

Exciton Bose-Einstein Condensation and Topology in Van Vleck-Type Mott Insulators

Von der Fakultät Mathematik und Physik der Universität Stuttgart zur
Erlangung der Würde eines Doktors der Naturwissenschaften (Dr. rer. nat.)
genehmigte Abhandlung

Vorgelegt von

Friedemann Aust

aus Stuttgart

Hauptberichterin: Prof. Dr. Maria Daghofer

Mitberichter: Prof. Dr. Ronny Nawrodt

Prüfungsvorsitzender: Prof. Dr. Sebastian Loth

Tag der mündlichen Prüfung: 02.12.2024

Institut für Funktionelle Materie und Quantentechnologien
der Universität Stuttgart

2024

Contents

1. Introduction	1
1.1. From Isolated Ion to the Octahedral Crystal Field	10
1.1.1. Single Atom	11
1.1.2. Crystal Field	14
1.1.3. T-P Correspondence	22
1.1.4. Size of the Crystal Field Splitting	24
1.1.5. Many-Body Effects: d^4 and t_{2g}^4	27
1.1.6. Tetrahedral Crystal Field and t_{2g}^4	32
1.1.7. Crystal Field Distortions	34
1.2. Spin-Orbit Coupling	38
1.2.1. Origin and Strength of Spin-Orbit Coupling	39
1.2.2. LS - and jj -Coupling Schemes	42
1.2.3. Dzyaloshinskii-Moriya Interaction	45
1.3. Coulomb Interaction	46
1.3.1. Coulomb Interaction in General	46
1.3.2. Kanamori Form	49
1.4. Extended Kitaev-Heisenberg Model for Hard-Core Bosons	51
1.4.1. Mott Insulator and Heisenberg Model	51
1.4.2. Kugel-Khomskii Models	53
1.4.3. Superexchange and Geometry	56
1.4.4. The Kugel-Khomskii Type Hamiltonian of Interest	60
1.4.5. Influence of Spin-Orbit Coupling and Singlet-Triplet Model	64

1.5.	The Language of Spin, Quadrupoles and Spin-Dimers	77
1.5.1.	Nematics for Spin-1/2 and Spin-1	78
1.5.2.	Spin-Dimer and Magnetic Moment	82
2.	Semiclassical Monte-Carlo Simulations for Spin-Orbital Triplons and Beyond	85
2.1.	Flavor-Wave or Linear Spin-Wave Theory	86
2.1.1.	Calculations for Flavor-Wave Theory	90
2.1.2.	Strengths and Weaknesses of Flavor-Wave Theory	93
2.2.	Exact Diagonalization and Related Methods	100
2.2.1.	Exact Diagonalization	100
2.2.2.	Application to the Triplon Model	102
2.2.3.	Advantages and Disadvantages	105
2.3.	Classical and Semiclassical Monte-Carlo	108
2.3.1.	Classical Monte-Carlo for the Triplon Kitaev-Heisenberg Model	109
2.3.2.	Semiclassical Monte-Carlo for the Singlet-Triplet model	110
2.3.3.	Semiclassical Monte-Carlo Beyond the Low-Energy Subspace	115
2.3.4.	Application to Ca_2RuO_4	120
2.3.5.	Use of Semiclassical Monte-Carlo Beyond This Thesis	126
3.	Analysis of the Triplon Honeycomb Model	131
3.1.	Quadrupoles and Higher-Order Terms	131
3.1.1.	Influence of the Quadrupole Bosons	133
3.1.2.	Higher-Order Terms	148
3.2.	Triplons in a Magnetic Field	171
3.2.1.	Triplon Condensation Driven by a Magnetic Field	175
3.2.2.	Triplon Kitaev-Heisenberg Model in a Magnetic Field	182

3.2.3.	Triplon Liquid and Magnetic Field	197
3.3.	Triplons in a Trigonal Crystal Field	206
3.3.1.	Strong and Weak Trigonal Field Regimes	212
3.3.2.	Spin-orbital Triplons in the Simple Trigonal Field Scheme	229
3.3.3.	Spin-orbital Triplons in the Full Trigonal Field Scheme	242
4.	Triplon Topology	253
4.1.	Triplon Hamiltonian	256
4.2.	Triplon Topology on the Honeycomb Lattice	262
4.2.1.	Kitaev Interactions and Limiting Cases	263
4.2.2.	Kitaev-Heisenberg Model	273
4.2.3.	Influence of Gamma	283
4.2.4.	Trigonal Crystal Field	292
4.3.	Triangular Lattice	297
4.3.1.	Topological Phase Diagrams	297
4.3.2.	Minimal Model	304
4.3.3.	Thermal Hall Effect	306
4.4.	Other Geometries and Interactions	317
4.4.1.	Kagome Lattice	317
4.4.2.	Square-Octagon Lattice	323
4.4.3.	Ca ₂ RuO ₄ -Based Lattice Model	325
4.4.4.	Triplon Topology in Other Dimensions	327
4.4.5.	Condensed Phase and Fractional Quantum Hall Effect	331
5.	Conclusion and Outlook	335
A.	Appendix	341
A.1.	Additional Magnetic Orders	341
A.2.	More Details: Crystal Field Analysis	344

A.3. Matrix Elements and States of the Full Crystal Field Model	349
A.4. Matrix Elements of the Triplon Model for Ca_2RuO_4	352
Bibliography	355
Acknowledgments	379

List of Abbreviations

BEC	Bose-Einstein Condensation/Condensate
SOC	Spin-Orbit Coupling
CF	Crystal Field
DM(I)	Dzyaloshinskii–Moriya Interaction
SSH	Su-Schrieffer-Heeger
ED	Exact Diagonalization
(s)MC	(semiclassical) Monte-Carlo
QMC	Quantum Monte-Carlo
CPT	Cluster Perturbation Theory
VCA	Variational Cluster Approach/Approximation
DMFT	Dynamical Mean-Field Theory
(I)RIXS	(Intermediate) Resonant Inelastic X-ray Scattering ...
MO	Molecular Orbital
PM	Paramagnet
FM	Ferromagnet
AFM/AF	Antiferromagnet
ZZ	Zigzag Antiferromagnet
ST	Stripy Antiferromagnet
TL	Triplon Liquid
c...	canted ...
Q...	quadrupolar ...

Abstract

In this thesis, we derive and investigate effective low-energy models based on compounds with d^4 transition metal ions like Ru^{4+} and Ir^{5+} . In these materials, one may expect a nontrivial interplay of the strong correlations of Mott insulator physics, the relativistic process of spin-orbit coupling and significance of the structural geometry. In particular, the energy scales of superexchange, spin-orbit coupling and distortions of the crystal are estimated to be of comparable size, thus implying their intricate competition.

At the center of this contest is the preference of spin-orbit coupling for a total angular momentum $J = 0$ singlet ground state which is at odds with the superexchange incorporating, for example, the higher $J = 1$ triplet. If the former dominates, the magnetism is solely carried by virtual excitations, i.e. the Van Vleck paramagnetism. Superexchange may, among other things, be able to induce a nontrivial magnetic moment into the singlet ground state via Bose-Einstein condensation of excitons, meaning superpositions of singlet and triplet (hard-core bosons) referred to as triplons. The superexchange itself is connected to the geometry of the crystal, for example edge-sharing ligand octahedra surrounding the $\text{Ru}^{4+}/\text{Ir}^{5+}$ ions, and this implies possible nontrivial magnetic states emerging from this process, e.g., a triplon-liquid resulting from Kitaev model physics, thus presenting an intriguing topic.

The key research issue we want to tackle in this context is a thorough study of a specific kind of this model, which is based on the geometric structure of, e.g., $\text{Ag}_3\text{LiRu}_2\text{O}_6$ and Li_2RuO_3 , that features the aforementioned octahedra and a honeycomb lattice of the Ru^{4+} ions. We consider the emerging extended Kitaev-Heisenberg model, where excitonic vector bosons replace the traditional pseudospin-1/2 as in-

herent degrees of freedom, and further inspect the role of quadrupole and multi-triplon interactions that are additionally induced by the superexchange. Moreover, we attempt to analyze the singlet-triplet model itself. The rich physics of the singlet-triplet structure has been well studied in spin-dimers, meaning dimers consisting of two spins (e.g. spin-1/2) coupling via antiferromagnetic Heisenberg interaction. In particular, Bose-Einstein condensation driven by magnetic field as well as pressure has been reported, as well as topologically nontrivial magnon/triplon excitations. As the $J = 0/J = 1$ setup involves a spin and orbital moment dimer with different (e.g. Kitaev) interactions and interplay with pressure and magnetic field, these features need to be reevaluated, which we attempt in this thesis.

Previous studies have either been superficially focused on basic aspects, such as the simple Kitaev-Heisenberg model, the pure Kitaev regime or a proof-of-concept for topologically nontrivial states. Here, we attempt to provide a more complete look at the problem. Moreover, a lot of research has been focused on related models, like the possible triplon physics and Higgs mode in Ca_2RuO_4 , which has different geometry and interactions, the traditional d^5 (pseudospin-1/2) Kitaev candidate $\alpha\text{-RuCl}_3$ or traditional spin-dimers, therefore leaving the subject of this thesis open.

Here we try to fill this gap by providing a thorough analysis of the model based on Exact Diagonalization, semiclassical (variational wave function based) Monte Carlo, flavor-wave theory and careful analytical study and derivation of effective models.

We provide a description of the impact of the multi-triplon terms, condensation behavior or absence thereof in magnetic field and under pressure, as well as an analysis of the emerging topology. While seemingly complicated at first glance, the trends can usually be gauged intuitively by careful consideration of the degrees of freedom or, in the case of topology, estimated by mapping to effective models in the limiting cases.

Deutsche Zusammenfassung

Dieser Abschnitt enthält die deutsche Übersetzung¹ des regulären englischsprachigen “Abstract” und kann demnach von Lesern des vorangegangenen Teils übersprungen werden.

In dieser Arbeit werden effektive Niedrigenergiemodelle auf der Basis von Verbindungen mit d^4 Übergangsmetallionen wie Ru^{4+} und Ir^{5+} hergeleitet und untersucht. In diesen Materialien kann man ein nicht-triviales Zusammenspiel der starken Korrelationen der Mott-Isolator-Physik, des relativistischen Prozesses der Spin-Bahn-Kopplung und der Bedeutung der Strukturgeometrie erwarten. Konkret werden die Energieskalen von Superaustausch, Spin-Bahn-Kopplung und Verzerrungen des Kristalls als vergleichbar groß eingeschätzt, was auf einen komplizierten Wettbewerb dieser Einflüsse schließen lässt.

Im Mittelpunkt dieses Konkurrenzkampfs steht, dass die Spin-Bahn-Kopplung einen Singulett-Grundzustand mit einem Gesamtdrehimpuls von $J = 0$ begünstigt, was einen Gegensatz zur Präferenz des Superaustauschs, z.B. für den Miteinbezug des höheren $J = 1$ Triplets, darstellt. Im ersteren Fall wird der Magnetismus ausschließlich durch virtuelle Anregungen, d.h. den Van-Vleck-Paramagnetismus, getragen. Der Superaustausch kann, unter anderem, in den Singulett-Grundzustand ein nichttriviales magnetisches Moment durch Bose-Einstein-Kondensation von Exzitonen, d.h. Überlagerungen von Singulett- und Triplett-Bosonen (Hardcore-Bosonen), die als Triplonen bezeichnet werden, induzieren. Da der Superaustausch selbst mit der Geometrie des Kristalls verflochten ist, z.B. mit Ligandenoktaedern die eine Kante teilen und die $\text{Ru}^{4+}/\text{Ir}^{5+}$ -Ionen umgeben, ist es möglich, dass aus diesem

¹Bei Teilen der Übersetzung wurde das Programm DeepL benutzt.

Prozess nichttriviale magnetische Zustände entstehen, z.B. eine Triplon-Flüssigkeit, die aus dem Kitaev-Modell resultiert, und somit ein per se interessantes Thema darstellt.

Die zentrale Forschungsfrage, die wir in diesem Zusammenhang angehen wollen, ist eine gründliche Untersuchung einer speziellen Art dieses Modells, das auf der geometrischen Struktur von z.B. $\text{Ag}_3\text{LiRu}_2\text{O}_6$ und Li_2RuO_3 basiert, die die oben erwähnten Oktaeder und ein Wabengitter der Ru^{4+} -Ionen aufweist. Wir betrachten das daraus resultierende erweiterte Kitaev-Heisenberg-Modell, das mit durch die inhärenten Freiheitsgrade die Eigenheit besitzt, exzitonische Vektorbosonen anstelle des traditionellen Pseudospins-1/2 einzubeziehen, und untersuchen die Rolle der Quadrupol- und Multi-Triplon-Wechselwirkungen, die ebenfalls durch den Superaustausch induziert werden. Außerdem versuchen wir, das Singulett-Triplett-Modell selbst zu analysieren. Die Singulett-Triplett-Struktur bietet bekanntermaßen eine reichhaltige Physik für die gut untersuchten Spin-Dimere, d.h. Dimere, die aus zwei Spins (z.B. Spin-1/2) bestehen, welche über antiferromagnetische Heisenberg-Wechselwirkungen koppeln, insbesondere im Hinblick auf die Bose-Einstein-Kondensation, die durch ein Magnetfeld sowie Druck angetrieben wird, sowie topologisch nichttriviale Magnon/Triplon-Anregungen. Da der $J = 0/J = 1$ Aufbau einen Dimer aus Spin- und Orbitalmoment mit unterschiedlichen (z.B. Kitaev) Wechselwirkungen und Interaktion mit Druck und Magnetfeld beinhaltet, müssen diese Eigenschaften neu bewertet werden, was wir in dieser Arbeit versuchen.

Bisherige Studien haben sich entweder oberflächlich auf grundlegende Aspekte konzentriert, wie das einfache Kitaev-Heisenberg-Modell, das reine Kitaev-Regime oder einen Konzeptnachweis für topologische nichttriviale Zustände. Hier versuchen wir, einen umfassenderen Blick auf das Problem zu werfen. Darüber hinaus hat sich ein Großteil der Forschung lediglich auf verwandte Modelle konzentriert, wie die mögliche Triplon-Physik und die Higgs-Mode in Ca_2RuO_4 , das eine andere Geometrie und Wechselwirkung aufweist, den traditionellen d^5 (Pseudospin-1/2) Kitaev-

Kandidaten α -RuCl₃ oder traditionelle Spin-Dimere, wodurch das Thema dieser Arbeit offen bleibt.

Hier versuchen wir, diese Lücke zu schließen, indem wir eine gründliche Analyse des Modells auf der Grundlage der exakten Diagonalisierung, der semiklassischen (Variationswellenfunktion) Monte-Carlo-Methode, der “flavor-wave” Theorie und der sorgfältigen analytischen Betrachtung und Herleitung effektiver Modelle vornehmen.

Wir beschreiben die Auswirkungen der Multi-Triplon-Terme sowie das Kondensationsverhalten oder dessen Abwesenheit im Magnetfeld und unter Druck. Des Weiteren liefern wir eine Analyse der entstehenden Topologie. Obwohl die Trends auf den ersten Blick kompliziert erscheinen, lassen sie sich in der Regel durch eine sorgfältige Betrachtung der Freiheitsgrade intuitiv erfassen oder, im Falle der Topologie, durch eine Abbildung auf effektive Modelle in den Grenzfällen abschätzen.

1

Introduction

Condensed matter physics and its subgenre of solid-state physics represent the great effort to try and describe the overwhelmingly rich and various properties of (rigid) matter. In one such attempt, Khaliullin [1] argued that a possible scenario for certain class of 4d and 5d transition metals, namely those with a t_{2g}^4 electron configurations such as Re^{3+} , Ru^{4+} , Os^{4+} and Ir^{5+} , could be the emergence of a nonmagnetic $J = 0$ ground state driven by spin-orbit coupling and magnetism that may be governed by a singlet-triplet model and Bose-Einstein condensation of excitons therein.

One of the big results of reference [1] is the endeavor to explain the magnetism of Ca_2RuO_4 using this line of thought. The first analysis provided in the paper makes estimates of the magnetic order, orbital moments and susceptibility in Ca_2RuO_4 that seem compatible with experimental data. It couples this prediction to the emergence of a Higgs mode, i.e. an amplitude mode representing the condensed matter analogue to the well known particle physics concept, as a consequence of exciton condensation. This Higgs mode has been subsequently found in an inelastic neutron scattering study [2] and via Raman scattering [3].

The other half of Khaliullin's paper describes a related scenario. For a model with the same setup for the, e.g., Ruthenium ion as in Ca_2RuO_4 but a structure motivated by Li_2RuO_3 , the form of the inherent interactions governed by the geometry dependent effective Kugel-Khomskii type Hamiltonian change while the singlet-triplet

degrees of freedom stay the same. A bond-dependent magnetic interaction results that is reminiscent of, but not equal to, the Kitaev model [4]. Here, the “spin” components travel along zigzag chains instead of being restricted to a single bond and the magnetic model is not one of spin-1/2 but hard-core spin-1 vector bosons.

In recent works [5–7] we have strived to further develop and analyze Khaliullin’s proposal by taking into account an additional direct exchange process resulting in the magnetic Hamiltonian taking the shape of an extended Kitaev-Heisenberg model and a complicated ensemble of higher-order multi-boson interactions. This thesis represents a direct continuation of that process.

As such, we sit at an intersection of interests that can be roughly grouped into three topics: Firstly, the direct motivation is to provide models that possibly describe materials and can be used to predict and search for novel features in them. Secondly, there is merit in the discussion of the model as a Kitaev or extended Kitaev-Heisenberg model with unconventional degrees of freedom. Thirdly, the local singlet-triplet structure and magnon condensation mechanism are themselves features that have enabled a plethora of discussions pertaining to dimer models and their novel physics, but here the fact that the “dimer” does not consist of spins but a spin and an angular momentum can drastically change motivations and results.

Subsequently, we further contextualize the three groups of interests and the points of discussion useful for the model in this thesis.

We first turn to the material-specific motivation. Primarily, our model can be seen as an attempt tailored to, e.g., $\text{Ag}_3\text{LiRu}_2\text{O}_6$, as geometrical features and degrees of freedom could be a candidate material for the models discussed in this thesis. Recent experimental results [8] establish a novel phase transition from $J = 0$ to another seemingly “nonmagnetic” (Van Vleck) state when the material is pressurized above a critical threshold. A theoretical analysis remains to be done and one needs to find out whether this effect is a consequence of Khaliullin’s line of thought or not.

Moreover, there are materials that might seem appropriate for a setup like ours, but

have seemingly different underlying physics such as Li_2RuO_3 , which can be seen as a parent compound of $\text{Ag}_3\text{LiRu}_2\text{O}_6$. While Li_2RuO_3 [9] features a structural phase transition that has been early on connected to a different physical origin, namely molecular orbit formation [10], there has been a lot of debate about the goings on in this material. The tendency to form spin-orbital singlets as discussed here became relevant again when it was directly compared to Na_2RuO_3 experimentally [11].

Additionally, the experimental side of the analysis of $\text{Ag}_3\text{LiRu}_2\text{O}_6$ -like materials is quite scarce and one may yet find inherent use of our model discussions for materials considered in the future. One should note that especially for ruthenates experimental data have recently become available due to the successful extension of resonant inelastic X-ray scattering to the intermediate (X-ray) regime (IRIXS) [12].

Furthermore, one can circle back to the discussions for Ca_2RuO_4 . The main difference between the two setups presented in [1] is the geometry of the (super-)exchange interactions and the form of the lattice model. Yet, the on-site degrees of freedom concerning a single Ruthenium atom, i.e. the Van Vleck-type d^4 Mott insulator characteristics, remain the same. As a result there is an overlap of interest concerning emerging effects where the precise form of the exchange interactions is not of central importance. In particular, quite a lot of discussion concerning Ca_2RuO_4 has been about the relative importance of spin-orbit coupling and tetragonal crystal field distortions [13–18] or the role of Hund’s coupling [19]. To the former discussion we even contribute directly [20] by use of the semiclassical Monte-Carlo scheme discussed in this thesis.

As a side note, it is useful to remember that Ca_2RuO_4 is extremely well studied not only because of the Higgs mode. A big part of the focus on Ca_2RuO_4 was caused by it having the same structure [21] as the hotly debated superconductor Sr_2RuO_4 [22, 23], which itself was first discovered by notably being isostructural to the cuprate high- T_c superconductor $\text{La}_{2-x}\text{Ba}_x\text{CuO}_4$. Another driver was the discovery of giant diamagnetism in non-equilibrium [24], which has since been found to be false [25]

but nevertheless sparked a lot of insightful discussions about the material [26].

Concluding the material interest section, we point out that a variety of other models share a similar relation to our setup like Ca_2RuO_4 , namely that the precise nature of Kugel-Khomskii type spin exchange might not be comparable but some or many aspects of the underlying physics are. Just to name a few: Similarities based on, but not limited to, $J = 0$ physics or lack thereof have been a point of discussion for, e.g., various $5d^4$ osmium based compounds [27, 28] and similarly in rhenates and iridates [29] (of note in particular is the debate about magnetism in Ba_2YIrO_6 [30–33]) as well as K_2RuCl_6 [34], $\text{Sr}_3\text{Ir}_2\text{O}_7\text{F}_2$ [35] and the d^8 compound NiRh_2O_4 [36]. Novel concepts like the very recent Ru-dimer model [37], where the ions seemingly share a d^4 - d^3 partnership are also clearly related.

We turn to the second class of interest: the form of the Hamiltonian being an extended Kitaev-Heisenberg model. For this explanation we can be briefer and less comparative, because the Kitaev and Kitaev-Heisenberg physics research field is extremely well established and well known. Several reviews already cover (obviously with some topical overlaps) Kitaev and Kitaev-Heisenberg models [38–40], specifically in magnetic fields [41] or quantum spin liquids in general [42, 43], with especially references [38, 39] focusing on the realization in materials.

A short summary can regardless be attempted in the following way: The Kitaev model [4] is a novel toy model hosting bond-dependent exchange interactions on a honeycomb lattice. For spin-1/2 the model (or its ground state and some other aspects) can be solved exactly(!) by mapping the spin-1/2 to four Majorana fermions (the number and thus spin-1/2 being an important aspect of the solution). Furthermore, Kitaev established the emerging spin-liquid phases and their use in topological quantum computation based on his earlier work [44].

On a side note, the quantum computer in general has gained a lot of traction during the last year with Google’s attempt to claim its supremacy [45] and the proof-of-principle demonstration of the topological computation also involving Kitaev as a

co-author [46]. However, the topological setup was carried out using the simpler Toric Code model and superconducting qubits, i.e. not a Kitaev model based setup. The quantum computation aspect of the Kitaev model itself has accordingly quieted down.

Back to the issue at hand: An important step was done by Jackeli and Khaliullin in their seminal paper [47] describing the possibility of finding Kitaev-like exchange interactions in realistic d^5 Mott insulators, where strong spin-orbit coupling causes the formation of a total angular momentum $j = 1/2$ ground state, which takes the role of the spin, and superexchange in edge-sharing ligand octahedra geometry enables bond-dependent spin interactions. Yet, this exchange is not the only process realistically happening in real materials, leading to the inception of Kitaev-Heisenberg models and other extensions [48–50].

As established by the mentioned above reviews, Kitaev-Heisenberg-like models turn out to be highly relevant¹ for material descriptions (although the exact form of the interactions is usually a topic of its own, see e.g. [51]). Therefore there is extensive interest in the model itself that we are here not attempting to do justice to at this point. We focus instead on two niches, the interest in magnetic fields and spin- S Kitaev and Kitaev-Heisenberg models. In all this the interest is driven by trying to find a material where the Kitaev or spin-liquid phase survives the competition with the other interactions.

For magnetic fields the relevance can be connected to one of the maybe most studied materials in contemporary Kitaev-Heisenberg physics: α - RuCl_3 . The material is a zigzag antiferromagnet. The antiferromagnetic order can be made to vanish in a magnetic field of sufficient strength, possibly leading to the emergence of a spin liquid [52]. Hence a lot of the Kitaev and Kitaev-Heisenberg debate has looked into

¹Topical side note: The aforementioned George Jackeli and Giniyat Khaliullin together with Hidenori Takagi (who leads, among other things, a neighboring research group under the common umbrella of the Institute for Functional Matter and Quantum Technologies in Stuttgart) have just been selected as 2025 recipients for the James C. McGroddy Prize for New Materials <https://www.aps.org/funding-recognition/prize/james-mcgroddy> (accessed 16.10.2024).

the behavior of the models in magnetic fields. This is a nontrivial issue for the Kitaev model itself and of course its various material specific extensions. The Kitaev model itself does not include a strong magnetic field, leading to the question of what kind of spin-liquid, e.g., gapped vs. gapless, can emerge.

Particularly α -RuCl₃ has raised the relevance of this discussion because of experimental evidence for a half-integer thermal Hall effect, whose “half” size was connected to the Majorana fermions [53]. While claims of successful reproduction and additional evidence [54, 55] caused noticeable hype, the discussion has since then turned out to be more complicated, see, e.g., references [56–58], and it has since been suggested that topological magnons may be the driver instead [59]. A very recent summary of this debate (end of last year) reiterates this [60].

Having established that there is interest in the magnetic field behavior of Kitaev-Heisenberg models we turn to the second niche: spin- S . Here, we can keep the introduction rather short as the idea is simple. The Jackeli-Khaliullin mechanism first employed in d^5 materials to obtain Kitaev-like interactions is based on the more general feature of Kugel-Khomskii type models in edge-sharing ligand octahedra geometry. For different setups with e.g. the same geometry, analogous interactions may arise. As such there are recent proposals of Kitaev-Heisenberg models for e.g. effective spin-3/2 [61–63] (instead of the $j = 1/2$ in d^5) or spin-1 [64]. With the hard-core spin-1 (note also: singlet-triplet structured) vector boson Kitaev-Heisenberg model [5] we are in medias res regarding this entire discussion. Additionally there is interest in spin-1 Kitaev physics also as a model study itself [65]. Of course, the nature of spin liquid [66] and magnetic field effects [67, 68] can be motivated quite similarly to the spin-1/2 scenario, however, giving different results.

Finally, we can turn to the third field of interest: the singlet-triplet structure and magnon condensation. Here the most use comes out of the description of trends, which we compare at points of need in the thesis. Hence we try to keep this introduction very brief.

Khaliullin's description of the emergence of magnetism in Ca_2RuO_4 is based on the mathematical language of singlet-triplet physics in dimer systems [69]. In a dimer consisting of two spin-1/2 (spin-1) coupled antiferromagnetically, it is clear that an analogous formation of singlet-triplet (-quintet) states exists. Similarly, the realization of magnetism via Bose-Einstein condensation involving the triplet excitations is an established concept [70]².

Dimer singlet-triplet systems have been a broad field of study as evidenced by the exhaustive review [71]. Of particular interest for this thesis is the quite famous example of TlCuCl_3 , where the Bose-Einstein condensation can be driven by pressure or magnetic field [72–74]. Additionally, the concept of an emerging Higgs mode has been discussed [75].

Another relevant and quite contemporary niche in this discussion is the role of uncondensed magnons as topological excitations [76, 77] where specifically triplon topology [78] has been established.

The language is not the only aspect that relates our model to dimer singlet-triplets. With a quick look at the degrees of freedom involved, one can see that we are in fact outright modeling an unusual dimer system. The main difference is that we do not couple two spins, but rather a $S = 1$ spin and an $L = 1$ angular momentum via spin-orbit coupling. This presents a clearly unique set of motivations and discussion if one considers e.g. that other types of spin interactions might become interesting (c.f. Kitaev) and the reaction to external influences like the magnetic field can be different. Hence one should be motivated to look for similarities and differences between the dimer setups. Although this sounds quite banal, the importance of this discussion and concept should not be discarded. A good example for this is the recent observation of the failure of the Curie-Weiss law for total angular momentum based systems [79]: It has been common practice to handle the j states found e.g.

²this review contains a useful dictionary of the Bose-Einstein condensation nomenclature in magnon systems

in α - RuCl_3 like spins, but this can lead to quantitatively wrong descriptions and analysis.

Having established the possible interests and motivations for our research, we can now turn to the structure of the thesis.

The remainder of this chapter introduces the fundamental concepts. We start with the physics for a single transition metal ion embedded in a solid, namely crystal field, spin-orbit coupling and Coulomb interaction. Thereafter we connect this to the lattice model by explaining superexchange via a Kugel-Khomskii model and subsequently projecting it onto an effective low-energy environment dictated by the single ion framework. This results in the extended Kitaev-Heisenberg model and interactions beyond. Finally, we make an important excursion into the textbook descriptions of spins and spin-dimer degrees of freedom (most importantly the singlet-triplet model), which either serve as an inspiration for the way the spin-orbital triplon model is presented and analyzed or enable the reader to directly compare and contrast both cases. Here, notable distinctions like the role and form of quadrupole and magnetic dipole moment are addressed.

In chapter two we present methods previously used for the analysis of this kind of model. We provide old results and amend, explain or extend them where necessary. This procedure naturally leads us to the description via spin-dimer inspired singlet-triplet ansatz. The use of this ansatz as a variational wave function whose parameters can be fixed by a classical Monte-Carlo simulation inspires the concept dubbed “semiclassical Monte-Carlo”, which is applied in large parts of this thesis. We provide information of its use even beyond the questions tackled in this thesis.

The centerpiece of this thesis is chapter three. Here, we apply the methods introduced in the previous chapter to the questions motivated in the previous paragraphs. Concretely, we attempt to explain how the interactions beyond the simple vector boson Kitaev-Heisenberg model, namely quadrupole contributions and multi-triplon terms, impact the system. Thereafter, we analyze the behavior of the emerging

model in a magnetic field. Lastly, inspired by experimental results for $\text{Ag}_3\text{LiRu}_2\text{O}_6$, we set out to describe the effect of trigonal crystal field distortions on the model.

Concluding, chapter four is a venture into a special kind of edge case of the model. For values solidly located in the paramagnetic regime, one might argue for a case where the flavor-changing part of the magnetic dipole moment has significance. As a result, the magnetic field can mix the triplon flavors and provide the pathway to a topologically nontrivial excitation structure. We set out to explain why and under what circumstances the nontrivial topology arises by connecting them to bosonic Dirac-cone physics. Subsequently we look at the influence of trigonal crystal field distortions and change of lattice structure and dimension in order to gauge the potential relevance of this model.

Before we move on with the introduction of the fundamental concepts, we address the extend of this chapter.

Purpose of this Chapter

In the introduction chapter we try to explain all concepts necessary to understand the thesis. As always, there can be quite a few different approaches concerning what and how much of it to cover, especially because most of it can be found in textbooks. Here, we focus on basic aspects of model construction and underlying degrees of freedom, maybe more broadly than needed. One reason for this is that, in our opinion, finding out what kind of approximations go into the model does not only aid the understanding, but can additionally suggest future ideas of how to improve this project to other readers. In contrast, we see no gain in discussing, e.g., what the basic idea behind numerical simulations like Monte-Carlo is or how the Lanczos algorithm for Exact Diagonalization works. We do not publish code³ so those discussions have no effect on the reproducibility or understanding. Moreover, we do

³and there are libraries out there that are way better than what we do anyways.

not see the point of one more introduction into basic topology were the ubiquitous pictures of donuts and coffee mugs are reiterated. There are textbooks out there for this purpose and an introduction of the tools established therein on a need to know basis seems to be sufficient.

The basic aspects we want to discuss are ones that can at least be connected to concrete statements about the model.

1.1 From Isolated Ion to the Octahedral Crystal Field

A key issue of the model addressed in this thesis is the incorporation of the crystal field. There are two distinct scenarios that need to be discussed in this context.

Firstly, there is the octahedral crystal field. The crystal field denotes the influence of the electrostatic potential of the environment of, in our present case, a transition-metal ion in a solid. In a crystal, the transition-metal ion is regularly surrounded by other ions, e.g. oxygen or chlorine, which in this work are always assumed to form an octahedron. It should be noted that this assumption is not such a strong restriction, as tetrahedral and octahedral structures emerge naturally by trying to pack spheres (in our case oxygen/chlorine) as dense as possible and then looking at what kind of interstices, i.e. empty space in between these spheres, remain for the transition metal [80].

As will be elaborated upon later, the octahedral crystal field is presupposed to be a dominant force. Its main role is the splitting of the five-fold degenerate d orbital of the transition-metal ion into two e_g and three t_{2g} orbitals, the latter of which present the starting point for all subsequent considerations.

Secondly, we need to account for possible deviations from the octahedral crystal field structure. These aberrations can occur for a multitude of reasons, the explana-

tion of which will follow in later sections, and can therefore be relevant for a variety of energy scales. Depending on the form and importance of these effects, one has to employ different strategies.

In order to not confuse these two discussions, we will henceforth refer to the second scenario as “crystal field distortion” in the course of the introduction chapter. Given that the first effect is only important for the setup and not the immediate points of interest in the thesis, we will however relax this distinction thereafter for simplicity’s sake.

Concluding, we want to give a comment about the purpose and format of the following sections. Some basic aspects will be discussed quite more detailed than necessary on first glance. One reason for this is avoiding impreciseness that we have encountered in even in well written scientific papers more often than we would like. For example in the case of the tetrahedral crystal d^8 model based on NiRh_2O_4 in a magnetic field (discussions in section 3.2.1) this can lead to significant discrepancies. Another reason is to try our hand at providing a neat practical introduction to people new to crystal field calculations, as we have seen some of the same starting difficulties repeatedly. Furthermore, we will refer to reference [81] as an excellent introduction with slightly different focus and reference [7] for a bare bones version of this kind of introduction, both of which serve as a basis for the discussion in 1.1.2.

1.1.1 Single Atom

The starting point for all subsequent discussions are the wave functions of the hydrogen atom:

$$\Psi_{nlm}(r, \theta, \phi) = R_{nl}(r)Y_{lm}(\theta, \phi), \quad (1.1)$$

where $R_{nl}(r)$ are the radial parts and $Y_{lm}(\theta, \phi)$ are the spherical harmonics [82]. Moreover $r \in [0, \infty)$, $\theta \in [0, \pi]$ and $\phi \in [0, 2\pi]$ are the radius, polar and azimuthal angles of spherical coordinates. Aside from many-body effects and occupation, which

we will cover later, this represents the single-particle wave function of an electron in the potential of an isolated ion.

The principal n , orbital/azimuthal l and magnetic m quantum numbers label the solutions. For a given n , the other numbers are restricted via

$$n = 1, 2, \dots, \tag{1.2}$$

$$l = 0, 1, \dots, n - 1, \tag{1.3}$$

$$m = -l, -l + 1, \dots, l. \tag{1.4}$$

Accordingly, each primary shell n has subshells labeled by l and each subshell $2l + 1$ orbitals labeled by m . The subshells are usually denoted by special names: $l = 0$ is named “ s ”, $l = 1$ as “ p ”, $l = 2$ as “ d ” and $l = 3$ as “ f ”.

After more or less naively filling the states with the available electrons for a given element, one can notice that some orbitals/shells are completely full and separated from the outermost states by a large energy gap. These core electrons are not expected to be particularly relevant if not explicitly prompted (e.g. in resonant inelastic X-ray scattering experiments). Focusing on the usually more interesting valence electrons, i.e. the highest occupied shells, one can introduce a shorthand notation describing the electron configuration for a given element: $n\langle\text{name}\rangle^{\langle\#\text{electrons}\rangle}$ (we ignore the standard noble gas part for simplicity). E.g. $3d^4$ represents 4 electrons in the d ($l = 2$) orbitals of the $n = 3$ primary shell. Henceforth, we will use shorthand notations like $3d$ for materials with valence electrons in the $3d$ shell.

At this point, one should note the nature of the previously mentioned many-body effects: Electrons are not non-interacting! Coulomb interaction between the electrons is an important feature in most of the subsequently introduced physical phenomena in a solid and beyond. Given the hierarchical nature of the energy scales in our setup, the relevant effects, e.g. on spin-orbit coupling, are best discussed separately at each point where they become important.

The first of these instances is the electron occupation of the hydrogen levels. First of all, the energies of the hydrogen states are shifted significantly resulting in e.g. the $4s$ levels being more favorable than the $3d$ levels [83]. This is reflected in the usual depictions of the periodic table of elements, where the transition metal Scandium ($4s^2 3d^1$) with 21 electrons follows Calcium with 20 ($4s^2$). Furthermore, the occupation of the shells can become nontrivial.

Considering Ruthenium as an illustration, the electron configuration is stated as $4d^7 5s^1$ [84], favoring the half-filled s -orbital and hence developing two distinct contributions to the valence electrons.

Yet, when embedding the single atom into a solid or molecule, ionic bonds can change the effective number of available electrons in situ. Ru^{4+} , Os^{4+} , Ir^{5+} and Re^{3+} , where the exponent denotes the number of ionized (for our purposes: missing) electrons, are all commonly denoted as ions with $4d^4$ or respectively $5d^4$ electron configuration [1]. The effective loss of the s -orbital character is an approximation that has, to our knowledge, not warranted any discussion in the context of the materials considered in this thesis. In fact, even established literature [85] explicitly ends this discussion at the same point. Violations of the simplification would be easily visible in many ab-initio simulations or experiments. There are however a few discussions of a small covalent character of the naively ionic bonds with the surrounding environment in materials related to our interest, e.g. [86], potentially leading to higher electron counts on the single ion. This should be kept in mind as a potential source of problems with our model. In fact the paper presents a scenario where without the compound in question, $\text{Ba}_2\text{NaOsO}_6$ (with $5d^1$ Osmium), is supposedly nonmagnetic if one ignores the extra electrons provided by ligand orbital admixture.

One should therefore note that the assumption of 4 electrons in a d orbital forms the basis of all following chapters.

1.1.2 Crystal Field

In a solid, a single atom is surrounded by its neighbors. This environment influences the previously discussed wave functions. Here we aspire to introduce the necessary tools for describing these effects and discuss the resulting changes, especially for d^4 systems.

1.1.2.1 Basics

As an example, we consider the real crystal structure of a material that could potentially host the effective physics we are interested in: $\text{Ag}_3\text{LiRu}_2\text{O}_6$. Figure 1.1 depicts the crystal structure found experimentally. The Ru^{4+} ions can be found in layers lying in the a-b-plane of the crystal, motivating the later employed description as a two-dimensional lattice model. Every Ruthenium locale consists of six oxygen atoms, which form, at least in the idealized case, an octahedron around it. Deviations from this ideal, which can even be spotted in the depicted structure upon close inspection, are pondered in section 1.1.7.

The primary concern resulting from the observation of the material is the embedding into the octahedral structure of oxygen atoms (which should be seen as a surrogate for many other possible ions not explicitly mentioned here). Historically, this process is referred to as “crystal field theory” or “ligand field theory” depending on the degree of involvement of the surroundings. Hereinafter we will refer to oxygen as the ligands regardless of the approach for simplicity.

It should be noted that we employ crystal field theory. Ligand field theory is relegated to the following small comment. The primary difference is that crystal field theory reduces the ligands to point charges, i.e. a simple electrostatic potential acting upon the wave function of the Ruthenium. In contrast to that, ligand field theory includes the involvement of the orbital wave functions of the ligands. Consequently,

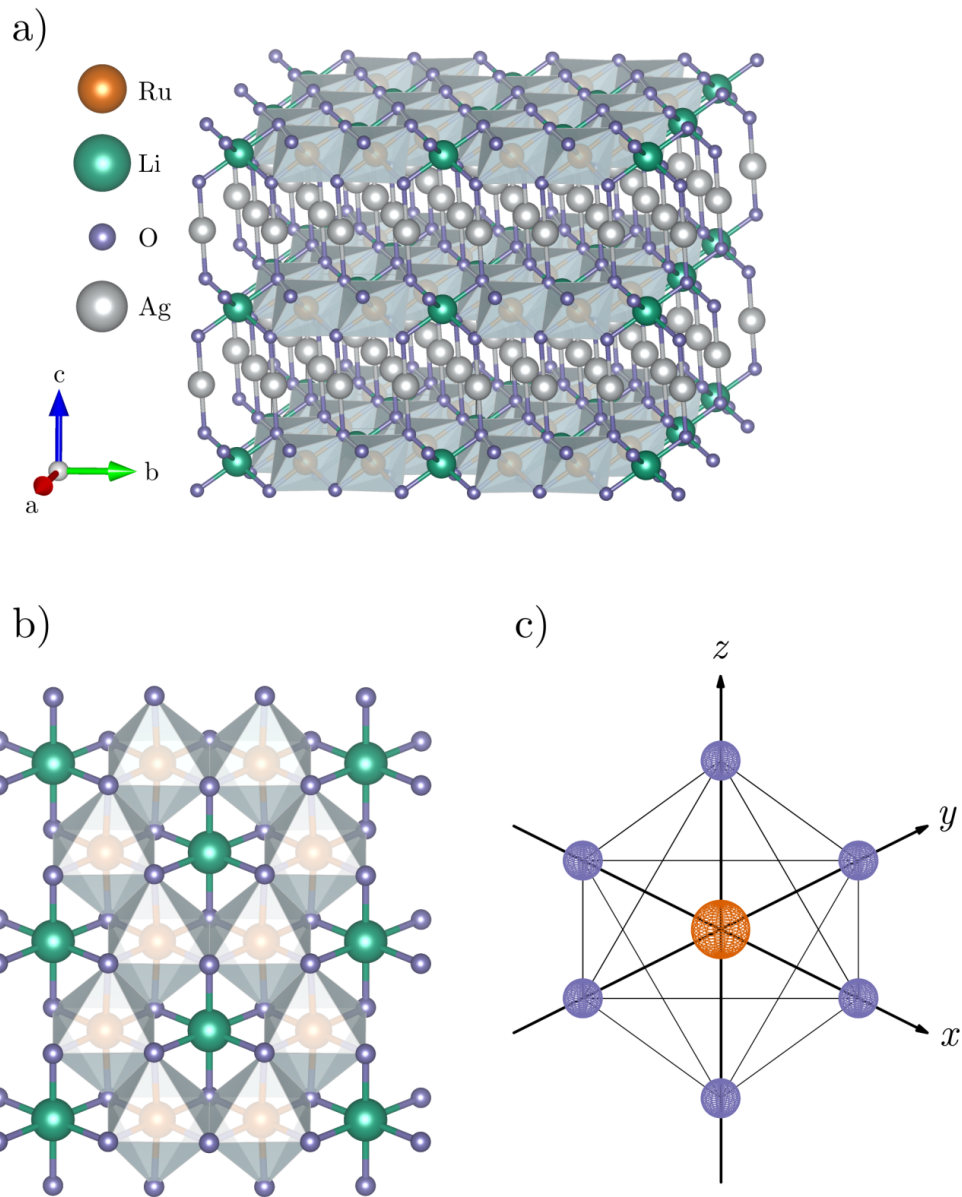


Figure 1.1. a) VESTA [87] depiction of the crystal structure of $\text{Ag}_3\text{LiRu}_2\text{O}_6$ as established experimentally in [8]. b) A single a/b-plane layer of the compound. The Ruthenium atoms form a honeycomb lattice and the oxygen octahedra share edges. One can spot distortions of the octahedra in b) from an idealized geometry in c), which is the basis of subsequent calculations.

crystal field theory can be seen as sufficient if the orbitals of ligands and transition-metal ion do not hybridize (ionic versus covalent bonding) or if the energy gap between the ligand and transition-metal state, the charge-transfer gap, is large.

Crystal and ligand field theory are old and well established, going back to the early 20th century (see reference [88] for a summary). Therefore we can limit our introduction of the reasons and restrictions of its use and instead make a short historical comment. Historically, the discussion goes back to the description of chemical bonds. Valence-bond theory, molecular-orbital and crystal field theory emerged as first explanations, with the latter one being extremely successful due to the work of Van Vleck, who of course is responsible for many things and provides the name for the excitonic magnetism discussed in this thesis. Interestingly, one of the early predictions was the quenching of the orbital momentum due to the crystal field, i.e. the topic of interest of section 1.1.3. From the historical point of view it is obvious that the ligand field theory can be viewed as a hybridization of all ideas, which can become necessary to engage with if the bonding is more nontrivial than just a theory of electrostatics in the crystal.

The starting point for crystal field theory calculations is the electrostatic Coulomb interaction of the ligand point charges:

$$V_{\text{CF}}(\mathbf{r}) = \sum_l \frac{q_l}{|\mathbf{r} - \mathbf{r}_l|}, \quad (1.5)$$

where l labels the ligands with charge q_l and \mathbf{r}_l the corresponding positions. There are elegant or direct ways to tackle this problem. On the elegant side there are explicit use of spherical harmonics and group theory. More direct would be a simple expansion of the root in cartesian coordinates and evaluation of the resulting integrals via computer. Due to its straightforward nature and the rarity of decently explicit literature, we find it prudent to present the concrete calculations in the latter format. For completeness and later discussions we will sketch the other approaches.

A useful identity that can be found in almost every electrodynamics textbook is that the multipole expansion of the electrostatic potential can be written in terms of spherical harmonics

$$\frac{1}{|\mathbf{r}_i - \mathbf{r}_j|} = \sum_{k=0}^{\infty} \frac{4\pi}{2k+1} \frac{r_{<}^k}{r_{>}^{k+1}} \sum_{m=-k}^k Y_{km}^*(\theta_i, \phi_i) Y_{km}(\theta_j, \phi_j), \quad (1.6)$$

where $r_{>}$ ($r_{<}$) is the larger (smaller) of both radii. As a result, the crystal field potential (1.5) can be rewritten as

$$V_{\text{CF}}(\mathbf{r}) = \sum_{k=0}^{\infty} \sum_{m=-k}^k f(k, m) Y_{km}(\theta, \phi), \quad (1.7)$$

where $f(k, m)$ contains constants, information about the geometry and (for point charges trivial) multipole moments of the charge distribution.

In the following we consider single-electron states (1.1) for simplicity and deal with the consequences of many electrons and their interactions later. Accordingly, introducing the electrostatic potential as a perturbation to the atomic wave function of the TM ion leads to the effective Hamiltonian

$$H_{nlm, n'l'm'} = \langle \Psi_{nlm} | V_{\text{CF}} | \Psi_{n'l'm'} \rangle \sim \langle Y_{lm} | Y_{l''m''} | Y_{l'm'} \rangle. \quad (1.8)$$

The integrals over three spherical harmonics are called Gaunt coefficients. They are straightforward to evaluate either numerically or via well known identities containing Wigner-3j symbols and the resulting selection rules [89].

The charm of this ansatz becomes apparent when contemplating symmetries. A perfect example is the derivation of the octahedral crystal field splitting found in reference [88]. The V_{CF} has to reflect the symmetries of the crystal, hence enforcing, e.g., the fourfold rotation $C_4 V_{\text{CF}} \stackrel{!}{=} V_{\text{CF}}$, ruling out a decent chunk of $Y_{l''m''}$ terms. Being able to use identities to calculate the important matrix elements also helps

when contemplating that crystal field theory predates computers.

A more explicit use of group theory can present an alternative approach. One should keep this in mind not only because of its potential usefulness as an elegant way of solving the crystal field problem, but also because the nomenclature involved in the calculations directly derives from it. The necessary background information can be readily found in standard textbooks [88, 90] and will be skipped due to the employment of the more direct approach in this thesis.

A quick run-through: The free ion has full rotational symmetry represented by the point group $SO(3)$. For example the octahedral crystal seen in figure 1.1c) has a different, lower symmetry O_h . Since $O_h \subset SO(3)$ they share representations. Yet, when $SO(3)$ becomes O_h , the irreducible representations of the former become reducible ones for the latter. You can decompose the reducible $SO(3)$ representations into a direct sum of irreducible O_h via character tables (a staple of group theory). The irreducible subspaces correspond to degeneracies. Concretely, we would start with fivefold degenerate d orbitals in $SO(3)$ and end up with a split into a twofold degenerate representation e_g and a threefold degenerate t_{2g} , where the names stem from group theory (all twofold parts are denoted as E , and threefold as T , with the additional aspects of the name referring to the nature of the system or involved symmetries).

Finally transitioning to explicit direct calculations, one can rewrite (1.5)

$$\begin{aligned}
 V_{\text{CF}}(\mathbf{r}) &= \sum_l \frac{q_l}{\sqrt{(x-x_l)^2 + (y-y_l)^2 + (z-z_l)^2}}, \\
 &= \sum_l \frac{q_l}{r_l \sqrt{1 + \frac{r^2}{r_l^2} - \frac{2(x_l x + y_l y + z_l z)}{r_l^2}}}, \\
 &= \sum_l \frac{q_l}{r_l \sqrt{1 + b + A}} = \sum_l \frac{q_l}{r_l \sqrt{1 + \epsilon}},
 \end{aligned} \tag{1.9}$$

where $b = r^2/r_l^2$ and A accordingly. While some sources [90] simply state that ϵ is small and one should expand $\sqrt{1 + \epsilon}$ around $r = 0$, one should note, that ϵ contains

multiple orders of the expansion parameter r/r_l , which is trivially seen by introducing the standard spherical coordinates ($x = r \cos(\phi) \sin(\theta)$, $y = r \sin(\phi) \sin(\theta)$ and $z = r \cos(\theta)$). Hence b is $\mathcal{O}((\frac{r}{r_l})^2)$ and A $\mathcal{O}(\frac{r}{r_l})$ seem to be clearer choices. Taylor expansion in r/r_l around 0 (the atom in the center of the ligands) then yields:

$$\begin{aligned}
 V_{\text{CF}}(\mathbf{r}) = \sum_l \frac{q_l}{r_l} \cdot & \left[1(\mathcal{O}((\frac{r}{r_l})^0)) - \frac{A}{2}(\mathcal{O}((\frac{r}{r_l})^1)) + \left(\frac{3A^2}{8} - \frac{b}{2}\right)(\mathcal{O}((\frac{r}{r_l})^2)) \right. \\
 & + \left(-\frac{5A^3}{16} + \frac{3Ab}{4}\right)(\mathcal{O}((\frac{r}{r_l})^3)) + \left(\frac{3b^2}{8} - \frac{15A^2b}{16} + \frac{35A^4}{128}\right)(\mathcal{O}((\frac{r}{r_l})^4)) \\
 & + \left(-\frac{15Ab^2}{16} + \frac{35A^3b}{32} - \frac{63A^5}{128}\right)(\mathcal{O}((\frac{r}{r_l})^5)) \\
 & \left. + \left(-\frac{5b^3}{16} + \frac{105A^2b^2}{64} - \frac{315A^4b}{256} + \frac{231A^6}{1024}\right)(\mathcal{O}((\frac{r}{r_l})^6)) + \dots \right].
 \end{aligned} \tag{1.10}$$

The effective Hamiltonian (1.8) consequently partitions into a sum of quick to calculate (at least via computer) integrals:

$$H_{nlm,n'l'm'} = \sum_{\tau=0}^{\infty} \left(\int_0^{\infty} dr R_{nl}^* R_{n'l'} r^2 V_{\text{CF}}^{\tau}(r) \right) \left(\int_0^{2\pi} d\phi \int_0^{\pi} d\theta Y_{lm}^* Y_{l'm'} \sin(\theta) V_{\text{CF}}^{\tau}(\phi, \theta) \right), \tag{1.11}$$

where τ refers to the order in r/r_l and the additions to V_{CF} denote that we split the corresponding terms and dependencies into the integrals. From here one straightforwardly calculates all matrix elements of the Hamiltonian up to a given order. We are interested in orbital rearrangement and thus can discard constant energy shifts. If one does not mix orders or atomic energy levels, the integral over r is just a global number (no dependence on m quantum number and thus the specific orbitals) and therefore it is often not evaluated but rather thrown (with other global factors like the q/r_l in V_{CF}) into the historically named ‘‘unit of energy’’ Dq . What remains is standard perturbation theory.

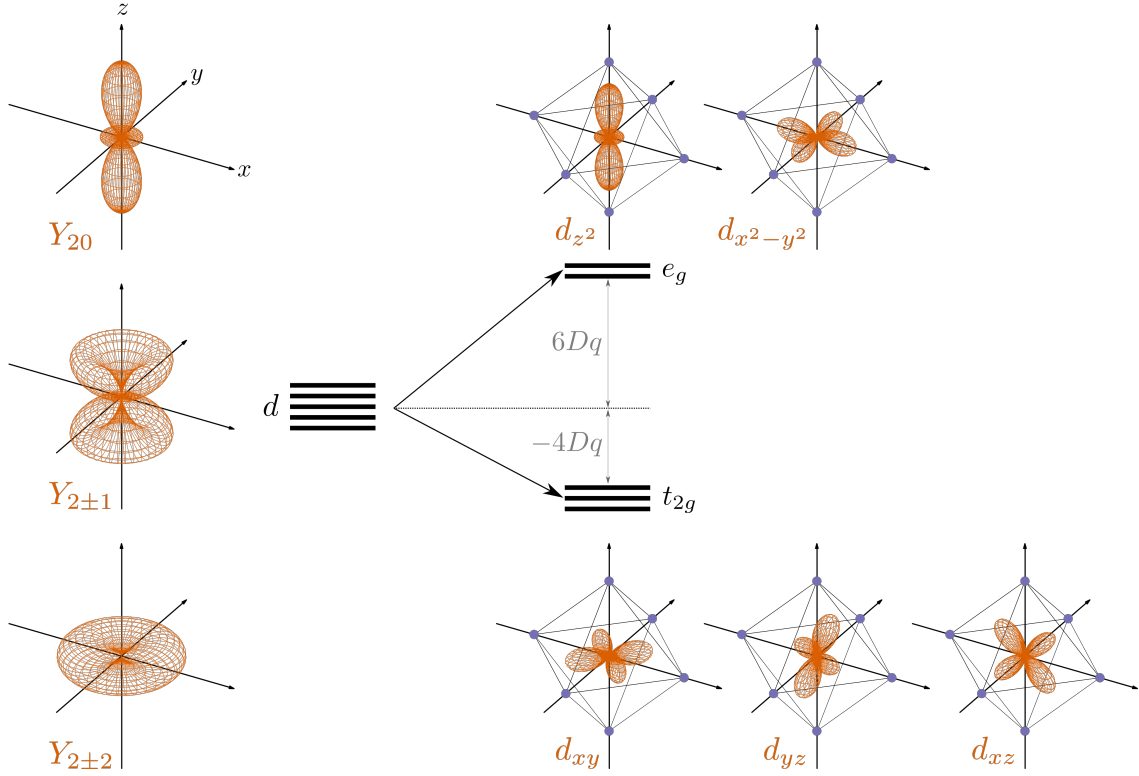


Figure 1.2. Electron wave functions represented by the square of the absolute values, e.g. $|Y_{20}(\theta, \phi)|^2$ for Y_{20} : On the left the wave functions for a free hydrogen like atom are shown. The right-hand side depicts the resulting e_g and t_{2g} orbitals described in the text. Additionally, the central part illustrates the energy splitting as a result of the octahedral crystal field environment schematically.

1.1.2.2 Octahedral crystal field

As established by figure 1.1, a point of interest in this thesis are materials with octahedral crystal field structure. Given the explanations of the previous chapter one has to establish the crystal structure geometrically, i.e. the positions of the ligands $((x, y, z)^T = (\pm a, 0, 0)^T, (0, \pm a, 0)^T, (0, 0, \pm a)^T)$, and their charges (all $q_i = -Q$). Furthermore, section 1.1.1 signals the focus on occupied d orbitals of transition metals. As a result the hydrogen wave functions are fixed by $l = 2$ and, since n is only contained in the radial part and thus Dq , the problem boils down to the five

$|Y_{2m}\rangle$ states.

Evaluation of the corresponding matrix elements yields its first nontrivial energy correction (neglecting constant shifts) to be in 4th order. The resulting effective Hamiltonian in the basis $\{|Y_{22}\rangle, |Y_{21}\rangle, |Y_{20}\rangle, |Y_{2-1}\rangle, |Y_{2-2}\rangle\}$ is

$$H = \begin{pmatrix} Dq & 0 & 0 & 0 & 5Dq \\ 0 & -4Dq & 0 & 0 & 0 \\ 0 & 0 & 6Dq & 0 & 0 \\ 0 & 0 & 0 & -4Dq & 0 \\ 5Dq & 0 & 0 & 0 & Dq \end{pmatrix}, \quad (1.12)$$

where $Dq = Q/6a^5 \cdot \langle R_{n2}|r^4|R_{n2}\rangle$.

Diagonalization yields the corrected hydrogen wave functions and energies. One finds the so called e_g orbitals

$$|d_{z^2}\rangle = |\Psi_{n20}\rangle, \quad (1.13)$$

$$|d_{x^2-y^2}\rangle = \frac{1}{\sqrt{2}} (|\Psi_{n22}\rangle + |\Psi_{n2-2}\rangle), \quad (1.14)$$

at $E_{e_g} = -4Dq$ and the t_{2g} orbitals

$$|d_{xy}\rangle = -\frac{i}{\sqrt{2}} (|\Psi_{n22}\rangle - |\Psi_{n2-2}\rangle), \quad (1.15)$$

$$|d_{yz}\rangle = -\frac{1}{\sqrt{2}} (|\Psi_{n21}\rangle - |\Psi_{n2-1}\rangle), \quad (1.16)$$

$$|d_{xz}\rangle = \frac{i}{\sqrt{2}} (|\Psi_{n21}\rangle + |\Psi_{n2-1}\rangle), \quad (1.17)$$

at $E_{t_{2g}} = 6Dq$. The result is illustrated in figure 1.2.

Obviously, the choice of the t_{2g} wave functions seems peculiar at first glance, as they are not the simple naive choices one would arrive at directly via matrix diagonalization but rather specific (allowed because of eigenvalue degeneracy) linear

combinations thereof. This choice, however, is convenient when talking about other aspects, such as the angular momentum of t_{2g} , which is discussed in the following section.

1.1.3 T-P Correspondence

The hydrogen d orbitals are characterized by their angular momentum $L = 2$ as the spherical harmonics are eigenfunctions of the angular momentum operator with the quantum numbers corresponding to the orbital l :

$$L^2 |Y_{lm}\rangle = l(l+1) |Y_{lm}\rangle, \quad (1.18)$$

$$L_z |Y_{lm}\rangle = m |Y_{lm}\rangle. \quad (1.19)$$

Here we introduced the common choice of angular momentum operators with $\hbar = 1$ for simplicity.

As pointed to in the short note about the history of the crystal field theory, Van Vleck established early on that a consequence of this formalism is that the angular momentum of the hydrogen orbitals is influenced or sometimes even completely quenched. What does this mean for the concrete case of the octahedral crystal field and the e_g and t_{2g} orbitals?

One can find the answer by simply using equations (1.18) and (1.19) (and the standard L^\pm , L_x and L_y definitions) to find their expressions in the $\{|d_{xy}\rangle, |d_{yz}\rangle, |d_{xz}\rangle, |d_{z^2}\rangle, |d_{x^2-y^2}\rangle\}$ basis:

$$L_x = \left(\begin{array}{ccc|cc} 0 & 0 & 0 & -\sqrt{3}i & -i \\ 0 & 0 & i & 0 & 0 \\ 0 & -i & 0 & 0 & 0 \\ \hline \sqrt{3}i & 0 & 0 & 0 & 0 \\ i & 0 & 0 & 0 & 0 \end{array} \right) \equiv \left(\begin{array}{c|cc} L_{t_{2g}}^x & -\sqrt{3}i & -i \\ \hline \sqrt{3}i & 0 & 0 \\ i & 0 & 0 \end{array} \right), \quad (1.20)$$

$$L_y = \left(\begin{array}{ccc|cc} 0 & 0 & -i & 0 & 0 \\ 0 & 0 & 0 & \sqrt{3}i & -i \\ i & 0 & 0 & 0 & 0 \\ \hline 0 & -\sqrt{3}i & 0 & 0 & 0 \\ 0 & i & 0 & 0 & 0 \end{array} \right) \equiv \left(\begin{array}{cc|cc} & & 0 & 0 \\ & L_{t_{2g}}^y & \sqrt{3}i & -i \\ & & 0 & 0 \\ \hline 0 & -\sqrt{3}i & 0 & \\ 0 & i & 0 & 0 \end{array} \right), \quad (1.21)$$

$$L_z = \left(\begin{array}{ccc|cc} 0 & i & 0 & 0 & 0 \\ -i & 0 & 0 & 0 & 0 \\ 0 & 0 & 0 & 0 & 2i \\ \hline 0 & 0 & 0 & 0 & 0 \\ 0 & 0 & -2i & 0 & 0 \end{array} \right) \equiv \left(\begin{array}{cc|cc} & & 0 & 0 \\ & L_{t_{2g}}^z & 0 & 0 \\ & & 0 & 2i \\ \hline 0 & 0 & 0 & \\ 0 & 0 & -2i & 0 \end{array} \right). \quad (1.22)$$

If the crystal field is dominant, effectively separating the e_g and t_{2g} subspaces is an option. The matrix elements in the e_g subspace are all 0. Hence the angular momentum is trivial and one refers to this as it being completely quenched.

In the t_{2g} subspace the matrices seem to take the form of the well known $L = 1$ angular momentum (at least with the choice of linear combinations in the degenerate states established in the previous section), hence we introduced the labels $L_{t_{2g}}^x/L_{t_{2g}}^y/L_{t_{2g}}^z$. However, upon closer inspection one can find an important detail: they are not really $L = 1$ matrices due to a wrong sign. Thus the commutator

$$\left[L_{t_{2g}}^x, L_{t_{2g}}^y \right] = -iL_{t_{2g}}^z \quad (1.23)$$

carries the wrong sign and we can not really use the orbitals as $L = 1$ angular momentum objects.

This sign problem however is easily fixable. A convenient way to do so is flipping the sign of all $L_{t_{2g}}^{\dots}$, i.e.

$$\mathbf{L} = -\mathbf{L}_{t_{2g}} = (-L_{t_{2g}}^x, -L_{t_{2g}}^y, -L_{t_{2g}}^z)^T, \quad (1.24)$$

which trivially leads to the right angular momentum algebra and $L = 1$ matrices for L .

Since $L = 1$ is the correct quantum number for hydrogen p orbitals, the t_{2g} triplet can be understood as p orbitals with a flipped sign in this aspect. This concept is called t-p correspondence and it is covered in standard textbooks like [85].

Flipping the sign however does come with an important caveat: If one wants to use the normal angular momentum language this sign change has to be applied to all objects that contain the L operators such as for example spin-orbit coupling and magnetic moment. For the later one finds

$$\mathbf{M}_{t_{2g}} = 2\mathbf{S}_{t_{2g}} + \mathbf{L}_{t_{2g}} = 2\mathbf{S} - \mathbf{L}, \quad (1.25)$$

where we used a standard choice of g factors $g_S = 2$ and $g_L = 1$ (other choices, like the ones used in [91], do not change the point we make here) and we used the fact that the spin is not involved in the spherical harmonics calculations. This change in expression of the magnetization is nothing new (see e.g. its use in [1, 85, 91]). Yet, one often finds that the minus sign is not used [92, 93] and, while this is often a very forgiving mistake, we find that in the case of [92] this might change the response to a magnetic field significantly!

As for the spin-orbit coupling: technically one has to change the sign of its Hamiltonian $\lambda\mathbf{L}\mathbf{S}$. However, because we work with holes instead of electrons later for convenience, there is an additional sign change which fixes it back to its original version.

1.1.4 Size of the Crystal Field Splitting

A direct follow up question regarding the previous t-p-correspondence argument is: Is it even reasonable to cleanly separate t_{2g} and e_g orbitals? More concretely, one might ask if the value of $10Dq$ is large or small compared to other influences.

There is a quick and hand-wavy answer to this. Established literature [94] states (rather roughly) that “it is not surprising that, experimentally, all ions studied in both the $4d$, $5d$ groups are found to belong to the strong ligand field”. Strong ligand field is contextualized explicitly as a single-electron calculation as employed in this thesis. Additionally the quoted book provides a table containing a list of $4d/5d$ and some $3d$ transition-metal ions it considers as having strong crystal fields. Hence, one might answer that the crystal field is sufficiently big enough as to not bother us anymore and go over to the next section. Furthermore, our focus on $4/5d$ states and not $3d$ is not primarily established by the crystal field but rather more complex reasoning involving other energy scales (charge-transfer gap, spin-orbit coupling, size of orbitals, see the related physics in [95]) and hence a more thorough investigation of the topic could be reasonably skipped.

Yet, while the crystal field being dominant is seemingly a solid assumption in the materials of our interest, there are reasons to answer the question a bit less shallowly. First of all, strong and weak are relative terms and there are reasons to expect that reality does not always follow the simple prediction. For example in some $5d$ materials one might have to start worrying about spin-orbit coupling induced $t_{2g}-e_g$ mixing [96]. One should be aware in which cases the simplicity might be dangerous. Secondly, there is a charm in writing things down in a more complete manner when the opportunity presents itself, especially when the discussion at hand neatly connects to other topics.

So how large is the splitting $10Dq$? The long answer is complicated and too elaborate to fully discuss here. A big issue is that crystal field theory, while useful for the easy calculation of the symmetries and orbitals, is far from the whole truth. In fact, the predictions of $10Dq$ (resulting from (1.12)) from the crystal field are regularly not even the largest contributions to $10Dq$ [83]. Rather, e.g. ligand field theory needs to be employed. In practice one can instead use crystal field theory to predict the orbitals and qualitative picture of the splitting and then use either

experimental data or more involved ab initio simulations to fix the quantitative value of $10Dq$.

Thus the question is rather: What rough trends in size can one expect and what concrete values do experiments/simulations provide? One might find the answer by considering example data compiled from textbooks in table 1.1. The size of $10Dq$ is obviously influenced by the choice of ligand. This increasing ligand strength is reflected in the more or less empirically constructed spectrochemical series found in standard textbooks [83, 94]. One should note that oxygen O^{2-} ligands, which are relevant in many of the later discussed/referred to compounds (e.g. $Ag_3LiRu_2O_6$), appear in this series between the values of F^- and H_2O found in the table.

One can also note that the central ion influences the splitting even when the electron configuration, e.g. $3d^5$ is the same. There are also semiempirical series of rows of d central metal ions reflecting this written down in literature [83, 85]. Moreover, the oxidization number (Fe^{2+}/Fe^{3+}) or number of electrons in general has an effect. Additionally, there is a clear increase $3d \rightarrow 4d \rightarrow 5d$.

The latter trend can be connected to a change in ion “size”, which is a useful concept for later discussions. For this one needs to consider integrals of the hydrogen radial wave function part R_{nl} and note that this trends continues to even to the radial integrals of crystal field theory in equation (1.11). The behavior of $r^2 |R_{nl}|^2$, which represent the radial probability density of the hydrogen wave function (r^2 is the contribution of the Jacobi determinant in spherical coordinates) can be seen in figure 1.3. As this represents the probability density of an electron, one may argue that increasing the principle quantum number n leads to a larger spatial extend of the orbital. An increase in nuclear charge Z however leads to a more compact probability distribution. Due to other electrons being around and screening the nuclear charge, the second trend is however more complicated and often accounted for by taking an effective nuclear charge Z_{eff} [83]. One may summarize this trend in the periodic table by stating that going down or to the left increases the size of the orbitals, which for

our purposes very roughly means that $5d$ orbitals are more spatially extended than $4d$ or $3d$. Similarly, the oxidization number trend is also obvious as it changes the effective charge of the ion (less screening), leading to a smaller size (often resulting in shorter metal-ligand distances).

All in all one may reasonably state that there are clear trends in the size of $10Dq$. This may be used to suggest materials if one finds the crystal field splitting to be the problem in establishing the model we are after.

What remains is to summarize what literature values for ions of interest, i.e. $\text{Ru}^{4+}/\text{Os}^{4+}, \text{Ir}^{5+}/\text{Re}^{3+}$ [1] or adjacent models of interest, are out there. Part of this is extremely topical as there has been quite a lot of progress in recent time such as the successful use establishment of IRIXS [12], i.e. RIXS in the intermediate X-ray regime, which provides easier access to ruthenium focused experiments.

Table 1.2 provides crystal field splitting estimates for a selection of materials. For the octahedral compounds $10Dq$ appears to be significantly larger than the other parameters (see next section). Notably, outright ignoring the e_g orbitals in the analysis, as marked by $10Dq = \infty$, is common practice. This represent the same of approximation we make in our model.

1.1.5 Many-Body Effects: d^4 and t_{2g}^4

In the first section of this chapter we established that our interest is focused on the assumption of 4 electrons occupying the d orbital, i.e. d^4 . As a consequence the technically single-electron crystal field calculations do not suffice – at least on a first glance.

The central point in this discussion is that, for the purpose of the excitonic magnetism model being relevant, one requires all four electron to be present in the t_{2g} orbital, i.e. t_{2g}^4 . From the angle of many-body effects, there are two prominent potential issues with that: spin-orbit coupling (SOC) and the Coulomb interaction of

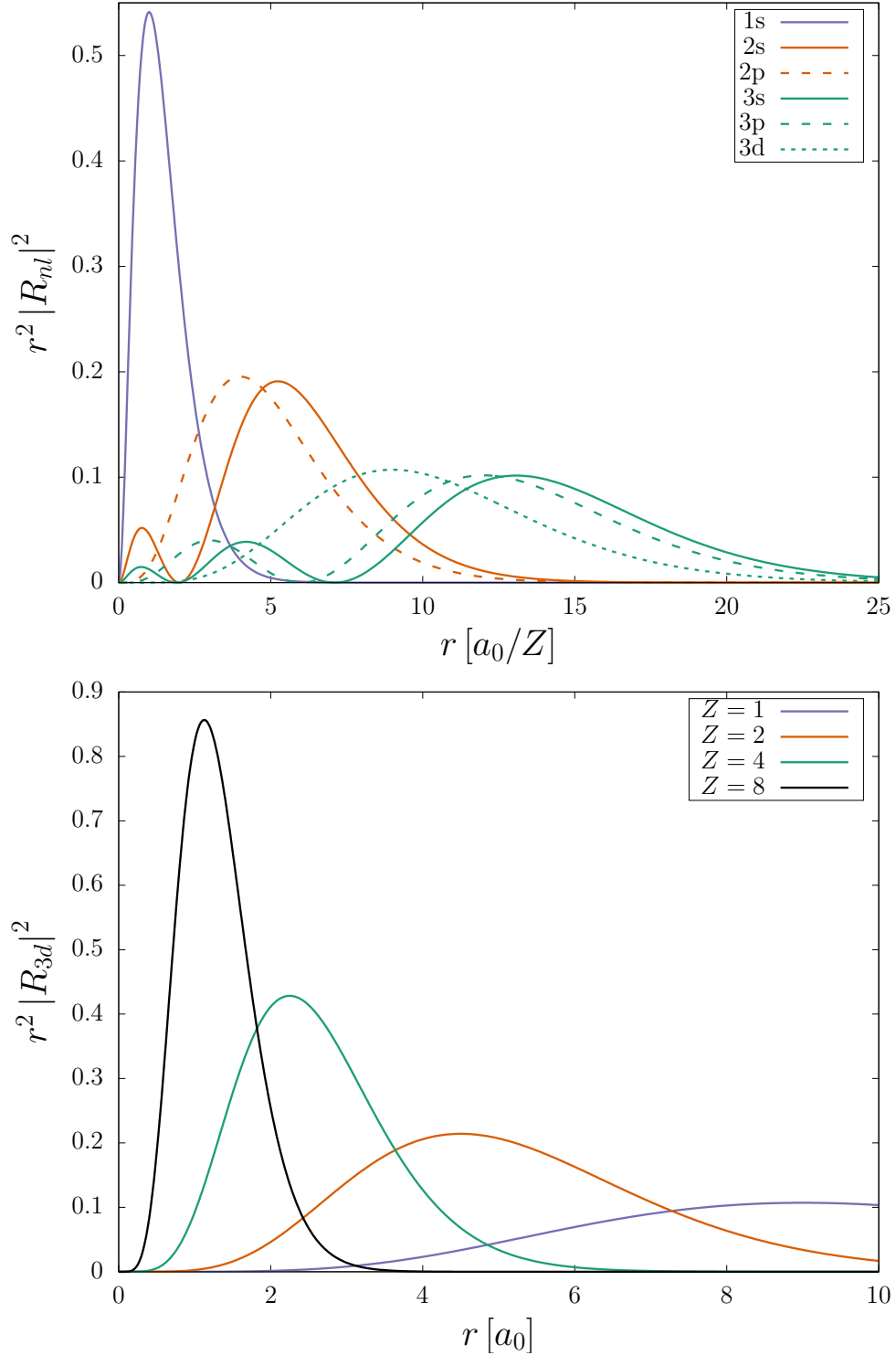


Figure 1.3. Evolution of the radial part (represented by $r^2 |R_{nl}|^2$) as a function of quantum numbers n/l (top) and central ion charge Z (bottom). The former suggests that the orbital size (radially) grows when turning to the bottom and right of the periodic table. The latter naively implies the opposite trend.

Table 1.1.: Compilation of data from textbooks [94] and [83] based on [97–99]: the numbers in the table, which have been converted to eV from the original sources, denote the octahedral crystal field splitting $10Dq$.

nd^x	Ion	Ligands					
		Cl ⁻	F ⁻	H ₂ O	NH ₃	en	CN ⁻
$3d^3$	Cr ³⁺	1.70	1.88	2.16	2.67	2.72	3.30
$3d^5$	Mn ²⁺	0.93		1.05		1.25	3.72
	Fe ³⁺	1.36		1.77			4.34
$3d^6$	Fe ²⁺			1.29			4.07
	Co ³⁺			2.57	2.84	2.88	4.31
$4d^6$	Rh ³⁺	2.53		3.35	4.22	4.29	5.64
$5d^6$	Ir ³⁺	3.10			4.96		
$3d^8$	Ni ³⁺	0.89	0.91	1.05	1.34	1.43	

the electrons with each other.

Spin-orbit coupling is best treated in its own chapter, because it is useful to establish the size and characteristics of it first. However, its effect can be established by a simple back-of-the-envelope calculation. SOC contains angular momentum operators, e.g. in the form $H = \lambda \mathbf{L} \mathbf{S}$, and hence the matrix elements outside of the e_g and t_{2g} in equations (1.20)-(1.22) will lead to e_g - t_{2g} mixing if they are not sufficiently smaller than the strength of the crystal field.

Coulomb interaction can be described by the Kanamori Hamiltonian, which is introduced in section 1.3. Explicit calculations involving the many-body Coulomb Hamiltonian are often complicated. Thankfully, this seems unnecessary for the project at hand, which we try to establish in the following paragraphs.

Leaving aside nuances about the nomenclature, the rough conflict of crystal field

Table 1.2.: Estimates of the size of the crystal field splitting parameter $10Dq$, the Hund's coupling J_H and spin-orbit interaction ξ for various compounds of direct or adjacent interest for this thesis. The parameters are established by experiments and/or comparison of model data to experimental results. All numbers are provided in units of [eV]. The ∞ implies that e_g orbitals were neglected in the modeling/fitting process.

Ion	nd^x	compound	$10Dq$	J_H	ξ	source
Ru ⁴⁺	$4d^4$	K ₂ RuCl ₆	2.9	0.42	0.103	[34]
Ru ⁴⁺	$4d^4$	Ca ₂ RuO ₄	3.1	0.34	0.13	[100]
Ru ⁵⁺	$4d^5$	α -RuCl ₃	2.4	0.34	0.15	[101] ^a
Ru ⁵⁺	$4d^5$	RuBr ₃	2.15	0.34	0.15	[102]
Ru ⁵⁺	$4d^5$	RuI ₃	2.05	0.34	0.15	[102]
Os ⁴⁺	$5d^4$	K ₂ OsCl ₆	3.3	0.43	0.34	[27] ^b
Os ⁴⁺	$5d^4$	K ₂ OsCl ₆	∞	0.28	0.41	[27] ^b
Os ⁴⁺	$5d^4$	K ₂ OsBr ₆	2.9	0.42	0.33	[27] ^c
Re ⁵⁺	$5d^2$	Ba ₂ YReO ₆	∞	0.38	0.26	[29] ^d
Os ⁵⁺	$5d^3$	Ba ₂ YOsO ₆	∞	0.335	0.275	[29] ^d
Ir ⁵⁺	$5d^4$	Ba ₂ YIrO ₆	∞	0.385	0.23	[29] ^d
Ru ⁴⁺	$4d^4$	RuO ₂	2.6	0.78 ^e	0.161	[103]
Ru ⁴⁺	$4d^4$	Ag ₃ LiRu ₂ O ₆	∞	0.75 ^f	0.140	[8]
Ni ²⁺	$3d^8$	NiRh ₂ O ₄	0.58	0.72	0.013	[104] ^g

^a except for $J_H = 0.32$ eV also [102]

^b same set of data is compared to two different models

^c Rb₂OsBr₆ not significantly different

^d analysis incorporates data from [31, 105, 106]

^e the source only provides the Slater integrals $F^{(2)}$ and $F^{(4)}$ (cf. 1.3), which we can use to get a slightly inaccurate estimate via the formula $J_H = 2.5/49 \cdot F^{(2)} + 22.5/441 \cdot F^{(4)}$ valid for a Kanamori Hamiltonian [107]

^f J_H simulation does not involve spin-orbit coupling

^g material has a tetrahedral crystal field

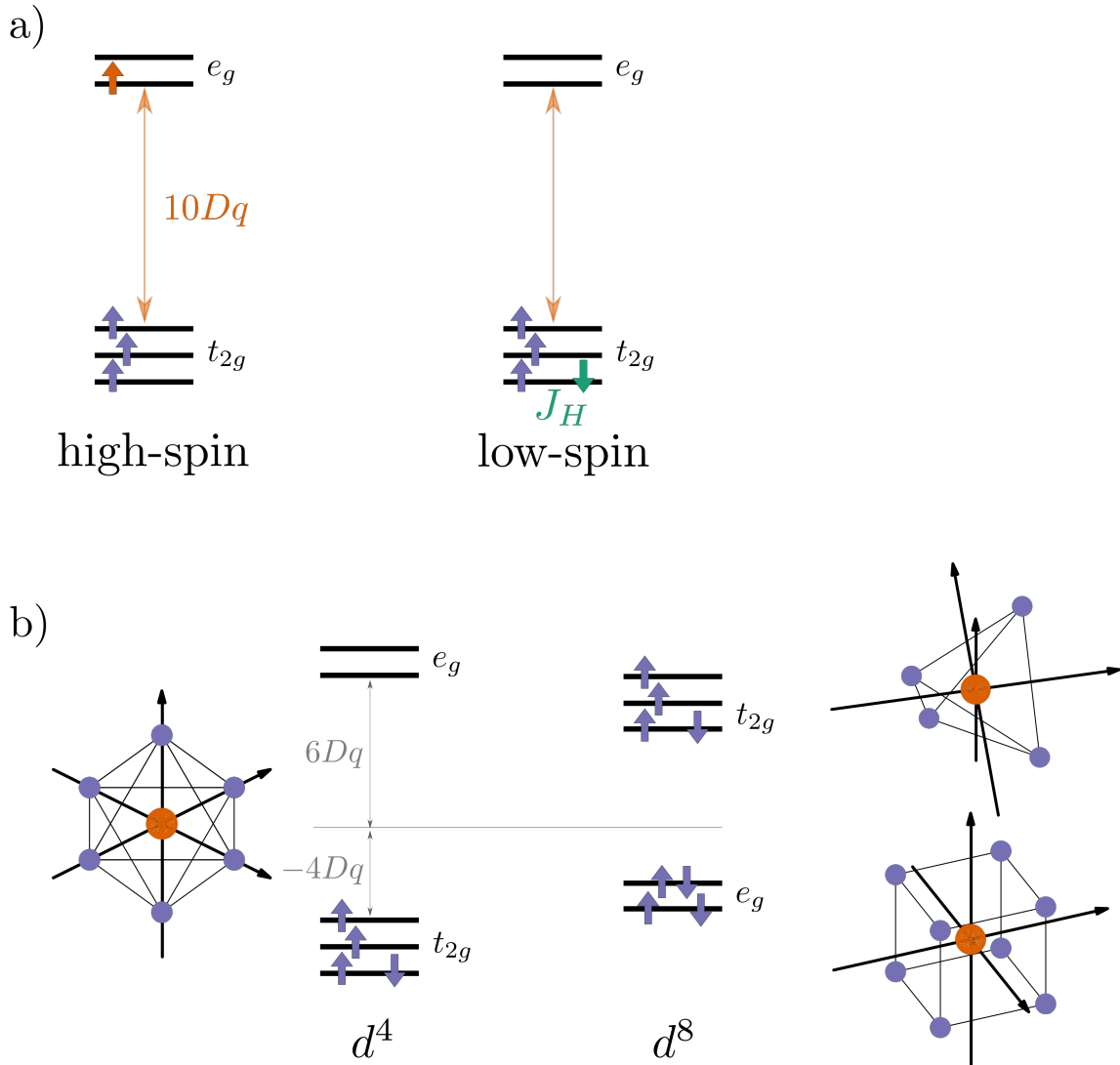


Figure 1.4. a) High- and low-spin configurations of a d^4 electron configuration in an octahedral crystal field environment: In the high-spin case the fourth electron is located in e_g , which is intertwined with an energy cost of $10Dq$. For the low-spin setting all electrons are in the t_{2g} orbital, i.e. t_{2g}^4 , which costs energy on the order of the Hund's coupling J_H due to the spin-alignment not maximizing its value. b) Tetrahedral and cubic crystal field provide the same kind of energy splitting, however inverse and of reduced strength. As a result, low-spin d^4 in an octahedron and d^8 in a cube/tetrahedron can end up with the same effective t_{2g}^4 electron configuration.

and Coulomb interaction is the Hund's coupling J_H , which more or less enforces the well-known Hund's rules when it comes to occupation of the orbitals. For the d^4 , or

rather t_{2g} and e_g orbitals this enables two rather simple edge cases: If one follows Hund's rules, i.e. if J_H is dominant compared to the $10Dq$ of the crystal field, one needs to maximize the spin when filling in the four electrons. Due to the Pauli principle this necessitates at least one electron to be in the higher e_g orbitals. If however the crystal field dominates, the energy gap separating t_{2g} and e_g , and hence the energy cost of an electron in the latter, is so large, that all electrons remain in t_{2g} . This is illustrated in figure 1.4a). As the first scenario results in a total spin $S = 2$ and the second one in $S = 1$, they are referred to as high-spin and low-spin respectively.

The excitonic magnetism scenario [1] is based on the assumption of excitations condensing into a $J = 0$ ground state, where J is the total angular momentum arising from SOC combining a spin $S = 1$ with an orbital $L = 1$, hence low-spin t_{2g}^4 is a viable option. As a result the restriction to a dominant crystal field is desirable.

Given the sizes of $10Dq$ and J_H established in table 1.2 this seems to be a decent choice in the desired $4d/5d$ materials.

1.1.6 Tetrahedral Crystal Field and t_{2g}^4

Repeating the crystal field calculations with a tetrahedral geometry (e.g. four ligands located at $(a, a, a)^T/\sqrt{3}$, $(a, -a, -a)^T/\sqrt{3}$, $(-a, a, -a)^T/\sqrt{3}$ and $(-a, -a, a)^T/\sqrt{3}$ as depicted in figure 1.4b)) yields the matrix of equation (1.12) with an additional factor of $-4/9$ for each element. This is a well known result stemming from the fact that octahedral and tetrahedral configurations both fall under the cubic symmetry group, which can be stated as [88]

$$\langle V_{\text{CF}}^{\text{octa}} \rangle = -\frac{9}{4} \langle V_{\text{CF}}^{\text{tetra}} \rangle = -\frac{9}{8} \langle V_{\text{CF}}^{\text{cubic}} \rangle, \quad (1.26)$$

where the superscript refers to the introduction of the respective geometry into equation (1.9) (and cubic alludes to a ligand on all corners of the cube as seen in the

bottom right of figure 1.4).

In regards to the excitonic magnetism model there are a few more or less important consequences of this result. Less important, but noteworthy, is the fact that the crystal field of the tetrahedral geometry (for unchanged materials and distances of ligands and central ion) is significantly smaller and thus more prone to discussions of e.g. high-spin state influences or SOC induced $t_{2g} - e_g$ mixing. Of crucial importance however is the fact that the tetrahedral crystal field results in the exact same t_{2g} and e_g orbitals as the octahedral one, aside from the aspect that the latter e_g lies lower in energy this time.

Consequently a d^8 tetrahedral geometry can potentially yield the desired effective t_{2g}^4 or $S = 1 = L$ of the excitonic magnetism scenario! Hence this should be kept in mind as a feasible application of many of our results in this thesis. One should note that, if the scenario applies, the form of all matrices and orbitals being effectively the same results in the formula (1.25) still being the valid way to write down the magnetization.

For a direct connection to this thesis one should keep in mind that the octahedral geometry has a few other important roles in the systems considered here. The most important difference is that the ligands, and thus the form of the crystal, mediate the exchange mechanism and are an important driver of the Kitaev-Heisenberg physics (cf. section 1.4).

Yet, NiRh_2O_4 , which is one such d^8 material, has been directly connected to the excitonic magnetism scenario [36]. It has also been proposed to host intriguing reentrance behavior in a magnetic field [92], which is what we will argue here and directly connect to the lengthy discussion of the magnetization formula for t_{2g} .

1.1.7 Crystal Field Distortions

1.1.7.1 General Discussion and Importance

Considering figures 1.1b) and c) closely, one might be able to spot, even with the naked eye, that the real crystal structure established by experiment does not contain perfect, idealized octahedra but rather slightly distorted ones. These distortions can arise “naturally”, e.g. via Jahn-Teller distortions [108], or as a consequence of orbital order [109]. Furthermore one might induce them by applying pressure [8] or has to deal with them as a result of otherwise induced phase transitions [26].

While estimating the size of these distortions in the sense of quantitative energy in the Hamiltonian is nontrivial (the discussions of section 1.1.4 obviously apply), the change in spacial structure is easily established and tabulated, e.g. [8, 26], and might provide a rough idea about the order of magnitude. Furthermore, experimental data might establish the size similar to $10Dq$.

For example Ca_2RuO_4 is thought to distort (in a significant way) tetragonally (see below) with a energy gap of $\Delta E = 0.25 \text{ eV}$ [100], while the significantly less distorted $\text{Ag}_3\text{LiRu}_2\text{O}_6$ is attributed to roughly $\Delta E \approx 0.05 \text{ eV}$ [8].

Hence, one can reasonably expect the effects of the distortion to be of or over the order of magnitude of spin-orbit coupling or the later introduced t^2/U . One needs to deal with these distortions explicitly.

Figure 1.5 shows examples of distortions of the ligand octahedra. Symmetry-wise one might talk about a few reasonable scenarios. In the full octahedral symmetry the distances to the ligands are the same in all three directions $\Delta x = \Delta y = \Delta z$. If one introduces an anisotropy in one axis, e.g. $\Delta x = \Delta y \neq \Delta z$ like in 1.5a), one talks about tetragonal distortion. Of course lengthening/shortening x and y and leaving z the same provides the same symmetry. These scenarios are only distinct by a possible global energy shift. In the discussions in this thesis this shift is discarded

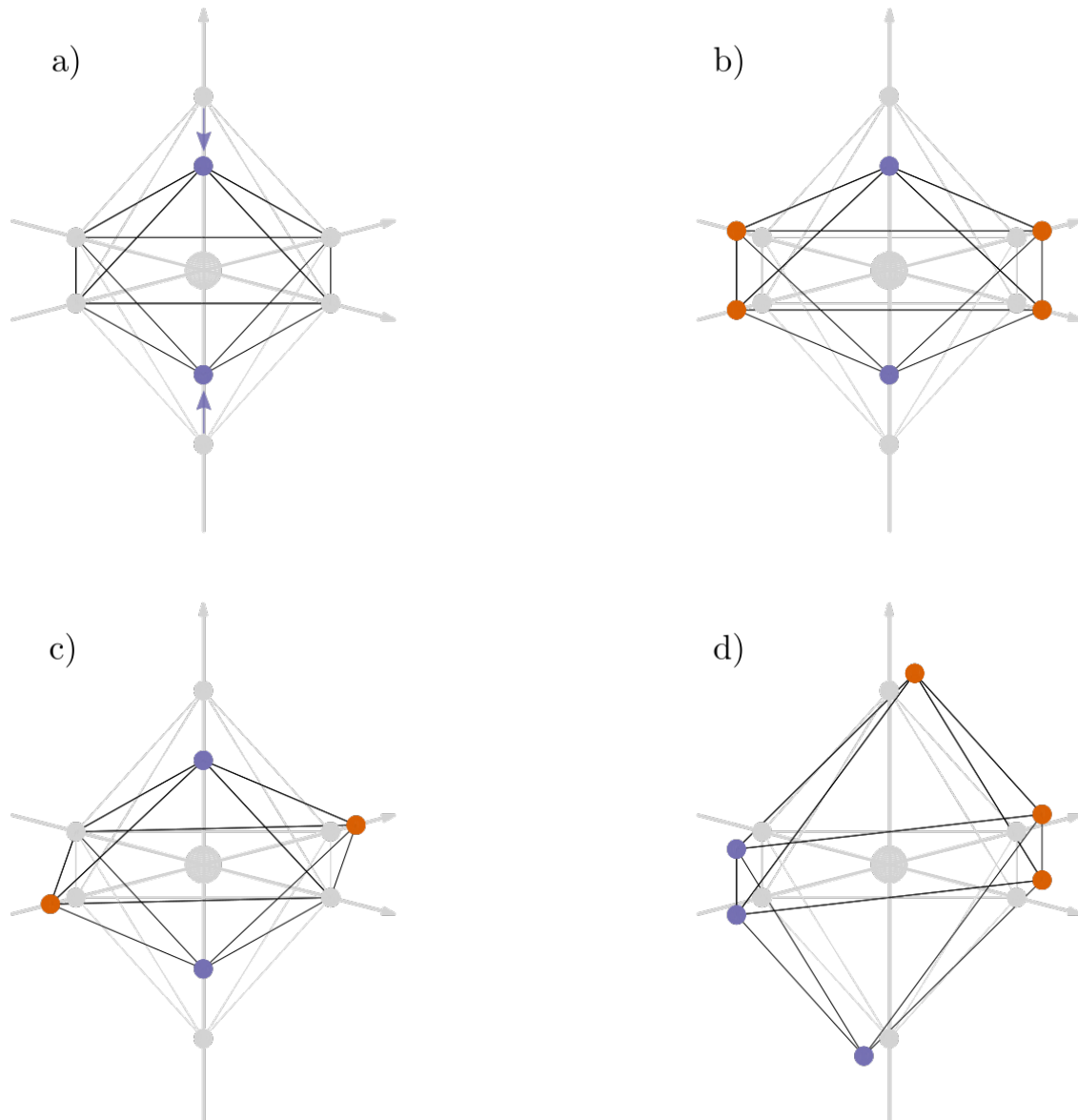


Figure 1.5. Sketches of distortions of an octahedral crystal environment with non-gray colors representing deviations from the original structure: a) tetragonal distortion $x = y \neq z$. b) If one cares about the total energy gain or loss (e.g. for the calculation of Jahn-Teller distortions) one can rewrite the (here also tetragonal) distortion as volume conserving symmetry modes. c) orthorhombic distortion d) trigonal distortion

and unimportant. In some scenarios like the Jahn-Teller distortions, however, one might need to account for them and hence use special setups, like 1.5b), which leaves the volume intact and represents the so called Q_3 symmetry mode [108].

As mentioned before, the tetragonal distortions is extremely prevalent in the discussions surrounding Ca_2RuO_4 , where a topic of interest is the origin of the magnetic behaviour, in particular the so called Higgs mode, and the question if the underlying physics can be best described as originating from effective $J = 0$ and excitonic magnetism (the topic of interest in this thesis), which necessitates the essential role of spin-orbit coupling, or a dominant tetragonal crystal field distortion and its resulting spin-1 model. Elements of this thesis contribute to this discussion [20] and hence we will cover this quickly.

If one goes lower in symmetry, i.e. $\Delta x \neq \Delta y \neq \Delta z \neq \Delta x$ one might talk about (ortho-)rhombohedral distortion 1.5c). While one might find scenarios where this applies on paper (which can be seen by, e.g., looking at measured values of the crystal axis in [8]), we are not aware of any relevant discussion where this impact is relevant for the material class of our interest. We will therefore skip this. Yet, one should keep this in mind as a possibility as, e.g., the analysis of the Pseudo-Jahn-Teller Effect in the iridate Sr_2IrO_4 [110] involves the orthorhombicity as a driving force.

A bit more unintuitive at first glance is trigonal distortion. Consider the plane described by the normal vector in $[x, y, z] = [1, 1, 1]$ direction. This also represents a symmetry of the octahedron, namely threefold rotation around the axis in said plane. Stretching/Compressing along the direction of the normal vector represent the trigonal distortion 1.5d).

Trigonal distortion is found to exist in materials of interest in this thesis, namely the ones involving the previously mentioned honeycomb lattice structure of TM ions instead of the square lattice found in Ca_2RuO_4 . In the discussion of in $\text{Ag}_3\text{LiRu}_2\text{O}_6$ for example [8], the trigonal distortions and their evolution under pressure are of key interest. Moreover $\alpha\text{-RuCl}_3$, the well studied d^5 cousin of our focus, is assumed

to host significant trigonal crystal field splitting [111]. Hence we will discuss the trigonal distortion and its effects quite thoroughly.

1.1.7.2 Calculating crystal field distortions

Given the strength of the crystal field distortions being either a rather free model parameter or hard to determine exactly in reality (cf. discussion in section 1.1.4) and our interest in how it perturbs the orbitals rather than total energy discussions, the calculation are quite straightforward in principle. Via the series expansion one can just handle the new structure (with an arbitrary small number for the displacement of position representing the distortion) via the known formulas in equations (1.10) and then subtract the terms of the original undistorted structure. Alternatively these well known results, or shortcuts to them, can be found in textbooks or papers [81, 88, 90].

On that note: one can easily verify that the extremely convenient short-hand formula [112] stating that the effect of the distortion manifests in its simplest form as

$$V = \Delta (\hat{\mathbf{n}} \cdot \mathbf{L}), \quad (1.27)$$

where $\hat{\mathbf{n}}$ is a normalized vector representing the distortion, works as intended for the common choices of tetragonal ($\hat{\mathbf{n}} = (0, 0, 1)^T$) and trigonal ($\hat{\mathbf{n}} = (1, 1, 1)^T/\sqrt{3}$) distortions. It should, however, be kept in mind what it takes to arrive at this formula and how one has to use and interpret this formula. The Hamiltonian therein is an effective Hamiltonian restricted to the t_{2g} basis (explaining the \mathbf{L} operator via equations (1.20)-(1.22)) and again uses assumptions like discarding total shifts in energy, which e.g. lets one freely deduct or add \mathbf{L}^2 to write down the result in convenient form. The expression obviously does not care about the sign change of the t-p-correspondence, as all angular momenta enter in pairs and the sign cancels out.

Both crystal field distortions are similar in a sense that they split up the t_{2g} triplet into a doublet and singlet. Concretely, the trigonal crystal field case yields (neglecting global energy shifts)

$$V = \frac{\Delta}{3} \begin{pmatrix} 0 & 1 & 1 \\ 1 & 0 & 1 \\ 1 & 1 & 0 \end{pmatrix}, \quad (1.28)$$

which after diagonalization results in the following energy shifts and eigenstates:

$$|s\rangle = \frac{1}{\sqrt{3}} (|xy\rangle + |yz\rangle + |xz\rangle) \quad \Longrightarrow \quad E_s = \frac{2\Delta}{3}, \quad (1.29)$$

$$|d_1\rangle = \frac{1}{\sqrt{2}} (|xy\rangle - |xz\rangle) \quad \Longrightarrow \quad E_{d1} = -\frac{\Delta}{3}, \quad (1.30)$$

$$|d_2\rangle = \frac{1}{\sqrt{2}} (|yz\rangle - |xz\rangle) \quad \Longrightarrow \quad E_{d2} = -\frac{\Delta}{3}, \quad (1.31)$$

where we introduced (for visual convenience) the hereinafter used notation for the t_{2g} orbitals $|d_{xy}\rangle \equiv |xy\rangle$ (others analogous). The resulting splitting of the triplet is visualized in figure 1.6. Depending on the sign either the singlet or the doublet is favored energetically and the splitting is linear.

The tetragonal case is even easier. The perturbation $V = \Delta L_z^2$ is already diagonal providing analogous results. A notable difference is that the t_{2g} orbitals do not mix (more concretely: the linear combination we chose to represent the t_{2g} triplet does not).

1.2 Spin-Orbit Coupling

Spin-orbit coupling is a key ingredient in our model and even beyond. For a look into its effect on ground states in iridates alone, one may look into the review [113], which also provides a rough overview about the $J = 0$ scenario that is the focal point

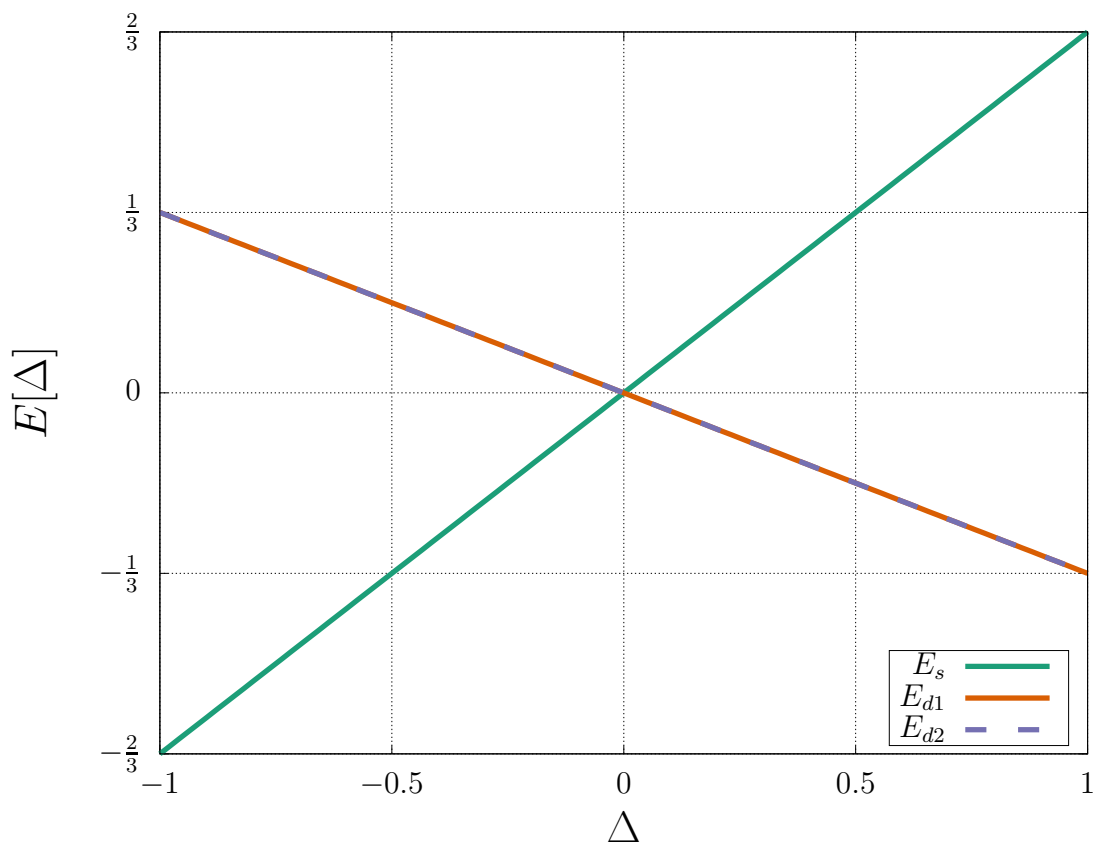


Figure 1.6. Effect of crystal field distortions on the energies of the t_{2g} orbitals: the triplet splits into singlet and doublet with the order depending on the sign of the distortion strength Δ .

of this thesis. Here, we want to give a basic general introduction to the topic.

1.2.1 Origin and Strength of Spin-Orbit Coupling

In this section we follow (up to and including the figures 1.7 and 1.8) the excellent introductory section of reference [114]⁴ and update/extend the discussion with a few added remarks and contemporarily produced data for the plots (which also fit the theory noticeably better).

Spin-orbit coupling is a relativistic effect. It emerges as a consequences of ap-

⁴And we are not the first to do so, see the review [115].

proximating the Dirac equation, i.e. the relativistic equivalent of the Schrödinger equation, for the nonrelativistic limit (full calculation in [82]). A resulting term in the Taylor expansion is the single-electron spin-orbit Hamiltonian

$$H_{\text{SOC}} = \frac{1}{2m^2c^2} \frac{1}{r} \frac{\partial V}{\partial r} \mathbf{l} \mathbf{s} \equiv \xi(r) \mathbf{l} \mathbf{s}, \quad (1.32)$$

where in the simplest case $V = -Ze^2/r$ is the standard hydrogen-like central potential and r is the radial position. Here \mathbf{l} emerges from the traditional position and momentum $\mathbf{r} \times \mathbf{p}$ and \mathbf{s} is a vector of Pauli matrices as a consequence of the structure of the Dirac equation (which famously knows about spin structurally).

How can one estimate ξ or rather $\langle \xi(r) \rangle$, which really represents the constant we are usually focusing on? The answer depends on the extend of “realism” one intends to involve in the construction of the average or in other words the wave function one tries to integrate over. Are there interacting or non-interacting electrons? Are the wave functions otherwise influenced by, e.g., a crystal field as discussed in the previous sections? This is the point where estimating the spin-orbit coupling strength becomes nontrivial and probably an exercise for ab-initio calculations or experimental estimates, which we turn to shortly.

Cheaper estimates are the use of hydrogen like expressions, resulting in

$$\xi_{nl} \sim \int_0^\infty dr |R_{nl}|^2 \xi(r) \implies \xi_{nl} = \frac{\alpha^2}{n^3 l(l + \frac{1}{2})(l + 1)} Z^4 \text{ [Ry]}, \quad (1.33)$$

where α is the fine-structure constant. Landau and Lifshitz [116], calculating an approximate probability of an outer shell electron being near the nucleus that is screened by the inner ones, rather estimate

$$\xi_L = A\alpha^2 Z^2 \text{ [Ry]}, \quad (1.34)$$

where A is a constant that needs to be estimated based on the situation (here we

are satisfied with assuming it to be of order of one).

Figures 1.7 and 1.8 visualize the estimates by plotting them against contemporary ab-initio data from reference [117] (instead of ancient Hartree-approximation based calculation cited in the original [114]). One finds that the Z^4 works decently for the inner electrons, e.g. p electrons if d is the outer shell. Z^2 seems to be a better estimate for outer electrons and hence for the objects we deem to be relevant in a solid.

However, it is clear from the preceding discussion that embedding the atom in a solid will lead to changes. In a solid the orbitals can be squished by the crystal field environment (also changing the effective Coulomb interaction, see the Kanamori discussion) and the electron count changes leading to more or less objects to interact with. These changes can be quite significant as reasoned by examples of tantalum and titanium in reference [114].

So how do we estimate the spin-orbit coupling strength in practice? As in the case of $10Dq$, experiments can provide the answer, at least as a rough estimate. For a compilation of thesis relevant or adjacent materials these values can be found in table 1.2. Additionally material specific ab-initio calculation could be employed. A very recent such try that might be of interest (as it explicitly involves α - RuCl_3) is reference [118].

From the theoretical estimates one should keep in mind the general trends. Iridium with $Z = 77$ is expected to have significantly larger spin-orbit coupling than Ruthenium ($Z = 44$). Furthermore, if the value estimated by experiments or ab-initio changes drastically from expectation, the underlying reason might be an interesting point to focus on. Case in point: Because Ba_2YOsO_6 and Ba_2YIrO_6 in table 1.2 do not follow naive expectations, the paper in question points to possible covalent ligand bonding effects that might be going on, suggestion a breakdown of the $J = 0$ ground state picture we are interested in.

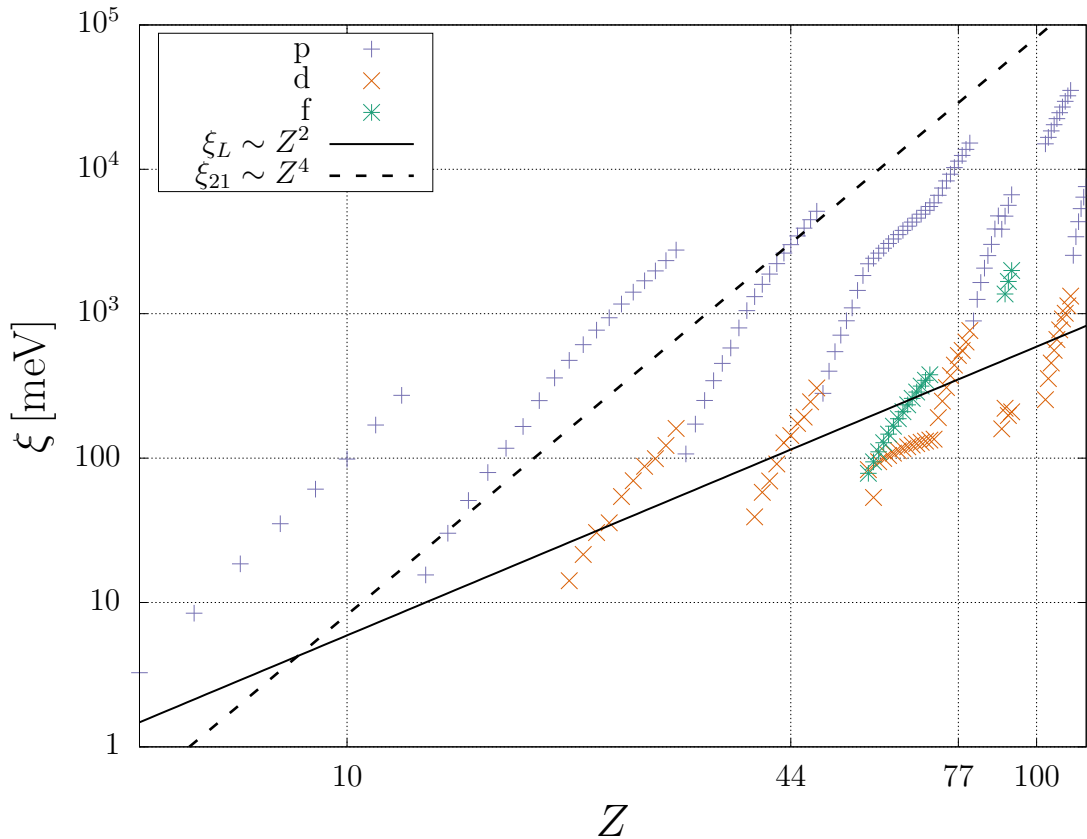


Figure 1.7. Values of the spin-orbit coupling strength ξ as estimated by [117] for elements labeled by their atomic number Z ($Z = 44$ represents Ruthenium and $Z = 77$ Iridium). Here $p/d/f$ are the orbitals (s is trivial for spin-orbit coupling). For comparison the estimates using the naive hydrogen like calculation ξ_{nl} for a given n/l and the Landau estimate ξ_L (using the arbitrary choice $A = 3$) are shown.

1.2.2 LS - and jj -Coupling Schemes

As in the case of low- and high-spin in the crystal field discussion, the next necessary step is the introduction of a many-particle description. As the previous result represents a single-particle Hamiltonian, a first step can be to make a sum over this term for many electrons:

$$H_{jj} = \xi \sum_i \mathbf{l}_i \mathbf{s}_i, \quad (1.35)$$

where i labels the electrons.

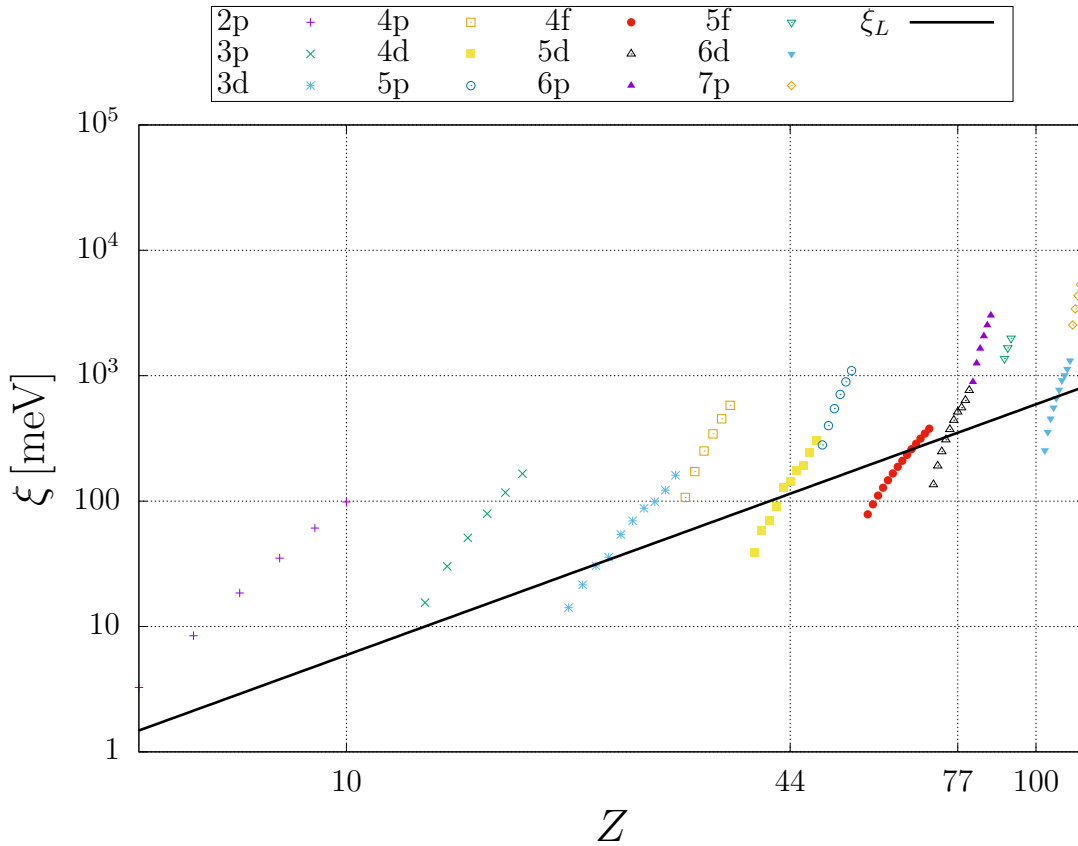


Figure 1.8. Data points of the previous figure for the outermost electrons of each element are shown with the corresponding nl orbital labels and the Landau estimate ξ_L .

If spin-orbit coupling is the dominant force or in other words if the electrons care more about its influence than about each other, the Hamiltonian is straightforwardly satisfied by minimizing each $\mathbf{l}_i \mathbf{s}_i$ term individually. This is accomplished by the combination into a total angular momentum $\mathbf{j}_i = \mathbf{l}_i + \mathbf{s}_i$ for each term in the usual way⁵. After this priority is satisfied one might start talking about a combination of all objects to a total angular momentum $\mathbf{J} = \sum_i \mathbf{j}_i$. Due to the order of operations, this process is called jj -coupling.

In the opposite case, i.e. the electron correlation being dominant over spin-orbit

⁵The calculation is a basic textbook exercise and the relevant formulas are covered when deriving the singlet-triplet model later.

coupling, the preeminent Hamiltonian is the Coulomb interaction (see 1.3). As described in the section introducing it, the problem can be summarized to the Hund's coupling J_{H} effectively enforcing Hund's rules, i.e. maximizing spin and angular momentum. As a result the combinations to total spin $\mathbf{S} = \sum_i \mathbf{s}_i$ and total angular momentum $\mathbf{L} = \sum_i \mathbf{l}_i$ happen first. The Hamiltonian can be simplified [85] to

$$H_{LS} = \lambda \mathbf{L} \mathbf{S}, \quad (1.36)$$

where $\lambda = \xi/2S$ or in the low-spin t_{2g}^4 case with $S = 1$ concretely $\lambda = \xi/2$.

Taking a glance into the realistic parameter estimates in table 1.2, one can surmise that, even though J_{H} is usually larger than ξ , we can't reliably expect to be in a pure LS -coupling regime. However, the entire description of the subsequently discussed Kugel-Khomskii model and its singlet-triplet low energy subspace require this limit.

Aside from the fact that the main motivation of our model study is the scenario itself, which is motivated by the possible feasibility of existence and not the necessity of a specific scenario dictated by a fixed material, the problem might not be as drastic as it appears to be on first glance. For one the total angular momentum in both jj - and LS - coupling for the ground state is $J = 0$. The main difference is more important for the specific look of the other states and the exact form of the Kugel-Khomskii Hamiltonian and resulting Kitaev-Heisenberg model. As we let the parameters in the model roam quite freely, care about the precise amount of interaction can be reasonably set aside. More importantly, while the Kugel-Khomskii model approach is limited in this regard, other angles of attack are not. In particular treatments of the entire problem in the form of a multi-orbital Hubbard model (orbital dependent electron hopping and full on-site Kanamori and spin-orbit coupling treatment of all t_{2g}^4 states) can serve as a comparison. For a Ca_2RuO_4 motivated model, this kind of problem has been extensively studied via the Exact Diagonalization based Variational Cluster Approach [119]. During the course of the study

the question of $LS-$ and $jj-$ picture being valid has been specifically analyzed for various parameter regimes.

Nevertheless it would be interesting to try to include the effects of going from the $LS-$ to the $jj-$ regime somehow. Maybe one could try to analyze the effects of the extra terms in H_{LS} compared to H_{jj} . Due to the difficulty to include anything other than the LS terms into the Kugel-Khomskii type model at hand, this is however beyond the scope of this thesis.

1.2.3 Dzyaloshinskii-Moriya Interaction

When considering the unconventional magnetism of $\alpha\text{-Fe}_2\text{O}_3$, Igor Dzyaloshinskii came up with a possible explanation by writing down a Landau theory for the problem and finding a symmetry allowed term that could explain the underlying ferromagnetic structure of the material [120]. Thereafter Moriya provided calculations and pointed out a direct connection to the involvement of spin-orbit coupling into the derivation of superexchange [121]. Moreover he formulated that a spin interaction (the Dzyaloshinskii–Moriya interaction hence referred to as DM interaction) of the form

$$\mathbf{D} \cdot (\mathbf{S}_i \times \mathbf{S}_j) \tag{1.37}$$

between sites i and j can exist if it the geometry fulfills 5 symmetry rules concerning inversion center, mirror planes and rotational axes. This anisotropic interaction scales linearly in λ and is in first order $\Delta g/g$ times the superexchange parameter, where g is the gyromagnetic factor of the free electron and Δg is its effective error. In order to better quantify that one can turn to two review papers of the field of DM interaction and its consequences [122, 123]. One of them derives the interaction in a way that matches the perturbation theory of sections 1.4.1 and 1.4.4 while the other outright states, rather roughly, that it is usually negligibly small in bulk materials, namely 1% of the Heisenberg interaction.

As a result we are not inclined to care about DM for our model calculations (only allowed starting at next nearest neighbors on the honeycomb and probably very small). That does not necessarily mean that it is the case for other systems (as implied by the mentioned reviews).

Of note are a lot of discussions involving DM as a driving force of topological phenomena in magnets, especially spin-dimer based singlet-triplet models that serve as a direct analogy to the spin-orbital $J = 0$ and $J = 1$ structure at the center of this thesis. Particularly, one should be aware of the topological triplons and magnetic Chern bands in the Shastry-Sutherland magnet $\text{SrCu}_2(\text{BO}_3)_2$ [78, 124, 125], which has since also approached novelties beyond this thesis like Dirac nodal loop [126] and Weyl-triplons [127]. DM is also involved in topological triplons in bilayer and ladder systems [128, 129] and has been shown to support higher-order topological states [130].

1.3 Coulomb Interaction

1.3.1 Coulomb Interaction in General

Condensed matter physics is intrinsically a many-body problem. When writing down the Schrödinger equation Hamiltonian of a solid one has to, in principle, account for many electrons having a kinetic energy and interaction, many ions possessing the same and last but not least interactions between electron and ions (see [131] for a proper introduction also concerning the following sentences). An exact solution of this object is seemingly unfeasible, so approximations have to be made. One can for example see that the ions are heavier than the electrons and employ the Born-Oppenheimer approximation. A more thorough dive into this topic is best left for established literature. We point out that one way of approximately treating the problem is to focus on the electrons via a Hamiltonian containing their kinetic energy,

electrostatic Coulomb repulsion between each other and an effective potential $V(\mathbf{r}_i)$ covering for other things, mainly interactions with the ions as e.g. the treatment of the crystal field in earlier chapters (but of course much more beyond that). This can read as

$$H = \sum_i \left(-\frac{\nabla_i^2}{2m} + V(\mathbf{r}_i) \right) + \frac{1}{2} \sum_{i \neq j} \frac{e^2}{|\mathbf{r}_i - \mathbf{r}_j|}, \quad (1.38)$$

where i labels the electrons, m is the electron mass, e its charge, V is the potential, \mathbf{r}_i the position of electron i and ∇_i the derivative resulting from the canonical momentum⁶.

The first part of the Hamiltonian consists of one-particle operators and represents what we have analyzed in the previous sections (aside from the spin-orbit coupling which is from the Dirac and not Schrödinger equation). In contrast to this, the last part is a two-particle operator representing the Coulomb repulsion between two electrons. All discussion of many-particle effects of previous sections stem from this term. Here, we aim to shortly explain its impact and how to possibly handle it.

As a two-particle operator the Coulomb Hamiltonian in second quantization environment translates to

$$H_{\text{Coulomb}} = \sum_{\alpha} \sum_{\beta} \sum_{\gamma} \sum_{\delta} U_{\alpha\beta\gamma\delta} c_{\alpha}^{\dagger} c_{\beta}^{\dagger} c_{\gamma} c_{\delta}, \quad (1.39)$$

where c_{α}^{\dagger} creates an electron in state α . Here α should label all relevant degrees of freedom such as e.g. the quantum number $n/l/m$ hydrogen-like solution discussed earlier, their spin σ or in position space the location of the electron \mathbf{r}_{α} . The matrix

⁶units like \hbar and ϵ_0 are left out for simplicity

element is then

$$\begin{aligned}
 U_{\alpha\beta\gamma\delta} &= \langle \alpha\beta | \frac{e^2}{|\mathbf{r}_i - \mathbf{r}_j|} | \gamma\delta \rangle \\
 &\sim \int d^3\mathbf{r}_i \int d^3\mathbf{r}_j \Psi_\alpha^*(\mathbf{r}_i) \Psi_\beta^*(\mathbf{r}_j) \frac{e^2}{|\mathbf{r}_i - \mathbf{r}_j|} \Psi_\gamma(\mathbf{r}_i) \Psi_\delta(\mathbf{r}_j),
 \end{aligned} \tag{1.40}$$

where $\Psi_\alpha^*(\mathbf{r}_\alpha = \mathbf{r}_i)$ represents the (complex conjugate of the) position space wave function of state α .

We have encountered this kind of problem earlier in this thesis, just in a significantly simpler form. For the crystal field calculation in 1.1.2 we had to deal with the same kind of electrostatic potential $1/|\mathbf{r}_i - \mathbf{r}_j|$ in a single-electron environment. The solution was to expand it as a function of spherical harmonics (cf. equation (1.6)) and then separate radial and angular degrees of freedom. Here this translates to

$$U_{\alpha\beta\gamma\delta} \sim \sum_{k=0}^{\infty} R_{\alpha\beta\gamma\delta}^{(k)} \cdot \frac{4\pi}{2k+1} \sum_{m=-k}^{m=k} (-1)^m \langle Y_{l_\alpha m_\alpha} | Y_{k(-m)} | Y_{l_\gamma m_\gamma} \rangle \langle Y_{l_\beta m_\beta} | Y_{km} | Y_{l_\delta m_\delta} \rangle, \tag{1.41}$$

where $R_{\alpha\beta\gamma\delta}^{(k)}$ represents the radial part. The radial part is referred to as Slater integral(s). For the later discussion the relevant part of these integrals is the one where we restrict ourselves to one orbital, i.e. l is uniform (obviously then also n) for all states and

$$\begin{aligned}
 F^{(k)} &= R_{\alpha\beta\gamma\delta}^{(k)} |_{l_\alpha=l_\beta=l_\gamma=l_\delta} \\
 &= \int_0^\infty dr_i \int_0^\infty dr_j r_i^2 r_j^2 R_{nl}^*(r_i) R_{nl}^*(r_j) \frac{r_{\leq}^k}{r_{>}^{k+1}} R_{nl}(r_i) R_{nl}(r_j).
 \end{aligned} \tag{1.42}$$

1.3.2 Kanamori Form

Given the form of the Coulomb interaction in equation (1.41), namely the spherical harmonics and their matrix elements, and the similarities to the crystal field potential discussion, it is unsurprising that the Hamiltonian can be simplified using symmetries. There are various ways to accomplish and parametrize this and one should point to [132] for a detailed discussion of the different schemes, comparisons between them and a detailed introduction of the Kanamori Hamiltonian of which we try to provide a rough sketch here.

As stated we can simplify the problem by choice of symmetry and thus spherical harmonics. Kanamori [133] did so to explain the ferromagnetism of nickel⁷. If one does restrict the choice of wave functions to either the t_{2g} or the e_g irreducible representations, i.e. their spherical harmonics, then the resulting interaction Hamiltonian remaining is

$$\begin{aligned}
 H_{\text{int}} = & U \sum_{i,a} n_{ia\uparrow} n_{ia\downarrow} + \frac{U'}{2} \sum_{i,\sigma} \sum_{a \neq \beta} n_{ia\sigma} n_{ib\bar{\sigma}} + \frac{1}{2} (U' - J) \sum_{i,\sigma} \sum_{a \neq b} n_{ia\sigma} n_{ib\sigma} \\
 & - \sum_{i,a \neq b} (J c_{ia\uparrow}^\dagger c_{ia\downarrow} c_{i,b\downarrow}^\dagger c_{ib\uparrow} - J' c_{ia\uparrow}^\dagger c_{ia\downarrow}^\dagger c_{ib\downarrow} c_{ib\uparrow}), \tag{1.43}
 \end{aligned}$$

where the intraorbital Hubbard U , interorbital U' and J/J' emerge as names for specific matrix elements of equation (1.39). Furthermore, a and b label the involved orbitals and σ the spin.

The Hamiltonian is rotationally invariant and this can be used [132]. First of all there are only two free parameters in this scheme as $J = J' \equiv J_{\text{H}}$ and $U' = U - 2J$. The former expression provides us with what we refer to as Hund's coupling J_{H} .

Furthermore, [132] describes the use of Casimir operators for e.g. the total spin \mathbf{S} to further simplify. If one follows true, a convenient form for the Hamiltonian in t_{2g}

⁷which is nontrivial to recognize as the mathematical “language”, as often in old papers, is quite different then the approach we choose here.

orbitals is

$$H_{\text{sym}} = (U - 3J_{\text{H}}) \frac{\hat{N}(\hat{N} - 1)}{2} - 2J_{\text{H}}\mathbf{S}^2 - \frac{J_{\text{H}}}{2}\mathbf{L}^2 + \frac{5}{2}J_{\text{H}}\hat{N}, \quad (1.44)$$

where the Hund's coupling enforcing Hund's rules, in particular maximizing total spin and angular momentum becomes extremely apparent. Here \hat{N} is the number operator for the total number of electrons.

All in all the equations tell us how to handle the Coulomb repulsion and how to compare it to other constituents like the crystal field splitting. Whenever one adds the need for multiple electrons and the energy scales are clearly hierarchical, then the Hund's rules are enforced by equation (1.44) for dominant Coulomb interaction or ignored if otherwise. Furthermore the equation dictates energies and multiplet structures for the local unperturbed Hamiltonian in the perturbation theory calculation of section 1.4.4, where we, however, approximate with Hund's rules purely for convenience.

A final, very important, remark needs to be made. How large is J_{H} in practice? While this could be calculated in principle, everything that influences the orbitals changes the calculation, hence experiments and/or ab-initio studies trying to include most effects are needed. As for the other topics we refer to the table 1.2. And we point to the following point of contention: As [132] analyzes, the scheme choice (i.e. way of writing down and simplifying) for the Coulomb interaction is important. Case in point: the thesis is concerned with a significant amount of studies using the Kanamori form for materials with a full set of d orbitals. Similarly the table 1.2 contains modeling for only t_{2g} ($10Dq = \infty$) and full d orbitals. These values of J_{H} are technically not the same objects. One should understand them (if not already doing so for other reasons) as rough estimates. Concluding we exemplify this with an example from [132]: Even though both e_g and t_{2g} lead to a Kanamori Hamiltonian,

their matrix elements and thus values for J_{H} are different:

$$U_{t_{2g}} = F^{(0)} + \frac{4}{49}F^{(2)} + \frac{36}{441}F^{(4)}, \quad (1.45)$$

$$J_{\text{H}}^{t_{2g}} = \frac{3}{49}F^{(2)} + \frac{20}{441}F^{(4)}, \quad (1.46)$$

$$U_{e_g} = F^{(0)} + \frac{4}{49}F^{(2)} + \frac{36}{441}F^{(4)}, \quad (1.47)$$

$$J_{\text{H}}^{e_g} = \frac{4}{49}F^{(2)} + \frac{15}{441}F^{(4)}, \quad (1.48)$$

where F are the Slater integrals introduced earlier.

1.4 Extended Kitaev-Heisenberg Model for Hard-Core Bosons

The purpose of this section is to write down the Hamiltonians covered in [6, 7], which is a direct extension of the one covered in [1] for the so called 90° scenario. We largely follow the explanations in [7]. If one needs additional information the 180° scenario of [1], which is analogous in large parts, is covered quite thoroughly in [134], even going over a more thorough incorporation of the Kanamori interaction. Additionally, similar models for slightly different scenarios pertaining to, e.g., the number of electrons involved have been around for a long time [135, 136].

1.4.1 Mott Insulator and Heisenberg Model

It is prudent to make a short detour. Consider the Hubbard model [137]

$$H = -t' \sum_{\langle i,j \rangle, \sigma} \left(c_{i,\sigma}^\dagger c_{j,\sigma} + h.c. \right) + U \sum_i n_{i,\uparrow} n_{i,\downarrow} \quad (1.49)$$

where t' is the hopping matrix element⁸, $c_{i,\sigma}^{(\dagger)}$ is the annihilation (creation) operator of an electron at site i with spin σ and U is the Hubbard repulsion (representing a simplified Coulomb repulsion). This famous model does not require a long introduction or discussion here, as this has been done elsewhere.

Our interest in this context is limited to the limit $t' \ll U$, which represents the Mott insulator [138]. In a Mott insulator the strong correlations of the electrons mediated by the Hubbard/Coulomb repulsion counter the hopping as double occupancy of energy levels becomes costly. In practice this leads to the opening of a (Mott) gap in the spectrum and insulating behavior due to localized electrons instead of the itinerant ones at $U = 0$. Mott insulators, the resulting “metal-insulator-transition” [139] and various consequences of these scenarios constitute an entire field of research.

For the present purpose one may restrict the relevant discussion to a small but important detail. What effectively happens if $t' \ll U$ holds (for half-filling)? A quick answer can be gained by employing perturbation theory, where the unperturbed Hamiltonian H^0 and perturbation V are represented by

$$H^0 = U \sum_i n_{i,\uparrow} n_{i,\downarrow} \quad \text{and} \quad V = -t' \sum_{\langle i,j \rangle, \sigma} \left(c_{i,\sigma}^\dagger c_{j,\sigma} + h.c. \right). \quad (1.50)$$

As the hopping acts on the bond between site i and j it is useful to restrict the discussion to this two-site problem and its pair states. For half-filling, the eigenstates are the single-occupied sites $|i, j\rangle = \{|\uparrow, \uparrow\rangle, |\uparrow, \downarrow\rangle, |\downarrow, \uparrow\rangle, |\downarrow, \downarrow\rangle\}$ at energy $E_g = E_i^0 + E_j^0 = 0$ and the double occupation on a site $|\uparrow\downarrow, \cdot\rangle$ and $|\cdot, \uparrow\downarrow\rangle$ at energy $E_e = U$. As $U > 0$ ⁹ the E_g states represent the ground state manifold, while E_e is separated by an energy gap. Standard degenerate perturbation theory yields an effective Hamiltonian

⁸emerges from the integral over the single-particle kinetic part of equation (1.38), thus caring about the position/overlap of involved orbitals

⁹attractive Hubbard models are tools for superconductivity but not reasonable here

in second order via

$$H_{\text{eff},\langle i,j \rangle} = |\alpha\rangle \langle \beta| \sum_{\gamma \notin \text{ground}} \frac{\langle \alpha|V|\gamma\rangle \langle \gamma|V|\beta\rangle}{E_{\alpha=\beta} - E_{\gamma}}, \quad (1.51)$$

but only for $|\downarrow, \uparrow\rangle$ and $|\uparrow, \downarrow\rangle$ (the others cannot gain energy because the Pauli principle blocks the hopping). Evaluating this resulting 2×2 problem results in

$$H_{\text{eff},\langle i,j \rangle} = -\frac{2t'^2}{U} \left(n_{i,\uparrow} n_{j,\downarrow} + n_{i,\downarrow} n_{j,\uparrow} - c_{i,\uparrow}^\dagger c_{i,\downarrow} c_{j,\downarrow}^\dagger c_{j,\uparrow} - c_{i,\downarrow}^\dagger c_{i,\uparrow} c_{j,\uparrow}^\dagger c_{j,\downarrow} \right). \quad (1.52)$$

The operators can be mapped onto spins via Pauli matrices $\boldsymbol{\sigma}$ and

$\mathbf{S}_i = \sum_{\sigma,\sigma'} c_{i,\sigma}^\dagger \boldsymbol{\sigma}_{\sigma,\sigma'} c_{i,\sigma'}$ [140]. This results in the structure of a Heisenberg model

$$H_{\text{eff},\langle i,j \rangle} = J \mathbf{S}_i \mathbf{S}_j + \text{const.} \quad (1.53)$$

with $J = \frac{4t'^2}{U}$ (thus antiferromagnetic).

1.4.2 Kugel-Khomskii Models

In that seminal paper Kugel and Khomskii [141] described a natural extension of the preceding discussion. If the degree of freedom on each site is not limited to a single level but rather a set of degenerate orbitals, the analogous strong-coupling perturbation theory calculation produces intriguing exchange interactions that then lift the orbital degeneracy as a potential driver of the Jahn-Teller effect.

Consider the processes sketched in figures 1.9a) and b). In the case of the previously discussed Hubbard model with one energy level the perturbation theory describes a virtual hopping back and forth, which in this simple scenario can only happen if the spins are anti-aligned due to the Pauli principle. Moreover the spin directions begin to influence each other because both $|\uparrow, \downarrow\rangle \rightarrow |\uparrow, \downarrow\rangle$ and $|\uparrow, \downarrow\rangle \rightarrow |\downarrow, \uparrow\rangle$ can happen. The connection of the spin sectors results in an effective spin model,

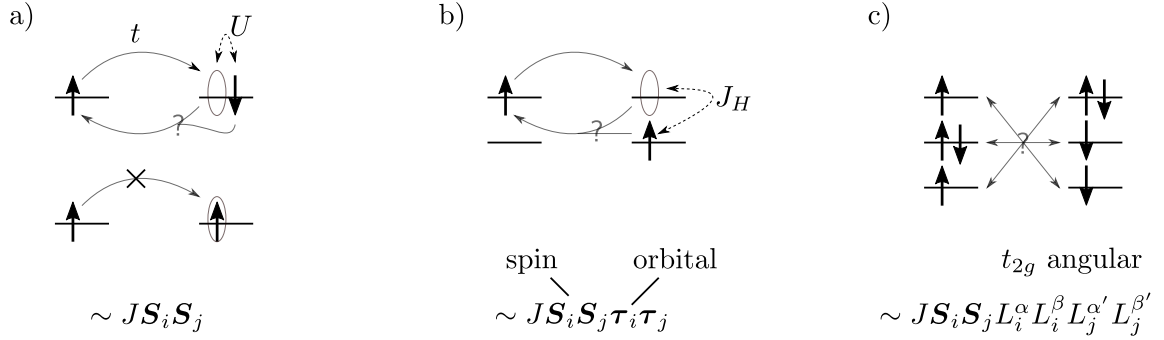


Figure 1.9. Sketches of virtual hopping processes in various models involving a dominant on-site Coulomb repulsion: a) represents a simple Hubbard model. This so called direct exchange cannot happen for both spins being in the same state (here up) due to the Pauli principle. Thus it results in an antiferromagnetic Heisenberg interaction. As the spins can effectively switch places the up and down spin sectors connect, resulting in the spin interaction. b) For orbital degeneracy, i.e. the original Kugel-Khomskii model the on-site interactions can become more complex (represented by the Hund’s coupling J_H), the restriction to the antiferromagnetic exchange is lifted and the orbital degree of freedom becomes involved. c) In our Kugel-Khomskii model the geometry dictates nontrivial hopping processes and the orbital degree of freedom can be mapped to an angular momentum as it represents a t_{2g} orbital.

which is antiferromagnetic due to the anti-aligned spins.

For two degenerate orbitals, e.g. e_g , one needs to account for a few things. For one, the Hamiltonians might change. Coulomb interaction in a multi-orbital scheme is more involved and might need to be covered by, e.g., a Kanamori Hamiltonian as introduced in equation (1.43). As a result, Hund’s coupling and nontrivial on-site eigenstates might need to be accounted for. Similarly the hopping might become complicated as discussed in the next example. Furthermore, different electron configurations might lead to nontrivial results.

Importantly, there are more possibilities when it comes to effective exchange interactions. Obviously a ferromagnetic exchange is not forbidden anymore due to the spins being able to occupy different orbitals. More general, the interplay, i.e. nonvanishing matrix elements in the perturbation theory, can not only involve changes of spin degree of freedom as before, but also deals with the orbital degree of freedom

or potentially a combination of both!

The resulting Hamiltonian and hence the physics in the system might therefore involve spin and orbitals and can result in (dis-)ordered states in one or both of the degrees of freedom. This can provide inherently new physics. Due to the importance of this line of thought for modeling materials and the plethora of shapes and forms of setups out there, a lot of different models analogous to this involving orbital degeneracy, material inspired hopping and Mott-like perturbation theory have been proposed and studied, see e.g. [109, 136]. These models fall under the umbrella of “Kugel-Khomskii models”.

A seminal result of the Kugel-Khomskii models, at least for this thesis, is the proposal that one could potentially realize Kitaev’s famous honeycomb model for t_{2g}^5 (5 electrons or 1 hole) orbital configurations with hopping mediated by edge-sharing ligand octahedra [47]. The central point is that Kitaev’s model requires bond direction dependent exchange interactions and due to orbitals becoming involved, one now has added an ingredient into the Hamiltonian that cares about a direction in position space via the geometry of the material. Trying to describe real materials, which of course can get increasingly complicated when one has to account for every potentially noteworthy exchange process, one naturally arrives at Kitaev-Heisenberg models and extensions of those [48–50].

The model we deal with in this thesis fits exactly into this line of thought. With a t_{2g}^4 electron configuration and novel hopping processes dictated by geometry (in fact the equivalent of the t_{2g}^5 Kitaev-Heisenberg materials) as sketched in figure 1.9c), we deal with a quite involved spin-orbital exchange interaction. Additionally one may recall that t_{2g} orbitals translating to angular momentum operators (cf. equations (1.20)-(1.22)), which is not the case for e_g . Hence we must, as is a central point for the original t_{2g}^5 Kitaev-Heisenberg models, deal with spin-orbit coupling, which further influences the S and L degrees of freedom in the effective resulting Kugel-Khomskii type Hamiltonian.

1.4.3 Superexchange and Geometry

In a material like $\text{Ag}_3\text{LiRu}_2\text{O}_6$ the derivation of effective Mott physics is similar but obviously more involved when it comes to computation. First of all, one now has to involve three orbitals (assuming the crystal field splitting is large enough), namely the t_{2g} orbitals $|xy\rangle$, $|xz\rangle$ and $|yz\rangle$. Secondly, one needs to account for 4 electrons (or 2 holes) per site instead of only a single one. Here the assumption of a dominant Hund's coupling aligning all spins is useful, shrinking the Hilbert space from 15 possible t_{2g}^4 configurations per site to a more manageable 6. If one does not care whether all unpaired spins point up or down, there are 3 configurations to be concerned about.

The Hund's coupling assumption is based on the energy levels of the Kanamori Hamiltonian, which in a multi-orbital t_{2g} model governs the role of on-site interactions and thus the unperturbed Hamiltonian H^0 . Due to the Kanamori Hamiltonian being a local quantity, the energies of site i and j are simply added like in the previous example. The main difference lies in the fact that the pair states are now $d_i^4 d_j^4 \rightarrow d_i^3 d_j^5 \rightarrow d_i^4 d_j^4$, or at least what remains of, e.g., d^4 after boiling it down to t_{2g}^4 via dominant crystal field and the aforementioned 6 configurations via Hund's coupling.

For the choice of convenience, it can be an option to do the calculations with two holes in t_{2g}^4 instead of four electrons, at least in practice when, e.g., calculating the hopping matrix elements of the perturbation theory or writing down the Kanamori eigenstates of H^0 . This should be kept in mind when handling the Hamiltonians involved, as there are a few points where this matters (not only here, but also when considering the sign of spin-orbit coupling later). But if one does not mix things up, the difference is only superficial. Given the straightforward nature of the calculations and the fact that most of it is covered elsewhere [6, 7, 134], we will handle this with a *laissez faire* attitude and neglect to mention this detail from here on.

We now know what changes for the on-site H^0 , but what happens to the hopping when going to the material inspired model? Recall figure 1.1b): In the compound the Ruthenium sites form a honeycomb. Each site is surrounded by ligand octahedra. These octahedra share edges. Each of the three types of bonds in the honeycomb can be connected to sharing a different edge (spatially) of the octahedra. Now consider that in each octahedron, the orbital wave functions are represented by the t_{2g} orbitals shown in figure 1.2.

As a result, what happens for a pair of edge-sharing octahedra in a given bond direction can be schematically handled as shown in figure 1.10. Before we do this we should recall that given the structure of the t_{2g} orbitals in figure 1.10 and the honeycomb lattice of Ruthenium in the material itself (cf. figure 1.1), there are three distinct bond directions and the orbitals switch roles when going from one bond type to another. Therefore we introduce $a/b/c$ as interchangeable orbital directions, where c represent the orbital in bond direction, i.e. $|xy\rangle$ in figure 1.10.

The orbitals in c direction point directly to each other. Consequently a direct hopping process between neighboring c orbitals can be feasible. The Hamiltonian would look like the hopping terms of equation (1.49), which is why we chose the nomenclature fitting to this discussion.

Not as intuitive but pretty well established, going back to analogous processes in [142], is the possibility of ligand mediated hopping¹⁰ or “superexchange”. The geometry here is such that hybridization between transition-metal d orbital and ligand/oxygen p orbital may be significant, leading to a nonzero overlap matrix element or hopping t_{pd} . The exchange process is not straightforward as one has to account for the Coulomb interaction (or at least Hubbard equivalent) on the TM (and technically, but usually not importantly ligand ion) and a new variable: the energy difference between TM d orbital and oxygen p orbital, which is called charge-transfer

¹⁰Often but not necessarily the ligand is oxygen and one talks about oxygen mediated hopping as a surrogate expression.

gap Δ_{CT} .

Detailed explanations [85] and calculations [81] are left to literature. One can find that the exchange process is technically quite involved, but one may simplify the situation depending on the dominance of either Mott gap or charge transfer gap. In the $4d/5d$ transition metals we are interested in, the simplification is not controversial¹¹ and the superexchange can be handled like a direct $d - d$ hopping with

$$t = \frac{t_{pd}^2}{\Delta_{\text{CT}}}. \quad (1.54)$$

This is however a topic that should be kept in mind. In $3d$ setups for example the significance can change as the charge-transfer gap is smaller [143]. Additionally, the trigonal crystal field introduced into later calculations can modify the effective importance of the process. In fact this is discussed in [144] for the related d^5 model paired with discussions for $\alpha\text{-RuCl}_3$ and Na_2IrO_3 . The paper also tries to quantify other simplifications that are usually made, like $t_{2g} - e_g$ processes, which have been mentioned as a possible motivation for different parameter signs in the very early Kitaev-Heisenberg model days [49]. Similarly one should revisit this topic if the geometry becomes important for another reasons, e.g. Floquet engineering, which was done in this kind of setup in [134, 145, 146].

If one accounts for different orbitals on each site of the oxygen in this geometry (cf. figure 1.10), one can write down the complete hopping Hamiltonian of this geometry along a bond c connecting lattice site i and j as

$$H^{(c),90^\circ} = \sum_{\langle i,j \rangle_{c,\sigma}} \left[t \left(a_{i,\sigma}^\dagger b_{j,\sigma} + b_{i,\sigma}^\dagger a_{j,\sigma} \right) - t' c_{i,\sigma}^\dagger c_{j,\sigma} + \text{h.c.} \right], \quad (1.55)$$

where the later term denotes the direct hopping explained before and 90° refers to the geometry of the superexchange.

The ignorance of the direct exchange in the name is historical. Naively one would

¹¹Mainly because we later let the exchange parameter quite free and a change in t is not critical.

expect the superexchange to dominate [81]. In particular, the first proposal of this type of model directly connected to the thesis focus [1] ignores it outright. Of course everything depends on the environment and things like e.g. the orbital size (cf. discussion connected to figure 1.3) or nature of the ligand can change the size of the exchanges.

We conclude the discussion with a side note: Ca_2RuO_4 has been frequently mentioned in this thesis as a related topic. In fact, the original paper discussing the excitonic magnetism physics at the center of the thesis [1] is split in half between the discussion of Ca_2RuO_4 and materials of similar structure (e.g. ABO_3 perovskites, where B is the TM in of interest) and the models as discussed above (e.g. ABO_2 delafossite mineral group or A_2BO_3). The main difference in the former case is that the structure does not consist of edge-sharing octahedra forming a honeycomb lattice, but rather corner-sharing octahedra forming a square lattice. The resulting superexchange geometry and Ca_2RuO_4 are sketched in figure 1.11 and result in a slightly different hopping Hamiltonian

$$H^{(c),180^\circ} = \sum_{\langle i,j \rangle_{c,\sigma}} \left[t \left(a_{i,\sigma}^\dagger a_{j,\sigma} + b_{i,\sigma}^\dagger b_{j,\sigma} \right) + \text{h.c.} \right]. \quad (1.56)$$

One can easily gauge that Ca_2RuO_4 can be quite distorted (and not trigonally), which is its own point of discussion.

Yet, some observations and results might be transferable both ways if they do not particularly rely on the exact form of the exchange interaction, but rather emerge, e.g., from the atomic physics picture of ruthenium.

1.4.4 The Kugel-Khomskii Type Hamiltonian of Interest

The last sections have laid the necessary ground work for this calculation. If deemed insufficient, one might consider the very similar calculation in [134].

As described, one needs to write down the d^4 , i.e. t_{2g}^4 states and use second order perturbation theory with H^0 being the Kanamori Hamiltonian and the 90° degree Hamiltonian of equation (1.55) as a perturbation, effectively inducing $d_i^4 d_j^4 \rightarrow d_i^3 d_j^5 \rightarrow d_i^4 d_j^4$ processes. It was also mentioned that restricting the Hilbert space of the Kanamori Hamiltonians by assuming a dominant Hund's coupling significantly shortens the calculation, as every on-site term becomes diagonal and the energy denominator in perturbation theory becomes $U_{\text{eff}} \equiv U$. As a rather free parameter study follows later, this kind of assumptions is as old as the model [48] and not known to be problematic if one is not interested in putting concrete values into the calculation.

One should mention that [134] incorporates J_H more thoroughly in the very similar Ca_2RuO_4 where there is direct motivation for concrete values because the discussion is centered on what kind of model is more successful for the material in question.

Simplified, the calculation is straightforward and explained in more detail in [6, 7]. One finds

$$H = \sum_c \left(H_{t^2}^{(c)} + H_{t'^2}^{(c)} + H_{tt'}^{(c)} \right), \quad (1.57)$$

with

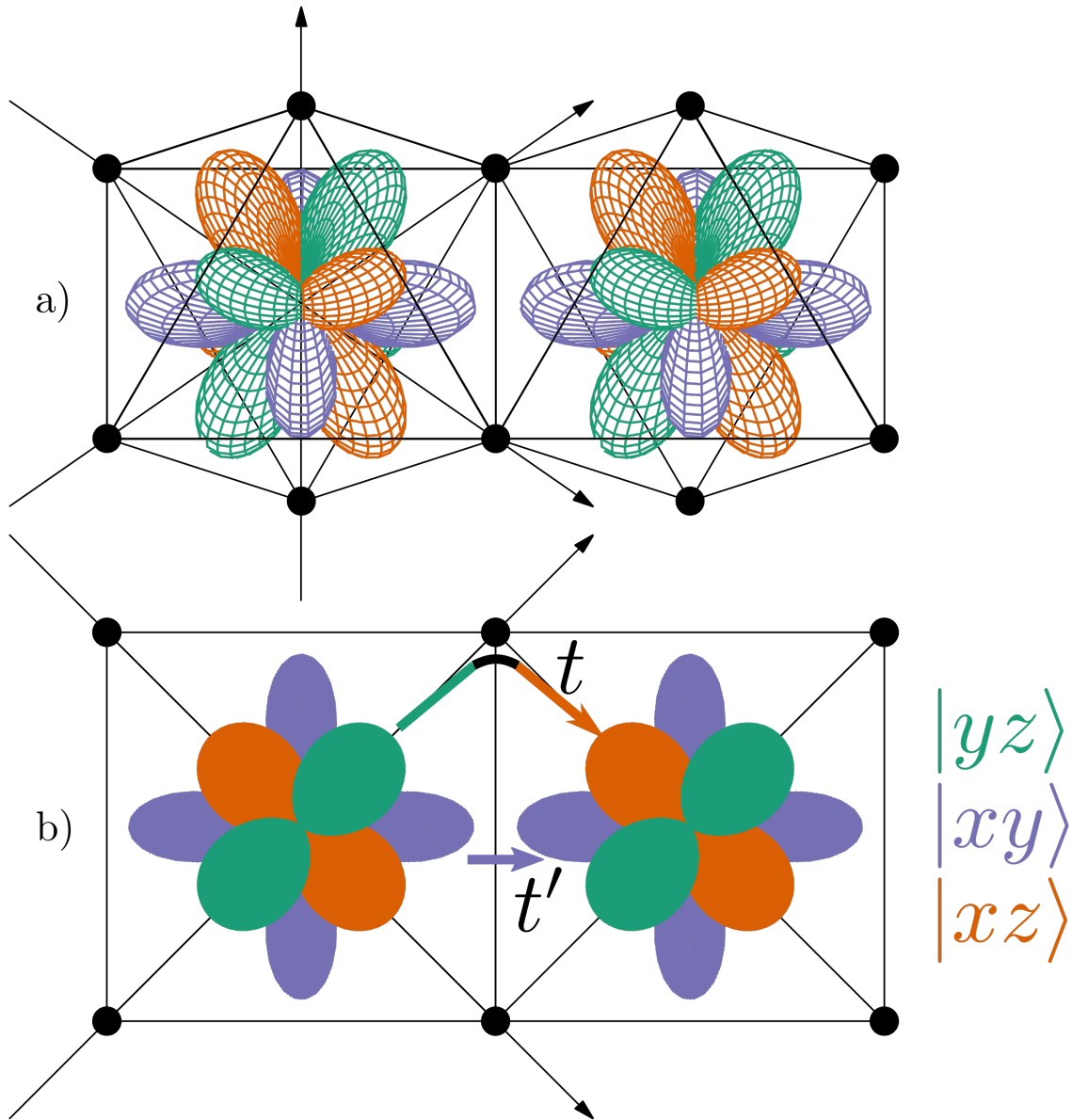


Figure 1.10. a) Corner-sharing octahedral structure with t_{2g} orbitals. b) Top-down view of the geometry: One orbital here exemplified by the $|xy\rangle$ orbital for bond in $[x, y, z] = [1, 1, 0]$ direction is in direct arrangement with the bond and thus possibly involved in direct overlap with the same orbital for the neighboring site. The other orbitals are aligned with the ligands and can partake in superexchange via them, leading to an interorbital exchange.

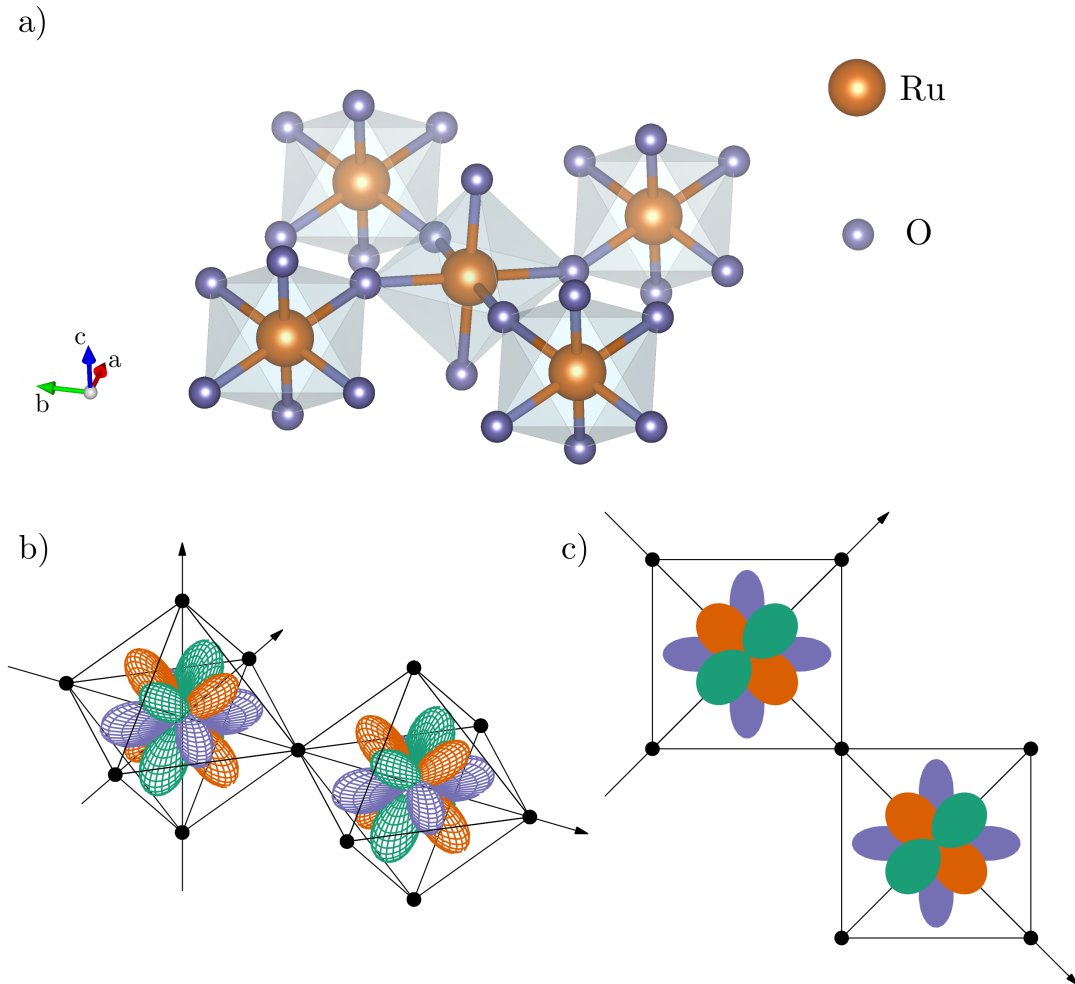


Figure 1.11. Superexchange geometry for the 180° geometry (corner-sharing octahedra) as employed for Ca_2RuO_4 : a) shows a VESTA [87] visualization of the crystal structure of experimental measurements in [147]. One can surmise the square lattice and corner-sharing structure (even though Ca_2RuO_4 can be quite away from the idealized structure due to distortions). b) illustrates the idealized structure of the superexchange geometry with the t_{2g} orbitals. c) is a top-down view of the scenario. Two of the three orbitals can superexchange via the corner-shared oxygen, while the third, here the green $|yz\rangle$ is almost orthogonal to the bond direction and therefore deemed inactive.

$$\begin{aligned}
 H_{t^2}^{(c)} &= \frac{t^2}{U} \sum_{\langle i,j \rangle_c} \left[\left(\mathbf{S}_i \mathbf{S}_j + 1 \right) \left((1 - N_{A,i})(1 - N_{B,j}) + (1 - N_{B,i})(1 - N_{A,j}) \right. \right. \\
 &\quad \left. \left. + A_i^\dagger B_i A_j^\dagger B_j + B_i^\dagger A_i B_j^\dagger A_j \right) \right. \\
 &\quad \left. - \left((1 - N_{A,i}) + (1 - N_{B_i}) + (1 - N_{A,j}) + (1 - N_{B,j}) \right) \right], \\
 H_{t'^2}^{(c)} &= \frac{t'^2}{U} \sum_{\langle i,j \rangle_c} \left[\left(\mathbf{S}_i \mathbf{S}_j + 1 \right) (1 - N_{i,C})(1 - N_{j,C}) - \left((1 - N_{i,C}) + (1 - N_{j,C}) \right) \right], \\
 H_{tt'}^{(c)} &= - \frac{tt'}{U} \sum_{\langle i,j \rangle_c} \left[\left(\mathbf{S}_i \mathbf{S}_j + 1 \right) \left(C_i^\dagger B_i A_j^\dagger C_j + C_i^\dagger A_i B_j^\dagger C_j + A_i^\dagger C_i C_j^\dagger B_j + B_i^\dagger C_i C_j^\dagger A_j \right) \right],
 \end{aligned} \tag{1.58}$$

where $A/B/C$ refer to the 3 discussed orbital configurations, meaning $A = bc$ with the lowercase operators denoting holes in the orbitals.

For the subsequent incorporation of spin-orbit into the model one needs to express the orbital degrees of freedom as angular momentum operators, which one knows is feasible due to the nature of t_{2g} . As $A/B/C$ consist of fermion operators $a/b/c$, one can easily verify that

$$L^x = i (B^\dagger C - C^\dagger B), \tag{1.59}$$

$$L^y = i (C^\dagger A - A^\dagger C), \tag{1.60}$$

$$L^z = i (A^\dagger B - B^\dagger A), \tag{1.61}$$

carry the correct (pseudo-)angular momentum commutation relations. There is no difference between real and pseudo angular momentum in the Hamiltonian as any minus sign is canceled by the at least pairwise appearance of operators.

Neglecting a constant energy shift, the Hamiltonian in spin-orbital form can be written as:

$$H^{(c)} = \sum_{\langle i,j \rangle_c} \left[(\mathbf{S}_i \mathbf{S}_j + 1) \left(\frac{t^2}{U} O_{ij}^{(c)} - \frac{tt'}{U} P_{ij}^{(c)} + \frac{t'^2}{U} Q_{ij}^{(c)} \right) + \frac{t^2 - t'^2}{U} ((L_i^z)^2 + (L_j^z)^2) \right], \quad (1.62)$$

$$O_{ij}^{(c)} = (L_i^x L_j^y)^2 + (L_i^y L_j^x)^2 + L_i^y L_i^x L_j^y L_j^x + L_i^x L_i^y L_j^x L_j^y, \quad (1.63)$$

$$P_{ij}^{(c)} = L_i^x L_i^z L_j^z L_j^y + L_i^y L_i^z L_j^z L_j^x + L_i^z L_i^x L_j^y L_j^z + L_i^z L_i^y L_j^x L_j^z, \quad (1.64)$$

$$Q_{ij}^{(c)} = (L_i^z)^2 (L_j^z)^2. \quad (1.65)$$

1.4.5 Influence of Spin-Orbit Coupling and Singlet-Triplet Model

Consider the Hamiltonian in equation (1.62): The Hamiltonian consists of total spin \mathbf{S} and orbital related angular momentum components $L^{x/y/z}$, or in other words it is a function $H = H(S, L)$. As explained previously, the total spin is fixed by the low-spin d^4 configuration and results in $S = 1$, while the angular momentum stems from t_{2g} and is therefore $L = 1$.

The influence and size of spin-orbit coupling has been introduced in a general context in section 1.2. As the spin-orbit interaction intertwines the spin and orbital degree of freedom, it is apparent that the concrete discussion of its effect needs to follow at this point.

In the original approach to our model [1], Khaliullin cites very rough estimates of spin-orbit coupling $\lambda = 50 - 200$ meV and superexchange $4t^2/U = 50 - 100$ meV. The former is compatible with the experimental data of table 1.2. The latter we can gauge as reasonable (at least on the lower end) based on citations of estimates and own ab-initio data in [13] for Ca_2RuO_4 ($U \approx 2$ eV and $t \approx 0.1 - 0.2$ eV).

For this reason one may reasonably reformulate the states in a picture of the

spin-orbit eigenstates and even propose an effective Hamiltonian treatment via perturbation theory as a first approach. We introduce these concepts in the following sections.

1.4.5.1 Spin-Orbit Eigenstates and the Low-Energy Subspace

As discussed in previous sections, LS- or Russel-Saunders coupling might not be a perfectly achieved limit given the material estimates of Hund's coupling J_H and spin-orbit interaction ξ in table 1.2, but it is the reasonable first guess. It is more importantly perfectly compatible with the Kugel-Khomskii type Hamiltonian $H(S, L)$ that combines spin intrinsically due to the approximation of the multiplet structure.

LS coupling introduces the total angular momentum $\mathbf{J} = \mathbf{S} + \mathbf{L}$ resulting in the splitting $J = 0, 1, 2$. Given the spin-orbit Hamiltonian (1.36) and the usual diagonalization trick $\mathbf{L}\mathbf{S} = \frac{1}{2}(\mathbf{J}^2 - \mathbf{L}^2 - \mathbf{S}^2)$, writing down the eigenstates and energies of the spin-orbit coupling is a trivial exercise, that is usually done in standard quantum mechanics lectures. The result is visualized in figure 1.12a).

The ground state of the spin-orbit coupling is given by $J = 0$ at energy $E = -2\lambda$. Above this there is a $J = 1$ triplet separated by an energy gap of λ , i.e. at energy $E = -\lambda$, and a $J = 2$ quintet that is split up by an even larger gap of 2λ (energy $E = \lambda$). If spin-orbit coupling is dominant or at least comparable to the superexchange energy $4t^2/U$, one may be inclined to use the fact that the gap between singlet and triplet is smaller to restrict the calculations on this subspace, which due to its four states encompasses not even half of the Hilbert space of the total problem. This is exactly what is described hereinafter.

In fact, this idea is very established. In the entire field of d^5 equivalent to our problem, Kitaev-Heisenberg models in materials such as α -RuCl₃, a central point of the interest is that spin-orbit coupling for a single hole in t_{2g} ($S = 1/2$ and $L = 1$) creates a $j = 1/2$ pseudospin in analogy to $J = 0$ here [47]. This then represents the

necessary degree of freedom for Kitaev's model [4], which bases its ideas on spin-1/2 for the description via Majorana fermions and gauge choices.

1.4.5.2 Projection onto the Singlet-Triplet Model

Here we derive the effective Hamiltonian for the $J = 0/1$ singlet-triplet low-energy subspace. Obviously the calculation is based on the usual (quasi-)degenerate perturbation theory, which is here employed up to first order:

$$\begin{aligned} H_{\text{eff},\alpha\beta} &= \delta_{\alpha\beta} E_\alpha + \sum_c \langle \alpha | H^{(c)} | \beta \rangle \\ &= \delta_{\alpha\beta} \sum_i E_{\alpha_i} + \sum_c \sum_{\langle i,j \rangle_c} \langle \alpha_i \alpha_j | H_{\langle i,j \rangle_c}^{(c)} | \beta_i \beta_j \rangle \end{aligned} \quad (1.66)$$

with the Kugel-Khomskii Hamiltonian H (cf. equation (1.62)) serving as a perturbation on the spin-orbit eigenstates, which are labeled $|\alpha\rangle$ and $|\beta\rangle$ for the entire lattice and carry a subscript if they describe a single site. $H_{\langle i,j \rangle_c}^{(c)}$ consists of spin and angular momentum operators. The Hilbert space is spanned by their eigenstates labeled by their projection onto the z-axis $|m_S, m_L\rangle$ ($m_S, m_L \in \{-1, 0, 1\}$) with

$$\begin{aligned} S_\pm |S, m_S\rangle &= \sqrt{S(S+1) - m_S(m_S \pm 1)} |S, m_S \pm 1\rangle, \\ S_z |S, m_S\rangle &= m_S |S, m_S\rangle, \\ \mathbf{S}^2 |S, m_S\rangle &= S(S+1) |S, m_S\rangle, \end{aligned} \quad (1.67)$$

where ($S_\pm = S_x \pm iS_y$) and \mathbf{L} analogous with eigenstates $|m_L\rangle$. Applying S and L operators on the eigenstates of the spin-orbit Hamiltonian, which are labeled by $|J, m_J\rangle$ leads to transitions in the energy scheme via

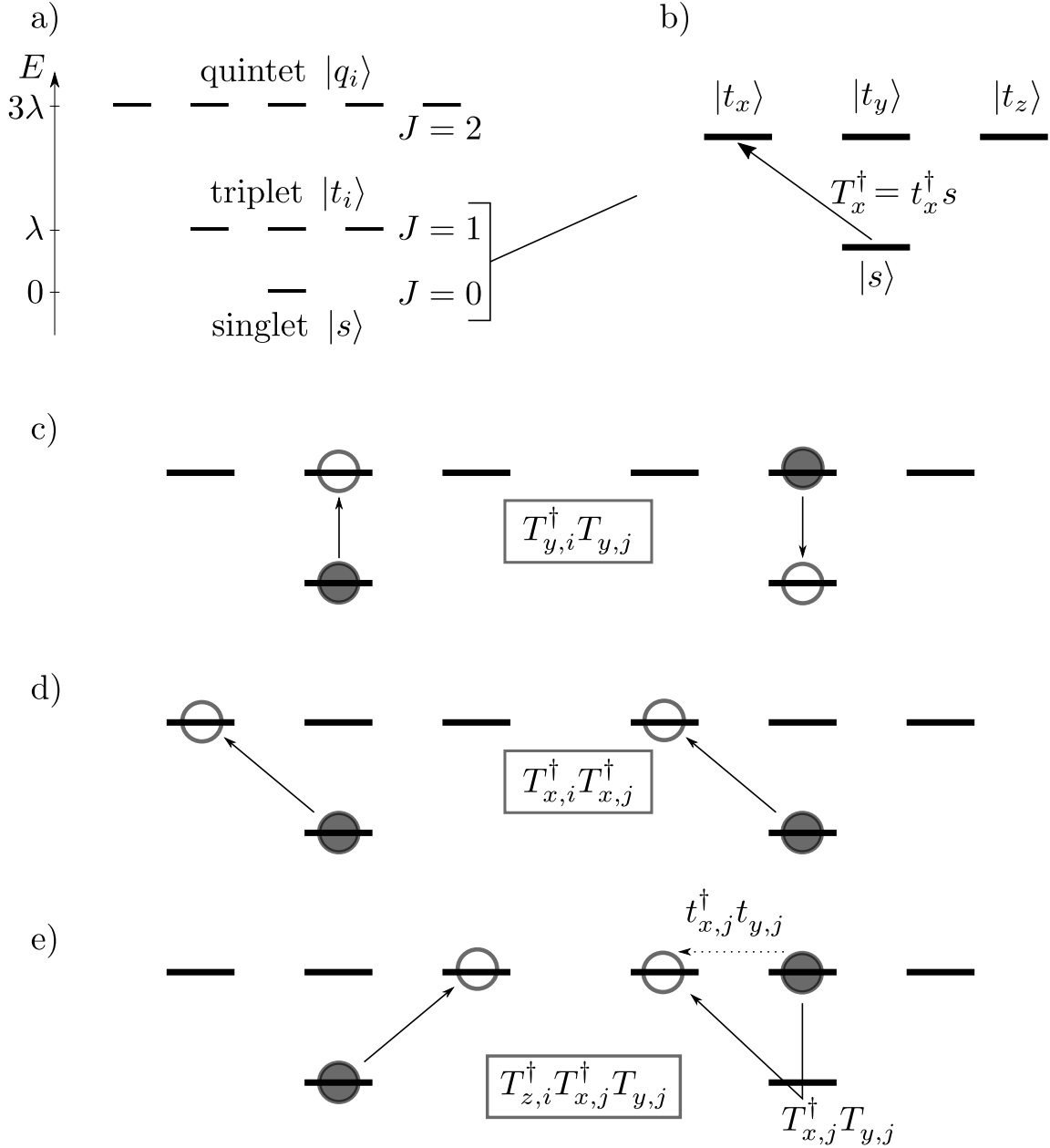


Figure 1.12. a) Energy levels resulting from LS-coupling of $S = 1$ and $L = 1$: the ground state is a $J = 0$ singlet. A constant shift for the later use of $\lambda \sum_i n_i$ has been incorporated. b) Low-energy subspace and resulting singlet-triplet model: the triplet states are chosen as specific linear combinations representing Cartesian components. Singlet s and triplet $t_{x/y/z}$ represent the energy levels. The triplon T , which is the degree of freedom involved in the Bose-Einstein condensation form of the Hamiltonian h_2 , represents the transition between them and therefore an exciton. c)-e) Schematic view of interaction processes of the Kugel-Khomskii Hamiltonian for sites i and j : hopping c) and pair creation d) process, which can also exchange flavor for the tt'/U terms or in higher orders represented by in e). One can note that on-site $t^\dagger t$ yields the same matrix elements as $T^\dagger T$.

$$\begin{aligned}
 S_{\pm} |J, m_J\rangle &= S_{\pm} \sum_{m_L=-1}^1 \sum_{m_S=-1}^1 \langle m_L, m_S | J, m_J \rangle |m_L, m_S\rangle, \\
 &= \sum_{m_L=-1}^1 \sum_{m_S=-1}^1 \sqrt{S(S+1) - m_S(m_S \pm 1)} \langle m_L, m_S | J, m_J \rangle |m_L, m_S \pm 1\rangle, \\
 &= \sum_{\tilde{j}} c_{\tilde{j}} |\tilde{J}, m_{\tilde{j}}\rangle,
 \end{aligned} \tag{1.68}$$

where $\langle m_L, m_S | J, m_J \rangle$ are the Clebsch-Gordan coefficients and $c_{\tilde{j}}$ are constants (involving Clebsch-Gordan coefficients and factors needed for the linear combinations building the eigenstates of $|J, m_J\rangle$). The other operators, S_z and any L type, also induce transitions analogously.

For the matrix elements of the first order the calculation consists of evaluations of matrix elements of e.g. this form:

$$\langle \alpha_i \alpha_j | H_{\langle i, j \rangle}^{(c)} | \beta_i \beta_j \rangle \stackrel{\text{e.g.}}{\approx} \langle \alpha_i \alpha_j | \mathbf{S}_i \mathbf{S}_j L_i^x L_i^y L_j^x L_j^y | \beta_i \beta_j \rangle = \langle \alpha_i | \mathbf{S}_i L_i^x L_i^y | \beta_i \rangle \langle \alpha_j | \mathbf{S}_j L_j^x L_j^y | \beta_j \rangle. \tag{1.69}$$

The calculation is straightforward in the $|m_S, m_L\rangle$ basis. There are 9 possible eigenstates. Every operator is defined by a 9×9 matrix (or two 3×3 matrices and a tensor product) via equations (1.67). Every $|J, m_J\rangle$ eigenstate is a linear combination $|m_S, m_L\rangle$ states with Clebsch-Gordan coefficients (cf. equation (1.68)) and thus a simple predefined vector.

Everything necessary for this calculation can therefore simply be handled by matrix and matrix-vector multiplication. The task reduces to simple bookkeeping that is, in our practical approach, handled by a Mathematica script going through a list of operators and adding the results. Any attempt to include the $J = 2$ states (or quintets q_i) can be trivially undertaken using more vectors in the states, i.e. $|\alpha_i\rangle$. For the current model this was never done due to lack of interest, especially because later introduce Monte-Carlo schemes can also trivially include the Hamiltonian $H(S, L)$

without the perturbation theory projection onto $J = 0/1$. Also, the pair states of singlet and triplet provide a 16×16 matrix, of which in the course of this thesis only a few terms turn out to be essential, and quintets would bloat the problem to a 81 dimensional Hilbert space.

A last comment remains to be made: for the singlet and triplet states we do not use the naive $|J, m_j\rangle$ choices in practice, but rather linear combinations (at least in the degenerate triplet) that represent the Cartesian vector components following [1]:

$$|s\rangle = \frac{1}{\sqrt{3}} (|1, -1\rangle - |0, 0\rangle + |-1, 1\rangle), \quad (1.70)$$

$$|t_x\rangle = \frac{1}{2i} (|1, 0\rangle - |0, 1\rangle + |-1, 0\rangle - |0, -1\rangle), \quad (1.71)$$

$$|t_y\rangle = \frac{1}{2} (-|1, 0\rangle + |0, 1\rangle + |-1, 0\rangle - |0, -1\rangle), \quad (1.72)$$

$$|t_z\rangle = \frac{i}{2} (|1, -1\rangle - |-1, 1\rangle), \quad (1.73)$$

where s is the $J = 0$ singlet state and t_i represents the $J = 1$ triplet. For a given site i the possible states are therefore $|\alpha_i\rangle \in \{|s\rangle, |t_x\rangle, |t_y\rangle, |t_z\rangle\}$. Standard evaluation of the matrix elements of perturbation theory can commence.

The resulting effective Hamiltonian for the singlet-triplet system has the general form [1]

$$H_{\text{eff}} = \lambda \sum_i n_i + \sum_c \sum_{\langle i,j \rangle_c} [h_2 + h_3 + h_4]_{\langle i,j \rangle_c}^{(c)}, \quad (1.74)$$

where $n_i = \sum_{\tau=x,y,z} t_{\tau,i}^\dagger t_{\tau,i}$, $t_{\tau,i}^\dagger$ creates a triplet state of type τ at site i and $h_2/h_3/h_4$ label the terms involving two, three and four triplet states respectively. There are two small caveats one might discuss here. The $\lambda \sum_i n_i$ represents the zeroth order contribution. Technically (compare with $J = 0$ and $J = 1$ eigenenergies) a constant energy shift is discarded to bring the operator into this form. The form itself is chosen because it looks exactly like a standard chemical potential, which is useful as the mechanism behind the later discussed triplon condensation then directly relate

to standard Bose-Einstein condensation language. Furthermore the obvious question of there not being h_1 terms can be raised. The answer lies in the on-site hard-core constraint

$$n_s + n_{t_x} + n_{t_y} + n_{t_z} = 1, \quad (1.75)$$

which has to hold (a remnant of the orbital configurations $A/B/C$ of which only one can exist on a given site). Hence h_1 terms are h_3 terms and energy shifts, as in every h_1 Hamiltonian one of the sites has to remain a singlet and the formula above can be inserted.

It is also clear that the Hamiltonian presents a hierarchical structure based on the triplet state count due to the chemical potential binding them to an energy cost λ of the spin-orbit coupling strength. When λ is dominant the singlet state is the ground state. For a slightly less dominant λ the h_2 (cf. h_1 discussion) term becomes active, which, as we will see, enables the admixture of triplets into the ground state. If then at some point enough triplet contribution exists, h_3 and h_4 gain relevancy.

The h_3 and h_4 terms have therefore been ignored in past analysis [6]. In this thesis we try to change that. While the perturbation theory results exist [7], the way the results have been written down in the past (in terms of e.g. quadrupole operators like in [1]), the terms are not directly useful, and errors can be made (and have been in the way they were written down in the past). Here and in [5] we try to remedy this and provide correct and directly useful Hamiltonians.

The full results of the perturbation theory in terms of singlet-triplet pair states as directly used in our simulations (at least in the current versions) is presented in figure 1.13.

The h_2 terms can simply be read off, resulting in

$$\begin{aligned}
 [h_2]_{\langle i,j \rangle}^{(c)} = & \frac{t^2}{U} \left[-\frac{5}{6} \left(s_i^\dagger t_{x,i} s_j^\dagger t_{x,j} + s_i^\dagger t_{y,i} s_j^\dagger t_{y,j} \right) + \frac{2}{3} \left(t_{x,i}^\dagger s_i s_j^\dagger t_{x,j} + t_{y,i}^\dagger s_i s_j^\dagger t_{y,j} \right) + h.c. \right] \\
 & - \frac{tt'}{U} \left[-\frac{1}{6} \left(s_i^\dagger t_{x,i} s_j^\dagger t_{y,j} + s_i^\dagger t_{y,i} s_j^\dagger t_{x,j} \right) + \frac{1}{3} \left(s_i t_{x,i}^\dagger s_j^\dagger t_{y,j} + t_{y,i}^\dagger s_i s_j^\dagger t_{x,j} \right) + h.c. \right] \\
 & + \frac{t'^2}{U} \left[-\frac{1}{6} \left(s_i^\dagger t_{x,i} s_j^\dagger t_{x,j} + s_i^\dagger t_{y,i} s_j^\dagger t_{y,j} \right) + \frac{1}{6} \left(t_{x,i}^\dagger s_i s_j^\dagger t_{x,j} + t_{y,i}^\dagger s_i s_j^\dagger t_{y,j} \right) \right. \\
 & \quad \left. - \frac{2}{3} s_i^\dagger t_{z,i} s_j^\dagger t_{z,j} + \frac{2}{3} t_{z,i}^\dagger s_i s_j^\dagger t_{z,j} + h.c. \right]. \tag{1.76}
 \end{aligned}$$

For the purpose of building and handling a simulation of this system one can stop reading here. Everything is technically established in the nomenclature of s and t states. However, for further analysis and interpretation, some different formulations can be useful. First and foremost one can borrow from the language of excitons [148], namely one can formulate everything in terms of triplon annihilation $T = s^\dagger t$ and creation $T^\dagger = t^\dagger s$ operators. Note that, for the effective model studied here, this merely represents a convenient way to analyze the model. The emerging exciton and its behavior in a t_{2g}^4 Hubbard model, of which we only represent a small part via perturbation theory, is its own topic of interest [149, 150] (notably, the Van Vleck-type triplons here might smoothly connect to the large SOC simple relativistic band insulator [151]). We hereinafter use “triplet” for the $J = 1$ states t and “triplon” for the excitons. While [148] also covers singlet-triplet systems explicitly, it also presents a way to find the equivalence to what one would more naively understand as excitons, i.e. spontaneous coherence between valence and conduction band. For this purpose one can for example consider Falicov-Kimball type models where two types of electrons (let’s call them α and β) exist separated by an energy gap. The exciton, which can arise due to various admixture terms, at least if feasible conditions exist, is then represented by a non-vanishing $\langle \alpha^\dagger \beta \rangle$.

1. Introduction

pair states $ k, j\rangle$	$ s, s\rangle$	$ s, x\rangle$	$ s, y\rangle$	$ s, z\rangle$	$ x, s\rangle$	$ x, x\rangle$	$ x, y\rangle$	$ x, z\rangle$	$ y, s\rangle$	$ y, x\rangle$	$ y, y\rangle$	$ y, z\rangle$	$ z, s\rangle$	$ z, x\rangle$	$ z, y\rangle$	$ z, z\rangle$
$ s, s\rangle$	$2t^2 + \frac{16t^2}{9}$	0	0	0	0	$-\frac{5t^2}{6} - \frac{1t^2}{6}$	$\frac{1}{3}(\frac{t^2}{3})$	0	0	$\frac{1}{3}(\frac{t^2}{3})$	$-\frac{5t^2}{6} - \frac{1t^2}{6}$	0	0	0	0	$-\frac{3t^2}{2}$
$ s, x\rangle$	0	$\frac{13t^2}{6} + \frac{3t^2}{2}$	$-\frac{1}{3}(\frac{t^2}{3})$	0	$\frac{3t^2}{6} + \frac{1t^2}{6}$	0	0	0	$-\frac{1}{6}(\frac{t^2}{3})$	0	0	$-\frac{1}{6}(\frac{t^2}{3})$	0	$-\frac{1}{2\sqrt{6}}(\frac{t^2}{3})$	$\sqrt{\frac{3}{8}}\frac{t^2}{6}$	0
$ s, y\rangle$	0	$-\frac{1}{3}(\frac{t^2}{3})$	$\frac{10t^2}{6} + \frac{3t^2}{2}$	0	$-\frac{1}{6}(\frac{t^2}{3})$	0	0	$\frac{2\sqrt{6}t^2 + 2\sqrt{6}t^2}{6}$	$\frac{3t^2}{6} + \frac{1t^2}{6}$	0	0	0	0	$-\sqrt{\frac{3}{8}}\frac{t^2}{6}$	$\frac{2\sqrt{6}}{6}(\frac{t^2}{3})$	0
$ s, z\rangle$	0	0	0	$2t^2 + \frac{7t^2}{3}$	0	$\frac{1}{2\sqrt{6}}(\frac{t^2}{3}) - \frac{1}{2\sqrt{6}}(\frac{t^2}{3})$	0	0	0	$\frac{1}{2\sqrt{6}}(\frac{t^2}{3}) + \frac{1}{2\sqrt{6}}(\frac{t^2}{3})$	$-\frac{1}{2\sqrt{6}}(\frac{t^2}{3})$	0	$\frac{3t^2}{6}$	0	0	0
$ x, s\rangle$	0	$\frac{3t^2}{6} + \frac{1t^2}{6}$	$-\frac{1}{3}(\frac{t^2}{3})$	0	$\frac{10t^2}{6} + \frac{3t^2}{6}$	0	0	$-\frac{2\sqrt{6}}{6}(\frac{t^2}{3})$	$-\frac{1}{6}(\frac{t^2}{3})$	0	0	$\sqrt{\frac{3}{8}}\frac{t^2}{6}$	0	0	$-\frac{1}{2\sqrt{6}}(\frac{t^2}{3}) - \frac{1}{2\sqrt{6}}(\frac{t^2}{3})$	0
$ x, x\rangle$	$-\frac{5t^2}{6} - \frac{1t^2}{6}$	0	0	$\frac{2t^2}{6} + \frac{3t^2}{6}$	0	$2t^2 + \frac{3t^2}{6}$	$-\frac{1}{3}(\frac{t^2}{3})$	0	$-\frac{1}{6}(\frac{t^2}{3})$	$-\frac{1}{6}(\frac{t^2}{3})$	$-\frac{1}{6}(\frac{t^2}{3})$	0	$\frac{1}{2\sqrt{6}}(\frac{t^2}{3})$	0	0	$-\frac{1t^2}{6} - \frac{1t^2}{6}$
$ x, y\rangle$	$\frac{1}{3}(\frac{t^2}{3})$	0	0	0	$-\frac{1}{6}(\frac{t^2}{3})$	$\frac{3t^2}{6} + \frac{1t^2}{6}$	$\frac{1}{6}(\frac{t^2}{3})$	0	$\frac{1}{6}(\frac{t^2}{3})$	$\frac{1}{6}(\frac{t^2}{3})$	$-\frac{1}{6}(\frac{t^2}{3})$	0	$\frac{1}{6}(\frac{t^2}{3})$	0	0	0
$ x, z\rangle$	0	0	$\frac{1}{2\sqrt{6}}(\frac{t^2}{3}) + \frac{1}{2\sqrt{6}}(\frac{t^2}{3})$	0	$-\frac{1}{2\sqrt{6}}(\frac{t^2}{3})$	0	0	$\frac{1}{2\sqrt{6}}(\frac{t^2}{3}) + 2\frac{t^2}{6}$	$-\sqrt{\frac{3}{8}}\frac{t^2}{6}$	0	0	0	0	$\frac{1}{2\sqrt{6}}(\frac{t^2}{3})$	0	0
$ y, s\rangle$	0	$-\frac{1}{6}(\frac{t^2}{3})$	$\frac{3t^2}{6} + \frac{1t^2}{6}$	0	$-\frac{1}{3}(\frac{t^2}{3})$	0	0	$-\sqrt{\frac{3}{8}}\frac{t^2}{6}$	$\frac{10t^2}{6} + \frac{3t^2}{6}$	0	0	$\frac{1}{2\sqrt{6}}(\frac{t^2}{3})$	0	$\frac{1}{2\sqrt{6}}(\frac{t^2}{3}) + \frac{1}{2\sqrt{6}}(\frac{t^2}{3})$	0	0
$ y, x\rangle$	$\frac{1}{3}(\frac{t^2}{3})$	0	0	0	$-\frac{1}{6}(\frac{t^2}{3})$	$\frac{1}{6}(\frac{t^2}{3})$	$\frac{1}{6}(\frac{t^2}{3})$	0	0	$\frac{10t^2}{6} + \frac{1t^2}{6}$	$-\frac{1}{6}(\frac{t^2}{3})$	0	$-\frac{1}{2\sqrt{6}}(\frac{t^2}{3}) - \frac{1}{2\sqrt{6}}(\frac{t^2}{3})$	0	0	0
$ y, y\rangle$	$-\frac{5t^2}{6} - \frac{1t^2}{6}$	0	0	$-\frac{1}{2\sqrt{6}}(\frac{t^2}{3})$	0	$-\frac{1}{6}(\frac{t^2}{3})$	$-\frac{1}{6}(\frac{t^2}{3})$	0	$\frac{10t^2}{6} + \frac{1t^2}{6}$	$-\frac{1}{6}(\frac{t^2}{3})$	$2t^2 + \frac{3t^2}{6}$	0	$-\frac{1}{2\sqrt{6}}(\frac{t^2}{3})$	0	0	$-\frac{1t^2}{6} - \frac{1t^2}{6}$
$ y, z\rangle$	0	$-\frac{1}{2\sqrt{6}}(\frac{t^2}{3}) - \frac{1}{2\sqrt{6}}(\frac{t^2}{3})$	0	0	$\sqrt{\frac{3}{8}}\frac{t^2}{6}$	0	0	0	$\frac{1}{2\sqrt{6}}(\frac{t^2}{3})$	0	0	$\frac{1}{2\sqrt{6}}(\frac{t^2}{3}) + 2\frac{t^2}{6}$	0	0	$\frac{1}{2\sqrt{6}}(\frac{t^2}{3})$	0
$ z, s\rangle$	0	0	0	$\frac{3t^2}{6}$	0	$\frac{1}{2\sqrt{6}}(\frac{t^2}{3})$	$\frac{1}{2\sqrt{6}}(\frac{t^2}{3})$	0	0	$-\frac{1}{2\sqrt{6}}(\frac{t^2}{3}) - \frac{1}{2\sqrt{6}}(\frac{t^2}{3})$	$-\frac{1}{2\sqrt{6}}(\frac{t^2}{3})$	0	$2t^2 + \frac{3t^2}{6}$	0	0	0
$ z, x\rangle$	0	$-\frac{1}{2\sqrt{6}}(\frac{t^2}{3})$	$-\sqrt{\frac{3}{8}}\frac{t^2}{6}$	0	0	0	0	$\frac{1}{2\sqrt{6}}(\frac{t^2}{3})$	$\frac{1}{2\sqrt{6}}(\frac{t^2}{3}) + \frac{1}{2\sqrt{6}}(\frac{t^2}{3})$	0	0	0	0	$\frac{1}{2\sqrt{6}}(\frac{t^2}{3}) + 2\frac{t^2}{6}$	0	0
$ z, y\rangle$	0	$\sqrt{\frac{3}{8}}\frac{t^2}{6}$	$\frac{1}{2\sqrt{6}}(\frac{t^2}{3})$	0	$-\frac{1}{2\sqrt{6}}(\frac{t^2}{3}) - \frac{1}{2\sqrt{6}}(\frac{t^2}{3})$	0	0	0	0	0	0	$\frac{1}{2\sqrt{6}}(\frac{t^2}{3})$	0	0	$\frac{1}{2\sqrt{6}}(\frac{t^2}{3}) + 2\frac{t^2}{6}$	0
$ z, z\rangle$	$-\frac{3t^2}{2}$	0	0	0	0	$-\frac{1}{6}(\frac{t^2}{3}) - \frac{1}{6}(\frac{t^2}{3})$	0	0	0	$-\frac{1}{6}(\frac{t^2}{3}) - \frac{1}{6}(\frac{t^2}{3})$	$-\frac{1}{6}(\frac{t^2}{3}) - \frac{1}{6}(\frac{t^2}{3})$	0	0	0	0	$2t^2 + 3\frac{t^2}{6}$

Figure 1.13. Matrix elements of the effective Hamiltonian resulting from first order perturbation theory result of the Kugel-Khomskii Hamiltonian in the low-energy subspace: Here $|x\rangle/|y\rangle/|z\rangle$ are shorthand for $|t_x\rangle/|t_y\rangle/|t_z\rangle$. For the Cartesian choice of triplet states the Hamiltonian remains real. This can and does change for other setups. The Hamiltonian for the other two bond types can be produced by cyclic permutation $x \rightarrow y \rightarrow z \rightarrow x$.

The Hamiltonian can thus be rewritten as

$$\begin{aligned}
 [h_2]_{\langle i,j \rangle}^{(c)} = & \frac{t^2}{U} \left[-\frac{5}{6} (T_{x,i}T_{x,j} + T_{y,i}T_{y,j}) + \frac{2}{3} (T_{x,i}^\dagger T_{x,j} + T_{y,i}^\dagger T_{y,j}) + h.c. \right] \\
 & - \frac{tt'}{U} \left[-\frac{1}{6} (T_{x,i}T_{y,j} + T_{y,i}T_{x,j}) + \frac{1}{3} (T_{x,i}^\dagger T_{y,j} + T_{y,i}^\dagger T_{x,j}) + h.c. \right] \\
 & + \frac{t'^2}{U} \left[-\frac{1}{6} (T_{x,i}T_{x,j} + T_{y,i}T_{y,j}) + \frac{1}{6} (T_{x,i}^\dagger T_{x,j} + T_{y,i}^\dagger T_{y,j}) \right. \\
 & \quad \left. - \frac{2}{3} T_{z,i}T_{z,j} + \frac{2}{3} T_{z,i}^\dagger T_{z,j} + h.c. \right].
 \end{aligned} \tag{1.77}$$

In this formulation the Hamiltonian has a structure analogous to the BCS-Hamiltonian of superconductivity [131] or the very established field of Bose-Einstein condensation of magnons [70, 71], which is the direct comparison and originator of the language. In this regard one should mention that a lot of the Bose-Einstein condensation language in particular for singlet-triplet models has been established for dimer systems, e.g. [69]. Later in section 1.5 we will discuss the degrees of freedom in the dimer setup and compare it to the triplons in this equation.

In the same vein one can borrow from established effective field theories for the singlet-triplet formalisms [69, 152] and use real fields (\mathbf{u}, \mathbf{v}) , which can be introduced via $\mathbf{T} = \mathbf{u} + i\mathbf{v}$.

Reformulating the Hamiltonian in terms of their real fields yields

$$\begin{aligned}
 [h_2]_{\langle i,j \rangle}^{(c)} = & \frac{4t^2}{U} \left[\frac{3}{4} (v_{x,i}v_{x,j} + v_{y,i}v_{y,j}) - \frac{1}{12} (u_{x,i}u_{x,j} + u_{y,i}u_{y,j}) \right] \\
 & - \frac{4tt'}{U} \left[\frac{1}{4} (v_{x,i}v_{y,j} + v_{y,i}v_{x,j}) - \frac{1}{12} (u_{x,i}u_{y,j} + u_{y,i}u_{x,j}) \right] \\
 & + \frac{4t'^2}{U} \left[\frac{1}{6} (v_{x,i}v_{x,j} + v_{y,i}v_{y,j}) + \frac{2}{3} v_{z,i}v_{z,j} \right].
 \end{aligned} \tag{1.78}$$

As discussed later the dipolar and thus usually important field is given by the \mathbf{v} vector boson and one may simplify the Hamiltonian even further by neglecting the

\mathbf{u} terms, yielding

$$H_{\text{eff}} = \lambda \sum_i n_i + 4J \sum_{\langle i,j \rangle} \mathbf{v}_i \mathbf{v}_j + 4K \sum_c \sum_{\langle i,j \rangle_c} v_i^c v_j^c + 4\Gamma \sum_c \sum_{\langle i,j \rangle_c} (v_i^a v_j^b + v_i^b v_j^a) \quad (1.79)$$

with

$$J = \frac{\frac{3}{4}t^2 + \frac{1}{6}t'^2}{U} \quad (1.80)$$

$$K = \frac{-\frac{3}{4}t^2 + \frac{1}{2}t'^2}{U} \quad (1.81)$$

$$\Gamma = \frac{-tt'}{4U}. \quad (1.82)$$

Vice versa one can parametrize the Kitaev-Heisenberg model in the usual way by introducing a magnitude A and angle α so that $J = A \cos(\alpha)$ and $K = A \sin(\alpha)$ and find

$$\frac{t^2}{U} = \frac{A}{3} (3 \cos \alpha - \sin(\alpha)) \quad (1.83)$$

$$\frac{t'^2}{U} = \frac{3A}{2} (\cos \alpha + \sin(\alpha)), \quad (1.84)$$

where $\frac{t^2}{U}$ being possibly negative might be considered a concession for the neglect of the multiplet, i.e Hund's coupling. One should note that $n_i = \sum_{\tau=x,y,z} t_{\tau,i}^\dagger t_{\tau,i} = \sum_{\tau=x,y,z} T_{\tau,i}^\dagger T_{\tau,i}$ as applications of hard-core bosons onto an on-site state work like fermions.

Clearly, the effective Hamiltonian in equation (1.79) has the form of an extended Kitaev-Heisenberg model [48, 50] just with vector bosons \mathbf{v} instead of spins(-1/2) as its constituents.

One should address why we use the seemingly arbitrary factor in the scaling, i.e. $4J$ instead of using just J . First of all, every simulation is done on the level of triplons and hence it is convenient to use a parametrization that scales obviously in

this case. Rewriting equation (1.79) in terms of triplons yields

$$\begin{aligned}
 H = & \lambda \sum_i n_i + J \sum_{\langle i,j \rangle} \left(\mathbf{T}_i^\dagger \mathbf{T}_j - \mathbf{T}_i^\dagger \mathbf{T}_j^\dagger + \text{h.c.} \right) \\
 & + K \sum_c \sum_{\langle i,j \rangle_c} \left(T_{c,i}^\dagger T_{c,j} - T_{c,i}^\dagger T_{c,j}^\dagger + \text{h.c.} \right) \\
 & + \Gamma \sum_c \sum_{\langle i,j \rangle_c} \left(T_{a,i}^\dagger T_{b,j} + T_{b,i}^\dagger T_{a,j} - \left(T_{b,i}^\dagger T_{a,j}^\dagger + T_{a,j}^\dagger T_{b,i}^\dagger \right) + \text{h.c.} \right) .
 \end{aligned} \tag{1.85}$$

Secondly, the transformation $\mathbf{T} = \mathbf{u} + i\mathbf{v}$ introduced in [1] is an idea that is in fundamental opposition of \mathbf{u} and \mathbf{v} in the director based interpretation, which is what motivates one to rewrite the terms in this manner, see sections 1.5 and 2.3.2. As explained therein, the ansatz, stems from a special choice singlet-triplet wave function. As a result one should usually carry the additional factor of the condensate density $\sqrt{\rho(1-\rho)}$ for each spin, which is optimized as $1/2$ for $\rho = 1/2$, thus canceling the “unnecessary” 4 in our Hamiltonian. Therefore the vector-bosons here are actually akin to spins with length $1/2$, which $\mathbf{T} = \mathbf{u} + i\mathbf{v}$ does not reflect.

Just to reiterate: the choice of [1] is not wrong, but inconvenient if you then want to directly understand \mathbf{v} as a spin, which is what the interpretation as a Kitaev-Heisenberg model does. This is why understanding the bosons as classical spins naively like in [6] shifts the phase borders by a factor of 4, because it did not account for the factor like we do here. Yet, when operating on the level of triplons, one can inherently avoid any formulation in terms of \mathbf{u} and \mathbf{v} bosons and the factor problem is just an inconvenient but ok way of handling the terms whenever the \mathbf{u} and \mathbf{v} picture is employed for interpretation purposes. The semiclassical Monte-Carlo later does not have this problem. The inconvenience is only in equation (1.79).

Similarly, one could also write down and or transform the h_3 and h_4 terms¹². One may use $t_{\tau,i}^\dagger t_{\tau',i} = T_{\tau,i}^\dagger T_{\tau',i}$, which we do as an example and for consistency with [5],

¹²We will ignore tt' for simplicities sake. All matrix elements can be read off from figure 1.13.

but the use of this formulation is limited. One finds

$$\begin{aligned}
 [h_3]_{\langle i,j \rangle}^{(c)} &= \frac{1}{\sqrt{24}} \frac{t^2 + t'^2}{U} \left(T_{x,i} T_{y,j}^\dagger T_{z,j} - T_{y,i} T_{x,j}^\dagger T_{z,j} \right) \\
 &+ \left(\frac{1}{\sqrt{6}} \frac{t^2}{U} + \frac{1}{\sqrt{24}} \frac{t'^2}{U} \right) \left(T_{y,i} T_{z,j}^\dagger T_{x,j} - T_{x,i} T_{z,j}^\dagger T_{y,j} \right) \\
 &+ \sqrt{\frac{3}{8}} \frac{t^2}{U} \left(T_{z,i} T_{x,j}^\dagger T_{y,j} - T_{z,i} T_{y,j}^\dagger T_{x,j} \right) + \text{h.c.} + i \leftrightarrow j .
 \end{aligned} \tag{1.86}$$

and cyclic permutations on the other bonds. The four-triplon-terms can conveniently be split into diagonal and off-diagonal parts $h_4 \equiv h_{4,\text{diag}} + h_{4,\text{off}}$. The diagonal part

$$\begin{aligned}
 [h_{4,\text{diag}}]_{\langle i,j \rangle}^{(c)} &= \frac{t^2}{U} \left[2 \left(n_i^s n_j^s + n_i^s n_j^z + n_i^z n_j^s + \vec{n}_i \cdot \vec{n}_j \right) \right. \\
 &+ \frac{9}{4} \left(n_i^x n_j^y + n_i^y n_j^x + n_i^x n_j^z + n_i^z n_j^x + n_i^y n_j^z + n_i^z n_j^y \right) \\
 &+ \left. \frac{13}{6} \left(n_i^s n_j^x + n_i^s n_j^y + n_i^x n_j^s + n_i^y n_j^s \right) \right] \\
 &+ \frac{t'^2}{U} \left[\frac{16}{9} n_i^s n_j^s + 3 n_i^z n_j^z + \frac{7}{3} \left(n_i^s n_j^z + n_i^z n_j^s \right) \right. \\
 &+ \frac{3}{2} \left(n_i^s n_j^x + n_i^s n_j^y + n_i^x n_j^s + n_i^y n_j^s \right) \\
 &+ \frac{5}{4} \left(n_i^x n_j^x + n_i^y n_j^y + n_i^x n_j^y + n_i^y n_j^x \right) \\
 &+ \left. 2 \left(n_i^x n_j^z + n_i^y n_j^z + n_i^z n_j^x + n_i^z n_j^y \right) \right] .
 \end{aligned} \tag{1.87}$$

The off-diagonal part is

$$\begin{aligned}
 [h_{4,\text{off}}]_{\langle i,j \rangle}^{(c)} &= - \frac{1}{4} \frac{t^2 + t'^2}{U} \left(T_{x,i}^\dagger T_{z,i} T_{x,j}^\dagger T_{z,j} + T_{i,y}^\dagger T_{z,i} T_{y,j}^\dagger T_{z,j} \right) \\
 &- \frac{1}{4} \frac{t^2}{U} T_{x,i}^\dagger T_{y,i} T_{x,j}^\dagger T_{y,j} \\
 &+ \frac{1}{4} \frac{t'^2}{U} \left(T_{x,i}^\dagger T_{z,i} T_{z,j}^\dagger T_{x,j} + T_{y,i}^\dagger T_{z,i} T_{z,j}^\dagger T_{y,j} \right) \\
 &+ \frac{1}{2} \frac{t^2}{U} T_{x,i}^\dagger T_{y,i} T_{y,j}^\dagger T_{x,j} + \text{h.c.} .
 \end{aligned} \tag{1.88}$$

1.4.5.3 Magnetization in the Low-Energy Subspace

It is essential to look into the effective degrees of freedom in the subspace. One should however note that these are themselves projection, i.e. $\langle \mathbf{S} \rangle_{s,t} \equiv \langle \alpha_i | \mathbf{S} | \alpha_j \rangle$. These objects should never be inserted into the perturbation theory itself.

Rewriting spin and angular momentum leads to (introducing the shorthand $\mathbf{J} = -i\mathbf{t}^\dagger \times \mathbf{t} = -i\mathbf{T}^\dagger \times \mathbf{T}$ for the total angular momentum)

$$\langle \mathbf{S} \rangle_{s,t} = -i\sqrt{\frac{2}{3}} (\mathbf{T} - \mathbf{T}^\dagger) + \frac{1}{2}\mathbf{J}, \quad (1.89)$$

$$\langle \mathbf{L} \rangle_{s,t} = i\sqrt{\frac{2}{3}} (\mathbf{T} - \mathbf{T}^\dagger) + \frac{1}{2}\mathbf{J}, \quad (1.90)$$

where there is an obvious point of interest in the first term compared to very naive free spins. However, this term is not unusual and these kind of formulas translate directly from normal spin-dimer singlet-triplet models [69].

However, the $\mathbf{M} = 2\mathbf{S} - \mathbf{L}$ (cf. equation (1.25)) reads

$$\langle \mathbf{M} \rangle_{s,t} = -i\sqrt{6} (\mathbf{T} - \mathbf{T}^\dagger) + \frac{1}{2}\mathbf{J} = \sqrt{24}\mathbf{v} + (\mathbf{u} \times \mathbf{v}). \quad (1.91)$$

This expression is quite unusual as we try to elucidate in the following section! Lastly however, we point out that \mathbf{M} represents the magnetic dipole and thus the first term suggest that \mathbf{v} does the same.

1.5 The Language of Spin, Quadrupoles and Spin-Dimers

In the previous section we have introduced \mathbf{u} and \mathbf{v} . As they emerge as a consequence of borrowed mathematical constructions from spin and spin-dimer physics, it is prudent to understand their origin. In fact, although [1] makes a few comments

about the dipole and quadrupole nature of \mathbf{u} and \mathbf{v} , the statements do not seem sufficient to understand the circumstances if one does not already know all the details ahead of reading them. Moreover, naively accepting that “ \mathbf{v} has dipole and \mathbf{u} quadrupole nature” can be misleading if not carefully applied. We try to remedy this by providing a quick run-through of all necessary concepts. For this purpose it seems convenient to follow established literature [153] to keep everything focused on essentials and add comments to connect it to the spin-orbital singlet-triplet model.

1.5.1 Nematics for Spin-1/2 and Spin-1

The \mathbf{u} and \mathbf{v} based description emerges as a natural way of aiding the search for multipolar or nematic order. This kind of order breaks the overall symmetry of the spin ($O(3)$) without possessing a magnetic moment, i.e. a dipole moment. As quadrupole is the simplest of these cases, we use it and nematic interchangeably here. Furthermore, we skip the importance or causes for interest in nematics as their relevance in this thesis is (sadly) not warranted (but that in itself is a result).

Precisely, when considering spins S , we are therefore looking for states $|\Psi\rangle$ with vanishing magnetic order or dipole moment $\langle\Psi|\mathbf{S}_i|\Psi\rangle \equiv \langle\mathbf{S}_i\rangle = \mathbf{0}$. Quadrupole order can then emerge, e.g., as anisotropic fluctuations $\langle(S_i^x)^2\rangle \neq \langle(S_i^y)^2\rangle = \langle(S_i^z)^2\rangle$.

One should, however, note that there always has to be a consideration of what kind of quadrupole one is interested in. For magnetic quadrupoles \mathbf{S} here takes the role of the magnetic moment \mathbf{M} , which is not written here because the objects are trivially more or less analogous.

The natural next step is to ask how one can accomplish this feat. One interesting answer, which makes, e.g., our spin-1 vector bosons intriguing on paper (compared to the $j = 1/2$ traditional Kitaev-Heisenberg systems), is the following: You can't accomplish this for (a single) spin-1/2. You need at least spin-1.

Consider a general spin-1/2 state $|\Psi\rangle = \alpha|\uparrow\rangle + \beta|\downarrow\rangle$. Naturally, both α and β are

complex parameters, leaving 4 free real numbers. Due to normalization and fixing of the arbitrary phase factor of the state, one can reduce the amount of parameters needed to 2. This is the same amount of parameters as an arbitrary rotation in three dimensions $\mathbf{\Omega}$ (represented by the spherical coordinates unit vector), hence we can write

$$\mathbf{\Omega} = (\cos(\phi) \sin(\theta), \sin(\phi) \sin(\theta), \cos(\theta))^T, \quad (1.92)$$

$$|\Psi_{\Omega}\rangle = \sin(\theta/2) e^{-i\phi/2} |\uparrow\rangle + \cos(\theta/2) e^{i\phi/2} |\downarrow\rangle, \quad (1.93)$$

$$\langle\Psi_{\Omega}|\mathbf{S}|\Psi_{\Omega}\rangle = S\mathbf{\Omega}, \quad (1.94)$$

where the calculations in the last equation use the known spin algebra also seen in equation (1.67). $|\Psi_{\Omega}\rangle$ shows that any kind of spin-1/2 state can be translated to any other via rotation. In other words: because we only need 2 real parameters, $|\Psi_{\Omega}\rangle$ can be any state¹³. Consequently, the last equation proves $\langle\mathbf{S}_i\rangle \neq \mathbf{0}$ for any spin-1/2 state.

Spin-1 however is described by three states, e.g. the eigenstates of the S^z operator $|m=1\rangle$, $|0\rangle$ and $|-1\rangle$. There are 6 free parameters, so even after using norm and phase fixing one can't just guarantee that it is possible to rotate one state into another. More importantly, it is trivial to calculate:

$$\langle 0|\mathbf{S}|0\rangle = \mathbf{0}, \quad (1.95)$$

$$\langle 0|(S^z)^2|0\rangle = 0, \quad (1.96)$$

$$\langle 0|(S^x)^2|0\rangle = \langle 0|(S^y)^2|0\rangle = 1. \quad (1.97)$$

Hence we have found a nematic state. There are even more. The following ($|z\rangle$ is

¹³The way of writing it down like this is called “spin ‘coherent state’”.

not really new) states are all nematic¹⁴:

$$|x\rangle = \frac{i}{\sqrt{2}} (|1\rangle - |-1\rangle), \quad |y\rangle = \frac{1}{\sqrt{2}} (|1\rangle + |-1\rangle), \quad |z\rangle = -i|0\rangle. \quad (1.98)$$

Additionally, any linear combination $|d\rangle = \sum_{\tau=x,y,z} d_\tau |\tau\rangle$ with real(!) coefficients d_τ is also nematic. Because the overall phase is immaterial, any linear combination with purely imaginary d_τ is also allowed. It is therefore convenient to write

$$|d\rangle = \sum_{\tau=x,y,z} d_\tau |\tau\rangle = \sum_{\tau=x,y,z} (u_\tau + iv_\tau) |\tau\rangle, \quad \mathbf{d} = \mathbf{u} + i\mathbf{v}, \quad (1.99)$$

where $\mathbf{u} \cdot \mathbf{v} = 0$ fixes the phase and $|\mathbf{u}|^2 + |\mathbf{v}|^2 = 1$ the norm. Here \mathbf{d} is called the director. It represents the axis (direction) perpendicular to the plane where the quadrupolar fluctuations happen.

We summarize: A single spin-1 state is nematic if only(!) either \mathbf{u} or \mathbf{v} are nonzero. Importantly, the dipole in this kind of state reads

$$\langle d | \mathbf{S} | d \rangle = 2(\mathbf{u} \times \mathbf{v}), \quad (1.100)$$

i.e. the dipole looks complicated on paper. This is the point where a direct comparison to equation (1.91) is warranted. The second term looks like a normal spin, while the first one, the one that makes \mathbf{v} a dipole in the spin-orbital model, is unusual. This term connects singlet and triplet while the usual one splits the triplet. The triplet splitting is basically the linear Zeeman splitting of a spin in a magnetic field and hence exists for normal spins. On the contrary the other term is connected to Van-Vleck magnetism. Because the Zeeman term represents the “usual” part it was convenient to reintroduce \mathbf{J} .

But what about the quadrupole? One can find arguments to state that the quadrupole has to be constructed out of products of spin operators, i.e. $Q^{\alpha\beta} \sim S^\alpha S^\beta$.

¹⁴and should appear familiar based on the cartesian triplets discussed before

The quadrupole tensor is

$$Q^{\alpha\beta} = S^\alpha S^\beta + S^\beta S^\alpha - \frac{2}{3}S(S+1)\delta_{\alpha,\beta}, \quad (1.101)$$

$$\langle d|Q^{\alpha\beta}|d\rangle = \frac{2}{3}\delta_{\alpha,\beta} - 2u_\alpha u_\beta - 2v_\alpha v_\beta. \quad (1.102)$$

In order to understand some papers, it is prudent to know that for convenience reasons the quadrupole tensor is often written in terms of its five linear independent components via

$$\mathbf{Q} = \begin{pmatrix} Q_{x^2-y^2} \\ Q_{3z^2-r^2} \\ Q_{xy} \\ Q_{yz} \\ Q_{xz} \end{pmatrix} = \begin{pmatrix} (S^x)^2 - (S^y)^2 \\ \frac{1}{\sqrt{3}}(3(S^z)^2 - S(S+1)) \\ S^x S^y + S^y S^x \\ S^y S^z + S^z S^y \\ S^z S^x + S^x S^z \end{pmatrix}. \quad (1.103)$$

What does that imply for the spin-orbital system? Citing [1] directly¹⁵: “Quadrupoles Q arise from the mapping of composite spin-orbital terms $S^\alpha L^\beta$ in H , e.g., $S^y L^z = \sqrt{2/3} \cdot u_x + 1/2 \cdot Q_x$. Note that \mathbf{u} enters here, revealing its quadrupole nature”.

First of all, one should mention that the nature of the order is maybe something one can discuss. In the spin-orbital system one may look for, e.g., order of the total angular momentum \mathbf{J} of only the spin \mathbf{S} , only the orbitals via \mathbf{L} , or, and this is what the above statement considers, order in the magnetic moment $\mathbf{M} = 2\mathbf{S} - \mathbf{L}$. That this choice might not be trivial can be seen by various choices in the VCA calculation in [119], which are of course educated guesses based on literature. Furthermore, the expression in [1] is actually an effective low-energy singlet triplet operator, i.e. the $\langle d|\dots|d\rangle$ “equivalent” $\langle \dots \rangle_{s,t}$ in, e.g., equation (1.91).

Accepting that the statement aims to describe quadrupoles of \mathbf{M} , one should keep in mind that these also contain terms like $S^\alpha S^\beta$ and $L^\alpha L^\beta$. However, with a bit of

¹⁵comment hidden in the bibliography of the paper

calculation one indeed finds

$$\begin{aligned}\langle S^y L^z \rangle_{s,t} &= \frac{1}{6} (s^\dagger t_x + t_x^\dagger s) - \frac{1}{2} (t_y^\dagger t_z + t_z^\dagger t_y), \\ &= \sqrt{\frac{2}{3}} u_x + \frac{1}{2} (-2u_y u_z - 2v_y v_z),\end{aligned}\tag{1.104}$$

where the introduction of \mathbf{u} etc... were done as before. The last term can be identified with Q (in our notation Q_{yz}) via (1.102). Like in the dipole, the first part is unusual while the last one is familiar from the spin system.

For completeness one might add that of course the $S^y S^z \sim S^x$ and hence the other elements look similar to a dipole, in a sense that $\sim \mathbf{v}$ (without i) could be argued:

$$\langle S^y S^z \rangle_{s,t} = \frac{1}{6} (s^\dagger t_x - t_x^\dagger s) + \frac{1}{2} t_y^\dagger t_z,\tag{1.105}$$

$$\langle L^y L^z \rangle_{s,t} = -\frac{1}{6} (s^\dagger t_x - t_x^\dagger s) + \frac{1}{2} t_y^\dagger t_z.\tag{1.106}$$

However, the fact that $M^x M^y + M^y M^x$ is the quadrupole and not only $M^x M^y$ takes care of the irregular terms via

$$\langle S^z S^y \rangle_{s,t} = -\frac{1}{6} (s^\dagger t_x - t_x^\dagger s) + \frac{1}{2} t_z^\dagger t_y,\tag{1.107}$$

i.e. each summand contains half of the ‘‘classical’’ Q_{yz} quadrupole while the other term cancels out. That in itself is a peculiar side note, because for the dipole the unusual Van Vleck term profits from $2\mathbf{S} - \mathbf{L}$ by adding up to three times the size compared to single \mathbf{S} , while the Zeeman term remains the same.

1.5.2 Spin-Dimer and Magnetic Moment

This section is kept short because nuances of the singlet-triplet ansatz are discussed later.

Previously, we established that a single spin-1/2 can't be nematic. However, a dimer consisting of two spin-1/2 can. Note that the spin-orbital singlet-triplet (quintet) model is technically a dimer of two spin-1 particles, but as the quintet is thrown out, the discussion covers both cases.

Consider an antiferromagnetic Heisenberg coupling between two spin-1/2 referred to as S_1 and S_2 . The eigenstates of $J\mathbf{S}_1\mathbf{S}_2$ possess a singlet-triplet structure with the ground state being at $E = -3J/4$ and an excited triplet at $E = J/4$ described by the states

$$|s\rangle = \frac{1}{\sqrt{2}} (|\uparrow\downarrow\rangle - |\downarrow\uparrow\rangle), \quad (1.108)$$

$$|x\rangle = \frac{i}{\sqrt{2}} (|\uparrow\uparrow\rangle - |\downarrow\downarrow\rangle), \quad (1.109)$$

$$|y\rangle = \frac{1}{\sqrt{2}} (|\uparrow\uparrow\rangle + |\downarrow\downarrow\rangle), \quad (1.110)$$

$$|z\rangle = \frac{-i}{\sqrt{2}} (|\uparrow\downarrow\rangle + |\downarrow\uparrow\rangle), \quad (1.111)$$

where we took the liberty to provide the cartesian linear combinations of the naive $|\mathcal{S}_{\text{tot}}, m_{\text{tot}}\rangle$ eigenstates of the total spin $\mathbf{S}_{\text{tot}} = \mathbf{S}_1 + \mathbf{S}_2$ regarding the degenerate triplet.

Given that we can write any state as a linear combination thereof, the basic form of the spin-1 $|d\rangle$ state can be reproduced

$$|\Psi\rangle = c_1 |s\rangle + c_2 \sum_{\tau=x,y,z} d_\tau |\tau\rangle, \quad (1.112)$$

where \mathbf{d} remains normalized and c_i are real constants with $c_1^2 + c_2^2 = 1$. The singlet is not important for the quadrupole discussion of the effective spin-1 triplet. Basic ideas of the previous discussions can be reiterated.

One important point remains to be made: how does the magnetic moment $\mathbf{M} = \mathbf{S}_{\text{tot}} = \mathbf{S}_1 + \mathbf{S}_2$ look? Projections onto the singlet-triplet model can be made with

the states described above and (again) simple application of the spin operators. We find (using t_x^\dagger and s like in the spin-orbital singlet-triplet model) [69]:

$$\langle \mathbf{S}_1 \rangle = \frac{1}{\sqrt{2}} (s^\dagger \mathbf{t} + \mathbf{t}^\dagger s) - \frac{i}{2} (\mathbf{t}^\dagger \times \mathbf{t}), \quad (1.113)$$

$$\langle \mathbf{S}_2 \rangle = \frac{1}{\sqrt{2}} (-s^\dagger \mathbf{t} - \mathbf{t}^\dagger s) - \frac{i}{2} (\mathbf{t}^\dagger \times \mathbf{t}), \quad (1.114)$$

$$\langle \mathbf{M} \rangle = -i (\mathbf{t}^\dagger \times \mathbf{t}). \quad (1.115)$$

Compared to equation (1.91) there is no Van Vleck term! The Zeeman term is additive. Spin-dimers will behave drastically different in magnetic fields.

2

Semiclassical Monte-Carlo Simulations for Spin-Orbital Triplons and Beyond

Hamiltonians presented in the introduction can be analyzed in various ways. In the course of this project, one idea, which had not been employed in its full potential in past studies [6], has shown a lot of promise. This extends to topics and schemes beyond what we cover in this thesis. Consequently, we want to provide an introduction to this approach, namely the semiclassical way of doing a Monte-Carlo (MC) simulation for our model.

While we use the semiclassical MC in chapter 3, the broader application and better examples for the usefulness of this method can be discussed in the context of Ca_2RuO_4 . Therefore we exemplify the use of semiclassical MC via the Ca_2RuO_4 based paper [20], which represents a case where we applied code written for this thesis with slight changes onto a related problem. In addition, the semiclassical MC procedure has seen use beyond what we cover here [134].

In order to set up the semiclassical MC procedure, we first provide a rough overview about methods used in previous or comparative (mainly Ca_2RuO_4) studies and lay out information about their strengths and weaknesses. In particular, we describe

flavor-wave or linear spin-wave theory as used in [1, 6, 7], exact diagonalization as employed in [6, 7, 119, 134] and the variational cluster approach/approximation (VCA) utilized in [119, 154] (with cluster perturbation theory in [7]). Furthermore, we look into classical Monte-Carlo calculations of [6]. We will not discuss quantum Monte-Carlo (QMC), which is expected to be hampered by the sign problem in systems of frustrated spins or bosons [155]. However, clever, often system specific, ways of handling the sign problem emerge regularly and in a very recent study one such approach has been showcased for α -RuCl₃ [156] and even our triplon Kitaev-Heisenberg model [157], so one might want to include this possibility at some point in the future.

After introducing the other approaches, we describe the idea behind the semiclassical Monte-Carlo simulations and point out which gaps or inconveniences of the other methods it can and can not fill. Thereafter, we exemplify this by noting the use for Ca₂RuO₄ calculations in [20, 134], which were done with the thesis code slightly adapted to the problem. Concluding, we talk about the use and possible use of this scheme beyond this thesis.

2.1 Flavor-Wave or Linear Spin-Wave Theory

In past studies [6, 7], what was referred to as linear spin-wave theory (LSWT) was employed in a rudimentary way to mainly gauge the extend of the paramagnetic phase of the triplon Kitaev-Heisenberg model for the honeycomb and triangular lattice. Here, we revisit spin-wave descriptions and apply them in different contexts, e.g., when interpreting the critical points in the magnetic field. Hence a more thorough introduction seems to be prudent before establishing the strengths and weaknesses of this scheme.

Moreover, we should note that the triplon framework should likely be labeled as a flavor-wave theory. The formalism consists of multiple boson flavors and works anal-

ogous to the spin-1 descriptions in reference [158] and the director based approach in reference [159], the latter of which is also covered in textbook [153] and thus section 1.5.1. Differences are, however, in practice regularly relegated to superficial nomenclature, as reference [159] points out when choosing to focus on the condensation of a specific boson. As a result, there is not much harm done when using the expressions spin-wave and flavor-wave interchangeably.

Both linear flavor-wave and spin-wave theory approach the problem of triplons or spins by focusing on an approximation of the Hamiltonian that restricts it to a quadratic form, which makes it accessible to Bogoliubov transformation for bosons or fermions.

Since the subject is mentioned later and this appears to be an adequate moment to provide a side note about the difference between hard-core and normal bosons, we shortly recap the Holstein-Primakoff transformation. Holstein and Primakoff proposed rewriting the spin in terms of canonical boson creation and annihilation operators $b^{(\dagger)}$ via [160]¹:

$$S^+ = b^\dagger \sqrt{2S} \sqrt{1 - \frac{n}{2S}}, \quad (2.1)$$

$$S^- = \sqrt{2S} \sqrt{1 - \frac{n}{2S}} b, \quad (2.2)$$

$$S^z = n - S, \quad (2.3)$$

where the spin operator and quantum number are as introduced in section 1.4.5.2 and $n = b^\dagger b$ is the number operator of the bosons.

For the reason of comparison we note that a spin-1/2 can alternatively be mapped

¹We switch the role of S^\pm via sign change of S_z compared to the original source.

to a single hard-core bosons h via identification of

$$S^+ |\downarrow\rangle = |\uparrow\rangle, \quad S^+ |\uparrow\rangle = 0, \quad S^- |\downarrow\rangle = 0, \quad S^- |\uparrow\rangle = |\downarrow\rangle, \quad (2.4)$$

$$h^\dagger |0\rangle = |1\rangle, \quad h^\dagger |1\rangle = 0, \quad h |0\rangle = 0, \quad h |1\rangle = |0\rangle, \quad (2.5)$$

resulting in

$$h^\dagger = S^+, \quad h = S^-, \quad n = h^\dagger h = S^+ S^- = S^z + \frac{1}{2}. \quad (2.6)$$

The identity $h^\dagger |1\rangle = 0$ is reminiscent of the Pauli principle for fermions. As one can easily calculate, this affects the commutation relations of the hard-core bosons. Adding an index denoting a lattice site leads to the commutation relations $[h_i, h_j^\dagger] = 0$ for $i \neq j$ and $\{h_i, h_i^\dagger\} = 1$, where $[\dots]$ refers to the commutator and $\{\dots\}$ the anti-commutator. Hence the hard-core bosons are neither canonical bosons $[b_i, b_j^\dagger] = \delta_{ij}$, nor canonical fermions $\{c_i, c_j^\dagger\} = \delta_{ij}$, which is logical when recalling the spin/angular momentum algebra.

Hard-core bosons do not commute like canonical bosons. This has profound consequences, such as unitary transformations working non-trivially [161] and the Bose-Einstein statistic of their canonical counterparts not being valid. All of these consequences are regularly ignored in the framework of spin- and flavor-wave, as can be seen, e.g., in the subsequent calculation of the flavor-wave theory or the thermal Hall conductance.

Looking back to the Holstein-Primakoff transformation, one might naturally ask why the spin can be described by canonical bosons b . Indeed n can technically take any value between $n = 0$ and $n = \infty$. However, the $n > 2S$ sector is never reached, as the roots vanish for, e.g., $S^+ |n = 2S\rangle = 0$, which recovers the hard-core nature. So if the roots are intact everything works as expected.

The bosonization is a way of describing spin-waves. Yet, we aim to employ lin-

ear(!) spin-wave theory. We exemplify this by considering the Heisenberg model $H = J \sum_{\langle i,j \rangle} \mathbf{S}_i \mathbf{S}_j$. Linear refers to restricting oneself to the quadratic form of the Hamiltonian, i.e., hopping, number operator and pair creation/annihilation terms. As such, terms like $S_i^z S_j^z \sim n_i n_j$ need to be approximated. This is akin to only considering h_2 terms while ignoring h_3 and h_4 in our triplon model.

More importantly, one needs to deal with the square roots in $S^{x/y}$ via S^\pm somehow, which is where Holstein-Primakoff and linear spin-wave connect to the hard-core constraint: The square roots can be expanded in powers of $\frac{n}{2S} \ll 1$, yielding

$$\sqrt{1 - \frac{n}{2S}} \approx 1 - \frac{n}{4S} - \frac{n^2}{32S^2} - \dots, \quad (2.7)$$

which for a spin-1/2 Heisenberg model leaves contributions to the linear terms via $S^+ = b^\dagger$ and $S^- = b$, hence the exact same expressions as for the hard-core boson mapping.

Ergo, the spin-1/2 linear spin-wave Heisenberg model is consistent with the formulation for hard-core bosons, assuming of course the $S_i^z S_j^z$ are approximated analogously. For the hard-core bosons, however, the use of mathematical operations like the Bogoliubov transformation and unitary transformations in general are problematic because of the commutation relations. Using those regardless is an approximation and the resulting problems are not obvious at first glance.

In contrast to this, the Holstein-Primakoff based approximation of the root enforcing the hard-core constraint implicitly makes the potential error obvious: It is exact if one accounts for all terms in the series expansion of the root, i.e. includes boson interaction terms such as $S^+ \sim b^\dagger n = b^\dagger b^\dagger b$ and so on. These interactions should systematically become more important when n increases, i.e. when a significant number of bosons are in the system. This provides an interpretation of the hard-core constraint and demonstrates that triplons are inherently interacting objects even in the absence of h_3 and h_4 terms.

With this interpretation in mind one may revisit discussions, e.g., in the spin-dimer triplon systems where a lot of theoretical and experimental work has been reformed for years [70], and realize why the wording and descriptions therein are as they appear. Concretely, the authors describe the use of Bose-Einstein statistics, spin-waves as well as phenomena like Bose-Einstein condensation (in momentum space) being warranted for small densities (n) and point out the potentially richness of new phenomena emerging when the interactions begin to matter.

Concluding, we point out that spin-wave descriptions are well established, even for spin-1/2, where the $\frac{n}{2S}$ expansion is most suspect [162].

2.1.1 Calculations for Flavor-Wave Theory

As mentioned in the preceding section, we neglect h_3 and h_4 terms in order to obtain a quadratic theory. Accordingly, we start with a Hamiltonian based on equation (1.85). The use in this thesis is restricted to the observation of a single flavor, which is feasible if $\Gamma = 0$ because the flavors do not mix and can therefore be considered separately. Hence we write $\mathbf{T} \rightarrow T$ and account for the differences of the flavors in the form of the interactions, which simplifies equation (1.85) to

$$H = \lambda \sum_i T_i^\dagger T_i + \sum_c \sum_{\langle i,j \rangle_c} \mu_{i,j}^c \left[T_i^\dagger \cdot T_j + \nu \cdot T_i T_j + \text{h.c.} \right], \quad (2.8)$$

where T may be seen as a surrogate for any triplon and $\mu_{i,j}^c$ denotes the interactions of the flavor on bond z . For example the z boson would have $(J + K)$ on bond $c = z$ and J on the x and y bond (we use the parametrization $J = A \cos(\alpha)$ and $K = A \sin(\alpha)$). We furthermore introduce ν for convenience and because it covers the \mathbf{u} boson case with the same calculation: While $\mathbf{v} = (\mathbf{T} - \mathbf{T}^\dagger)/(2i)$ yields pair terms with negative sign for $\mathbf{v}_i \mathbf{v}_j$, hence $\nu = -1$, $\mathbf{u}_i \mathbf{u}_j$ would instead use $\nu = 1$ due to $\mathbf{u} = (\mathbf{T} + \mathbf{T}^\dagger)/2$.

In the subsequent derivations we try to formulate the equations in a form consistent with [163] (and the associated thesis [164], which is more explicit and an excellent resource), which provides identities for generalized bosonic Bogoliubov transformations for a Holstein-Primakoff spin-wave calculation, which we can adapt in some circumstances.

In others, the Fourier transformed Hamiltonian matrix can be written down in an analogous way as the subsequent case and then diagonalized with help of a transformation [164]. This would be the case for $\Gamma \neq 0$, due to flavor mixing requiring solutions of a 12×12 matrix and larger unit cells like the kagome lattice. As these cases are not useful for the points we try to make in this thesis, we skip these discussions. We do, however, want to point out that this is feasible. In the same vein, [163] provides different identities one can use for a single atom in the unit cell as seen in the analysis of the triangular lattice in [7]. In principle the flavor-wave description can be used in all those cases.

Here, however, the useful points can be made for the honeycomb lattice. Given its structure (cf. 4.17), the well known way of solving this problem is to label the two atoms in the unit cell and write:

$$H = \lambda \left(\sum_{i \in s_1} T_{1,i}^\dagger T_{1,i} + \sum_{i \in s_2} T_{2,i}^\dagger T_{2,i} \right) + \sum_c \sum_{i \in s_1} \sum_{\delta \in \text{NN}_c} \mu_{i,\delta}^c \left[T_{1,i}^\dagger \cdot T_{2,\delta} + \nu \cdot T_{1,i} T_{2,\delta} + \text{h.c.} \right], \quad (2.9)$$

where the index 1/2 denotes the sublattice. For the honeycomb lattice the nearest neighbors can be labeled by the position of their unit cell, e.g., $\mathbf{r}_\delta = \mathbf{r}_i + (0, 0)^T$ for the $c = z$ -bond, $\mathbf{r}_\delta = \mathbf{r}_i - \mathbf{v}_1$ for y and $\mathbf{r}_\delta = \mathbf{r}_i - \mathbf{v}_2$ for z , where \mathbf{v}_i are the primitive lattice vectors.

A Fourier transformation is trivially applied, which usually is covered in standard

exercise classes, leading to

$$H = \sum_{\mathbf{k}} \left[\lambda \cdot \left(T_{1,\mathbf{k}}^\dagger T_{1,\mathbf{k}} + T_{2,\mathbf{k}}^\dagger T_{2,\mathbf{k}} \right) + \epsilon_{\mathbf{k}} T_{1,\mathbf{k}}^\dagger T_{2,\mathbf{k}} + \nu \cdot \epsilon_{\mathbf{k}}^* T_{1,\mathbf{k}} T_{2,-\mathbf{k}} + \text{h.c.} \right], \quad (2.10)$$

where, e.g., for the z triplon $\epsilon_{\mathbf{k}} = J + K + J e^{-i\mathbf{k}v_1} + J e^{-i\mathbf{k}v_2}$. In order to use [163], one needs to rewrite the Hamiltonian into the subsequent Nambu form, which can be accomplished using the trivial identities $\epsilon_{-\mathbf{k}} = \epsilon_{\mathbf{k}}^*$ and $\sum_{\mathbf{k}} f(\mathbf{k}) = \frac{1}{2} \sum_{\mathbf{k}} (f(\mathbf{k}) + f(-\mathbf{k}))$ as well as boson commutation relations, resulting in

$$H = \frac{1}{2} \sum_{\mathbf{k}} \Psi^\dagger \begin{pmatrix} A_{\mathbf{k}} & B_{\mathbf{k}} & C_{\mathbf{k}} & D_{\mathbf{k}} \\ B_{\mathbf{k}}^* & A_{\mathbf{k}} & D_{\mathbf{k}}^* & C_{\mathbf{k}} \\ C_{\mathbf{k}} & D_{\mathbf{k}} & A_{\mathbf{k}} & B_{\mathbf{k}} \\ D_{\mathbf{k}}^* & C_{\mathbf{k}} & B_{\mathbf{k}}^* & A_{\mathbf{k}} \end{pmatrix} \Psi - \lambda, \quad (2.11)$$

where we introduced the Nambu spinor $\Psi = \left(T_{1,\mathbf{k}}, T_{2,\mathbf{k}}, T_{1,-\mathbf{k}}^\dagger, T_{2,-\mathbf{k}}^\dagger \right)^T$ and the labels $A_{\mathbf{k}} = \lambda$, $B_{\mathbf{k}} = \epsilon_{\mathbf{k}}$, $C_{\mathbf{k}} = 0$ and $D_{\mathbf{k}} = \nu \epsilon_{\mathbf{k}}$. It should be noted that $A_{\mathbf{k}}$ and $C_{\mathbf{k}}$ are real and would carry the next-nearest neighbor terms (if one is interested in introducing those to the problem).

The Bogoliubov transformation yields a new diagonalized Hamiltonian, with the quasiparticles α and β constructing the eigenstates. The energies are

$$E_{\alpha,\beta} = \sum_{\mathbf{k}} \left[\omega_+(\mathbf{k}) \alpha_{\mathbf{k}}^\dagger \alpha_{\mathbf{k}} + \omega_-(\mathbf{k}) \beta_{\mathbf{k}}^\dagger \beta_{\mathbf{k}} + \frac{1}{2} (\omega_+(\mathbf{k}) + \omega_-(\mathbf{k})) \right] - \lambda. \quad (2.12)$$

Consequently, one obtains a quantum mechanical correction to the ground state energy of $n_\alpha = n_\beta = 0$ and excitations characterized by

$$\omega_\pm(\mathbf{k}) = \sqrt{\Omega_{\mathbf{k}} \pm X_{\mathbf{k}}}, \quad (2.13)$$

where

$$\Omega_{\mathbf{k}} = A_{\mathbf{k}}^2 - C_{\mathbf{k}}^2 + |B_{\mathbf{k}}|^2 - |D_{\mathbf{k}}|^2, \quad (2.14)$$

$$X_{\mathbf{k}} = \sqrt{4|A_{\mathbf{k}}B_{\mathbf{k}} - C_{\mathbf{k}}D_{\mathbf{k}}|^2 + (D_{\mathbf{k}}B_{\mathbf{k}}^* - B_{\mathbf{k}}D_{\mathbf{k}}^*)^2}. \quad (2.15)$$

For the choices of $A_{\mathbf{k}}-D_{\mathbf{k}}$ describing our model, one concretely obtains

$$\omega_{\pm}(\mathbf{k}) = \lambda \cdot \sqrt{1 \pm \frac{2}{\lambda} |\epsilon_{\mathbf{k}}| + \frac{(1 - \nu^2)}{\lambda^2} |\epsilon_{\mathbf{k}}|^2}. \quad (2.16)$$

For either purely \mathbf{v} or \mathbf{u} bosons, which are represented by $\nu = \pm 1$, the quadratic terms drop out, resulting in

$$\omega_{\pm}(\mathbf{k}) = \lambda \cdot \sqrt{1 \pm \frac{2}{\lambda} |\epsilon_{\mathbf{k}}|}. \quad (2.17)$$

2.1.2 Strengths and Weaknesses of Flavor-Wave Theory

First and foremost, the preceding section shows that linear flavor-wave theory discards h_3 and h_4 terms as well as the hard-core constraint. Secondly, the theory is limited to the paramagnetic regime, meaning the area of the singlet $J = 0$ ground state, where the triplons excitations exist and before the magnetism can emerge by their Bose-Einstein condensation [70]. For the condensed phase, one can no longer easily legitimize ignoring the hard-core constraint (and the h_3/h_4 like terms). In that case, one would have to rephrase the model in terms of a suitable new vacuum and restart the analysis.

A polarized paramagnet in a magnetic field for example, is still a scenario where a spin-wave theory can be very successfully applied even for spin-1/2 [165]². Therein one also finds trends, which are quite analogous to subsequent discussions, like the phase transitions estimated by classical Monte-Carlo and spin-wave theory matching

²Details can be found in the supplemental material of the reference.

exactly.

Furthermore, one can rewrite the theory for the condensed magnetic phases by creating a new set of states via linear combination of singlet and condensing triplon. This approach, which transforms the entire Hamiltonian, is of limited use in our thesis. One may however obtain information, e.g., about the emergence of Goldstone and Higgs mode in Ca_2RuO_4 [1], which is done quite detailed in reference [166] to discuss crystal field effects. Similarly, reference [6] makes a few points about the condensation in the triplon Kitaev-Heisenberg model. Nevertheless, transforming the Hamiltonian for each phase separately only to still ignore the h_3 and h_4 terms is a nontrivial amount of work for a questionable extend of gain.

Regarding its strength, the flavor-wave description can boast its quantum mechanical nature. As a results, quantum fluctuations and corrections are addressed, which can be a clear advantage compared to classical descriptions quantitatively, e.g., for estimating the magnetization [165].

Another advantage of the flavor-wave approach is that it does not really care whether \mathbf{u} and \mathbf{v} bosons are involved. If both have the same form of interactions, the overall effect can be calculated by just changing the value of ν . When that is not the case, one needs to adapt the dispersions in $B_{\mathbf{k}}$ and $D_{\mathbf{k}}$, which is still feasible. As far as the subsequent point about condensation goes, this might be a bit of a disadvantage in some regards, as \mathbf{v} represents the dipole and \mathbf{u} the quadrupole (cf. section 1.5.1), and discriminating between them is therefore an essential aspect of the magnetic order parameter.

The greatest advantage of the flavor-wave or spin-wave theory is that it is very established for normal spin and therefore also triplons (the orbital aspect does not matter here), which provides clear guidelines of handling and interpreting the results, especially regarding the Bose-Einstein condensation summarized in reference [70]. Following this review, we can make the ensuing claims about the flavor-wave results:

When the SOC λ dominates, the ground state consists of singlets $J = 0$ (states

$|s\rangle$) and thus represents a paramagnet (triplon vacuum). When A increases, one reaches a critical point where the gap to the triplon excitations closes [ω_{\pm} in equation (2.17) touches 0] at a given wavevector \mathbf{k}_0 , at which point a Bose-Einstein condensation takes place. The degeneracy results in a new coherent superposition $|\Psi\rangle = c_1 |s\rangle + c_2 |t\rangle$, where $|t\rangle$ represents the condensing triplet $J = 1$ state and c_i are coefficients. Hence $\langle T = s^\dagger t \rangle$ can become nonvanishing, in analogy to, e.g., $\langle S^x \rangle$ or $\langle S^y \rangle$ for normal spins and $\langle b^{(\dagger)} \rangle$ for regular Bose-Einstein condensates. Because the degeneracy is located at a given wave vector \mathbf{k}_0 , the wave function of the condensate has to modulate in space via the Fourier transformation $e^{i\mathbf{k}_0 \mathbf{r}}$, where \mathbf{r} is the position. For spin $\langle S^x \rangle$ this directly translates to a modulation in magnetic moment and therefore magnetic order. For the triplon one might think about the dipole or quadrupole nature of this order parameter, although in practice the \mathbf{v} interaction clearly dominates in strength and no argument is necessary.

Concretely, for the \mathbf{v} Kitaev-Heisenberg model in equation (1.79) (or equivalently the triplon Hamiltonian in equation (2.9) with $\nu = -1$), this leads to the phase diagram introduced below. First, we need to mention that the following spin-wave analysis was attempted in reference [6], but there are errors in the results, like the condensation happening at both Γ and K points in the Heisenberg limit. There are, however, no overall changes to the result, as reference [6] only uses the critical points and establishes the magnetic order via Monte-Carlo simulations and not condensation arguments. Our results here match the minima observed in the CPT study [7].

Following equation (2.10) and comments below it, one finds for the z -triplon with $J = A \cos(\alpha)$ and $K = A \sin(\alpha)$, that

$$|\epsilon_{\mathbf{k}}|^2 = A^2 \left[1 + 2 \cos^2(\alpha) (1 + \cos(\mathbf{k}\mathbf{v}_1) + \cos(\mathbf{k}\mathbf{v}_2) + \cos(\mathbf{k}(\mathbf{v}_1 - \mathbf{v}_2))) \right. \\ \left. + 2 \cos(\alpha) \sin(\alpha) (1 + \cos(\mathbf{k}\mathbf{v}_1) + \cos(\mathbf{k}\mathbf{v}_2)) \right], \quad (2.18)$$

while for the other flavors the three different cosine terms containing \mathbf{v}_i cycle in the

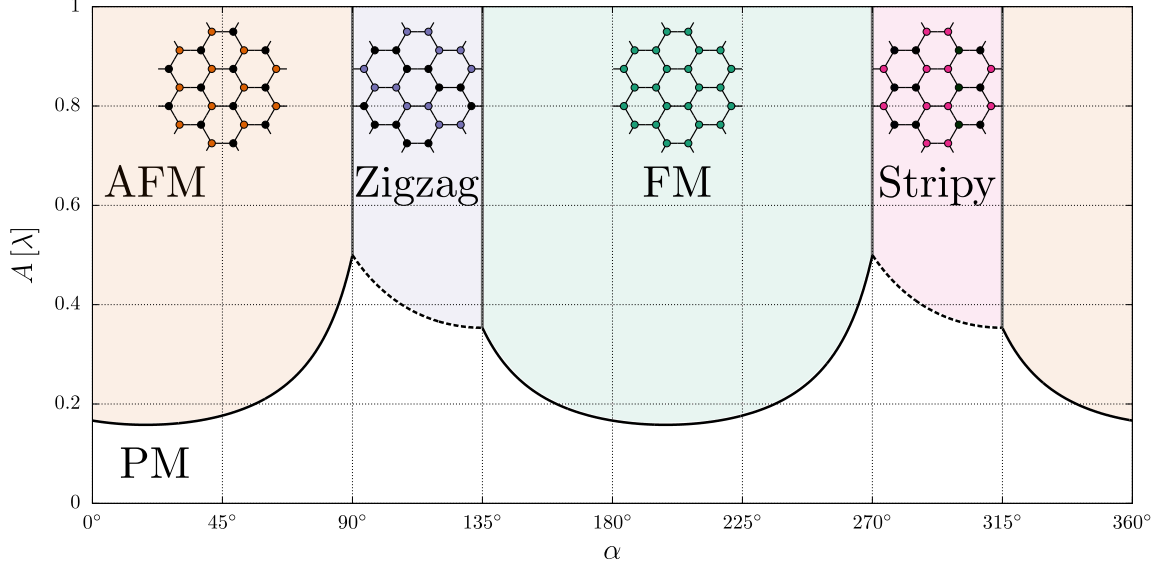


Figure 2.1. Spin-wave phase diagram for the triplon Kitaev-Heisenberg model restricted to \mathbf{v} bosons: The Heisenberg and Kitaev interactions are parametrized by $J = A \cos(\alpha)$ and $K = A \sin(\alpha)$, while λ denotes the spin-orbit coupling. The continuous black line labels condensation at the Γ point and the dashed one condensation at the M points. In the pure Kitaev limit ($J = 0$), the condensation happens simultaneously in the entire Brillouin zone while in the bond selecting case $J = -K$ entire lines from M to the Γ point vanish simultaneously. The phases are the antiferromagnetic (AFM) order, ferromagnetic order (FM), zigzag and stripy order. The sketches in each phase illustrate the order (black site denotes the opposite spin direction). Aside from the phase labels (FM \rightarrow AF and Zigzag \rightarrow Stripy)

$\cos(\alpha) \sin(\alpha)$ part.

Accordingly, the critical points where the ω_- solution in equation (2.17) vanishes are

$$A_{\text{crit},\Gamma}(\alpha) = \frac{\lambda}{2\sqrt{1 + 8 \cos^2(\alpha) + 6 \cos(\alpha) \sin(\alpha)}}, \quad (2.19)$$

for $\alpha \leq 90^\circ$, $135^\circ \leq \alpha \leq 270^\circ$ and $315^\circ \leq \alpha$ (2π periodicity of J and K via α) at the Γ point in the Brillouin zone, as well as

$$A_{\text{crit},M}(\alpha) = \frac{\lambda}{2\sqrt{1 - 2 \cos(\alpha) \sin(\alpha)}}, \quad (2.20)$$

when condensation takes place at the M point, which is feasible in regions where

$\cos(\alpha)$ and $\sin(\alpha)$ have different signs and $\cos(\alpha) \leq \sin(\alpha)$, meaning $90^\circ \leq \alpha \leq 135^\circ$ and $270^\circ \leq \alpha \leq 315^\circ$. Furthermore, at the Kitaev points ($J = 0$), the dispersion $|\epsilon_{\mathbf{k}}|$ is flat and the entire Brillouin zone serves as a condensation point, while in the bond selective case $J = -K$ at $\alpha = 135^\circ$ and $\alpha = 315^\circ$, entire lines connecting M and Γ points are reaching zero.

Based on these results we can construct the phase diagram seen in figure 2.1. In areas where the critical points are not reached, the quantum disordered or paramagnetic (PM) phase exists.

Since the Fourier transformation as introduced in the flavor-wave calculations regards the periodicity of the entire unit cell, the Γ point condensation results in a static (e^0) modulation of the entire unit cell magnetic moment. So if one moves along a real space lattice vector, the magnetic moment stays intact. This is the case for both the antiferromagnetic (AFM) and ferromagnetic (FM) order in figure 2.1, so technically the spin-wave, as it is written down, can not discriminate between those cases. Extra work is necessary, such as the exact diagonalization constructing the spin-structure factor in the first and second Brillouin zone to cover the real space modulations inside the unit cell.

In practice, however, one might compare with the order emerging in other methods like Monte-Carlo or argue/estimate which magnetic structure should emerge, e.g., by writing down the classical energy of a single site and its surroundings. More importantly, the order emerging in all Monte-Carlo and exact diagonalization simulations has always (aside from the nature of the liquid phase) been the one found in the “regular” (no singlet, just spin-1/2, spin-1, ...) Kitaev-Heisenberg model and thus one may establish the precise nature by comparison. Therefore one may reasonably attempt to draw the flavor-wave phase diagram exactly like the one in figure 2.1, which makes the flavor-wave a very useful and powerful approach.

Concluding, we fill the rest of the phase diagram. Condensation at an M point,

e.g., the one at, $\frac{\mathbf{b}_1}{2}$ ³ where \mathbf{b}_i are the reciprocal lattice vectors constructed from the real space \mathbf{v}_i , yields a modulation of the unit cell magnetic moment with $e^{i\mathbf{b}_1\mathbf{r}/2}$. The definition of the reciprocal vectors in two dimensions $\mathbf{v}_i\mathbf{b}_j = \delta_{i,j}2\pi/a$ ($a \equiv 1$ is the lattice constant) implies that there is no modulation implies that when one travels along lattice vector \mathbf{v}_2 . In \mathbf{v}_1 direction the modulation is exactly -1 per lattice vector and therefore the spins flip, which depending on the structure inside the unit cell itself being AFM or FM yields the stripy or zigzag magnetic orders. Similarly, the flat bands in the Kitaev limit result in a modulation with every possible \mathbf{k} vector, which represents a classical Kitaev spin-liquid, i.e. a disordered state.

For the zigzag phase there is a peculiarity that one should be aware of, e.g., when considering possible results of numerical simulations. Each triplon flavor $x/y/z$ condenses at a separate set of M points simultaneously, as evident by equation (2.18) and the comment below it. As a result, one flavor modulates in the \mathbf{v}_1 direction, while the others do so in \mathbf{v}_2 and $\mathbf{v}_1 - \mathbf{v}_2$ lines. When one builds a biased lattice (more bonds in one direction than the other), like the $N = 12$ site exact diagonalization simulations in this thesis, or if one considers any type of imbalance inherent in real materials, the degeneracy may be lifted and only one flavor condenses providing a clean zigzag phase as pictured in figure 2.1. Otherwise one might obtain a superposition of up to all three modulations happening in parallel, which might look (only) superficially different. We visualized it in figure 2.2. The thermal fluctuations of the Monte-Carlo simulation seem to prefer this modulation. The triplon specific condensation does in principle present the opportunity to lift this degeneracy differently and should be kept in mind.

³Side note: The high symmetry points of the hexagonal Bravais lattice can be found in [90]. In coordinates $(n, m) = n\mathbf{b}_1 + m\mathbf{b}_2$, the M point can be reached by $(\frac{1}{2}, \frac{1}{2})$, $(\frac{1}{2}, 0)$ and $(0, \frac{1}{2})$ (and equivalently subtractions of integer reciprocal lattice vectors), while the K/K' point is at $(\pm\frac{2}{3}, \pm\frac{1}{3})$. The form of \mathbf{b}_i does not matter, which is why squishing the honeycomb into a “square lattice”, i.e. $\mathbf{v}_1 = (1, 0)^T$ and $\mathbf{v}_2 = (0, 1)^T$ can be a great practical approach to the calculations.

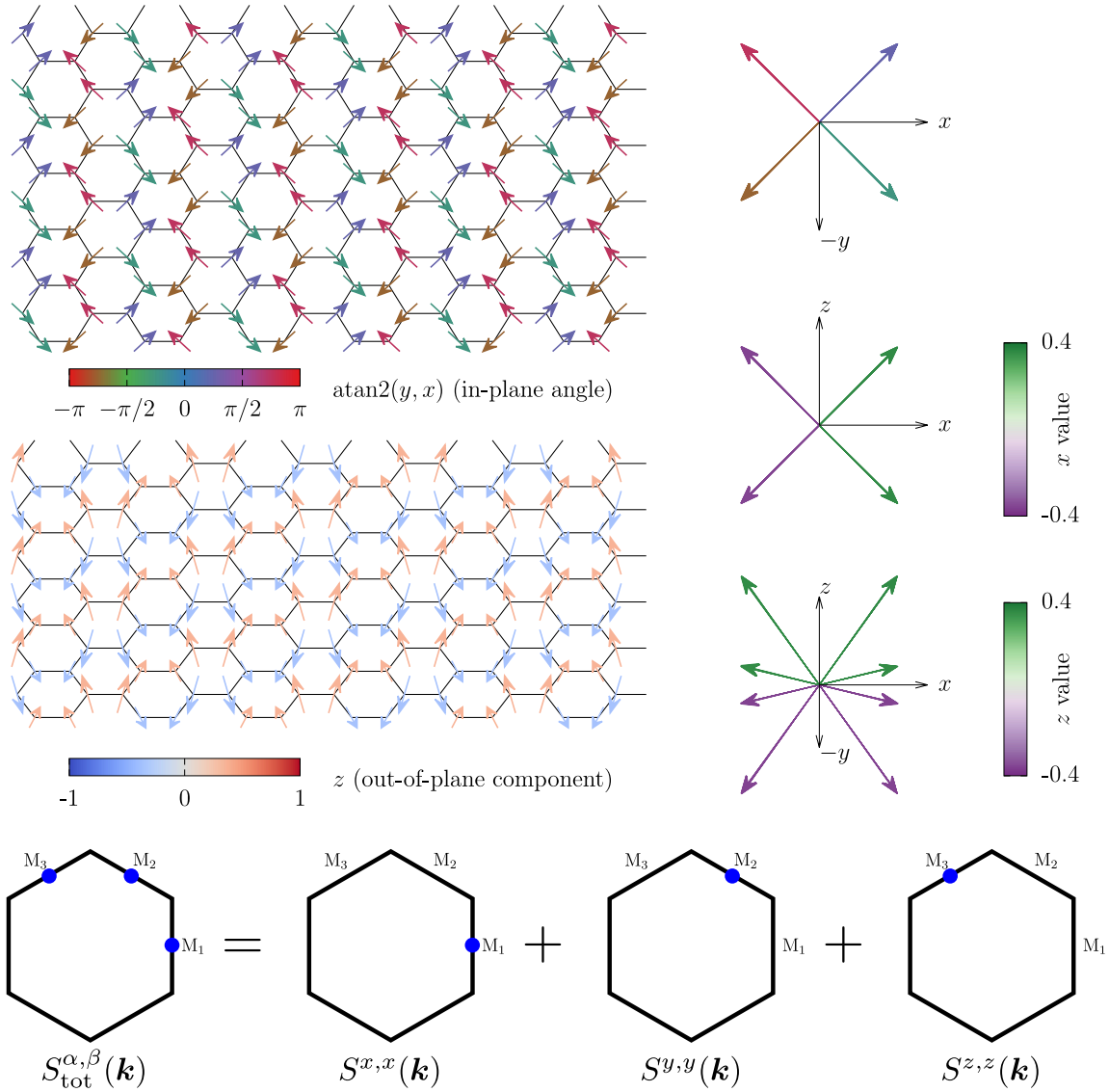


Figure 2.2. Simultaneous zigzag order of the \mathbf{v} boson components as established by semiclassical Monte-Carlo: The upper lattice plot represents a top down view where the in-plane angles are colored in, while the bottom lattice plot is the same structure tilted at 60° from the in-plane level with the out-of-plane component colored in. The structures on the right represents all spins on the lattice plotted from a common origin depicted by (from top to bottom) a top-down view of the x - y -plane (in-plane color scheme), a top-down view of the x - z -plane and an overview from a tilted angle (spherical coordinate $\theta = 54.74^\circ$). The spin pictures with a common origin are to scale (also in subsequent figures). Roughly rounded maximal values for the noted components are provided for the two plots on the bottom right as maximum scaling for the color maps. At the bottom, the significant contributions to the spin-structure factor of each boson are depicted by blue dots. The honeycombs represent the first Brillouin zone.

2.2 Exact Diagonalization and Related Methods

2.2.1 Exact Diagonalization

For the following methods there is no need for a thorough discussion. Exact diagonalization (ED) and classical Monte-Carlo (MC) methods for our model have been introduced in reference [6]. One may look into that reference for more details. Moreover, the key idea of the Lanczos method has been around for a long time, including in the condensed matter physics context [167]. For a comprehensive guide including the use of symmetries (e.g., translation symmetry as a result of periodic boundary conditions) we suggest reference [168].

The idea behind ED is simple: Why not solve the entire quantum mechanical problem outright? In order to accomplish this, one needs to construct the Hilbert space of the problem. For our lattice model, one might label the wave functions on each lattice site i as $|\Psi_i\rangle$, where $|\Psi_i\rangle \in \{|s\rangle, |t_x\rangle, |t_x\rangle, |t_z\rangle\}$ (cf. section 1.4.5.2), leading to the Hilbert space being spanned by the product states

$$|\Psi\rangle = \bigotimes_i |\Psi_i\rangle. \quad (2.21)$$

One may quickly realize the crucial problem: the Hilbert space scales with (in this case) 4^N , where N is the number of lattice sites. The scaling is exponential and hence increasing N is unsustainable. Case in point: Every state is characterized by a complex linear combination of the 4^N basis states. Therefore one requires $2 \cdot 4^N$ (ideally) double precision numbers to just write down a single state (let alone even attempting a diagonalization of the Hamiltonian). Every double precision number needs 64 bit, i.e. 8 byte, of memory space. For $N = 24$ this results in roughly 4.5

petabytes, which is not feasible.

It is possible to reduce the number using symmetries to only require a fraction of the space. Yet, when talking about a macroscopic object, like the pellet of $\text{Ag}_3\text{LiRu}_2\text{O}_6$ studied in [8], one has to, at least on paper, think in magnitudes of the Avogadro number $N_A = 6.022 \cdot 10^{23}$ atoms/mole regarding N . Moreover, one strives to describe, e.g., continuous symmetry breaking, which is only defined in the thermodynamic limit and can require careful thought in ED [169].

Nevertheless, ED turns out to be an excellent method. For problems not requiring a macroscopic number of degrees of freedom this is obvious. In our case the idea is to mimic an infinite lattice by using periodic boundary conditions. The problem of actually diagonalizing the matrix is (if full diagonalisation is not feasible) handled by, e.g., the previously mentioned Lanczos method, which is an iterative approach that necessitates the explicit memory capacity of saving two vectors and the Hamiltonian (more if one wants to remedy problems with orthogonalization).

The most obvious shortcoming of ED in our practical use is the lattice size in regards to the spin order it needs to host. This can be exemplified (next to of course trying to draw the order on a cluster with periodic boundary conditions without contradictions arising) when recalling the spin-waves and the translation of modulations in k and real space. As done in reference [5], the magnetic order can be gauged using the magnetic (spin) structure factor

$$S^{\alpha,\beta}(\mathbf{k}) = \left\| \sum_i e^{i\mathbf{k}\mathbf{r}_i} (T_{i,\alpha}^\dagger - T_{i,\beta}) |\Psi_{\text{ground}}\rangle \right\|^2, \quad (2.22)$$

where $S^{\alpha,\beta}$ here interprets the $\mathbf{v} \sim \mathbf{T} - \mathbf{T}^\dagger$ as spins. Similar magnetic structure factors regarding the quadrupole \mathbf{u} or the full magnetization (cf. equation (1.91)) can be constructed analogously.

The Fourier transformation is connected to the translation invariance provided by the specific choice of periodic boundary conditions. For $N/2$ unit cells (honeycomb

with N lattice sites), i.e. $N/2$ positions in real space, it provides $N/2$ momenta \mathbf{k} , which carry values directly resulting from the periodicity choice.

Every momentum \mathbf{k} is connected to a magnetic structure via its modulation in real space (cf. spin-wave condensation in section 2.1). If the lattice is build inappropriately or just too small to fit the magnetic order unit cell, this is equivalent to not being able to access $S^{\alpha,\beta}(\mathbf{k})$ or even the correct ground state $|\Psi_g\rangle$. For the Kitaev-Heisenberg model in magnetic fields, classical simulations suggest that extremely large lattices could be necessary to describe the magnetic orders involved [165].

2.2.2 Application to the Triplon Model

ED results for the triplon Kitaev-Heisenberg model can be found in figure 2.3 and associated publication [5] and thesis [6]. Next to the magnetic structure factor, the phase borders are also evaluated using derivatives of the ground state energy $E = \langle \Psi_g | H | \Psi_g \rangle$ and the ground state fidelity, the latter of which presents the overlap between the wave function of an old and current simulation $F = \langle \Psi_g(\text{old}) | \Psi_g(\text{new}) \rangle$ (here the angle $F = \langle \Psi_g(\alpha - d\alpha) | \Psi_g(\alpha) \rangle$). The simulation was done on a $N = 12$ site lattice [6], which represents the minimum size able to host stripy and zigzag phase simultaneously with one set of periodic boundary conditions. Full credit for the result in figure 2.3 goes to the author of [6]. We, however, had to rewrite parts of the code and reproduce the results in order to compare them with higher-order terms included in (the supplementary of) reference [5], which is why we adapt the picture and use it to provide the necessary foundation for the results in chapter 3.

The phase diagram contains the new aspect of a paramagnetic regime (cf. section 2.1) and the known (condensed) magnetic phases found in the spin-1/2 Kitaev-Heisenberg model [49, 50]. Moreover, like in the spin-1/2 case, the Kitaev phase gains a stable surrounding area of influence. Here the degrees of freedom consisting of triplons should indicate new physics, as the Majorana description of the original

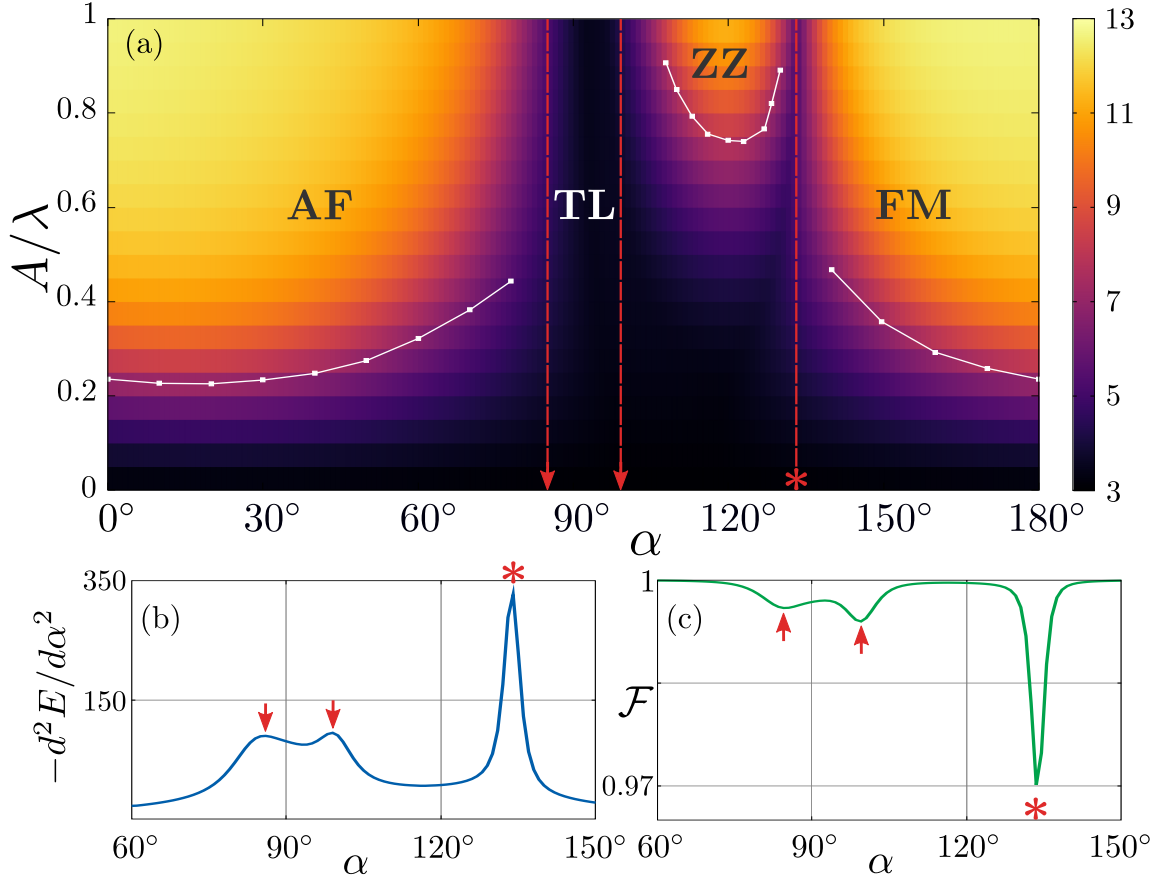


Figure 2.3. Exact diagonalization phase diagram for the triplon Kitaev-Heisenberg model restricted to \mathbf{v} bosons: The Heisenberg and Kitaev interactions are parametrized by $J = A \cos(\alpha)$ and $K = A \sin(\alpha)$, while λ denotes the spin-orbit coupling. The phase borders are fixed by analysis of the ground state fidelity F and second derivative of the ground state energy E (red vertical lines). The transition from the paramagnet (white horizontal lines) is fixed by the reversal points of the maximal magnetic structure factor, which also represents the color map. The phase are the antiferromagnetic (AF) order, ferromagnetic order (FM), triplon liquid (TL) and zigzag order (ZZ). Aside from the phase labels (FM \rightarrow AF and zigzag \rightarrow stripy), the phase diagram is symmetric regarding $\alpha \rightarrow \alpha + 180^\circ$. This figure has been previously published in references [5] and [6] and has been created by the author of the latter source.

Kitaev model is connected to rewriting spin-1/2 [4]. Therefore, this phase has been labeled triplon liquid.

Following [5], there have been new studies and insights, which motivate shortly

discussing this old result.

Characterizing this “triplon liquid” phase is a nontrivial issue attempted in detail in [170] and, as of last year, via QMC simulations in [157]. The first approach finds that it represents a strongly correlated paramagnetic phase, which transitions to a plaquette-VBS (valence bond solid) of triplon dimers when the sign of λ is flipped (more or less when translating their parametrization to our language in section 1.4.5.2). The sign flip is, of course, not covered in our model (and there is no reason aside from conceptual interest to do so). In the quantum Monte-Carlo study it is found to be a correlated, quantum paramagnetic state, which extends in a finite regime.

We do not strive to discuss the nature of the Kitaev phase in detail in this thesis. Rather, our interest is relegated to the topics [170] and [157] reference as other open questions, such as the inclusion of multi-particle interactions (h_3 and h_4 terms) as well as magnetic fields.

One should mention, that there has been increased interest in Kitaev and Kitaev-Heisenberg models with different spins. The ED study comparing regular spin-1 (and other spin- S) Kitaev regimes predates [5] by just a year [171] and motivated a closer look at the thermodynamic properties and emerging liquid in the model. The spin-1 Kitaev-Heisenberg model [65] actually postdates our triplon study. Since then, the investigation has been extended to spin- S systems [172], where the most obvious difference is the size of the finite area the Kitaev phases survive in, which decrease in a logical manner when going from the most quantum $S = 1/2$ to the classical limit $S \rightarrow \infty$, with only a minuscule area in the $S \geq 2$ case.

There is an intriguing observation implied in figure 2.3 and explicitly visible in the QMC equivalent in reference [157]: While the normal spin Kitaev models have a significantly smaller ferromagnetic Kitaev (meaning $J = 0$ and $K < 0$) phase than the corresponding antiferromagnetic Kitaev limit, the phases (specifically the boundaries as, e.g., AFM Heisenberg still becomes FM Heisenberg) are not symmet-

ric regarding $\alpha \rightarrow \alpha + 180^\circ$. For the triplons this is, however, clearly the case. This is a peculiarity that may be worth looking into, but not in this thesis, especially because in a magnetic field the trends fit the spin-based expectations (cf. chapter 3). Yet, this could also be an indicator of the Kitaev “limit” only existing cleanly in the $A \rightarrow \infty$ case and the paramagnet enforcing the symmetry.

As for the phase borders in general, reference [157] argues that those are fluctuation-induced first-order transitions, at least based on a Landau theory. This theory, as they admit, is not valid for h_3 and h_4 terms or flavor mixing (Γ interactions or crystal and magnetic field), as the symmetries are different. Regarding the condensation, one may observe that there are quantitative differences compared to the spin-wave and Monte-Carlo methods, which, in reference to the former, need to be attributed to interactions and finite size effects.

2.2.3 Advantages and Disadvantages

The clear advantage of ED is the direct solution of the quantum mechanical problem. On the other hand, this is connected to the disadvantage of the exponential scaling Hilbert space (and resulting nontrivial scaling of the expenditure of time). Compared to previous studies in [6], this problem has become significantly worse for the simulations in this thesis. In the absence of h_3 , h_4 and Γ interactions, the ground state always contains an even number of bosons (due to the pair creation and annihilation terms), meaning that the scaling is not 4^N (or a fraction of that because of, e.g., use of translational invariance), but [6, 7]

$$\dim(\text{even, even, even}) = \sum_{k=0}^N \sum_{k'=0}^N \sum_{k''=0}^N \binom{N}{2k} \binom{N-2k}{2k'} \binom{N-2k-2k'}{2k''}. \quad (2.23)$$

Even then, $N = 12$ seems to be a practical limitation.

The h_3 and h_4 terms or the magnetic or trigonal crystal field mixing flavors similar

to Γ interactions make this simplification impossible and therefore the full 4^N scaling needs to be taken into account.

Additionally, for large Hilbert spaces the evaluation of observables like the magnetic structure factor in equation (2.22) can be time consuming in itself. As saving the ground state for each simulation is unfeasible for large dimensions, which observable to analyze needs to be, in practice, decided beforehand. As will be apparent in the course of chapter 3, this choice might not always be obvious.

Another disadvantage connected to this is the comparatively more problematic way finite size effects may appear in the simulation. Consider, e.g., a $N = 2$ lattice with periodic boundary conditions. The possible states are $|ss\rangle$ and (we restrict ourselves to one flavor of triplons) $|tt\rangle$ in the even sector and $|st\rangle$ as well as $|ts\rangle$ in the odd one. Due to the finite size, the hopping terms $T^\dagger T$ can only(!) happen in the odd sector, while the pair creation and annihilation terms are restricted to the even sector. For $N = 4$ the terms are not forbidden on the other sector, but still have different chances of influencing the model (providing nonzero matrix elements). This of course would not happen on a real infinite lattice, as the differences disappear and the even and odd sector become comparable. In the simulations of [6] this has not been a problem (not only because the Hilbert space was constructed that way), but due to, e.g., the crystal field bringing the first excited state (odd) closer to the ground state (even), purely finite size based level crossing due to the imbalance of hopping and pair terms can happen.

ED also has significant advantages. In contrast to the spin-wave approach, which required a specific form of the Hamiltonian, ED can be done on any level. For Ca_2RuO_4 ED calculations have been employed on the low-energy triplon and Kugel-Khomskii Hamiltonian $H(S, L)$ (cf. equation (1.62)) levels [134]. Furthermore, a full electron based three-band Hubbard model has been analyzed [119]. Of course, the scaling of the latter (15^N) and the Kugel-Khomskii approach (enforced J_H) decrease the lattice size that is accessible to ED, which would not be a good idea for the

honeycomb where $N = 12$ is already barely enough for the magnetic orders. However, the square lattice Ca_2RuO_4 with slightly different interactions is more tolerant in this regard. Also, due to the complicated interplay of interactions, nontrivial analysis can be relevant even for a two-site model or the atomic limit [173–175].

Another advantage is the ability to (at least approximately) construct Green’s functions via the spectral representation [131], which for zero temperature is

$$G_{AB}^r(\omega \pm i\eta) = \sum_n \left[\frac{\langle \Psi_g | A | \Psi_n \rangle \langle \Psi_n | B | \Psi_g \rangle}{\omega - (\omega_n - \omega_g) + i\eta} - \frac{\langle \Psi_g | B | \Psi_n \rangle \langle \Psi_n | A | \Psi_g \rangle}{\omega + (\omega_n - \omega_g) + i\eta} \right], \quad (2.24)$$

where r denotes the retarded Green’s function, Ψ_n denotes an eigenstate of energy ω_n , ω_g is the ground state energy and η is the artificial factor keeping the poles of the real axis. Here A and B are arbitrary operators. This provides access to correlation functions and can be used to analyze, e.g., dynamical magnetic susceptibilities as seen in [6, 20].

Additionally the Green’s function provides a pathway to clever further manipulations, such as the cluster perturbation theory (CPT) and variational cluster approach/approximation (VCA) [176], which have been employed for the triplon model [7] and the Ca_2RuO_4 based calculations [13, 119]. For the latter, even a finite temperature analysis VCA analysis, which is highly nontrivial, has been published [154, 177]. Also, the Green’s function and impurity based dynamical mean-field theory (DMFT) has contributed to Ca_2RuO_4 research [26, 178]

We mention VCA, because the results connect to semiclassical Monte-Carlo applications in the subsequent discussion and [20, 134]. VCA strives to interpolate the thermodynamic limit by use of boundary conditions and a self-energy functional, which for appropriate structure of interactions and single-particle Green’s function (see [176], also for points made subsequently) is stationary if the Green’s function fulfills the Dyson equation of the infinite lattice. As such, the search for magnetic order becomes a variational problem where a so called Weiss field pushing the system

toward predetermined order can be added and the strength is set by calculating a stationary point (which necessitates repeated solution of the ED problem like any, e.g., minimization of a function would). The Weiss field needs to be added. If one suspects AFM order on a square lattice model for Ca_2RuO_4 , one may write

$$H'_M = M \sum_{\mathbf{r}} e^{i\mathbf{Q}\mathbf{r}} (n_{\mathbf{r}\uparrow} - n_{\mathbf{r}\downarrow}) \quad (2.25)$$

with $\mathbf{Q} = (\pi, \pi)$ and \mathbf{r} is the positions and then go on and vary M to find out if the stationary point is at $M = 0$ or at a finite value, thus signaling possible magnetism. We will revisit this discussion after the introduction of the semiclassical Monte-Carlo approach.

2.3 Classical and Semiclassical Monte-Carlo

The semiclassical Monte-Carlo (sMC) approach we introduce here represents a natural evolution of thinking about the classical Monte-Carlo simulations in the triplon model and may be useful when applied analogously to other problems. Importantly, the sMC scheme arises intuitively by writing down the triplon dimer wave function and this introduction of a quantum mechanical ansatz can directly explain why the classical MC simulations in reference [6] work as well as they do. Moreover, such an ansatz can indicate where the classical approach is not appropriate, as will become apparent when considering the Kugel-Khomskii type spin and angular momentum based Hamiltonian.

2.3.1 Classical Monte-Carlo for the Triplon Kitaev-Heisenberg Model

In order to discuss the idea we start with the classical MC scheme introduced in [6]. The starting point is trying to simulate the pure \mathbf{v} boson excitonic Kitaev-Heisenberg model constructed in equation (1.79). Consider the Hamiltonian

$$H = \lambda \sum_i |\mathbf{S}_i|^2 + \tilde{J} \sum_{\langle i,j \rangle} \mathbf{S}_i \mathbf{S}_j + \tilde{K} \sum_c \sum_{\langle i,j \rangle_c} S_i^c S_j^c, \quad (2.26)$$

where \mathbf{S}_i is a spin on site i and S_i^c ($c \in \{x, y, z\}$) its component. The first term is unusual compared to normal Kitaev-Heisenberg models and represents a first approach to describe the condensate.

In classical MC simulations \mathbf{S} is just a $O(3)$ unit vector, which can be parametrized by spherical coordinates $S^x = \cos(\phi) \sin(\theta)$, $S^y = \sin(\phi) \sin(\theta)$ and $S^z = \cos(\theta)$. This continuous variation of the spin components may be interpreted as $S = \infty$ when recalling the role of n in the Holstein-Primakoff transformation (cf. section 2.1), which is why one refers to this as the classical limit. Due to the first term only being a constant shift, the simulations result in a regular classical Kitaev-Heisenberg model found, e.g., in [50]. The phase diagram is the same as figure 2.1 at $A \rightarrow \infty$ (or effectively what you see at any $A > 1/2$).

So what about the first term introduced in equation (2.26) (or [6])? Triplons (or triplet states) cost energy λ , so reflecting this via punishing the length of the vector is a reasonable first approach. Naturally, the author of reference [6] reintroduced the radius r of the spherical coordinates and allowed it to take values from $0 < r < 1$ (the full occupation of the triplet, which represents a regular spin-1, is then $r = 1$ where the unit vector is recovered). The Monte-Carlo simulation of this model results exactly (aside from a global factor of $\tilde{A} = 4A$ explained subsequently) in the same

phase diagram as the spin-wave calculation in figure 2.1!

The next step was to reason that the magnetic moment should have the size corresponding to the expression of the condensate terms in [1], namely $|\mathbf{S}_i|^2 = r_i^2 = \rho_i$ and $\mathbf{S}_i = \sqrt{\rho_i(1 - \rho_i)}\mathbf{v}_i$ (an inconsistent transformation):

$$H = \lambda \sum_i \rho_i + \tilde{J} \sum_{\langle i,j \rangle} \sqrt{\rho_i(1 - \rho_i)}\sqrt{\rho_j(1 - \rho_j)}\mathbf{v}_i\mathbf{v}_j \quad (2.27)$$

$$+ \tilde{K} \sum_c \sum_{\langle i,j \rangle_c} \sqrt{\rho_i(1 - \rho_i)}\sqrt{\rho_j(1 - \rho_j)}v_i^c v_j^c.$$

The spin interaction reaches its maximal strength for $\rho = 1/2$, which exactly eliminates the factor 4 in the calculation and reproduces the phase borders of the spin-wave.

Two questions arise naturally: First of all: Why does MC work so well (meaning the perfect reproduction of the quantum mechanical spin-wave approach)? Secondly: Is there a way to straightforwardly arrive at the Hamiltonian in equation (2.27)?

2.3.2 Semiclassical Monte-Carlo for the Singlet-Triplet model

At this point, one may recall the spin and spin-dimer definitions found in equations (1.99) and (1.112). On a given site i , the wave function of the singlet-triplet system may be written as

$$|\Psi_i\rangle = c_s |s\rangle + \sum_{\tau=x,y,z} c_\tau |\tau\rangle = \left[c_s s^\dagger + \sum_{\tau=x,y,z} c_\tau t_\tau^\dagger \right] |\text{vac}\rangle, \quad (2.28)$$

where c_i are complex coefficients and $|\text{vac}\rangle$ is the vacuum state. Equation (1.112) also contains the concept of the director $\mathbf{d} = \mathbf{u} + i\mathbf{v}$ as a possible way to conveniently describe the wave function. Reintroducing this, enforcing normalization via ρ and

using the global arbitrary phase to fix the singlet to a real coefficient yields

$$|\Psi\rangle = \bigotimes_i |\Psi_i\rangle = \bigotimes_i \left[\sqrt{1 - \rho_i} s_i^\dagger + \sqrt{\rho_i} \sum_{\tau=x,y,z} d_{i,\tau} t_{i,\tau}^\dagger \right] |\text{vac}\rangle, \quad (2.29)$$

where $|\mathbf{u}_i|^2 + |\mathbf{v}_i|^2 = 1$ and we furthermore provided an ansatz for the wave function of the full lattice by considering a tensor product of the states for a single site. On a side note: this leaves 6 real parameters from the original 8 (4 complex c_{\dots}), with ρ being additionally restricted to values between 0 and 1.

The direct analogy to this ansatz (aside from a site-independent ρ) can be found in the spin-triplon based model for iron pnictides in reference [179], where it is referred to as ‘‘Gutzwiller-projected condensate of spin-1 T bosons’’. In the context of a more general discussion of spins and their Bose-Einstein condensation, this ansatz would fall under the umbrella of a mean-field variational ground state [71] with almost fully generalized parameters. Interestingly, the latter reference mentions the potential equivalence between this ansatz and classical spins, as we discuss a few paragraphs below.

The main problem of this ansatz in the context of the Kitaev-Heisenberg model here is its direct product approach not enabling the description of some states, e.g., some kind of fluctuating valence bonds the Kitaev interaction tries to enable. One can easily illustrate this problem with an example: Consider two spin-1/2 particles. Both have general wave functions $|\Psi_{1/2}\rangle = \alpha_{1,2} |\uparrow\rangle + \beta_{1,2} |\downarrow\rangle$, where the index labels the spin. Their product state

$$|\Psi_1\rangle \otimes |\Psi_2\rangle = \alpha_1 \alpha_2 |\uparrow\uparrow\rangle + \alpha_1 \beta_2 |\uparrow\downarrow\rangle + \beta_1 \alpha_2 |\downarrow\uparrow\rangle + \alpha_1 \alpha_2 |\downarrow\downarrow\rangle \quad (2.30)$$

can not be used to describe the singlet $1/\sqrt{2} \cdot (|\uparrow\downarrow\rangle - |\downarrow\uparrow\rangle)$, which is the textbook example for entanglement. Consequently, states where entanglement between different sites is important can not be described accurately.

However, aside from this restriction, the ansatz describes the degrees of freedom adequately and a minimization of its parameters ρ , \mathbf{u} and \mathbf{v} is akin to the use of the variational method [82], which according to the source “can be especially used sometimes for astonishingly excellent estimations of the ground-state energy of a physical system”.

Leaving this discussion aside, we continue with the application of the ansatz. It is useful to calculate

$$\langle \Psi | \frac{1}{2i} (\mathbf{T}_i - \mathbf{T}_i^\dagger) | \Psi \rangle = \sqrt{\rho_i(1-\rho_i)} \mathbf{v}_i, \quad \langle \Psi | \frac{1}{2} (\mathbf{T}_i + \mathbf{T}_i^\dagger) | \Psi \rangle = \sqrt{\rho_i(1-\rho_i)} \mathbf{u}_i, \quad (2.31)$$

or vice versa $\langle \Psi | \mathbf{T}_i | \Psi \rangle = \sqrt{\rho_i(1-\rho_i)} (\mathbf{u}_i + i\mathbf{v}_i)$. Note that the $\sqrt{\rho(1-\rho)}$ not being there in quantum mechanical operator ansatz $\mathbf{T} = \mathbf{u} + i\mathbf{v}$ in [1, 6] leads to a factor 4 discrepancy between the introduction of the couplings J and K for the triplon or \mathbf{v} boson Hamiltonian (cf. equations (1.79) and (1.85)).

Applying this ansatz onto the Hamiltonian in equation (1.85) (for $\Gamma = 0$) or (2.8), which was the starting point of the flavor-wave calculation, results in:

$$\begin{aligned} \langle \Psi | H | \Psi \rangle &= \lambda \sum_i \langle n_i \rangle + J \sum_{\langle i,j \rangle} \left(\langle \mathbf{T}_i^\dagger \rangle \langle \mathbf{T}_j \rangle - \langle \mathbf{T}_i^\dagger \rangle \langle \mathbf{T}_j^\dagger \rangle + \text{h.c.} \right) \\ &\quad + K \sum_c \sum_{\langle i,j \rangle_c} \left(\langle T_{c,i}^\dagger \rangle \langle T_{c,j} \rangle - \langle T_{c,i}^\dagger \rangle \langle T_{c,j}^\dagger \rangle + \text{h.c.} \right) \\ &= \lambda \sum_i \rho_i + J \sum_{\langle i,j \rangle} \left(4\sqrt{\rho_i(1-\rho_i)} \sqrt{\rho_j(1-\rho_j)} \mathbf{v}_i \mathbf{v}_j \right) \\ &\quad + K \sum_c \sum_{\langle i,j \rangle_c} 4\sqrt{\rho_i(1-\rho_i)} \sqrt{\rho_j(1-\rho_j)} v_{i,c} v_{j,c}, \end{aligned} \quad (2.32)$$

where we introduced the short-hand $\langle \mathbf{T}_i^\dagger \rangle \langle \mathbf{T}_j \rangle = \langle \Psi_i | \mathbf{T}_i^\dagger | \Psi_i \rangle \otimes \langle \Psi_j | \mathbf{T}_j | \Psi_j \rangle$ for later convenience.

For the emergence of magnetism, the essential property is the maximal energy gain it can provide. For this $\sqrt{\rho(1-\rho)} = 1/2$ cancel the factors 4 exactly and one

is left with the perfect equivalent of Hamiltonian (2.27) (and aside from the factor 4 length-based discussion in complete analogy to the classical spin model in equation (2.26)).

Importantly, this equivalence makes it clear why the classical spin simulation perfectly reproduces the quantum mechanical spin-wave calculation: the classical spins are mimicking a real quantum mechanical wave function based on the on-site singlet-triplet ansatz (or vice versa). Additionally, it makes the result of these simulations obvious: In [6] the MC simulations perfectly reproduces the spin-wave phase diagram in figure 2.1, which is therefore also true for the semiclassical version.

Moreover, this provides a more general framework for possible semiclassical MC simulations. The idea is straightforward: Minimize $E = \langle \Psi | H | \Psi \rangle$ (like the iron pnictide ansatz [179]), which is a real function of the parameters $(\rho_i, \mathbf{v}_i, \mathbf{u}_i)$ for every lattice site i . In our case, this requires a minimization in a $6N$ dimensional (recall $|\mathbf{u}_i|^2 + |\mathbf{v}_i|^2 = 1$) parameter space. This is where classical MC simulations come into play for the the minimization of E . Since H is always hermitian and E therefore a real function akin to a classical energy, all concepts like importance sampling via Markov chain and the Metropolis Algorithm requiring, e.g., $e^{-\beta E}$, where β is the inverse temperature $\beta = 1/(k_B T)$ can be applied like for any other classical MC simulation [168].

The recipe is as follows: On every lattice site the parameters are $0 \leq \rho \leq 1$ as well as \mathbf{u} and \mathbf{v} , which can be defined by a five-dimensional unit sphere, i.e. four angles from $0 \leq \phi \leq \pi$ and one angle $0 \leq \theta \leq 2\pi$. With these value the on-site part of equation (2.29) can be build as a complex four-dimensional vector in the $\{s, t_x, t_y, t_z\}$ basis. For pure on-site terms like SOC this is enough. For the interactions between different lattice sites one needs to build a second state for the other involved site and use a tensor product to obtain a sixteen-dimensional (complex numbers) pair state $|\Psi_{\text{pair}}\rangle = |\Psi_i\rangle \otimes |\Psi_j\rangle$. The calculation of the interaction is now trivially a simple matrix vector multiplication with the terms of the Hamiltonian, e.g. $\langle \Psi_{\text{pair}} | H | \Psi_{\text{pair}} \rangle$,

where H is the matrix in figure 1.13.

This way of conducting Monte-Carlo simulations has a few key advantages compared to the classical versions even beyond directly explaining their origin and success. First and foremost, using objects like the matrix in figure 1.13 directly, makes the incorporation of h_3 , h_4 and \mathbf{u} obvious and trivial⁴. For the classical scheme this is not the case. More importantly, the semiclassical approach can tell us directly that the classical MC can work perfectly, but also directly predict that (here for the h_3 and h_4 terms) the classical model will become insufficient for given interactions. We make this point in the subsequent $H(S, L)$ discussion, where it can be exemplified in a really basic manner. For us, however, this means that aside from the Kitaev limit, we may use the sMC simulation in any context of chapter 3.

Another advantage compared to the linear flavor-wave is the incorporation of the hard-core constraint at least on the mean-field level of the wave function itself. Also, the framework is quantum mechanical in nature. Additionally, the Hilbert space scaling with $6N$ instead of 4^N makes larger lattice sizes possible (essential, e.g., for the Kitaev-Heisenberg model in magnetic fields [165]) and saving the end result ground state for later postprocessing feasible. It also enables flexibility of calculating observables after or during the simulation. It should be noted that expectation values of an operator A are simply calculated via matrix vector multiplication with the ground state $\langle \Psi | A | \Psi \rangle$.

In contrast to ED or flavor-wave, the sMC method requires the inclusion of a temperature. This can be an advantage or disadvantage. Nevertheless, the trivial inclusion of temperature can be used to naturally obtain finite temperature results to contribute to relevant discussions, an example of which we mention later.

The big disadvantage, however, is the form of the ansatz restricting the validity of the results. In practice, not being able to describe the Kitaev phase is not ideal. Yet,

⁴On a practical note: Both ED and sMC schemes can now use the same definition of interactions via this matrix, meaning that incorporating new terms into one program directly translates to the other.

the direct connection between wave function and result might be used to gauge what can and can not be involved in the object of study based on the form of the ansatz. Furthermore, one may rethink the ansatz by trying to include, e.g., a valence bond basis in a future study. Another disadvantage is that there is a point of diminishing returns when comparing time and computation effort with ED for small lattices.

Finally, we conclude this part by commenting on the practical details of the implementation and use of sMC compared to the classical methods in [6]. The simulations are more complicated and should, in our experience (and the analogous problem of the Kitaev-Heisenberg model in a magnetic field [165]), be attempted using the parallel tempering method [180]. First of all, this makes parallelization easy. Secondly, there are a lot of competing ground states, as mentioned in [165], and a single simulation can strand in local minima quite easily.

2.3.3 Semiclassical Monte-Carlo Beyond the Low-Energy Subspace

We mentioned one advantage of ED being its possible use outside of the triplon framework. This leads to the question if something similar can be achieved for sMC as well.

In the hierarchy of approximations, the Kugel-Khomskii type Hamiltonian $H(S, L)$ in equation (1.62) presents an opportunity to attempt such an extension. There is direct and obvious gain: $H(S, L)$ is not restricted to the low-energy subspace and therefore able to cover, e.g., the influence of the quintet states.

Given the sMC calculations in the previous discussion, the implementation is straightforward: According to the definitions in section 1.4.5.2, the matrix form of \mathbf{S} and \mathbf{L} and their nine $|m_S, m_L\rangle$ basis states (for $S = 1$ and $L = 1$) with complex numbers (18 real coefficients) can be used to construct single site or pair states in complete analogy to the singlet-triplet system. The energy $E = \langle \Psi | H | \Psi \rangle$ is then

recovered via simple application of tensor and matrix vector products.

Here, one might ask if this kind of effort is even necessary, because it would be way cheaper to construct two classical unit vectors, i.e. a four parameter simulation, given that the earlier sMC method was directly equivalent to the classical model. Here, however, a look at the Hamiltonian can make the inadequacy of the classical model directly obvious.

Consider

$$\langle \Psi | H(S, L) | \Psi \rangle \sim \lambda \sum_i \langle \mathbf{L}_i \mathbf{S}_i \rangle + \sum_{\langle i, j \rangle} \left(c_1 \langle \mathbf{S}_i L_i^\alpha L_i^\beta \rangle \langle \mathbf{S}_j L_j^\gamma L_j^\delta \rangle + c_2 \langle L_i^\alpha L_i^\beta \rangle \langle L_j^\gamma L_j^\delta \rangle \right), \quad (2.33)$$

where we restricted ourselves to write down some paradigmatic terms in the Hamiltonian (with c_i being arbitrary coefficients). Transition to the classical interpretation of the results is provided by the expectation values $\mathbf{L}_{\text{classical}} = \langle \mathbf{L} \rangle$. For some terms like $\langle \mathbf{L}_i \mathbf{S}_i \rangle$, the nature of the product states $|m_S, m_L\rangle = |m_S\rangle \otimes |m_L\rangle$, which acts effectively like the two operators being on different sites, the classical formulation is equivalent. But clearly $\langle L_i^\alpha L_i^\beta \rangle \neq \langle L_i^\alpha \rangle \langle L_i^\beta \rangle$. Thus the classical is not expected to lead to the same results. More concretely, if a classical vector \mathbf{L} is aligned in z-direction, then $L_{\text{classical}}^x = 0 = L_{\text{classical}}^y$ and hence $\langle L^x \rangle = 0 = \langle L^y \rangle$. But, because $[L^x, L^y] = iL^z$, even only $\langle L^z \rangle \neq 0$ should imply $\langle L^x L^y \rangle \neq 0$.

More concretely, as we consider the Ca_2RuO_4 based 180° geometry (section 1.4.3), the Hamiltonian on the square lattice (has only two bond types) is given by [1]

$$H = \frac{t^2}{U} \sum_c \sum_{\langle i, j \rangle_c} [(\mathbf{S}_i \mathbf{S}_j + 1) O_{ij}^{(c)} + (L_i^c)^2 + (L_j^c)^2] \quad (2.34)$$

$$O_{ij}^{(c)} = (L_i^a L_j^a)^2 + (L_i^b L_j^b)^2 + L_i^a L_i^b L_j^b L_j^a + L_i^b L_i^a L_j^a L_j^b.$$

For classical vectors, the previously described superfluous ways of creating a vanishing orbital angular momentum can lead to degenerate solutions that are un-physical

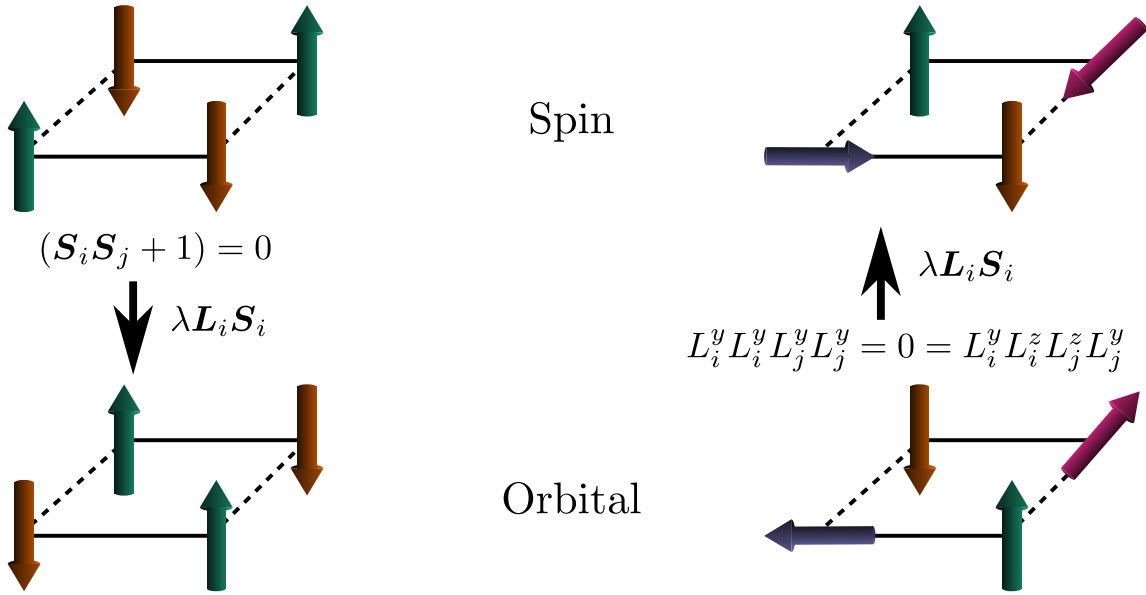


Figure 2.4. Problems in a classical MC simulation of the Kugel-Khomskii Hamiltonian: The lattices on the top depict spin and the ones on the bottom orbital angular momentum vectors. The antiferromagnetic spin order on the left side is a possibility consistent with the quantum mechanical simulation and based on the vanishing of $(\mathbf{S}_i \mathbf{S}_j + 1) = 0$ on each bond. Via spin-orbit coupling λ this kind of order enforces the orbital structure. For classical vectors, however, orbital orders can produce degenerate solutions due to the flawed treatment of $\langle L^\alpha L^\beta \rangle \neq \langle L^\alpha \rangle \langle L^\beta \rangle$.

for the quantum mechanical case. One of those scenarios is depicted in figure 2.4.

Hence, a classical simulation of the Kugel-Khomskii model should be avoided. Similarly, h_3 and h_4 terms in the triplon model, which carry, e.g., on-site $T_{i,\alpha}^\dagger T_{i,\beta}$, should adhere to the same arguments. Therefore, the classical MC simulation, which works perfectly for the \mathbf{v} bosons, should not be employed for the more general model, while the sMC scheme does not have any problems with the inclusion of other interactions per se.

Finally, we want to introduce a useful approximation. Of course, one can attempt a sMC simulation of $H(S, L)$ with the full 18 parameter (17 if one normalizes) on-site degrees of freedom. Yet, if one is not interested in the paramagnet (singlet) to triplon condensed magnet transition, but rather in a complementary model estimating if anything beyond the singlet-triplet model, e.g. via quintet influence for $t^2/U > \lambda$,

can occur, one may reasonably simplify the problem.

First, one may observe almost all choices of VCA calculation Weiss fields in [119], which are well informed by, e.g., previous attempts to describe similar models [181], are spin or orbital orders, meaning separate entities in S and L . This is easy to understand, as the main influence making these quantum numbers a bad choice (rather promoting the total angular momentum J) is the spin-orbit coupling, which loses influence when t^2/U or the crystal field Δ are increasing in size.

As a result one might try the ansatz

$$|\Psi\rangle = \bigotimes_i (|S_i\rangle \otimes |L_i\rangle) \quad |L_i\rangle = c_1 |m_L = -1\rangle + c_2 |m_L = 0\rangle + c_3 |m_L = 1\rangle, \quad (2.35)$$

and $|S_i\rangle$ analogously, where c_i are complex coefficients and m_L is the eigenvalue of L^z . The $J = 0$ singlet can not be described by these states in complete analogy to equation (2.30).

Nevertheless, every spin or orbital order, where S and L do not mix, can be described and due to normalization the complete parameter space is only $10N$, i.e. marginally more expensive than the singlet-triplet model. In the subsequent section this scheme is applied.

This line of thought also provides an opportunity to classify our sMC scheme in the context of known literature. While we arrived at the model via clear line of thought stemming from the evolution of the classical MC for triplons, the general idea of more or less writing down a variational wave function ansatz is obviously not a new concept. Even the subsequently discussed reference [182] notes analogous attempts going back to the 1990s. Yet, there is a reason why [182] describes the method and its implication in detail: The idea behind semiclassical MC simulations is quite powerful.

Importantly, reference [182] considers a model with biquadratic couplings $(\mathbf{S}_i \mathbf{S}_j)^2$. The form and inherent problems with a classical calculation regarding this term

should be analogous to the $(L_i^a L_j^a)^2$ terms in our model, so it is not surprising that the authors argue a classical simulation to be fatally flawed (they focus on quadrupolar correlations in their argument). More importantly, they work with a single spin-1, for which they neatly explain the semiclassical Monte-Carlo simulation. They baptize their model sSU(3) (semiclassical SU(3)) Monte-Carlo. Consequently, the $10N$ product state of S and L is a semiclassical $SU(3) \otimes SU(3)$ scheme.

We summarize the results of [182] discussing the power of their sMC scheme: Via cumulant expansion of the full quantum partition function they find the sMC scheme to be exact for high temperatures and approaching the variational (method) result for $T \rightarrow 0$. They argue that, while the model reduces to a mean-field treatment at $T = 0$, it provides advantages by capturing the thermal fluctuations more appropriately, displaying exact critical behavior and avoiding some difficulties regarding the Mermin-Wagner theorem. Nevertheless, the quantum fluctuations are not fully covered so the sMC is expected to be unreliable when it comes to quantitative assessments.

It should also be noted that sSU(3) remains quite topical, see, e.g., its use in [183]. Similarly, the $sSU(3) \otimes SU(3)$ could be a very prudent approach for Kugel-Khomskii type Hamiltonians. We try to establish this via the example in the subsequent section.

Moreover, after we found the semiclassical MC simulations to be a useful approach in [20], a 63 page guide focused on semiclassical simulations of spin-1 magnets based on a U(3) algebra (the basic idea is using dipole and quadruple moments on equal footing) was published [184]. This paper illustrates the power and potential usefulness of this kind of concept. In particular, during the writing of this thesis the bilinear-biquadratic model with Kitaev interactions was thoroughly analyzed with the U(3) sMC method [185], resulting in novel phases like an eight-color chiral spin liquid.

All in all, semiclassical Monte Carlo simulations could be a useful concept in the

singlet-triplet model and beyond. We go on to exemplify this for our model in particular with the results in reference [20].

2.3.4 Application to Ca_2RuO_4

As previously mentioned, many advantages of the sMC method only become apparent when discussing problems other than those analyzed in chapter 3. Because the application of sMC to triplons and Kugel-Khomskii type Hamiltonians is a result of this thesis, it seems prudent to provide an example for its usefulness. In order to do this, we quickly summarize the contribution of our sMC code to reference [20].

We quickly address to what extent we had a hand in each presented point. Fundamentally new and not published anywhere is the sMC data in figure 2.5, i.e. the triplon model sMC simulation. For both the triplon ED and $\text{SU}(3)\otimes\text{SU}(3)$ sMC simulations, we adapted and debugged code written for this thesis to the Ca_2RuO_4 based model and performed preliminary simulations on small $N = 4$ lattices. Yet, full credit for the execution and interpretation of the published simulations and their results goes to the author of reference [134], who also derived the model in equations(2.38)-(2.40) and conducted the Kugel-Khomskii based ED without any of our input. As for the projection onto the low-energy singlet-triplet subspace in analogy to section 1.4.5.2: The projection was accomplished with our Mathematica script and, even though an analysis of the triplon model has been done in reference [20], the low-energy model has never been published. In order to make the simulations transparent and reproducible, we add the triplon model in appendix A.4.

A hotly debated point of contention for Ca_2RuO_4 is the importance of tetragonal crystal field distortion Δ and spin-orbit coupling λ (cf. sections 1.1.7, 1.2 and introductory remarks or references [119, 134]), which are on-site terms described by

$$H_{\text{on-site}} = H_{\text{SOC}} + H_{\text{CF}} = \lambda \sum_i \mathbf{S}_i \mathbf{L}_i + \Delta \sum_i (L_i^z)^2. \quad (2.36)$$

The debate itself will not be a point of discussion here. Rather, we point out that it can obviously serve as a motivation for a parameter study of λ and Δ , which is what the subsequent phase diagrams display.

The superexchange interaction between neighboring sites is based on the 180° geometry discussed in section 1.4.3 with the additional inclusion of Hund's coupling into the Kugel-Khomskii perturbation theory as well as a next-nearest neighbor hopping (hereinafter referred to as bond "3" of the square lattice). According to [134], one finds

$$H = H_{\text{OF}} + H_{\text{OP}} + H_{\mathbf{L}\cdot\mathbf{L}} \quad (2.37)$$

$$H_{\text{OP}} = \sum_{c=1}^3 \sum_{\langle i,j \rangle_c} \sum_{\alpha \neq \beta} \left[t_{\beta,c}^2 \frac{U + J_{\text{H}}}{U(U + 2J_{\text{H}})} (\mathbf{S}_i \mathbf{S}_j - 1) (1 - \mathcal{L}_\alpha^2)_i (1 - \mathcal{L}_\alpha^2)_j \right. \\ \left. + \left(t_{\gamma \neq (\alpha,\beta),c}^2 \frac{(U + J_{\text{H}})}{U(U + 2J_{\text{H}})} - \frac{(t_{\alpha,c}^2 + t_{\beta,c}^2) J_{\text{H}}}{U(U - 3J_{\text{H}})} \right) (\mathbf{S}_i \mathbf{S}_j - 1) (1 - \mathcal{L}_\alpha^2)_i (1 - \mathcal{L}_\beta^2)_j \right], \quad (2.38)$$

$$H_{\text{OF}} = \sum_{c=1}^3 \sum_{\langle i,j \rangle_c} \sum_{\alpha \neq \beta} \left[-t_{\alpha,c} t_{\beta,c} \frac{J_{\text{H}}}{U(U + 2J_{\text{H}})} (\mathbf{S}_i \mathbf{S}_j - 1) (\mathcal{L}_\beta \mathcal{L}_\alpha)_i (\mathcal{L}_\beta \mathcal{L}_\alpha)_j \right. \\ \left. + \left(t_{\alpha,c} t_{\beta,c} \frac{(U - J_{\text{H}})}{U(U - 3J_{\text{H}})} \right) (\mathbf{S}_i \mathbf{S}_j + 1) (\mathcal{L}_\beta \mathcal{L}_\alpha)_i (\mathcal{L}_\alpha \mathcal{L}_\beta)_j \right], \quad (2.39)$$

$$H_{\mathbf{L}\cdot\mathbf{L}} = \sum_{c=1}^3 \sum_{\langle i,j \rangle_c} \sum_{\alpha \neq \beta} \left[t_{\alpha,c} t_{\beta,c} \frac{2J_{\text{H}}}{U(U - 3J_{\text{H}})} (\mathcal{L}_\beta \mathcal{L}_\alpha)_i (\mathcal{L}_\alpha \mathcal{L}_\beta)_j \right. \\ \left. - (t_{\alpha,c}^2 + t_{\beta,c}^2) \frac{1}{(U - 3J_{\text{H}})} (1 - \mathcal{L}_\alpha^2)_i (1 - \mathcal{L}_\beta^2)_j \right], \quad (2.40)$$

where the labels $\alpha/\beta/\gamma$ (kept matching to [20]) refer to the t_{2g} orbitals $xy/yz/xz$ (cf. section 1.1.2.2). Furthermore, $L^x = \mathcal{L}_{yz}$, $L^y = \mathcal{L}_{xz}$ and $L^z = \mathcal{L}_{xy}$ recover the

$H(S, L)$ framework. The parameters are based on the geometry and reference [13] (using ab-initio based values for Ca_2RuO_4). In all subsequent calculations $t_{xy,1} = t_{xy,2} = t_{xy} = 0.2 \text{ eV}$, $t_{xy,3} = t_{\text{NNN}} = 0.1 \text{ eV}$, $t_{zx,1} = t_{zx} = t_{yz} = t_{yz,2} = 0.137 \text{ eV}$ and all remaining $t_{\alpha,c} = 0$. Moreover, Hubbard repulsion and Hund's coupling are fixed to $U = 2 \text{ eV}$ and $J_{\text{H}} = 0.34 \text{ eV}$. For $J_{\text{H}} = 0$, the model reduces to the one in [1], which is why we used this case to establish the inadequacy of classical simulation in the previous section.

Projection onto the singlet-triplet ground state (cf. 1.4.5.2) provides the singlet-triplet model. One should note that $\Delta \sum_i (L_i^z)^2$ was also projected onto the low-energy subspace, which could be questioned to be a bad approximation in parts of the subsequently presented triplon phase diagram.

The results of ED and sMC for the triplon model are presented in figure 2.5. As mentioned in the previous section, sMC is not expected to be correct quantitatively. One may also argue that ED on small clusters (here $N = 8$) also underestimates hopping and pair creation/annihilation for the even/odd sectors as a finite size effect. Both aspects likely provide the main difference between the two phase diagrams: The extend of the paramagnetic phase is larger for ED (condensation happens "later"). This is in direct accordance to ED and sMC data for the triplon Kitaev-Heisenberg model found in figures 2.3 and 2.1 (sMC and spinwave phase borders correspond perfectly). Aside from this, the phase diagrams are comparable and both not unexpected given the analysis of a similar model in [166], which also explains the easy axis phase winning for $\Delta = 0$. Further details beyond that are discussed in [20].

For later discussions in this thesis there are two aspects worth pointing out. First of all, there is no simplification of the triplon Hamiltonian (in regards to discarding \mathbf{u} , h_3 and h_4 terms). Therefore one may realize that the higher order h_3 and h_4 terms do not seem to change the magnetic order even deep in the condensed phase where a lot of triplons are available. In fact, due to the projection of Δ , one partially ends up in a physically questionable scenario where the triplets are lower in energy (on-

site) than the singlet. Still no change is visible. This search for possible differences also represents the reason of equally spacing the simulation parameters in figure 2.5 instead of focusing on the (expected to be quantitatively wrong) position of the phase transition.

Secondly, the magnetic order is produced only by the \mathbf{v} bosons. This is unsurprising given the condensation mechanism in reference [1] is based on them, but could have feasibly changed as the \mathbf{u} and higher order terms are not discarded.

Continuing with the Kugel-Khomskii model in figure 2.6, one may first of all observe that the simple $SU(3)\otimes SU(3)$ sMC reproduces all magnetic orders of ED beyond the paramagnet. When comparing with the triplon model, one may attribute the two new phases for very small SOC λ to the influence of the quintet states. As a result, the $SU(3)\otimes SU(3)$ sMC can be a useful counterpart to the triplon model, gauging the breakdown of the low-energy limit. If the results are not straightforward, one may attempt to simulate the ground state of the same Hamiltonian with a full $18N$ parameter ansatz.

In regards to the phase borders, one may find the expected quantitative disagreements. However, the estimation of the borders for the Kugel-Khomskii model is very rough, which can be seen when considering the evaluated samples for each method provided in reference [20]. The borders of the paramagnet, for example, are not recalculated but recovered from the triplon model, which one can solve quite quickly for the same $N = 8$ lattice. The paper can also be consulted when interest in further information such as spin-structure factor calculations for the sMC and ED models arises.

An essential argument for the usefulness of the sMC scheme can be given when recounting the relationship to other studies. Reference [20] can be seen as a continuation of the analysis in reference [13] (and hence [119]), which is mainly based on VCA. Aside from a slightly different focus, e.g., in regards of the parameter space, the magnetic orders found should be reasonably comparable. Yet, reference [13] lacks

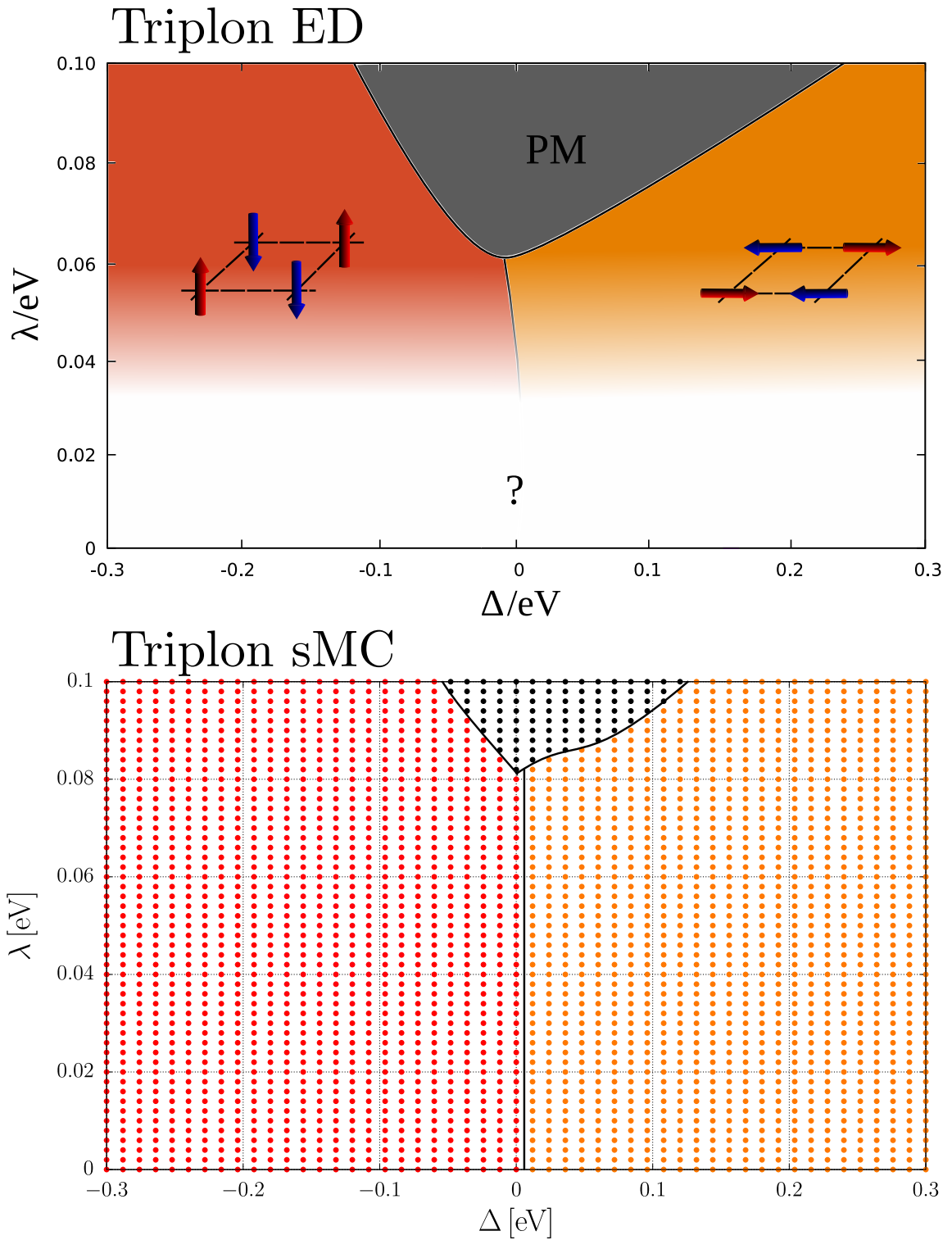


Figure 2.5. ED and sMC phase diagrams for the triplon model based on Ca_2RuO_4 : The cartoons provide orders of the \mathbf{v} bosons and thus the magnetic moment. For large spin-orbit coupling λ a paramagnetic regime exists. The sMC phase diagram reproduces ED aside from quantitative changes of the critical points. The ED phase diagram has been adapted from reference [20].

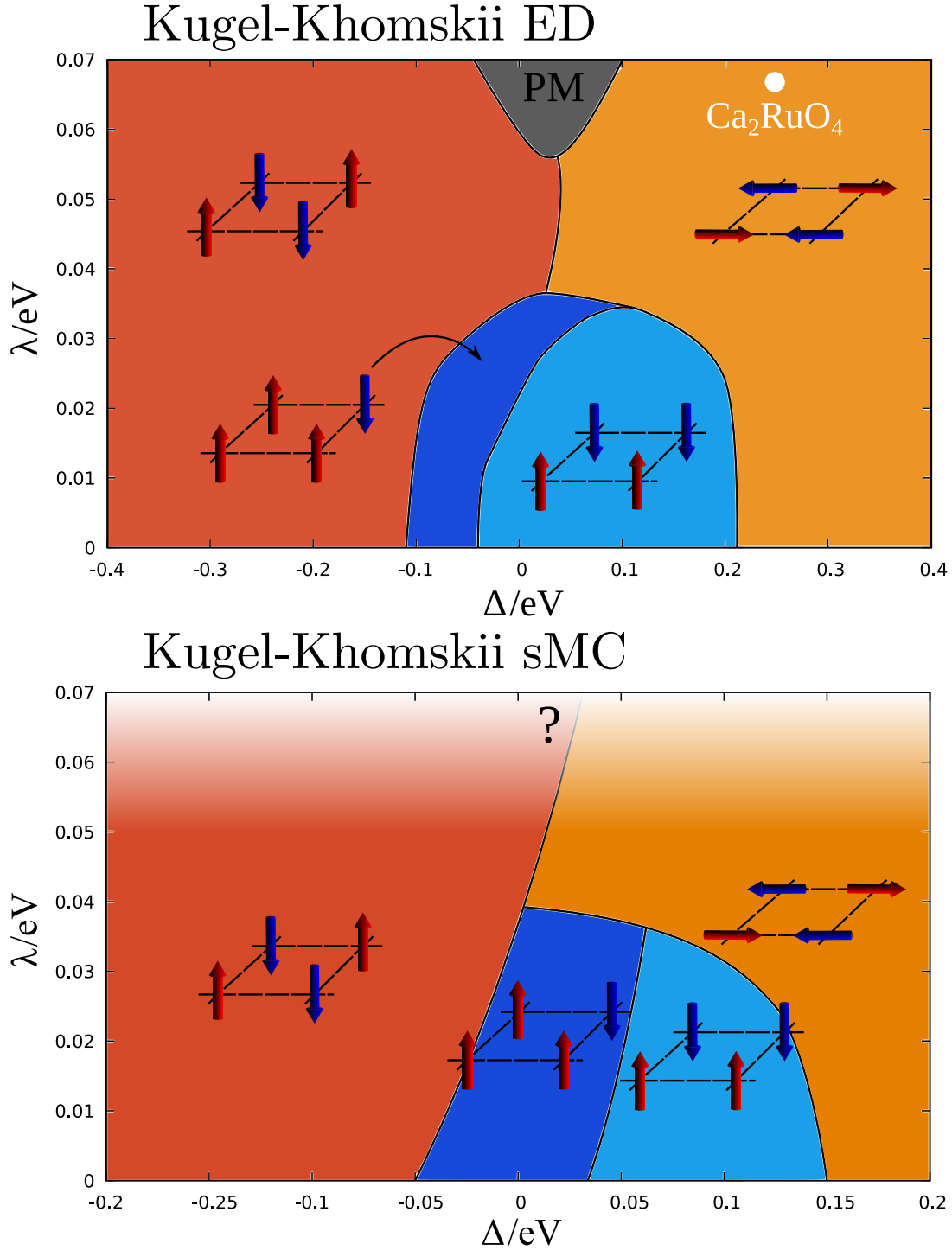


Figure 2.6. ED and $SU(3)\otimes SU(3)$ sMC phase diagrams for the Kugel-Khomskii model based on Ca_2RuO_4 : The cartoons provide orders of the spin \mathbf{S} . The sMC model is able to reproduce all magnetic orders found in ED, except for the paramagnet (as a result of ansatz choice). In particular, a 3-up-1-down order previously undetected in VCA simulations is established. The figure has been adapted from reference [20].

the 3-up-1-down spin order (dark blue in both diagrams). The reason for this is the high computational effort of VCA (ED, here on an $N = 4$ site three-band Hubbard model needs to be evaluated many times to optimize the order parameter) paired with the fact that a Weiss field (cf. equation (2.25)) needs to be set in the correct form. The 3-up-1-down phase has not been considered in the VCA simulations.

For the more thorough but only ED based analysis in reference [20], the 3-up-1-down order was found with support of the sMC model checking the result for a bigger lattice and unbiased choice of observable regarding its direction (details see [134]).

Consequently, the comparatively cheap sMC evaluation could have improved (and likely reduced the need for a few Weiss-field choices) the VCA calculation by providing a second opinion regarding the possible magnetic orders. Naturally, one could have been aware of a possible 3-up-1-down order beforehand given the related model in [186] establishing such as phase. Yet, in practice one may not be aware of all relevant literature and the sMC model provides a quick check, e.g., for ED lattice size and VCA Weiss-field choice. Thus, sMC should be considered in future VCA studies.

2.3.5 Use of Semiclassical Monte-Carlo Beyond This Thesis

As mentioned before, the subject matter of this thesis does not present the ideal showcase for the full extend of usefulness of the sMC scheme. There are a few projects that have been attempted or could be considered in the future. Here, we quickly point these topics out.

Monte-Carlo is bound by the necessity of a temperature for the partition function and probabilities. As a counterpart to ED simulations at $T = 0$ this is an inconvenience. Yet, especially when implemented via parallel tempering, the existence

of a plethora of temperatures can be used as an advantage when looking into finite temperature properties of models. Moreover, reference [182] points out that the semiclassical scheme is expected to capture the thermal fluctuations more appropriately than a mean-field treatment would.

With our code, a finite temperature study of the Ca_2RuO_4 based model in the $\text{SU}(3)\otimes\text{SU}(3)$ scheme has been attempted by the author of [134]. In the reference, one may find that the sMC method seems to capture the magnetic Neel transition in the Mott regime of Ca_2RuO_4 reasonably well. Observables such as specific heat and magnetization can be easily implemented in sMC. As a finite temperature VCA study finds nontrivial intermediate orbital order in the vicinity of this transition [154, 177], an intriguing project could be to go beyond the simplified $\text{SU}(3)\otimes\text{SU}(3)$ scheme to try and capture this behavior.

In the course of the finite temperature study, a recipe to set the temperature choice via feedback optimization [187] according to Fick's law of diffusion has been tried (also [134]). Again, we contributed the code, but full credit for finishing this side project (and in this case the explicit implementation of how the new temperatures are chosen) goes to the author of reference [134]. The main idea is to track the copies (sets of parameters which are exchanged between the temperatures in parallel tempering Monte-Carlo) that have been at the highest and lowest temperatures respectively and count their location (i.e. temperature) at each exchange. If the temperatures are set inadequately, e.g. because of a phase transition producing a sharp change in energy, the copies might not make it to the other end and their average position is akin to a step function. Ideally, a linear statistical occupation is expected and the feedback loop tries to extrapolate what kind of temperatures one may choose in order to obtain that behavior. However, as expected by the claims of [187], our model falls under the category of being too simple to really profit from the extra effort.

We finally turn the discussion to projects that have not been attempted but could

be relevant. First of all, future VCA studies could profit from a sMC calculation.

Secondly, one might attempt to include a novel way of post-processing the simulation results. The machine-learning base (TK-)SVM code (tensorial-kernel support vector machine) [188] is published (source code publicly available) and designed to find order parameters for classical Monte-Carlo simulations. As the end result of the sMC simulation recovers the vector interpretation of the spin (or boson or angular momentum) via the expectation value, there is no reason to expect any incompatibility. TK-SVM has been used (with partially surprising results) for a Kitaev based model [189, 190] and hence provides a potentially relevant motivation for triplon Kitaev-Heisenberg focused analysis, especially because, at least on paper, similar models (triplons in pnictide [179] or biquadratic spin-1 dimers with qunitet involvement [191]) have complicated quadrupolar order and even octupolar order for excitons has been discussed for $5d^2$ $J = 2$ states [192]. Moreover, the expressions of dipole and quadrupole (cf. section 1.5.1, in particular the Van-Vleck contribution for the magnetic moment) operators in the spin-orbital model have more an extra contribution compared to spins. However, during our simulations the order has always been obvious so far, so the need to use TK-SVM has not been there.

Thirdly, the recent emergence of the previously mentioned $U(3)$ semiclassical spin-1 simulation scheme [184] provides a plethora of potential ideas. One may, on the one hand, try to directly adapt the results in a $U(3) \otimes U(3)$ scheme or think about translating the degrees of freedom of the full $18N$ parameters or the triplon model to a form where direct use of the results in [184] can be gained. To exemplify this one might point, e.g., to the combination of sMC with the equations of motion ([184] refers to this as molecular dynamics simulations providing access to dynamic properties). For triplons, this could be done with in real space with a part-wise definition of the hard-core (anti-)commutation relations. For the $H(S, L)$ Kugel-Khomskii model the dynamics of angular momentum and spin can be written down

quite trivially. On for example finds for the honeycomb model in equation (1.62):

$$\begin{aligned} \frac{dS_h^d}{dt} &= -i \left[S_h^d, \sum_c H^{(c)} \right] \\ &= \sum_c \sum_{\langle i,j \rangle_c} \sum_{\tau=x,y,z} (\delta_{h,i} \varepsilon_{d\tau k} S_i^k S_j^\tau + \delta_{h,j} \varepsilon_{d\tau k} S_i^\tau S_j^k) \left(\frac{t^2}{U} O_{ij}^{(c)} - \frac{tt'}{U} P_{ij}^{(c)} + \frac{t'^2}{U} Q_{ij}^{(c)} \right), \end{aligned} \quad (2.41)$$

where ε is the Levi-Civita symbol. Analogously, the angular momentum dynamics are described by

$$\begin{aligned} \frac{dL_h^z}{dt} &= \sum_{\langle i,j \rangle_z} (\mathbf{S}_i \mathbf{S}_j + 1) \left[\frac{t^2}{U} \left(\delta_{h,i} (L_i^x L_i^y + L_i^y L_i^x) ((L_j^y)^2 - (L_j^x)^2) \right. \right. \\ &\quad + \delta_{h,j} (L_j^x L_j^y + L_j^y L_j^x) ((L_i^y)^2 - (L_i^x)^2) \\ &\quad \left. \left. - \frac{tt'}{U} \left(\delta_{h,i} (L_i^y L_i^z L_j^z L_j^y - L_i^x L_i^z L_j^z L_j^x + L_i^z L_i^y L_j^y L_j^z + L_i^z L_i^x L_j^x L_j^z) + i \leftrightarrow j \right) \right] \right. \\ &\quad \left. + \dots \quad (\text{x and y bond}). \right. \end{aligned} \quad (2.42)$$

The x and y bonds are qualitatively different but also straightforward to calculate. As we are not trying to analyze the dynamics in this thesis but rather point out interesting projects, a look at the above terms is sufficient. One can easily see (cf. definitions in section 1.5.1), that a lot of quadrupole terms are involved in the dynamics (very obvious for $\Gamma \sim tt'/U = 0$), which clearly presents a potential point of interest that could warrant a closer look.

All in all, sMC provides a multitude of potentially interesting future projects.

3

Analysis of the Triplon Honeycomb Model

3.1 Quadrupoles and Higher-Order Terms

The triplon model in the 90° bonding geometry derived in section 1.4.5.2 has been analyzed previously in some limited cases. In the original inception of the model [1], analysis was limited to the rough, flavor-wave based description of the quadratic terms h_2 in what amounts to the bond-selecting $J = -K$ case of the Kitaev-Heisenberg model. Additionally, past studies of the Kitaev-Heisenberg(Γ) model [5–7] have been primarily focused on the \mathbf{v} boson terms in the Hamiltonian. Consequently, the nature of the quadrupoles \mathbf{u} and the higher-order terms, namely h_3 and h_4 interactions provided in equations (1.86)–(1.88), are comparatively unknown quantities. Both quadrupoles and higher-order terms are noticeably intriguing on paper.

For \mathbf{u} , one may recall the introduction via spin-dimer nematics in section 1.5. In the case of spins, both boson types \mathbf{u} and \mathbf{v} are, if only one of them is present, designed to be indicators of the nematic or quadrupole order. The dipole in those systems is described by $(\mathbf{u} \times \mathbf{v})$. Yet, in the spin-orbital dimer, the magnetization adheres to the formula in equation (1.91) (instead of equation (1.115)), thus carrying

a term proportional to \mathbf{v} , which via the previous analysis (e.g. figure 2.3) established excitonic magnetism via condensation. Nevertheless, the \mathbf{u} terms remain part of the spin-orbital quadrupole (cf. equation (1.104)). Given that they exist in the Hamiltonian (equation (1.78)) in more or less equal form, one might ask whether dipole and quadrupole can be treated on similar footing and if the latter might even be made to condensate. Moreover, one should answer how the \mathbf{u} terms affect the triplon Kitaev-Heisenberg model of dipoles studied in [5]. Lastly, one might point to related triplon models like the one for iron pnictide [179], where quadrupole order is important.

The higher-order terms present an even greater unknown. There are a plethora of terms in the Hamiltonian. Some of them can be clearly identified as potentially drastic changes to the system. Khaliullin [1] notes the biquadratic exchange $(\mathbf{J}_i \cdot \mathbf{J}_j)^2$, where $\mathbf{J} = -i\mathbf{T}^\dagger \times \mathbf{T}$ and its potential to cooperate with the pair creation terms via similar structure $(T_i^\dagger T_j^\dagger T_i T_j)$. Aside from this possibility of exotic consequences, the straightforward question is whether the inclusion of the higher order terms leaves the Kitaev-Heisenberg magnetic phases, in particular the triplon liquid, intact. This relates back to the Bose-Einstein condensation of spin-based magnons in reference [70]: Condensation takes place, but the resulting density facilitates the importance of the interactions and therefore potentially rich new physics.

We are, however, not going to focus on the Γ interaction of the extended Kitaev-Heisenberg model. The reason for this is that within the derivation of the sMC scheme, we pointed out the equivalence of the quadratic model to classical spins. As a result one suspects the Γ terms to reproduce known results from the extended Kitaev-Heisenberg model of regular spins [50] (which itself can be topical and nontrivial [193]), with the distinctions of a possible different behavior of the triplon liquid (here the behavior in the magnetic field is the more prominent discussion due to the possible half-integer thermal Hall effect in α -RuCl₃ [53]) and the existence of a paramagnetic regime.

3.1.1 Influence of the Quadrupole Bosons

We begin this analysis with the focus on the \mathbf{u} terms. The spin-wave theory of the quadratic Hamiltonian based on equation (1.78) with more general parametrization is

$$\begin{aligned}
 H &= \lambda \sum_i n_i + 4J_v \sum_{\langle i,j \rangle} \mathbf{v}_i \mathbf{v}_j + 4K_v \sum_c \sum_{\langle i,j \rangle_c} v_i^c v_j^c + 4J_u \sum_{\langle i,j \rangle} \mathbf{u}_i \mathbf{u}_j + 4K_u \sum_c \sum_{\langle i,j \rangle_c} u_i^c u_j^c \\
 &= \lambda \sum_i n_i + (J_v + J_u) \sum_{\langle i,j \rangle} \left(\mathbf{T}_i^\dagger \mathbf{T}_j + \text{h.c.} \right) + (K_v + K_u) \sum_c \sum_{\langle i,j \rangle_c} \left(T_{c,i}^\dagger T_{c,j} + \text{h.c.} \right) \\
 &\quad + (-J_v + J_u) \sum_{\langle i,j \rangle} \left(\mathbf{T}_i^\dagger \mathbf{T}_j^\dagger + \text{h.c.} \right) + (-K_v + K_u) \sum_c \sum_{\langle i,j \rangle_c} \left(T_{c,i}^\dagger T_{c,j}^\dagger + \text{h.c.} \right). \quad (3.1)
 \end{aligned}$$

With λ , J_v , J_u , K_v and K_u there are five free parameters. In order to gain some intuition we start with a more limited case and increase the complexity step by step.

Consider the case $J_v = J_u$ and $K_v = K_u$. If one leaves the magnitude $A = J_v + J_u$ as a single parameter, the ν and the rest of the flavor-wave theory in equation (2.9) are recovered. The main difference is that now there is a motivation to lift the restriction of $\nu = \pm 1$ representing the pure \mathbf{u} or \mathbf{v} cases and let the parameter take arbitrary values. In essence, we strive to obtain information about the influence of the pair creation and annihilation terms.

The solutions are provided in equation (2.16). The critical points still emerge from the (unchanged) maximal values of $|\epsilon_{\mathbf{k}}|$, i.e. the M and Γ point depending on the sign and size of α , where $J = J_v + J_u \equiv A \cos(\alpha)$ and $K = K_v + K_u \equiv A \sin(\alpha)$. Only now (at least for $\nu \neq \pm 1$), the critical points emerge from solving the quadratic equation

$$1 - 2|\epsilon_{\mathbf{k}}/A| \frac{|A|}{\lambda} + (1 - \nu^2) |\epsilon_{\mathbf{k}}/A|^2 \left(\frac{|A|}{\lambda} \right)^2 \stackrel{!}{=} 0 \quad (3.2)$$

for $x = A/\lambda$ ($\epsilon_{\mathbf{k}}/A$ is independent of A) the first possible \mathbf{k} value. One finds the same solutions as in equations (2.19) and (2.20), with the difference that the factor

$\frac{1}{2}$ in front of the square root is switched for $1/(\nu + 1)$ or $-1/(\nu - 1)$ depending on the sign of ν .

The resulting critical points are sketched in figure 3.1. One may find that the overall effect of increasing $|\nu|$ and therefore the addition of the pair terms lowers the threshold of the critical point. That trend is expected, as the increase in ν more or less acts like a growth of the interactions parameters like J_ν . The sign of ν dictates which boson condenses (see subsequent examples within slightly different parametrizations). For $\nu < 0$ the \mathbf{v} boson condenses resulting in magnetic order. For $\nu > 0$, however, the \mathbf{u} boson is dominant and, as a result, all Kitaev-Heisenberg phases can emerge as quadrupole variants. For $\nu = 0$ both solutions are degenerate. Semiclassical Monte-Carlo simulations picks one of the phases at random as both represent rather deep and disconnected energy minima.

For showcasing the emerging magnetic and quadrupole orders we switch to a more systematic approach. In general, one might parametrize the Kitaev-Heisenberg model parameters in the following way:

$$J_v \equiv A \cos(\alpha) \cos(\xi), \quad K_v \equiv A \sin(\alpha) \cos(\xi), \quad (3.3)$$

$$J_u \equiv A \cos(\beta) \sin(\xi), \quad K_u \equiv A \sin(\beta) \sin(\xi), \quad (3.4)$$

where α and β are the angles varying the two distinct Kitaev-Heisenberg interactions and ξ is the angle mixing the models, with $\xi = 0$ representing the pure dipolar \mathbf{v} boson model, $\xi = \pi/2$ the quadruple and there is freedom to vary the overall signs when including angles up to 2π . It should be noted that we redefine A compared to the previous parametrization.

For an intermediate analysis we assume $\alpha = \beta$, i.e. both boson types carrying the same kind of interaction. In this case the excitations can be calculated analogously

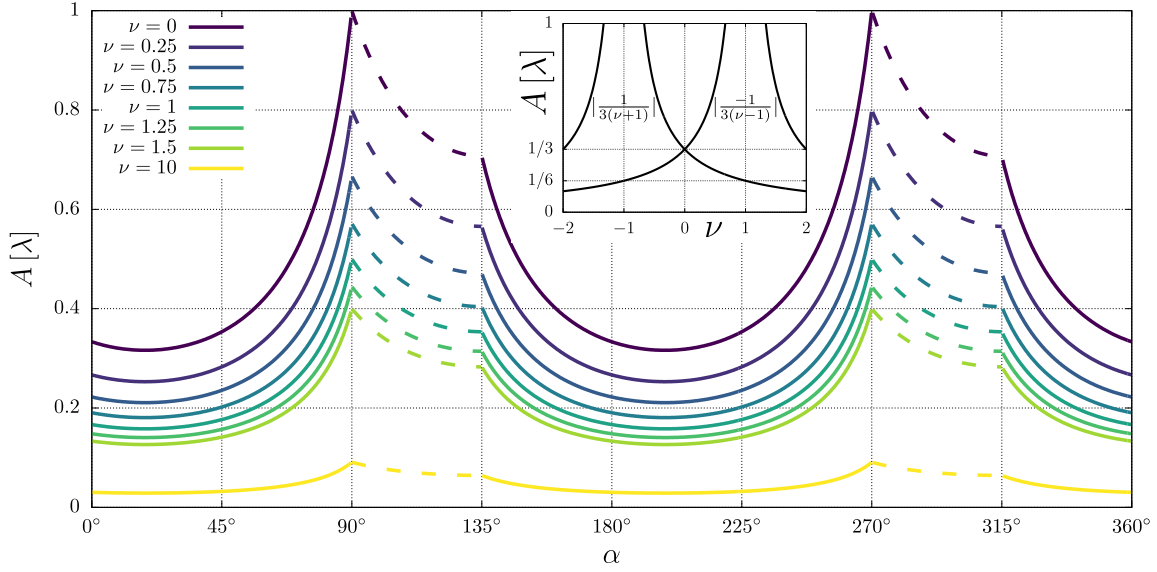


Figure 3.1. Critical points signaling condensation for various values of the pair term factor ν ($\nu = \pm 1$ represent a model of purely \mathbf{u} or respectively \mathbf{v} vector bosons) for various value of α (labeling the Kitaev-Heisenberg model via $J = A \cos(\alpha)$ and $K = A \sin(\alpha)$): The continuous line depicts the condensation at the Γ point while the dashed one denotes the critical point being at M. The overall allocation of Γ and M point phases is identical to the Kitaev-Heisenberg model. The sign of ν , however, decides which boson condenses. In the inset, critical behavior in the Heisenberg limit $\alpha = 0$ is sketched in dependence of ν .

to the previous cases and the result is

$$\omega_{\pm} = \lambda \left\{ 1 \pm 2 \left(\frac{|A|}{\lambda} \right) |\cos(\xi) + \sin(\xi)| |\epsilon_{\mathbf{k}}^{\text{old}}| + \left(\frac{|A|}{\lambda} \right)^2 [(\cos(\xi) + \sin(\xi))^2 - (\cos(\xi) - \sin(\xi))^2] |\epsilon_{\mathbf{k}}^{\text{old}}|^2 \right\}^{\frac{1}{2}}, \quad (3.5)$$

where ϵ^{old} constitutes the dispersion with regular $J = J_v$ and $K = K_v$ from below equation (2.10) (without A like in equation (3.2)). Hence, ϵ^{old} provides a known quantity with identified maxima and minima in dependence of α from the normal Kitaev-Heisenberg model. As a result, the nature of the critical points does not change, only the value of $|A|/\lambda$ needed to reach them, just like ν . Yet, now we can observe the effect systematically without increasing the overall magnitude of the

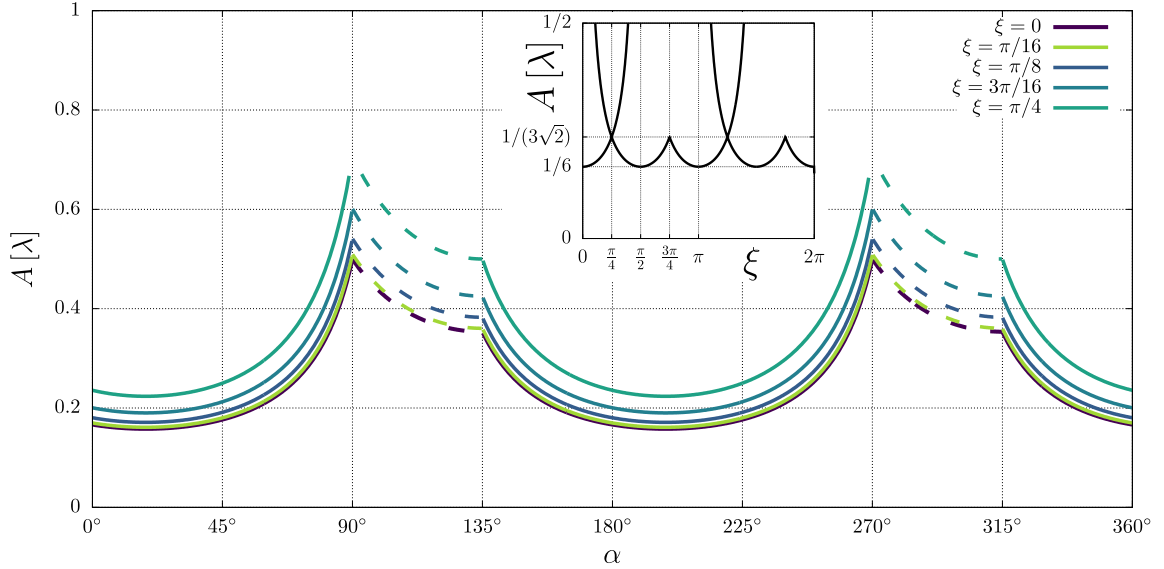


Figure 3.2. Critical points signaling condensation for various values of the mixing angle ξ : The Kitaev-Heisenberg couplings for both \mathbf{u} and \mathbf{v} vector boson models are $J_v = A \cos(\alpha) \cos(\xi)$, $K_v = A \sin(\alpha) \cos(\xi)$, $J_u = A \cos(\alpha) \sin(\xi)$ and $K_u = A \sin(\alpha) \sin(\xi)$ (the index denotes the type). The continuous line depicts the condensation at the Γ point while the dashed one denotes the critical point being at M. The overall allocation of Γ and M point phases is identical to the Kitaev-Heisenberg model. The inset depicts the critical points in dependence of ξ in the Heisenberg $\alpha = 0$ limit.

interactions. The result is depicted in figure 3.2. The critical points in the figure are calculated by $\omega_- \stackrel{!}{=} 0$ as before.

We therefore obtain the critical points quite easily. Nevertheless, one should analyze what kind of condensation can actually take place. Of course, one could argue via classical energies or the overall size of the dominant coupling. However, semiclassical Monte-Carlo trivially solves this problem. Figure 3.3 depicts the phase diagram for the $\alpha = 0$ Heisenberg limit with varying mixing angle. Depending on the dominant mixing term ($\cos(\xi) > \sin(\xi)$ or vice versa), the order switches between quadrupole and dipole, which is natural as the models exist in parallel on equal footing. Due to the mixing angle covering sign changes from the $J < 0$ to $J > 0$ regime, this change in type (\mathbf{u} or \mathbf{v}) boson order is paired with a change in magnetic (or quadrupole)

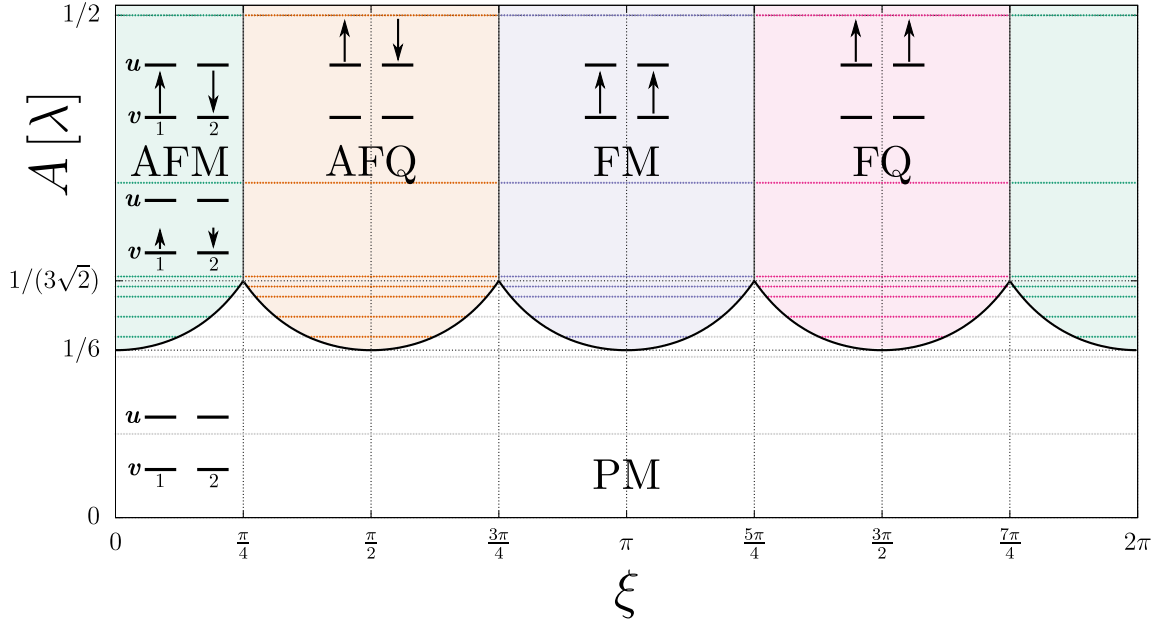


Figure 3.3. Phase diagram of the $\alpha = 0$ Heisenberg model with various mixing angles ξ between \mathbf{u} and \mathbf{v} bosons: The Kitaev-Heisenberg couplings for both \mathbf{u} and \mathbf{v} vector boson models are $J_v = A \cos(\alpha) \cos(\xi)$ and $J_u = A \cos(\alpha) \sin(\xi)$ (the index denotes the type). The points represent semiclassical Monte-Carlo simulations in the singlet-triplet framework verifying the phases, while the line depicts the critical points calculated via flavor-wave theory. One finds perfect agreement between both approaches. Moreover, the phases interchange between quadrupole ((anti-)ferroquadrupolar (A)FQ) and dipole ((anti-)ferromagnetic (A)FM) on even footing as predicted by the sign and size of $\cos(\xi)$ and $\sin(\xi)$. Below the critical points, the paramagnet (PM) is located. The pictograms depict order and length $\sqrt{\rho}$ of the vectors qualitatively (1 and 2 represent the sublattice).

order changing from ferro- to antiferromagnet (or quadrupole).

The behavior of the spin length $\sqrt{\rho}$ depicted in the pictograms on the left side of figure 3.3 remains completely unchanged from the old \mathbf{v} based analysis [6]. This is, however, trivially explained by its role in the ansatz of the singlet triplet wave function in equation (2.29) and not worth a closer look.

It is also natural that the other magnetic phases in the Kitaev-Heisenberg model, namely zigzag and stripy (cf. figure 2.1), work analogously. The respective example for $\alpha = 120^\circ$ can be found in figure 3.4. One may hence claim, that the possibility

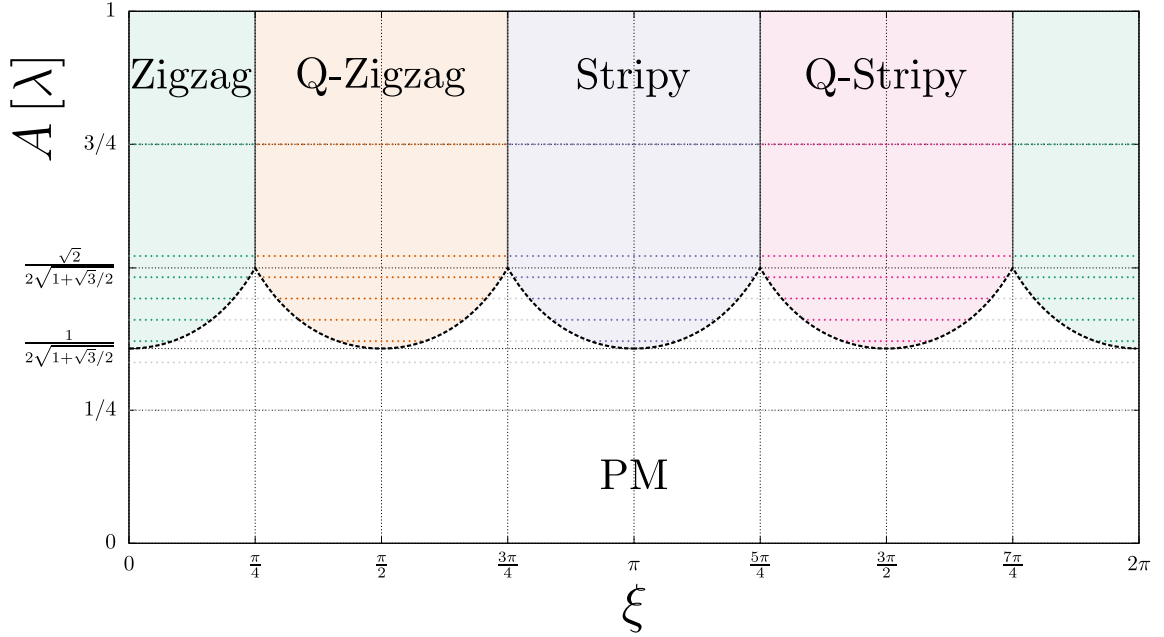


Figure 3.4. Phase diagram of the $\alpha = 120^\circ$ Kitaev-Heisenberg model (zigzag phase) with various mixing angles ξ between \mathbf{u} and \mathbf{v} bosons: The Kitaev-Heisenberg couplings for both \mathbf{u} and \mathbf{v} vector boson models are $J_v = A \cos(\alpha) \cos(\xi)$ and $J_u = A \cos(\alpha) \sin(\xi)$ (the index denotes the type). This figure is the counterpart to 3.3. The points represent semiclassical Monte-Carlo simulations in the singlet-triplet framework verifying the phases, while the line depicts the critical points calculated via flavor-wave theory (dashed because the condensation happens at the M point). Next to the known zigzag and stripy orders one finds their quadrupole counterparts. PM denotes the paramagnetic regime.

of finding quadrupole zigzag or stripy orders in this kind of model exists, at least on paper.

The evolution of phases is straightforward. The reason for this is that both \mathbf{u} and \mathbf{v} exist basically non-interacting next to each other. The only connection is the spin-orbit coupling $\lambda \sum_i n_i$, which for the wave function ansatz (2.29) results in $\langle \lambda \sum_i n_i \rangle = \lambda \sum_i \rho_i (|\mathbf{u}_i|^2 + |\mathbf{v}_i|^2) = \lambda \sum_i \rho_i$, as $(|\mathbf{u}_i|^2 + |\mathbf{v}_i|^2) = 1$. For the quantum mechanical operators $n_i = \mathbf{T}_i^\dagger \mathbf{T}_i = |\mathbf{u}|^2 + |\mathbf{v}|^2 \leq 1$ [1]. As a result, the \mathbf{u} and \mathbf{v} bosons are exclusive. If one can save an infinitesimally small bit of energy more by ordering \mathbf{v} instead of \mathbf{u} , then maximizing this energy gain enforces $|\mathbf{v}|^2 = 1 \rightarrow |\mathbf{u}|^2 = 0$. Basically, both models exist completely exclusive to each other, but as one needs to

pay energy for spin length, the more efficient model wins outright.

As a corollary, this means that any kind of quadrupole counterpart to the magnetic phases in the extended Kitaev-Heisenberg models [50] should surface for the corresponding choices of spin interactions. Notably, this seems to extend to the triplon liquid. ED calculations for $A = 1$ reproduce the results of figure 2.3 perfectly, assuming one switches the sign in the spin-structure factor of equation (2.22) from $-$ to $+$ to observe the \mathbf{u} bosons.

We now move to the general model with $\alpha \neq \beta$. Coming from the perspective of two models just existing next to each other, it is clear what can be expected. Whichever model can provide the lowest energy for itself wins. However, as the energies are a function of α (analogous β), and the energy gain for both models scales with $A \cos(\xi)$ and $A \sin(\xi)$ respectively, the exact form of the phase borders might not always be obvious at first glance. This is especially true when doing calculations in spin-wave theory, where everything is written in the same \mathbf{T} triplons and the relevant trends might be superficially obscured. Yet, the solutions are straightforward. Consequently, the essential features are always the dispersions, which are described by

$$\begin{aligned} |\epsilon_{\mathbf{k},\text{h/p}}|^2 = & J_{\text{h/p}}^2 + K_{\text{h/p}}^2 + 2J_{\text{h/p}}^2(1 + \cos(\mathbf{k}\mathbf{v}_1) + \cos(\mathbf{k}\mathbf{v}_2) + \cos(\mathbf{k}(\mathbf{v}_1 - \mathbf{v}_2))) \\ & + 2J_{\text{h/p}}K_{\text{h/p}}(1 + \cos(\mathbf{k}\mathbf{v}_1) + \cos(\mathbf{k}\mathbf{v}_2)) \end{aligned} \quad (3.6)$$

for the z bosons (and cycling the three cosine terms through the summand in the second line of the equation for the others). Here we indexed the Kitaev-Heisenberg parameters for the hopping (h) and pair terms (p), which are fixed by $J_{\text{h/p}} = \pm J_v + J_u$ and $K_{\text{h/p}} = \pm K_v + K_u$. Therefore, the search for minima and maxima of these terms remains in complete analogy to the previously discussed cases, i.e. we can restrict the discussion to Γ and M points in the Brillouin zone.

Similarly, the solutions of $\omega_- = 0$, which provide the critical points, are $A_{\text{crit}}/\lambda =$

$|1/(|\epsilon_{\mathbf{k},h}| \pm |\epsilon_{\mathbf{k},p}|)|$ (the minimal A_{crit} decides the condensation). One can use these spin-wave solutions and extensively discuss the possible phase diagrams for any values of α , β and ξ rather quickly, especially because the resulting magnetic or quadrupole order is quite obvious as evidenced by the previously described ξ based phase diagrams. We, however, restrict ourselves to one example.

The almost worst case scenario for the influence of the \mathbf{u} bosons can be gauged from the $\beta = 0$ case. “Almost” here refers to the fact that one compares energies and the lowest possible one (also clear from how low the critical value A_{crit} is, e.g., in figure 2.1 or the classical energy discussion in [6]) is in vicinity of the Heisenberg limit, shifted slightly to the area where J and K have the same sign. Nevertheless, the pure Heisenberg $K = 0$ case is close to that and nicer to interpret and visualize. As the energy of \mathbf{u} bosons is therefore close to the optimum, their competition with the \mathbf{v} ground state will be the comparatively most fierce one.

The resulting phase diagram for the $\beta = 0$ case can be seen in figure 3.5. Therein, we visualized the competition by depicting the lowest A_{crit} solution at each the Γ and M point. The observations are restricted to $0^\circ \leq \alpha \leq 180^\circ$, as the spin-wave results do not change for the remaining angles (as evident by the preceding discussions). When a \mathbf{u} solution becomes relevant, a flat line emerges, as the interactions of this boson are not dependent on α . As long as the \mathbf{u} terms do not outright take over, the phase borders can remain completely unchanged in regards to α , as one can observe for all transitions in the $\xi = 0$ and $\xi = \pi/16$ cases as well as the zigzag to FM critical point for $\xi = \pi/8$. The point of condensation given by the lowest A_{crit} , however, can change as expected by earlier studies the $\alpha = \beta$ case.

At $\xi = \pi/8$, where the size of the \mathbf{u} terms scaling with $\sin(\xi)$ is still multiple times smaller than its dipole counterpart, there is already a significant area where the quadrupoles enforce the order. They do so by replacing the energetically most unfavorable (at least from a spin-wave or classical energy standpoint) area around the Kitaev phase, which is why one should ensure its survival in a full ED simulation.

3.1. Quadrupoles and Higher-Order Terms

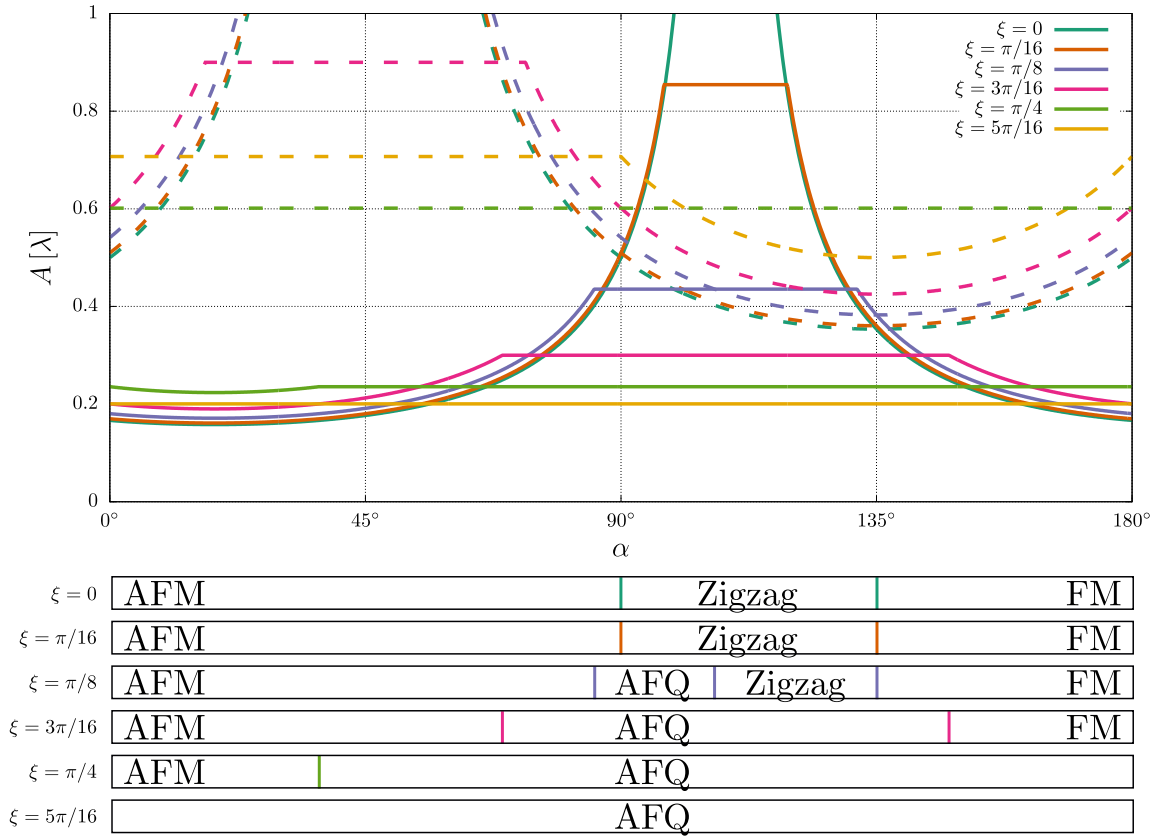


Figure 3.5. Flavor-wave critical points and corresponding phase diagram of the \mathbf{u} and \mathbf{v} based Kitaev-Heisenberg model: The interactions are defined by the Heisenberg and Kitaev couplings $J_v = A \cos(\alpha) \cos(\xi)$, $K_v = A \sin(\alpha) \cos(\xi)$, $J_u = A \cos(\beta) \sin(\xi)$ and $K_u = A \sin(\beta) \sin(\xi)$. Here, exemplarily, the \mathbf{u} bosons are restricted to the antiferromagnetic Heisenberg case $\beta = 0$. In order to visualize the behavior of the critical points, we illustrated the minimal value solutions at the Γ point (continuous line) and M point (dashed line) for various angles of ξ . The flat lines represent the \mathbf{u} solution, which does not vary with α , taking over. At the bottom, the resulting phase diagrams are presented with the magnetic orders being labeled by (A)FM for the (anti-)ferromagnet, AFQ for the antiferroquadrupole and zigzag as known from the regular Kitaev-Heisenberg model. One should note that at $\xi = \pi/4$, where dipoles and quadrupoles are on equal footing, there is a degeneracy between AFQ and FM at $\alpha = 180^\circ$. Moreover, due to the bosons not interacting but being exclusive, the α -dependent phase borders do not necessarily change with ξ .

In fact, the critical angle ξ at which the quadrupole order emerges is $\tan(\xi) = 1/3$, i.e. roughly $\xi = \pi/10$. Further increase of the importance of \mathbf{u} via ξ leads to the expected enhanced prominence of the quadrupole phase. When both scalings are

the same at $\xi = \pi/4$, the critical points are located at the energy degeneracies of the pure Heisenberg limits $\alpha = 0^\circ$ and $\alpha = 180^\circ$, with AFM winning in areas where the Kitaev interaction benefits the energy and losing where the opposite is true. At some point beyond that, the quadrupole order spans the entire phase diagram.

As for ED investigating the Kitaev phase: This is the point where due to nontrivial effort being necessary for each simulation, a free parameter study becomes unpleasant. Consequently, we switch to a discussion of how important one may expect the quadrupole terms to be based on the model derived in section 1.4.5.2. As discussed subsequently, the effect is expected to be minute. Regarding the spin-liquid one may look ahead to the higher order terms based discussion and figure 3.17. On the scale presented therein, the data of the model with \mathbf{u} bosons would (if included) look indistinguishable to the “original” (only \mathbf{v} terms).

There are two main reasons for the unimportance of the \mathbf{u} terms. First of all, the overall strength characterized by the mixing angle ξ is expected to be small enough to not care even when following the “almost worst case” spin-wave results established above. Secondly, the interactions are not even close to the almost worst case. On the contrary, they are much closer to the opposite limit. Given the form of the interactions in equation (1.78), one finds that $\beta = 135^\circ$, i.e. $J = -K$ has to hold. As observing the \mathbf{u} terms isolated should be the same as the \mathbf{v} terms, it is clear (cf. 2.1) that the vector bosons are directly on the border between FQ and Q-Zigzag phases and in a regime where the classical or spin-wave energies are comparatively high (meaning not as stable). Hence, relatively larger angles of ξ compared to the Heisenberg \mathbf{u} case visualized in figure 3.5 are required in order for the quadrupoles to affect the magnetic phases of the dipoles.

Coming back to the first argument, the mixing angle resulting from the Hamiltonian in equation (1.78) can be calculated. With $\cos(\beta) = -1/\sqrt{2} = -\sin(\beta)$ fixing

the interactions of \mathbf{u} , the solution follows from the system of equations

$$\begin{aligned} J_v &= A \cos(\alpha) \cos(\xi) \stackrel{!}{=} \frac{\frac{3}{4}t^2 + \frac{1}{6}t'^2}{U}, & K_v &= A \sin(\alpha) \cos(\xi) \stackrel{!}{=} \frac{-\frac{3}{4}t^2 + \frac{1}{2}t'^2}{U}, \\ J_u &= A \left(-\frac{1}{\sqrt{2}} \right) \sin(\xi) \stackrel{!}{=} -\frac{\frac{1}{12}t^2}{U} = -K_u, \end{aligned} \quad (3.7)$$

resulting in

$$\tan(\xi) = \frac{\sqrt{2}}{9} \left(\cos(\alpha) - \frac{1}{4}(\cos(\alpha) + \sin(\alpha)) \right). \quad (3.8)$$

The maximum possible value of this function is reached at $\xi \approx 0.04\pi$, meaning that the influence of the \mathbf{u} terms in the explicitly derived model is, at most, roughly halfway between the $\xi = 0$ and $\xi = \pi/16$ solutions in figure 3.5. Consequently, one would expect no quadrupole phase but a minute shift of the critical points. However, when drawing the flavor-wave solutions with the angle of equation (3.8) and the correct $J_u = -K_u$ interactions, the line matches that of $\xi = 0$, as the $\beta = 135^\circ$ regime influences the \mathbf{v} bosons significantly less drastic than the $\beta = 0^\circ$ “almost worst” case scenario. Hence, it is reasonable and expected that the inclusion of \mathbf{u} terms does not change the results noticeably.

Concluding, one might ask the question if this is a more general feature of this kind of model. Are the \mathbf{u} terms always negligible? An extremely general statement is unfeasible, as the derivation of the triplon Hamiltonians involves two very non-trivial perturbation theories: One establishing the Kugel-Khomskii model and one projecting to the low-energy singlet-triplet subspace. However, one can try to find out the trends within those Hamiltonians.

Consider, for example, the Ca_2RuO_4 based model in equations (2.38)-(2.40). An advantage of the model is the more complete incorporation of the on-site multiplet structure into the derivation of the Kugel-Khomskii Hamiltonian, thus possibly allowing access to more insights. Projecting this model down onto the singlet-triplet

low-energy subspace according to section 1.4.5.2 yields

$$H = \lambda \sum_i n_i + \sum_{\langle i,j \rangle, x \text{ bond}} h_x + \sum_{\langle i,j \rangle, y \text{ bond}} h_x(x \leftrightarrow y) + \sum_{\langle i,j \rangle, \text{NNN bond}} h_{\text{NNN}}. \quad (3.9)$$

Restricting ourselves to quadratic terms, i.e. hopping and pair creation, and introducing the shorthand $t_l = t_{xy}$ as well as $t_s = t_{yz} = t_{zx}$ results in (appendix A.4 provides all other matrix elements of the effective Hamiltonian for potential future use)

$$h_x = \frac{J_{\text{H}}^2(12t_l^2 + \mathbf{3}t_l t_s + 7t_s^2) + U J_{\text{H}}(8t_l^2 - t_l t_s + 4t_s^2) - U^2(4t_l^2 + t_s^2)}{6U(U - 3J_{\text{H}})(U + 2J_{\text{H}})} T_{x,i}^\dagger T_{x,j} \quad (3.10)$$

$$- \frac{J_{\text{H}}^2(12t_l^2 + \mathbf{2}t_l t_s + 7t_s^2) + U J_{\text{H}}(8t_l^2 - t_l t_s + 4t_s^2) - U^2(4t_l^2 + \mathbf{1}t_l t_s + t_s^2)}{6U(U - 3J_{\text{H}})(U + 2J_{\text{H}})} T_{x,i}^\dagger T_{x,j}^\dagger$$

$$+ (t_l \leftrightarrow t_s \text{ for y and z triplon terms}) + \text{h.c.}$$

and

$$h_{\text{NNN}} = -t_{\text{NNN}}^2 \frac{U^2 - 4J_{\text{H}}U - 7J_{\text{H}}^2}{6U(U - 3J_{\text{H}})(U + 2J_{\text{H}})} \left(T_{x,i}^\dagger T_{x,j} - T_{x,i}^\dagger T_{x,j}^\dagger \right) \quad (3.11)$$

$$- \sum_{\alpha \neq x} \frac{t_{\text{NNN}}^2}{3} \left(\frac{1}{U} + \frac{1}{U + 2J_{\text{H}}} \right) \left(T_{\alpha,i}^\dagger T_{\alpha,j} - T_{\alpha,i}^\dagger T_{\alpha,j}^\dagger \right) + \text{h.c.},$$

where we highlighted the differences of pair and hopping terms (aside from the global minus sign) with red color.

There are some direct observation one can make. First of all, gaining or losing quadrupole contributions by changing the size of U and J_{H} is possible for the nearest neighbor terms, but it is not critical and there are significantly more important conclusions to draw. Secondly, quadrupole contributions are completely absent in the quadratic next-nearest neighbor terms. Hund's coupling J_{H} and Hubbard interaction do not change this. Furthermore, one can draw parallels to the absence of \mathbf{u} terms in the t^2/U direct overlap exclusive processes. Indeed, it is the orbital conserving

Kugel-Khomskii terms and the absence of the quadrupole within them that seemingly heavily disfavor the \mathbf{u} contributions taking over. We will discuss this subsequently. Thirdly, we notice that the quadrupoles in the Ca_2RuO_4 based model are overall expected to be even less significant, as the hopping and pair terms in equation (3.10) are almost perfectly identical with a flipped sign and therefore overwhelmingly \mathbf{v} dipoles.

In order to understand the effect of the orbital conservation, one can recall the structure of the Kugel-Khomskii Hamiltonians, e.g., in equation (1.62). For the $\langle i, j \rangle$ terms there are contributions of the form (neglecting the on-site energy shifts) $\langle S_i^\alpha L_i^\beta L_i^\gamma \rangle_i \langle S_j^\alpha L_j^\delta L_j^\epsilon \rangle_j$ and $\langle L_i^\beta L_i^\gamma \rangle_i \langle L_j^\delta L_j^\epsilon \rangle_j$, where $\langle \dots \rangle_i$ denotes the projection onto the singlet-triplet states on site i in accordance with equation (1.69) and section 1.4.5.2. Hence, one should calculate the projections and observe the nature of the quadratic contributions (linear on-site) regarding their dipole and quadrupole nature. A table of projections for the quadratic terms has been created in [6]. As one can easily state the terms more compactly and with higher-order contributions we write them down here. One finds

$$\begin{aligned} \langle L_i^\beta L_i^\gamma \rangle_i &= \varepsilon_{\beta\gamma\tau} \left(-\frac{1}{\sqrt{6}} \right) \left(T_{\tau,i} - T_{\tau,i}^\dagger \right) + (1 - \delta_{\beta\gamma}) \frac{1}{2} T_{\beta,i}^\dagger T_{\gamma,i} \\ &+ \delta_{\beta\gamma} \left(\frac{2}{3} n_i^s + \frac{1}{2} n_i^x + \frac{1}{2} n_i^y + n_i^z \right) = -i\varepsilon_{\beta\gamma\tau} \sqrt{\frac{2}{3}} v_{\tau,i} + \dots, \end{aligned} \quad (3.12)$$

i.e. $\langle L^x L^y \rangle \sim v_z$ and no \mathbf{u} terms in the quadratic Hamiltonian.

Moreover,

$$\begin{aligned}
 \langle S_i^\alpha L_i^\beta L_i^\gamma \rangle_i &= \delta_{\alpha\gamma} \delta_{\beta\gamma} \left(-i\sqrt{\frac{2}{3}} \right) (T_{\alpha,i} - T_{\alpha,i}^\dagger) + (1 - \delta_{\alpha\beta}) \delta_{\beta\gamma} \left[\left(\frac{-i}{\sqrt{6}} \right) (T_{\alpha,i} - T_{\alpha,i}^\dagger) \right. \\
 &\quad \left. - \frac{i}{2} \varepsilon_{\alpha\beta\tau} (T_{\beta,i}^\dagger T_{\tau,i} - T_{\tau,i}^\dagger T_{\beta,i}) \right] + (1 - \delta_{\beta\gamma}) \left[\left(\frac{-i}{\sqrt{6}} \right) (\delta_{\alpha\beta} T_{\gamma,i} - \delta_{\alpha\gamma} T_{\beta,i}^\dagger) \right. \\
 &\quad \left. - \frac{i}{2} \varepsilon_{\beta\gamma\tau} (\delta_{\alpha\beta} T_{\alpha,i}^\dagger T_{\tau,i} + \delta_{\alpha\gamma} T_{\tau,i}^\dagger T_{\alpha,i}) \right] - i\varepsilon_{\alpha\beta\gamma} \left(\frac{1}{3} n_i^s + \frac{1}{2} n_i^\alpha \right) \quad (3.13) \\
 &= \delta_{\alpha\gamma} \delta_{\beta\gamma} \sqrt{\frac{8}{3}} v_{\alpha,i} + (1 - \delta_{\alpha\beta}) \delta_{\beta\gamma} \sqrt{\frac{2}{3}} v_{\alpha,i} \\
 &\quad - i\sqrt{\frac{2}{3}} (1 - \delta_{\beta\gamma}) (\delta_{\alpha\beta} (u_{\gamma,i} + iv_{\gamma,i}) - \delta_{\alpha\gamma} (u_{\beta,i} - iv_{\beta,i})) + \dots,
 \end{aligned}$$

where the \mathbf{u} terms appear in the $\beta \neq \gamma$ cases with appropriate spin contributions. In both equations we implied the Einstein summation convention for the τ index. The second part of the equations introduces the vector bosons and shifts the non-quadratic terms (and on-site singlets) into “...”.

What can we learn from the preceding equations regarding the importance of quadrupoles in the quadratic terms? Importantly, the Kugel-Khomskii terms carrying both spin and orbital interactions are required. Importantly, the nature of the orbital interplay seems to be essential. Recall that the angular momentum operators translate directly to orbital occupations via equations (1.59)-(1.61). Furthermore, one should remember the Kugel-Khomskii theory describing virtual hopping processes like $d_i^4 d_j^4 \rightarrow d_i^3 d_j^5 \rightarrow d_i^4 d_j^4$ and there is thus one orbital with double occupation of the electrons, which translates to the angular momenta, which is hereinafter referred to as “orbital occupation”.

In the $\beta = \gamma$ case, e.g. $(L_x)^2$ on-site terms in the Hamiltonian, the orbital occupation is conserved. For these orbital conserving terms, the quadratic interactions are purely dipolar. A large part of the Kugel-Khomskii Hamiltonians in this thesis consists of these kind of terms. Combined with the spinless $\langle L_i^\beta L_i^\gamma \rangle_i$ contributions only allowing \mathbf{v} , the quadrupoles are dominated. In particular, the direct overlap,

t' for the honeycomb model and the next nearest neighbor terms for the Ca_2RuO_4 terms are orbital conserving, as only one orbital is involved in the exchange. Hence, the absence of quadrupoles in the t'^2/U and NNN terms is expected.

On the contrary, the $\beta \neq \gamma$ case, which can be understood as an electron starting in, e.g., orbital a and ending up in b , can host dipoles and quadrupoles on even footing for spin involvement, at least two out of three components thereof. Again, one should not forget the $\langle L_i^\beta L_i^\gamma \rangle_i$ terms favoring dipoles and hence expect the quadrupoles to be smaller. However, if only these orbital occupation changing terms exist, the difference between the energy scales can be smaller. Case in point: The Γ interactions in the honeycomb model, i.e. tt'/U terms, have to change orbital occupations, because t facilitates electrons moving in a and b orbitals, while the way back needs to involve a c electron via t' . As a result, the quadrupoles in equation (1.78) are quite comparable with $\Gamma_v = 3\Gamma_u$, so by coincidence exactly the value of the critical point for the Kitaev limit breaking down in the scenario of figure 3.5 (of course energy scales and thus the exact value should be different here). So if there is another purely v interaction frustrating Γ_v , for example by dipolar exclusive NNN terms, one might have a chance to expect quadrupole order based on the quadratic Hamiltonian. The question about this being a realistic scenario in materials is, of course, another one. One should note, however, that prominent Γ (and the related Γ') terms, are a feature in many suggestions for $\alpha\text{-RuCl}_3$ [51]. Yet, one may note that the Kugel-Khomskii Hamiltonian results in different interactions for one and two holes respectively and this feature might not translate necessarily. In summary, one should not expect the quadrupoles to be important aside from very special cases.

Finally, this result might be used to gauge the importance for \mathbf{u} by introducing the following rule of thumb: If the Kugel-Khomskii Hamiltonian in the d^4 system does not overwhelmingly include orbital non-conserving terms, the quadrupoles in the quadratic model might be reasonably discarded. Vice versa: If one is interested in the \mathbf{u} terms, one might seek out a geometry where the superexchange or orbital

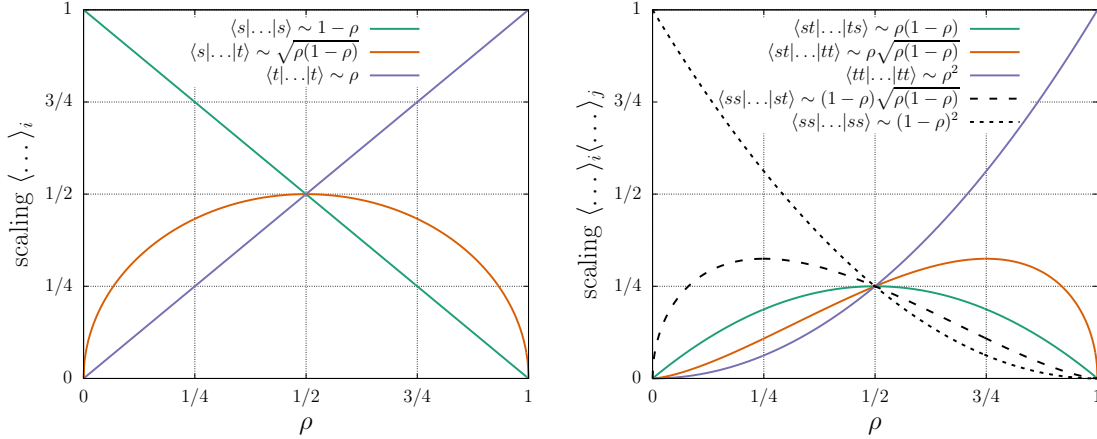


Figure 3.6. Dependency of matrix elements of the triplon model Hamiltonian on the triplon density ρ assuming the wave function ansatz used for the semiclassical Monte-Carlo simulations: The states can contain a singlet s or (arbitrary) triplet t , with the shorthand notation $\langle st|\dots|ts\rangle = \dots s_i^\dagger t_i t_j^\dagger s_j$, where the latter terms denote the usual hard-core creation and annihilation operators. The dashed lines represent terms that can be translated to the other orders and on-site energy shifts and strain terms by explicit elimination the hard-core constraint ($s_i^\dagger s_i = 1 - \sum_\alpha t_{i,\alpha}^\dagger t_{i,\alpha}$).

overlap based electron tunnelings can mainly happen between different orbitals, like the mixed tt' scenario.

3.1.2 Higher-Order Terms

We subsequently turn to an analysis of the remaining parts of the Hamiltonian: The h_3 and h_4 terms introduced in equation (1.74) and explicitly stated in equations (1.86)-(1.88) as well as figure 1.13. Henceforth, these terms are dubbed “higher-order”, as they contain the interactions involving three and four triplons T (or triplets t) respectively. Nevertheless, one should note that the complete matrix in figure 1.13 also contains what could be dubbed h_1 terms, for example $\langle s_i t_j|\dots|s_i s_j\rangle = \dots s_i^\dagger s_i t_j^\dagger s_i$. Due to the hard-core constraint permitting only one hard-core boson per site, namely $n_i^s + n_i^x + n_i^y + n_i^z = 1$, where n are the number operators belonging to singlet and triplet states, one may argue (or replace $s_i^\dagger s_i$ in the Hamiltonian

explicitly) that these interactions are h_3 terms and on-site energy shifts (and possibly strain terms). Hence, we include them into the higher-order terms in our analysis.

These multi-triplon interactions, like the ones produced by the hard-core constraint itself (cf. section 2.1), are expected to become significant after the condensation process, i.e. when a considerable amount of triplons exist in this system. This kind of scaling with the triplon number (or density) can be useful to keep in mind for the subsequent analysis. It is also neatly visualized when recalling the form of the singlet-triplet wave function ansatz in equation (2.29), which is used in the semiclassical Monte-Carlo simulations. Assuming a constant density ρ on each lattice site¹ leads to the scaling behaviors of the matrix elements pictured in figure 3.6.

In the figure one can observe, that the $\mathbf{v}_i\mathbf{v}_j$ and $\mathbf{u}_i\mathbf{u}_j$, i.e. the h_2 terms, reach their optimal strength at $\rho = 1/2$, which should be kept in mind as an effective spin-length when performing regular spin-wave calculations in this model. As the spin-orbit coupling λ couples this spin-length, or rather the parameter ρ , with an energy cost, the h_2 model results in a density $\rho < 1/2$ for finite values of A (usually significantly for the values of A considered in this thesis) and $\rho = 1/2$ for $A \rightarrow \infty$ [6].

Contrary to this, the higher-order terms have a clear preference for $\rho > 1/2$ values. When completely overwhelming the SOC λ , one should expect the density to strive towards $\rho = 3/4$ for the h_3 and $\rho = 1$ for the h_4 terms. All in all, this means that the density ρ reaching values of about or over $1/2$ could be seen as an indicator for the importance of higher-order terms significantly influencing the h_2 based results.

¹Side note: We do not have to defend this assumption here, because neither Monte-Carlo nor ED simulations assume anything in this regard and the results are clear. Yet, one may note that this seems to be a quite powerful and prudent simplification. The previously mentioned iron pnictide triplon paper [179] just assumes this outright. Our Monte-Carlo code gives us the opportunity to test this (although simple two-site model estimates can do that as well). Seemingly, one has to take drastic actions in order to obtain triplon density modulations: even for significant next-nearest neighbor interactions allowing the unit cell sites of the honeycomb lattice to act isolated from each other, one has to switch off the spin-orbit coupling λ on one of the sites to see (only) a moderate effect. This topic is, however, beyond the scope of this thesis.

Another indicator could be the importance of the “quadrupole” \mathbf{u} , which we found to be negligible in the last section. We put quadrupole in quotes here, because one does not need quadrupolar order to find \mathbf{u} significantly contributing to the model. In order to see this and discover some of the possible influences of the higher-order contributions, one may combine the results of equations (3.12) and (3.13) with the definitions of dipoles and quadrupoles in section 1.5. There are, of course a lot of quadrupole contributions (quadrupoles are not just \mathbf{u} terms). For example $(1 - \delta_{\beta\gamma})\frac{1}{2}T_{\beta,i}^\dagger T_{\gamma,i}$ and $(1 - \delta_{\beta\gamma})\frac{1}{2}\varepsilon_{\beta\gamma\tau}\delta_{\alpha\beta}T_{\alpha,i}^\dagger T_{\tau,i}$ contain the necessary on-site products. Regardless, when the dipoles order and prominently feature in the model, one should mention their contributions to the higher orders, in particular

$$-\frac{i}{2}(1 - \delta_{\alpha\beta})\delta_{\beta\gamma}\varepsilon_{\alpha\beta\tau} \left(T_{\beta,i}^\dagger T_{\tau,i} - T_{\tau,i}^\dagger T_{\beta,i} \right) \sim \frac{i}{2}J_{i,\alpha} \rightarrow \langle J_{i,\alpha} \rangle = -2i(\mathbf{u} \times \mathbf{v})_{i,\alpha}, \quad (3.14)$$

where \mathbf{J} is the total angular momentum, which is at the foundation of the singlet-triplet model. Hence, the higher-order terms contain dipole-dipole interactions via (components of) $\mathbf{v}_i(\mathbf{u} \times \mathbf{v})_j$ and $(\mathbf{u} \times \mathbf{v})_i(\mathbf{u} \times \mathbf{v})_j$.

There are three main takeaways from this one should be aware of. First of all, with h_3 and h_4 interactions (as well as the magnetic field later, which enters via the complete dipole moment $M = \alpha\mathbf{v} + \beta(\mathbf{u} \times \mathbf{v})$) the \mathbf{u} boson now has a reason to exist instead of being completely cannibalized via the maximization of the energy gain of \mathbf{v} by $|\mathbf{u}|^2 + |\mathbf{v}|^2 = 1$. Therefore, a non-vanishing \mathbf{u} can be seen as a sign of the higher-order terms being influential.

Secondly, one should recall the discussion of the degrees of freedom in a normal spin system (section 1.5). The normal spins and spin-dimer singlet-triplet systems have a magnetic dipole moment that is just the $(\mathbf{u} \times \mathbf{v})$ part. The orders are more straightforward: check $(\mathbf{u} \times \mathbf{v})$ and if that is zero one has either \mathbf{u} or \mathbf{v} , which for normal spins are quadrupoles if they exist alone, or for spin-dimers a pure singlet (paramagnet). For our spin-orbital singlet-triplet, the regular dipole magnetic mo-

ment can be quite involved at first glance, because the excitonic degree of freedom also contributes and both \mathbf{v} and $(\mathbf{u} \times \mathbf{v})$ can exist at the same time (or even nontrivially influence each other via $\mathbf{v}_i(\mathbf{u} \times \mathbf{v})_j$). Yet, the order behind it is still effectively an ordinary dipole. In fact, the more the triplet (which isolated has the structure of a normal spin-1) gets involved in its entirety, the more the magnetic moment will look like the regular spin.

Lastly, we point out a corollary of the previous point: It is not obvious if h_3 - h_4 terms and h_2 terms actually mainly fight or cooperate. An overall trend towards an AFM can be hidden in h_2 via \mathbf{v} and h_3 - h_4 via $(\mathbf{u} \times \mathbf{v})$, but their end result is the same. If so, there might not be any drastic change in magnetic order via the inclusion of higher-order terms. In this light, it might be interesting to revisit the results for the Ca_2RuO_4 based model in figure 2.5, where the magnetic order does not change even though the crystal field in switches the on-site ground state of singlet and triplet in some areas, i.e. clearly presents an opportunity for $\rho > 1/2$ to be the main actor. Still, the order remains purely \mathbf{v} boson based. However, the Ca_2RuO_4 is not the focus of this thesis and therefore this should be investigated at another point in time.

Undoubtedly, a pure parameter study of this model with rather free choices of interaction strengths of the various higher order terms could be interesting in itself. However, due to the plethora of different influences, most of them bond-dependent, this approach is not practical, at least when it comes to discussions in this thesis. Instead, we include the h_3 - h_4 terms by treating them as an extension of the h_2 based Kitaev-Heisenberg model. Equations (1.80) and (1.81) introduce the Kitaev-Heisenberg parametrization as a function of the effective hopping and Hubbard interaction (t^2/U and t'^2/U) of the underlying d^4 electron model. This choice of parameters is rather free (e.g. possible negative sign of t^2/U), which represents an attempt to account for other influences like Hund's coupling exerting influence and is very established in the Kitaev-Heisenberg model context (cf. [50]). Vice versa,

the variation of $J = A \cos(\alpha)$ and $K = A \sin(\alpha)$ fixes t^2/U and t'^2/U to given values via equations (1.83) and (1.84). The strength of the higher-order terms, at least the ones we derived in our approximate perturbation theories of Kugel-Khomskii model and low-energy projection, are fixed by this and hence the parameters A and α will hereinafter be used in direct analogy to the h_2 discussion.

Finally, we move to concrete results. In figure 3.7 one can see the phase diagrams established by Monte-Carlo simulations of the singlet-triplet model ($N = 144$ sites) for the Kitaev-Heisenberg model with only h_2 terms (both \mathbf{u} and \mathbf{v}) as well as with the inclusion of the higher orders h_3 and h_4 . First of all, the addition of \mathbf{u} terms does not change the overall result in any drastic way. Even the data points located very close to critical points predicted by the \mathbf{v} boson flavor-wave solution stay in the expected phase (this is sometimes hard to spot with pure eyesight in figure 3.7, but certainly the case upon closer inspection). Therefore the results are a reproduction of the ones in figure 2.1 or the classical simulations in reference [6]. The phase borders correspond to roughly the flavor-wave predictions, i.e. the classical Kitaev spin-liquid (which for Monte-Carlo is often represented by general disordered nonsense) and the bond selecting $J = -K$ cases at $\alpha = 135^\circ$ and $\alpha = 315^\circ$, where in the spin-wave Γ and M points (among others) are condensing concurrently and the semiclassical Monte-Carlo simulation is an arbitrary mixture of FM and zigzag.

When introducing the higher-order terms, most of the phase diagram remains unchanged. If one compares the emerging phases closely with the spin-wave solution, there are slight discrepancies. Condensation leading to AFM and stripy regimes seems to require slightly larger A values, while the FM and zigzag phases gain influence. The phase borders at the Kitaev cases and $\alpha = 315^\circ$ appear to work as before, at least when observed at this scale. Nevertheless, there is one very drastic change compared to the previous phase diagram: Between zigzag and FM regimes a new distinct phase, which we dub “canted zigzag”, emerges. The existence of this new phase demands further investigation.

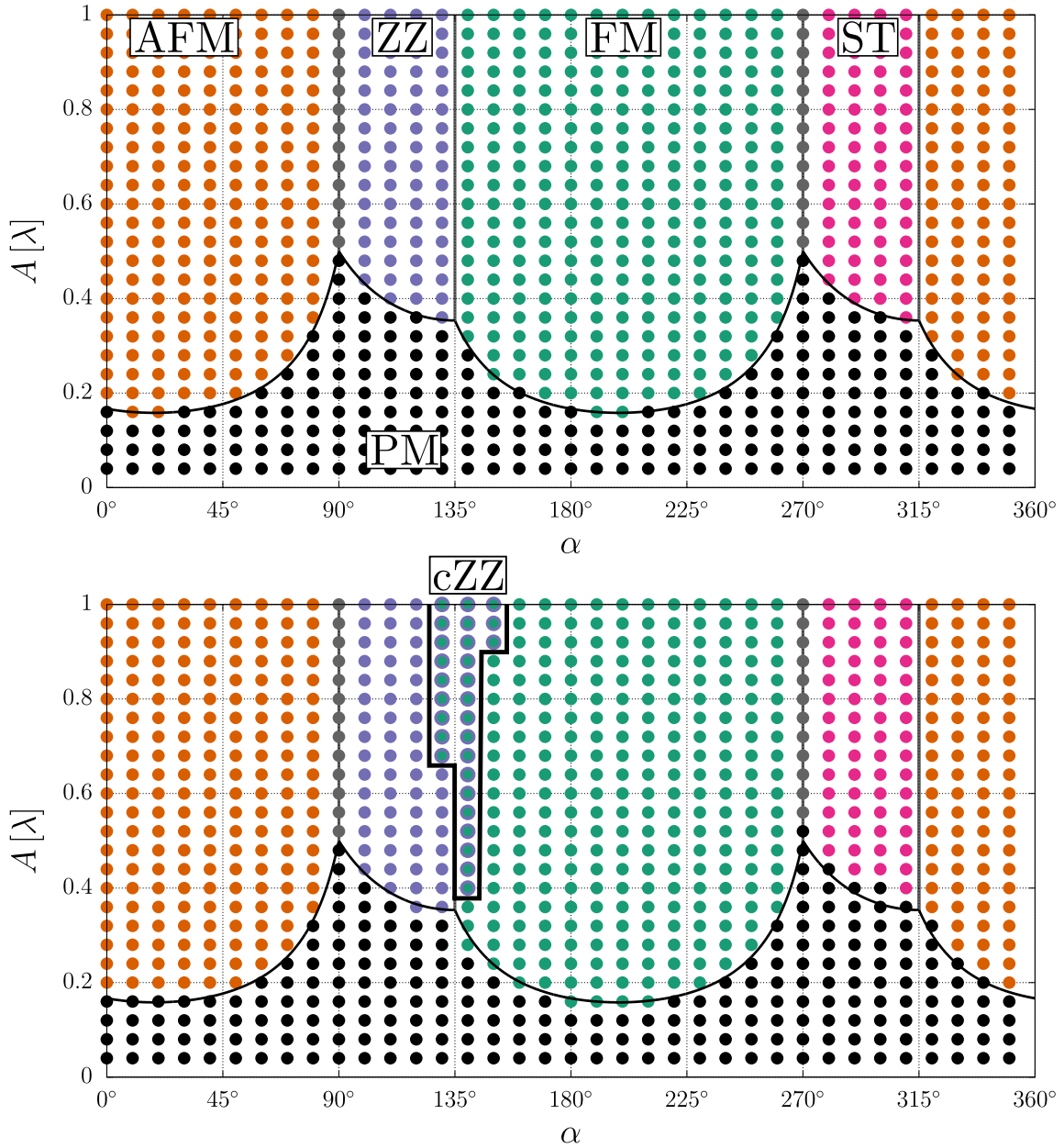


Figure 3.7. Semiclassical Monte-Carlo phase diagrams of the triplon model parametrized by $J = A \cos(\alpha)$ and $K = A \sin(\alpha)$ (higher-order terms and \mathbf{u} Hamiltonian fixed by resulting values for t^2/U and t'^2/U): The diagram at the top represents the full h_2 model with both \mathbf{u} and \mathbf{v} boson types, while the one at the bottom further includes the higher-order h_3 and h_4 terms. The phases are the paramagnet PM, the (anti-)ferromagnet (A)FM, zigzag (ZZ) as well as stripy (ST) phases, all of which known from earlier results. The black lines depict the critical condensation points estimated by the flavor-wave calculations. On this scale, even the full h_2 model perfectly corresponds to the flavor-wave solution. For h_3 and h_4 , the FM (+ zigzag) regime seems to gain importance while the AFM (+ stripy) phases emerge for higher interaction values than expected by the flavor-wave. Notably, a new phase emerges: The canted zigzag (cZZ) phase between the FM and ZZ regimes.

3. Analysis of the Triplon Honeycomb Model

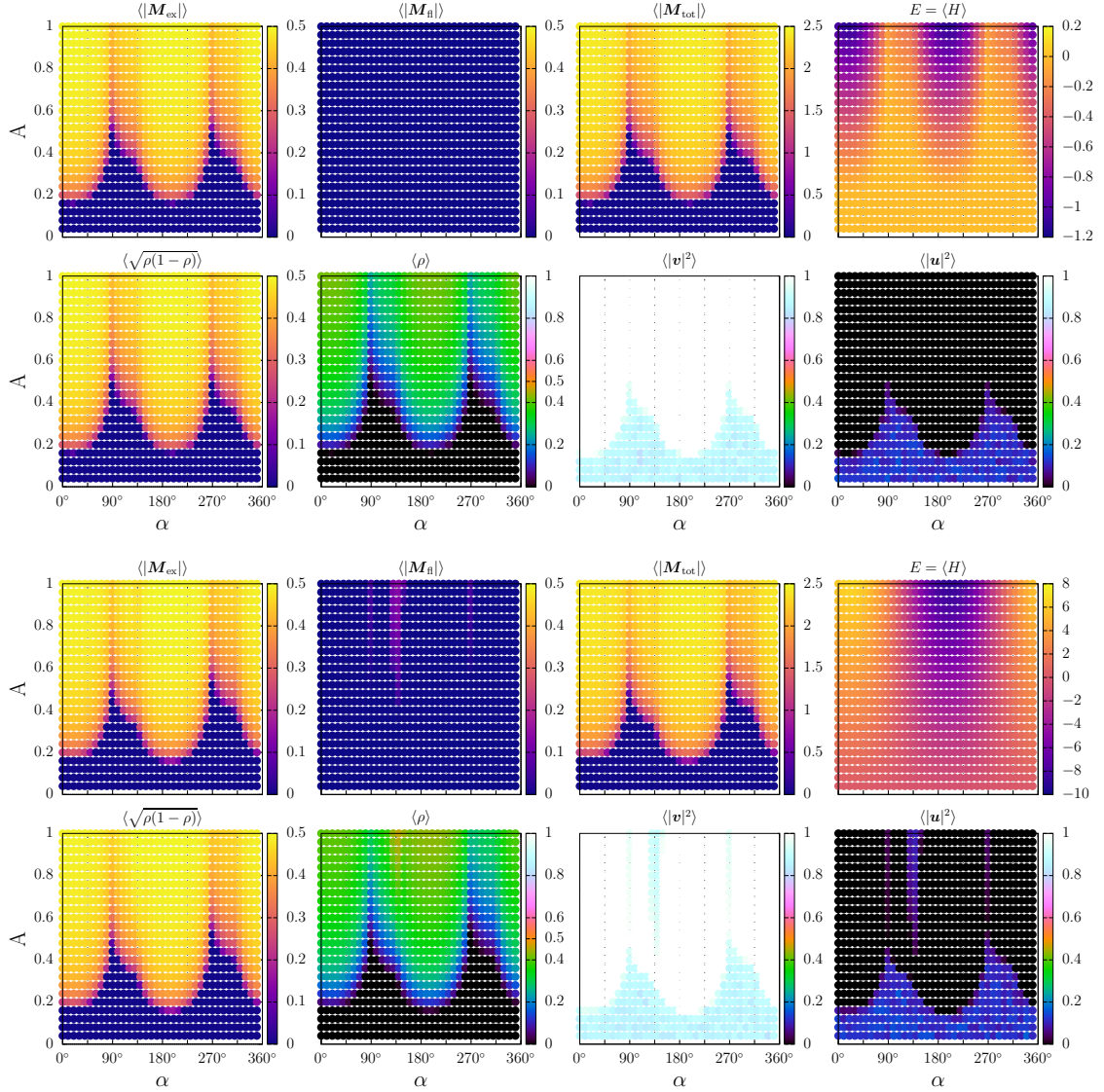


Figure 3.8. Observables for the semiclassical Monte-Carlo simulations in figure 3.7, i.e. of the triplon model parametrized by $J = A \cos(\alpha)$ and $K = A \sin(\alpha)$ (higher-order terms and \mathbf{u} Hamiltonian fixed by resulting values for t^2/U and t'^2/U): The diagram at the top represents the full h_2 model with both \mathbf{u} and \mathbf{v} boson types, while the one at the bottom further includes the higher-order h_3 and h_4 terms. Overall, the differences between both models (the ones at the $J = 0$ Kitaev limit can be discarded, as Monte-Carlo just results in disorder) are only evident in details (e.g. slight changes in ρ) aside from the area where the new canted zigzag phase can be found. There, $\rho \approx 1/2$, a noticeable \mathbf{u} contribution as well as significant flavor-changing magnetic moment $\mathbf{M}_{\text{fl}} = \rho(\mathbf{u} \times \mathbf{v})$ signal the influence of the higher-order terms and the new order. All observables are introduced in previous sections. Moreover, one may spot the change in energy behavior for both cases, which will be discussed later. Averages $\langle \dots \rangle$ correspond to lattice means $1/N \cdot \sum_i O_i$, where O_i is any observable on lattice site i .

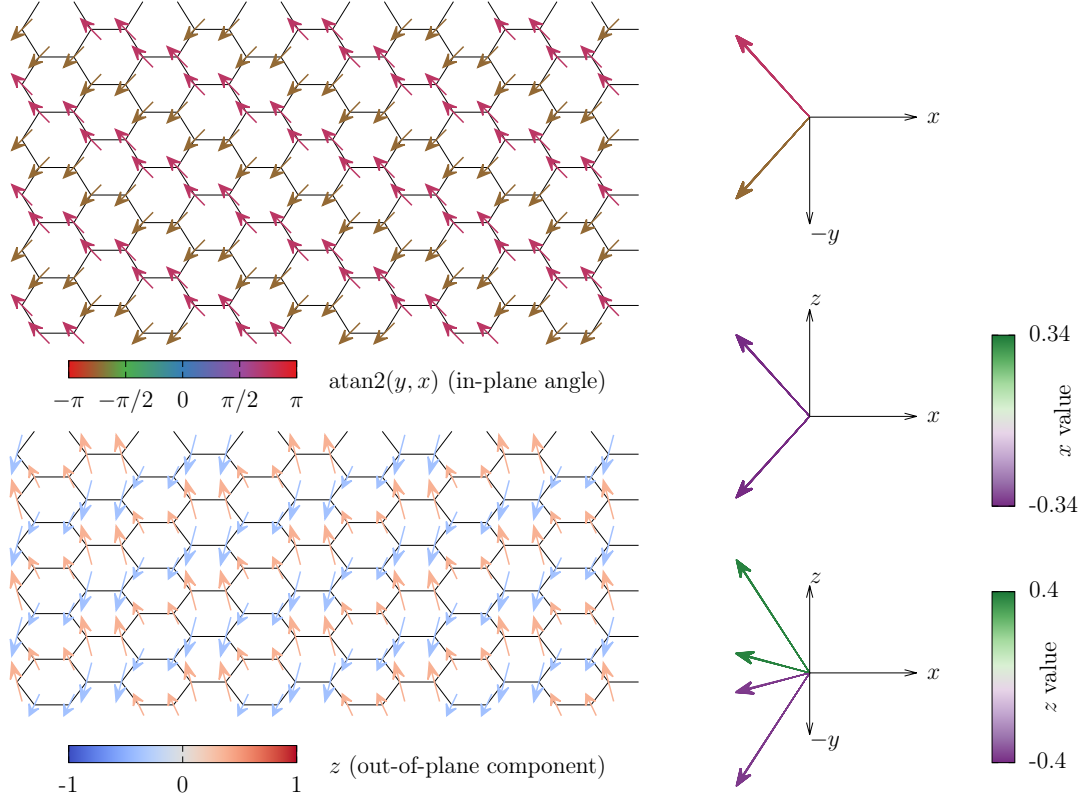


Figure 3.9. Order of the \mathbf{v} bosons in the canted zigzag phase as established by semiclassical Monte-Carlo: The upper lattice plot represents a top down view where the in-plane angles are colored in, while the bottom lattice plot is the same structure tilted at 60° from the in-plane level with the out-of-plane component colored in. The structures on the right represents all spins on the lattice plotted from a common origin depicted by (from top to bottom) a top-down view of the x - y -plane (in-plane color scheme), a top-down view of the x - z -plane and an overview from a tilted angle (spherical coordinate $\theta = 54.74^\circ$). Roughly rounded maximal values for the noted components are provided for the two plots on the bottom right as maximum scaling for the color maps.

In figure 3.8 we present a few observables calculated for the ground states established by the semiclassical Monte-Carlo simulations. The parameters ρ , \mathbf{u} and \mathbf{v} are the degrees of freedom in the wave function ansatz of equation (2.29). For the

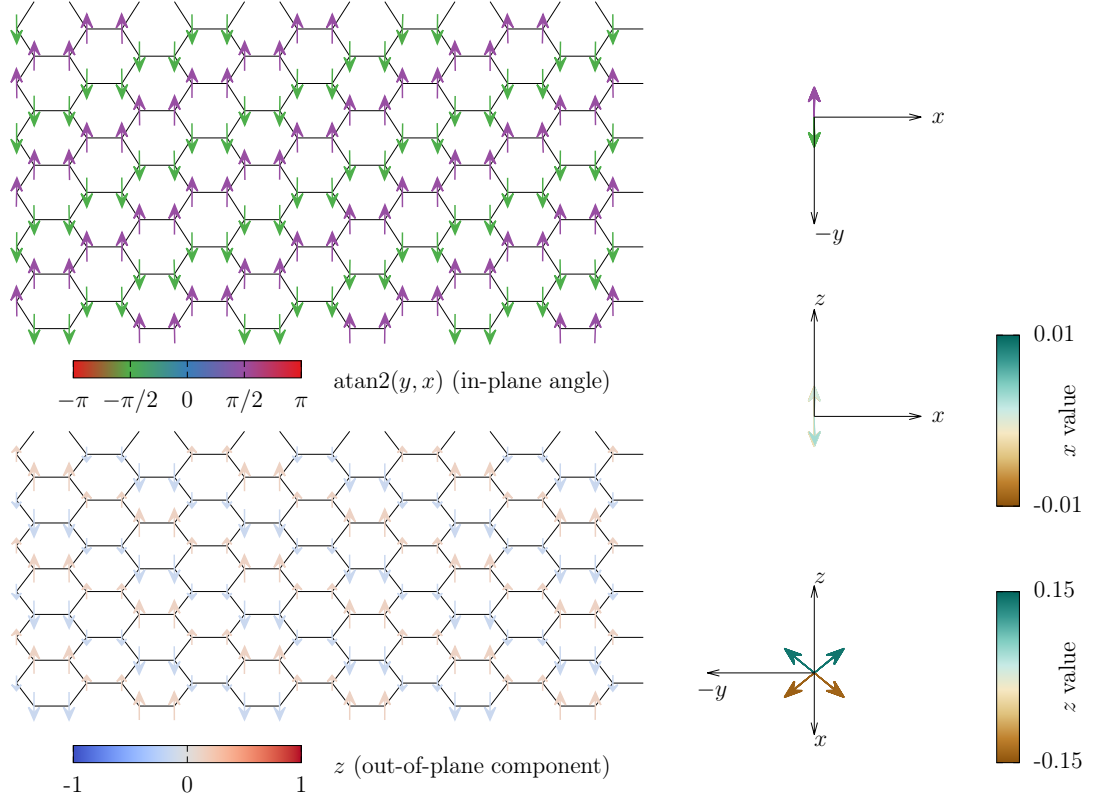


Figure 3.10. Order of the \mathbf{u} bosons in the canted zigzag phase as established by semiclassical Monte-Carlo: The upper lattice plot represents a top down view where the in-plane angles are colored in, while the bottom lattice plot is the same structure tilted at 60° from the in-plane level with the out-of-plane component colored in. The structures on the right represents all spins on the lattice plotted from a common origin depicted by (from top to bottom) a top-down view of the x - y -plane (in-plane color scheme), a top-down view of the x - z -plane and an overview from a tilted angle (spherical coordinate $\theta = 54.74^\circ$). Roughly rounded maximal values for the noted components are provided for the two plots on the bottom right as maximum scaling for the color maps.

magnetization, this ansatz yields (using equation (1.91)).

$$\mathbf{M} = 2\sqrt{6}\sqrt{\rho(1-\rho)}\mathbf{v} + \rho(\mathbf{u} \times \mathbf{v}) \equiv 2\sqrt{6}\mathbf{M}_{\text{ex}} + \mathbf{M}_{\text{fl}}, \quad (3.15)$$

where we introduced a distinction between the excitonic or Van-Vleck terms and the

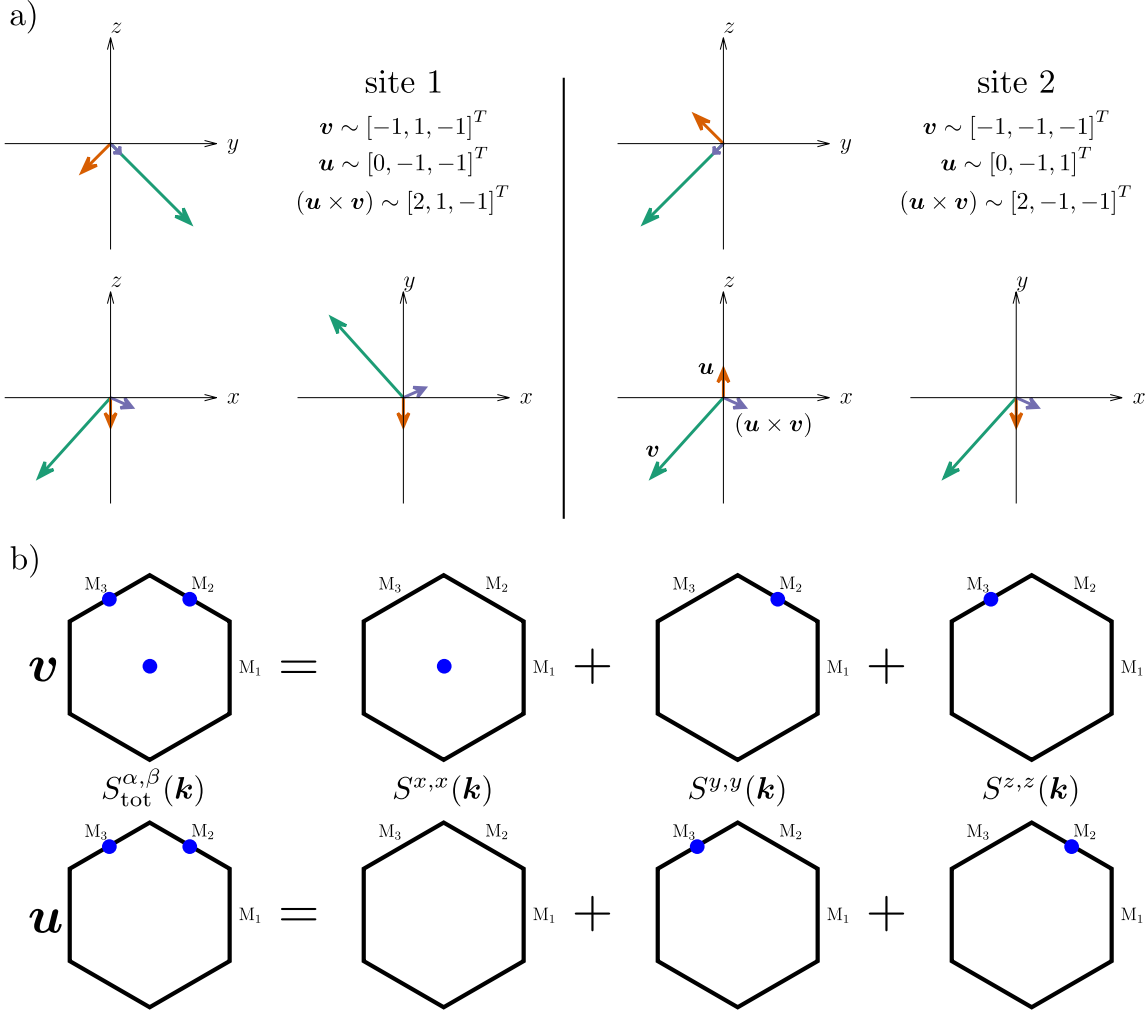


Figure 3.11. Additional information for the canted zigzag phase depicted in figures 3.9 and 3.10: Site 1 represents the lattice site at the bottom left of figure 3.9 and site 2 is the one reached by the only lattice vector translation not requiring periodic boundary conditions. Subfigure a) depicts the dipole boson \mathbf{v} , quadrupole \mathbf{u} and resulting additional dipolar $(\mathbf{u} \times \mathbf{v})$ contributions. Notably, $(\mathbf{u} \times \mathbf{v})$ is perfectly aligned with \mathbf{v} in y and z components and differs by relative size and direction for the canting axis x . Consequently, the \mathbf{u} order could possibly be a byproduct of a more efficient way of aligning the dipoles emerging from the higher-order terms. Subfigure b) shows the significant spin-structure factors (corresponding to each boson type) in the first Brillouin zone (which is the only one required here). Compared to the concurrent zigzag order in figure 2.2, the x boson is no longer located at M_1 but rather the Γ point, corresponding to the effective ferromagnetic order in that direction.

flavor-changing (Zeeman-like) ones. The new canted zigzag phase is clearly distinguishable by a non-vanishing \mathbf{M}_fl and consequently \mathbf{u} contribution. Additionally, the triplon density ρ is noticeably close to $\rho \approx 1/2$, as evidenced by the orange colored slice near 135° for large A . One can also see, that the overarching appearance of the results aside from this is quite comparable, with only minor details like small changes in ρ being discernible.

One may take a close look at this phase. We do this by visualizing the order of the \mathbf{v} bosons in figure 3.9 and \mathbf{u} bosons in 3.10. For the former, the spins seem to be antiferromagnetic in y and z directions and angled toward x (of course the axes are interchangeable, also the canting can happen around a concurrent mixture of axes akin to the zigzag order, e.g., around the $y = \pm z$ axis), similar to what they would do in a magnetic field (cf. [41, 165]). This is why we refer to this as “canted”. There is another way to interpret the result. Recall the zigzag phase simultaneously happening in all boson types and lattice vectors direction picture in figure 2.2. On that note, everything, e.g., from a pure AFM phase to the polarized paramagnet (basically FM) is referred to as canted AFM/zigzag/... Importantly, this is also the case when the FM-like contribution is dominant, which is how one should understand the canted phase here (meaning more like the FM regime than the AFM one, therefore helping condensation in that region of the phase diagram). Superficially, the new phase selects half of the spin directions, namely all the ones with positive x components, therefore realizing a kind of FM-zigzag mix, where y and z are zigzag and the x component is a FM. There is one very important distinction that should be called out. As established in the figure, the value of the x component, which was equal to the z one in the simultaneous zigzag phase, is now slightly decreased. So one should ask where this part of the canting angle goes. The answer seems to lie in the \mathbf{u} bosons, which order in the y - z -plane and thus the magnetic x -component of $(\mathbf{u} \times \mathbf{v})$. In this plane, the \mathbf{u} bosons also exhibit a concurrent y and z direction zigzag order. Of course, speculations about quadrupole

order is pointless because the dipole does not vanish.

In order to provide additional insights, we illustrate the spin order of two sites and the significant values of the spin-structure factor of the canted zigzag phase in figure 3.11. Site 1 is the one at the bottom left of figure 3.9, while site 2 is one lattice vector removed in the only direction that does not require periodic boundary conditions. As a result, the z component of the \mathbf{u} boson is AFM and the y boson FM (zigzag modulation along the vector belonging to the z boson condensation point). The \mathbf{v} boson does the same but for switched directions. Additionally it harbors a FM x component. The $(\mathbf{u} \times \mathbf{v})$ follows the \mathbf{v} boson perfectly in y and z components, while the x direction is noticeably reversed and more pronounced, thus resulting in an effective canting of the magnetic moment along this axis. For the spin-structure factors, one finds significant contributions at the M points for y and z in complete accordance to the concurrent zigzag phase, but the x boson now has a dominant feature at the Γ point in the first Brillouin zone reflecting the FM order. As the emerging order is usually connected to the flavor-wave condensation points, these predictions also neatly connect to the new phase. It emerges around $\alpha = 135^\circ$, where the Γ and M point are equivalently favorable. Details are discussed in connection with the subsequent point.

There are a few questions that should be addressed. First of all, why is there no canted stripy phase visible in the diagram? In fact, we verified with detailed sweeps on a $N = 16$ lattice, e.g., at $A = 1$, that the phase transition from AFM to stripy at $\alpha = 315^\circ$ works as expected: Namely, at the critical point there is a superposition of AFM and stripy orders (see [6] for details). An explanation could be, that the stripy phase can be understood as having an additional AFM modulation inside the unit cell and, as a result, the significant spin-structure factor at the Γ point in the second Brillouin zone. Hence, the canted order and stripy phase seem as not as compatible as the zigzag one. This fight against each other instead of cooperation is also implied by the delay of the condensation in stripy and AFM phases as opposed to the earlier

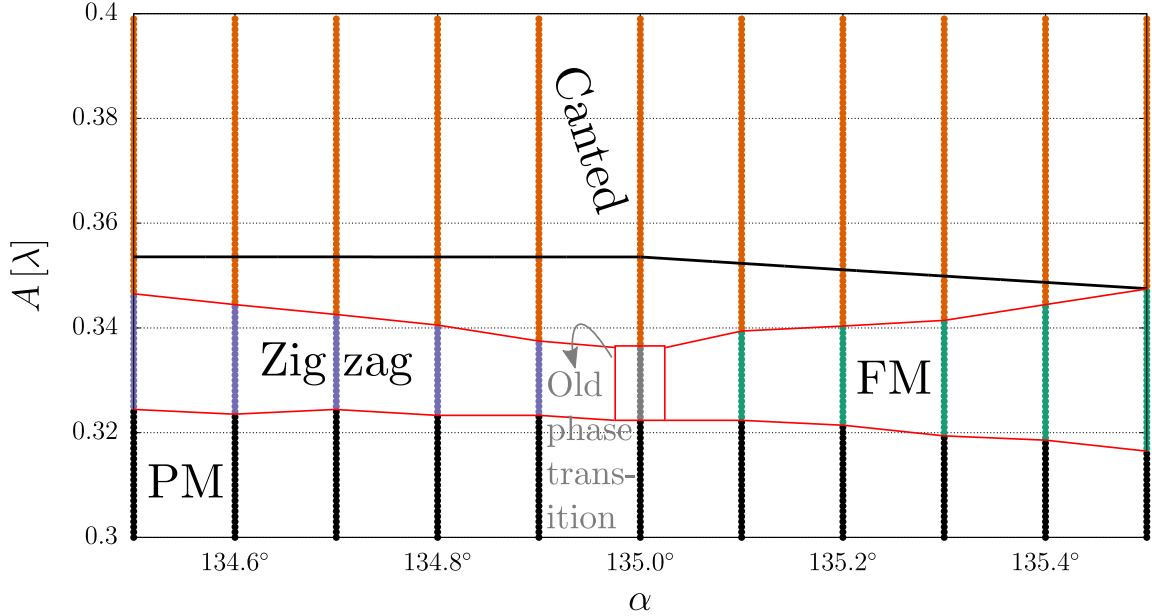


Figure 3.12. Detailed semiclassical Monte-Carlo sweeps in vicinity of the critical condensation around the Kitaev-Heisenberg parameter $\alpha = 135^\circ$: The canted phase does not emerge directly from first condensation, but rather after the system first establishes phases and phase transitions just like in the absence of h_3 and h_4 (ferromagnet FM, paramagnet PM, zigzag and a superposition of FM and zigzag at $\alpha = 135^\circ$). The black line depicts the flavor-wave solution, showing that the condensation point is moved.

(smaller A) one in the FM and zigzag regimes.

Moreover, this question is connected to the emergence of the canted zigzag phase around $\alpha = 135^\circ$. In order to study this in detail, we undertook the analysis seen in figure 3.12. Therein, we can get the following essential insights: The canted phase does not emerge directly from the condensation points. At the critical points, the old (read: no higher-order terms) FM and zigzag phases emerge. More importantly, the phase transition between them is exactly the one known from the case with absent higher-order terms, i.e. the superposition of both phases as covered and illustrated in [6], which is in direct analogy to the (semi-)classical AFM to stripy scenario. For larger values of A , the canted phase starts to emerge from the $\alpha = 135^\circ$ point, which is expected given the importance of both Γ and M points. The finite recovery of the

old phase diagram provides a possible explanation for the behavior of the $\alpha = 315^\circ$ phase transition: It is expected to remain intact until the h_3 and h_4 terms become strong enough to take over, which has seemingly not happened at $A = 1$.

Secondly, one might continue to ask, especially prompted by the previously discussed insight, what one should expect for larger values $A > 1$. One should note that there is only qualitative interest here, as the perturbation theory done via low-energy subspace projection starts to become more and more suspect. The gap from $J = 1$ to the $J = 2$ quintet (which we eliminate) is 2λ . As $\lambda = 1$, the perturbation theory is basically legitimized by $A \ll 2(\lambda)$. Hence, we have no interest to do anything more than provide a general overview.

We have attempted a Monte-Carlo study for the $N = 16$ lattice for steps $\Delta\alpha = 1$ at $A = 2$. The results neatly fit to expectations. In particular, the higher order terms are now strong enough to finally overcome the old transition at $\alpha = 315^\circ$. In its place, a very small area consisting of $313^\circ \leq \alpha \leq 315^\circ$ shows a new magnetic phase with participation of the \mathbf{u} boson. Similarly, the classical Kitaev cases start to become obsolete, but notably also only in similarly small parameter ranges of the phase diagram. The new phases emerge at $86^\circ \leq \alpha \leq 92^\circ$ and $269^\circ \leq \alpha \leq 272^\circ$. We visualize these new magnetic orders in figure 3.13 and their spin-structure factors in 3.14. All other orders are known from the $A = 1$ case. The AFM phase is located at $0^\circ \leq \alpha \leq 85^\circ$ and $\alpha \geq 315^\circ$, the zigzag at $93^\circ \leq \alpha \leq 124^\circ$, the canted zigzag at $125^\circ \leq \alpha \leq 156^\circ$, the FM at $157^\circ \leq \alpha \leq 268^\circ$ and finally the stripy phase at $273^\circ \leq \alpha \leq 312^\circ$. All in all one might subsume, that for unrealistically large interaction strength h_3 and h_4 terms become important in very small areas around Kitaev phases and the zigzag to AFM transition.

Thirdly, one could try to observe what only the higher-order terms want to establish at $A = 1$, i.e. the value we expect them to have the most impact in our phase diagram. For this, we have repeated the Monte-Carlo simulations for the smaller $N = 16$ cluster with $A = 1$ and all h_2 terms set to zero. Spin orders, phase diagram

3. Analysis of the Triplon Honeycomb Model

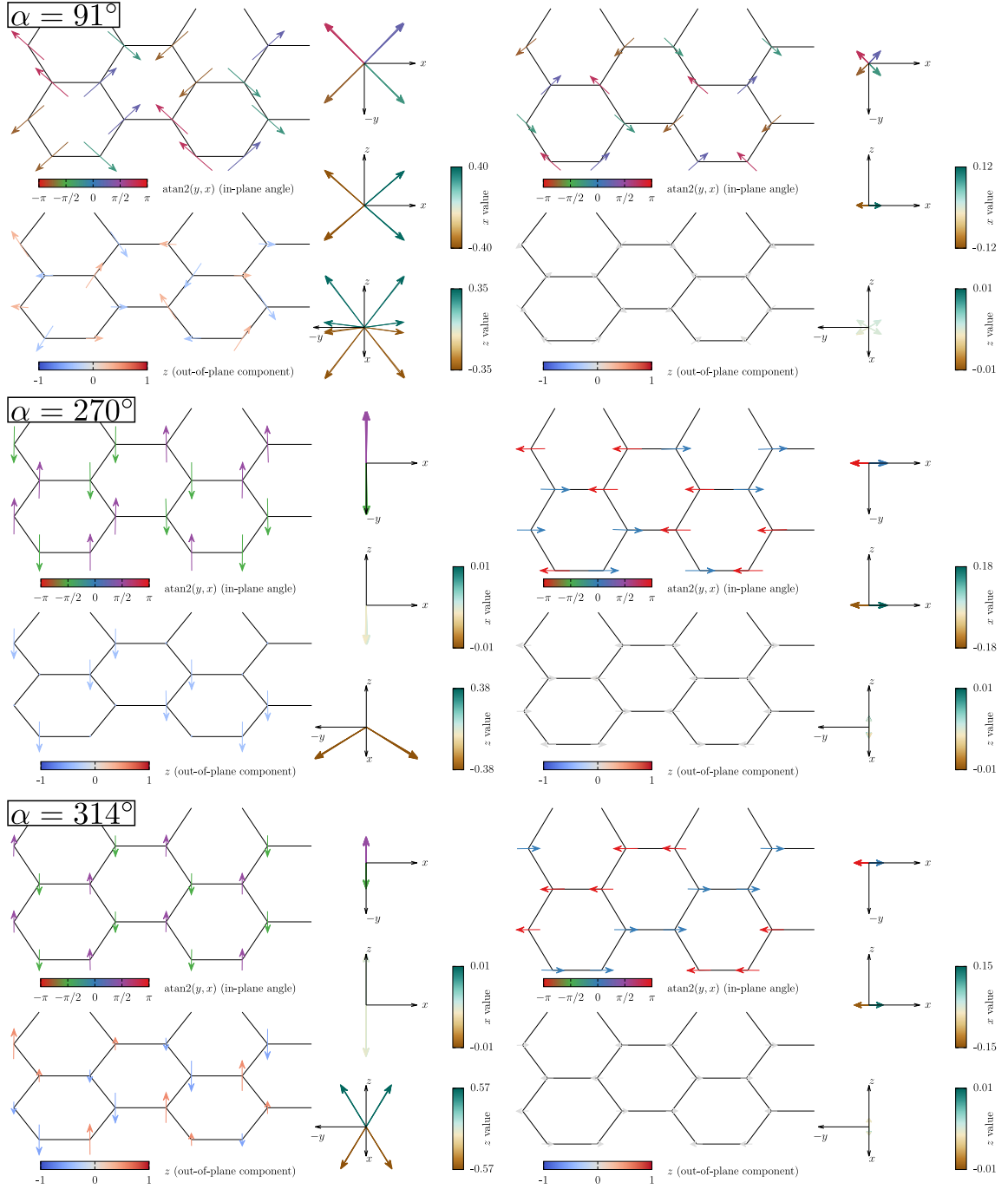


Figure 3.13. Order of the \mathbf{v} (left) \mathbf{u} (right) bosons for the new emerging phases at $A = 2$ in vicinity of the Kitaev and stripy to AFM transition regimes as established by semiclassical Monte-Carlo: The depiction is analogous to previous figures. Notably, the Kitaev phases seem to display very similar structures to the neighboring uncanted zigzag or stripy orders, with the addition of \mathbf{u} contributions that serve as a clear distinction.

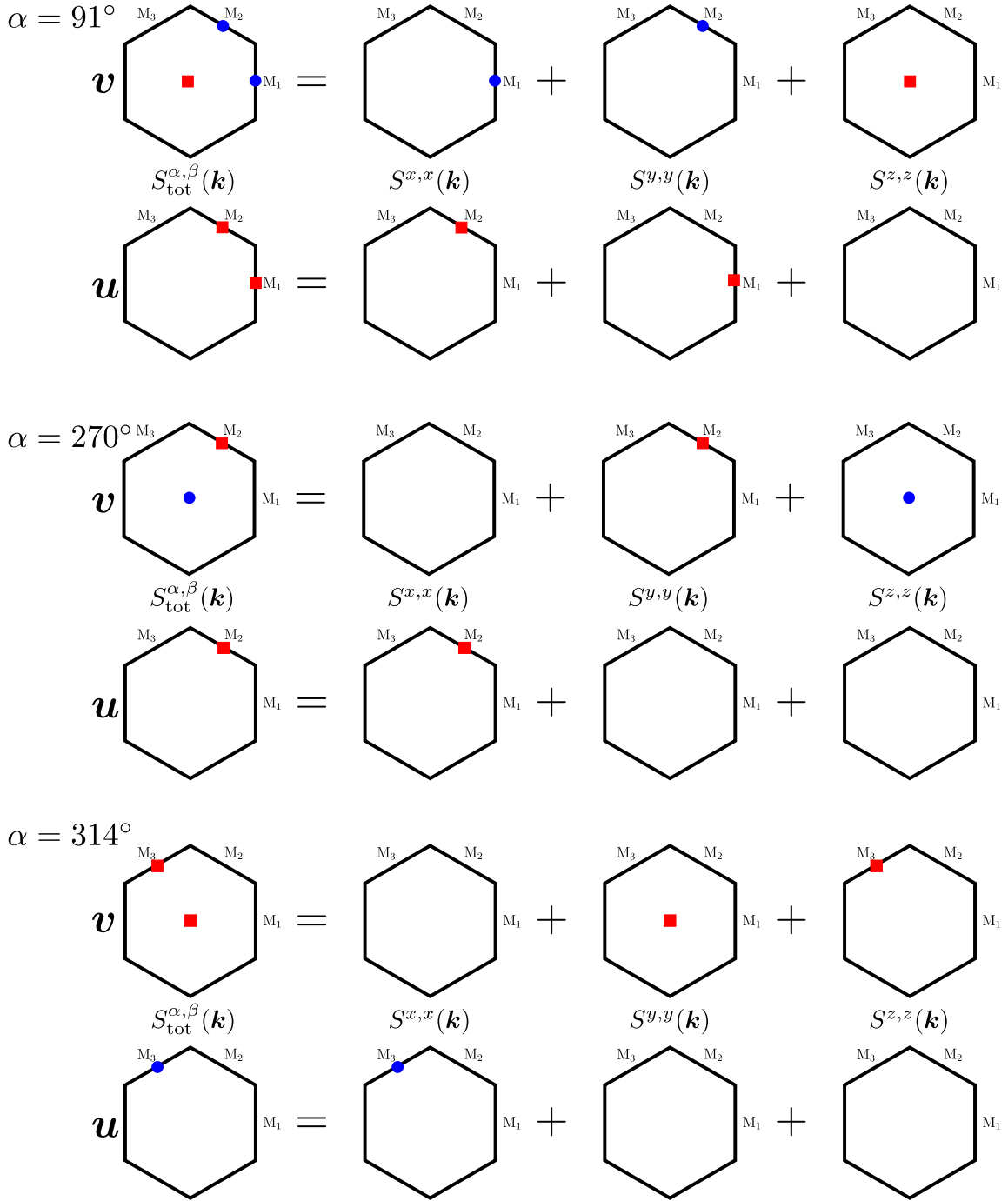


Figure 3.14. Significant spin-structure factors as established by semiclassical Monte-Carlo simulations for the orders displayed in figure 3.13: The blue dot denotes the contribution in the first Brillouin zone while the red square represents the second Brillouin zone (shifted by a reciprocal lattice vector). For the M points, which exist in both, we exclusively display the bigger contribution.

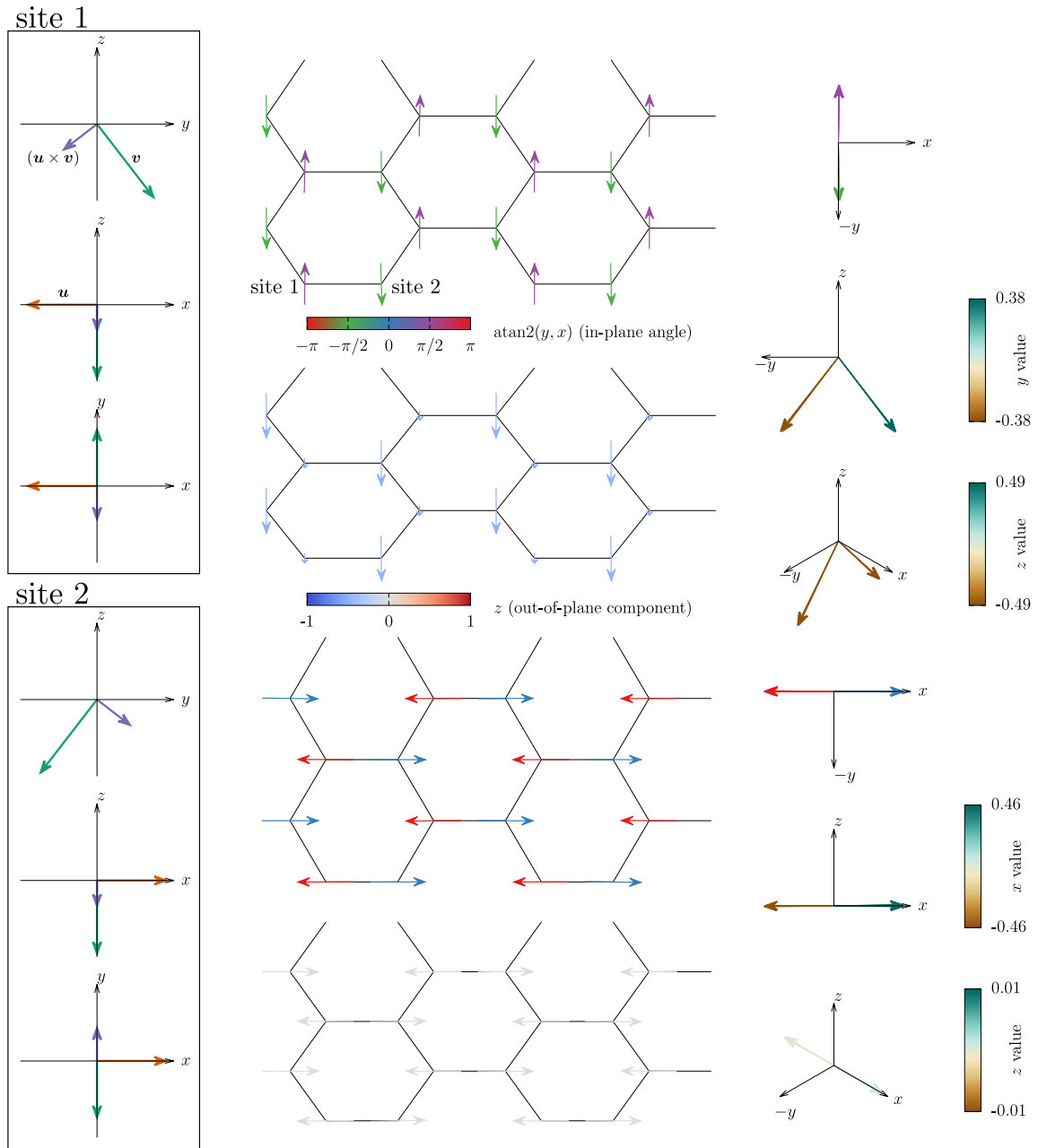


Figure 3.15. Order of both the v bosons (top) and u bosons (bottom) for the canted antiferromagnet phase produced by only considering the h_3 and h_4 terms for Kitaev-Heisenberg parameters $\alpha = 0^\circ$ and $A = 1$ as established by semiclassical Monte-Carlo: The color schemes and views are described in previous figures. Each boson type is limited to its own area: The u bosons are located on the x axis, while v orders in the y - z plane. As a result, the dipolar contribution is amended by a $(\mathbf{u} \times \mathbf{v})$ canting angle toward the z -axis. This is depicted in detail for two representative sites on the left side of the lattice plots. Further information regarding observables can be found in the subsequent figure.

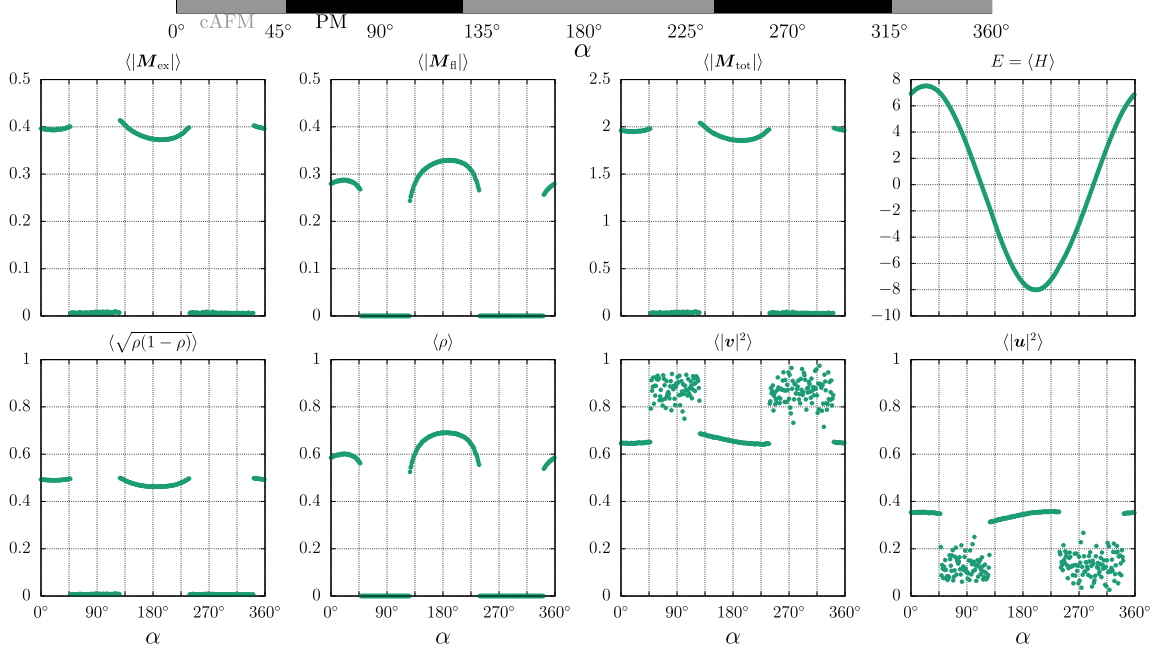


Figure 3.16. Semiclassical Monte-Carlo phase diagram (top) and observables for Kitaev-Heisenberg parameters $A = 1$ and varying α for the model with solely h_3 and h_4 terms: The emerging phases are the paramagnet (PM) and canted antiferromagnet (cAFM) as depicted in the previous figure. While the AFM phases are analogous, the concrete directions of the \mathbf{v} boson in relation to their \mathbf{u} counterparts is different, i.e. the resulting canting ($\mathbf{u} \times \mathbf{v}$) points in different directions. For the $\alpha = 0^\circ$ regime the canting has opposite sign in one component and same sign in the other, effectively pointing \mathbf{v} towards a common axis, while the $\alpha = 180^\circ$ phase has completely aligned (between different sites) ($\mathbf{u} \times \mathbf{v}$) contributions suggesting an overall ferromagnetic contribution.

and observables can be found in figures 3.15 and 3.16. The phase diagram consists of two canted AFM phases and paramagnetic regimes. The paramagnets extend (lattice size dependent and here $\Delta\alpha = 1^\circ$ step size) in the areas $48^\circ \leq \alpha \leq 126^\circ$ and $239^\circ \leq \alpha \leq 341^\circ$. Hence, the h_2 stripy to AFM transition at $\alpha = 315^\circ$ is an area where the higher-order terms seem to be relatively weak. On the contrary, the zigzag to FM counterpart $\alpha = 135^\circ$ falls within the magnetic regime of h_3 and h_4 at $A = 1$. The canted AFM phases are distinct by the directions of ($\mathbf{u} \times \mathbf{v}$) contributions, i.e. the direction of the canting.

As a consequence of the $A = 1$ phase diagram, one might try to investigate further

values $A > 1$ to observe if the paramagnet can be overcome in more scenarios by the higher-order terms. A sweep at $A = 2$ results in the two canted AFM phases existing in the areas $0^\circ \leq \alpha \leq 71^\circ$ ($\alpha \geq 309^\circ$) as well as $140^\circ \leq \alpha \leq 251^\circ$. The paramagnet is restricted to the area $265^\circ \leq \alpha \leq 308^\circ$. Two new phases with canted zigzag-like features emerge at $72^\circ \leq \alpha \leq 101^\circ$ respectively $252^\circ \leq \alpha \leq 264^\circ$, hinting at the overall agreeableness of the higher-order terms with zigzag kind of order. We provide figures in appendix A.1. In the remaining part of the phase diagram, the semiclassical Monte-Carlo results do not converge cleanly and hint at the lattice size being too small to establish the magnetic order. This is not entirely surprising, as canting effects in certain magnetic field directions (c.f. [165]) are known to result in similarly complicated structures. However, a detailed study of the $A = 2$ effects is a topic beyond this thesis and will not be attempted here.

Finally, we turn to the ED analysis. There are three main points of interest here. First of all, the fate of the Kitaev triplon liquid phase, which necessitates the full quantum treatment, needs to be discussed. Secondly, one should see if the new canted zigzag phase survives quantum fluctuations. Thirdly, ED could tell us if there are new phases which we can not find with the wave function ansatz of the semiclassical Monte-Carlo, e.g., one induced by the biquadratic exchange discussed in [1].

In a twist of irony, our analysis of this topic predates the emergence of the semiclassical Monte-Carlo studies performed in this thesis. In figure 3.17 one can find the ED results (partly) published in [5] representing a look at the parameter range of the data in figure 2.3 with additional h_3 and h_4 terms. “Original” refers to the \mathbf{v} boson model while “complete” denotes the addition of \mathbf{u} and higher-order contributions. What we do not plot explicitly here is the information about the \mathbf{k} value at which the spin-structure factor is maximal, but this information is in complete analogy to [6] and we arrange our presentation in accordance to [5]. All in all, the higher order terms do not seem to destroy the Kitaev phase at $A = 1$, i.e. the most problematic case of the area of interest. “Complete” and “original” are the data published in

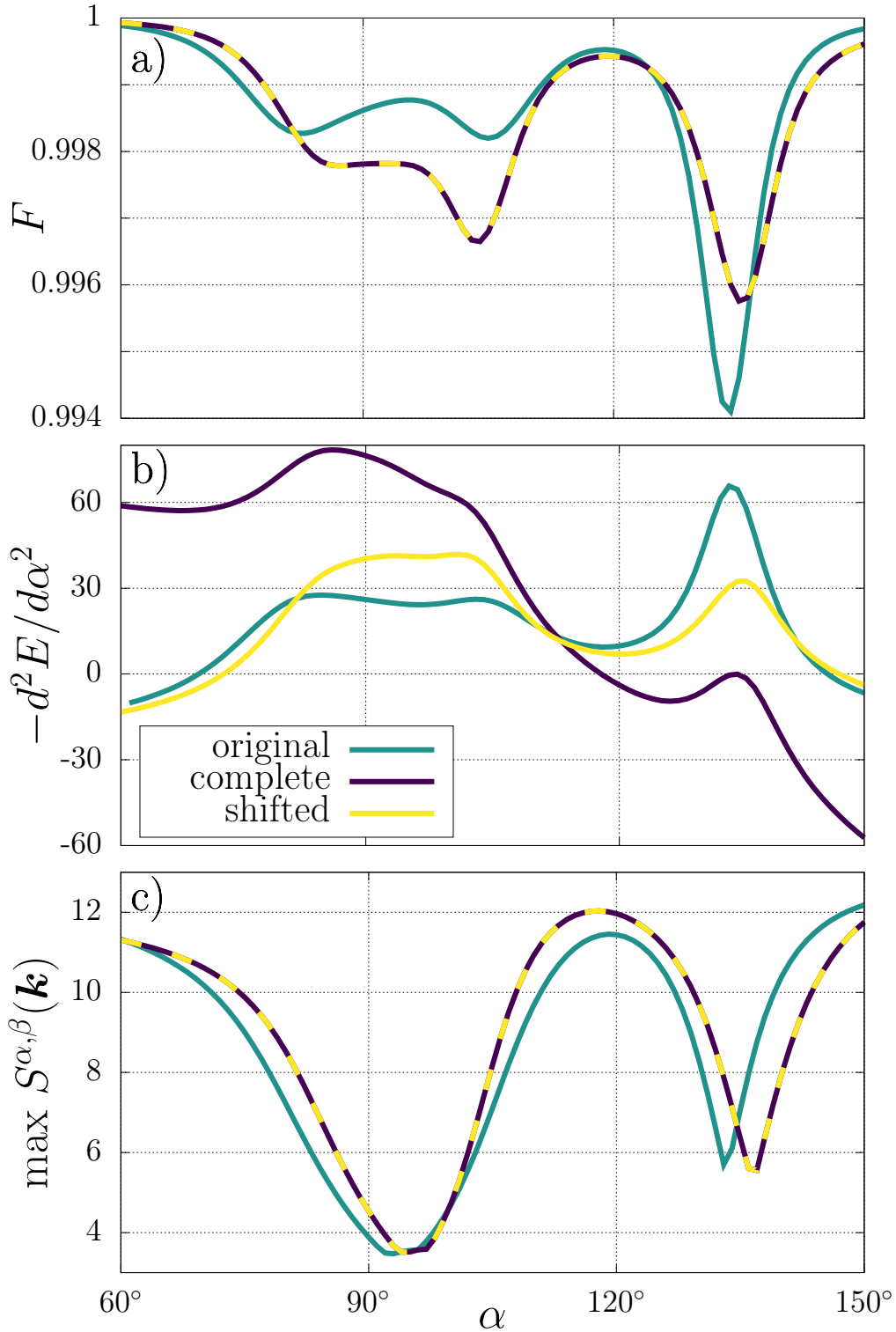


Figure 3.17. Ground state fidelity, energy derivative and maximal spin-structure factor resulting from ED simulations of the triplon Kitaev-Heisenberg model without (“original”) and with (“complete”) higher-order terms (previously published in [5]). The Kitaev phase is indicated to survive the higher-order contributions. The “shifted” line presents an attempt to eliminate the superfluous α dependent energy shift.

[5]. Additionally, we can note here that the sole addition of \mathbf{u} terms results in no visible shift of the observables, which is why we neglect to show it. Importantly, we point out the absence of the canted zigzag phase, which like the degeneracy at the $\alpha = 135^\circ$ bond-selecting Kitaev-Heisenberg point in the classical phase diagram, seems to be absent for the quantum mechanical treatment (in contrast to the Kitaev phase, which now encompasses a finite area).

Furthermore, one may spot the overall α dependent trend of the energy derivative introduced by the higher-order terms, which seems to shift or obfuscate the position of the maxima. The reason for this dependence seems to lie at the overall carelessness regarding the separation of singlet-triplet and triplon model in past studies [1, 5–7]. Concretely, one might take a closer look at the simplifications using the hard-core constraint and discarding of energy shifts. For example, the spin-orbit coupling is written in a way to conveniently look like a chemical potential for triplets/triplons by shifting the energy, even though the projection of the operator to the singlet triplet results in $\lambda \sum_i (-2n_i^s - n_i^x - n_y^i - n_z^i)$. Similar simplifications are done with the Kugel-Khomskii Hamiltonian. One can attempt to fix this by rewriting the model by, e.g., eliminating the singlet explicitly via the hard-core constraint and discarding all resulting energy shifts. In order to do this one can just take all matrix elements of the Hamiltonian in figure 1.13 in which there is an on-site $s_i^\dagger s_i$ term and introduce $s_i^\dagger s_i = 1 - \sum_\tau t_{i,\tau}^\dagger t_{i,\tau}$. Then one adds the new triplon based terms to the appropriate matrix elements and discards the identity operator. This is the “shifted” line in figure 3.17, which seems to work perfectly as the fidelity (ground state change) and spin-structure factors remain unchanged. Nevertheless, since this also leads to discarded on-site strain terms that are clearly not energy shifts, we largely ignore this and just accept that the energy signatures are less reliable. In future studies, we suggest leaving everything singlet-triplet based (no triplons) from the start.

A central question raised in reference [1] is the fate of the bond-selecting interaction case in this model. The model in the reference represents the $t' = 0$ case

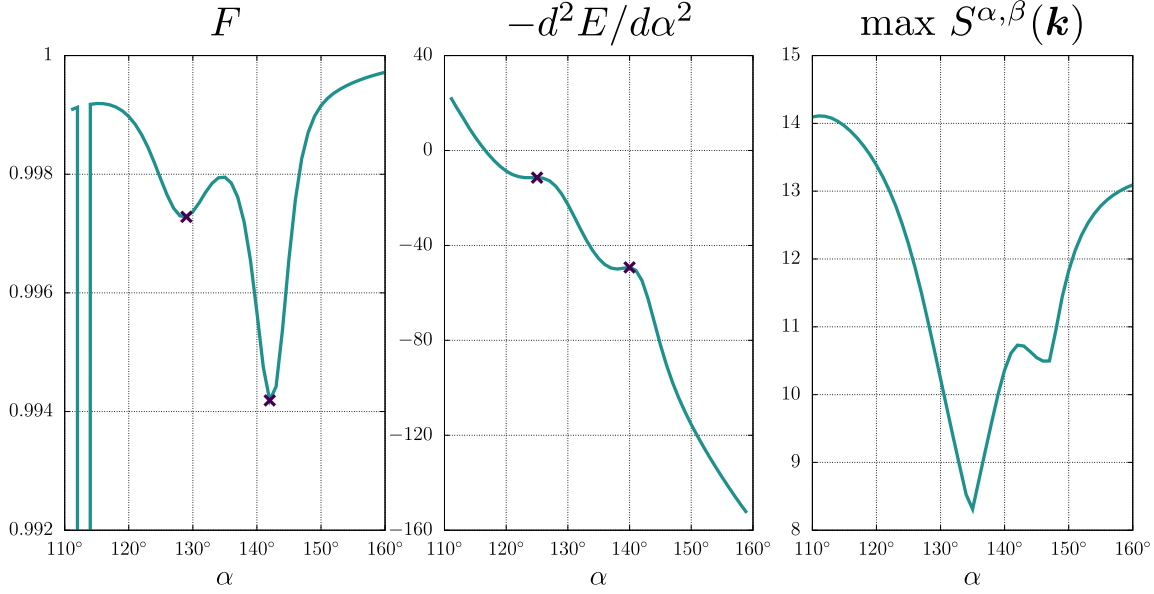


Figure 3.18. ED ground state fidelity, energy derivative and spin-structure factor for $A = 2$ in vicinity of the zigzag to ferromagnet transition: The canted zigzag phase emerges in the quantum model. One may note the ground state change represented by $F = 0$ at $\alpha = 113^\circ$. The purple crosses depict the local maxima of fidelity and energy derivative.

and thus exactly $\alpha = 315^\circ$ (or its sign flipped version at $\alpha = 135^\circ$). In that paper, it has been pointed out that the higher order terms should decide the fate of the condensate. Moreover, a lot of novel possible scenarios have been suggested based on that line of thought. After over 10 years, we can now finally provide an answer: In the semiclassical scheme there is a finite area of stability of the h_2 critical point. Thereafter, for the $\alpha = 135^\circ$ case, a canted zigzag phase with \mathbf{u} contributions is established. However, this seems to be the case because of the higher-order terms preferring a similar structure, as the stripy to AFM transition, which has the analogous choice to make, just recovers the h_2 structure up to unrealistically high interaction strength. Now, with the quantum mechanical simulation, we find that for $A = 1$ both the h_2 degeneracy structure and canted zigzag phase do not occupy a finite area in the phase diagram. There is no choice to make. zigzag and FM, i.e. small t' contributions, cannibalize the interesting scenario completely.

3. Analysis of the Triplon Honeycomb Model

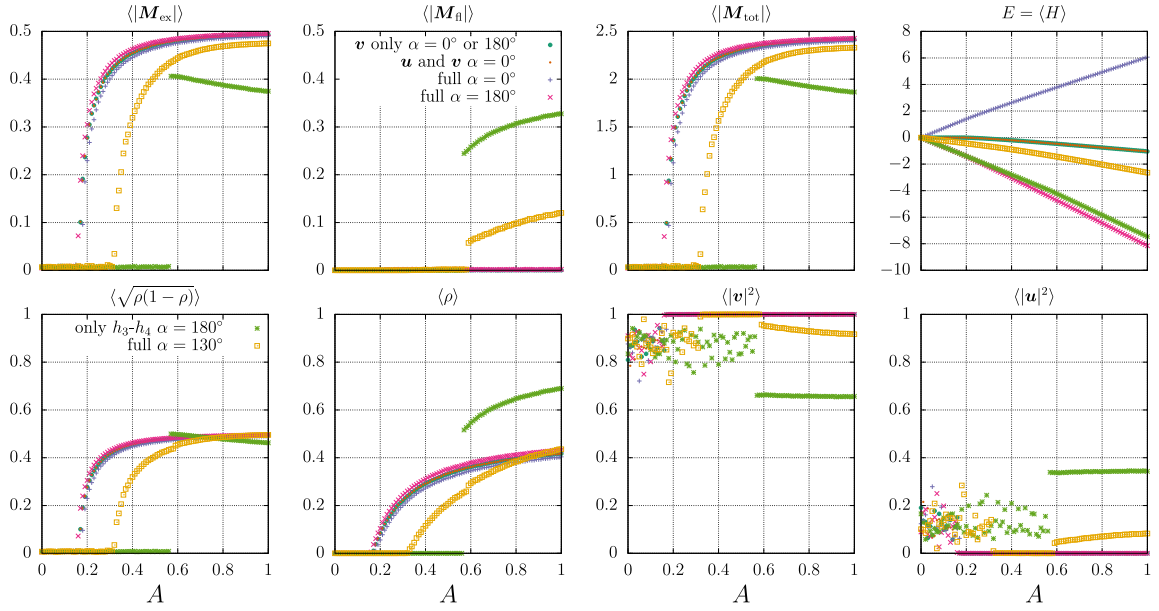


Figure 3.19. Semiclassical Monte-Carlo observable for various scenarios: The usual contribution of \mathbf{u} terms is negligible, while the higher-order h_3 and h_4 terms cause slight shifts. In the case of new phases caused by the higher-order terms ($\alpha = 130^\circ$ canted zigzag phase and solely h_3 - h_4 model), there are clear jumps in the observables, signaling a ground state change. Additionally, the new phases seem to strive for a maximum in the flavor-changing \mathbf{M}_{fl} contribution of the dipole.

Yet, based on the semiclassical Monte-Carlo results one might ask whether the canted zigzag phase completely vanishes or is recovered for larger A . Hence, we have performed an ED simulation at $A = 2$, which can be found in figure 3.18. Therein, the canted zigzag phase is recovered based on fidelity and energy derivative extrema as well as spin-structure factor signatures (both significant contributions at Γ and M , with the M point taking over for $\alpha > 135^\circ$). So the canted zigzag phase does exist in the quantum mechanical case. But why does it only emerge so late? There are two possible reasons. First of all, this could be the effect of quantum fluctuations. Secondly, this could be a finite size effect. For the latter, one should note the comparatively (to semiclassical Monte-Carlo) late emergence of the magnetic phases in figure 2.3. Hence, the question is connected to the reason for the general disagreement between sMC and ED condensation points. Of course, sMC is not expected

to be correct quantitatively. Yet, ED is not without its faults. When discussing the strengths and weaknesses, we mentioned that ED systematically underestimates the hopping and pair term contributions depending on lattice size (even and odd boson number subspaces). As a result, one should attempt a systematic finite size evaluation of the critical condensation point. However, this should be done in the simpler model based on Ca_2RuO_4 , as both Hamiltonian (for $J_{\text{H}} = 0$) and lattice form can be handled more conveniently. This is beyond the scope of this thesis. Nevertheless, a systematic undervaluing of interactions could in theory motivate $A > 1$ as a more realistic regime. Alternatively, the Quantum Monte Carlo simulation in [157] could be repeated with higher-order contributions and focus on the possible canted zigzag regime. All in all, the question of relevancy of the canted zigzag phase remains to be answered.

Finally, we should address the remaining feature of figure 3.18. There is clearly a change in ground state between $\alpha = 110^\circ$ and $\alpha = 120^\circ$. It is nontrivial to identify if this is a legitimate feature of the higher-order terms or a finite size effect. For this discussion we provide some observables of the semiclassical Monte-Carlo simulation in figure 3.19. One can see, that the magnetism of the h_3 and h_4 terms emerges not via the regular condensation, but rather a drastic discontinuous change in the ground state. Hence, this feature might not necessarily be a finite size effect. Yet, there seems to be no change in energy and spin-structure factor in ED, so the first suspect would be the temporary emergence of the one-boson sector, which should try to establish the same magnetic order, below the triplon vacuum. This again hints at the importance of a finite size effect study.

3.2 Triplons in a Magnetic Field

Regarding the triplon model in a magnetic field, there are three main avenues of interest we want to approach here. First of all, the magnetic field has been an

important tool to drive Bose-Einstein condensation of triplons in spin-dimer models [70] such as, e.g., TlCuCl_3 [74, 194, 195]. As the magnetic field for the spin-orbital dimers found in our system couples to the magnetic dipole moment \mathbf{M} in equation (1.91) and not the one in equation (1.115) for regular spins, this very established phenomenon of driving the condensation needs to be reevaluated.

The second point of interest is directly connected with the previous subject. Kitaev-Heisenberg physics in magnetic fields, even for normal spins, are highly non-trivial [41, 165] and have gained a lot of relevance as a result of experiments surrounding $\alpha\text{-RuCl}_3$. In this compound, a magnetic field can be used to suppress the magnetic order, possibly leading to the emergence of a spin-liquid phase [38]. The material itself has been around for some time as a possible Kitaev material showing intriguing magnetic field behavior [111, 196]. Yet, the focus on this material increased dramatically when a series of experiments in 2017-2018 established the potential spin-liquid [52, 197–201]. Of particular interest was the claim of an unusual thermal Hall effect in the material [53, 55], which, due to the apparent half-integer quantization, has been connected to the Majorana fermions inherent in the Kitaev spin-liquid. A lot of attention regarding the magnetic field (extended) Kitaev-Heisenberg model studies is naturally focused on the spin-1/2 d^5 scenario or even more directly material specific context of $\alpha\text{-RuCl}_3$ [51, 202, 203]. With the investigation of the triplon Kitaev-Heisenberg model in reference [5], we more or less concurrently provided a related model, which due to its degrees of freedom (singlet-triplet instead of spin-1/2, variable spin-length via condensate, higher-order terms) and the aforementioned different coupling to the magnetic field may either provide new novel effects or, if its found to work analogously to the normal spin, a case where a lot of insights can be adapted. Hence, we investigate the general behavior of the triplon Kitaev-Heisenberg model in a magnetic field.

It should be mentioned that the initial intrigue about the half-integer thermal Hall effect has died down a bit. While supporting evidence like further quantized mea-

measurements for different magnetic fields hosting a Kitaev-like bond-dependent sign structure [54] was established, questions have been raised regarding sample dependence [56, 204] and even absence of the half-integer plateau [58], with oscillations taking its place. While some argue that the half-integer effect is robust [57], the topic remains under debate. Following a very recent summary of this subject [60], there are a lot of arguments suggesting that there is no half-integer thermal Hall effect caused by Majorana fermions, but rather a thermal Hall effect of magnons, which still explains features like the sign structure [59]. This is, however, not directly important for the discussions in this thesis.

The third and final area of interest discussed in this thesis is specifically focused on the fate of the triplon liquid phase in magnetic fields. It is also directly motivated by the result of the α -RuCl₃ thermal Hall experiment leading to a surge of interest in this kind of subject. The previously discussed suppression of magnetic order in α -RuCl₃ necessitates large magnetic fields. As the famous Kitaev model [4] exact solution is not valid for large magnetic fields, the obvious question connected to the experimental results is: What kind of spin-liquid could be established? One of the approaches to obtain an explanation is to study the behavior of a pure Kitaev model in a magnetic field (instead of, e.g., a Kitaev- Γ or other Kitaev-Heisenberg schemes emerging from a more material tailored starting point). In spin-1/2 models, one finds that the FM Kitaev phase polarizes almost instantly, while the AFM Kitaev regime is more robust and can be driven to another spin-liquid intermediate phase before eventually succumbing to the magnetic field [205–208] (note that the field direction influences this). The intermediate phase may also be connected to a topologically nontrivial phase [209–211].

Obviously, the spin-1/2 characteristics (often connected explicitly to the Majorana fermions) should not be expected to translate to out singlet-triplet model consisting of a $J = 0$ ground state and $J = 1$ triplets. Yet, what the investigation into the spin-1/2 regime and the resulting intermediate spin-liquid phase has motivated

a closer look at Kitaev models with other spin types, e.g., a general spin- S [212] or the subsequently discussed spin-1. The spin-1 Kitaev phases are distinct from the spin-1/2 case, e.g., via the nature of their excitations [213]. Nevertheless, they share the intriguing feature of an unstable FM, stable AFM and the existence of an intermediate phase driven by the magnetic field [66–68, 171, 214]. Reference [67] also points out a key motivation: The spin-1/2 Kitaev candidate materials are primarily expected to be in the FM regime, while spin-1 can be different in this regard. Quite analogously, our d^4 Kugel-Khomskii model is expected to result in different effective spin interactions than its d^5 counterpart (e.g. Kitaev in d^5 and bond-selecting $J = -K$ via a pure 90° exchange in our d^4 model). More importantly: As we have our own distinct degrees of freedom, i.e. the on-site singlet-triplet, we obtain our own Kitaev phase [157, 170] and therefore potentially a different intermediate spin-liquid, if one exists at all.

Subsequently, we start the analysis by looking at the first point, i.e. the magnetic field as a driver of triplon condensation.

3.2.1 Triplon Condensation Driven by a Magnetic Field

We start by choosing a useful parametrization of the magnetic dipole moment. Following equation (1.91), one may introduce the influence of the magnetic field via

$$\begin{aligned}
 H &= h \sum_i \hat{\mathbf{h}} \mathbf{M}_i = h \sum_i \hat{\mathbf{h}} \left(-\sqrt{6}i(\mathbf{T}_i - \mathbf{T}_i^\dagger) - \frac{i}{2} \mathbf{T}_i^\dagger \times \mathbf{T}_i \right) \\
 &= h \sum_i \hat{\mathbf{h}} \left(\sqrt{6} \mathbf{M}_{\text{ex},i} + \frac{1}{2} \mathbf{M}_{\text{fl},i} \right) \\
 &\equiv h \sum_i \hat{\mathbf{h}} (\cos(\tau) \mathbf{M}_{\text{ex},i} + \sin(\tau) \mathbf{M}_{\text{fl},i}), \tag{3.16}
 \end{aligned}$$

where h is the strength of the magnetic field, $\hat{\mathbf{h}}$ its normalized direction and we split the contributions into an excitonic part (ex), which creates or annihilates a triplon/exciton and the flavor-changing part, which solely serves as an on-site interaction with fixed triplon number. We also introduce the parameter τ to facilitate a more general discussion, with $\tan(\tau) = (1/2)/\sqrt{6}$ recovering the real magnetic moment. It should be noted that the sign (even when different for both terms) does not matter in the subsequent discussion.

As mentioned previously, using the magnetic field to drive triplon condensation is a well established subject for normal spin-dimers. A dimer consisting of two spin-1/2 adheres to equation (1.115) and is therefore recovered via $\tau = \pi/2$ (due to the sign not playing a role we restrict ourselves to $0 \leq \tau \leq \pi/2$). Hence, the spin-dimer is only influenced by the flavor-changing term, which results in a regular linear Zeeman splitting as seen in figure 3.20. According to [70], the Bose-Einstein condensation of triplons is then facilitated by the Zeeman splitting effectively reducing the gap between singlet and triplet. As a result, one may expect a finite region around the energy crossing point of singlet and lowered triplet state where a condensation can become possible. Of course, the behavior in the condensed phase needs to be accounted for after the critical point, so how long the condensate survives is another

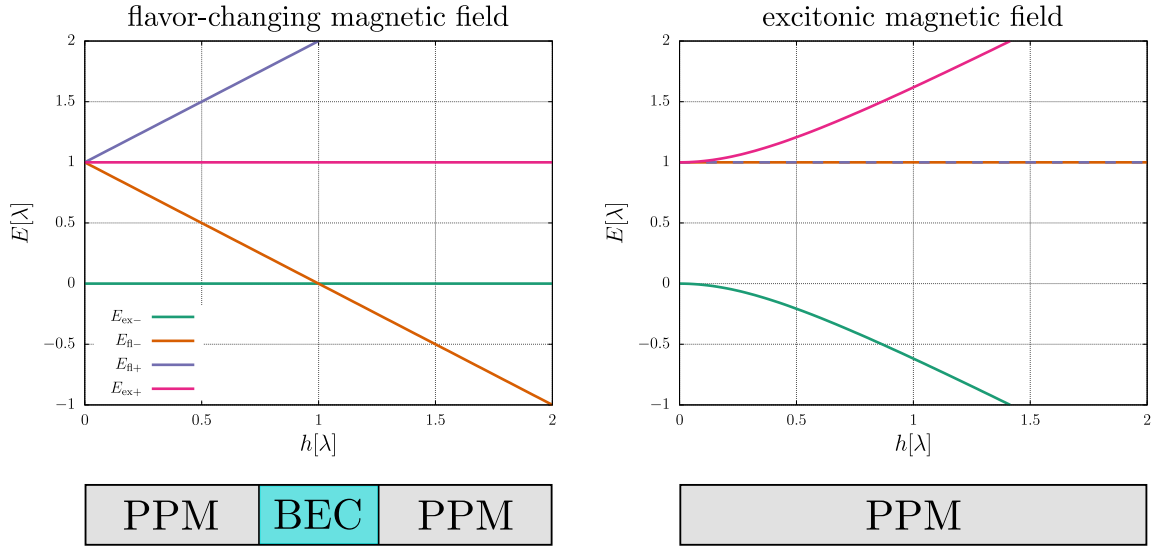


Figure 3.20. Effect of the two contributions to the magnetic dipole moment on the on-site energies: Regardless of the magnetic field direction, a distinct pair of energies is influenced by each term, which is represented by the labels $E_{n,\pm}$ for the ones dictated by the flavor-changing magnetic field term and $E_{ex,\pm}$ for the excitonic contribution. Spin-dimers, e.g., a singlet-triplet model consisting of two coupled spin-1/2, only have the flavor-changing contribution. Therefore, the (polarized) paramagnet (P)PM can possibly be driven into a magnetic phase via Bose-Einstein condensation (BEC) by effective reduction of the gap between singlet and triplet. In contrast to this, the excitonic contribution stabilizes the ground state.

discussion. However, at some point the magnetic field is expected to itself introduce a gap that can not be overcome, hence resulting in a polarized paramagnet.

For a spin-1 dimer, i.e. a singlet-triplet-quintet model, this behavior might repeat, as first singlet and triplet condense and eventually a quintet state (Zeeman splitting can be twice as strong) will catch up with the triplet. One can therefore leave and reenter the condensate (although the second one of course is a different entity). For the sake of simplicity, we henceforth limit the discussion to the directly relevant singlet-triplet model. Yet, this does not invalidate the arguments we make subsequently. Pictures illustrating this condensation behavior with the addition of the quintet can be found in reference [92].

In the spin-orbital singlet-triplet model we have both excitonic and a flavor-

changing contributions. Naturally, one should ask the question what to expect as a result of this peculiarity. Reference [157], which is a quantum Monte-Carlo study of the triplon Kitaev-Heisenberg model (slightly different parameters) suggests the following: “The system couples to the external field through the van Vleck magnetic moments as well as the triplon magnetic moments, both of which can drive the condensation of triplons”. Furthermore, reference [92], which considers a model based on the d^8 compound NiRh_2O_4 and therefore a scenario where the magnetic field coupling should be the same as in our model, implies the feasibility of driving (and reentering) the Bose-Einstein condensate in more or less complete analogy to the spin-dimer systems.

There are likely issues with both these statements/results which we try to point out in the remainder of this section. In fact, we imply that driving the condensation with a magnetic field seems to be a nonviable approach in practice!

In order to do this, we first look at the effect of both terms in isolation. Figure 3.20 contains the eigenenergies of the magnetic field Hamiltonian for a single site singlet-triplet model. The energies can be calculated trivially. They are (independent of field direction)

$$\begin{aligned}
 E_{\text{fl},\pm} &= \lambda \pm h \sin(\tau), \\
 E_{\text{ex},\pm} &= \frac{\lambda}{2} \pm \sqrt{\left(\frac{\lambda}{2}\right)^2 + h^2 \cos^2(\tau)}.
 \end{aligned}
 \tag{3.17}$$

Accordingly, the contributions exist completely disjoint from each other. It is also obvious and illustrated in figure 3.20, that the excitonic contribution does not reduce the singlet-triplet gap. Instead, the opposite is the case.

Coming back to the statement of reference [157] one should therefore note that it can be misleading. For normal spin-dimers the support for condensation is explained by the on-site contribution of the magnetic field. For the spin-orbital model the excitonic (Van Vleck) term does not facilitate condensation in this way (it adds

3. Analysis of the Triplon Honeycomb Model

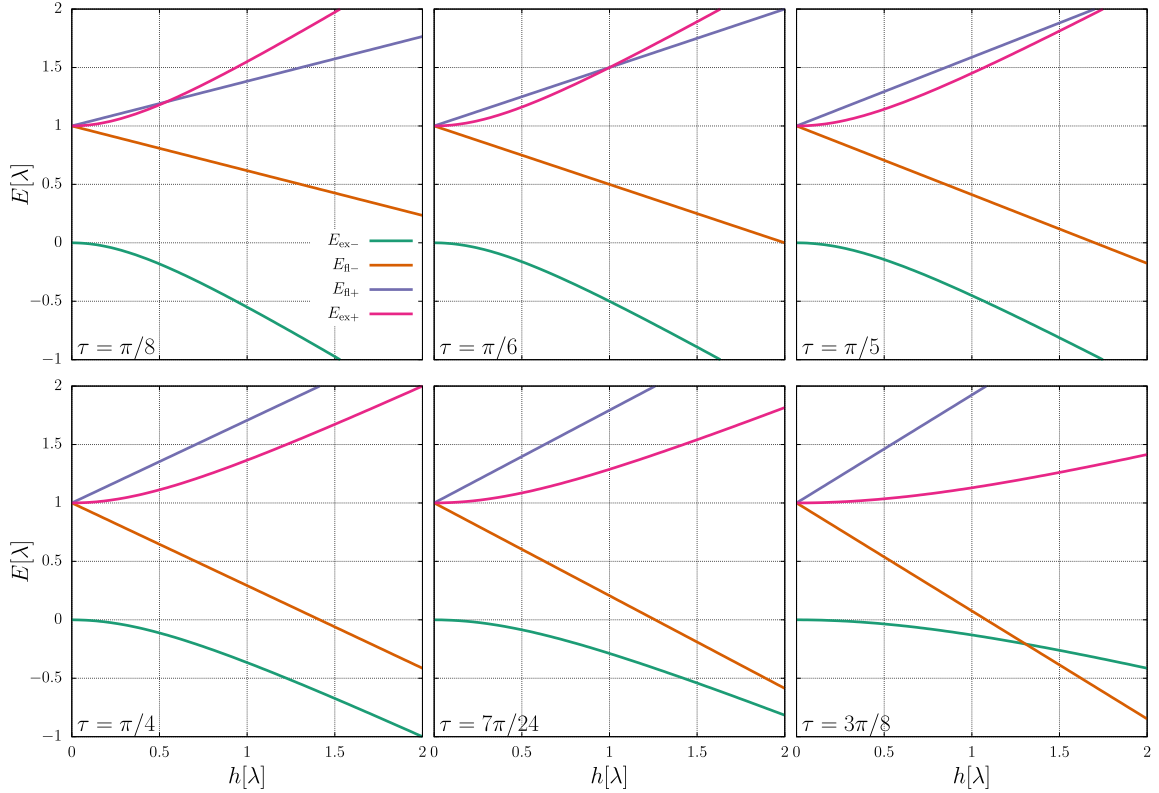


Figure 3.21. Various examples of the on-site singlet-triplet under influences of a magnetic field with both flavor-changing (fl) and excitonic field (ex) being active: The angle τ represents the relative strength of both contributions via $\mathbf{M} = \cos(\tau)\mathbf{M}_{\text{ex}} + \sin(\tau)\mathbf{M}_{\text{fl}}$ (sign irrelevant, therefore $0 \leq \tau \leq \pi/2$ with the edge cases being illustrated in figure 3.20). Each term influences its own distinct pair of energies, which is reflected by the index.

triplons but not via BEC). The statement could still be technically correct when considering that the Van Vleck term increases the number of bosons, which could under certain circumstances help, e.g., higher-order contributions to gain importance and help overcome the singlet-triplet gap. Yet, one needs to investigate if this nontrivial scenario is even feasible.

We now turn to the discussion of the NiRh_2O_4 based model [92]. Aside from being a $3d^8$ model with different kind of intersite interactions, NiRh_2O_4 could possibly share a lot of similarities with the d^4 Van Vleck-type models suggested for Ca_2RuO_4 and $\text{Ag}_3\text{LiRu}_2\text{O}_6$. We explicitly noted the similarities over the course of the introductory

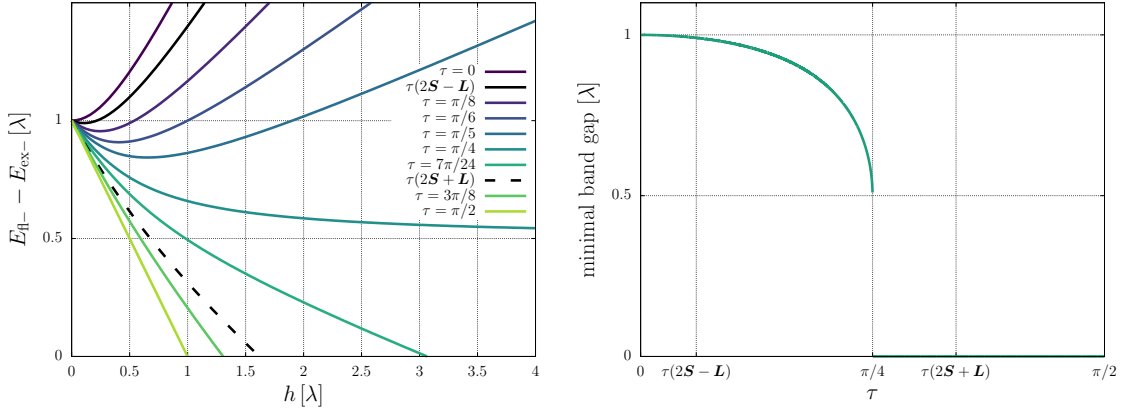


Figure 3.22. Evolution of the band gap between the singlet and lowest triplet state as a function of the magnetic field strength h (left) and resulting minimal band gap (right) as a function of τ (relative strength of the flavor-changing and excitonic contribution): The parametrization is $\mathbf{M} = \cos(\tau)\mathbf{M}_{\text{ex}} + \sin(\tau)\mathbf{M}_{\text{fl}}$, with the index denoting the contribution. The sign error resulting from use of $2\mathbf{S} + \mathbf{L}$ instead of the t-p-correspondence based $2\mathbf{S} - \mathbf{L}$ puts the magnetic field response into the realm of a more spin-dimer like (only flavor-changing) scenario, where the gap always closes and a condensation of triplons can be driven with the magnetic field. In contrast to this, driving a condensation is almost impossible in the $2\mathbf{S} - \mathbf{L}$ as the reduction of the singlet-triplet gap is minute.

chapter. Even the discussion whether one should understand it as a spin-orbital singlet-triplet model or rather a regular spin-1 due to a large tetragonal crystal field distortion [36, 215], is very reminiscent of the one for Ca_2RuO_4 [119, 134]. As a result, one should expect the magnetic field to have the same characteristics for both our model and NiRh_2O_4 . Their prediction [92] is an outright level crossing akin to the $\tau = \pi/2$ pure spin-dimer case and therefore driven condensation and reentrance behavior leading to novel magnetic phases via BEC.

In order to understand the possible issue with this model we turn to an analysis of the mixed model, i.e. $0 < \tau < \pi/2$. As the analytical expressions dictate, the two sets of energies are disjoint and one trivially obtains the eigenvalues illustrated in figure 3.21. Hence, the reduction of the singlet-triplet gap and eventual level crossing are dictated by the size of the magnetic field contributions and therefore the angle τ .

Concretely, one can look at the singlet-triplet gap by considering the energy difference $E_{\text{fl},-} - E_{\text{ex},-}$. This term reaches zero, i.e. accomplishes a level crossing and therefore guaranteeing condensation, only for $\tau > \pi/4$ (h needs to be real and positive because it represents the length of the magnetic field vector), where $h_{\text{cross}}/\lambda = -\sin(\tau)/\cos(2\tau)$. This is expected, because $\tau = \pi/4$ represents the equal strength of both contributions to the magnetic moment. Furthermore, one obtains the effective evolution of the singlet-triplet band gap found in figure 3.22. For $0 \leq \tau \leq \pi/4$ there is a finite minimum, which moves from $h = 0$ at $\tau = 0$ to $h \rightarrow \infty$ at $\tau \rightarrow \pi/4$. Interestingly, the spin gap can be, at most, halved in this scenario. This is also illustrated in the figure by explicit use of the analytical expression for the minimum location, which is $h_{\text{min}} = \tan(\tau)/(2\sqrt{\cos^2(\tau) - \sin^2(\tau)})$.

What remains is to establish the value of the angle τ belonging to our model, which we accomplished at the start of this section. It is represented in figure 3.22 via the expression $\tau(2\mathbf{S} - \mathbf{L})$, reflecting the magnetic moment $\mathbf{M} = 2\mathbf{S} - \mathbf{L}$ derived in the introduction in equations (1.25) and (1.91). As a result, our model is in a regime where the excitonic term is very dominant and hence the singlet-triplet gap is only reduced by a very minuscule amount. Therefore, one may only think about driving condensation if one is more or less directly at the critical point already.

How does that fit to the results of the NiRh₂O₄ based model? It could be the case that their results are erroneous due to neglect of the sign change enforced by the use of t-p-correspondence. In reference [92] they use $\mathbf{M} = 2\mathbf{S} + \mathbf{L}$, which they are allowed to do if \mathbf{L} is the pseudospin and not a normal angular momentum operator. As we have covered the tetrahedral geometry d^8 case in the introduction and found it to be analogous to our model, there seems to be no apparent reason to not have the pseudospin-angular momentum argument leading to $\mathbf{M} = 2\mathbf{S} - \mathbf{L}$. If they have indeed used the wrong expression, it would lead to (analogous to equations (1.89)

and (1.90))

$$\langle \mathbf{M}_i \rangle_{s,t} = 2\langle \mathbf{S}_i \rangle_{s,t} + \langle \mathbf{L}_i \rangle_{s,t} = -i\sqrt{\frac{2}{3}}((\mathbf{T}_i - \mathbf{T}_i^\dagger)) - i\frac{3}{2}\mathbf{T}_i^\dagger \times \mathbf{T}_i, \quad (3.18)$$

where $\tau = \tan^{-1}(3/2/(\sqrt{2/3}))$, i.e. the $\tau > \pi/4$ regime and the values illustrated in the previously mentioned figures.

Assuming our parameters to be correct, it is very straightforward what to expect if one starts applying a magnetic field to the triplon model in its paramagnetic regime: Aside from a freak accident or somehow nontrivial interplay with the intersite terms, the model will stay a (polarized) paramagnet. One can (at least for semiclassical Monte-Carlo, where the critical point is known and identical to the flavor wave), for example, start in the AFM Heisenberg with $A/\lambda = 0.166$, i.e. extremely close to the critical point $A/\lambda = 1/6$, and the Monte-Carlo simulation will result in a polarized paramagnet for any value of the magnetic field strength.

Finally, we point out that this should have been expected from the start. Reference [92] points out the difference between their model and the one in FeSc_2S_4 . This compound is a different singlet-triplet scenario enforced by a d^6 setup with spin $S = 2$ and spin-orbit coupling. As such, however, it shares the spin-orbital nature of the singlet-triplet model. In reference [216], they look at the excitations, which they deem extremely close to condensation via an almost gapless INS spectrum. Yet, an application of the magnetic field does not condense the triplets but leads to a shift of the excitations to higher energies, i.e. what we expect based on our calculations as well. They point this out as a feature of the spin-orbital singlet in contrast to a spin-spin one. In other words regarding the same compound, this is referred to not being in the linear Zeeman regime anymore [217]. Given our previous arguments, NiRh_2O_4 and our model should behave similarly.

Moreover, we point out that the precise balance between the excitonic term and flavor-changing usual Zeeman splitting is important. Hence, one should always be

careful when establishing the magnetic dipole moment. The overall discussion of spin-orbital moments being distinct in behavior from normal spins is a very banal but important point, which is not always respected. In a similar vein, the importance of this concept was also pointed out relatively recently in reference [79]. Therein, the authors argue that the Curie-Weiss law is a pure spin model and needs to be modified in order to capture the total angular momentum resulting from spin-orbit coupling correctly. Not doing so leads to significant deviations, e.g., for estimating the Kitaev interaction scale in α -RuCl₃. All in all, one should always carefully evaluate differences between spin and total angular momentum degrees of freedom.

3.2.2 Triplon Kitaev-Heisenberg Model in a Magnetic Field

As a result of the previous section, we can restrict our analysis of the Kitaev-Heisenberg model in a magnetic field to starting points in the condensed regime. Hence, we set $A = 1$ unless otherwise mentioned. Furthermore, we point out the analysis of the classical Kitaev-Heisenberg model done in reference [165] and further mentioned in reference [41]. One of the main results of this section is that the model can be understood quite easily when knowing the classical phase diagram, which is why one may refer to reference [165] for more detailed descriptions of the phases. Furthermore, the supplementary material of this paper explains and derives the spin-wave solutions we use.

Based on the results of that paper, we expect the $\mathbf{h} = [0, 0, 1]^T$ magnetic field direction to be the better regime for the initial analysis, as the $\mathbf{h} = [1, 1, 1]^T$ case results in a multitude of complicated large magnetic unit cell phases. Accordingly, we restrict ourselves to that field unless otherwise mentioned.

We start with the simplification $\mathbf{M}_f = 0$ and only \mathbf{v} bosons, although the latter restriction is not important. With this, we strive to find out the effect of a variable

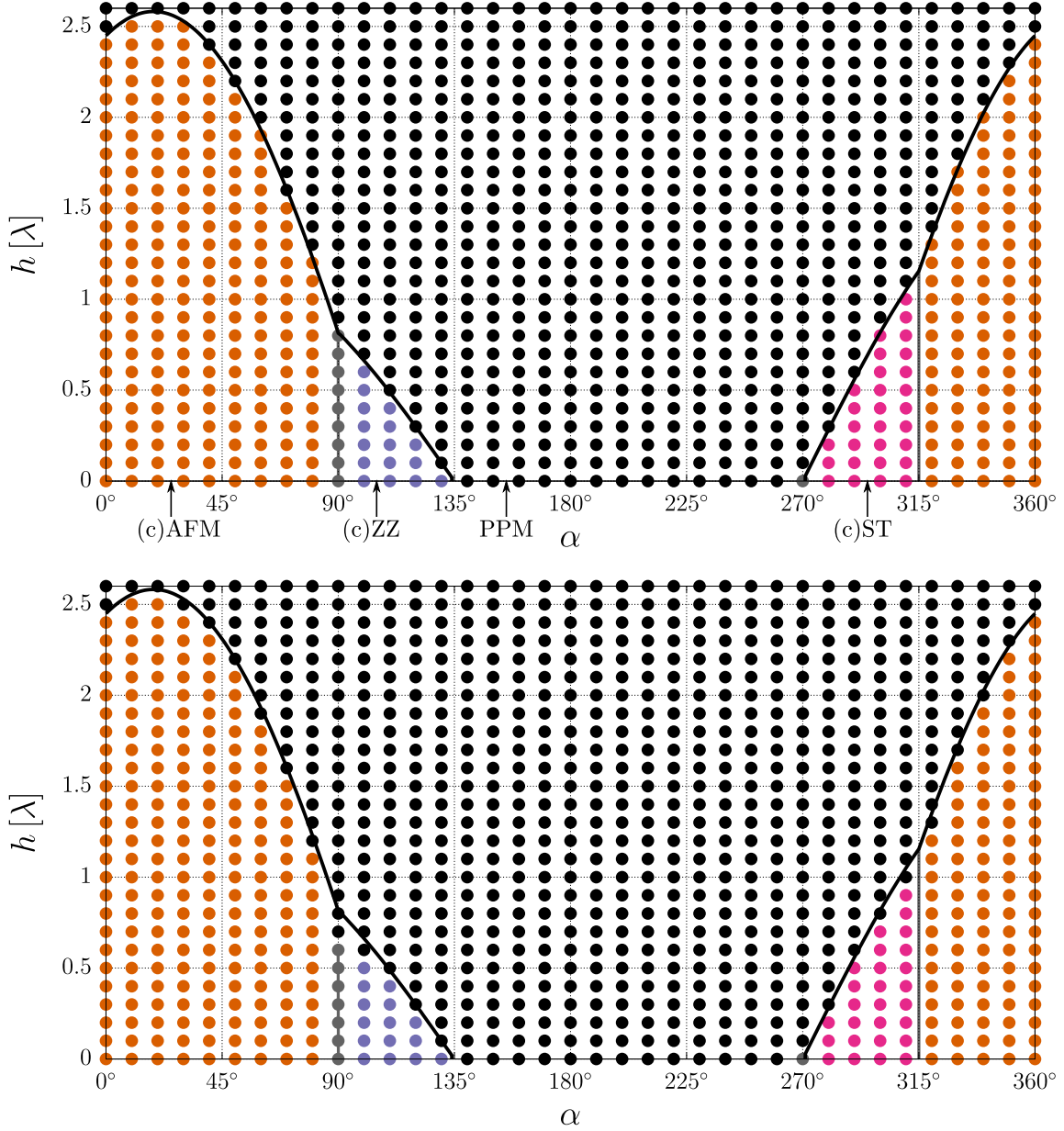


Figure 3.23. Phase diagram for the triplon model in dependence of the Kitaev-Heisenberg parameter α ($A = 1$) for fixed spin-length $1/2$ (effectively $\lambda = 0$ limit) and the semiclassical ansatz with variable spin-length (bottom): Observables can be found in figures 3.24 and 3.25 and the magnetic field is limited to the excitonic contribution. The black line represents the spin-wave calculations for spin-length $1/2$, which the top figure is in perfect agreement with. As the variable spin-length $\sqrt{\rho(1-\rho)}$ is only fixed to $1/2$ at $A \rightarrow \infty$ in the model with variable spin-length, it is unsurprising that there are slight corrections compared to the spin-wave solution. Overall, the top diagram is analogous to the classical Monte-Carlo simulation in reference [165], which is where detailed descriptions of the phases can be found. Consequently, we adopt the label of a canted (c) magnetic phase. The lattice size is $N = 144$.

spin-length. Indeed the Hamiltonian with the semiclassical ansatz (cf. equation (2.29)) is

$$\begin{aligned} \langle H \rangle = & \lambda \sum_i \rho_i + \sum_c \sum_{\langle i,j \rangle} 4\sqrt{\rho_i(1-\rho_i)}\sqrt{\rho_j(1-\rho_j)}(J\mathbf{v}_i\mathbf{v}_j + Kv_{i,z}v_{j,z}) \\ & + 2\sqrt{6}h \sum_i \sqrt{\rho_i(1-\rho_i)}\hat{\mathbf{h}}\mathbf{v}_i. \end{aligned} \quad (3.19)$$

For fixed $\rho = 1/2$, one recovers a classical Hamiltonian with a magnetic field that is $\sqrt{6}$ times stronger than in the regular spin parametrization [165] and a constant energy shift $\lambda/2$. Therefore, one may use the spin-wave solution of reference [165], which is based on the large magnetic field limit and a Holstein-Primakoff transformation where the spin quantization axis is parallel to \mathbf{h} :

$$\mathbf{e}_1 = \frac{(\mathbf{e}_z \times \mathbf{h}) \times \mathbf{h}}{|(\mathbf{e}_z \times \mathbf{h}) \times \mathbf{h}|}, \quad \mathbf{e}_2 = \frac{\mathbf{e}_z \times \mathbf{h}}{|\mathbf{e}_z \times \mathbf{h}|}, \quad \mathbf{e}_3 = \frac{\mathbf{h}}{h}, \quad (3.20)$$

$$\mathbf{v}_{s,i} = (v - b_{s,i}^\dagger b_{s,i})\mathbf{e}_3 + \sqrt{\frac{v}{2}}(b_{s,i} + b_{s,i}^\dagger)\mathbf{e}_1 + i\sqrt{\frac{v}{2}}(b_{s,i} - b_{s,i}^\dagger)\mathbf{e}_2, \quad (3.21)$$

where the s index labels the two sublattices of the honeycomb lattice and $b^{(\dagger)}$ is a regular boson creation/annihilation operator and v is the spin-length. We calculate and draw the critical points in the phase diagrams. A lengthy analyzes regarding the critical points and resulting magnetic phases can be found in reference [165]. Solutions are obtained analogous to the flavor-wave calculation in this thesis.

From these considerations, it is also obvious what the effect of the spin-length could be. Naturally, the spin-orbit coupling λ is not a constant energy shift anymore. Yet, at $h = 0$ it effectively sets a spin-length $\sqrt{\rho(1-\rho)}$ depending on α and A ($J = A \cos(\alpha)$ and $K = A \sin(\alpha)$). It does not care about any direction or nature of the magnetic order of the bosons, just their length. If $\rho = 0$, i.e. A is below the critical condensation point, we will almost certainly obtain the polarized

paramagnet in the entire parameter space of h and α due to the previous discussion about driving the BEC with a magnetic field. If one is in a condensed phase, λ fixes $\sqrt{\rho(1-\rho)}$ to an A and α dependent value smaller than $1/2$. Yet, due to the root-shaped form of the increase of condensate density ρ and resulting $\sqrt{\rho(1-\rho)}$ (cf. figure 3.19 and 3.6), one expects to be decently close to $\sqrt{\rho(1-\rho)} = 1/2$ relatively quickly. Consequently, the only thing ρ is naively expected to change here is that the effective h and A values of spin-wave theory have slightly different values. Instead of $A_{\text{eff}} = 4A\sqrt{\rho_i(1-\rho_i)}\sqrt{\rho_j(1-\rho_j)} = A$ for $\rho = 1/2$ and accordingly $h_{\text{eff}} = 2\sqrt{6}h\sqrt{\rho_i(1-\rho_i)} = \sqrt{6}h$, a starting point of $\rho = 0.4$ would result in $A_{\text{eff}} \approx 0.96A$ and $h_{\text{eff}} \approx 0.98\sqrt{6}h$, i.e. even a relatively large change in condensate density might lead to a minute change in effective classical spin interactions.

The resulting semiclassical Monte-Carlo phase diagrams for a scenario with fixed $\rho = 1/2$ and one with the normal variable ρ can be found in figure 3.23. Observables for both simulations can be found in figures 3.24 and 3.25. As expected, the scenario with fixed spin-length reproduces the spin-wave solution exactly. For the variable spin one finds small deviations where the polarized paramagnet is more prominent (A_{eff} decreases quicker than h_{eff}). The most noticeable change is in the area of the AFM Kitaev phase (only because the FM vanishes instantly anyways), because ρ is very significantly smaller in that area (see observables). Additionally, the behavior of the observables is just as expected from classical simulations when further considering that the excitonic magnetic field will slowly push the condensate density toward $1/2$ by trying to maximize its strength and energy gain via the factor $\sqrt{\rho(1-\rho)}$ in the Hamiltonian. The trivial trends of some observables should be noted for subsequent discussions.

Of course, a decrease in A (as long as it still remains in the condensed phase) will result in a more pronounced deviation from the $\rho = 1/2$ spin-wave solution and a more prominent polarized paramagnet in the phase diagram. These changes, however, can be estimated via the spin-wave theory by either fixing v or introducing

3. Analysis of the Triplon Honeycomb Model

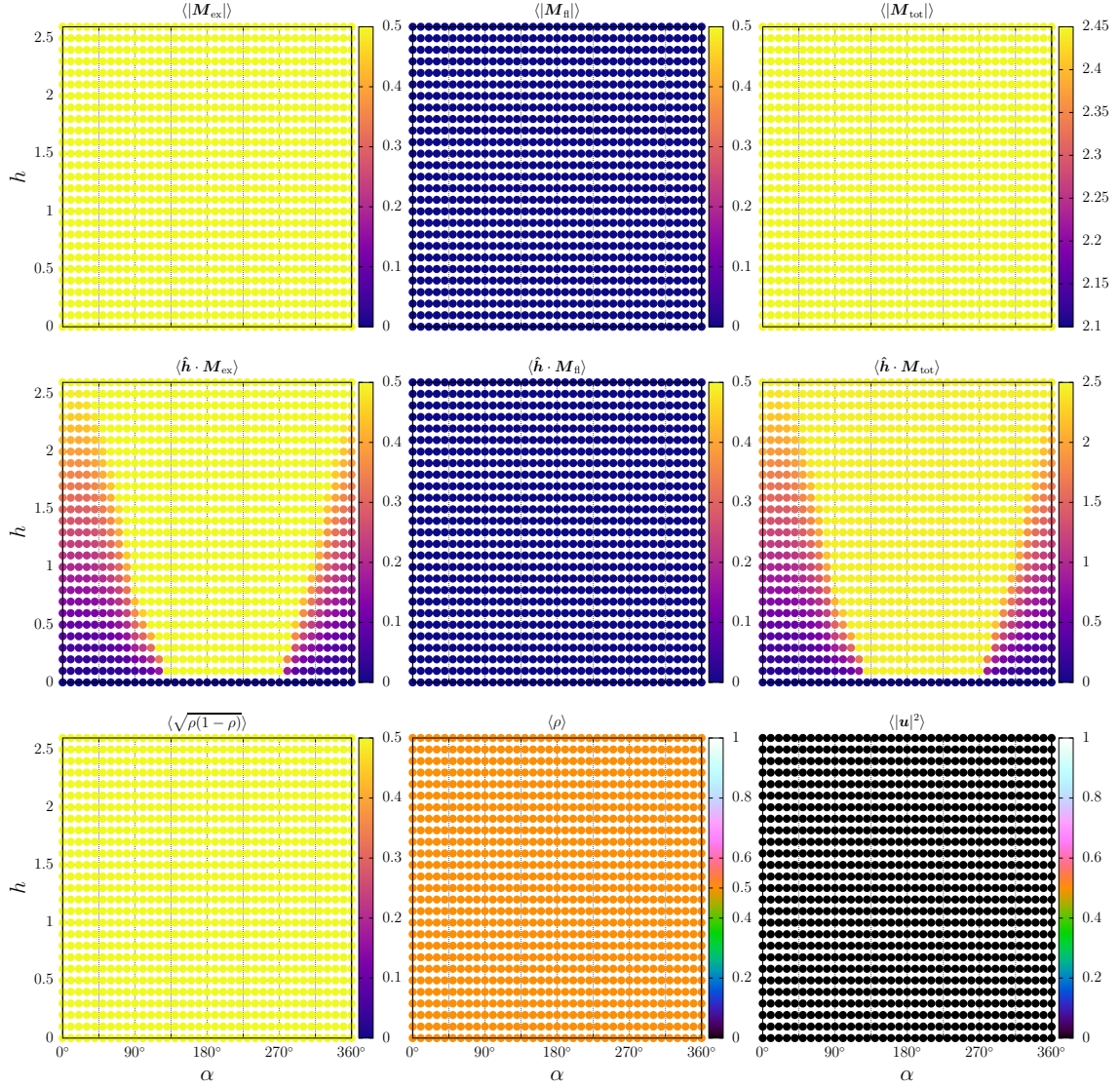


Figure 3.24. Observables for the triplon model in dependence of the Kitaev-Heisenberg parameter α ($A = 1$) for fixed spin-length $1/2$ (effectively $\lambda = 0$ limit): The connected phase diagram can be found in figure 3.23 (top). Most observables show trivial trends (sometimes enforced) and serve mainly as a comparison to subsequent analogous figures. Here \hat{h} is the magnetic field unit vector (strength h). The remaining parameters are explained in the text.

A_{eff} and h_{eff} . This decrease in stability of the magnetic phase continuously connects to the critical condensation point, where $\rho = 0$ and the paramagnet emerge.

One should note, that all magnetic phases are established at length in [165] and

3.2. Triplons in a Magnetic Field

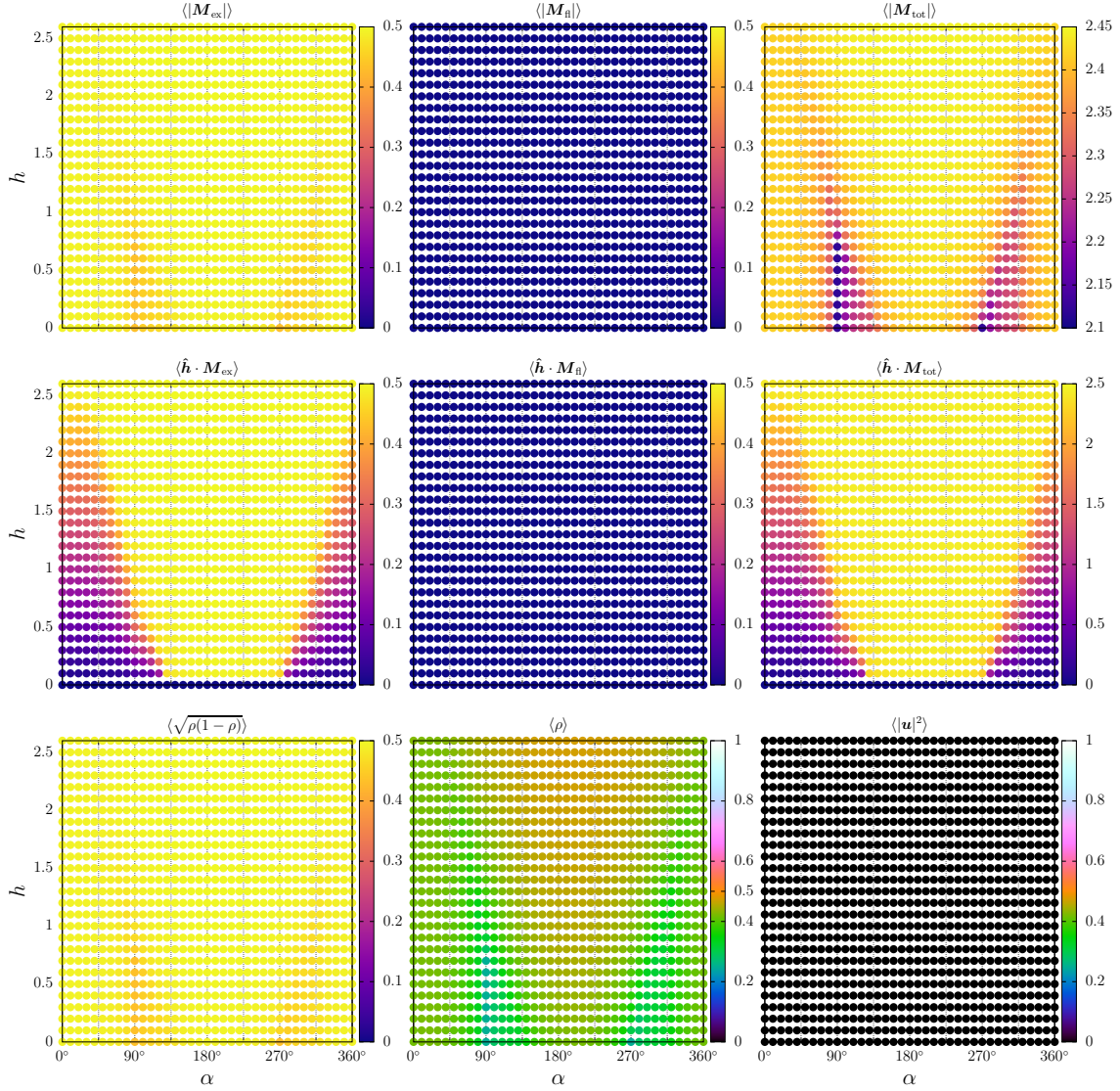


Figure 3.25. Observables for the triplon model in dependence of the Kitaev-Heisenberg parameter α ($A = 1$) for variable spin-length: The connected phase diagram can be found in figure 3.23 (bottom). The main difference to the fixed spin-length (regular spin) model is impact of the $h = 0$ spin-length best visualized by $\langle \rho \rangle$. Moreover, some interactions like the Kitaev limit seem to keep this quantity relatively fixed. The phases with reduced spin-length are the ones with the most noticeable changes compared to the spin-length $1/2$ spin-wave solution, which is obviously expected. All in all, the spin-length $1/2$ guess seems to be a decent estimate. The parameters are explained in the text.

[41]. Therefore, they will not be discussed here. Nevertheless, the canting in the magnetic field does not involve the \mathbf{u} degree of freedom (yet) and is different from the one induced by the higher-order terms. It consists solely of a continuous tilt towards the magnetic field direction with increasing strength of h .

In summary, the condensed phases of the excitonic Kitaev-Heisenberg model in a magnetic field work extremely similar to a regular spin, with the excitonic term of the magnetic field entering the equation in the same form as sole spin coupling to the magnetic field. This is surprising when considering that the previous section is based on the difference between spin-orbital- and spin-dimers. Yet, it is obvious when considering the triplet or triplon in isolation being akin to a normal spin-1 Hilbert space. The uncondensed phase is expected to remain a paramagnet, which prevails as a clear difference to normal spins.

There are two more aspects of our model we should analyze. First of all, there is the influence of the flavor-changing magnetization. Secondly, the influence of the higher-order terms need to be discussed. For this, we first consider the $K = 0$ AFM Heisenberg case in isolation. Observables calculated via semiclassical Monte-Carlo can be found in figure 3.26. The flavor-changing magnetization, which translates to $\rho(\mathbf{u} \times \mathbf{v})$ in the semiclassical ansatz, facilitates a small orthogonal \mathbf{u} component as seen in figure 3.27. Still, the impact of the \mathbf{u} terms in the Hamiltonian remains minute. Nevertheless, the flavor-changing magnetic field contribution leads to a small increase in the surviveability of the magnetic phase, which is logical due to the term trying to decrease the singlet-triplet gap a bit. Also, the scaling with ρ means that \mathbf{M}_f pushes the condensate density and thus also $\rho(1 - \rho)$ towards the $\rho = 1/2$ maximum and thus towards the spin-length $1/2$ spin-wave solution. In other words, we lose slightly less stability as a result of not starting with $\rho = 1/2$. Combined, this explains the tiny but noticeable discrepancy. Because the impact is the same for $\alpha \neq 0$ and almost not noticeable on the overarching scale, we do not present a new phase diagram.

3.2. Triplons in a Magnetic Field

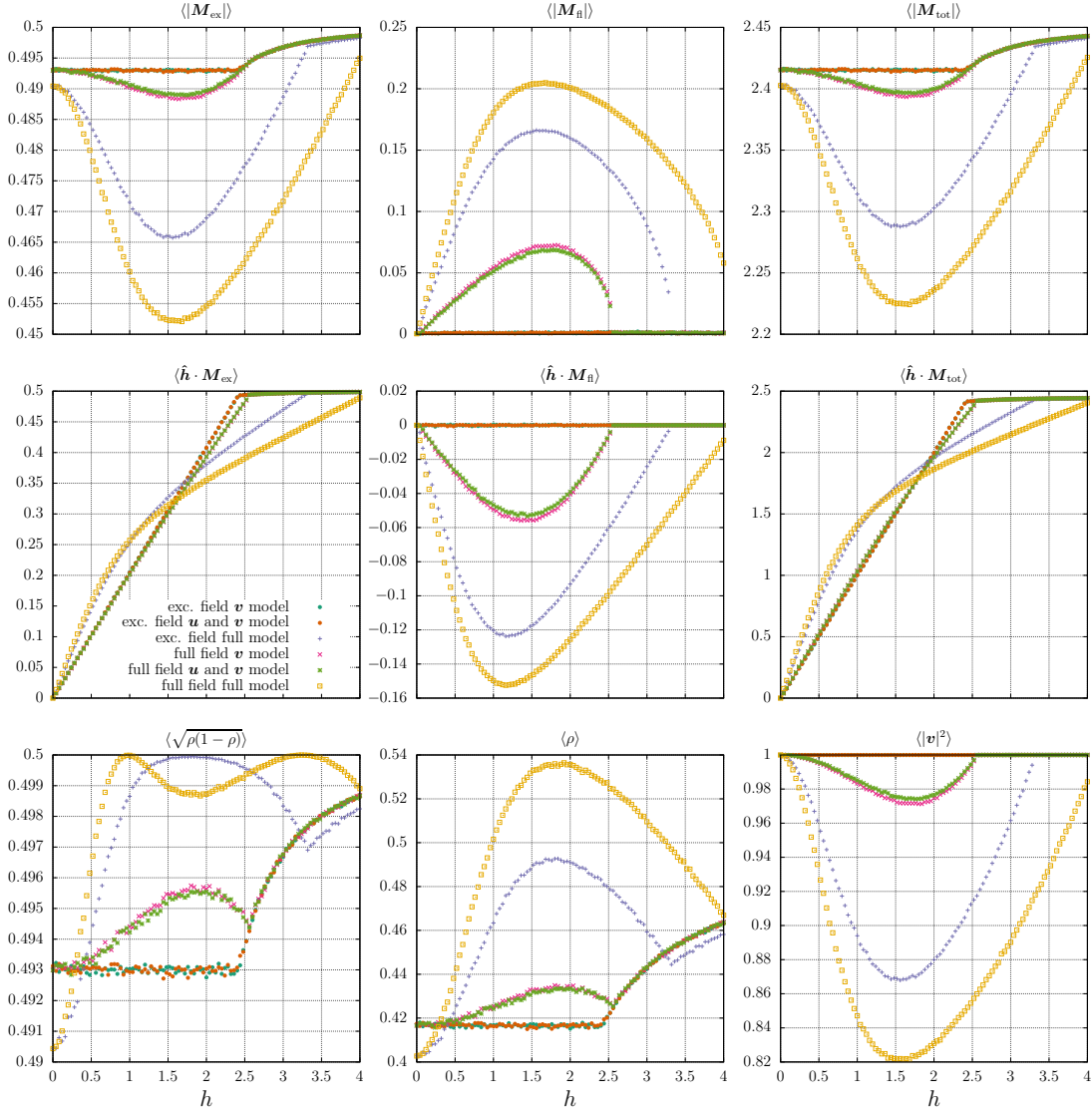


Figure 3.26. Semiclassical Monte-Carlo observables for different models with only the excitonic (exc. field) magnetic field contribution and the full dipole moment including the flavor-changing terms (full field): The label “ v model” denotes the pure v boson Kitaev-Heisenberg Hamiltonian. Furthermore, “ u and v ” includes the quadrupole terms and the full model also includes the h_3 and h_4 terms. The sole inclusion of higher-order terms and addition of flavor-changing field seem to have noticeably shared features. All simulations represent the $\alpha = 0$ AFM Heisenberg phase with $A = 1$.

3. Analysis of the Triplon Honeycomb Model

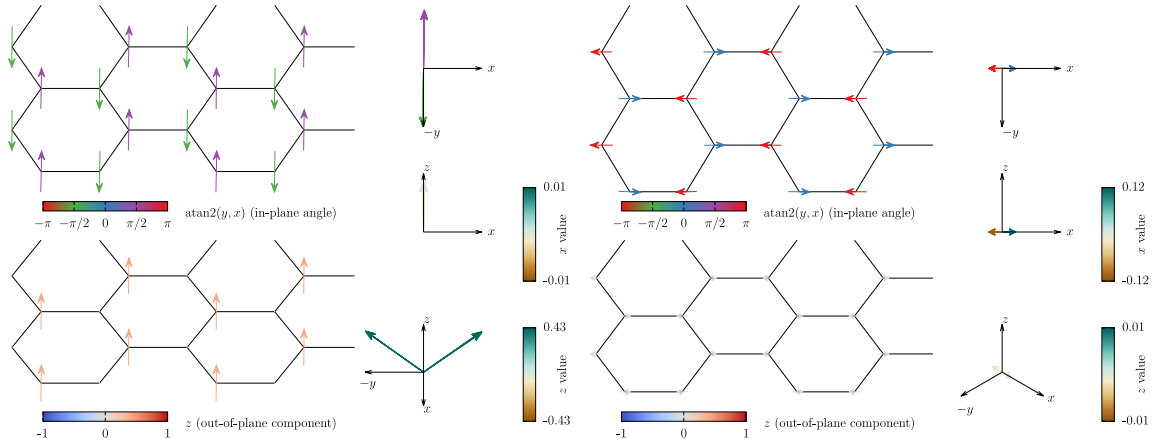


Figure 3.27. Order of both the \mathbf{v} bosons (left) and \mathbf{u} bosons (right) in the canted AFM phase: The color schemes and views are described in previous figures. The \mathbf{v} order is known from the regular spin Kitaev-Heisenberg model in the magnetic field. Its canting angle increases linear with the magnetic field strength. Due to the flavor-changing $\mathbf{u} \times \mathbf{v}$ contribution, there is orthogonal dipole moment and consequently \mathbf{u} order enforced by the \mathbf{v} bosons. Aside from details like the relative magnitude of \mathbf{u} and the variable canting angle, this phase is identical with the one found in figure 3.15.

We now turn to the higher-order terms. Again, we first discuss the case of a purely excitonic magnetic field contribution. Naively, the previously discussed bias of the h_3 and h_4 terms to the ferromagnetic regime might lead one to expect that the only phase that might gain prominence is the polarized paramagnet, maybe except for the (canted) zigzag phase which also profits from the inclusion. Yet, the data in figure 3.26 shows two surprising things: First of all, the AFM phase is a lot more resistant to the magnetic field than expected. Secondly, the higher-order terms in the $\alpha = 0$ case seem to work very analogously to the flavor-changing magnetic field contribution. The h_3 and h_4 terms create the same kind of $\mathbf{u} \times \mathbf{v}$ contribution mainly orthogonal to the magnetic field direction. In fact, they do so at a noticeably bigger scale.

Thankfully, the explanation of this phenomenon seems to be quite straightforward when recalling the impact of the higher-order terms themselves. In the preceding analysis of the higher-order terms, we tried to figure out the impact of the h_3 and

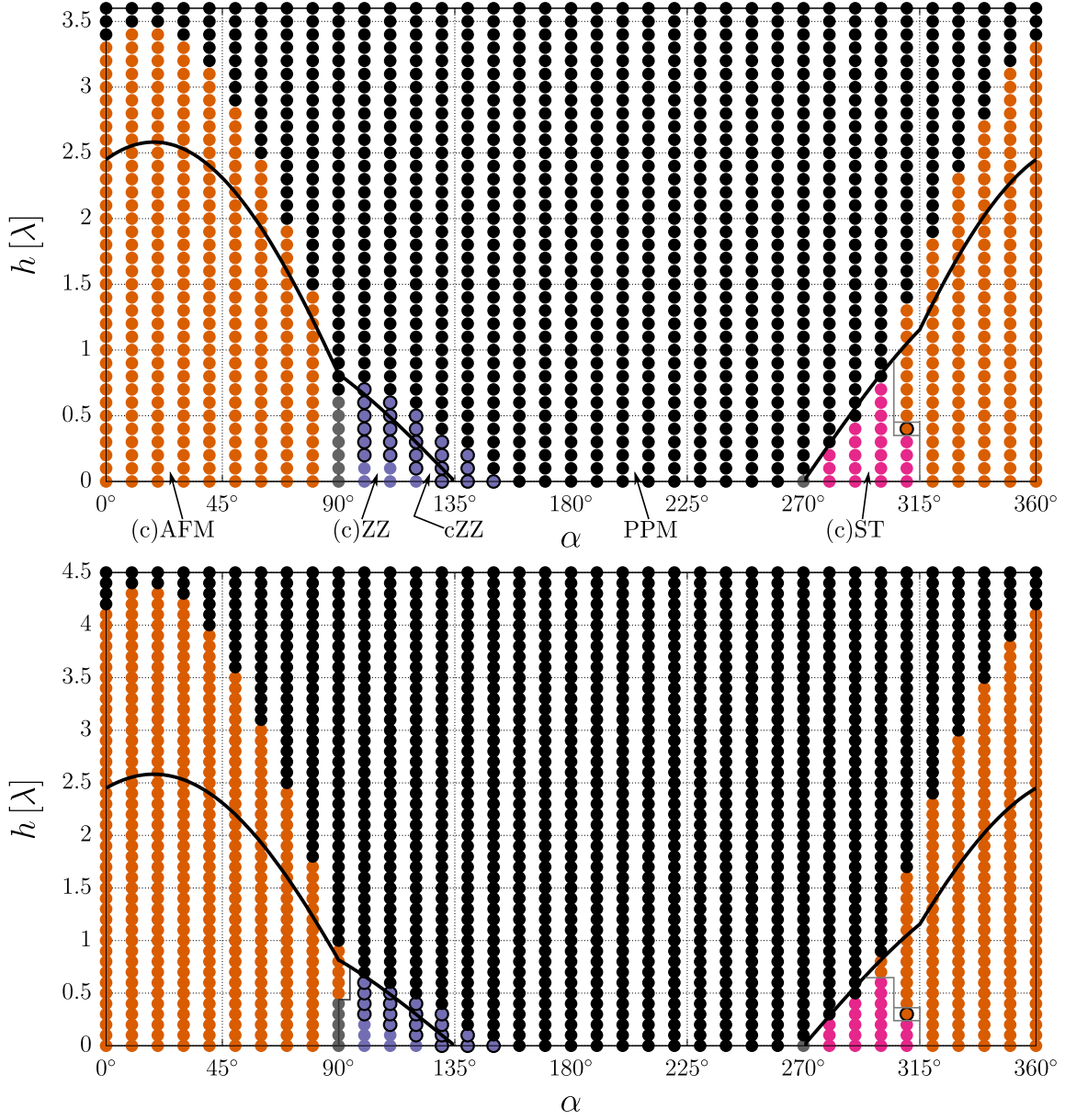


Figure 3.28. Phase diagram for the triplon model in dependence of the Kitaev-Heisenberg parameter α ($A = 1$) including h_3 and h_4 terms with only the excitonic magnetic field (top) and the full magnetic field (bottom): Observables can be found in figures 3.29 and 3.30. The black line represents the spin-wave calculations for spin-length 1/2. Compared to the h_2 based model, the most significant change is the extend of the canted antiferromagnetic field phase, which further gain prominence by reintroducing the flavor-changing magnetic field contribution, which tries to enforce the same kind of spin-canting and thus supports the (c)AFM regime. All in all, a material in the AFM regime is expected to show a fundamentally different behavior compared to a normal spin, while the remaining areas (aside from the cZZ canted zigzag regime, which is, however, hard to discern from the magnetic field canted one (c)ZZ) remain relatively similar. The lattice size is $N = 144$.

3. Analysis of the Triplon Honeycomb Model

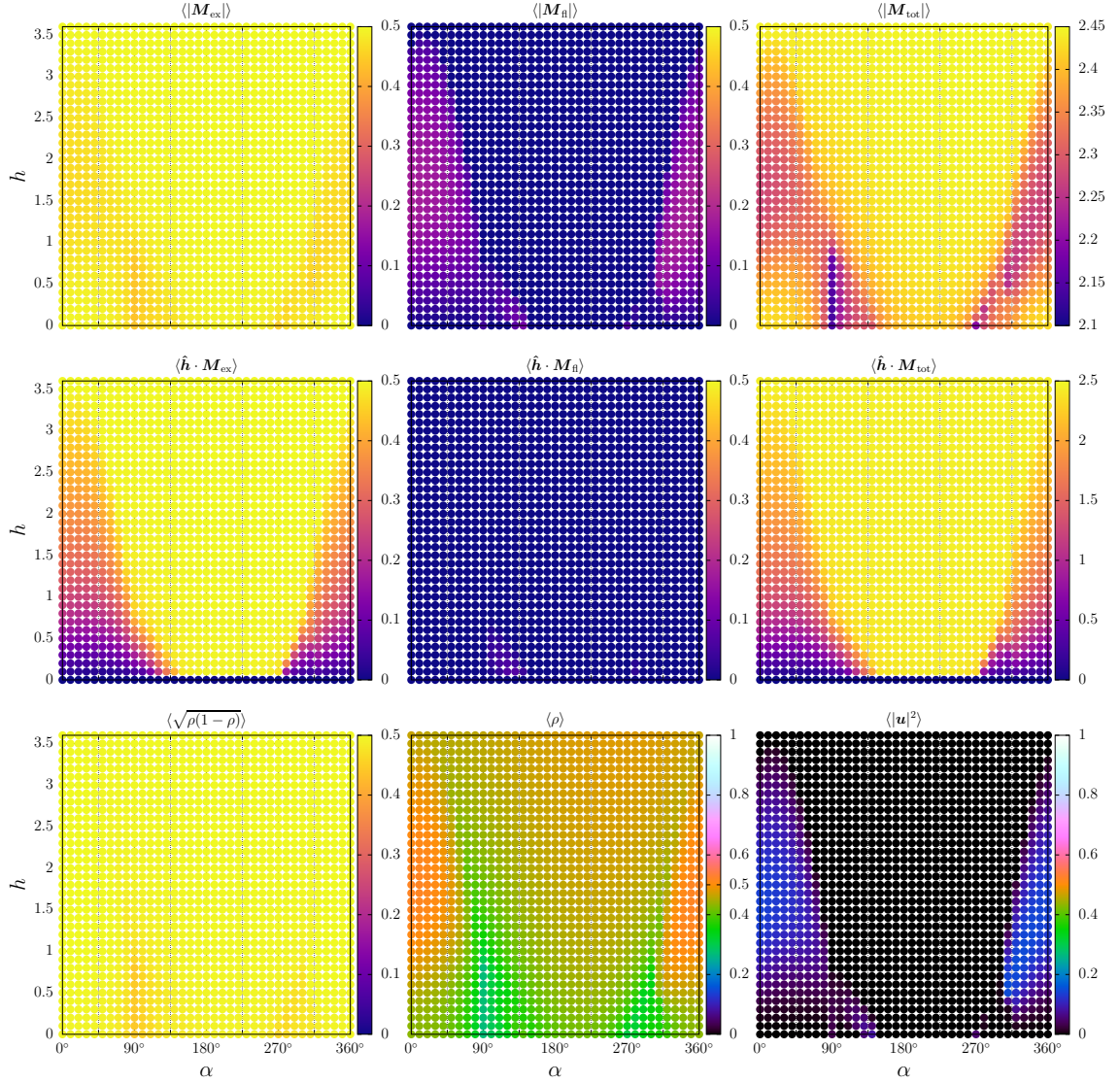


Figure 3.29. Observables for the phase diagram in figure 3.28 (top): There are noticeable \mathbf{u} , which increase with the magnetic field in some areas. Mainly the canted AFM seems to profit. Note that the flavor-changing contribution is perpendicular to the magnetic field, except for a tiny area where the h_3 - h_4 canted magnetic field has a small out of plane component.

h_4 as their own entity, i.e. the magnetic orders created in the absence of h_2 terms. Recall the magnetic order in figure 3.15, which is established by the higher-order terms at $\alpha = 0$ and $A = 1$. This looks like a canted antiferromagnet in a magnetic

3.2. Triplons in a Magnetic Field

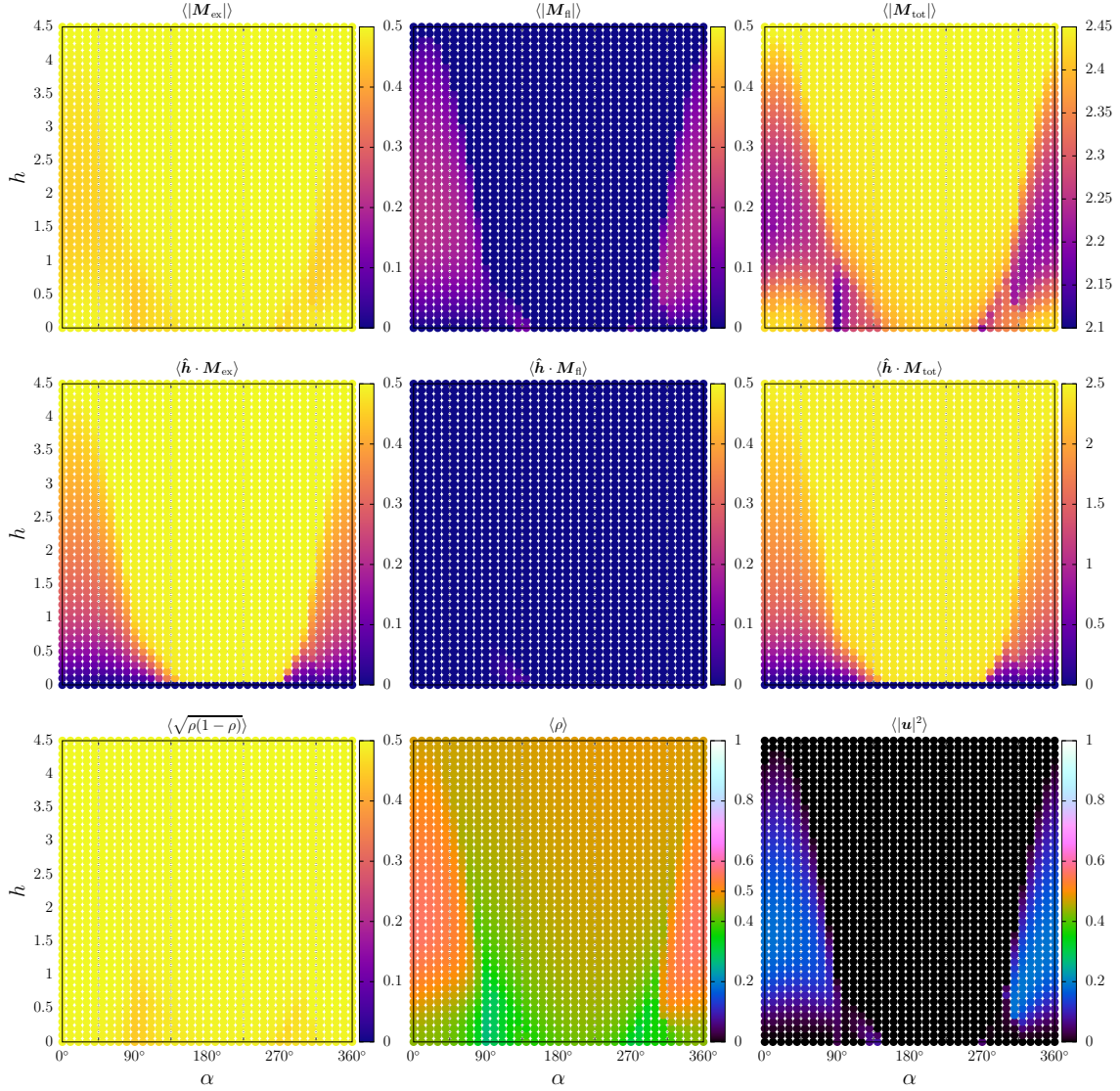


Figure 3.30. Observables for the phase diagram in figure 3.28 (bottom): Compared to the case without the flavor-changing magnetic field contribution in figure 3.29, the \mathbf{u} contributions (note $|\mathbf{v}|^2 = 1 - |\mathbf{u}|^2$) and condensate density ρ in the canted AFM phase are significantly more prominent.

field, with the differences that the \mathbf{u} bosons are significantly larger than they would be for the rather small $\mathbf{u} \times \mathbf{v}$ flavor-changing terms and the fact that the phase has a more or less fixed (changes minutely) canting angle, which is very roughly 40° measured from the z axis. All in all, this phase and the magnetic field cooperate.

3. Analysis of the Triplon Honeycomb Model

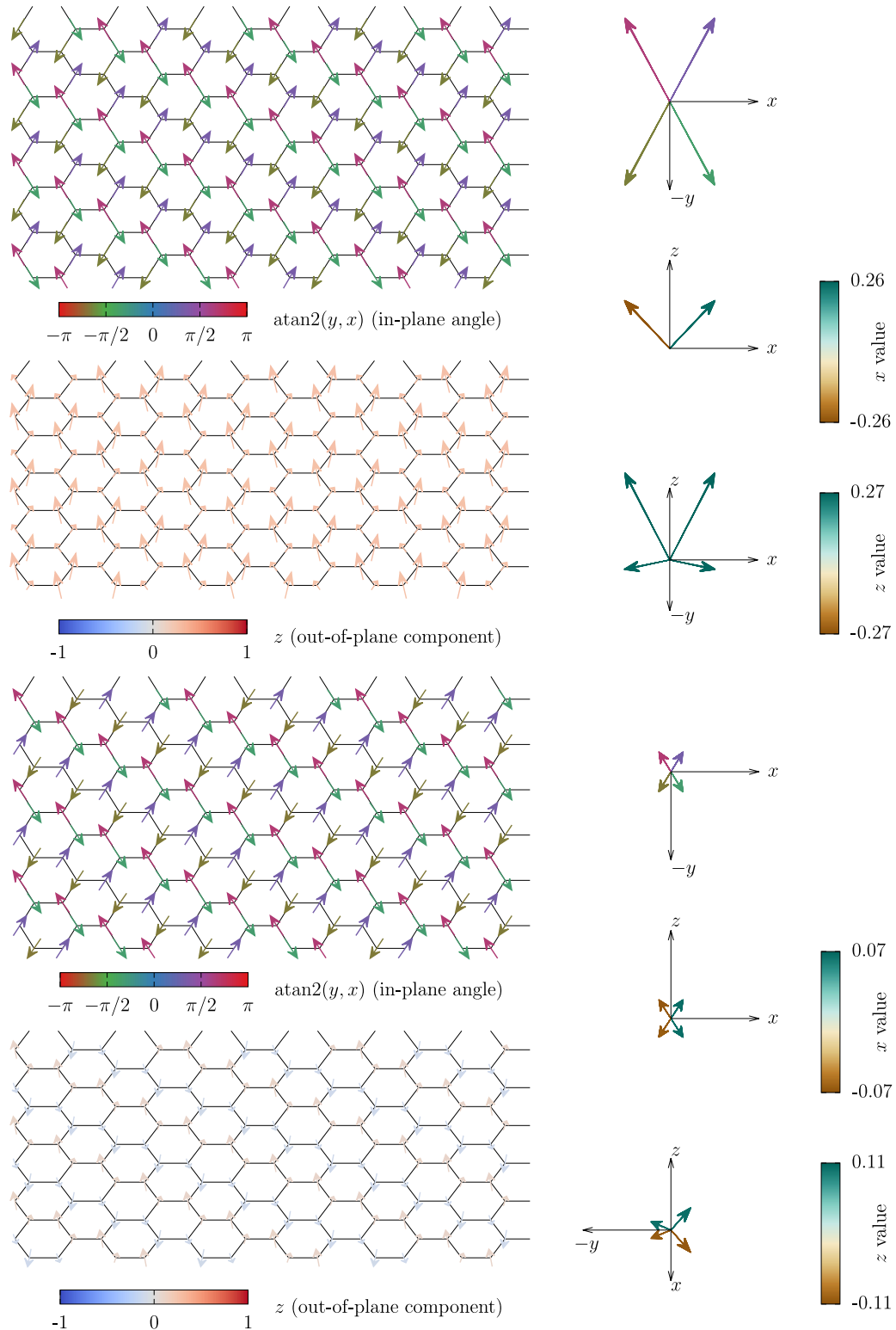


Figure 3.31. Order of both the \mathbf{v} bosons (top) and \mathbf{u} bosons (bottom) for the new intermediate phase between canted stripy and canted AFM for active higher-order terms: The color schemes and views are described in previous figures.

Consequently, allowing the flavor-changing magnetic field term supports this trend and leads to a further significant increase in the stability of the AFM phase. The position of the \mathbf{u} bosons orthogonal to the \mathbf{v} dipoles is in perfect agreement between both terms. This would not be the case for the canted zigzag phase produced by the higher-order terms in vicinity of $\alpha = 135^\circ$. Also, as the flavor-changing term forces a \mathbf{u} order based on $\mathbf{u} \times \mathbf{v}$, the pattern of the quadrupoles themselves found for the canted zigzag cZZ phase is at odds with this and rather expected to be incompatible.

Finally, we turn to the phase diagrams (figure 3.28) and observables (figures 3.29 and 3.30) established by semiclassical Monte-Carlo simulations of the full model with an excitonic and full magnetic field respectively. Most of the trends seem straightforward to interpret based on the preceding points. The main differences for the excitonic field is the existence of the canted zigzag cZZ ($h = 0$) phase, which can be discerned from the regular canting by the \mathbf{u} contribution. As it promotes at least a kind of canting, it is unsurprising that it wins out compared to the regular magnetic field canted zigzag order (c)ZZ. Increase, or for the stripy regime decrease, of ρ based on the higher-order terms can further help or harm compared to the $\rho = 1/2$ spin-wave scale. The main difference, however, is the prominence of the AFM phase explained by the cooperation with h_3 and h_4 . A clearly visible aspect visualizing the impact of the higher-order terms is the nontriviality of the observable $|\mathbf{u}|^2$. The areas of cZZ and (c)AFM are distinct. Moreover, the triplon density ρ serves as a potential signal.

We also note the appearance of an intermediate phase between the canted AFM and canted stripy phases for a small (in our simulation single data point) area of the phase diagram. Figure 3.31 shows this new intermediate magnetic order. As the canted AFM also more or less represents the order established solely by the h_3 and h_4 terms, it is reasonable that something very akin to other higher-order exclusive magnetic orders can appear close to a phase transition. It also could motivate further more detailed studies about the fate of the $\alpha = 315^\circ$ transition in the magnetic field.

Yet, we remain focused on the overarching trends.

Adding the flavor-changing magnetic term further promotes the AFM phase and noticeably the density ρ in the impacted areas. Furthermore, the canted zigzag phase decreases in prominence, likely due to the aforementioned disagreement about the order of the \mathbf{u} bosons. All in all, the most important point seems to be, like in the $h = 0$ phase diagram, that cooperation with the higher-order terms, if possible, can significantly alter the phase diagram. Areas where the orders disagree seem to be more or less easy to understand in a more traditional spin picture.

All in all, the overarching trends in the phase diagram seem to be expected when first considering what the h_3 and h_4 terms themselves strive for and subsequently analyzing if anything of the h_2 orders may be similar. Cooperation, either with the canted AFM or the admixture of zigzag and FM characteristics in the cZZ regime, seems to be where noticeable influence of the higher-order terms can drastically change the situation.

Concluding, we want to add two comments. First of all, the detailed study of the $\mathbf{h} = [1, 1, 1]^T$ phase diagram, which even for normal spins is extremely complicated [165], is beyond the scope of this thesis. Nevertheless, we have looked into this subject a bit. That the \mathbf{v} boson model in the excitonic magnetic field necessarily reproduces the basic aspects of the normal spin model is evident by the semiclassical ansatz providing the equivalent formulation and the spin-wave theory, even when adding the variable spin-length either via v or effective A and h , being usable. Yet, it is also clear that flavor-changing magnetic field and higher-order terms lead to changes. As our model has 3 times the amount of variational parameters and calculations may need to be done multiple times to account for the different schemes of interactions and magnetic field, this task is highly time consuming and nontrivial due to the large lattice sizes necessary to cover all possible complicated orders found for regular spins. Secondly, the Monte-Carlo simulations for the phase diagrams with higher-order contributions were done with the “shifted” scheme, i.e. the elimination of

energy shifts and strain terms via hard-core constraint. We have since rechecked essential parts of the result without this assumption and found only tiny quantitative disagreements (as expected by strain terms). Hence, this needs to only be kept in mind when aiming for exact numerical reproduction of our results.

3.2.3 Triplon Liquid and Magnetic Field

As established in the introductory part of this section, the phase in the Kitaev limit, which has been dubbed triplon liquid [5] or just correlated paramagnet [157], is worth a closer look when it comes to its evolution in the magnetic field. The many sources mentioned in the introduction of this section imply a lot of potentially interesting investigations being possible. For example, one might look at the impact of different magnetic field directions, nature of the transition or even the excitations, which could be different for the singlet-triplet model. Yet, the studies are nontrivial and were extremely new at the point in time when we ourselves looked into the magnetic field impact. Our model having to deal with higher-order terms being potentially relevant, two distinct magnetic field terms as well as potentially much more noticeable finite size effects due to the smaller cluster size (the singlet-triplet Hilbert space is significantly larger than that of a spin-1/2 or spin-1 model), drastically increases the amount of effort necessary for each analysis. As such, a full investigation into this topic seems to be unfeasible, at least in the context of this thesis. However, it should be mentioned that we attempted a few simulations not covered in here. For example, we also attempted the analysis shown in figures 3.37 to 3.39 in a $\mathbf{h} = [1, 1, 1]^T$ magnetic field without noticing a qualitative change. Moreover, we confirmed that an analysis akin to figure 3.32 with higher-order terms is plagued by finite size effects. Additionally, we always simulated in both the normal and “shifted” regime to find out whether there is a difference.

So what do we strive to do here? We focus on one of the major results for regular

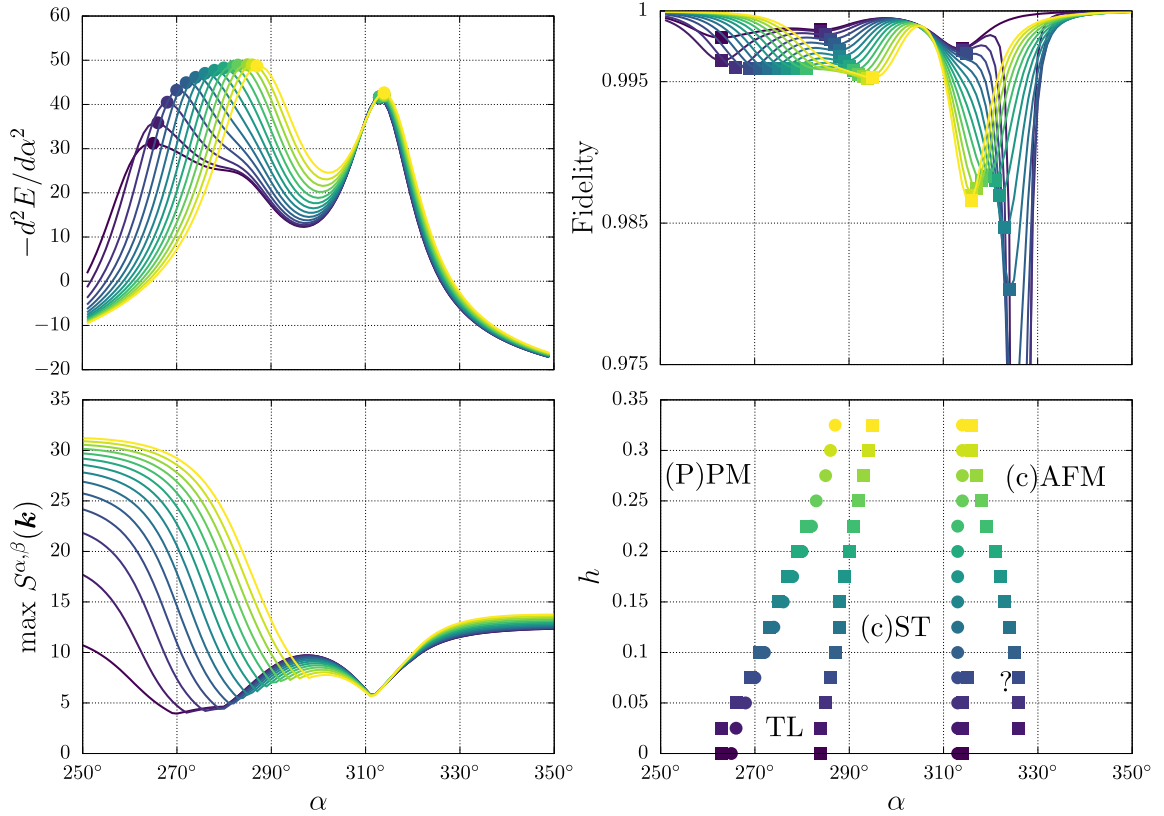


Figure 3.32. Exact diagonalization results for a $N = 12$ lattice with Kitaev-Heisenberg parameters $A = 1$ and angles in vicinity of $\alpha = 270^\circ$ (FM Kitaev phase): The phase diagram in the bottom right is established via minimal values of fidelity F (squares), maximal derivatives of the ground state energy E (circles) and spin-structure factor S (magnetic phase label corresponding position of maximal value in Brillouin zone). The color scheme correspond to the values magnetic field strength h . At exactly $\alpha = 270^\circ$ the Kitaev phase vanishes quickly. Its survival to other angles might be interesting to investigate for normal spin. The rightmost phase border is seemingly a finite size effect, as the spin-structure factor does not change its significant contribution and overall behavior.

spins. A shared feature between spin-1/2 and spin-1 model seems to be the existence of a novel intermediate spin-liquid phase, which is located between Kitaev regime and fully-polarized paramagnet in the AFM case. In essence, we try to find out if anything peculiar happens when we destroy the Kitaev phase. This feature has been established via ED simulations, so the potential observables are clear. In order to keep the discussion focused on this essential question, we neglect the higher-order

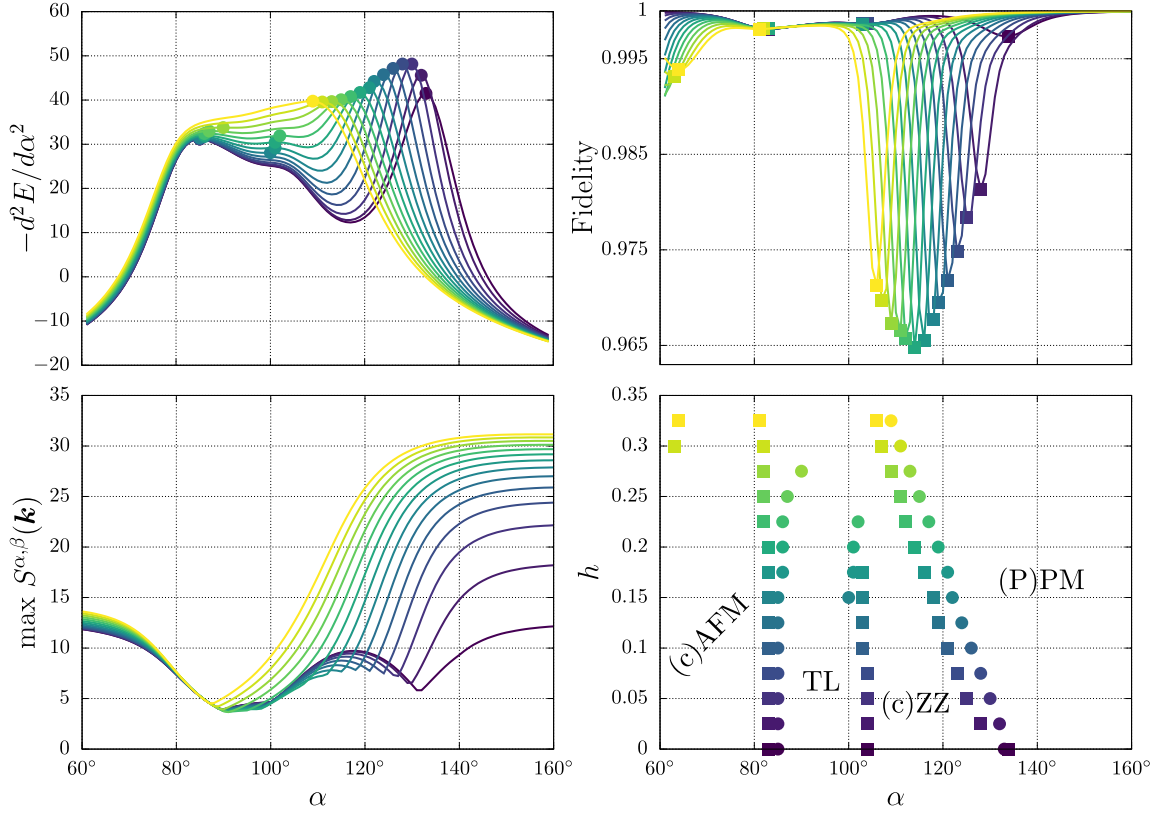


Figure 3.33. Exact diagonalization results for a $N = 12$ lattice with Kitaev-Heisenberg parameters $A = 1$ and angles in vicinity of $\alpha = 90^\circ$ (AFM Kitaev phase): The phase diagram in the bottom right is established via extremal values of fidelity F (squares), derivatives of the ground state energy E (circles) and spin-structure factor S (position of maximal value in Brillouin zone). The color scheme correspond to the values magnetic field strength h . In contrast to the FM Kitaev phase, the AFM regime seems to be rather stable, which is in accordance to regular spin Kitaev phases.

terms unless otherwise mentioned. The Hamiltonian consists of the full h_2 setup and full magnetic field, although the \mathbf{u} bosons and flavor-changing term are found to not impact the central result of this analysis, as will be shown later.

Figure 3.32 contains ED results for various sweeps of the parameter α in the vicinity of the FM Kitaev phase. When staying in the pure Kitaev limit $\alpha = 270^\circ$, the FM Kitaev phase is polarized quickly. The apparent persistence to other angles might be worth an investigation, but not in the scope of this thesis. Canted stripy, AFM

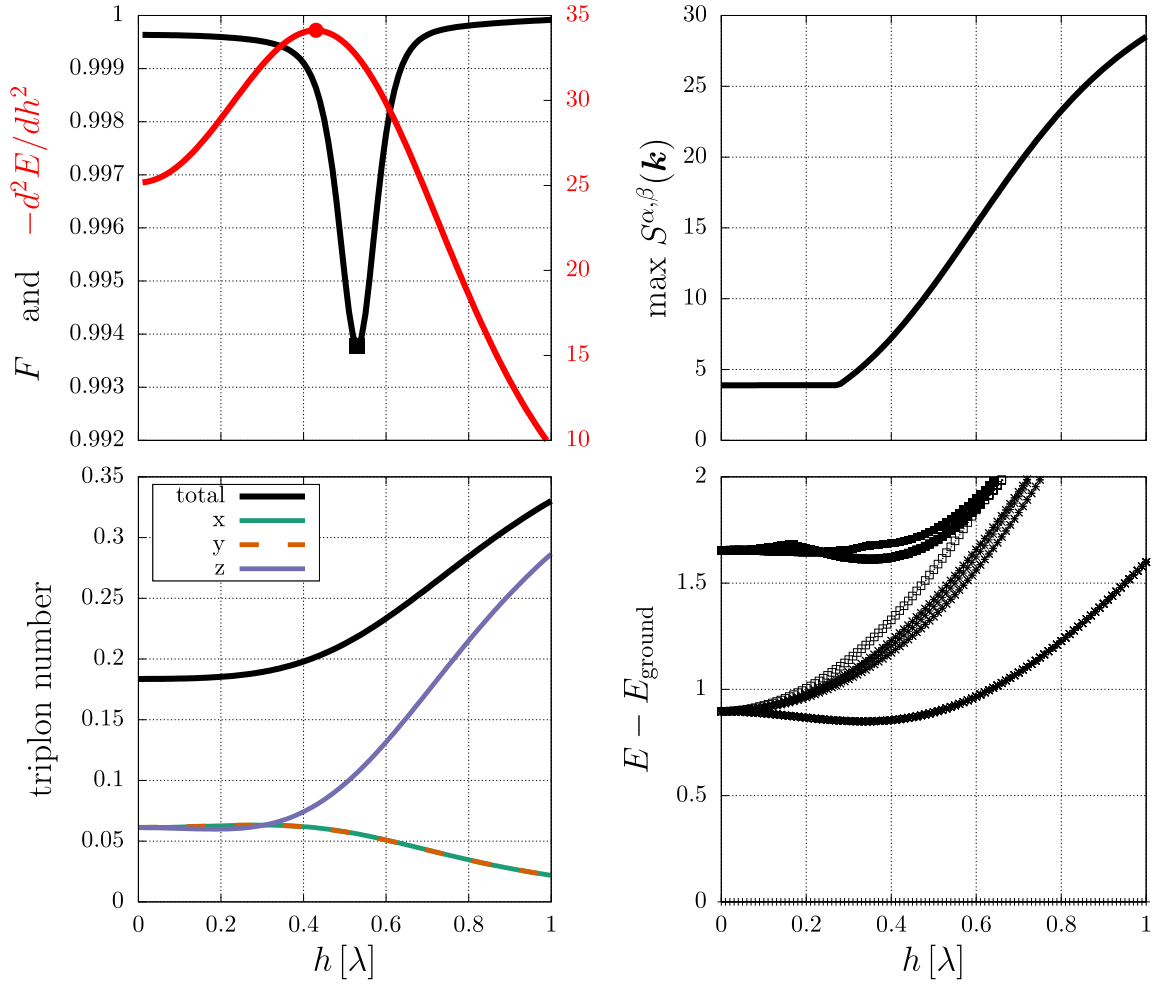


Figure 3.34. $N = 12$ ED data for the ν boson model AFM Kitaev phase with purely the excitonic magnetic field contribution: Even though the equivalence to normal spin models is as perfect as it can feasibly be, there are no signs of an intermediate liquid phase. In fact: There is just the correlated paramagnet where the boson numbers stay equivalent and the spin-structure factor maximum is ambivalent and flat.

and polarized paramagnet phases are showing trends expected from the semiclassical simulations and can be identified clearly by the Brillouin zone location and behavior of the maximal spin-structure factor. Yet, the fidelity feature labeled with a question mark in the phase diagram is unexpected. In fact, no other observable seems to show any change in behavior. Moreover, the fidelity maximum changes drastically and subsequently moves back toward the expected transition point. As no higher-order

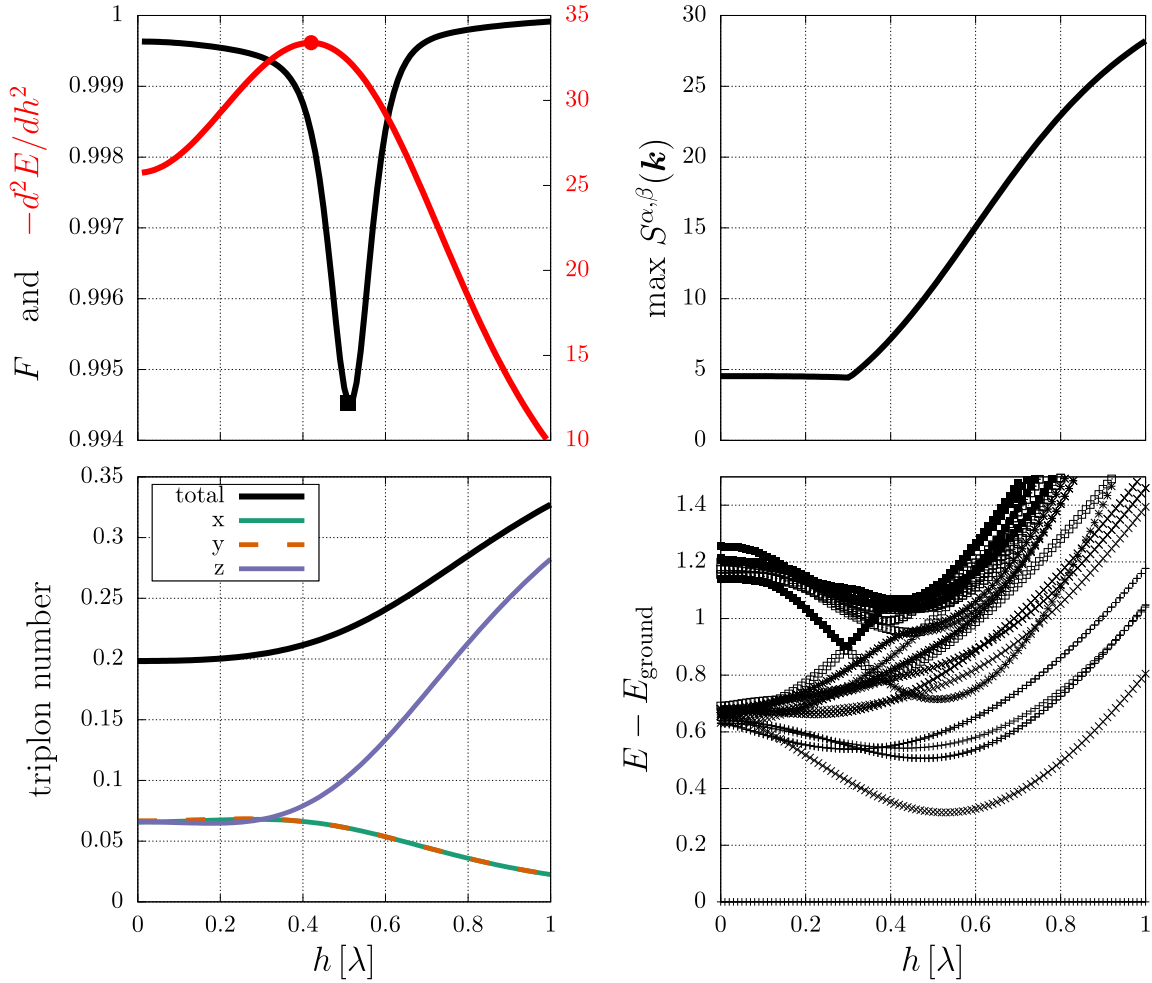


Figure 3.35. $N = 12$ ED data for the full boson model, including h_3 - h_4 terms, AFM Kitaev phase with purely the excitonic magnetic field contribution: There is no drastic change in regards to possible phase transitions and spin-gap compared to the regular \mathbf{v} boson model.

terms are active, a finite new phase in this area is not predicted by other means, e.g. the semiclassical Monte-Carlo results. Consequently, we propose that this feature is merely a finite size effect. As noted previously, a proper look into the finite size scaling is not practical in our setup due to the Hilbert space dimension scaling.

Additionally, figure 3.33 contains the analogous plot for the AFM Kitaev regime. The Kitaev phase is implied to be noticeably more stable, although the sweeps in α direction are, of course, not able to guarantee this by themselves. Otherwise,

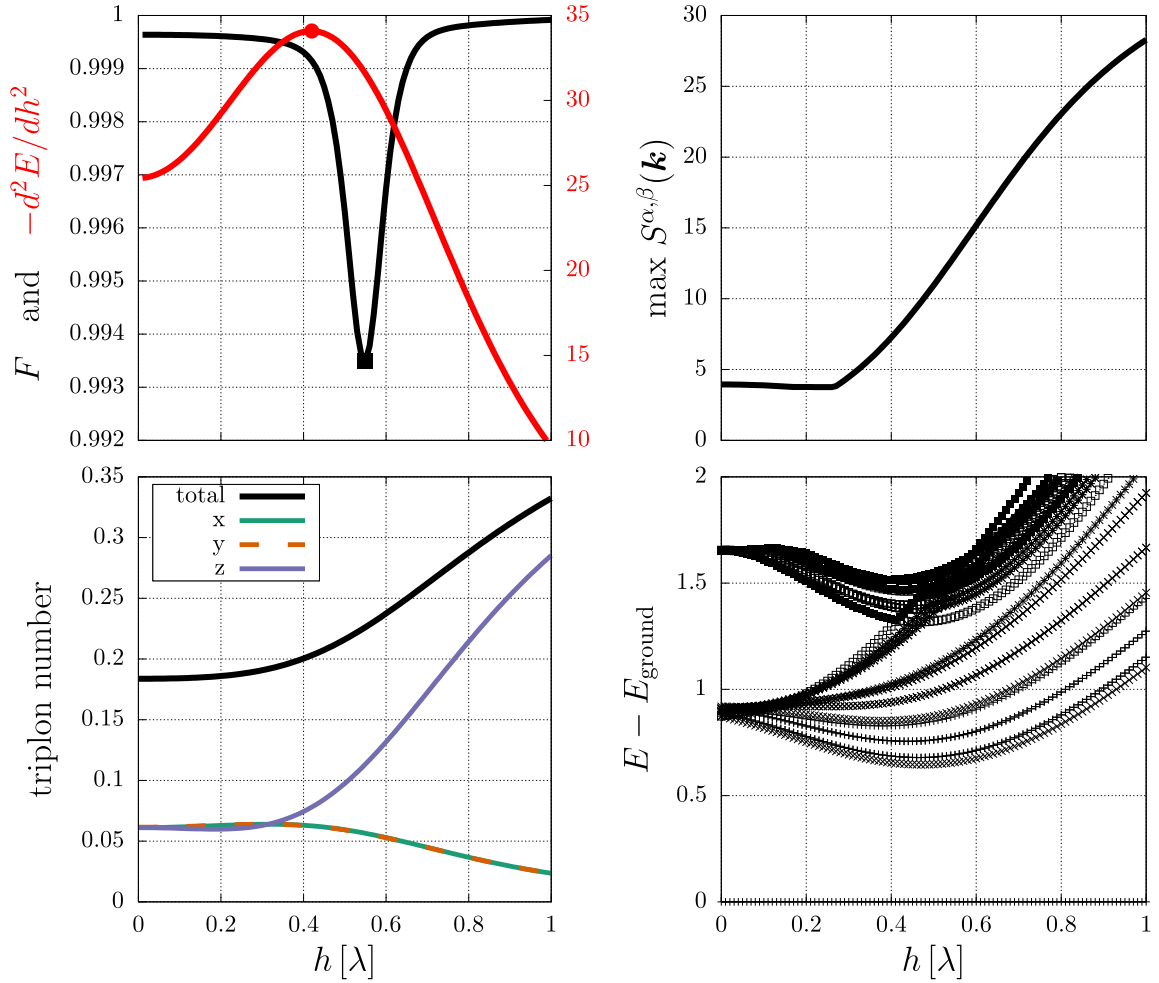


Figure 3.36. $N = 12$ ED data for the full h_2 (\mathbf{u} and \mathbf{v}) boson model AFM Kitaev phase with purely the both magnetic field contributions: The qualitative behavior is analogous to the \mathbf{v} and excitonic magnetic field model.

the overall shape of the phases seems to agree with the semiclassical Monte-Carlo simulations. One may note at this point, that the symmetry of the AFM and FM Kitaev phases regarding their extend in the α parameter range does not survive the magnetic field.

We move to parameter sweeps in direction of the magnetic field strength. Having found no signs of the intermediate liquid phase yet, we first look at the model consisting only of the \mathbf{v} bosons and the excitonic magnetic field contribution. The resulting ED data are shown in figure 3.34. In both the spin-1 and spin-1/2 models,

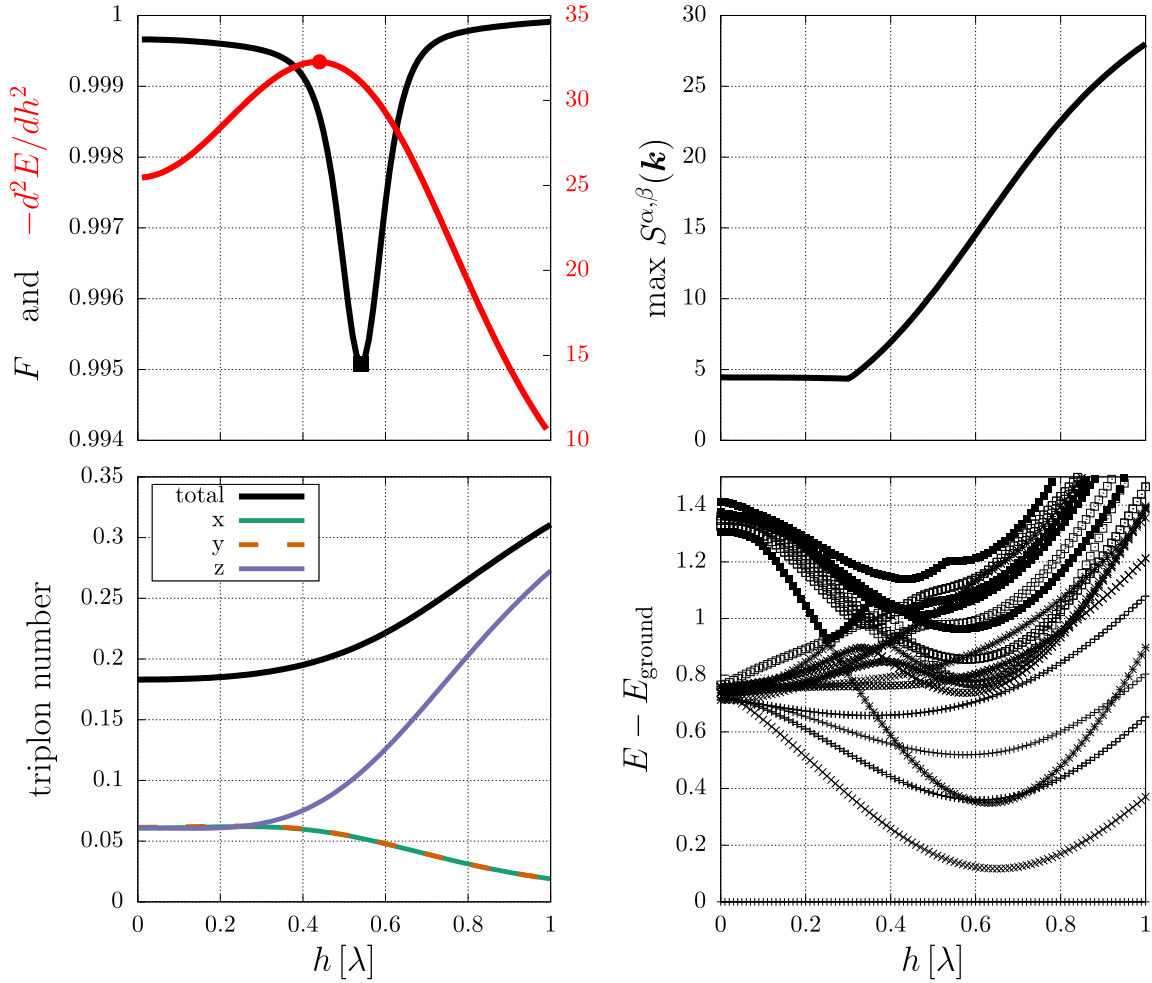


Figure 3.37. $N = 12$ ED data for the full boson model, including h_3 - h_4 terms, in AFM Kitaev phase with both magnetic field contributions: There is no drastic change compared to the purely excitonic model. One may notice the reduced spin-gap. However, the lowest excited energy emerges from the single-boson sector, has the same preferred \mathbf{k} momentum value as the ground state and is therefore likely a finite size effect if it ever starts to come close to the ground state.

the energy derivative reliably signals the transition in and out of the intermediate phase [67, 205]. Yet, we seemingly find only one phase transition in all observables. There seems to be a finite region of stability where the Kitaev interaction keeps the triplon number of each flavor equal. Contemporary with the phase transition the boson in magnetic field direction separates. The spin-structure factor switches from the \mathbf{k} ambivalent small maximum to a clear maximum at the Γ point in the first

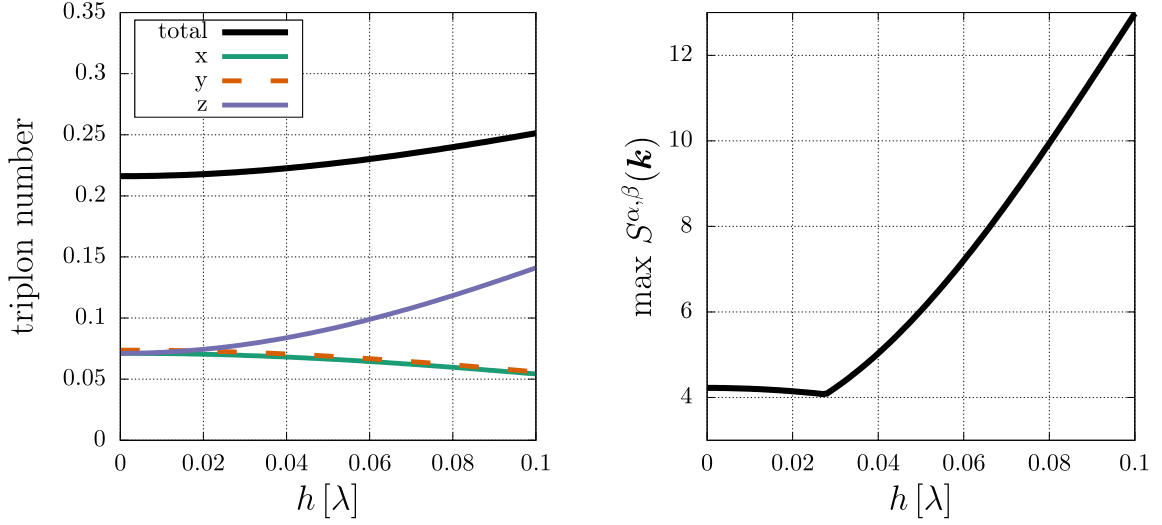


Figure 3.38. Full triplon model including h_3 - h_4 and both contributions of the magnetic field for the FM Kitaev limit: As expected from normal spins, the FM has no intermediate liquid regime and vanished roughly an order of magnitude earlier than its AFM counterpart.

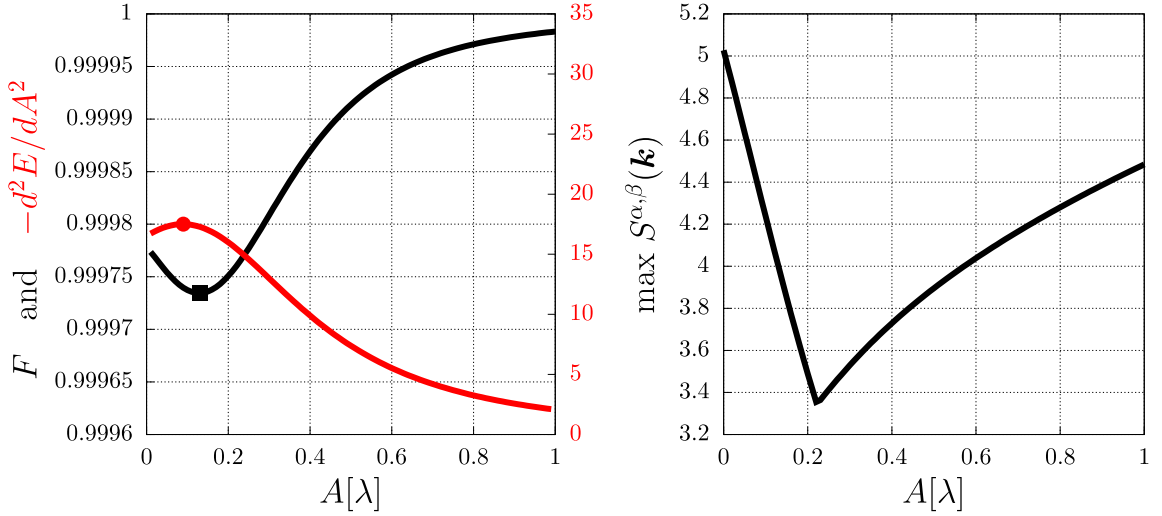


Figure 3.39. Full triplon model including h_3 - h_4 and both contributions of the magnetic field for the AFM Kitaev limit: The magnetic field is fixed to $h = 0.1$. Obviously, the phase transition indicated by fidelity and energy derivative happens to early to be connected to triplon condensation and is therefore likely a reflection of the classical Kitaev energy scale.

Brillouin zone, thus signaling the emergence of the polarized paramagnet. Another possible signal in past spin-1/2 and spin-1 is the energy spectrum. Due to finite

size, one is not always expected to see an approximate gap closing. Yet, there is not even an area where the excitations change behavior. As a result, there does not seem to be a signal for a possible intermediate phase. We have also looked at other observables like the overlap with the magnetic field eigenstate (only on-site terms in h and λ) and alternative spin-structure factors. As mentioned before, we also tried the $[1, 1, 1]^T$ magnetic field to cover possible direction dependence as predicted in the spin-1/2 model [205]. The result does seemingly not change.

Additionally, we provide the analogous sweeps for other iterations of the model. In figure 3.35 the higher-order terms are included as well. Figures 3.36 and 3.37 cover the case of the full magnetic field, i.e. excitonic and flavor-changing contributions, for the full h_2 model and again the inclusion of higher-order terms (here even without strain and shift terms). The only noticeable change between all scenarios happens in the excitation spectrum. However, the change is merely a single low-lying energy state that is relative close to the ground state. A closer look identifies this as a seemingly clear finite size effect. As mentioned before, even and odd boson number sectors should behave similarly in the thermodynamic limit, but can not do that on a finite cluster. If the sectors are disjoint, the vacuum is connected via pair creation and annihilation terms with the states containing two, four and other even numbers of bosons. The pair terms drive the boson condensation. The sector with one boson does the same for the odd numbered states. Hence, the odd “ground state” and even ground state are identical in behavior aside from finite size effects and a shift of λ . As we can clearly identify the low-lying state by its \mathbf{k} number and other observables as well as $h = 0$ starting point in the plots, we know that it is the same polarized paramagnet emerging from the odd subspace.

Before explaining the single phase transition, it is prudent to consider the FM Kitaev regime. Figure 3.38 shows that the FM Kitaev phase shows analogous trends but vanishes an order of magnitude earlier. This result is quite universal among the Kitaev models of any spin and usually interpreted as a reflection of the underlying

spin correlations being opposed or compatible with the field [205] and more or less expected from the classical and semiclassical simulations.

If this is the case, the phase transition might not reflect any condensed magnetic phase but rather a (classical) energy scale of the correlations in the paramagnet. In order to prove this, we consider the following: Figure 3.39 shows the ED data for a finite value of the magnetic field $h = 0.1\lambda$ polarizing the paramagnet. The observables imply a phase transition roughly where $A = h$, which takes place way before any condensation can feasibly happen. Switching roles leads to analogous results. Hence, this phase transition seems to reflect the trivial competition of the spin correlation energy scales.

This result of basically only seeing a correlated paramagnet is compatible with the recent QMC results in reference [157]. Consequently, it would be reasonable to expect this and interesting to see if a QMC simulation involving the magnetic field works out analogously. Even in the detailed analysis of the Kitaev phase in reference [170], the sign of the spin-orbit coupling had to be flipped in order to find anything else but the paramagnet. More efforts should be undertaken to find out how to characterize this Kitaev phase and see how to access it in simulations on finite clusters.

3.3 Triplons in a Trigonal Crystal Field

Similar to the magnetic field discussion, the impact of a (trigonal) crystal field distortion is connected to a few concrete questions. Here we try to focus on two of those. First of all, we revisit the general exploration of the field influence in direct analogy to the magnetic field. Namely, we want to find out whether driving the Bose-Einstein condensates via crystal field, i.e. pressure, is feasible and how the crystal field affects the magnetic phases. Regarding the condensation process, one should note that for normal spin-dimer systems like TlCuCl_3 , pressure can induce

the Bose-Einstein condensation (see, e.g., reference [218] for an early experiment, [72] for a theoretical description and [73, 75] for focus on excitations and nature of the phase transition). In fact, while the nature of the quantum critical point for pressure alone is described differently, namely via condensation of multiple flavors and driven by an overall pressure induced change in interaction (coupling and dimer energy gap) parameters, the resulting magnetic phase is the same as the one induced by the magnetic field, as implied by the $H - p$ (magnetic field strength and pressure) phase diagram in reference [72].

Regarding our model, this look at spin-dimers leads to a very peculiar dichotomy: On the one hand, the magnetic field has not been found to be a feasible way of inducing Bose-Einstein condensation of triplons. On the other hand, enhancing (tetragonal) crystal field distortion with or without the simplification onto a triplon model seems to be able to support magnetism in the related material Ca_2RuO_4 [20, 119, 134, 166]. Moreover, the impact of the crystal field distortion has been a major focus in this material due to the debate over the importance of spin-orbit coupling and crystal field interpretations of the on-site degrees of freedom [119]. Additionally, one should note that tetragonal and trigonal (like in the subsequently discussed $\text{Ag}_3\text{LiRu}_2\text{O}_6$ or related $\alpha\text{-RuCl}_3$) distortions should have roughly comparable influence as they can be made to be of similar form when changing the quantization axis [91]. Consequently, we should try to look into this dichotomy and find out whether the pressure can in fact induce Bose-Einstein condensation in the spin-orbital singlet-triplet model.

Here one may note that the orbital degree of freedom and the spin-orbit coupling enforcing the singlet-triplet gap may actually present a distinct advantage compared to regular spin-dimer systems. The crystal field (distortion) as described in section 1.1.7 enters via the orbital degree of freedom, i.e. the t_{2g} \mathbf{L} operator and hence directly as one of the “spin” species in our dimer. Additionally, the SOC could potentially be large enough to facilitate the inclusion of the crystal field as a projection

onto the singlet-triplet model itself. As a result, one is not restricted to the way reference [72] includes the distortion as an effective change of all coupling parameters.

Turning back to the concrete questions: The second focus in this section is motivated by a recent experiment analyzing the compound $\text{Ag}_3\text{LiRu}_2\text{O}_6$ under pressure. This also connects directly to the question whether or not the crystal field can be expected to drive triplon condensation. For $\text{Ag}_3\text{LiRu}_2\text{O}_6$, the experiment in reference [8] implies that the material might realize a $J = 0$ singlet state at ambient pressure. When the pressure is increased, corresponding to an approximately trigonal distortion, there seem to be two subsequent phase transitions to other nonmagnetic phases, i.e. no exciton condensation. The phase at very high pressures is attributed to a formation of molecular bonds like the one suggested for the parent compound Li_2RuO_3 [9, 10], which is claimed to be not unusual for this kind of compound. However, the emergence of the nonmagnetic intermediate phase is novel and the authors try to explain it via spin-orbital singlet-triplet calculations with a trigonal crystal field (in what we will later introduce as the “simple crystal field” scheme). Yet, the triplon model is a very rough back of the envelope estimate that serves more as a plausibility argument than a direct explanation. Here, we have the opportunity to find out if a more thorough analysis actually yields an explanation or if the effect requires another influence not in our model. As a result, the issue of the crystal field resulting in a different singlet phase instead of Bose-Einstein condensation based magnetism needs to be looked into.

For a more complete introduction to the discussion, we reiterate the arguments of reference [8] regarding the phase diagram established therein and explain the suggested connection to Li_2RuO_3 . Figure 3.40 shows sketches illustrating the points we make in the subsequent paragraphs. In reference [8], $\text{Ag}_3\text{LiRu}_2\text{O}_6$ is investigated under pressure. The compound itself is deemed a paramagnet (Van Vleck-type susceptibility) at ambient pressure and connected with the $J = 0$ singlet structure of our triplon model. When pressure is applied, two successive phase transitions are

identified. Both of these emerging phases are found to have a paramagnetic response, i.e. some kind of vanishing magnetic moment ground state (we will hence use the slightly simplistic label “nonmagnetic” to refer to this).

By keeping track of the structure, they argue that roughly trigonal distortion takes place and the bond lengths of the honeycombs in the material become anisotropic in the new phases. As there is a very significant shortening reminiscent of the structure in the parent compound Li_2RuO_3 in the high pressure phase, they connect this to the Ru-Ru molecular orbital (MO) dimer structure in this material (cf. [9, 10]), which they note as not unusual when considering similar effects in, e.g., $\alpha\text{-RuCl}_3$ [219]. This MO state also consists of a singlet, although of different origin (cf. sketch in figure 3.40).

The intermediate pressure phase consisting of a slightly less distorted structure is not expected based on $\alpha\text{-RuCl}_3$. Hence, it seems to present a novelty and raises the question about its origin. The authors of reference [8], while providing no definite description, argue for a stabilization due to admixture of triplets and base some of their argument on calculations (in the supplementary material) based on the triplon Kitaev-Heisenberg model that we analyzed in reference [5], which is also the center of attention for this thesis. There is a supporting argument for a ground state admixture $|ss\rangle + |TT\rangle$ on a bond. It would provide a Van Vleck response together with the anti-bonding states, which are shifted to higher energies and therefore explain the qualitative change in susceptibility. But beyond that no concrete proof is provided.

This leaves the door open for us to provide a more thorough analysis of the triplon Kitaev-Heisenberg problem in order to find out if anything hinting at the intermediate phase can be found in this scheme. One should note, that the intermediate phase might outright be of a different origin, as the $\alpha\text{-RuCl}_3$ discussion in reference [219] argues for a breakdown in spin-orbital physics (and Kitaev interaction). As a result, even the likely inability of the triplon model to establish the intermediate phase could provide an important hint about its origin. In a big picture sense, this

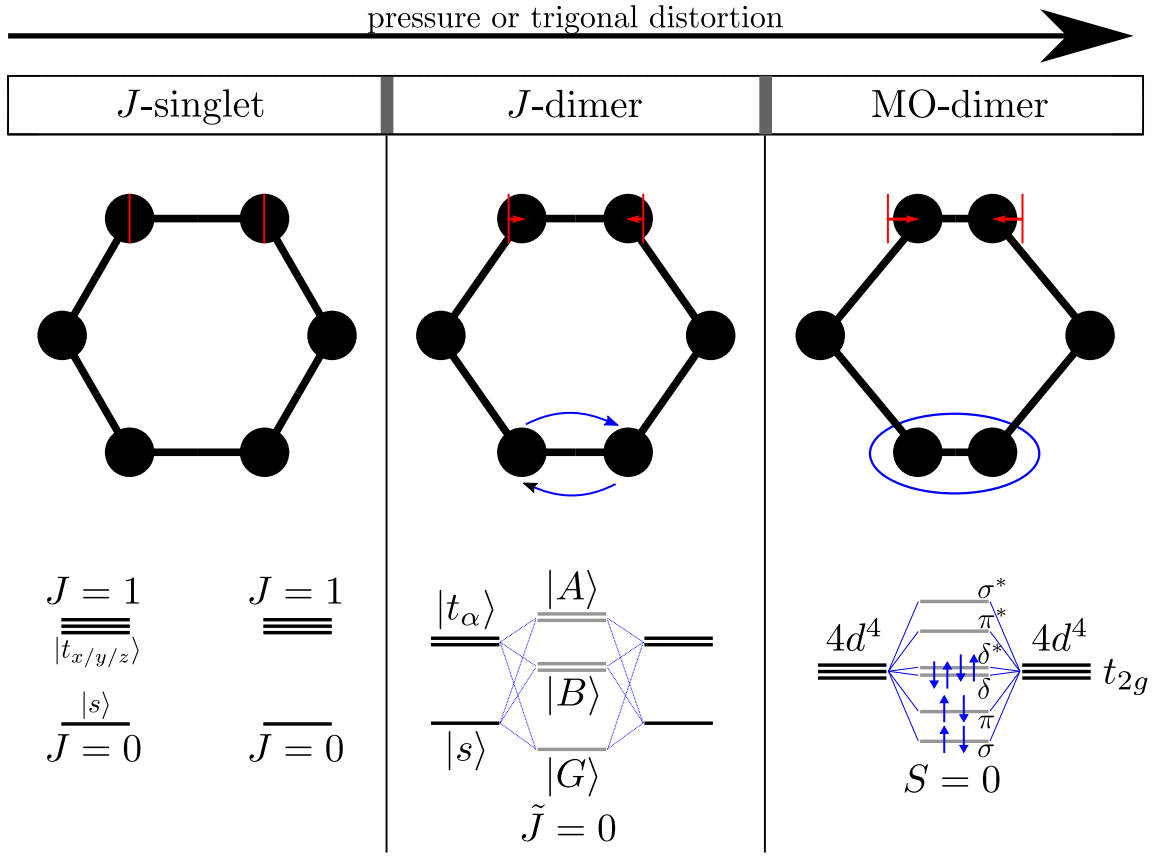


Figure 3.40. Cartoons of the experiment based interpretation of the phases of $\text{Ag}_3\text{LiRu}_2\text{O}_6$ under pressure in reference [8] (with the molecular orbital (MO) level structure adapted from reference [9]): All three regimes are found to have a magnetically trivial ground state. At ambient pressure (left), one may expect the spin-orbital singlet-triplet model with interactions that are too small to overcome the gap, thus enabling a singlet $|s\rangle$ ground state on each site individually. On the MO side of things, the full t_{2g} orbitals may combine fully to form molecular orbitals ($\sigma/\pi/\delta$) for a pair of sites. Trivially filling in the four electrons of each Ruthenium yields a total spin $S = 0$. In the intermediate state, an admixture of the two remaining triplets into the singlet ground state on a bond $|G\rangle$ is suggested. The excited states split into a bonding $|B\rangle$ and antibonding $|A\rangle$ state. The two successive phase transitions are connected to structural shortening of the corresponding bond length.

problem connects to the competition of covalent bonding (here in the sense of the MO) against magnetism in transition-metal compounds [220].

Before starting the modeling and analysis, we turn to a small side note about Li_2RuO_3 for completeness. When talking about the MO structure for Li_2RuO_3 , the

reference is made to the molecular Ru-Ru bond formation proposed in the early study in reference [9]. This suggestion was later underlined with band-structure calculations [10], although one should be aware that correlations and Mott picture may be important in this kind of problem in general [220]. However, there is also a strong coupling description proposal for the mechanism [221], which is based on a Kugel-Khomskii model without SOC but rather a phonon-induced collaborative Jahn-Teller process lifting the degeneracy. This model might be useful to keep in mind for future studies.

One may also note, that the physics in Li_2RuO_3 might be more complicated than the straightforward way described in the early references. Importantly, there seems to be a discrepancy between polycrystalline or powder based measurement where the nonmagnetic singlet is deemed to exist [222], and a single crystal based experiment suggesting a magnetic ground state in two distinct samples and connects this to the structural conditions [11]. This may hint at a competition between magnetic and nonmagnetic phases. Yet, there is some caveat as a later study with Na substitution seems to reproduce the polycrystalline results [223]. Finally, especially when proposing future looks into the issue, it might be useful to be aware that Li_2RuO_3 has been found to be anisotropic [224], deemed to possibly show valence bond liquid behavior even beyond the structural phase transition and that it is very sensitive to disorder and synthesis procedure.

As a concluding side note, we point out that the idea of creating a silver-intercalated counterpart, meaning $\text{Ag}_3\text{LiRu}_2\text{O}_6$ from Li_2RuO_3 , is also topical concept in the d^5 system, where $\text{Ag}_3\text{LiIr}_2\text{O}_6$ (inspired by Li_2IrO_3) has been put forward as a Kitaev material candidate [225] (although controversially [226, 227]). Similarly, $\text{H}_3\text{LiIr}_2\text{O}_6$ has been synthesized and studied [228, 229]. These very related discussions may be prudent to keep in mind for future studies.

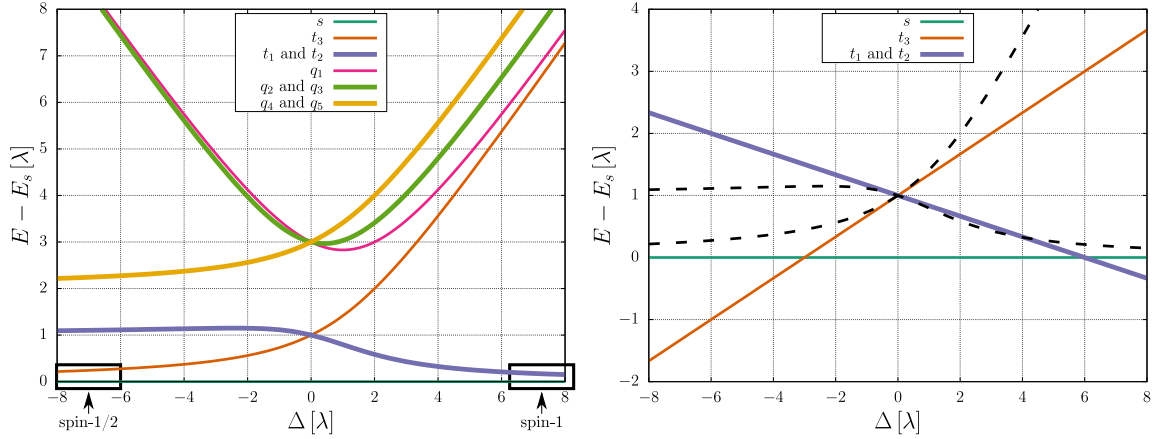


Figure 3.41. Single site energies as a function of the crystal field strength Δ for the spin-orbit coupling and trigonal crystal field Hamiltonians: The “full” scheme (left) represents the solution of both Hamiltonians on equal footing, which is appropriate for any values of both parameters. In contrast to this, the “simple” scheme (right) denotes a perturbation theory inclusion of the crystal field onto the spin-orbit coupling induced singlet s and triplet t_i states (quintet q_i is neglected), which is legitimate for comparatively weak crystal fields. Thicker lines represent double degenerate energy levels and the dashed lines in the simple diagram visualize the full scheme energies for comparison. The full model degeneracy at $\Delta \rightarrow \pm\infty$ can be used to motivate effective spin-1/2 and spin-1 models.

3.3.1 Strong and Weak Trigonal Field Regimes

Given the discussion surrounding equation (1.27), there are two obvious ways to include the (trigonal) crystal field. If it is strong enough to compete on the level of spin-orbit coupling, the on-site level structure should account for both influences. Therefore, the resulting Hamiltonian is

$$\begin{aligned}
 H &= H_{\text{SOC}} + H_{\text{CF}} \\
 &= \lambda \sum_i \mathbf{L}_i \mathbf{S}_i + \frac{\Delta}{3} \sum_i (L_i^x L_i^y + L_i^y L_i^x + L_i^x L_i^z + L_i^z L_i^x + L_i^y L_i^z + L_i^z L_i^y),
 \end{aligned} \tag{3.22}$$

where the first term is the LS-coupling SOC Hamiltonian introduced in equation (1.36) and the last term describes trigonal crystal field distortion of the t_{2g} orbitals as

derived in equation (1.27) (constant energy shift neglected). For convenience when writing down the subsequent analytical expressions, we introduce the shorthand $D = \Delta/3$.

The singlet-triplet model establishing the $|s\rangle$ and $|t_{x/y/z}\rangle$ states is based on the single-site diagonalization of the SOC Hamiltonian and subsequent neglect of the quintet states. If we strive to include the crystal field on the same footing, we need to build new singlet and triplet states out of the eigenstates of the SOC+CF Hamiltonian. We hereinafter refer to this scheme as the “full crystal field”. Diagonalization² leads to the following energies:

$$E_{1/2} = -\frac{\lambda + D}{2} \pm \frac{\sqrt{3}}{2} \sqrt{3\lambda^2 - 2D\lambda + 3D^2} \quad (3.23)$$

$$E_{(3/4)/5} = D \pm \lambda, \quad (3.24)$$

$$E_{(6/7)/(8/9)} = -\frac{D}{2} \pm \frac{1}{2} \sqrt{4\lambda^2 - 9D^2}, \quad (3.25)$$

where the brackets in the latter expressions denote twofold degenerate sets of energies and the minus solution of \pm always labels by the higher number. In contrast to earlier investigations, we do not shift the singlet to $E = 0$. Thus, the singlet is $E_2 \equiv E_s$ ($E = -2\lambda$ for $D = 0$) and the triplet states are $E_5 = E_{t_3}$ and $E_{(8/9)} = E_{t_1/t_2}$ at $E = \lambda$. The energies are shown in figure 3.41. For positive Δ , i.e. the trigonal contraction relevant for the $\text{Ag}_3\text{LiRu}_2\text{O}_6$ pressure experiment in reference [8], the t_1 and t_2 triplon gap is reduced, while the remaining eigenstates shift to comparatively higher energies.

At $\Delta \rightarrow \infty$, the two triplons and the singlet combine to a threefold degenerate state. A structure like this can be described as an effective spin-1 model. In fact, one of the prominent discussions for Ca_2RuO_4 is about which influence (SOC or crystal field) should be seen as dominant and hence whether the model is primarily a spin-orbital singlet-triplet influenced by Δ or a spin-1 perturbed by λ (see, e.g., reference

²via the computer algebra system interface wxMaxima

[119] and note that Ca_2RuO_4 is distorted tetragonally, although with analogous results regarding the energies). Naturally, both regimes seem to be a decent idea, as they are well motivated by the underlying physics and the three lowest eigenstates are well isolated rather quickly (spin-1). Moreover, the singlet-triplet projection becomes more and more exact due to the quintet shifting to higher energies. The primarily ill-motivated aspect is the incorporation of t_1 , which should be outright neglected at large positive Δ . Of course, an additional state in the perturbation theory does not make it worse per se. All in all, the spin-1 regime has been looked at extensively and our singlet-triplet theory is not expected to break down. Therefore, we can ignore this aspect.

Analogously, the $\Delta \rightarrow -\infty$ limit results in a degeneracy of two states, namely the singlet and t_1 triplet. This can motivate an effective spin-1/2 description. In the limit, a novel transversal-field Ising model emerges. Yet, the interesting results were published at the start of this year in reference [91]. Thus, there is no need to cover this limiting case in this thesis either. One should note, however, that the case of negative Δ does not improve the singlet-triplet projection. On the contrary, a twofold degenerate part of the quintet may become relevant.

Turning back to the general description, the Hamiltonian in equation (3.23) dictates the new singlet and triplet via the eigenstates. One finds:

$$N_s = \sqrt{(9\sqrt{3}\lambda - 3\sqrt{3}D)\sqrt{3\lambda^2 - 2\lambda D + 3D^2} + 27\lambda^2 - 18\lambda D + 27D^2}, \quad (3.26)$$

$$\begin{aligned} |s\rangle = \frac{1}{N_s} & \left(\sqrt{2}D(|m_L = 1, m_S = 1\rangle - |-1, -1\rangle) - (1+i)|D|(|1, 0\rangle + |0, 1\rangle) \right) \quad (3.27) \\ & + \frac{i}{\sqrt{2}} \frac{|D|}{D} (\sqrt{3}\sqrt{3\lambda^2 - 2\lambda D + 3D^2} + 3\lambda - D)(-|1, -1\rangle + |0, 0\rangle - |-1, 1\rangle) \\ & - (1-i)|D|(|-1, 0\rangle + |0, -1\rangle). \end{aligned}$$

Before continuing, it should be noted that $|D|/D$ needs to be, at least technically, treated with care when $D \rightarrow 0$. The limits $D \rightarrow 0^+$ and $D \rightarrow 0^-$ lead to the

discontinuity $|D|/D \rightarrow \pm 1$. Yet, a closer look at the $D = 0$ case reveals that the difference can be accounted for by a global phase factor. As a result one may choose a limit consistently and apply it in the numerical simulations. For us this will be $\lim_{D \rightarrow 0} |D|/D = 1$. This sudden change in base choice can result in some superficial discontinuities, which have no impact on the underlying physics, in the subsequent parameter plots.

We continue with the comparatively trivial t_3 triplon

$$|t_3\rangle = \frac{1}{\sqrt{6}} \left(|1, 0\rangle - |0, 1\rangle - \frac{1+i}{\sqrt{2}} (|1, -1\rangle - |-1, 1\rangle) - i(|0, -1\rangle - |-1, 0\rangle) \right), \quad (3.28)$$

which is independent of λ and D . The other two triplons can be described by

$$N_{t_1} = \sqrt{12\lambda^2 + 27D^2 - 9D\sqrt{4\lambda^2 + 9D^2}} \quad (3.29)$$

$$\begin{aligned} |t_1\rangle = \frac{1}{N_{t_1}} & \left(0|1, 1\rangle - \frac{1-i}{4} (-\sqrt{2}\sqrt{4\lambda^2 + 9D^2} + \sqrt{8}\lambda + 3\sqrt{2}D) |-1, -1\rangle \right. \\ & + \lambda|1, 0\rangle - \frac{\lambda(1+i)}{\sqrt{2}} |1, -1\rangle - \frac{1}{2} (\sqrt{4\lambda^2 + 9D^2} - 3D) |0, 1\rangle \\ & - \frac{1+i}{4} (-\sqrt{2}\sqrt{4\lambda^2 + 9D^2} + \sqrt{8}\lambda + 3\sqrt{2}D) (|0, 0\rangle + |-1, 1\rangle) \\ & \left. + \frac{i}{2} (2\lambda - 3D + \sqrt{4\lambda^2 + 9D^2}) (|0, -1\rangle - |-1, 0\rangle) + \frac{(1+i)\sqrt{8}\lambda}{4} |-1, 1\rangle \right) \end{aligned} \quad (3.30)$$

and

$$N_{\tilde{t}_2} = \left(8\lambda^4 + \sqrt{4\lambda^2 + 9D^2}(4\lambda^3 - 6\lambda^2 D + 9\lambda D^2 - 9D^3) - 12\lambda^3 D + 30\lambda^2 D^2 - 27\lambda D^3 + 27D^4 \right)^{\frac{1}{2}} \quad (3.31)$$

$$\begin{aligned} |\tilde{t}_2\rangle = \frac{1}{N_{\tilde{t}_2}} & \left(\lambda |D| |1, 1\rangle + 0 |1, 0\rangle + \frac{i|D|}{2D} (\lambda \sqrt{4\lambda^2 + 9D^2} + 2\lambda^2 - \lambda D) |1, -1\rangle \right. \\ & - \frac{1+i}{4} (\sqrt{2} |D| \sqrt{4\lambda^2 + 9D^2} + \sqrt{8}\lambda |D| - 3\sqrt{2}D |D|) |0, 1\rangle \\ & + \frac{i}{2} (|D| \sqrt{4\lambda^2 + 9D^2} - 3D |D|) |0, 0\rangle \\ & + \frac{1}{2} (|D| \sqrt{4\lambda^2 + 9D^2} - 3D |D| + 2\lambda |D|) |1, 1\rangle \\ & - \frac{(1-i)|D|}{4D} (\sqrt{2}(D-\lambda)\sqrt{4\lambda^2 + 9D^2} - \sqrt{8}\lambda^2 + \sqrt{2}D\lambda - 3\sqrt{2}D^2) |0, -1\rangle \\ & + \frac{(1-i)|D|}{4D} (\sqrt{2}(D-\lambda)\sqrt{4\lambda^2 + 9D^2} - \sqrt{8}\lambda^2 + 3\sqrt{2}D\lambda - 3\sqrt{2}D^2) |-1, 0\rangle \\ & \left. - \frac{i|D|}{2D} ((\lambda - D)\sqrt{4\lambda^2 + 9D^2} + 2\lambda^2 - D\lambda + 3D^2) |-1, 1\rangle \right). \end{aligned} \quad (3.32)$$

As the latter triplets are not orthogonal, the real $|t_2\rangle$ (which is even more inconvenient to write down explicitly) is provided by the Gram-Schmidt process as

$$|t_\perp\rangle = |\tilde{t}_2\rangle - \langle t_1 | \tilde{t}_2 \rangle |t_1\rangle, \quad \longrightarrow \quad |t_2\rangle = \frac{|t_\perp\rangle}{\| |t_\perp\rangle \|}. \quad (3.33)$$

The new singlet and triplet states should be valid for any value of λ and Δ . Nevertheless, this comes at the price of a highly nontrivial and unintuitive structure. It is therefore prudent to take a closer look at the new contributions. Figure 3.42 illustrates the $|m_L, m_S\rangle$ basis states involved in each boson. One finds that the additional terms adhere to a more or less palpable structure, with partly paired changes in old and new terms. Notably, a part of the influence resulting from the quintet states is directly apparent via the $m_J = \pm 2$ contributions becoming quite significant in the $|t_1\rangle$ and $|t_2\rangle$ states.

3.3. Triplons in a Trigonal Crystal Field

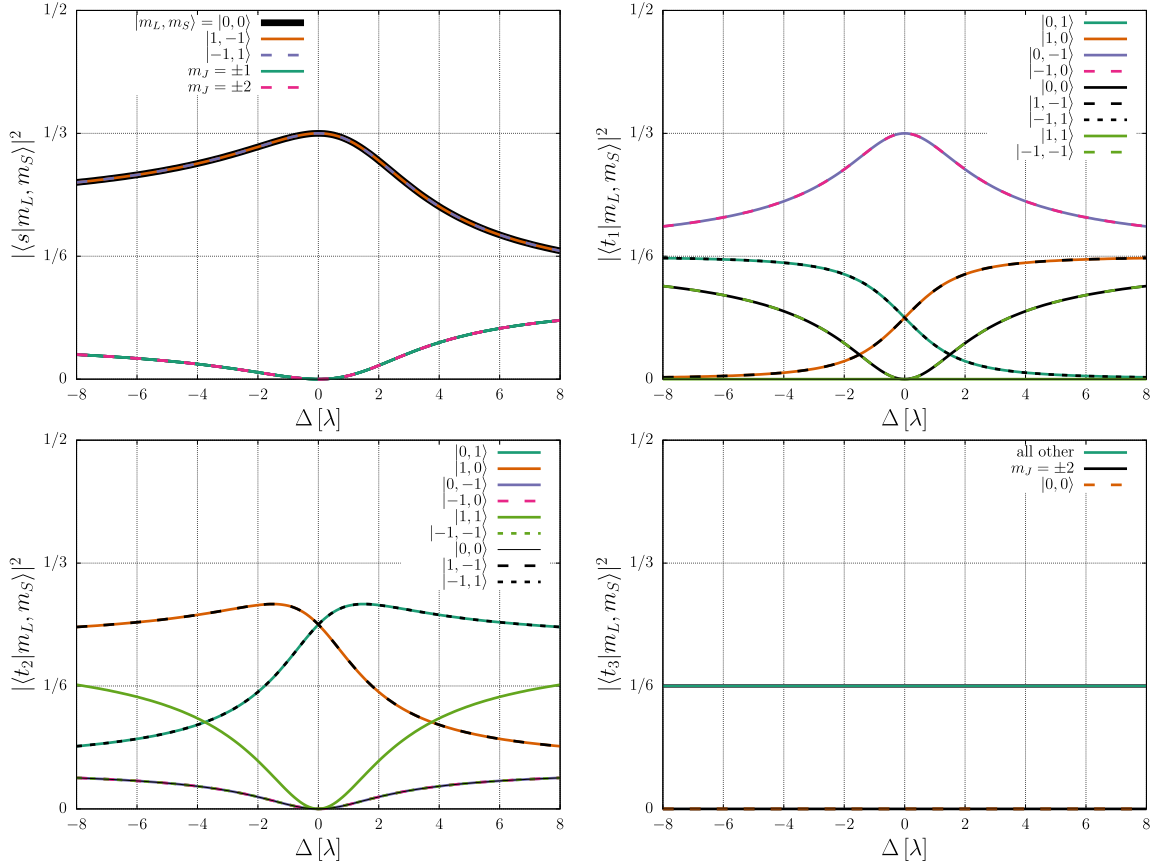


Figure 3.42. Visualization of the singlet-triplet basis of the full crystal field scheme as a function of the crystal field strength Δ : The eigenstates of the full Hamiltonian effectively mix different $|m_L, m_S\rangle$ states into the original singlet and triplet. Without change in quantization axis, the triplet t_3 does not change.

More importantly, one may look into the overlap with the old singlet and triplet states in order to gauge where the overall changes originate from. This is shown in figure 3.43. Here, one may immediately spot an aspect hidden in the previous figure. The singlet and triplet states do not mix. This is notable due to reference [8], which does not include the crystal field on equal footing to SOC but rather as a perturbation, suggesting that adding triplons to the ground state might support the new crystal field induced intermediate phase. Yet, from the pure on-site picture it is not obvious why this should help. More precisely, it is not obvious why the triplon admixture to the singlet should be different (in a clearly supportive fashion)

3. Analysis of the Triplon Honeycomb Model

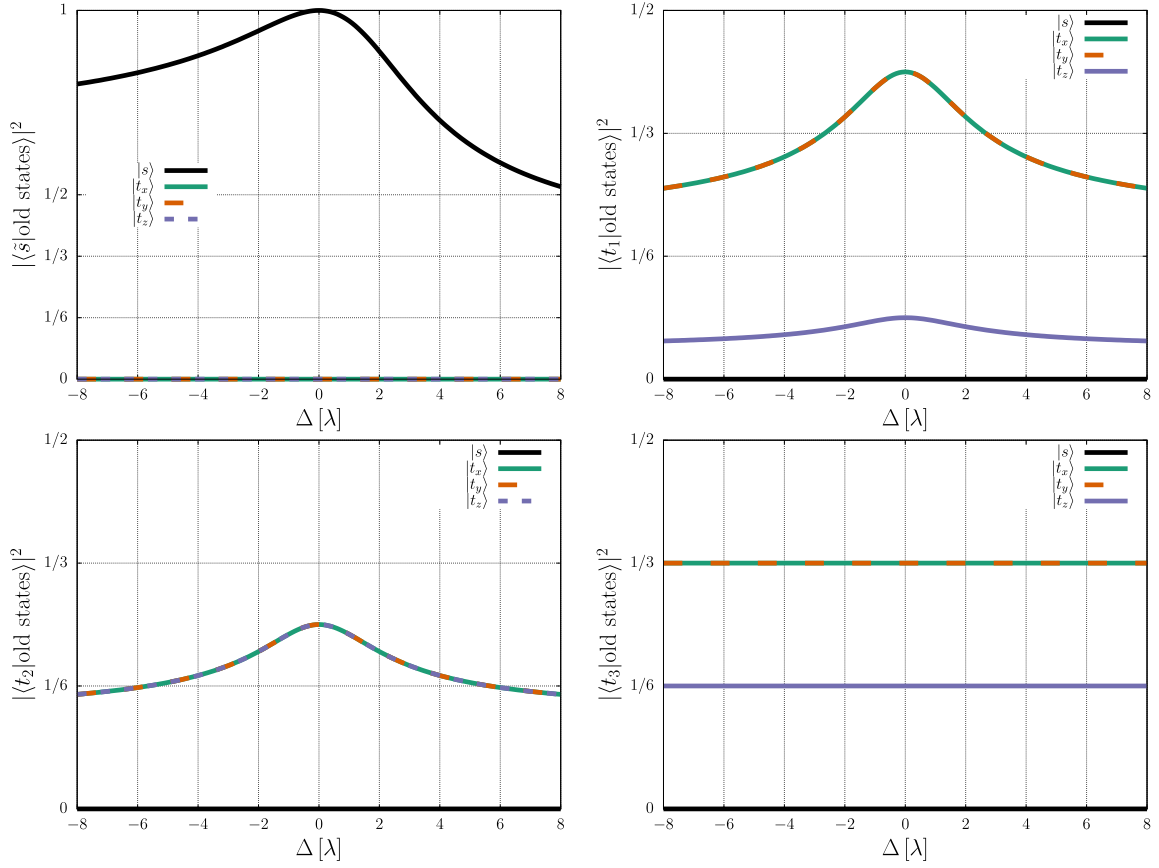


Figure 3.43. Comparison between old (no crystal field) and new (full crystal field scheme) singlet-triplet basis as a function of the crystal field strength Δ : Even in full crystal field scheme singlet and triplet states do not mix via trigonal distortion. As a result, the main change, along with mixing of the triplet itself, seems to be the influence of old quintet states that need to be accounted. Note that the new singlet is $|\tilde{s}\rangle$ in order to clearly label the objects.

compared to the $\Delta = 0$ case. Moreover, considering what changes and what remains the same, a large amount of the new structure has to be accounted for with the former quintet states.

One should note that this is not the only possible way to describe the singlet-triplet system. One may change the quantization axis of the angular momentum to the direction of the crystal field distortion like in reference [91]. That, however, comes at the price of converting the Kugel-Khomskii Hamiltonian. Additionally, one may try to choose any different recombination of the degenerate $|t_1\rangle$ and $|t_2\rangle$

states. Yet, one definitely loses the ability to choose the “natural” $|t_{x/y/z}\rangle$ basis, which necessitates the degeneracy of all three triplet states, for $\Delta \neq 0$. As a result, one needs to account for a complex pair state Hamiltonian (i.e. matrix analogous to the one in figure 1.13 but with potentially complex values). Concretely, this is a result of the projection onto the low-energy subspace (cf. section 1.4.5.2) involving the new singlet and triplet states.

An emerging problem for the practical analysis is the obfuscation of the interaction parameters, i.e. the Heisenberg and Kitaev couplings not being obvious. In the natural basis, e.g., the hopping matrix elements $\langle t_\tau, s | H_{(i,j)}^{(c)} | s, t_\tau \rangle$, where $H_{(i,j)}^{(c)}$ is the Kugel-Khomskii Hamiltonian introduced in equation (1.62) and $\tau \in \{x/y/z\}$ for a given bond in c direction, are real and for the Heisenberg case $\alpha = 0$ equivalent for all flavors τ . As a result, we obtain a Heisenberg model (equivalent hopping and pair terms) of \mathbf{v} bosons (real and opposite sign hopping and pair terms) in this case. When rewriting the $|t_\tau\rangle$ (and $|s\rangle$) into new complex linear combinations (with additional involvement of quintet state contributions), you lose the equivalence in couplings, making the effective Heisenberg interaction nonobvious. Additionally, the interaction can become complex, which according to the semiclassical wave function ansatz from equation (2.29) will result in a mixing of \mathbf{u} and \mathbf{v} contributions. Still, the order remains unchanged when taking into account full dipole magnetic moment. It is just not as straightforward to gauge what happens based on the interactions.

Nevertheless, we can attempt to find out how the coupling parameters change via the influence of the crystal field. In order to accomplish this, we visualize the h_2 matrix elements, i.e. $\langle \alpha_i \alpha_j | H_{(i,j)}^{(c)} | \beta_i \beta_j \rangle$ with $\alpha, \beta \in \{s, t_1, t_2, t_3\}$ and restriction onto the hopping and pair term matrix elements, in figure 3.44. We use the usual Kitaev-Heisenberg parametrization to fix t^2/U and t'^2/U (same as the previous uses) and fix $A = 0.1\lambda$, because part of the discussion is motivated by the paramagnetic regime suggested for $\text{Ag}_3\text{LiRu}_2\text{O}_6$. However, A is just an overall global factor that can be set arbitrarily for this discussion. It should also be noted that we consider the

3. Analysis of the Triplon Honeycomb Model

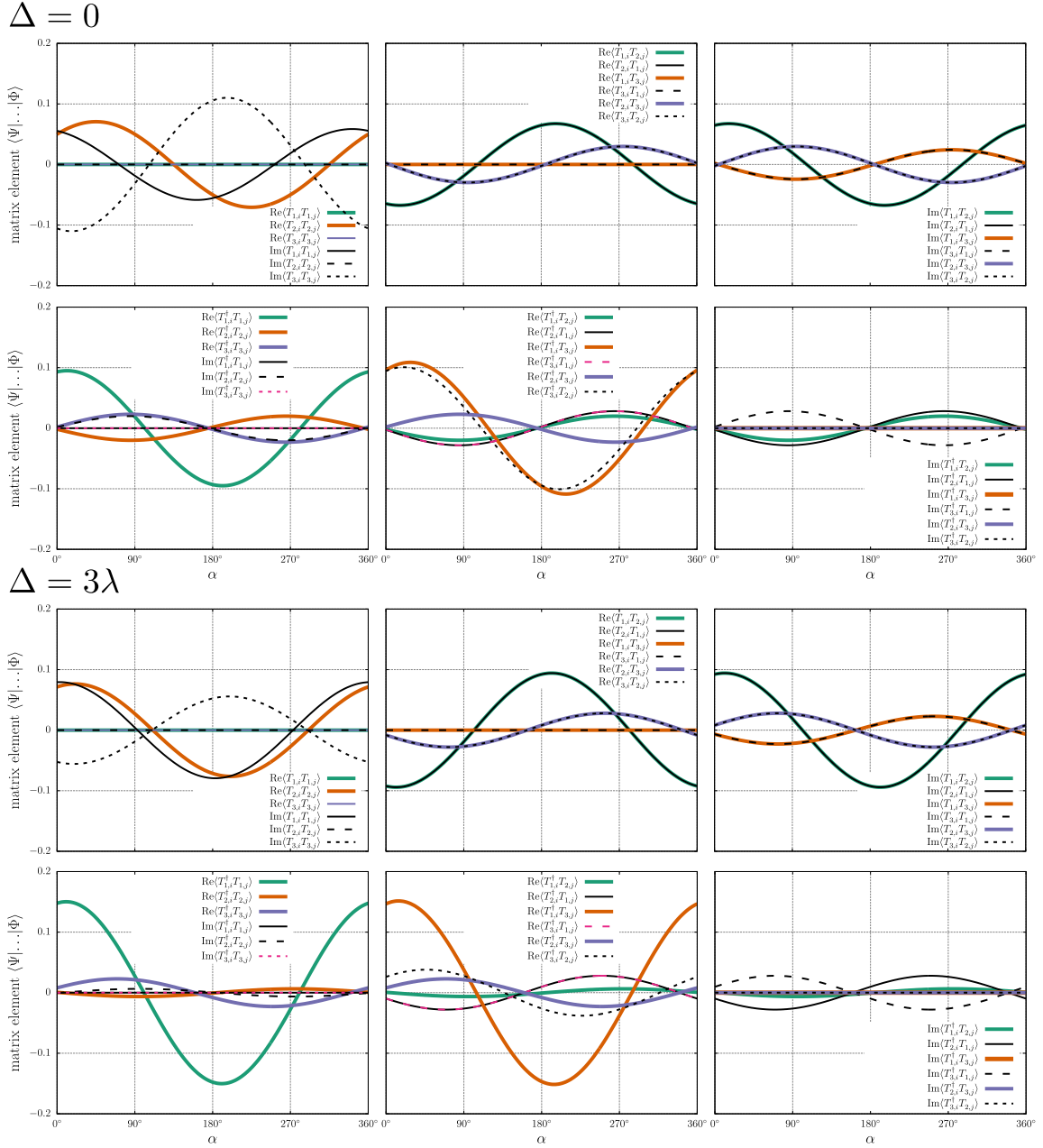


Figure 3.44. Matrix elements of the h_2 terms of the triplon model Hamiltonian (next neighbor pair states) on the z bond in the crystal field singlet-triplet basis: The values are obtained by fixing the Kugel-Khomskii interaction parameters t^2/U and t'^2/U to the Kitaev-Heisenberg parameters A and α . Here, A is a global factor and set to $A = 0.1\lambda$ (as in later analysis of the paramagnetic phase). The top half denotes the model in the absence of the crystal field. The interaction parameters are not trivially identifiable as a Kitaev-Heisenberg model due to the basis change. In the lower half, a noticeable crystal field value has been chosen for comparison. Most matrix elements do not seem to show drastic changes.

$c = z$ bond (meaning that we analyze the respective Kugel-Khomskii Hamiltonian in equation (1.62)).

For the traditional $x/y/z$ components the interactions would look straightforward, with $\langle T_{x/y,i}^\dagger T_{x/y,j} \rangle = A \cos(\alpha)$, $\langle T_{z,i}^\dagger T_{z,j} \rangle = A(\cos(\alpha) + \sin(\alpha))$ and pair terms the same but for a sign flip. All other contributions are trivial. In the new basis, the interactions look superficially complicated in the equivalent $\Delta = 0$ case (cf. top of figure 3.44). Yet, this represents the Kitaev-Heisenberg model and reproduces the phase diagrams (including h_3 and h_4 when incorporated) exactly.

While we can not directly make sense of the effective interactions parameters, we can still estimate the overall change when comparing these with the ones we obtain by involving a finite Δ . One can do this analysis quite extensively. Nonetheless, we restrict ourselves to the scenario deemed relevant for $\text{Ag}_3\text{LiRu}_2\text{O}_6$. In reference [8], they mention $\lambda = 70 \text{ meV}$ and $\Delta = 100 \text{ meV}$ as well as $\Delta = 200 \text{ meV}$ as “realistic parameters” (later they also use $\lambda = 50 \text{ meV}$ and $\Delta = 100 \text{ meV}$ for a triplon based explanation). Hence, we choose $\Delta = 3\lambda$ and therefore a round value roughly at the top end of the estimate. The resulting h_2 Hamiltonian terms are shown at the bottom of figure 3.44. Even for this comparatively large value, the changes are not drastic. Limiting the observations to the most prominent interactions, one may spot a noticeable decrease in $\text{Im}\langle T_{3,i} T_{3,j} \rangle$ and $\text{Re}\langle T_{3,i}^\dagger T_{2,j} \rangle$ contributions. Other prominent interactions gain significantly.

All in all, we may attempt to formulate how one can naively expect the trigonal crystal field compression to impact the model. The interactions do not change extremely drastically. They may induce a different magnetic phase, but their overall magnitude does not seem to collapse. On the contrary, there might even be an increase. The more notable change becomes apparent when recalling that the on-site gap of singlet and triplet is roughly halved at $\Delta = 3\lambda$ according to the energies displayed in figure 3.41. Therefore, the naive expectation is that the crystal field distortion drives the system toward a BEC. Or in a back-of-the-envelope argument:

Starting in the Heisenberg case with $J = A = 0.1\lambda$ and halving the gap results in $J/\lambda \approx 0.2$ (some Kitaev or other terms might enter) and thus a value beyond the critical condensation point of the Heisenberg limit at $A_c/\lambda = 1/6$. Due to the other interactions one may end up with a magnetic order (e.g., stripy or even something new instead of AFM or vice versa) and the point of condensation might not be obvious. Consequently, one could also imagine a case where the condensate is destroyed due to the interactions changing the necessary critical strength (different A_c values, cf. spin-wave phase diagram in figure 2.1). However, as the singlet-triplet gap changes drastically and the interactions do not, this scenario is very improbable. Concluding, we expect a BEC to emerge when the trigonal distortion is increased.

This expectation is, in contrast to the magnetic field, perfectly in line with the one for spin-dimer systems [70, 71]. For a spin-1/2 dimer like TlCuCl_3 [73], there is an intra-dimer coupling J_{intra} and inter-dimer coupling(s) J_{inter} . The first interaction produces the singlet-triplet gap (taking the role of λ for the spin-orbital model), while the latter is responsible for driving the magnon condensation. When pressure p is applied, both become functions of the new parameter, i.e. $J_{\text{intra}}(p)$ and $J_{\text{inter}}(p)$, which denotes both a singlet-triplet gap change and slightly different coupling parameters. Value-wise, these changes are used to explain the condensation. A notable difference for spin-dimer systems is that, all three triplons are driven toward condensation at the same time, while in our example one (or for negative Δ two) of them is shifted to higher energies and hence becomes irrelevant.

At this point it is prudent to look at the triplon model analysis used to argue about the nature of the intermediate pressure singlet phase in the supplementary material of [8]. The authors consider the h_2 Kitaev-Heisenberg model (only a single value of J and K are considered explicitly) on a single bond and provide the eigenstates and energies, i.e. they do ED with two sites and open boundary conditions. They also use the simplified crystal field scheme valid for weak distortions (which we are going to explain a few paragraphs later) instead of the full model we introduced previously.

The arguments and results of this analysis are very superficial. The essential parts can be summarized as: J and K promote admixture of triplon pair states $|T_\tau, T_{\tau'}\rangle$ into the singlet $|s, s\rangle$, which they argue to support the intermediate phase. Furthermore, the Van-Vleck magnetic response, i.e. finite magnetic moment due to second order perturbation theory proportional to $|\langle J \neq 0 | \mathbf{M} | J = 0 \rangle|^2$, connects to the “antibonding” states which are pushed up in energy by J and K interactions. The latter part is obvious and seemingly not useful for differentiating between ambient pressure and intermediate singlet based phases. Moreover, the former aspect is too vague to really describe any concrete characteristic of the intermediate phase. The admixture also happens in ED simulations of the ambient pressure phase (in contrast to (s)MC or infinite lattice tight binding model calculations, where ρ is zero outside of the magnetic phase). The authors seemingly did not evaluate if there is any qualitative change in this parameter and hence a real hint at this aspect being involved in the phase transition and thus the creation of the new intermediate singlet.

Consequently, we should give this model a more thorough look and find out if the triplon based description could really explain an intermediate singlet phase. One may note however, that this would be in direct contrast to the naive expectations formulated in previous paragraphs.

As mentioned, the analysis in reference [8] is based on the simplified or weak field model, which is not trivially a good idea for the values of λ and Δ deemed as realistic parameter, because it necessitates $\Delta \ll \lambda$ (details follow later). Here, we have already calculated the full crystal field model equivalent via the interactions shown in figure 3.44. With this, appropriate energies using the analytical expressions provided previously and possibly h_3 and h_4 terms, we could in principle provide a more thorough version of their analysis. The matrix elements shown for a bond are equivalent to the open boundary condition two site ED treatment. Yet, their results are so vague and universally true that there is no need to do so. We instead provide larger cluster sMC and ED analyses later.

We directly move to the last piece of model introduction we require for the subsequent analysis: What is the simplified weak crystal field scheme used in reference [8] (but also, e.g., in chapter 4 of this thesis)? If $\Delta \ll \lambda$, the crystal field operator can be projected onto the low-energy subspace in the same way all terms are handled in section 1.4.5.2. As the low-energy structure is provided solely by λ again, the original singlet-triplet choices s and $t_{x/y/z}$ can be used. The resulting Hamiltonian for a given site i is

$$\begin{aligned}
 & \frac{\Delta}{3} \langle L^x L^y + L^y L^x + L^x L^z + L^z L^x + L^y L^z + L^z L^y \rangle_{s,t} \\
 &= \frac{\Delta}{6} (T_x^\dagger T_y + T_y^\dagger T_x + T_y^\dagger T_z + T_z^\dagger T_y + T_z^\dagger T_x + T_x^\dagger T_z) \\
 &= \frac{\Delta}{6} (s^\dagger, t_x^\dagger, t_y^\dagger, t_z^\dagger) \begin{pmatrix} 0 & 0 & 0 & 0 \\ 0 & 0 & 1 & 1 \\ 0 & 1 & 0 & 1 \\ 0 & 1 & 1 & 0 \end{pmatrix} \begin{pmatrix} s \\ t_x \\ t_y \\ t_z \end{pmatrix}.
 \end{aligned} \tag{3.34}$$

Notably, there is no interplay between singlet and triplet degrees of freedom. The Hamiltonian is very reminiscent of the flavor-changing part of the magnetization (equation (3.16)) and thus to the magnetic field in normal spin-dimer systems!

Naively, one may therefore expect the simplified crystal field for the spin-orbital model to have comparable effects to the magnetic field in spin-dimer models. Thus, one would expect the crystal field to support and drive the Bose-Einstein condensation by reduction and eventual elimination of the singlet-triplet gap for a given flavor combination! This becomes apparent when diagonalizing the Hamiltonian in the previous equation. The eigenenergies are shown and compared to the full crystal field gap in figure 3.41. Their analytical expressions are

$$E_s = 0, \quad E_{t_3} = \frac{\Delta}{3}, \quad E_{t_1} = E_{t_2} = -\frac{\Delta}{6}, \tag{3.35}$$

with eigenstates (singlet trivial)

$$\begin{aligned} |t_3\rangle &= \frac{1}{\sqrt{3}} (|t_x\rangle + |t_y\rangle + |t_z\rangle), \\ |t_2\rangle &= \frac{1}{\sqrt{2}} (|t_x\rangle - |t_y\rangle), \\ |t_1\rangle &= \frac{1}{\sqrt{6}} (|t_x\rangle + |t_y\rangle - 2|t_z\rangle), \end{aligned} \tag{3.36}$$

where any linear combination of $|t_1\rangle$ and $|t_2\rangle$ is also acceptable.

As expected, the splitting is linear and the main difference to the magnetic field for the spin-dimer systems is that the triplet state crossing the singlet is twofold degenerate in the $\Delta > 0$ case. Hence, the resulting $\Delta \rightarrow \infty$ phase might not necessarily be just a polarized paramagnet like entity. Of course, the incorporation via perturbation theory dictates that the regime at or beyond the crossing point is not well motivated anyways and should be discarded. It should, nevertheless, be mentioned that degenerate triplons condensing in the pressure induced problem is also a feature analyzed for normal spin-dimer systems (e.g., the aforementioned case of TlCuCl_3 , where all three flavors condense at the same time). Otherwise, the energy structure suggests direct comparability to the magnetic field driven spin-dimers.

It is therefore even more puzzling that the authors of reference [8], which use this simplified scheme in their try to explain the triplon involvement, suggest that this explains anything other than a direct drive towards a BEC phase. Naturally, we try to subsequently test the naive estimate and provide a more thorough analysis of the triplon Kitaev-Heisenberg model in the crystal field. One may also mention that the great unknown of the h_3 and h_4 terms and their possible interplay with the crystal field, which could be drastic when recounting, e.g., the extend of the canted AFM phase in the magnetic field discussion. We will also subsequently try to find out if those could be the reason for the intermediate singlet.

On a side note, we may try to find out what the wave function ansatz used in the

semiclassical Monte-Carlo simulation can tell us about the crystal field. For the full crystal field this is not that useful, because of the plethora of interactions. Yet, as mentioned before, a complex coupling implies both \mathbf{u} and \mathbf{v} to be active at all times. For the simple crystal field, the resulting expression is straightforward. One finds

$$\frac{\Delta}{6} \langle (T_x^\dagger T_y + T_y^\dagger T_x + T_y^\dagger T_z + T_z^\dagger T_y + T_z^\dagger T_x + T_x^\dagger T_z) \rangle = \rho \frac{\Delta}{6} \sum_{\tau=x,y,z} \sum_{\tau' \neq \tau} (v_\tau v_{\tau'} + u_\tau u_{\tau'}) \quad (3.37)$$

and thus a term that scales with ρ like the flavor-changing magnetic field part. The expression is, however, not the dipole $\mathbf{u} \times \mathbf{v}$, but rather a very similar flavor interaction that notably leaves the boson types isolated. As a result, one would expect (in regimes where the higher order terms can be neglected), that both \mathbf{v} and \mathbf{u} bosons behave trivially like in section 3.1, meaning that the more suitable boson type wins completely and the other one can be neglected. The behavior should therefore be expected to be rather straightforward. In fact, the only thing that makes the model not fully “classical” (cf. section 2.3) is that, e.g., $\langle v_x v_y \rangle \neq \langle v_x \rangle \langle v_y \rangle$.

As a final part of this section, we want to provide a few notes about how the crystal field simulations were implemented in practice. For the simple crystal field, the analysis of the Hamiltonian in our simulations is completely analogous to the inclusion of the magnetic field, meaning no nontrivial extra work was necessary to conduct the analyses. Nevertheless, some care needs to be taken if one is interested in the spin-structure factor in ED simulations (see subsequent discussion in this section). The simulation of the full triplon model is more elaborate. As mentioned in the discussion surrounding figure 3.44, the new triplon basis needs to be taken into account, thus changing the Hamiltonian. Concerning the practical implementation details, one should not forget that the pair state Hamiltonian can now be complex valued and that the Hamiltonians on different bonds can not be translated into each other by cycling indices. As a result, the Kugel-Khomskii model of equation (1.62) for all three bonds needs to be projected onto the low-energy subspace separately.

Because the Kugel-Khomskii Hamiltonian per se remains unchanged, we can retain the parametrization of the interaction parameters t^2/U and t'^2/U by the Kitaev-Heisenberg parameters A and α in direct equivalence to the previous cases. All Kugel-Khomskii terms and thus all matrix elements of the low-energy projection can be accounted for this way. The procedure is the same as for the inclusion of the higher-order terms in previous section. We again neglect the Γ terms for consistency and because they do not present an obvious interest (we expect to inherit the properties of the normal extended Kitaev-Heisenberg model, which are already known quantities with Γ). Here, the inclusion may even be less important as the original Kitaev-Heisenberg interactions are translated to superficially different ones, including Γ -like terms, by basis change. Moreover, a full ab-initio study is not attempted (and difficult, see, e.g., the case of α -RuCl₃ [51, 230]) and, e.g., next-nearest neighbor interaction likely present in real materials are expected to drastically change any phase diagram (can be gauged via the spin-wave expressions in section 2.1).

Additionally, we want to comment on some practical details of the projection. The most straightforward way is to insert the singlet and triplet definitions of equations (3.27)-(3.33) into, e.g., Mathematica and calculate the matrix elements completely analogous to the regular case. There is, however, another option that might be extremely useful when attempting simulations beyond the current problem. Because of this potential usefulness, we set up the codes (sMC and ED) with this alternative, subsequently introduced scheme. Mathematica can handle the projection into an arbitrary singlet-triplet basis, meaning unspecified complex parameters, e.g., $|s\rangle = (s_1, s_2, s_3, s_4, s_5, s_6, s_7, s_8, s_9)$ as a vector in the $|m_L, m_S\rangle$ basis. The program can also generate a “Fortran output”, which is reasonably close to compatible with a real Fortran code. Fixing the expressions to fully compatible code can be achieved with a text editor and the “find and replace” function. This is arduous work, mainly because a single bond matrix of, e.g., the t^2/U terms has roughly 20000 lines (assuming a Fortran character limit of 130 per line), but achievable in the time frame

of minutes/hours rather than days.

The advantage of this scheme is clear: Any form of low-energy basis (e.g. other crystal fields) can be analyzed without extra effort. This might not be an extreme benefit in this thesis, but may be useful in the future. Also, the new matrix can be checked trivially in the $\Delta = 0$ case by choosing the regular singlet-triplet basis (setting s_i and triplet parameters). This is only an option because the basis is left arbitrary and can be changed on a whim. The $\lambda = 0$ case can be reasonably checked as well. For the intermediate values, future studies might check their code using the matrix elements in figure 3.44. In order to help with reproduction or refutation of our results, we provide the full 16×16 matrix (akin to figure 1.13) for intermediate values in appendix A.3.

Lastly, we make some notes about the behavior of the magnetization or its surrogate observables like the spin-structure factor in equation (2.22). The magnetization $\mathbf{M} = \alpha \mathbf{v} + \beta(\mathbf{u} \times \mathbf{v})$ of equation (1.91) ($\mathbf{M} = (M_x, M_y, M_z)^T$) is in the Cartesian $x/y/z$ basis. Even though the simple crystal field formalism keeps the triplon directions intact, the magnetic order emerges in the easy-plane or easy-axis direction of the crystal field distortion ($[1, 1, 1]$ direction or orthogonal plane). While this is not a particularly practical issue with sMC, the ED spin-structure factors should be chosen in the appropriate directions if one is explicitly interested in that observable.

For the full crystal field scheme one rewrites the directions. Thus the magnetization, which is a product of the low-energy projection as well, needs to be reevaluated. One can rephrase the old triplets in the new basis like reference [91]. We rather choose to compare apples to oranges for simplicity and talk about the magnetic moment in $t_{1/2/3}$ direction. The reason for this is that nothing in the discussion in this thesis is particularly connected to tracing the exact behavior of the spin-structure factor (some kind of magnetism or not is a sufficient answer). Rather, the central question concerns the intermediate non-magnetic singlet phase. Nevertheless, future studies might have to keep this in mind.

Finally, we can move on to explicit simulation results.

3.3.2 Spin-orbital Triplons in the Simple Trigonal Field Scheme

We start with a disclaimer: The simple and full crystal field models can be analyzed extensively. There are many intriguing questions, e.g., about the being able to drive the Kitaev phase and/or its survival analogous to the magnetic field case. Moreover, the magnetic orders in the Kitaev and zigzag/stripy regimes, especially in the simple case with higher-order terms, seem to be nontrivial. Additionally, the evolution of the magnetic order might be discussed.

However, this thesis is long enough and especially the former problem involves a lot of extra work beyond the crystal field discussion (as has become apparent in the magnetic field analysis). Therefore, we remain focused on the general ability to drive BEC and the issue motivated by the experimental findings of reference [8]: Does the triplon Kitaev-Heisenberg model (and eventually the higher-order terms) have an explanation for the distinct non-magnetic phase, which emerges when the trigonal distortion is induced via pressure.

We start with simulations of the Heisenberg FM and AFM cases using sMC. Observables for $N = 16$ site simulations can be found in figure 3.45. Therein, we consider Heisenberg interactions of strength $A = 0.1\lambda$ and $A = \lambda$, i.e. respective values deep in the paramagnetic and magnetic regimes. One should recall, that the simple trigonal crystal field scheme is based on perturbation theory of the SOC induced singlet-triplet states. As a result, the on-site gap closings (cf. figure 3.41) at $\Delta = -3\lambda$ and $\Delta = 6\lambda$ represent a definite maximum for the extend of the scheme being well motivated. Overall discrepancies to the full theory can be expected even earlier. Nevertheless, we provide data for more parameter values for completeness and in order to compare the results to spin-dimers in a magnetic field, where this

3. Analysis of the Triplon Honeycomb Model

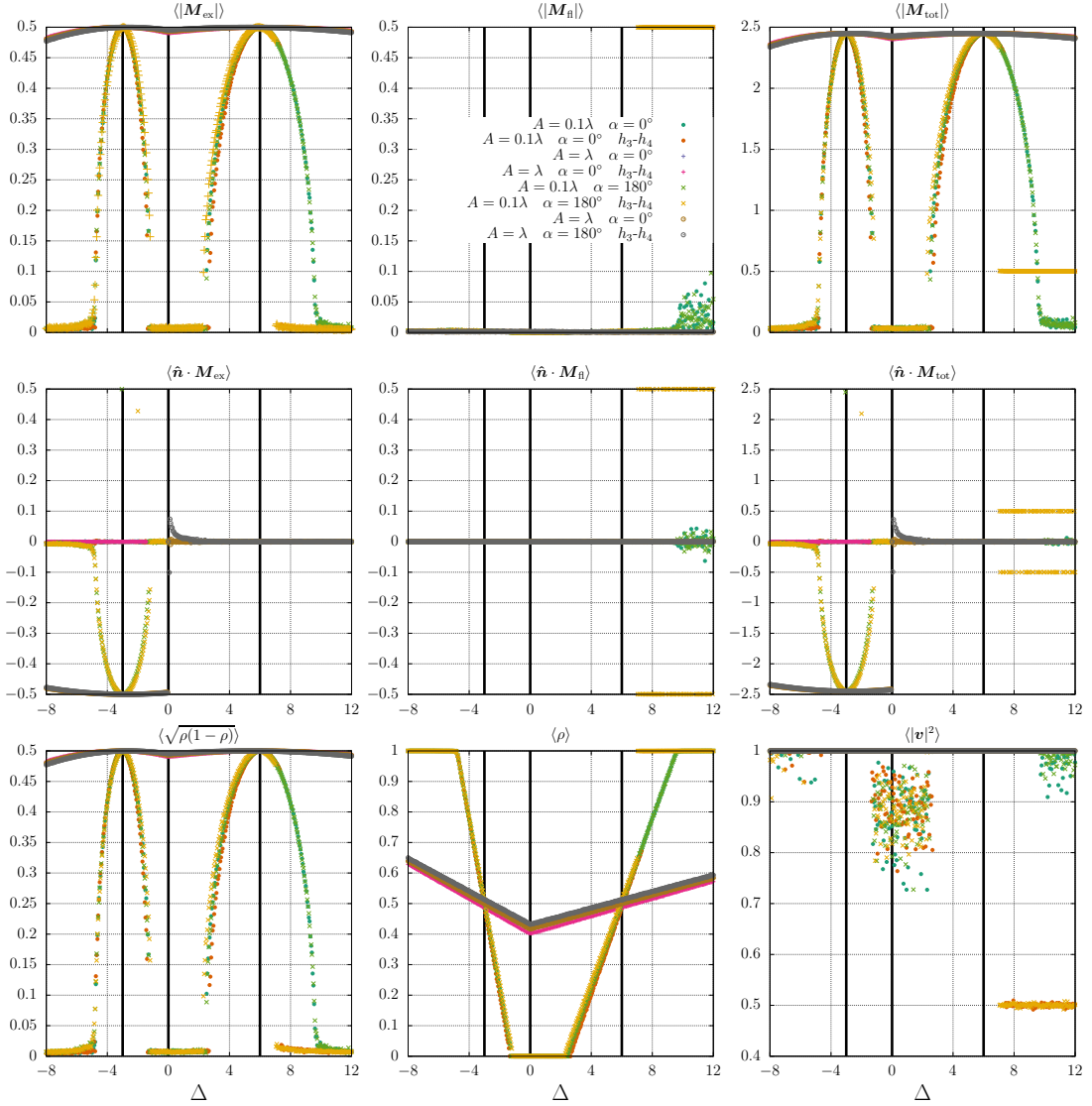


Figure 3.45. Observables calculated via semiclassical Monte-Carlo for the AFM and FM Heisenberg model in the simple crystal field scheme: Each case is analyzed deep in the magnetic $A = \lambda$ and paramagnetic $A = 0.1\lambda$ phase respectively. Here, $\hat{n} = [1, 1, 1]^T/\sqrt{3}$ is the direction of the trigonal distortion. Notably, the simple crystal field scheme is definitely ill-motivated when the singlet-triplet gap induced by spin-orbit coupling closes, which is represented by the vertical black lines at $\Delta = -3\lambda$ and $\Delta = 6\lambda$. Parameters beyond that are only visualized for the sake of completeness. In the acceptable parameter range, the magnetic phases evolve trivially (in contrast to the magnetic field discussion) and the paramagnetic phases are driven toward Bose-Einstein condensation with a look comparable to the spin-dimer singlet-triplet models in a magnetic field. The magnetic phases are \mathbf{v} boson based, except for a h_3-h_4 term based novelty in the ill-motivated $\Delta > 6\lambda$ area.

kind of restriction does not apply in the same way. Similarly, one might be tempted to keep the direction of the trigonal distortion $\hat{\mathbf{n}} = [1, 1, 1]^T/\sqrt{3}$ as a kind of magnetic field direction analogue.

The magnetic phases in figure 3.45 evolve trivially. The phases stay magnetic. One may find that the FM/AFM order is purely excitonic (\mathbf{v} based) and (cf. FM and $\hat{\mathbf{n}} \cdot \mathbf{M}$) changes at $\Delta = 0$ from an easy-axis (aligned with $\hat{\mathbf{n}}$) to an easy-plane (orthogonal to $\hat{\mathbf{n}}$) phase. The higher-order terms induce the usual support for the FM regime and slight penalty for AFM, which is most obvious in the ρ data. There might be a slight resistance to aligning with the easy-plane axis in the FM case for small $\Delta > 0$.

The more or less trivial evolution of the magnetic phases is a contrast to the magnetic field discussion, where the canting, the form of the semiclassical Hamiltonian being comparable to a regular spin and $\mathbf{u} \times \mathbf{v}$ contributions are responsible for a more complex behavior. Also, the complete analogy between FM and AFM cases (except for higher-order term induced differences) is different than the magnetic field effects. Yet, those features can be expected when considering the crystal field Hamiltonian in the semiclassical wave function ansatz in equation (3.37). Instead of coupling \mathbf{u} and \mathbf{v} bosons, they are left isolated so the latter can win outright as established in the quadrupole analysis in section 3.1. Also, the Hamiltonian does not induce canting and hence the higher-order terms, which we found to often be compatible with that, may reasonably have less impact. With this explanation, the slight deviation in the FM case for small $\Delta > 0$, which is close to the canted zigzag phase in the Kitaev-Heisenberg model without a magnetic field, seems plausible, as the higher-order terms in this region of the phase diagram might have some prominence and, due to a fixed $x/y/z$ axis aligned canting angle, may prefer a direction other than $\hat{\mathbf{n}}$ (or the orthogonal plane). Also, the values of ρ probably seem to increase slowly enough to not enable the higher-order terms to dominate in the physically relevant regime. Also, the implied reduction of magnetization for very big absolute

values of Δ is expected as the effective magnetic coupling resulting from A should be suppressed.

We, subsequently, turn to the paramagnetic regime ($A = 0.1\lambda$). Importantly, except for the case of active \mathbf{M}_f in the un-physical $\Delta > 6\lambda$ regime with active higher-order terms, the data imply Bose-Einstein condensation and magnetization curves that are directly analogous to the “textbook” examples of spin-dimer systems in a magnetic field [70, 71]. In other words, we seem to find directly what we introduced as naive expectations in the previous section. In the figure and in other observables like the energy, no signs of anything other than the straightforward condensation process can be found in the physical regime. Hence, sMC of the triplon Heisenberg model in a simple crystal field implies that one should not expect another singlet based nonmagnetic phase. On the contrary, the crystal field (as opposed to the magnetic field) should be considered as a possible way to establish magnetic order in compounds with paramagnetic Van Vleck-type singlet-triplet models.

One should note that, in the simple crystal field regime, the on-site singlet-triplet gap is guaranteed to close at a certain value, so triplet influence has to happen at some point if all the compound does is adhere to the triplon model at hand. The only possible exceptions are, first of all, additional influences not covered in this model, e.g., structural transitions caused by something else. Secondly, the higher-order terms could, at least in principle, induce nontrivial transitions, which they seemingly not do in the physically relevant regime of the Heisenberg model (the $\Delta > 6\lambda$ phase still hints at the possibility). Thirdly, regimes where the condensation is not straightforward, like the Kitaev case, might be a possible way to avoid the obvious trend toward condensation. Models beyond the Heisenberg case are analyzed in later parts of this section, covering at least part of the latter two issues. Aside from that, our comment in regards to the triplon and simple crystal field considerations in reference [8] would be that something outside the model might be needed for an explanation of the novel nonmagnetic phase. Beyond that, the full crystal field

possessing the essential component is still on the table.

Continuing the overall description and interpretation of the results, we find that the magnetic order emerges as expected from the behavior of the $A = \lambda$ data. For example in the FM Heisenberg case, the FM order is driven and aligns in easy-plane and easy-axis directions respectively. Irregularities are limited to the ill-motivated regimes.

Beyond the energy gap closings, for the fully polarized $\rho = 1$ regime the data seem ambivalent. As no further analysis has been done (we restrict ourselves to the question of condensation), we can not be sure if this is a physical effect or just numerical difficulties in the MC simulations (A should be suppressed in importance and thus one might need to lower the temperature). It could therefore be interesting to look at this regime, which represents the counterpart to the polarized paramagnet in the spin-dimer magnetic field problem. But we will not cover this here.

The remaining noticeable feature is the (again un-physical) phase with \mathbf{u} contribution in the $\Delta > 6\lambda$ regime with higher-order interactions being included. First of all, one finds equal contribution of \mathbf{u} and \mathbf{v} bosons. Additionally, the magnetic order is not excitonic, but purely $(\mathbf{u} \times \mathbf{v})$ based. In fact, the magnetization is fixed at the maximal possible value of the flavor-changing contribution (recall $|\mathbf{u}|^2 + |\mathbf{v}|^2 = 1$, $0 \leq \rho \leq 1$ and semiclassical $\mathbf{M}_{\text{fl}} = \rho(\mathbf{u} \times \mathbf{v})$). The flavor-changing term also appears to be easy-axis, but this is trivial to explain as the semiclassical expression for Δ only enforces the \mathbf{u} and \mathbf{v} bosons to be easy-plane and the flavor-changing term is orthogonal to those contributions by construction.

While un-physical, this new magnetic phase is quite compelling conceptually. As illustrated by the right side of figure 3.46, it consists of disordered \mathbf{u} and \mathbf{v} moments and AFM/FM ordered magnetic dipole moment \mathbf{M} . It is therefore easy to explain in the following way: As $\rho = 1$ holds, the triplet is the sole contributor. The triplet itself, i.e. isolated from the rest of the system, is just a regular spin-1 type entity. In section 1.5.1, the language of the spin-1 is introduced. For the regular spin-1,

3. Analysis of the Triplon Honeycomb Model

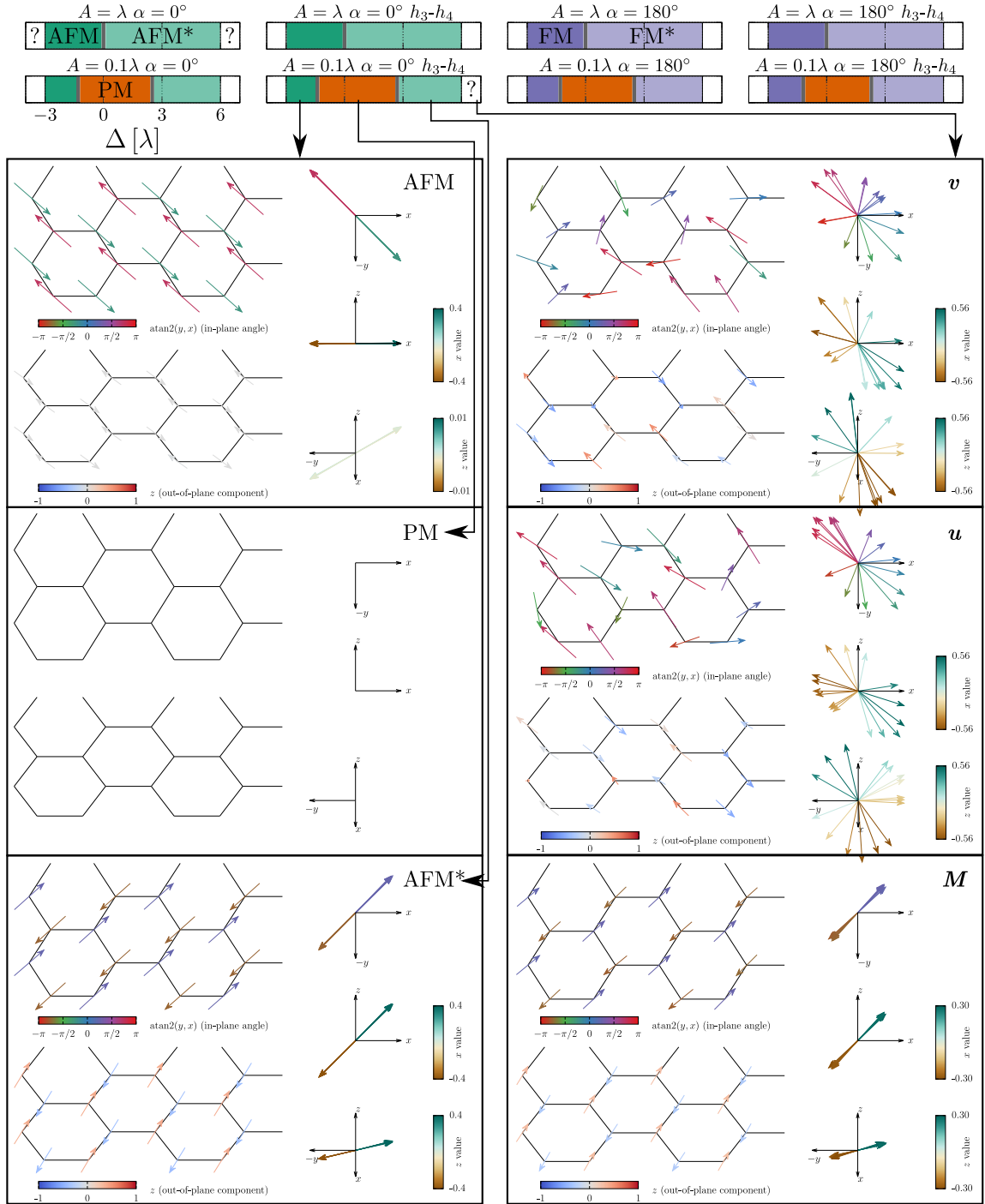


Figure 3.46. Phase diagrams and exemplary boson orders (left: \mathbf{v} only) for the previously discussed FM and AFM Heisenberg models: At $\Delta < 0$, the order is easy-axis in trigonal field direction and at $\Delta > 0$ easy-plane (labeled by $*$). Changes between models are minute: The $A = \lambda$ cases are trivial and the size of the paramagnet is only changed slightly by inclusion of the higher order h_3 - h_4 terms in the expected way (FM is favored). The novelty at $\Delta > 6\lambda$ is visualized on the right and found to represent a disorder in \mathbf{u} and \mathbf{v} and AFM/FM order in the full dipole moment \mathbf{M} .

the \mathbf{u} and \mathbf{v} bosons are actually both quadrupoles, which remain trivial here. The dipole magnetic moment is covered solely by $\mathbf{u} \times \mathbf{v}$. Hence, we have actually found a regular triplet AFM/FM order that is completely analogous to the normal spin. As the triplet-triplet interactions are located in the higher-order terms, the phase is only established if these contributions are included. In fact, the “regular spin-1 like” feature is the total angular momentum $J = 1$, thus implying that the relevant terms are $\mathbf{J}_i \mathbf{J}_j$. Intriguingly enough, this is not directly connected to the disorder of the bosons themselves.

As a final note about this phase, we point out an aspect that is very likely irrelevant but could be an interesting point to keep in mind. A conceptual problem for using a finite triplet/triplon contribution like in reference [8] to explain the a non-magnetic phase, is to write down such a state concretely. How does one handle finite triplet/triplon contribution without creating a magnetic moment³? As soon as a triplon is in the ground state, the excitonic dipole contribution is nonzero. One conceptual way would actually be the pure triplet (like in the novel phase) rather than the triplon admixed ground state. The excitonic contribution vanishes by necessity for $\rho = 1$ and $\mathbf{u} \times \mathbf{v}$ can be zero if the bosons are aligned.

Moving back to more relevant discussions, the aforementioned figure 3.46 provides the phase diagrams and visualization of the (AFM) spin orders for the previously discussed Heisenberg model simulations. Overall, the results are as expected. The higher-order terms induce slight changes in the critical condensation points. The magnetic order directions conform to the eigenstates of the simple trigonal crystal field. Beyond the on-site gap closings, the results of the model should not be used to produce a phase diagram.

In summary, the sMC simulations of the Heisenberg cases confirm the naive predictions of the behavior: One should expect condensation analogous to the spin-dimer

³The admixture arguments in the reference and triplon number in our subsequent ED data are not relevant. ED is a simulation on a finite cluster without well defined order parameters and therefore a finite triplon number everywhere.

in a magnetic field and nothing else. How should this be interpreted and connected to the experiment in reference [8]? Primarily, we should confirm that our assessment of the model is correct. A sMC simulation is restricted by the chosen form of the wave function ansatz, which might not cover the degrees of freedom correctly (although it should cover the suggestions of reference [8] reasonably well). Moreover, quantum fluctuations might be important in establishing the nonmagnetic intermediate phase. We need to provide further analysis with ED, which should be able to address these shortcomings.

Figures 3.47 and 3.48 provide exemplary ED results for the AFM Heisenberg model. The ground state based observables are known from previous discussions. We substitute the spin-structure factor for the triplon number, as the latter is the object of interest given arguments in reference [8] and the former just reiterates the obvious fact that one arrives in a magnetically ordered phase, which at least for the simple crystal field model has to happen at some point. For the cluster we chose the $N = 6$ one analyzed in studies of the normal Kitaev-Heisenberg model in reference [6]. There is a small caveat that needs to be mentioned here. If the nonmagnetic intermediate phase requires a biased cluster, our analysis has no chance of finding it. That, like possible anisotropy of the bond interactions, is beyond the considerations in this thesis and might be worth a look in the future.

A smoking gun signature would be the appearance of either two phase transitions or hitherto unknown trends in the triplon number. None of that seems to happen. There is solely one transition into the magnetic phase. If one starts in the magnetic regime, there seems to be no sign of a phase transition at all. Naturally, the observables on the finite cluster do not perfectly agree when it comes to the quantitative value of the critical point, but that is expected. For completeness, we provide the Δ sweep with more paramagnetic values of A in appendix A.2.

Finally, there is an obvious extension of the preceding discussions that needs to be covered. What if the Heisenberg model is not enough and Kitaev interactions

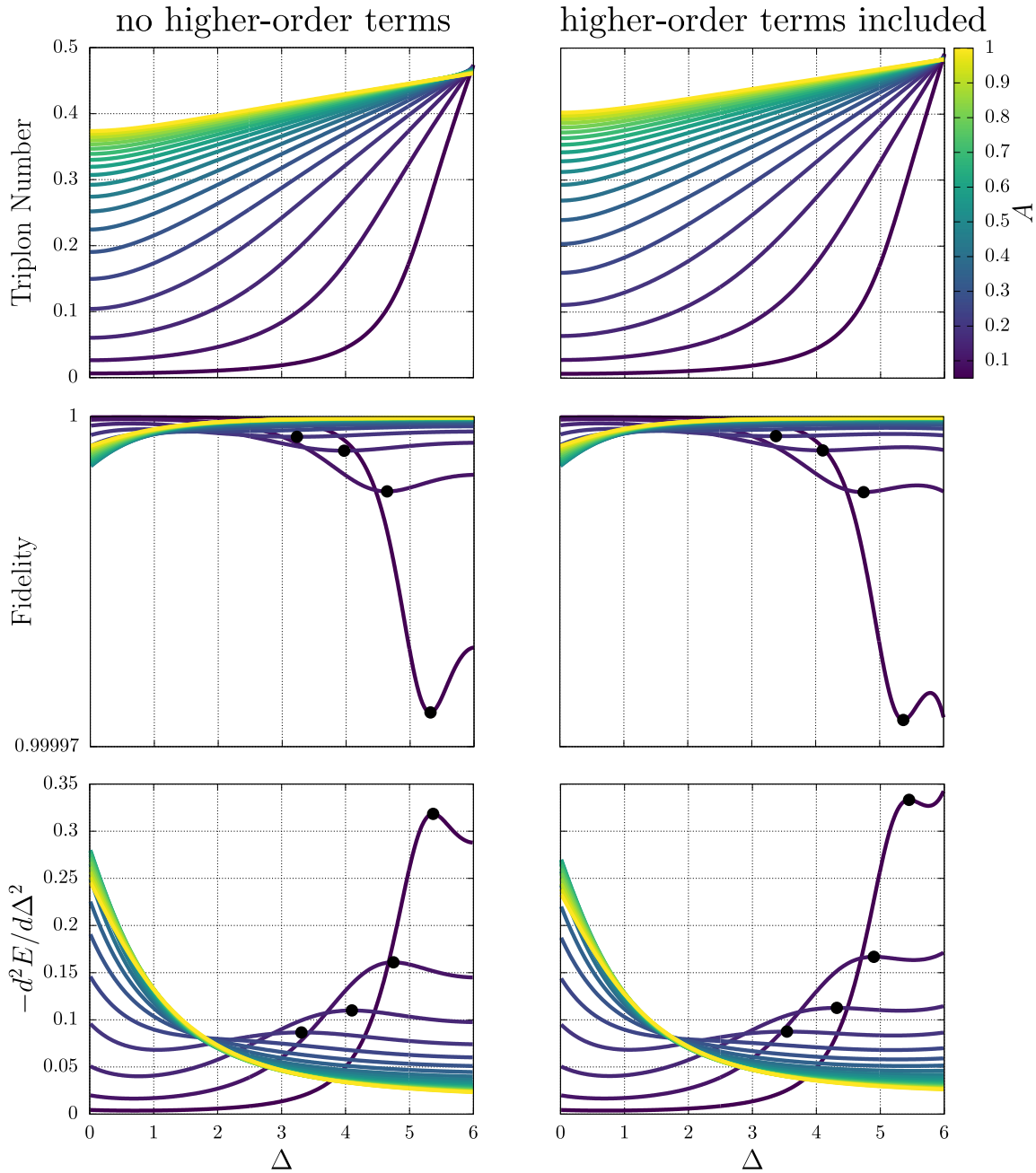


Figure 3.47. Ground state properties calculated via ED for the AFM Heisenberg model with coupling strength A as a function of the crystal field strength Δ : Total triplon number, ground state fidelity (step size 0.01λ) and second energy derivative are analyzed for potential signatures of a phase transition. For the latter two, these are expected to be indicated by a maximum/minimum and marked by a black dot if available. These roughly correspond to turning points in the triplon number and found to signal the transition from the paramagnet to the regular magnetic phase. No other signs of a phase transition (e.g. from a singlet to another singlet with involvement of the triplon density) seem to be visible.

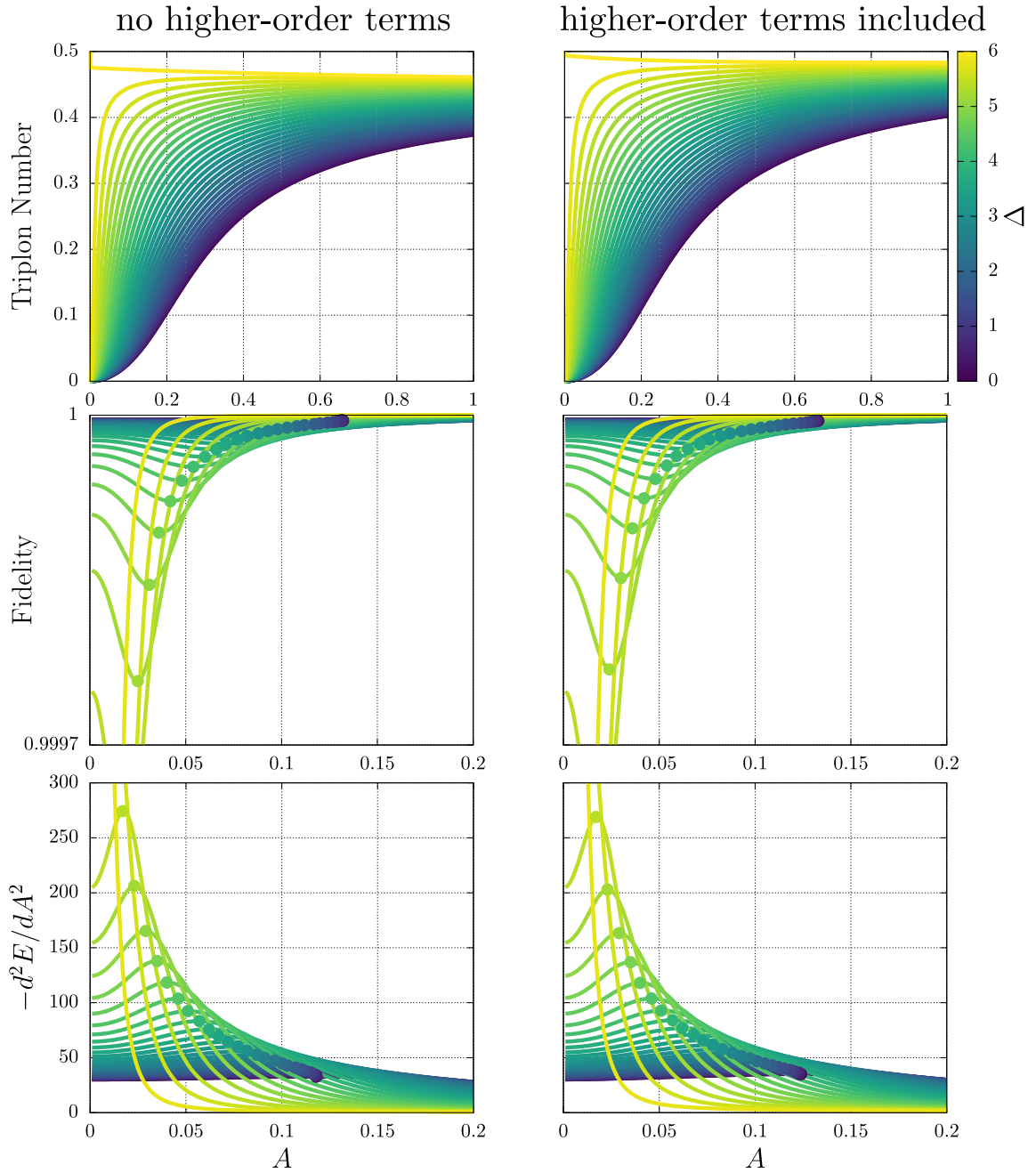


Figure 3.48. Ground state properties calculated via ED for the AFM Heisenberg model for various values of the crystal field Δ as a function of the Heisenberg coupling A : As before, the total triplon number, ground state fidelity (step size 0.001λ) and second energy derivative are analyzed for potential signatures of a phase transition and maxima/minima for the latter two are marked with color map corresponding dots. Again, only the expected drive into the magnetic phase seems to be visible.

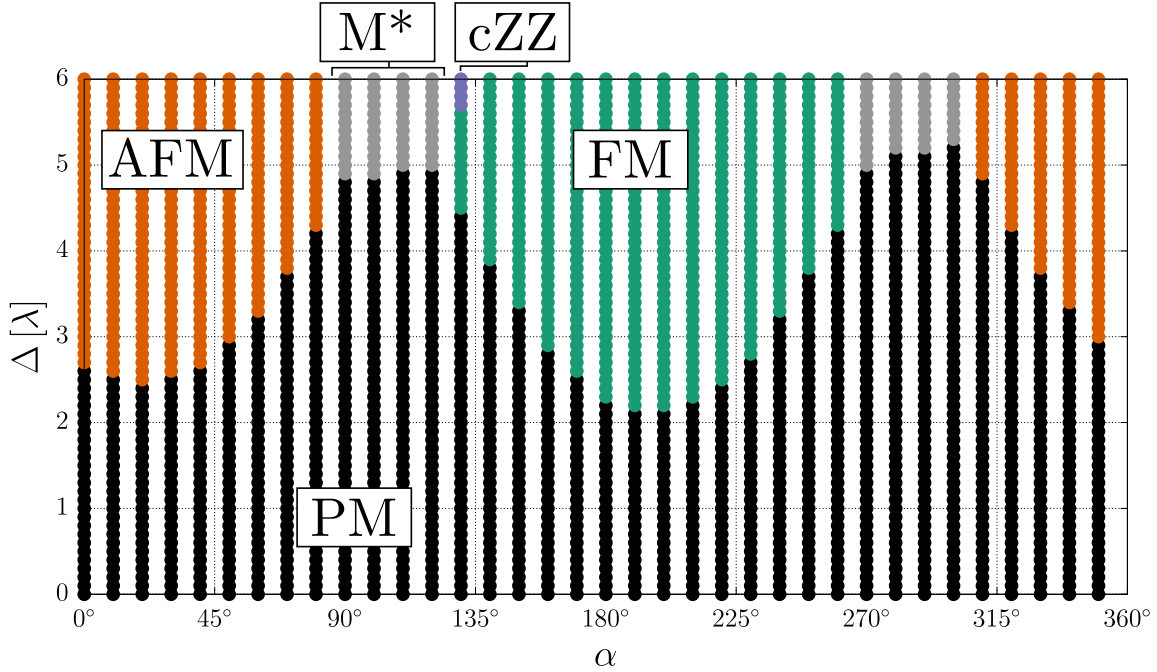


Figure 3.49. Phase diagram for the Kitaev-Heisenberg model with higher-order h_3 - h_4 terms, $A = 0.1\lambda$ and various values of interaction angle α and crystal field Δ : The semiclassical Monte-Carlo simulations describe the regular paramagnet and drive into various magnetic phases. For the purpose of shortening the discussion, the possibly more complicated regime of magnetic phases is labeled by M^* . One should note, that there is nontrivial behavior induced by the crystal field, as the FM seems to exist at $\alpha = 130^\circ$, i.e. in an area where the regular Kitaev-Heisenberg model would be expected to host a zigzag phase.

are necessary? Thus, we provide a full phase diagram of the Kitaev-Heisenberg model with $A = 0.1\lambda$ and higher-order terms in figure 3.49. In appendix A.2 one can find the equivalent analysis without h_3 and h_4 terms, which does not change the overarching result. Similarly, ED simulations on the $N = 6$ cluster also do not provide any new insights.

As expected, one finds the AFM, FM and canted zigzag phase. Due to the higher-order terms, there is a slight preference for FM when critical condensation points are compared. Notably, there is nontrivial behavior, which is best exemplified by the AFM and FM order usurping the $\alpha = 130^\circ$ and $\alpha = 310^\circ$ angles of stripy and zigzag phase. The M^* area denotes magnetic phases that we do not specify explicitly.

Most importantly, we find that there is still just the regular singlet and magnetic phases. The Kitaev-interaction in the simple crystal field scheme does not seem to be a sufficient explanation for the intermediate nonmagnetic phase.

The model preferring FM/AFM order compared to zigzag/stripy seems to be curious at first glance. Naively, the simple crystal field seems to be a purely local quantity that does not care about the boson order except for forcing overall direction axes. Yet, the crystal field having an effective momentum preference is reasonable when comparing it to the interplay between magnetic field and Kitaev interaction in our reference [5] or the topology chapter of this thesis in figure 4.4. The Kitaev interaction itself (in absence of higher-order terms or Γ terms) provides flat bands due to each flavor being constricted to the bond where it can be created. The magnetic field can change the flavor and hence enable a dispersion on the other bonds, thus creating a momentum dependent structure. Obviously, the flavor-changing also happens analogously in the simple crystal field.

Lastly, we should comment on the M^* part of the phase diagram. First of all, one should reiterate that the phase summarized under this label are all magnetic, which is all that is important for the question at hand. Secondly, one might look at the next section and attest that none of those phases seem to survive the rigor of the full crystal field model (although there is a reasonable chance that values other than $A = 0.1\lambda$ closer to the respective condensation points could change that). Thirdly, we estimate that a more thorough analysis should be done before giving definite statements about everything going on in this regime. As those phases are not important for this thesis, we will not provide this here. We, subsequently, roughly state what to expect and what the problems are. The Kitaev phase seems to survive. Although in that case one needs to always carefully evaluate at what point, if at all, the AFM or FM takes over and discern this from sMC reliably finding a local energy minimum instead, which is a nontrivial amount of work. Additionally, there is one data point next to the cZZ phase suggesting a higher-order induced (active \mathbf{u}

moment) new phase. Moreover, the area should be evaluated on very large lattices, because the crystal field shares features with the $[1, 1, 1]$ magnetic field, which has highly nontrivial features [165]. While there is no outright canting behavior caused by the crystal field, at least the neighboring cZZ phase has an axis preference (hence the name “canted” we chose as a label in previous sections). Similarly, the spin-1 Kitaev-Heisenberg model with a spin anisotropy in $[1,1,1]$, i.e. an operator $\Delta(\mathbf{n}\mathbf{S})^2$ very similar to the trigonal distortion, was proposed to induce a vortex state [231]. All in all, this area is seemingly not important but might be interesting on a conceptual level, which could be evaluated in a future study.

In summary, the simple crystal field does not seem to explain the intermediate nonmagnetic phase. It rather reliably enforces the emergence of magnetic phases by driving the BEC like a magnetic field would do for a spin-dimer. Explanations of the intermediate phase seem to necessitate at the very least the inclusion of additional influences. One attempt would be the incorporation of the crystal field without perturbation theory, which is described in the previous section as the “full crystal field” and analyzed in the next part.

3.3.3 Spin-orbital Triplons in the Full Trigonal Field Scheme

The differences between simple and full crystal field scheme are explained in section 3.3.1. We can move on to the results. For sake of comparison with the simple scheme we chose the same parameter ranges and follow the order of analysis. Hence, we start with sMC simulations of the Heisenberg case.

Figure 3.50 contains the sMC observables in direct analogy to the preceding figure 3.45. Turning to descriptions of the results, we first notice that all magnetic phases are a mixture of \mathbf{u} and \mathbf{v} bosons, which we deemed as expected in our formulation of naive expectations due to the basis change and resulting complex interaction parameters. The ratio of the boson types remains neatly fixed and a well defined quantity in each magnetic regime. This may possibly serve as a new indicator of absence of significant higher-order term influence.

In contrast to the simple crystal field scheme, the simulations do not change drastically beyond $\Delta = -3\lambda$ and $\Delta = 6\lambda$, because there is no extreme change like an energy gap closing. In fact, the energy gap remains finite (cf. figure 3.41) and there is no distinctly different behavior expected for very large absolute values of Δ (in contrast to, e.g., the polarized paramagnet equivalent where one state becomes more and more isolated). As a result, the magnetization does not reduce for large Δ , but seems to strive towards a constant, which appears to be the same whether one starts in the magnetic $A = \lambda$ regime or in the $A = 0.1\lambda$ paramagnet.

The last aspect points to an important difference between simple and full crystal field model. In the simple crystal field, the semiclassical picture implies $\Delta\rho(\dots)$ as a scaling and hence that the crystal field is optimized for $\rho = 1$, i.e. the pure triplet $J = 1$ state. At the band gap closing at $\Delta = -3\lambda$ and $\Delta = 6\lambda$, both magnetic and paramagnetic starting points agree that $\rho \approx 1/2$ and then continue towards a pure

3.3. Triplons in a Trigonal Crystal Field

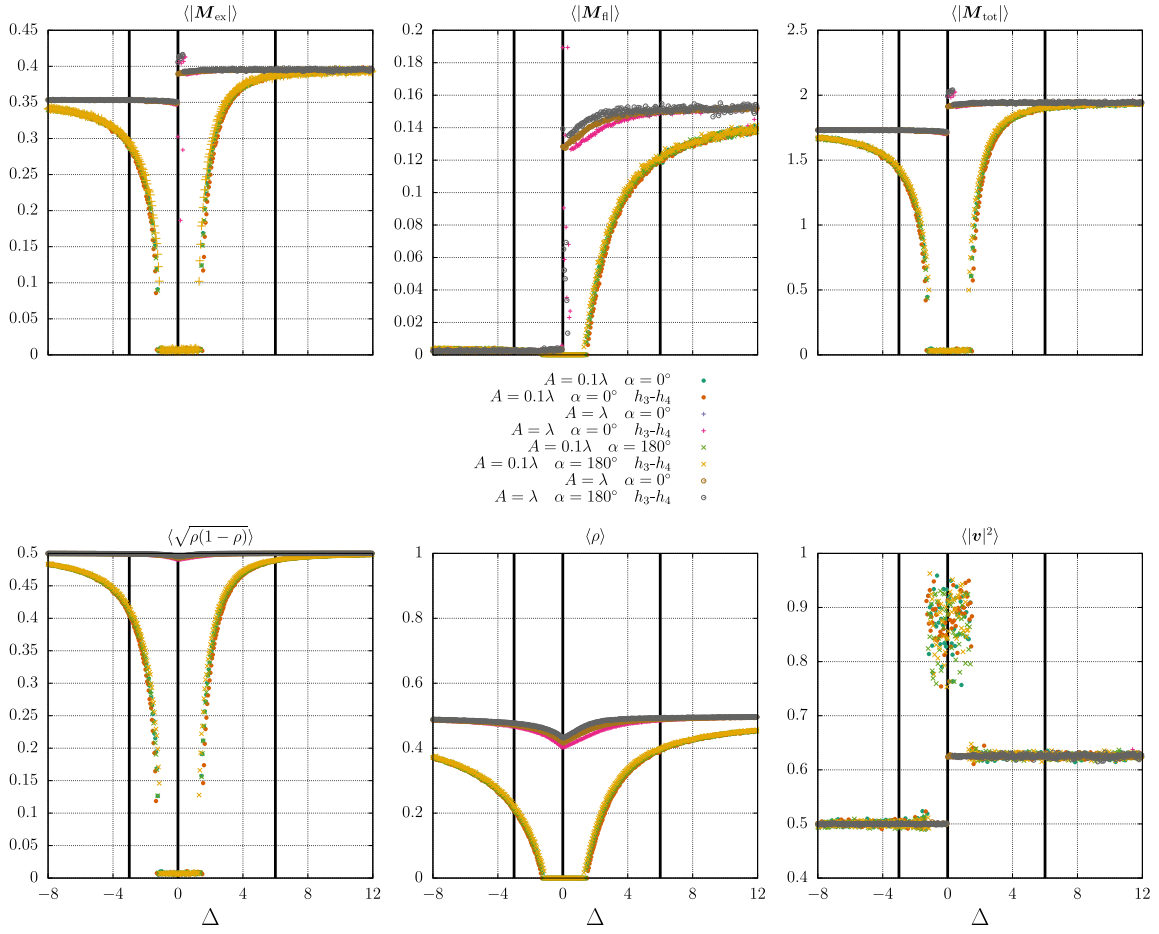


Figure 3.50. Observables calculated via semiclassical Monte-Carlo for the AFM and FM Heisenberg model in the full crystal field scheme: Each case is analyzed deep in the magnetic $A = \lambda$ and paramagnetic $A = 0.1\lambda$ phase respectively. The black vertical lines at $\Delta = -3\lambda$ and $\Delta = 6\lambda$ are a remnant of the simple crystal field kept only as a comparative element (no physical importance here). The overall trends remain the same as in the simple crystal field case: The magnetic phases evolve trivially and the paramagnetic phases are driven toward Bose-Einstein condensation. Due to the basis change and resulting complex interaction parameters, both \mathbf{u} and \mathbf{v} bosons are involved, although the proportion of each in the magnetic phase remains at a constant value.

triplet. Yet, in the full model the gap never closes and the crystal field strives toward $\rho = 1/2$, i.e. the optimal filling for the h_2 terms and the triplons in general. Thus, the crystal field remains perfectly compatible with the triplon condensation process.

Similar to the simple crystal field model, the fully magnetic $A = \lambda$ simulations are

3. Analysis of the Triplon Honeycomb Model

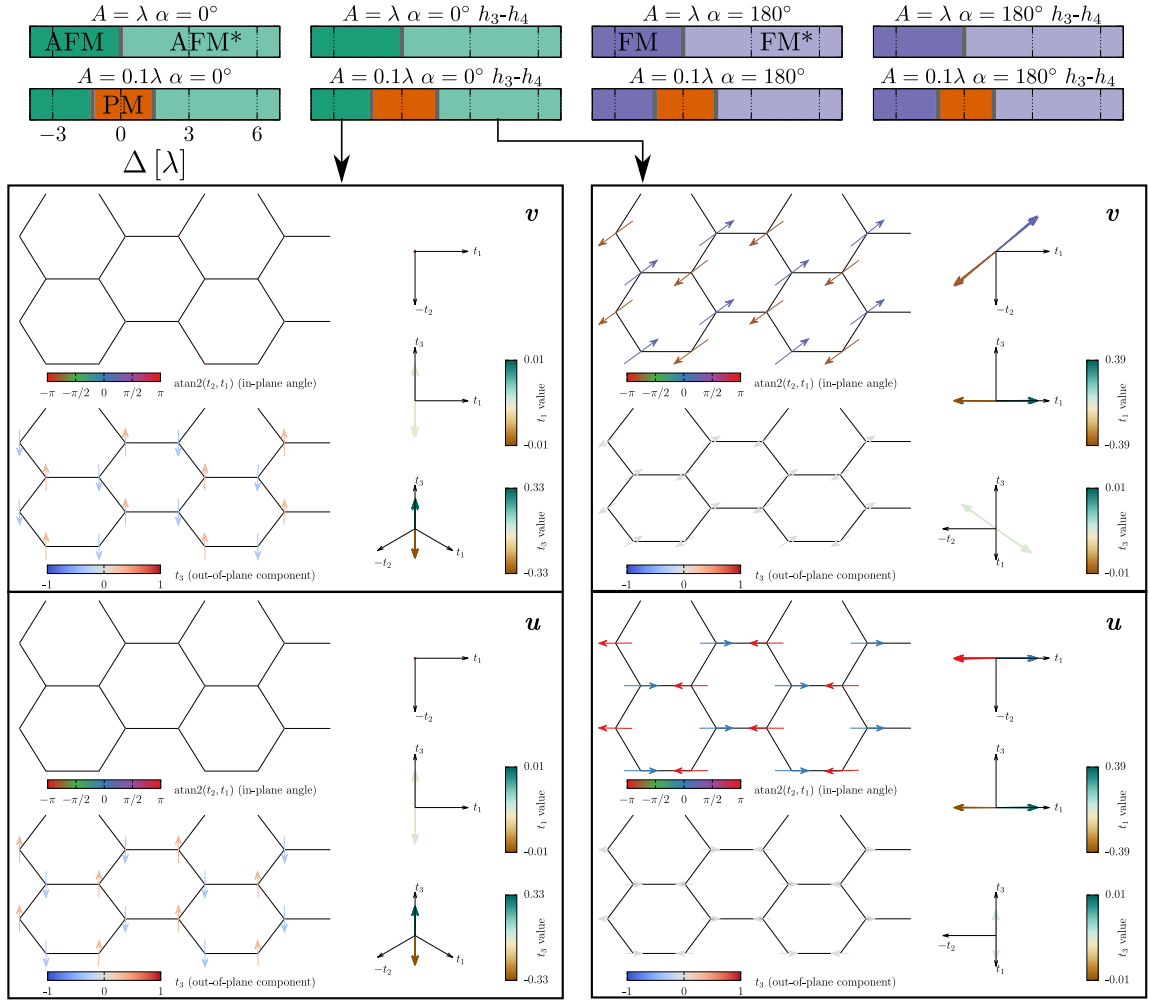


Figure 3.51. Phase diagrams and exemplary boson orders for the previously discussed FM and AFM Heisenberg models: Here t_i represent the triplon basis states in the full crystal field scheme and hence directions in the semiclassical Monte-Carlo evaluation of the order. The $\Delta < 0$ easy-axis is thus represented by the t_3 direction and the $\Delta > 0$ easy-plane (labeled by *) by the t_1 - t_2 plane. Changes between models are still minute. The main differences to the simple scheme is that $\Delta < -3\lambda$ and $\Delta > 6\lambda$ can be analyzed and all orders are involving both boson types.

mostly trivial. There is an abnormality for small $\Delta > 0$ when higher-order terms are involved (and due to $A = \lambda$ noticeable), which is expected based on a similar feature appearing in the simple scheme. Aside from that, there is the usual higher-order terms induced slight imbalance between AFM and FM condensation points.

We turn to the paramagnetic $A = 0.1\lambda$ starting point. As in the simple model,

we only observe a BEC. Noticeably, the condensation takes place at significantly lower values of Δ than in the simple scheme, which is surprising if one assumes the reduction of the effective on-site band gap (which evolves very analogously in both schemes, cf. figure 3.41) to be the main contribution. Consequently, the Heisenberg interactions, i.e. the other entities that change in the full scheme, seem to gain significant prominence. Aside from the easier condensation point, there seem to be no irregularities that point towards a nonmagnetic intermediate phase. In fact, the support for condensation seems to be in direct opposition to that.

Before making a final point about the flavor-changing magnetization, we turn to the phase diagrams and examples for a magnetic order depiction in figure 3.51. Changing the basis from Cartesian $t_x/t_y/t_z$ (resulting in vector components $x/y/z$ of \mathbf{v} and \mathbf{u}) to the $t_1/t_2/t_3$ (henceforth interchangeably used as vector component labels) frame of reference necessitates a short introduction of the geometry. Comparison with the simple field eigenstates and hence equation (3.36), dictates that t_3 inherits the easy-axis direction, i.e. the role of $\hat{\mathbf{n}}$. This is also evident when recalling that the t_3 on-site state is a purely constant entity. The ever-changing (with Δ) t_1 and t_2 directions are hence the easy-plane vectors. As expected, the system chooses an easy-axis order of both boson types for $\Delta < 0$, while aligning in the orthogonal plane for $\Delta > 0$.

We may now focus on the final abnormality in figure 3.50: Why is there a flavor-changing magnetization for $\Delta > 0$? Reflexively, one might discard this as an artifact of the way we consider the magnetization. As mentioned before, we refrained from tracking the $x/y/z$ magnetization by transferring the expression into the new basis, but rather changed to the $t_1/t_2/t_3$ directions, because we do not try to compare quantitative values (which would be akin to comparing apples to oranges). Yet, this does not seem to explain the following effect⁴. First and foremost, one can trivially

⁴At least we do not find an obvious issue with the projection behaving differently when considering $M = 2S_{t_{1/2/3}} - L_{t_{1/2/3}}$ in the $t_{1/2/3}$ basis, but that would be the point where one should look for possible inaccuracies.

see why there is no flavor term for $\Delta < 0$, because both boson types are forced onto the t_3 axis. For $\Delta > 0$ only a plane is enforced. On this plane there does not seem to be an obvious influence dictating that the bosons align their axes. Hence, one might be able to have a $\mathbf{u} \times \mathbf{v}$ component and hence a magnetic moment orthogonal to the plane. As this is something that one might be able to measure, a more formal and thorough way of bookkeeping the magnetic dipole moment could be a worthwhile project for future studies. However, for the current topic we do not care where the magnetic moment points to, so we finish the discussion at this instant.

Like for the crystal field, we should look at ED and α dependence. We start with the former. Figure 3.52 shows the resulting ground state observables. Importantly, there seem to be no features pointing to an intermediate nonmagnetic phase. Additional data can be found in appendix A.2. This is enough analysis for the purpose of this thesis. One should, however, be aware of some caveats regarding this simulation.

The Δ parameter sweeps have certain problems, which is why the fidelity and energy derivative should be handled with caution (the triplon number and other observables still seem to validate our result). With Δ , our basis changes. Thus the ground state fidelity, which consists of the overlap between old and new state, loses its well defined nature. If one really needs to rely on this quantity in future simulations, one should save the old and new basis and expand the new states in the old ones or vice versa. Similarly, the energy (and hence its derivative) has the problem of having an overall nontrivial total energy shift with Δ (a problem known from the higher-order terms analysis). However, sweeps in other parameters like A may not suffer from the same kind of problem.

There is another caveat. We might ask the reasonable question why the $\Delta = 0$ results are not identical with the simulation in absence of a trigonal field or the ones for the same value in the simple scheme (with $\Delta = 0$). Yet, there is a very straightforward explanation. Recall that we should expect a significant finite size effect for the ED cluster, e.g., for $N = 2$ the even particle sector may only have

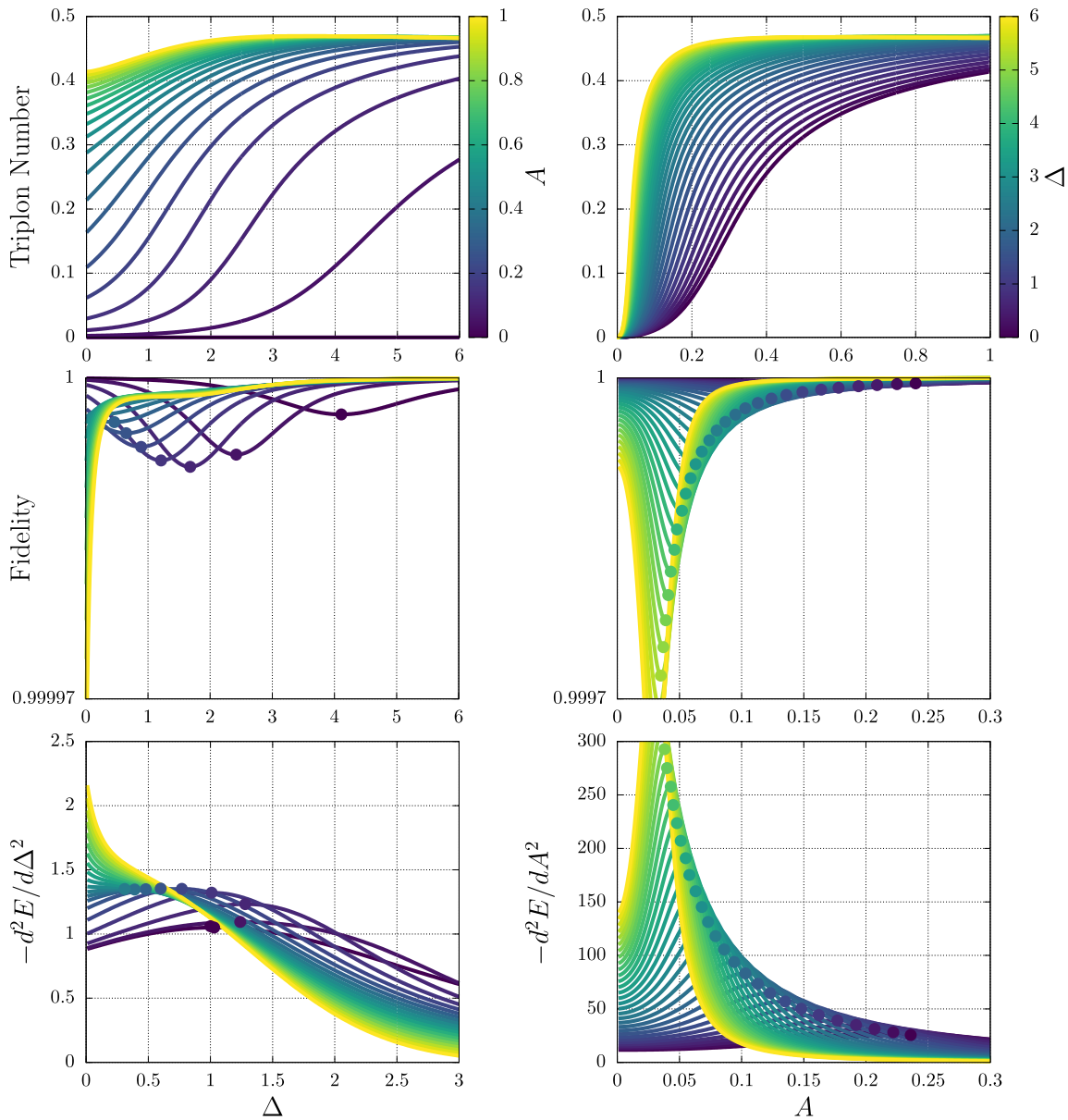


Figure 3.52. Ground state properties calculated via ED for the AFM Heisenberg model: Sweeps in Δ (left) as well as A (right) are shown. Higher-order terms are included. Extrema in the fidelity and energy derivative are marked by color map conforming dots. The fidelity and energy derivative as a function of Δ are less useful due to nontrivial energy shifts and basis change, which does not happen for A . However, no simulation shows a second transition point. The model is still found to drive from regular singlet paramagnetic phase to magnetic phase in the accustomed way.

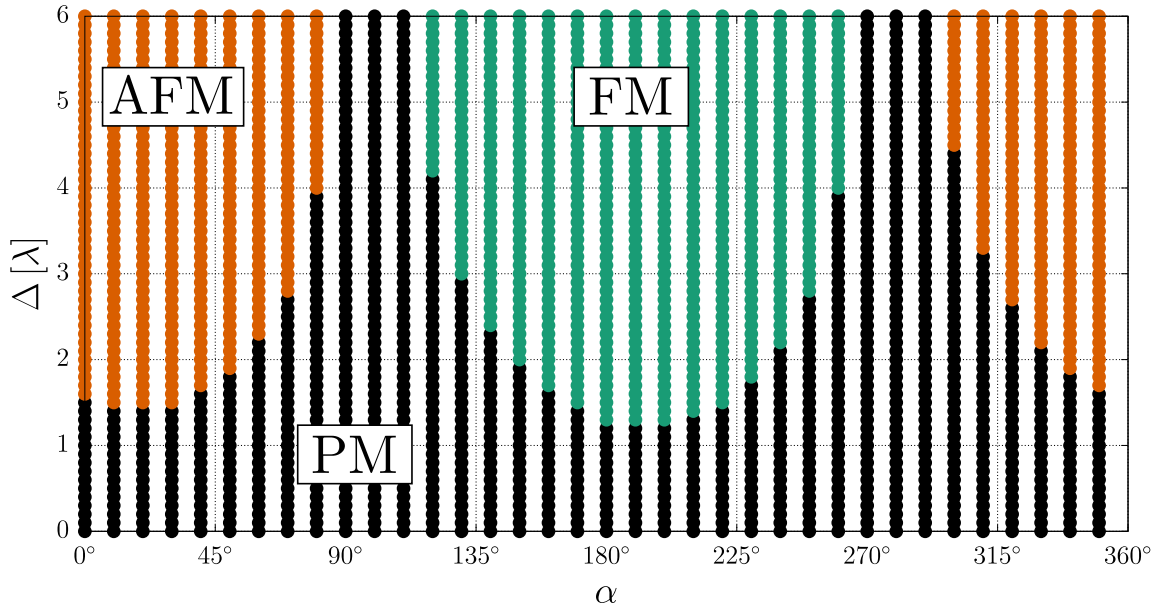


Figure 3.53. Phase diagram for the Kitaev-Heisenberg model with higher-order h_3 - h_4 terms, $A = 0.1\lambda$ and various values of interaction angle α and crystal field Δ : Even for the full crystal field model the semiclassical Monte-Carlo simulations describe the regular paramagnet and drive into magnetic phases. Here, only FM/AFM phases seem to be involved. For angles where no magnetic phase is present at $\Delta = 6\lambda$ (not enforced by a gap closing like in the simple scheme), the condensation is found to emerge at larger values as described in the text.

pair creation while the odd one can only account for triplon hopping. If one rotates the $x/y/z$ basis into a new basis, these finite size problems should be expected to change significantly. New problems can appear when, e.g., needing to account for flavor-changing terms, and the issues arise nontrivially for each bond and each flavor. Hence, the quantitative differences are no problem in principle. However, one should note that a clear sanity check is lacking for the ED simulation as a result of this. We can rotate (at least for $\Delta = 0$) to the old $x/y/z$ basis and check that our Hamiltonian is seemingly correct, but potential bugs, e.g., with the complex values being introduced, can not be completely discarded. At this point we reiterate that the complete Hamiltonian may be checked for future attempts at reproduction of our results by turning to appendix A.3.

Finally, we may turn to the α dependence, i.e. the inclusion of the Kitaev interaction. Figure 3.53 depicts the phase diagram with higher-order contributions (appendix A.2 has the analogue without h_3 and h_4). We can make the following observations: We seemingly find no other singlet than the usual PM phase. There seem to be only PM and FM/AFM. The FM/AFM phases gain prominence in both additional α values as well as a smaller Δ being sufficient to cause condensation of triplons. Additionally, no canted zigzag phase seems to exist. Moreover, there is no guaranteed condensation for all regimes at $\Delta = 6\lambda$.

The features can seemingly be explained or made plausible quite straightforwardly. Condensation is not enforced as the singlet-triplet gap does not close in the full scheme. If the crystal field, which in the full scheme alters the matrix elements, has a bias towards the Heisenberg interactions, it explains both significant decrease in condensation requirements and prominence in the α direction. We should recall that a small part of this seems to exist in the simple scheme as well.

When considering the areas where the paramagnet still remains at $\Delta = 6\lambda$, we might first note that this is a detail that may explain the absence of condensation in real materials. The zigzag order, for example, is a prominent feature in Kitaev-Heisenberg model candidate materials like Na_2IrO_3 or $\alpha\text{-RuCl}_3$ [38] (both d^5 , but this feature could possibly extend to d^4). Hence, one might have a lot of “time” before condensation has to happen and thus a lot of options to do something else under pressure, e.g. a structural transition. But does condensation take place at all? When continuing the sMC simulation to larger value we find a condensation into AFM order for $\alpha = 90^\circ$ at $\Delta \approx 7.4\lambda$, FM order at $\alpha = 110^\circ$ for $\Delta \approx 7.3\lambda$, while the $\alpha = 120^\circ$ case avoids condensation even at $\Delta = 12\lambda$. Hence, the trend seems to mostly continue as expected from the $\Delta < 6\lambda$ results.

We note that the absence of a Kitaev phase in sMC, if correctly assessed, might not mean anything as the existence should be evaluated with a thorough ED simulation in order to fully account for the quantum fluctuations. Nevertheless, the deemed

breakdown of Kitaev physics in α -RuCl₃ under pressure [219] makes this an intriguing question. Additionally, the $\alpha = 120^\circ$ case might be worth a look in future studies. However, for the purpose of this thesis we reiterate that an $N = 6$ ED simulation does not find the intermediate nonmagnetic phase either and conclude the investigation.

In summary, the incorporation of the crystal field, no matter if simple or full, seems to overall induce condensation if one is not in a very particular case of, likely frustrated, interactions. The model does not seem to be able to explain the intermediate phase found in [8].

One should therefore look for a different origin of the phase or try to modify the triplon model. In that sense, we might shortly go over the likely extensions. Next nearest neighbor interactions are expected to be able drastically change the magnetic order based on rudimentary simulations and as trivially evident in the formulas of spin-wave theory. This topic might be interesting in general. Yet, this kind of interaction does not seem suitable to explain a phenomenon located on a single dimer bond, which is a nearest neighbor problem. A different, but maybe more feasible approach, would be anisotropic bond interactions. E.g., one could start multiplying the interactions of the z bond by a given factor (for an analysis of the classical anisotropic Kitaev-Heisenberg model see reference [232]). This would likely enforce dimer like features. But it does not seem to be trivially evident how this should promote a nonmagnetic phase. Another, probably unlikely (e.g. due to it breaking down in the related α -RuCl₃ [219]), candidate explanation would be closeness to the Kitaev regime, which according to [170] is connected to valence bond (solid) features, which would connect to discussion for Li₂RuO₃. Another possible angle of attack, which we think to have a lot of promise to at least lead to interesting results, is to try and solve the problem from the Li₂RuO₃ side of things. In essence, one could try to gauge how the valence bond state suggested for Li₂RuO₃ overlaps with the triplon definitions on the two-site problem. This may give hints about the form of the interactions necessary to drive triplons into this kind of state, if this

is at all a feasible idea (like the Kugel-Khomskii and phonon based description in reference [221]). Nevertheless, the question remains unanswered and the possible connection to Li_2RuO_3 intriguing. Finally, it would be prudent to try to write down the competition between covalent bond and magnetic (triplon based) interaction explicitly and directly connect to reference [220].

4

Triplon Topology

In references [5, 6], first numerical results establishing topological phases of the triplon Kitaev-Heisenberg model were reported. Here we try to explain the nature of the topological effects, widen the scope of the analysis to other lattices and interaction types, and furthermore try to gauge in what way the discussions in other topological singlet-triplet and magnon systems [76, 77] can be adapted to our results and vice versa.

A key for this discussion is to identify what similarities and differences our setup shares with the more conventional, spin-dimer based, singlet-triplet models like $\text{SrCu}_2(\text{BO}_3)_2$ [78]. Here one should first mention the form of the spin interactions considered.

Naturally, some of the more per se model- and not material-based studies contain a broader range of interactions, e.g. a full Kitaev-Heisenberg model for a pure spin system like in the spin-ladder and bilayer based discussions in references [128, 129]. However, as mentioned in section 1.2.3, both of these and other past efforts concerning the topological spin-dimer singlet-triplet have been primarily driven by the Dzyaloshinskii–Moriya interaction. Results here have been various, even going into concepts like Dirac nodal loops [126], Weyl-triplons [127] and higher-order topological states [130].

DM interaction is allowed for our honeycomb model, but it is not expected to be

essential, neither for triplon topology nor for the nature of the spin interactions in general. Instead, the obvious discussions in the spin-orbital triplon model concern Kitaev or Γ (Γ') type interactions arising naturally due to the orbital nature of the model (as they did in the spin-1/2 Kitaev-Heisenberg model [51]).

This is part of the big overall difference concerning geometry-based motivations. A large part of the focus of dimer-based singlet-triplet discussions has been interactions arising in models based on materials like $\text{SrCu}_2(\text{BO}_3)_2$ [78, 124, 125] or $\text{Ba}_2\text{CuSi}_2\text{O}_6\text{Cl}_2$ [233], where the geometry and in particular the positioning of the dimers, i.e. the orientation of the lattice sites concerning each other, dictate the spin exchange. In particular, the form of DM interactions set restrictions for the geometry.

We, however, are technically limited by the ligand octahedra, i.e. the environment of each lattice site (that is usually just assumed implicitly) and their bond, i.e. the edge-sharing connection. While this of course in principle represents a restriction as materials of interest in the real world are not created by magically wish-fulfilling entities, the bond problem is not as strict as it appears. In theory one can still build all kinds of lattices out of these bonds. Additionally a rather free parameter study might not care about edge-sharing geometry that much, because analogous processes like d-p-p-d hopping (also discussed for the usual Kitaev-Heisenberg setups [39]) is still orbital based and can provide the anisotropic Kitaev or Γ (Γ') type interactions.

All in all, this naturally prompts a more qualitative approach regarding the availability of topologically nontrivial states in our kind of setups. Hence, we try to extend the scope, primarily to different geometries.

Another big difference concerning the spin-dimers are the energy scales involved. The case of DM interactions illustrates this point. Furthermore, in, e.g., a spin-1/2 dimer the antiferromagnetic exchange separates singlet and triplet while for us the spin-orbit coupling takes this role. For previously cited $\text{SrCu}_2(\text{BO}_3)_2$ [125], the energy scales were favorable enough to make signatures of topological triplons well

accessible for experiments. One might have to discuss if the spin-orbital models are expected to perform similarly, better or worse in this regard.

Other differences arise from our discussions above: Due to the spin-orbital nature of the dimer creating our singlet-triplet model, magnetic field and crystal field distortions might have different impact. Especially for the magnetic field, which is usually directly responsible for the nontrivial topology, this distinction is important.

Last but not least, one should acknowledge that there is general interest in Kitaev-Heisenberg based topology stemming from the recent thermal Hall effect discussion for α -RuCl₃. There are features such as a special sign structure in the thermal Hall response and specific heat [54, 234], whose origin has been a point of analysis [235, 236] as it has been connected to the spin-liquid and Majorana fermions as well as more conventional magnons [59]. It is therefore inherently interesting to find out what happens in our model, which represents a related setup.

This chapter tries to provide answers to these questions in the following way: First, in section 4.1, we introduce the triplon model whose topology we subsequently try to analyze and talk about approximations that need to be made in order to do so. Next, in section 4.2, we revisit the honeycomb lattice model where first numerical results have been found in references [5, 6]. However, we significantly broaden the scope of the previous studies by performing more exhaustive numerical evaluations, considering arbitrary magnetic field directions and explaining the emerging topological phenomena based on models we derive for the high- and low field limits as well as discussing the underlying spin- L bosonic Dirac-cone physics. Moreover, we include the trigonal crystal field in this analysis.

Thereafter, we search for triplon topology as in our model in other kinds of setups, starting with a detailed analysis of the triangular lattice in section 4.3, where some noticeable distinctions compared to the honeycomb can be made. Finally, we provide an overview over other geometries and interactions in 4.4.

4.1 Triplon Hamiltonian

Based on previous discussions (cf. sections 1.4.5.2 and 2.1), we consider the following Hamiltonian:

$$\begin{aligned}
 H = & \lambda \sum_{i,\alpha} n_{i,\alpha} + J \sum_{\langle i,j \rangle} \left(\mathbf{T}_i^\dagger \mathbf{T}_j - c_J \mathbf{T}_i^\dagger \mathbf{T}_j^\dagger + \text{h.c.} \right) \\
 & + K \sum_{\gamma} \sum_{\langle i,j \rangle_{\gamma}} \left(T_{\gamma,i}^\dagger T_{\gamma,j} - c_K T_{\gamma,i}^\dagger T_{\gamma,j}^\dagger + \text{h.c.} \right) \\
 & + \Gamma \sum_{\gamma} \sum_{\langle i,j \rangle_{\gamma}} \left(T_{\alpha,i}^\dagger T_{\beta,j} + T_{\beta,i}^\dagger T_{\alpha,j} - c_{\Gamma} \left(T_{\beta,i}^\dagger T_{\gamma,j}^\dagger + T_{\gamma,j}^\dagger T_{\beta,i}^\dagger \right) + \text{h.c.} \right),
 \end{aligned} \tag{4.1}$$

where $c_J/c_K/c_{\Gamma}$ are real constants. For their values see equation (1.77); they are roughly of order one and were at times set to one for simplification. Furthermore, $\gamma \in \{x, y, z\}$ labels a bond and thus triplon flavor, with α and β representing the other ones via cyclic permutation.

This Hamiltonian is, however, not the one we analyze in this thesis. An important assumption is missing and needs to be included. We assume a regime located well inside the paramagnetic phase of the model, meaning $\lambda \gg J/K/\Gamma$. In the subsequent paragraphs we explain the hows and whys of this assumption. It should be noted that this scenario is directly equivalent to previous studies in dimers, e.g. in reference [78], where the excitations, which represent the topological objects of interest, are also uncondensed triplets/triplons.

First, we try to establish why this distinction should probably be made. Topological states of matter are an extremely broad topic with a plethora of effects and phenomena, as one can easily gauge from reviews such as references [237, 238], which do not even touch the subcategory of topological magnetic excitations [77] that we discuss here, or by considering the Nobel Prize awarded for this field of research to Thouless, Haldane and Kosterlitz in 2016. We try to break it down in terms of

the historically important quantum Hall effect (even though the many variations of quantum Hall effects could also be its own topic) in a quick and rough manner.

With the experimental sensation of the integer quantum Hall effect [239] came explanations about the underlying physics, one of which was given by Thouless et al. by considering an electron gas in a two-dimensional periodic potential, i.e. a band structure based picture. This description of the quantization of the Hall conductance by a (so called TKKN) invariant was later connected to the more or less equivalent, more mathematically based, Chern number [240]. In a physical sense, the Hamiltonian $H(\mathbf{k})$ depends on momentum \mathbf{k} , which takes the role of the adiabatically changing parameter in the Berry phase [241]. The Chern number is then the total amount of Berry curvature in the entire Brillouin zone.

This interpretation and way of establishing topology necessitates the existence of a band to carry the \mathbf{k} . Therefore, it is limited to a non-interacting system (i.e. electron gas) or effective single-particle description. However, it is also clear that any kind of particle forming a band will do. Hence one is not limited to electrons like in the original quantum Hall effect. Bosons can have topologically nontrivial states. Similarly having a band structure in ground or excited states is not important as long as there is a band. As a result, the topological magnons/triplons, which are excitations forming bands, are not a surprise and covered by the well known formulas for the Chern number¹.

Going into situations where many-particle interactions or impurities become important requires extra work [242, 243], as the single-particle formulations and having a band structure per se become equivocal. Many-particle effects can change the situation drastically, which is probably most famously evidenced by the fractional quantum Hall effect [244]. Here the Coulomb interaction between the electrons is essential, which is to be expected as the original experiment set out to find a Wigner

¹But not the Hall effect: The particles are not charged and hence the thermal Hall effect needs to be discussed instead.

solid, i.e. a structure where the Coulomb repulsion is so strong that the electrons themselves form a lattice in order to maximize their distance from each other.

Hard-core bosons are intrinsically interacting via the on-site hard-core constraint. This can be directly related to an effective Coulomb repulsion: In a normal Bose-Hubbard model the so called “hard-core limit” is established by going to the limit of $U \rightarrow \infty$ for the Hubbard-interaction equivalent (cf. equation (1.49)) for bosons [245].

Consequently, discriminating between a regime where boson interactions are relevant or not is essential for the approach of the discussion and topological invariants. Finally, the nature of restricting ourselves to the paramagnetic regime becomes apparent: With enough distance to the critical point where triplons condense, there should not be enough bosons around to make hard-core interactions crucial for the description of the material and hence a topology can manifest itself in a band structure picture. In the condensed phase one has to rethink as triplon numbers become sizable.

Therefore, we focus on the paramagnetic regime and resulting topological band structure of triplon excitations. Remarks concerning the condensed phase and fractional quantum Hall effect are relegated to section 4.4.5.

It should, however, be pointed out that neglecting interactions can be a quite forgiving assumption even in non-obvious cases. $\text{SrCu}_2(\text{BO}_3)_2$ has been argued to exhibit experimental signatures consistent with topological triplons, which may survive (of course with changes) the influence of a two-triplon bound state crossing into the area of band-structures of the single-triplon environment [125].

Coming back to the Hamiltonian in equation (4.1) one can now ask what kind of approximations are suitable in the paramagnetic phase. Naturally, just the Hamiltonian alone emerging from h_2 terms with neglect of h_3 and h_4 (cf. section 1.4.5.2) is one such simplification. Moreover, one can take a closer look at the pair creation and annihilation terms. Technically one could handle them via Bogoliubov

transformation (cf. section 2.1), because the Bogoliubov quasiparticles look like free single-particle solutions. There are however arguments for outright ignoring the pair terms, which is useful because this saves a lot of work.

Firstly, one can note that the pair terms connect particle sectors with $N \pm 2$ bosons, e.g. the empty vacuum state with the one filled by $N = 2$ particles or the first excited state $N = 1$ with $N = 3$. As each boson costs λ and we strive for $\lambda \gg J/K/\Gamma$, there is a large energy gap of 2λ separating the states and they would enter only perturbatively.

Secondly and more importantly, there has been progress since reference [5] regarding the understanding of the model. In this thesis we explicitly link the topology to Dirac-cone physics in the limiting cases. Furthermore, we survey the intermediate regime to find that this might continue to explain the model beyond its limiting cases. In reference [246] bosonic Dirac-cone physics in general have been linked to fermionic models, which hugely helps with handling and interpreting them. Therein, the triplon model of reference [5] has been explicitly mentioned as falling into this category.

A big result of reference [246] is that the neglect of pair terms is not necessary to establish the Dirac-cone topology, i.e. we obtain the same physics either way. This is an incredibly powerful result as the approximation of pair terms is done with a given regularity, which the authors also point out by explicitly citing a large array of models (ours included) where the assumption is of this nature. It is therefore expected that neglect of pair terms changes the exact value of phase boundary but not the Dirac-cone physics establishing the topological band structure. One can therefore rephrase equation (4.1) by setting all c_{\dots} constants to 0.

Given that there is now no entity connecting the particle sectors of the model, one can just observe each one separately. As a result, λ as an energy scale is just reduced to a constant energy shift, e.g. in the one particle sector, and can be discarded for the calculation of the Chern number. One should however not discard the term

when the absolute energy scale becomes important, as is the case for the thermal Hall conductivity, where the temperature needs to set the occupation of the excited states via the Bose-Einstein distribution.

Even so, there is one more approximation that can and maybe needs to be made for the topological band structure analysis. We want to introduce a magnetic field, i.e. add the following term (cf. equation (1.91)) to the Hamiltonian

$$H_{\text{mag}} = h \sum_i \hat{\mathbf{h}} \cdot \langle \mathbf{M}_i \rangle_{s,t} = h \sum_i \hat{\mathbf{h}} \cdot \left[-i\sqrt{6} (\mathbf{T} - \mathbf{T}^\dagger) - \frac{i}{2} (\mathbf{T}^\dagger \times \mathbf{T}) \right], \quad (4.2)$$

where h is the strength of the magnetic field and $\hat{\mathbf{h}}$ a normalized vector representing its direction.

Here one should recall the discussions comparing the nature of the terms in the magnetization in, e.g., section 1.5.2: $(\mathbf{T}^\dagger \times \mathbf{T})$ is the Zeeman term splitting the triplons. It is the term found usually in spin-dimers and involved in the usual discussions of triplet topology like in reference [78]. But here we also have the Van Vleck term $(\mathbf{T} - \mathbf{T}^\dagger)$ to deal with and in discussions regarding the condensation we found it to dominate. Furthermore, the Van Vleck term destroys the non-interacting nature of the model by connecting the particle sectors.

One can argue that very deep in the paramagnetic phase the Zeeman term is relevant and maybe even dominant. Formally the term is also suppressed by an energy gap λ to the $N \pm 1$ particle sectors. Also the stabilization of the ground state is not that important and changing the exact values of the splitting will turn out to be inconsequential. So there are reasons not to outright discard this model, even apart from pure interest in the topology, removed from direct material based motivations. Yet, this (and the thermal Hall signature being minute because of the energy scales involved) is probably the biggest issue when it comes to the possibility of a the direct experimental realization based on at least the material class we aim to describe with the broader scenario of the excitonic Kitaev-Heisenberg model. Nevertheless, we will

ignore the Van Vleck term in the subsequent calculations.

It should be noted that the spin-dimers not only have no Van Vleck term, but the Zeeman splitting is additive (cf. equation (1.115)) and thus relatively larger (aside from comparing apples to oranges in regards to spin-dimer and spin-orbital dimer magnetizations). Therefore this triplon model would gain significant importance if Kitaev interactions could arise for ordinary spin-dimers.

Naturally, there is a reason for the ubiquitousness of Kitaev model approaches based on the Jackeli-Khaliullin mechanism [47] and thus our problem, as the orbital involvement making the directional anisotropy possible is exactly what provides the Van Vleck term.

Nonetheless, there exist suggestions for alternative ways to produce Kitaev interactions in which the situation may be better. For example the fundamental toolbox papers for ultracold atoms [247] and polar molecules [248] in optical lattices both include the possibility. Especially the later is noteworthy as very similar topology implicitly based on a (manipulated) hard-core boson singlet-triplet setup for molecules with dipole-dipole interactions [249], where the molecule rotations are governed by a $H \sim \mathbf{J}^2$ Hamiltonian, exists. Yet, research into Kitaev physics themselves is not prominent. A recent study [250] for example established that any Kitaev spin-liquid phase would be destroyed for ultracold polar molecules due to the long range nature of the interactions. For our purposes, the existence of Kitaev type interactions is essential and not them being in any form dominant or able to establish a spin-liquid, so that might be worth to keep in mind. Moreover, sometimes topical proposals still emerge in completely new setups, like the quantum dot and magnetic field manipulation based model in reference [251]. Furthermore, even without material based motivation, one can write down and study Kitaev-type Hamiltonians with normal spins.

For the latter case, there is a noteworthy paper which has been published very recently during the creation of this thesis [252]. Therein, a Kitaev-Heisenberg model

is studied on the star lattice. In the valence bond solid phases the spins combine on given bonds, motivating a singlet-triplet model on an effective kagome lattice. The topological band structure of the triplets in a magnetic field is analyzed. Following the subsequent discussions of the topological triplon model, one can understand why their model works and moreover even predict many features of the, at first glance, kaleidoscopic mess of a phase diagram, even down to some significant values of the Chern numbers. This creates a direct motivation of gauging the overall trends of the triplon topology in our model.

Finally, after the approximations, the Hamiltonian analyzed for its (or the lowest excitations') topological band structure is

$$\begin{aligned}
 H = & J \sum_{\langle i,j \rangle} \mathbf{T}_i^\dagger \mathbf{T}_j + \sum_{\gamma} \sum_{\langle i,j \rangle_{\gamma}} \left[K T_{\gamma,i}^\dagger T_{\gamma,j} + \Gamma \left(T_{\alpha,i}^\dagger T_{\beta,j} + T_{\beta,i}^\dagger T_{\alpha,j} \right) \right] + \text{h.c.} \\
 & + i h \sum_i \hat{\mathbf{h}} \cdot (\mathbf{T}^\dagger \times \mathbf{T}), \tag{4.3}
 \end{aligned}$$

where we re-scaled h for later convenience and consistency with old results [5, 6]. Recall that the Kitaev-Heisenberg part can be parametrized via $J = A \cos(\alpha)$ and $K = A \sin(\alpha)$. We can now start the analysis of this model.

4.2 Triplon Topology on the Honeycomb Lattice

The triplon topology on the honeycomb lattice has been the subject of study in references [5] and [6]. Regardless, there are reasons to give it another look. First of all, the results are limited to purely numerical analysis of the Kitaev-Heisenberg model in $\mathbf{h} = [1, 1, 1]^T$ direction and $\Gamma \neq 0$ in $[1, 1, 1]$ and $[0, 0, 1]$. These numerical results were important to establish existence and interest, but they are flawed either by computational difficulties (unfinished areas and merged band interpretations),

some mistakes in the phase diagrams of the latter two cases and a non-normalized magnetic field making the interpretation more difficult. Furthermore, the in-plane magnetic fields were omitted as topologically trivial.

Here, we reestablish the old results cleanly. Additionally we derive models in the limits of large magnetic field $h \gg J/K/\Gamma$ and dominant coupling (vicariously via) $K \gg h$ and analyze them thoroughly. We also establish an interpretation of the topology as being based on bosonic Dirac-cone physics. Moreover, we take a closer look at the parameter space regarding orientation of the magnetic field and size and form of interactions, in particular by including a trigonal field distortion. Discussions of the latter have in the past been relegated to a (illustrating) side note in reference [5], where it was established that the magnetic field could also be substituted by next-nearest neighbor DM interactions and a trigonal splitting resulting in a reproduction of the famous Haldane model [253].

We start by assessing the topological band structure by taking a closer look at the Kitaev limit $J = \Gamma = 0$.

4.2.1 Kitaev Interactions and Limiting Cases

The Chern number of band n can be calculated by finding the eigenstates and energies of the Hamiltonian in equation (4.3) and using

$$\begin{aligned}
 C_n &= -\frac{1}{2\pi} \text{Im} \int_{\text{BZ}} d\mathbf{S} \cdot \boldsymbol{\Omega}_n(\mathbf{k}), \\
 &= -\frac{1}{2\pi} \text{Im} \int_{\text{BZ}} d\mathbf{S} \cdot \sum_{m \neq n} \frac{\langle n(\mathbf{k}) | (\nabla_{\mathbf{k}} H(\mathbf{k})) | m(\mathbf{k}) \rangle \times \langle n(\mathbf{k}) | (\nabla_{\mathbf{k}} H(\mathbf{k})) | m(\mathbf{k}) \rangle}{(E_n(\mathbf{k}) - E_m(\mathbf{k}))^2} \\
 &= -\frac{1}{2\pi} \text{Im} \int_{\text{BZ}} d^2\mathbf{k} \sum_{m \neq n} \frac{\langle n(\mathbf{k}) | (\partial_{k_x} H(\mathbf{k})) | m(\mathbf{k}) \rangle \langle n(\mathbf{k}) | (\partial_{k_y} H(\mathbf{k})) | m(\mathbf{k}) \rangle - x \leftrightarrow y}{(E_n(\mathbf{k}) - E_m(\mathbf{k}))^2},
 \end{aligned} \tag{4.4}$$

where the integrand represents the Berry curvature² $\boldsymbol{\Omega}_n(\mathbf{k})$, $|n(\mathbf{k})\rangle$ the eigenstate

²We call the z-component of it, i.e. the integrand in the last line of the equation, just Berry curvature hereinafter for convenience.

with energy E_n and we used its well known gauge-independent formulation [240] and inserted the two-dimensional structure of the Brillouin zone.

The Kitaev limit provides a phase diagram with three distinct Chern number configurations [figure 4.1a)]. In the low magnetic field limit $h \ll K$ the Chern numbers are $C = \{-1, 0, 1, -1, 0, 1\}$ (lowest to highest band). For dominant magnetic fields $h \gg K$ the topological invariant is instead fixed to $C = \{-1, 1, -1, 1, -1, 1\}$. Transitions to and out of an intermediate phase $C = \{-1, 0, 0, 0, 0, 1\}$ happen at $h = K$ and $h = 2K$. For most of the discussions in this thesis, the upper three bands can be inferred from the lower ones as in this example. Therefore, we will subsequently limit ourselves to providing the lowest three band Chern numbers.

The phase diagram in the Kitaev limit can be understood in its entirety. The main reason is that in the absence of a magnetic field the Kitaev interactions produce a nondispersive band structure (and vice versa), i.e. an obvious degeneracy that is lifted in a topologically nontrivial way. Although the combination of magnetic field and Kitaev terms introduces intriguing dispersive behavior [figure 4.5a)] by allowing an on-site flavor change coupled to an imaginary phase i , the gaps produced by the energy scales are straightforward and dictate the topological phase transition via band touching points. As a result, the $h \ll K$ phase is expected to exist up to $h = K$ and the $h \gg K$ limit emerges at $h = 2K$.

These results have been known from reference [6] (although fixing the norm of the vector makes the energy scales more obvious here). But what happens when we try to find out how the degeneracy in the limiting cases is actually lifted?

4.2.1.1 Analysis of the High- and Low-Field Limit

The spectral structure in both limits motivates the construction of effective Hamiltonians as a way to interpret the topological invariant and its origin. The degeneracy is provided by the triplon flavors $\alpha \in \{x, y, z\}$ and the two sublattices of the honeycomb lattice. We choose a basis of the correspondingly labeled states $|x_1\rangle, |y_1\rangle, |z_1\rangle,$

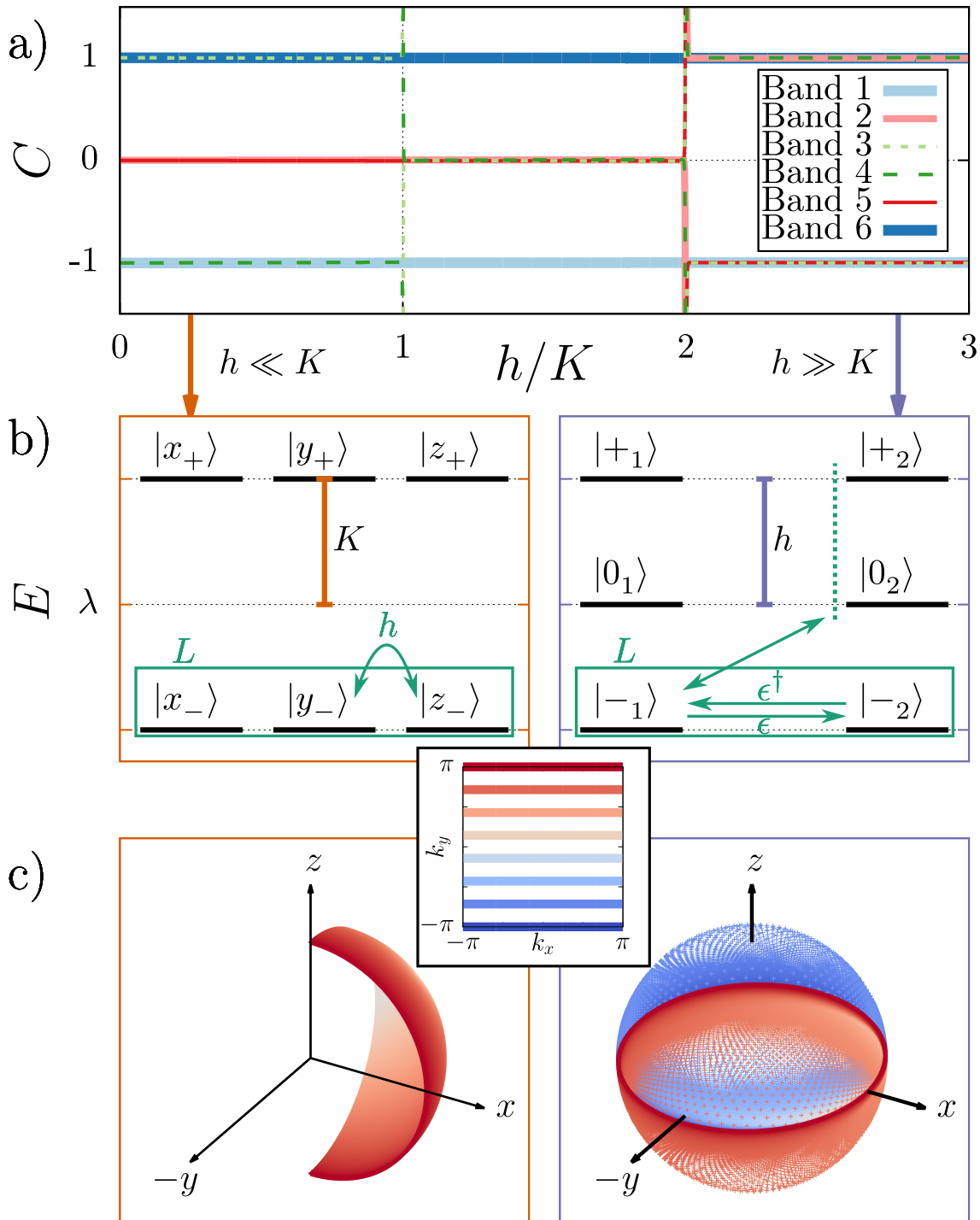


Figure 4.1. a) Chern numbers of the triplon excitations in the pure Kitaev model as a function of the magnetic field \mathbf{h} in $[1, 1, 1]$ direction. b) Schematic sketch of the ideas behind the effective Hamiltonians in each limit: In the limit of large Kitaev interaction $K \gg h$ the bonding and anti-bonding states of the sublattices are degenerate while in the $h \gg K$ limit the sublattices themselves are degenerate. c) Position of the winding number $\hat{n}(\mathbf{k})$ throughout the Brillouin zone (distorted to a square for simplicity).

$|x_2\rangle$, $|y_2\rangle$ and $|z_2\rangle$, where the index denotes the sublattice. The Hamiltonian takes the form

$$H = \left(\begin{array}{c|c} \mathbf{h}_m & \boldsymbol{\epsilon} \\ \hline \boldsymbol{\epsilon}^\dagger & \mathbf{h}_m \end{array} \right), \quad \boldsymbol{\epsilon} = \begin{pmatrix} \epsilon_x & \gamma_z & \gamma_y \\ \gamma_z & \epsilon_y & \gamma_x \\ \gamma_y & \gamma_x & \epsilon_z \end{pmatrix}, \quad \mathbf{h}_m = \frac{h}{|\mathbf{h}|} \begin{pmatrix} 0 & -ih_z & ih_y \\ ih_z & 0 & -ih_x \\ -ih_y & ih_x & 0 \end{pmatrix}, \quad (4.5)$$

where ϵ_α and γ_α denote the standard Fourier transformation of the triplon hopping terms in equation (4.3) (cf. section 2.1) and \mathbf{h}_m represents on-site magnetic field terms with direction \mathbf{h} being introduced in equation (4.2). For the discussion of the Kitaev case here $\gamma_\alpha = 0$ and ϵ_α consist only of a single Kitaev term.

The limiting cases consist of threefold ($h \ll K$) and twofold ($h \gg K$) degenerate energy manifolds [figure 4.1b)]. When $K \gg h$ one needs to build new eigenstates using the off-diagonal matrix elements of equation (4.5), i.e one creates a bonding and anti-bonding state for each flavor $|\alpha_\pm\rangle = c_{\alpha,1,\pm} |\alpha_1\rangle + c_{\alpha,2,\pm} |\alpha_2\rangle$. The states (for each flavor) live at the (for the Kitaev case \mathbf{k} independent) energy $E_\pm = \pm K$. The flavors themselves stay degenerate. For $h \gg K$ the on-site magnetic field results in three eigenstates and eigenenergies and the degeneracy is based on the sublattices.

We strive to apply an interpretation of both limits via winding numbers, or more precisely, spin- L generalized Dirac-cone physics. This has been described in reference [78]. It requires the Hamiltonian to be rewritten in the form of $H = n_0 \mathbb{1} + \mathbf{n} \mathbf{L}$, where $\mathbb{1}$ and $\mathbf{L} = (L^x, L^y, L^z)^T$ represent unit and angular momentum matrices and \mathbf{n} as well as n_0 are parameters.

In these spin- L physics setups the form of \mathbf{n} characterizes the topology of the $(2L + 1)$ band system. If there is no band touching point, i.e. if $\mathbf{n} \neq 0$, one can establish a map from the 2D Brillouin zone to the unit sphere in three dimensions via the normalized vector $\hat{\mathbf{n}}$. The winding number, or skyrmion count (there are no real-space skyrmions here, but this interpretation is common, see e.g. reference

[254]), $W_n \in \mathbb{Z}$ of \mathbf{n} is then calculated via

$$W_n = \frac{1}{4\pi} \int_{\text{BZ}} dk_x dk_y \hat{\mathbf{n}} \cdot \left(\frac{\partial \hat{\mathbf{n}}}{\partial k_x} \times \frac{\partial \hat{\mathbf{n}}}{\partial k_y} \right), \quad (4.6)$$

where $\hat{\mathbf{n}}$ represents the normalized vector \mathbf{n} .

The Chern number of the two respectively three bands is related to the skyrmion count via $C = 2m_n W_n$, where m_n relates to the m quantum number of the angular momentum, which here can be connected to each band [78]. In particular $C = \{W_n, -W_n\}$ for $L = 1/2$ and $C = \{2W_n, 0, -2W_n\}$ for $L = 1$.

This formula is the generalization of the well known and used winding number interpretation normally employed for two-band systems [238]. Obviously, any(!) two-band system can be written in the required form via Pauli matrices $H = n_0 \mathbb{1} + \mathbf{n} \boldsymbol{\sigma}$ as this is a general feature of 2×2 hermitian matrices.

For the three-band model, being able to rewrite the Hamiltonian in this form is not obvious. Being able to do it is a handy direct proof of underlying spin- L Dirac-cone physics being present. Using the spin-1 matrices $(L_\alpha)_{\beta\gamma} = -i\epsilon_{\alpha\beta\gamma}$ and the unitary transformations $x \rightarrow xe^{-i\mathbf{k}\mathbf{r}_x/2}$ and $y \rightarrow ye^{i\mathbf{k}\mathbf{r}_y/2}$ we find

$$H_{h \ll K} = K \mathbb{1} - \begin{pmatrix} 2h_x \cos(\mathbf{k}\mathbf{r}_y) \\ 2h_y \cos(\mathbf{k}\mathbf{r}_x) \\ 2h_z \cos(\mathbf{k}(\mathbf{r}_x - \mathbf{r}_y)) \end{pmatrix} \cdot \begin{pmatrix} L^x \\ L^y \\ L^z \end{pmatrix}, \quad (4.7)$$

and analogous for the $E = -K$ system (we get two spin-1 copies for the two threefold degenerate $K \gg h$ and three spin-1/2 for the twofold degenerate $h \gg K$). Here we deformed the honeycomb lattice by the (free) choice of lattice vectors to a square lattice and the vectors $\mathbf{r}_x = (1, 0)^T$ and $\mathbf{r}_y = (0, 1)^T$ denote the distance to the nearest neighbor unit cell. However, any other choice could be used by inserting different vectors \mathbf{r}_x and \mathbf{r}_y .

The resulting Chern numbers are $C = \text{sign}(h_x h_y h_z) \cdot \{-1, 0, 1\}$ if $h_{x/y/z} \neq 0$. If

one of the components $h_{x/y/z} = 0$, then the Chern number is ill-defined because of a remaining degeneracy and would remain trivial even if this problem did not exist. In regards to the winding number [cf. figure 4.1c)], $\hat{\mathbf{n}}$ covers the entire sphere multiple times, but requires more than one Brillouin zone to do so.

A direct consequence of this calculation is the insight that the magnetic field being perpendicular, i.e. in $[1, 1, 1]$ direction, is not the make-or-break criterion for topologically nontrivial bands! Case in point, the field in $[1, 1, -2]$ direction, which corresponds to a vector parallel to the honeycomb plane direction produces the same Chern numbers but with an overall change of sign. The limiting factor for topological triviality is any \mathbf{h} component being zero, as would have been the case for a more naive choice of in-plane field $[1, -1, 0]$, but also for $[1, 1, 0]$, which has a perpendicular component. Topologically nontrivial bands thus exist for all directions with three nonzero components of the magnetic field.

We subsequently investigate the $h \gg K$ limit. The magnetic field provides three eigenstates $|0\rangle$ and $|\pm\rangle$ with energies $E_0 = 0$ and $E_{\pm} = \pm h$ [figure 4.1b)]. Being a pure on-site interaction, the energies of the honeycomb lattice are twofold degenerate due to the unit cell. For a given twofold degenerate system of states belonging to sublattices 1 and 2, a general effective Hamiltonian (up to an energy shift) takes the form (basis $\{|0\rangle_1, |0\rangle_2\}$ where the index denotes the sublattice)

$$H = \begin{pmatrix} \mu_1 & \rho^* \\ \rho & \mu_2 \end{pmatrix}, \quad \implies \quad \mathbf{n} = \begin{pmatrix} \text{Re}(\rho) \\ \text{Im}(\rho) \\ \frac{\mu_1 - \mu_2}{2} \end{pmatrix}, \quad (4.8)$$

where Re/Im denotes the real/imaginary part and ρ as well as $\mu_{1/2}$ are general parameters discussed later.

Due to the winding number interpretation always being possible in a two-band system, we derive the essential formulas in a more general context. The fundamental consequence of the form of \mathbf{n} is that if $\mu_1 = \mu_2$, i.e. in cases where the sublattice

symmetry is upheld, the resulting band structure is at best topologically trivial if not even ill-defined. Therefore, one can instantly conclude that next-nearest neighbor interactions, which stay on a sublattice and are real, are not essential for the topology in this limit and do not contribute to it.

The block structure of the Hamiltonian (4.5) implies the form of the relevant processes as illustrated in figure 4.1. Straightforwardly, we find

$$\begin{aligned} \rho_{|0\rangle} &= \langle 0_2 | \epsilon | 0_1 \rangle = \frac{1}{|h|^2} \left(h_x^2 \epsilon_x + h_y^2 \epsilon_y + h_z^2 \epsilon_z \right. \\ &\quad \left. + 2h_x h_y \gamma_z + 2h_x h_z \gamma_y + 2h_y h_z \gamma_x \right), \\ \rho_{|\pm\rangle} &= \langle \pm_2 | \epsilon | \pm_1 \rangle = \frac{1}{2|h|^2} \left((h_y^2 + h_z^2) \epsilon_x + (h_x^2 + h_z^2) \epsilon_y + (h_x^2 + h_y^2) \epsilon_z \right. \\ &\quad \left. - 2h_x h_y \gamma_z - 2h_x h_z \gamma_y - 2h_y h_z \gamma_x \right). \end{aligned} \tag{4.9}$$

For Kitaev interactions in the perpendicular $[1, 1, 1]$ case, the ρ terms resemble the dispersion produced by Heisenberg interactions, implying that there always is a degeneracy at the K points in the Brillouin zone for $n_z = 0$.

The n_z component is derived in second order perturbation theory describing virtual excitations to the other energy levels on the opposite sublattice [figure. 4.1b)] (formula cf. equation (1.51)). Inherent symmetries and aspects of the eigenstates such as $|-\rangle = (|+\rangle)^*$ can be used to simplify the calculation significantly. As a result the $|\pm\rangle$ shares the same terms as the $|0\rangle$ levels, with reduced numerical values. Additionally the $|\pm\rangle$ have unique contributions via $|\pm\rangle \rightarrow |\mp\rangle \rightarrow |\pm\rangle$ processes. Here, we discuss n_z on the $|0\rangle$ level, as an example, but provide all terms for later analysis of the limit in the phase diagram.

We find

$$\begin{aligned}
 \mu_1^{(0)} &= \sum_{\pm} \left(\frac{\langle 0|_1 \epsilon^\dagger |\pm\rangle_2 \langle \pm|_2 \epsilon |0\rangle_1}{E_{\pm} - E_0} \right) \\
 &= \frac{\langle 0|\epsilon^\dagger|+\rangle \langle +|\epsilon|0\rangle}{|h|} - \frac{\langle 0|\epsilon^\dagger|-\rangle \langle -|\epsilon|0\rangle}{|h|} \\
 &= \frac{|\langle +|\epsilon|0\rangle|^2}{|h|} - \frac{|\langle -|\epsilon|0\rangle|^2}{|h|} \\
 &= \frac{|\langle +|\epsilon|0\rangle|^2}{|h|} - \frac{|\langle +|\epsilon^\dagger|0\rangle|^2}{|h|},
 \end{aligned} \tag{4.10}$$

where we drop the sublattice index because the on-site states are the same. The last lines are a peculiarity of the system, which is possible due to $|-\rangle = (|+\rangle)^*$, $|0\rangle = (|0\rangle)^*$, $\epsilon^\dagger = \epsilon^*$, $\langle \Phi|A|\Psi\rangle = (\langle \Psi|A^\dagger|\Phi\rangle)^*$ and $|c\rangle = |c^*\rangle$.

For μ_2 the roles of ϵ^\dagger and ϵ switch, which is compensated by the minus sign and factor 1/2 in n_z . We find

$$\begin{aligned}
 n_z^{(0)} &= \mp \frac{1}{|h|} \left(|\langle \pm|\epsilon|0\rangle|^2 - |\langle \pm|\epsilon^\dagger|0\rangle|^2 \right) \\
 &\equiv \frac{1}{|h|^4} \left(\Delta\mu_{\epsilon\epsilon}^{(0)} + \Delta\mu_{\epsilon\gamma}^{(0)} + \Delta\mu_{\gamma\gamma}^{(0)} \right),
 \end{aligned} \tag{4.11}$$

where we separated the contributions of different parts of the ϵ matrix for discussion. Without Γ contributions (which are discussed later), only $\Delta\mu_{\epsilon\epsilon}$ is active. We find

$$\Delta\mu_{\epsilon\epsilon}^{(0)} = \frac{h_x h_y h_z}{2} \text{Im} \left[\epsilon_x (\epsilon_y^* - \epsilon_z^*) + \epsilon_y (\epsilon_z^* - \epsilon_x^*) + \epsilon_z (\epsilon_x^* - \epsilon_y^*) \right]. \tag{4.12}$$

For $|\pm\rangle$, perturbation theory works analogously. There is always a contribution from the $|0\rangle$ state that has familiar form. New terms might appear via $|+\rangle \rightarrow |-\rangle$ suppressed by an energy gap of $2|h|$. The big differences appear in $\Delta\mu_{\epsilon\gamma}^{(\pm)}$ and $\Delta\mu_{\gamma\gamma}^{(\pm)}$ discussed for the $\Gamma \neq 0$ regime. For $\Delta\mu_{\epsilon\epsilon}^{(\pm)}$ the terms stay analogous and thus $\Delta\mu_{\epsilon\epsilon}^{(+)} = \frac{3}{2} \Delta\mu_{\epsilon\epsilon}^{(0)}$ and $|-\rangle$ correspondingly³.

³The Chern numbers of the lowest three bands dictate the others.

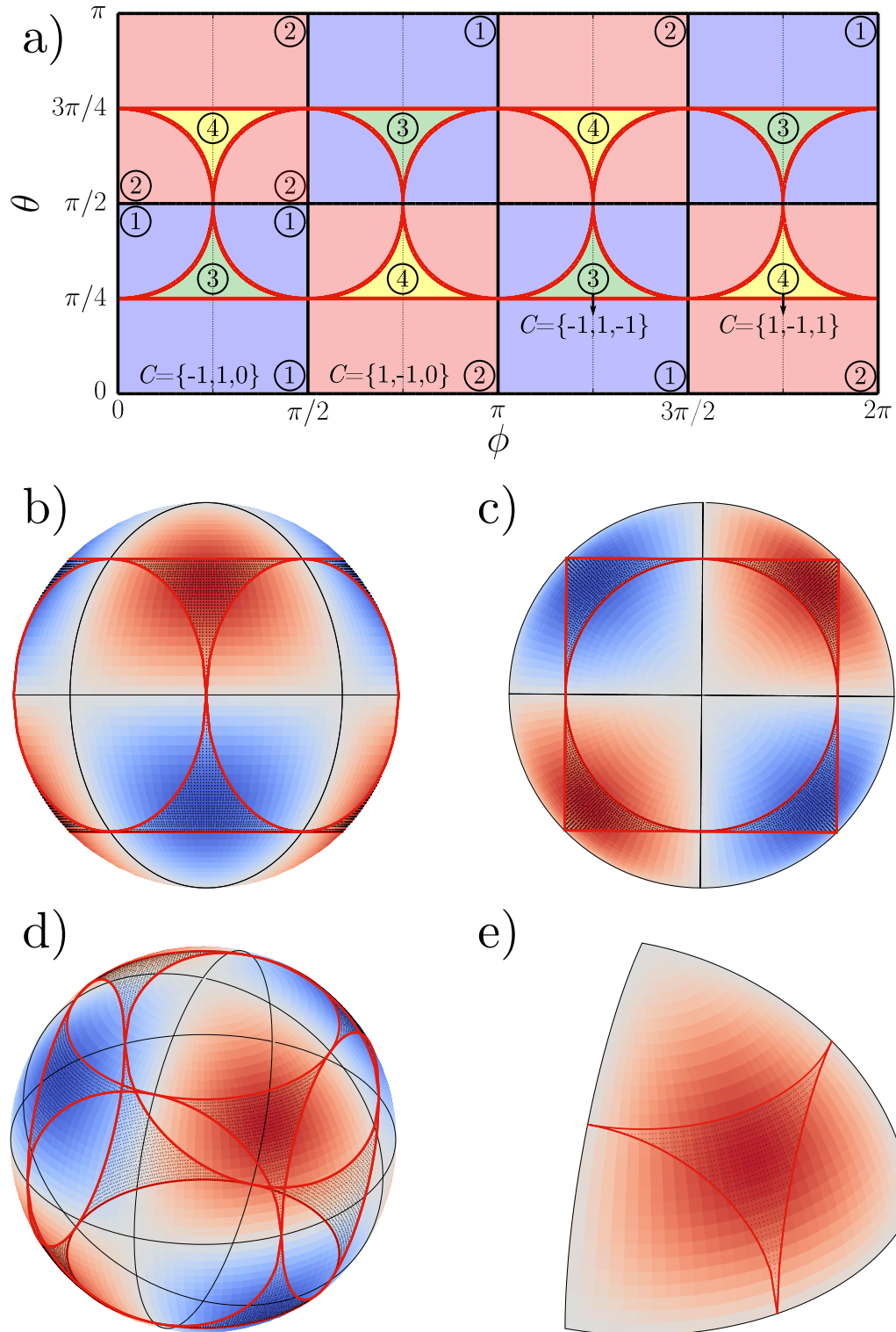


Figure 4.2. a) Topological phase diagram of the effective $h \gg K$ model: ϕ and θ are spherical coordinates parametrizing the direction of the magnetic field. Phase transitions are connected to triangle equalities of the field components and a clear sign structure based on them emerges, which is visualized on the sphere in b)-e).

This relation for n_z has two immediate consequences: First, Kitaev terms are essential for lifting the degeneracy and gaining a topological phase. In the case without Kitaev terms, the $(\epsilon_x^* - \epsilon_y^*)$ terms vanish completely because the Heisenberg terms look the same for all flavors. As a result the degeneracy at the K points (vanishing n_x and n_y) cannot be lifted by a nonzero n_z ($|\mathbf{n}|$ represents the band gap and $|\mathbf{n}| = 0$ a degeneracy). Even if that was not the case for n_x and n_y , a trivial z component forbids a nontrivial winding number, at least when operating in two dimensions. Secondly, all three components of the magnetic field need to be active. The winding number for $|0\rangle$ in the nontrivial $[1, 1, 1]$ case is visualized in figure 4.1c).

In figure 4.2 we analyze the $h \gg K$ effective model for different magnetic fields. Here the magnetic field is described by the spherical coordinate unit vector $h_x = \cos(\phi) \sin(\theta)$, $h_y = \sin(\phi) \sin(\theta)$ and $h_z = \cos(\theta)$. We find a rich phase diagram even in just this limit.

There are two notable aspects in the phase diagram. First of all, the phases where all three (six) bands carry a nontrivial Chern number are exactly the areas where the components h_x , h_y and h_z fulfill the triangle inequalities, similar to K_x , K_y and K_z -dependent spin liquid phases in the original Kitaev model [4]. Ergo, if one of the components is much larger than the others, one of the band pairs stays trivial. Second, there is a clear sign structure dictated by the overall sign of the product of $h_x h_y h_z$. The sign of the lowest band is consistent in a sector. As the lowest band is filled first thermally by a Bose-Einstein distribution and the sign represents the direction of the edge state gradient, one would expect this sign structure to directly translate to the thermal Hall conductivity (cf. section 4.3.3). Hence, we provide one more indication that the sign structure of the thermal Hall effect is a general feature of Kitaev interactions and not necessarily connected to Majorana fermions (see discussion in the introduction of this chapter). Moreover, we note that there are differences between our effective model and the very recent results for an in-plane polarized Kitaev magnet (i.e. regular spin based model), where, e.g., large

topologically trivial areas exist [255].

4.2.2 Kitaev-Heisenberg Model

We now consider the Kitaev-Heisenberg model ($\Gamma = 0$).

For the high-field limit we can use the previous calculations to obtain results beyond the Kitaev limit. Analysis of the high-field limit can be performed using equations (4.9) and (4.11). Naturally, changes due to magnetic field direction and Kitaev to Heisenberg ratio influence each other.

In the low-field limit the winding number interpretation using $L = 1$ Dirac-cone physics loses its usefulness and one is in reasonable practice limited to brute force calculations. However, according to reference [246] the entire system retains its Dirac-based nature.

The Kitaev-Heisenberg model with a magnetic field in perpendicular direction can be found to offer a rich phase diagram containing a multitude of distinct topological configurations (see figure 4.3, and references [5, 6] for the old plot without limit case and clean phase borders). The phase diagram is invariant for $\alpha \rightarrow \alpha + 180^\circ$. In contrast to reference [5], we eliminated unclear areas by careful numerical evaluation of the Chern number and additional explicit calculation of the band gap closings. Furthermore, we normalize the magnetic field vector direction. The focus on the band gap closings is useful because it does not have the same problems as the gauge-independent formulation of the Berry curvature and thus Chern number in equation (4.4), namely the energy difference in the denominator diverging when bands touch. The winding number interpretation has the same issue via $\hat{\mathbf{n}} = 0$.

One can notice the phase transitions seemingly originating from select points in the $h = 0$ limit. Three distinct phase transitions continue into the high-field limit: the ferro- and antiferromagnetic Heisenberg case as well as at $\alpha = 108.5^\circ$. Amid a closer look at the band structure, or more fundamentally at the Hamiltonian (4.1), one can

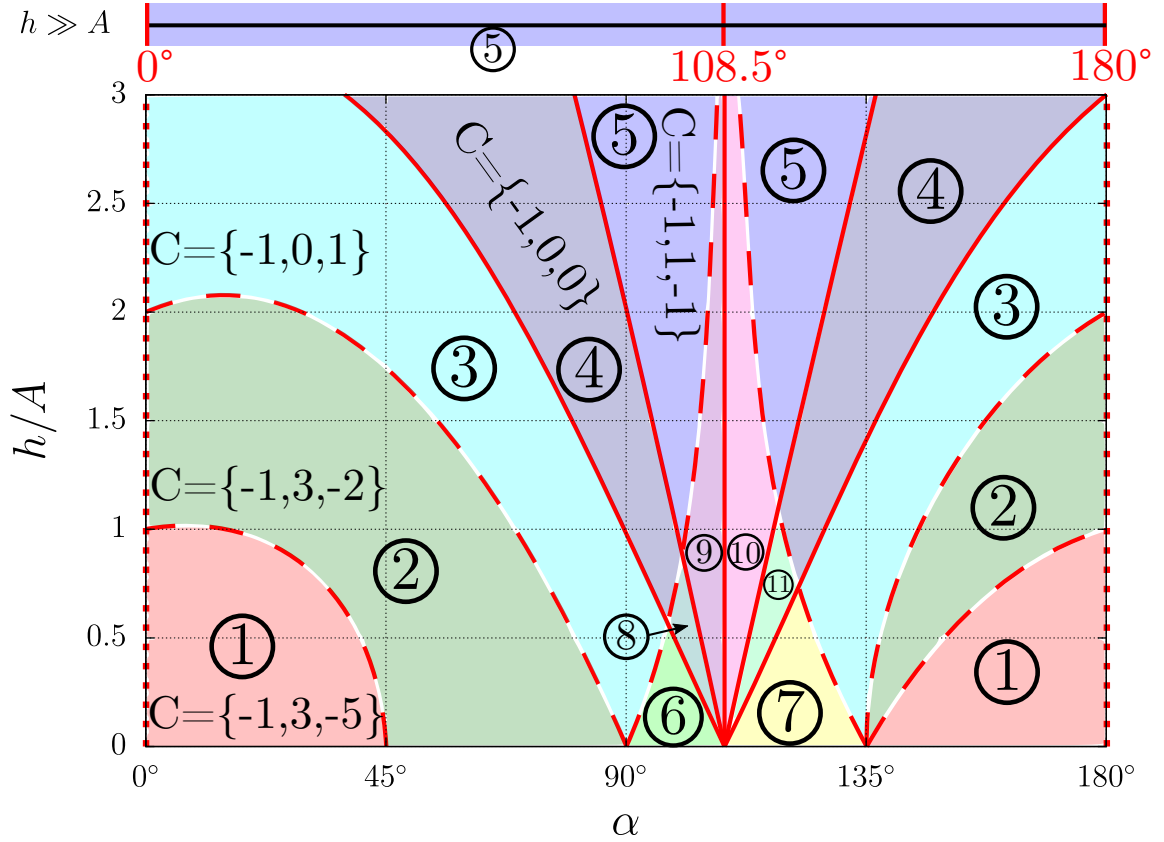


Figure 4.3. Topological phase diagram for the Kitaev-Heisenberg model parametrized by $J = A \cos(\alpha)$ and $K = A \sin(\alpha)$ for a magnetic field in $[h_x, h_y, h_z] = [1, 1, 1]$ direction (normalized): the numbers in brackets denote the Chern numbers of lowest three bands (the others are fixed by mirroring and changing sign). Calculated band gap closings (not in the $h \gg A$ limit) at Γ (solid line), M (dashed) and K (dotted) symmetry points in the Brillouin zone are sketched to provide clean phase borders. A full list of the phases can be found in table 4.1. The top contains the phase diagram of the effective minimal model winding number calculations.

find these phase transitions to be trivial aspects of sublattice symmetry. For a pure Heisenberg interaction the dispersion vanishes $\epsilon = \mathbf{0}$ at the K points of the Brillouin zone. Similarly, at the Γ point we find $\epsilon_{x/y/z} = 3J + K = A(3 \cos(\alpha) + \sin(\alpha))$, which becomes trivial for $\alpha = 108.5^\circ$. The latter observation, i.e. trivial dispersion, easily extends to the results in the high-field limit. Additionally we earlier discussed the pure Heisenberg case to lead to $n_z = 0$ and, as a consequence, to a gapless system. Similarly all other phase transitions can be evaluated analytically when the band

touching points are known. All phase transitions not belonging to the high-field limit inherit the sinusoidal and cosine shapes of the J/K parameters. We find band gap closings at Γ , K (only Heisenberg $K = 0$) and M points in the Brillouin zone. Each touching point originates at distinct points in the $h = 0$ limit, prompting a closer investigation. Additionally, one can notice a clear trend in regards to Chern number changes at these transitions. Except for the special angle $\alpha = 108.5^\circ$, a gap closure at the M point provides $\Delta C = \pm 3$ while the Γ point introduces changes of $\Delta C = \pm 1$.

A full list of Chern numbers for the phases of this and the subsequent $[1, 1, -2]$ phase diagram is shown in table 4.1.

Through analysis of the $h = 0$ band structures and the Berry curvatures (figures 4.5 and 4.4) for a representative part of the phase diagram $0^\circ < \alpha \leq 90^\circ$, we can procure an explanation for the origin and influence of the M point phase transition as well as the realization of the highest Chern number $C = 5$.

The introduction of a minute Heisenberg term to the Kitaev limit changes the degeneracy, leaving three distinct twofold degenerate flavor pairs on the K-K' lines. The Berry curvature then originates at the M points. Each of the three distinct points can gap and potentially introduce a change in Chern number. Due to the form of the dispersion, the magnetic field is expected to provide a mix of these solutions. Yet, the middle bands, and not the two highest (lowest) ones naively deduced from the $h = 0$ limit, inherit all three distinct lifted degeneracies. This can be observed by considering the phase transition at $h \neq 0$. As a result the $h = 0$ limit, though useful for the nature of the topological phase, does not immediately dictate the Chern numbers.

At $\alpha = 45^\circ$, the Heisenberg interaction takes over, causing a touching point between bonding and antibonding solutions. Again, three distinct points for the flavor pairs are formed, this time between the middle bands. Here, the Chern numbers follow directly from the $h = 0$ limit. The Chern number is additive through all these

Table 4.1.: Chern numbers of the lowest three bands for $\mathbf{h} = [1, 1, 1]^T$ and $\mathbf{h} = [1, 1, -2]^T$. Chern numbers of $[1, 1, 1]$ also appear in the $[1, 1, -2]$ phase diagram with a global sign change (which would not be there for $[1, 1, 2]$). Phase labels can be found in figures 4.3 and 4.6.

[1, 1, 1]			new for [1, 1, -2]				
phase	C_1	C_2	C_3	phase	C_1	C_2	C_3
1	-1	3	-5	A	1	-3	3
2	-1	3	-2	B	1	-2	1
3	-1	0	1	C	1	-1	0
4	-1	0	0	D	-1	1	0
5	-1	1	-1	E	0	0	-1
6	2	-3	1	F	1	-3	4
7	-1	0	4	G	-1	2	-1
8	2	-3	0	H	-1	2	0
9	2	-2	-1	I	-1	1	1
10	-1	1	2	J	1	-1	-1
11	-1	0	3	K	1	0	-2

cases.

Additionally the underlying bosonic Dirac physics become apparent. Going backwards from the near Heisenberg regime in 4.4d) to the $\alpha = 45^\circ$ case in 4.4c), one can see that the flavors touch via Dirac-cone shaped dispersions, which split up depending on their flavor type and travel to different M points in the Brillouin zone. Moreover, if any lifted Dirac point contributes a Chern number ± 1 , the 3 distinct flavors reaching the M points directly explain the aforementioned $\Delta C = \pm 3$.

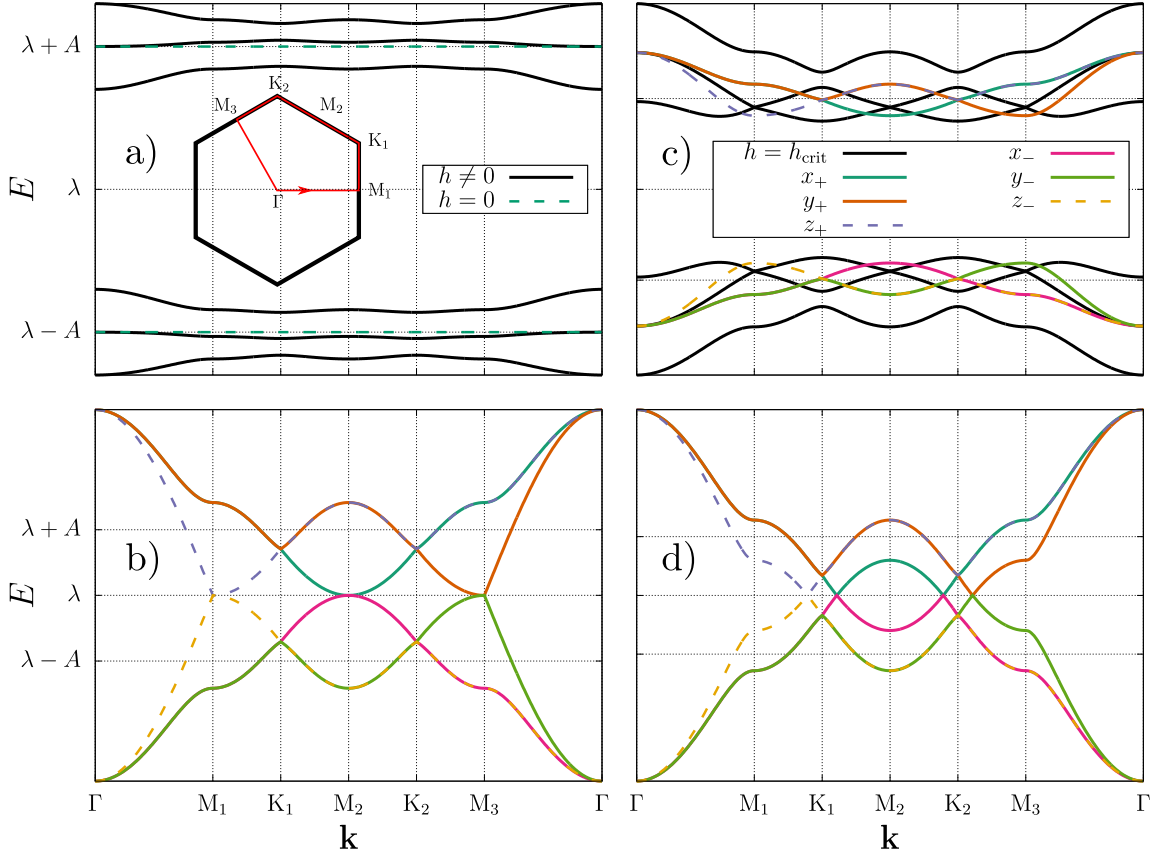


Figure 4.4. a) Band structure for the Kitaev model with and without a magnetic field: The magnetic field can induce a dispersive behavior (cf. [5]). b) Band structure in the regime $45^\circ < \alpha < 90^\circ$ at the $h = 0$ and first $h \neq 0$ phase transition: The degeneracies lie within the bonding and anti-bonding sublattice states. The band gaps close at the K and M points respectively. c) At $\alpha = 45^\circ$ the Heisenberg interaction is strong enough to allow additional touching points between bonding and anti-bonding regimes. d) Moving closer to the Heisenberg regimes all degeneracies move to the K points. Flavors have spatially dependent touching points (threefold rotation to exchange them) and therefore travel on distinct lines.

This splitting and movement of the Dirac points can also be gauged by the observation of the Berry curvature in figure 4.5. The nontrivial Berry curvature regularly emerges from the K points, then splits up into three distinct entities, and moves toward different M point. Furthermore the splitting makes the Berry curvature appear to have the structure of a decorated honeycomb lattice, which fits the role of the flavors on each site and thus to interpretations used in reference [5].

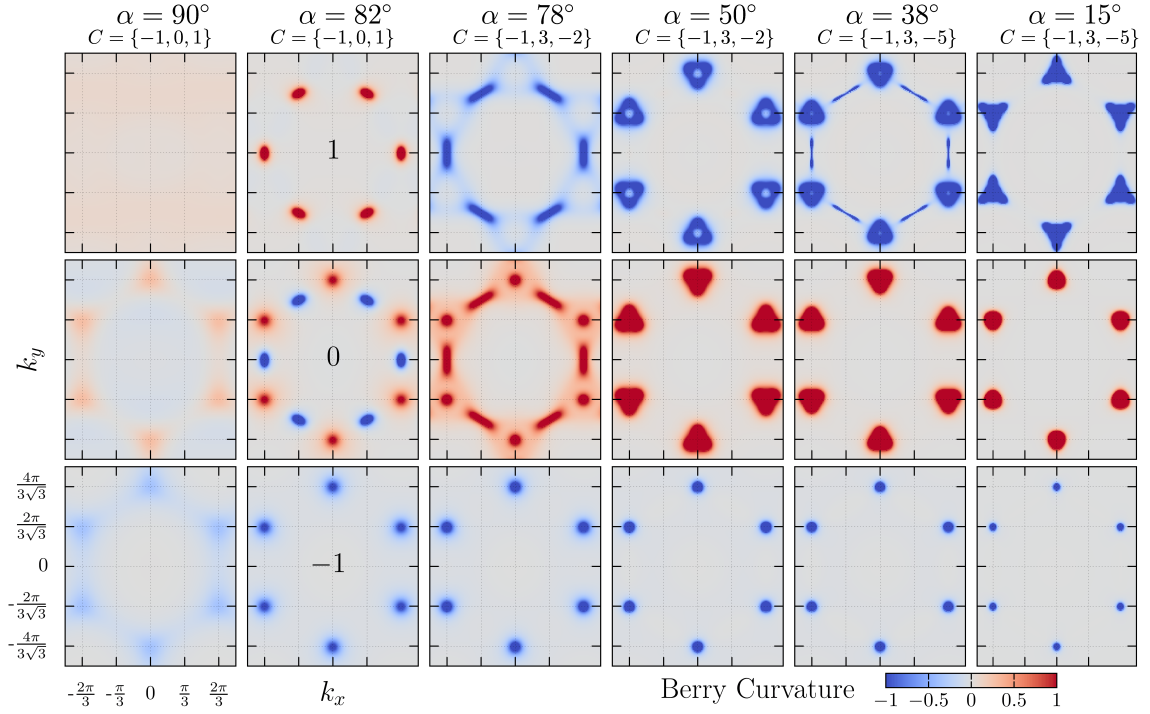


Figure 4.5. Berry curvature of the lowest three bands (lowest band on bottom) at $h = 0.5$: The points of nontrivial Berry curvature emerge and then split up to travel towards different K points, where in the Heisenberg limit all degeneracies unite. Close to the Heisenberg limit a decorated honeycomb structure emerges.

In summary, the $[1, 1, 1]$ magnetic field establishes a topological phase diagram that can be understood in terms of a high magnetic field limit, a low-field Kitaev limit and the form of the dispersion relations for $h = 0$. The high Chern number is partly caused by the lifting of the degeneracy of the three distinct flavor pairs at the M points and accumulation of different broken symmetries.

With this knowledge we can interpolate the topological phase diagram for arbitrary magnetic field directions, which was not done before, as reference [6] discarded the in-plane magnetic fields as trivial (probably by only testing $[1, -1, 0]$). Note that $[1, 1, 1]$ is perpendicular, so any other vector with vanishing scalar product with it is in-plane.

However, the previous discussions of the limiting cases point a different picture.

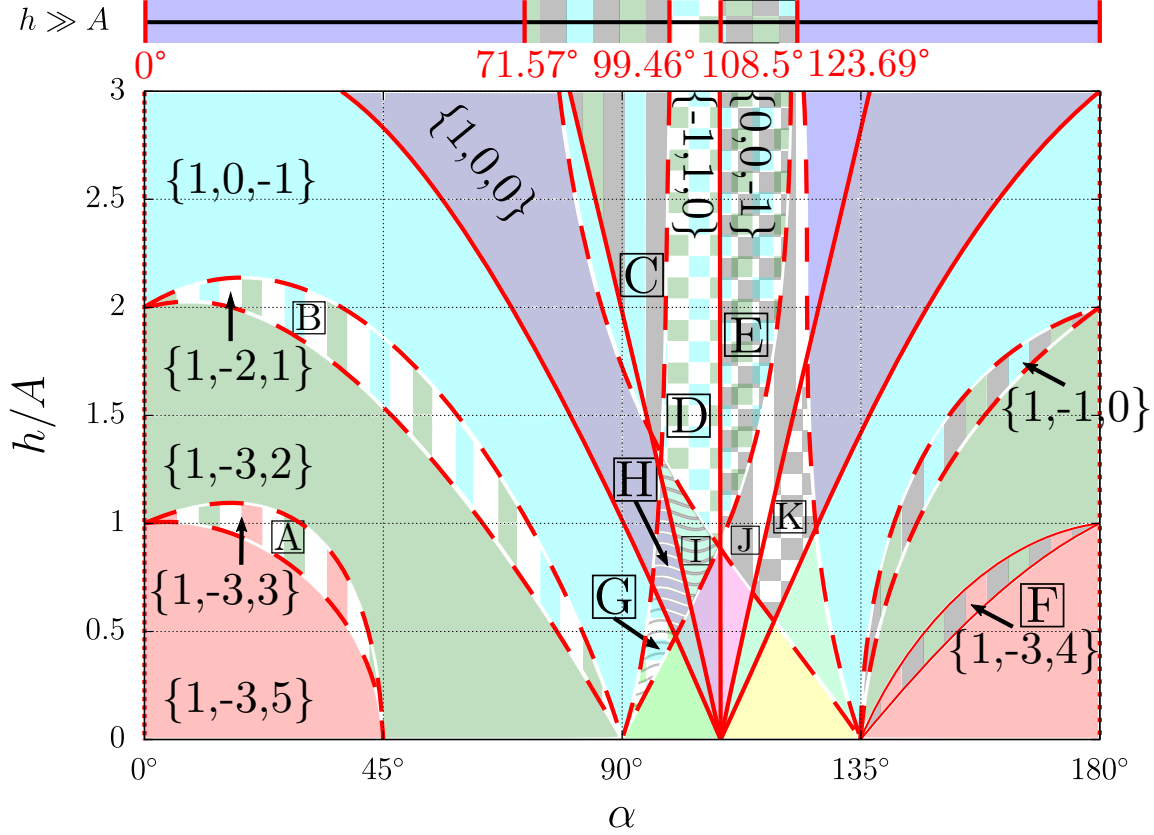


Figure 4.6. Topological phase diagram for the Kitaev-Heisenberg model parametrized by $J = A \cos(\alpha)$ and $K = A \sin(\alpha)$ for a magnetic field in $[h_x, h_y, h_z] = [1, 1, -2]$ direction (normalized): the numbers in brackets denote the Chern numbers of lowest three bands (the others are fixed by mirroring and changing sign). Calculated band gap closings (not in the $h \gg A$ limit) at Γ (solid line), M (dashed) and K (dotted) symmetry points in the Brillouin zone are sketched to provide clean phase borders. A full list of the phases can be found in table 4.1. The top contains the phase diagram of the effective minimal model winding number calculations. Unlabeled phases are the ones found at comparable positions in 4.3 aside from a global sign change (which would not be necessary for $[1, 1, 2]$).

The essential ingredient for nontrivial structures can be pinned to having all three components of the magnetic field vector being finite. Another insight was the sign structure of the Chern number. These findings continue to the whole phase diagram. Indeed any field direction with a trivial component e.g. $[h_x, h_y, 0]$ can be found to be topologically trivial. This obviously does not include any restriction on the

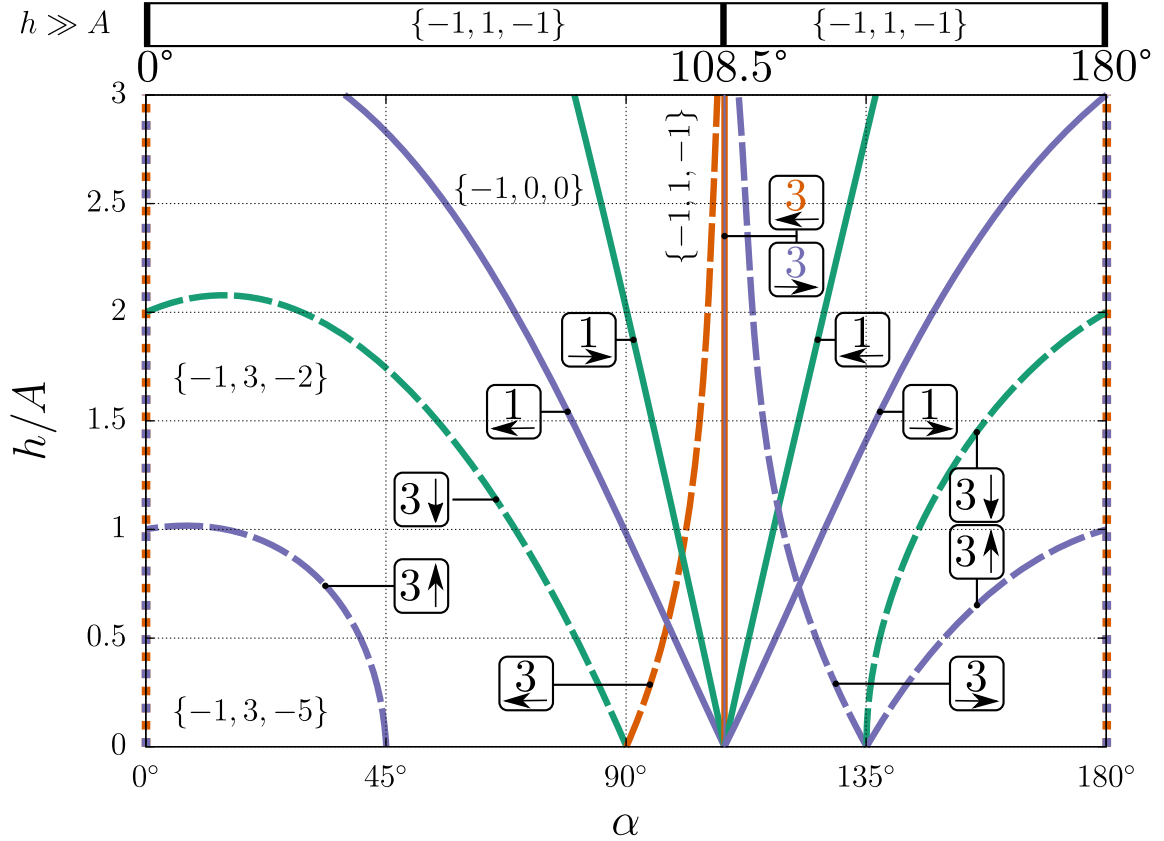


Figure 4.7. Alternative scheme to visualize the phase diagram in figure 4.3 (the $[1, 1, 1]$ magnetic field). Dashed, dotted and normal lines still refer to the K, Γ and M points. Numbers in brackets denote the Chern numbers of the lowest three bands $\{C_1, C_2, C_3\}$. The colors refer to which gap closes (see also legend in figure 4.9): orange labels the lowest gap and crossing the line in arrow direction yields $C_1 + x$ and $C_2 - x$. The next highest gap is represented by green and the one between band three and four by violet.

perpendicular or in-plane directions.

The remaining magnetic-field results can be explained via the example of the $[1, 1, -2]$ direction, which is in-plane. The phase diagram can be found in figure 4.6. As demonstrated by the limit-based model, the low-field Kitaev phase only changes its global sign. Moreover all familiar Chern number combinations develop an overall sign change. This is not the case for $[1, 1, 2]$ where the signs stay consistent with $[1, 1, 1]$. Similarly $[1, 1, -1]$ has a sign flip compared to $[1, 1, 1]$ and $[1, -1, -1]$ does

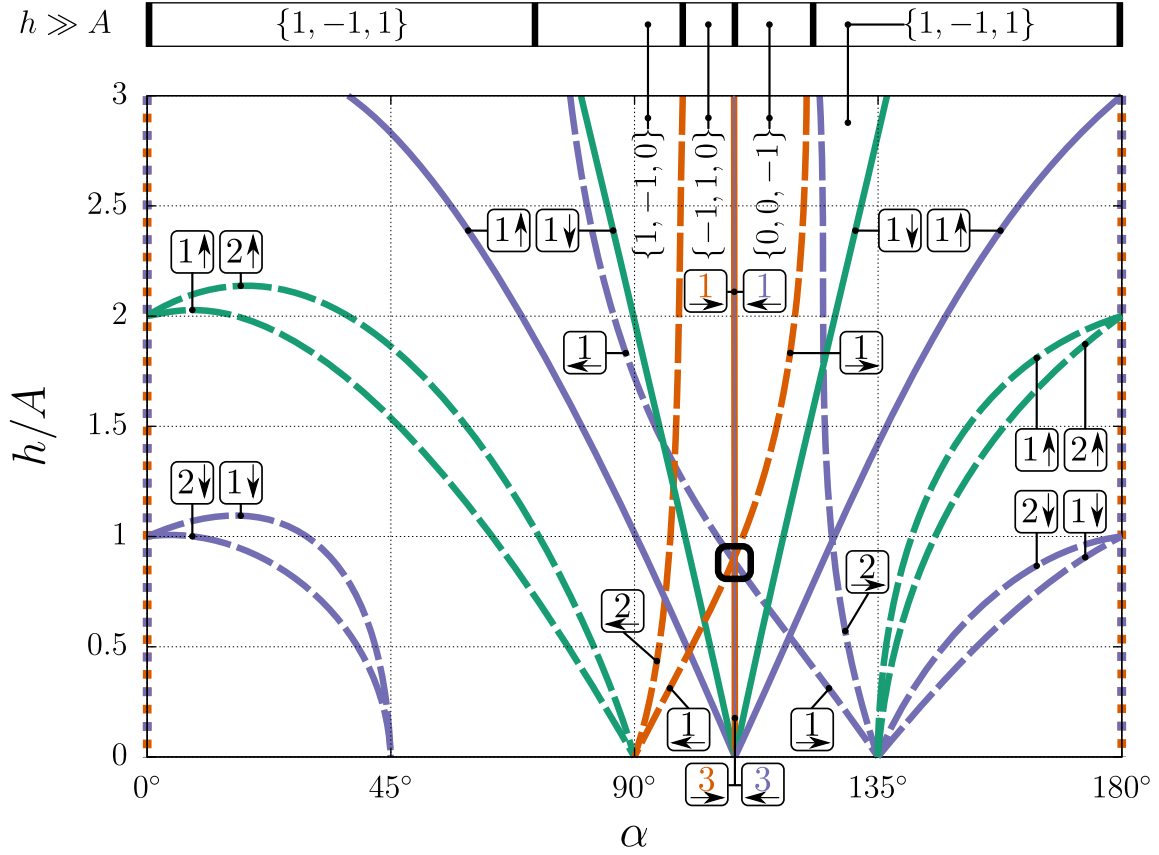


Figure 4.8. Alternative scheme to visualize the phase diagram in figure 4.3 (the $[1, 1, -2]$ magnetic field). Dashed, dotted and normal lines still refer to the K, Γ and M points. Numbers in brackets denote the Chern numbers of the lowest three bands $\{C_1, C_2, C_3\}$. The colors refer to which gap closes (see also legend in figure 4.9): orange labels the lowest gap and crossing the line in arrow direction yields $C_1 + x$ and $C_2 - x$. The next highest gap is represented by green and the one between band three and four by violet. The black box labels an area of more complicated nature where the lines within intermingle and arrow labels change.

not. One may ignore the overall sign change and discuss the remaining features, which are partly $h_x = h_y \neq h_z$ based. Unsurprisingly, Heisenberg and $\alpha = 108.5^\circ$ remain unchanged as well as the number of Γ touching points, where no explicit flavor distinction exists.

However, each of the M transitions is split into two separate instances, one with $\Delta C = \pm 2$ and another with $\Delta C = \pm 1$, which effectively introduces a new intermediate phase. The origin of this phase is easily explained by the three distinct flavor

pairs. The magnetic field constitutes the interaction of the flavors. If one interaction is different it will inherit slightly changed dynamics implying an earlier/later gap closure. Consequently, three different components $h_{x/y/z}$ can further split the M transitions, resulting in three subsequent $\Delta C = \pm 1$ changes. The resulting new phases are therefore straightforward.

Additionally the high-magnetic-field limit changes as previously established. Notably this leads to an intriguing evolution of the phase transitions from the low- to the high-field limit. The unintuitive change is thus relegated to strong magnetic fields, which are not expected to be important in realistic models (see reference [6] for an estimate for the involved units).

Summarizing, the topological phase diagram for arbitrary magnetic fields with three nonvanishing components is rich and not limited to perpendicular magnetic fields. Many of its properties can be intuitively understood. At this point providing a plethora of slightly different phase diagrams stops being useful. Therefore we leave it at these two. One should note that, as evidenced by the discussions, this time the various topological band structures for the different magnetic field directions have been thoroughly checked.

Nevertheless, one point remains to be made here. Due to the multitude of different topological phases and the fact that there is no trivial one in sight (as long as the entire setup is nontrivial), drawing and labeling the phase diagram in its entirety is neither well-arranged nor convenient. Moreover, the situation when including the Γ terms is an order of magnitude more complex and the resulting kaleidoscope of a phase diagram is just not practical for a mistake free and reproduceable analysis (cf. reference [6]).

Essentially, the problem can be reduced to a compilation of wildly intersecting band touching points representing fixed symmetries and thus behaviors. Therefore, the important information can be communicated via these lines, at least if one accepts that 1) there are topologically nontrivial phases everywhere (assuming any single one

exists) and if the Chern numbers somehow cancel in a particular area that would be a coincidence⁴ and 2) that there are so many approximations involved that predicting specific Chern numbers (or locations in the phase diagram) of a realistic material can not be expected, so that bothering which Chern numbers in each area are present is not the most important aspect.

One can try to reproduce the earlier phase diagrams with this in mind. This has been attempted in figure 4.7 for $[1, 1, 1]$ and figure 4.8 for $[1, 1, -2]$. When interest in a precise area arises, the Chern numbers can be easily “calculated” by following the arrays and adding the numbers for the relevant bands. A legend explaining the rules can be found in figure 4.9. The colors are designed to be colorblind safe [256].

In this way, the relevant information can be conveyed in a format that is hopefully concise and little prone to errors. This format should still be seen to imply a thorough evaluation of the Chern numbers and band gaps, the latter of which can more often than not be calculated analytically when the touching-point coordinates, e.g. M , are known and inserted as \mathbf{k} into the Hamiltonian.

4.2.3 Influence of Gamma

Flavor changing interactions Γ are expected to contribute in real materials, which can be inferred from the derivation of the model in this thesis and general experiences based on other Kitaev-Heisenberg models [39]. In the subsequent paragraphs we investigate their influence.

In the low-field Kitaev limit, Γ terms enter as competition to the magnetic field in the flavor changing matrix elements of bonding/anti-bonding states. This has two immediate consequences: First of all, the existence of complex matrix elements impedes the analysis via $L = 1$ winding number. However, based on [246], one can still recognize the physics as Dirac-cone based. Moreover, the limiting case $h \gg \Gamma$

⁴that so far has not appeared in any regime

always works and the other limit can be calculated by brute force. Therefore the existence of topological bands can be quickly determined, because if it works in both limits, the nontrivial topology cannot easily disappear. Accordingly, evaluation of a plethora of phase diagrams, at least as a survey and explicitly also in the Γ regime, yielded non-trivial phases.

Similar to the approach we used in the discussion of the topological band structure of the pure Kitaev-Heisenberg model, there is an argument to be made that just creating one of countless possible phase diagrams is, even though it might look complicated and superficially important, not an adequate approach to understand the model. It seems functional to explain why and when one should expect to find nontrivial topology. Moreover, describing the big picture structure from which one can infer the overall behavior, like the flavors becoming disparate in the $\Gamma = 0$ $[1, 1, 1]$ to $[1, 1, \pm 2]$ case resulting in a split of M touching points, seems to be prudent.

We therefore choose the following approach in this thesis: As reference [6] looks at the $\Gamma \neq 0$ $[1, 1, 1]$ and $[0, 0, 1]$ cases and provides flawed phase diagrams based purely on numerical results, the first step is to cleanly describe these known cases. We then work out what to expect for the behavior concerning general magnetic fields, of course based on implicit evaluations of the Chern number in various cases. One should note that in contrast to the $\Gamma = 0$ discussion where only the $[1, 1, 1]$ was previously known and just slightly but acceptably off regarding clean phase borders and merged bands, the $\Gamma \neq 0$ plots are flawed in a more significant sense (understandably so considering the sheer amount of phases and numerical difficulties⁵). Next to merged bands, slight inaccuracies regarding the phase boundary and the inconvenience of an unnormalized magnetic field vector, there are also errors concerning some Chern numbers. Hence, it is prudent to reestablish those. Also, it gives the reader an opportunity to recheck aspects of the simplified way of displaying the phase diagram via band touching

⁵Reference [252] for example only provides 3 phases explicitly in a comparative but simpler scenario, which is perfectly reasonable

points and arrows used in this thesis.

For the new aspect of the topology that is beyond numerics we start, as was the case for the $\Gamma = 0$ model, with the limiting case.

In the general high-field limit the γ terms in ρ and n_z need to be considered. The ρ terms are established in equation (4.9). For the latter this leads to non-vanishing summands $\Delta\mu_{\epsilon\gamma}$ and $\Delta\mu_{\gamma\gamma}$, which can be found to be

$$\Delta\mu_{\epsilon\gamma}^{(0)} = \text{Im} \left[h_x h_y (\epsilon_x - \epsilon_y) (h_x \gamma_y^* + h_y \gamma_x^*) + h_x h_z (\epsilon_z - \epsilon_x) (h_x \gamma_z^* + h_z \gamma_x^*) \right. \\ \left. + h_y h_z (\epsilon_y - \epsilon_z) (h_y \gamma_z^* + h_z \gamma_y^*) \right], \quad (4.13)$$

$$\Delta\mu_{\gamma\gamma}^{(0)} = \text{Im} \left[h_x (h_y^2 + h_z^2 - h_x^2) \gamma_y^* \gamma_z + h_y (h_x^2 + h_z^2 - h_y^2) \gamma_z^* \gamma_x \right. \\ \left. + h_z (h_x^2 + h_y^2 - h_z^2) \gamma_x^* \gamma_y \right], \quad (4.14)$$

on the $|0\rangle$ manifold ($|\pm\rangle$ are analogous and provided after the subsequent discussion). Beyond changes in the high-field limit, this implies that the requirement of three non-vanishing components of \mathbf{h} can be dropped. For example, two corresponding γ components $\gamma_{x/y}$ can introduce a nonzero term with h_z in n_z and therefore potentially substitute for $h_{x/y}$.

However, this new freedom introduces a “new” (previously also trivial) range of bad choices in regard to topological phases. For $h_y = -h_x$ and $h_z = 0$, i.e. the $[1, -1, 0]$ case or equivalent combinations of the flavors, we find $\Delta_{\epsilon\epsilon} = 0$, $\Delta\mu_{\gamma\gamma} = 0$ trivially caused by the magnetic field and $\Delta\mu_{\epsilon\gamma}$ vanishing due to the form of γ and ϵ and thus no topological band structure. However, an anisotropy of Γ in γ_x and γ_y can remedy this. This fact seems to extend to the entire phase diagram. All in all, one can find scenarios where no topological band structure can be established, but one has to actively seek them out.

In summary, the nonzero Γ allows for a plethora of new acceptable choices for the magnetic field direction. While for $\Gamma = 0$ one needed all three components to

be active, the γ dispersion can substitute breaking the flavor symmetry and thus allow e.g. $[0, 0, 1]$. However, in some “unlucky” (of course based on symmetries of the dispersion relations etc...) cases like $[1, -1, 0]$, the γ can not do its job because the symmetries align somewhere in the Brillouin zone (closing of band gaps can now happen away from the symmetry points). One can move this unlucky coincidence by e.g. anisotropy of Γ (or K or J), which might just exist in a realistic compound per se or be induced via pressure (in practice one would probably just move the magnetic field a tiny bit).

For completeness one should mention, that an analogous analysis follows for the $|\pm\rangle$ states. The new terms in the n_z component are ($|-\rangle$ via $(|+\rangle)^* = |-\rangle$):

$$\begin{aligned} \Delta\mu_{\epsilon\gamma}^{|\pm\rangle} = \frac{\Delta\mu_{\epsilon\gamma}^{(0)}}{2} + \frac{1}{2}\text{Im} \left[h_z^2(\epsilon_x - \epsilon_y)(h_x\gamma_y^* + h_y\gamma_x^* - h_z\gamma_z^*) \right. \\ \left. + h_y^2(\epsilon_z - \epsilon_x)(h_x\gamma_x^* - h_y\gamma_y^* + h_z\gamma_z^*) \right. \\ \left. + h_x^2(\epsilon_y - \epsilon_z)(-h_x\gamma_x^* + h_y\gamma_y^* + h_z\gamma_z^*) \right], \end{aligned} \quad (4.15)$$

$$\begin{aligned} \Delta\mu_{\gamma\gamma}^{|\pm\rangle} = \frac{\Delta\mu_{\gamma\gamma}^{(0)}}{2} + \text{Im} \left[h_x(h_y^2 + h_z^2)\gamma_y^*\gamma_z \right. \\ \left. + h_y(h_x^2 + h_z^2)\gamma_z^*\gamma_x \right. \\ \left. + h_z(h_x^2 + h_y^2)\gamma_x^*\gamma_y \right]. \end{aligned} \quad (4.16)$$

Before considering how to make predictions about the topological nature of the low-field limit, it is useful to look at the phase diagram. We turn to a pure observational look at the result.

In figure 4.9 we present the topological phase diagram for $\Gamma = 0.1A$ and a magnetic field in the $[1, 1, 1]$ direction. Similar to the previous case the explicit analysis of phase transitions via a search for vanishing bandgaps is a powerful tool. The new energy scale of Γ discussed in the Kitaev case permeates through the entire phase diagram at $h = \sqrt{3}\Gamma$ (Γ is akin to an unnormalized vector in $[1, 1, 1]$ direction), introducing a phase transition with $\Delta C = \pm 2$. We refer to a subsequent discussion

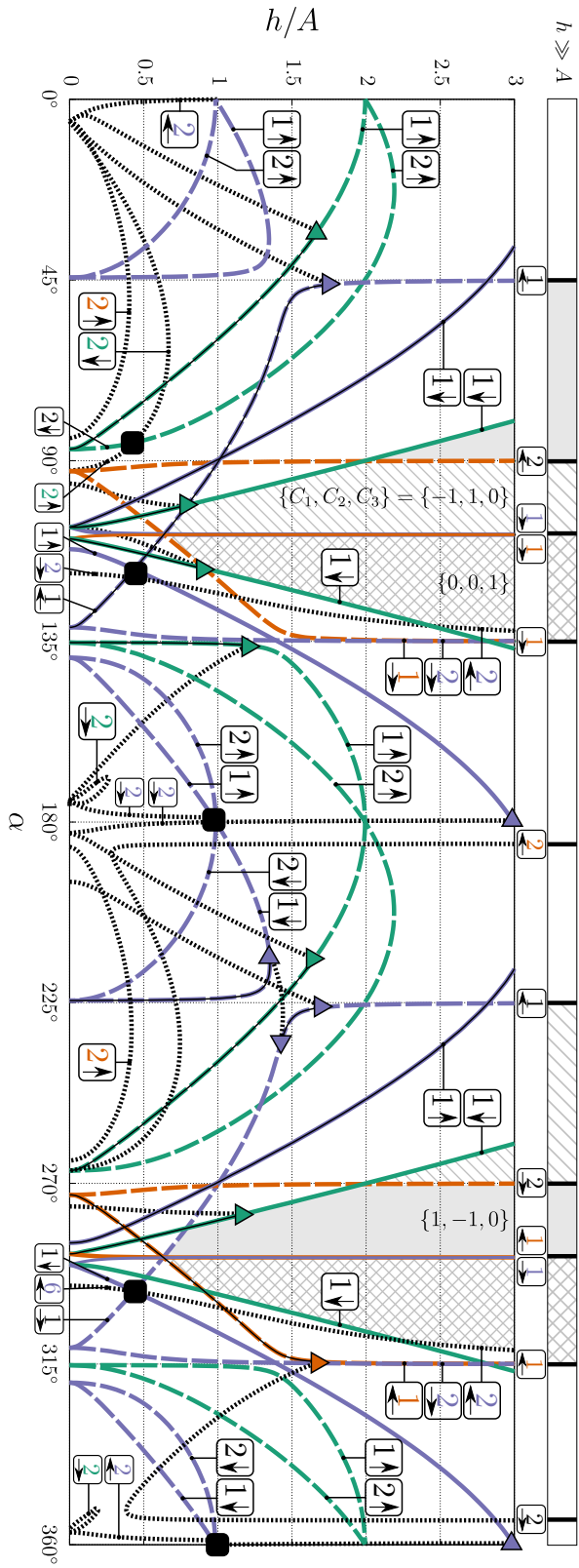


Figure 4.10. Phase diagram for $[0, 0, 1]$ and $\Gamma \neq 0$: Numbers in brackets denote the Chern numbers of the lowest three bands $\{C_1, C_2, C_3\}$. Colorful dashed, dotted and normal lines refer to the K, Γ and M points. The colors refer to which gap closes: orange labels the lowest gap and crossing the line in arrow direction yields $C_1 + x$ and $C_2 - x$ (see also key of 4.9 for more detailed explanations). The next highest gap is represented by green and the one between band three and four by violet. Gap closings away from the symmetry points are shown as black, more finely dashed lines.

of the triangular lattice for an analysis of this particular symmetry.

Γ introduces new phase transition points in the Brillouin zone. These new participants introduce the most significant changes in the phase diagram, most notably a Chern number of $C = 8$. Furthermore, the introduction of Γ leads to an inequivalence of $\alpha \rightarrow \alpha + 180^\circ$, which can be flipped by a sign change of Γ . Additionally, pure Heisenberg and $\alpha = 108.5^\circ$ cases are not trivial anymore, because Γ changes the form of the dispersion. In fact, the trivial points move in a way that depends on Γ . This includes the Heisenberg limit, which ceases to be trivial. Instead the straight phase border reaching into the high-field limit, which was formally at the $\alpha = 0^\circ$ Heisenberg case, shifts toward the Kitaev regime also by roughly the order of magnitude of Γ . The shifts have been observed to follow this trend for other values of Γ .

Another noticeable feature can be visualized when looking at the “old” phases, i.e. the ones known from the $\Gamma = 0$ $[1, 1, 1]$ diagram. In figure 4.9 these are highlighted by a gray coloring⁶. In the first half of the diagram, i.e. $0^\circ \leq \alpha \leq 180^\circ$ where K and Γ have the same sign, the topological phases are largely new, except for the area where the high-field phase permeates. In contrast to this, the other half more or less repeats the $\Gamma = 0$ phase diagram above the magnitude threshold of the new interaction. In one case the interactions seem to cooperate while in the other there is a competition.

Lastly, one might notice that the gap closings away from the symmetry points seem to be connected to a Chern number change of $\Delta C = \pm 6$. This, however, can be rationalized, as the M points (at least pairwise) can be translated into one another by a reciprocal lattice vector. A point away from a phase boundary will, however, not repeat and therefore inherit the sixfold rotational symmetry of the Brillouin zone. Hence, a Dirac point connected to this could be expected to produce such a change.

⁶Of course, due to the huge amount of phases, some Chern number combinations reappear at other points. These have not been included in the coloration.

Continuing with explanations of the purely observational discussion, one can go back to the issue of the low-field limit. As mentioned before, explicit formulation as a $L = 1$ winding number does no longer work. Technically one can try to use multiple layers of perturbation theory or the fact that the 3×3 structure is still solvable, which can help a lot for analytical expressions of the gap closings via the discriminant. Yet, the Dirac physics is set by reference [246] for the entirety of the model so there is no gain in that. This also does not solve the core issue: is the low-field limit topologically non-trivial or not? Or at least: are there some areas of topological non-triviality?

Naturally, one can always go back to brute-force calculations in the low-field limit and thus establish that both limits work and there should be a kaleidoscope of topological phases. However, there is at least a very good plausibility argument that also explains features in the phase diagram.

Here one can recall a tool that has seen use for Kitaev-Heisenbergs model in other contexts: sublattice transformations. In one of the first papers considering the Kitaev-Heisenberg model [48] a four-sublattice transformation was employed to rewrite the model in pure Heisenberg form, solve it and then recover the “real” solution by transforming back, in this case from a FM-Heisenberg to a stripy AFM phase. Ever since these kinds of mappings of one point in the Kitaev-Heisenberg model to another have been employed and extended, e.g. by reference [257], where different lattices are analyzed and the transformation is generalized as an application of the Klein four-group $\mathbb{Z}_2 \times \mathbb{Z}_2$. All in all, one may summarize this as there being clear mappings from some sets of Kitaev-Heisenberg couplings to others.

For the extended Kitaev Heisenberg model including the Γ terms, these “hidden symmetries” were systematically analyzed in reference [258] using combinations of transformations on two, four and six sites. While the paper is more focused on magnetic phases instead of pure coupling parameters, the idea behind it can be sketched by a (trivializing) example: Suppose neighboring sites i and j are coupled

via Kitaev and Γ interactions with $K = \Gamma$. Now switch $x \rightarrow y$ on site j , i.e. $\mathbf{T} = (T_x, T_y, T_z) \rightarrow \tilde{\mathbf{T}} = (\tilde{T}_x, \tilde{T}_y, \tilde{T}_z) = (T_y, T_x, T_z)$:

$$KT_{z_i}T_{z_j} + \Gamma(T_{x,i}T_{y,j} + T_{y,i}T_{x,j}) \rightarrow KT_{z,i}\tilde{T}_{z,j} + (T_{x,i}\tilde{T}_{x,j} + T_{y,i}\tilde{T}_{y,j}) = K\mathbf{T}_i\tilde{\mathbf{T}}_j. \quad (4.17)$$

Hence one can make Kitaev and Γ couplings of the same size look like a Heisenberg model on a given bond. Of course that change the interactions on the other bonds, which is why the real story is more complicated and one needs to apply (usually multiple) transformations as described in reference [258]. And, naturally, the on-site magnetic field changes, although in perturbation theory one would solve the model without it first and moreover the direction of the magnetic field (when all three components are nonzero) has been important for the specific Chern number but not the topology being trivial or not.

The major point of the sublattice transformation is that combinations of Kitaev, Heisenberg and Γ couplings can be made to look like each other. While the exact form of their characteristics might not be the same (in other words: Chern numbers and phase borders are subject to change), the overarching symmetries are. The previous back-of-the envelope example directly explains the earlier observation of the Heisenberg point becoming nontrivial and the straight phase border moving: Heisenberg $J + \Gamma$ has a bit of Kitaev in it while $\Gamma + K$ may look like Heisenberg if of equal size. Hence one would expect $\alpha = 0$ to become nontrivial and the border to move to where Kitaev and Γ are comparable, which is exactly what we observe in figure 4.9.

And for the overarching model this leads to the following plausibility argument: When varying the parameters of the $JK\Gamma$ model one almost inevitably move through dual points of the normal Kitaev-Heisenberg model, which was topological nontrivial for the majority of magnetic field choices. Therefore, one should reasonably expect at least some points in the low-field limit to inherit this trait.

With this in mind, it is not surprising that aside from the previously established choices like $[1, -1, 0]$, after many rough numerical evaluations of the phase diagrams for, e.g., different values of Γ and magnetic field choices as well as anisotropic couplings, the model seems to stay topologically nontrivial everywhere. Given that the trends in the phase diagram are expected in the case of some previously described overarching trends, but probably too complicated to predict before calculations are explicitly done, one could reasonably stop the explanation here.

For the purpose of completeness we however add the second scenario attempted in [6], i.e. the $[0, 0, 1]$ magnetic field, in figure 4.10 in order to make this point and subsequently refrain from such endeavors.

In summary, flavor changing interactions do not destroy the topological band structure. On the contrary, they facilitate the potential for higher Chern numbers and additional magnetic field directions.

4.2.4 Trigonal Crystal Field

In light of the above discussion we refrain from studying additional terms like the Γ' interactions, but there is one influence that, at least on paper, presents a qualitatively different scenario. The trigonal distortion $H_{\text{CF}} = \Delta_{\text{CF}} \sum_i \sum_{\alpha \neq \beta} T_{i,\alpha}^\dagger T_{i,\beta}$ (size Δ rescaled for convenience compared to previous discussions), represents an on-site term. Given previous discussions, it is also expected to be of quite significant size in real materials. Recall from earlier sections that in Ca_2RuO_4 the (tetragonal, but that does not matter explicitly) crystal field is of comparable size or more significant than spin-orbit coupling, i.e. larger than the $J/K/\Gamma$ interactions here. Also, its on-site nature represents a new situation.

In the high-field case this problem can be solved easily. The crystal field terms only enter μ_1 and μ_2 as they are on-site. Additionally the terms look the same for both sites, so the contribution to $n_z \sim \mu_1 - \mu_2$ vanishes exactly. Thus, a constant

4.2. Triplon Topology on the Honeycomb Lattice

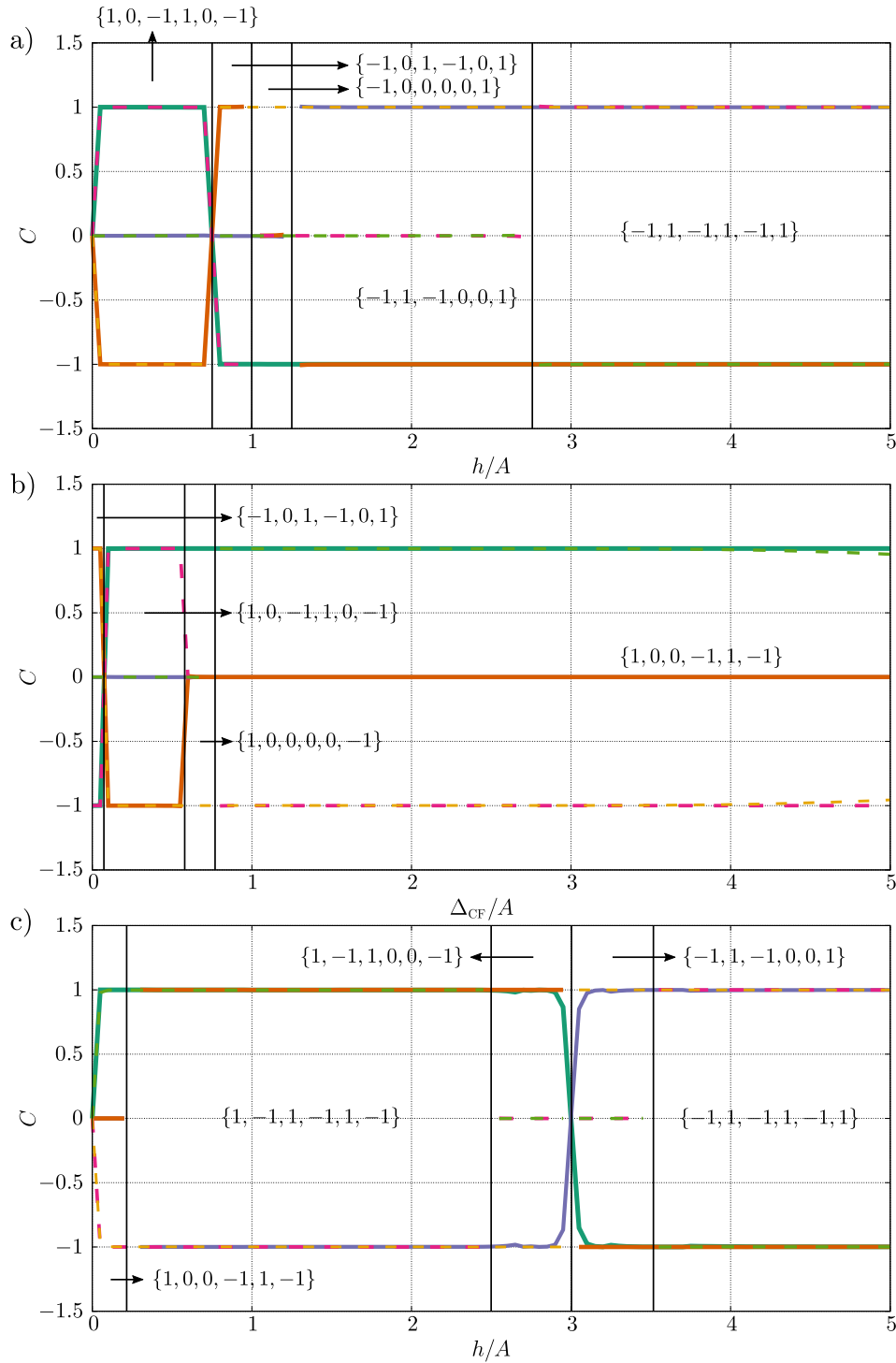


Figure 4.11. Phase diagrams for a) Kitaev coupling $K = A = 1$, crystal field strength $\Delta_{\text{CF}} = A/4$, b) $K = A$, magnetic field strength $h = A/4$ and c) $K = A/4$, $\Delta_{\text{CF}} = A$: Phase borders are visualized by black vertical lines. Chern numbers are provided for each phase starting with the energetically lowest band and increasing in energy from left to right. The Chern numbers of the highest three bands are represented by the dashed lines.

crystal field (no matter if tetragonal, trigonal or any other form) does not change anything in the high-field limit.

For the low-field calculations Δ_{CF} poses a problem. One can however approach it qualitatively. If the exchange interaction, e.g. Kitaev, is larger than the crystal field, then it only enters perturbatively, which for a topological problem where change can only happen when bands touch is basically a nonissue. So the crux of the topological nature boils down to the problem of $\Delta_{\text{CF}} \gg J/K$ and cases where all parameters are of similar size.

At this point there is no way around plausibility arguments and explicit calculations. First of all, Δ_{CF} splits the energies into two-fold and “one-fold” degenerate states. If lifting the two-fold degeneracy still works analogous to the threefold, one might have the expectation that the Chern numbers should be smaller until the magnetic field is large enough to overcome the energy gap to the third. Similarly, the point (formally $J = K$ at $\alpha = 45^\circ$) where bonding and anti-bonding flavors touch is not forbidden by adding Δ_{CF} , only the exact point and flavors change.

Explicit numerical evaluations match these expectations exactly. Interestingly, the straight horizontal line feature of the Γ term in the $[1, 1, 1]$ field case reappears. However, the most important statement is the following: through trial and error we did not manage to make the model trivial for any previously unknown case. The crystal field does not seem to break the topologically nontrivial structure.

However, we refrain from providing full phase diagrams as before. There are two main reasons: Firstly, while it is easy to generate a rough overall structure and a reliable list of Chern numbers for the larger phases (usually not near band gaps so the denominator $(E_n - E_m)^2$ is unproblematic), providing a full presentable phase diagram for the entire parameter space is a lot of cleanup work. Also one would only provide representative scenarios anyways (like $[1, 1, 1]$ and $[0, 0, 1]$ and/or Γ involvement). Secondly, the time saving feature of the lowest three Chern numbers being sufficient information breaks down. This would make big phase diagrams even

harder to read.

The non-symmetric structure of the Chern number can be made plausible rather easily: Since a large crystal field would split the six bands into sets of four and two with a large energy gap, the four bands have more opportunities to be degenerate, e.g., in regards to the bonding and anti-bonding states possessing overlaps. Therefore, a certain delay or even qualitative change of, e.g., lower four and upper two bands is expected and as a result a difference between lowest three and highest three bands regarding Chern numbers. Actually, it could be seen as intriguing that Γ does not have a similar effect. However, we always calculate and list all six Chern numbers in our numerical evaluations so one can be reasonably sure of this. It is also somewhat understandable, because the $\gamma_{x/y/z}$ dispersion relations vanish at certain points in the Brillouin zone and may therefore not present a clear energy scale of imbalance like the crystal field.

Returning to the original point of discussion, we limit the presentation of explicit Chern number results to the representative examples (all in $[1, 1, 1]$ direction) shown in figure 4.11. In figure 4.11a) one can see the case of a small crystal field of $\Delta_{\text{CF}} = A/4$ compared to Kitaev coupling $K = A = 1$. For the Kitaev case the energy scales of the critical points are transparently coinciding with very “rounded” numbers. Naturally the $h = 0$ case is uniquely trivial as no complex phase is involved in the model. Aside from this, the critical points are at $h_c = 3A/4$, $h_c = A$, $h_c = 5A/4$ and finally the transition to the high-field limit phase at $h_c = 11A/4$. Of note is in particular the large area of non-symmetric Chern numbers (concerning the three lowest and highest bands) and the global sign switch in the area of the former spin- L $L = 1$ low-field winding number phase.

In figure 4.11b) the parameters are $h = A/4$ and $K = A$, i.e. one starts in the low-field spin- L phase and then increases the crystal field value until $\Delta_{\text{CF}} \gg K$. Again the sign flip of the low-field phase emerges. More importantly, the crystal field drives the bands into a stable high-“field” phase at $\Delta_c = 3A/4$, which has the

non-symmetric Chern number structure. The small deviations near $\Delta_{\text{CF}} = 4A$ are just bad evaluations of the integral, which can be fixed but naturally become more and more problematic as the band gaps become progressively smaller (until they touch at $\Delta_{\text{CF}} = \infty$).

For completeness, figure 4.11c) provides the, on paper, interesting case of $\Delta_{\text{CF}} = A$ being significantly larger than $K = A/4$. Again the trivial case is restricted to exactly $h = 0$. Moreover, the phase transitions materialize at $h_c = A/4$, $h_c = 5A/2$, $h_c = 3A$ and the one into the high-field limit at $h_c = 7A/2$. Around $h_c = 3A$ the effort put into the evaluation of the integral had to be increased significantly, because one band gap is minute.

There is one more argument left to make. The Hamiltonian H_{CF} is the projection of the crystal field onto the low-energy singlet-triplet subspace (cf. section 1.4.5.2). What happens if the crystal field is included in the creation of the singlet-triplet model itself (cf. section 3.3.1), which is what one should reasonably do when it is larger than or comparable to the SOC λ ? One aspect is an emerging energy gap in the triplet (cf. figure 3.41), but that should work analogous to the projected case (non-symmetric Chern numbers). Additionally the form of the interactions ($J/K/\Gamma$ and beyond) change (cf. figure 3.44), but that one we deemed unimportant for the overall fact of topological non-triviality by analysis of the extended $J/K/\Gamma$ model. The only caveat is of course that now technically the high-field limit is influenced, but obviously not in an essential manner regarding its non-triviality.

4.3 Triangular Lattice

4.3.1 Topological Phase Diagrams

The excitonic Kitaev-Heisenberg model is not limited to honeycomb lattice scenarios. In a delafosite structure for example, the same form of interactions can be relevant for a triangular lattice geometry [1]. Beyond that, the results of honeycomb and triangular lattice might be used to assess the possible emergence of triplon topology for related scenarios. We sketch most of the geometries talked about in this thesis in figure 4.17. Of those, we focus the analysis on the triangular lattice, for reasons that will become apparent when considering our results.

For a triangular lattice the lack of a nontrivial unit cell leads to a fundamentally different scenario for nontrivial topology. First and foremost, the large magnetic field limit leads to a trivial topology, because there is no degeneracy that can be lifted. Secondly, all dispersion relations ϵ_α and γ_α are real. This influences the competition of h and Γ , which share the same matrix elements. Additionally, the Heisenberg interaction acts only as an overall momentum dependent energy shift and is therefore not important for the formation of topologically nontrivial bands.

Without the Heisenberg terms the triplon Hamiltonian is

$$H = \begin{pmatrix} \epsilon_x & \gamma_z - ih_z & \gamma_y + ih_y \\ \gamma_z + ih_z & \epsilon_y & \gamma_x - ih_x \\ \gamma_y - ih_y & \gamma_x + ih_x & \epsilon_z \end{pmatrix}, \quad (4.18)$$

with $\epsilon_\alpha = \sum_{\mathbf{r}_\alpha} 2K \cos(\mathbf{k}\mathbf{r}_\alpha)$ and $\gamma_\alpha = \sum_{\mathbf{r}_\alpha} 2\Gamma \cos(\mathbf{k}\mathbf{r}_\alpha) + \Delta_{\text{CF}}$, where we included the influence of a trigonal crystal field Δ_{CF} analogous to earlier discussions. Moreover, \mathbf{r}_α denotes the vector to the nearest neighbor along a bond of type $\alpha = x/y/z$ (cf. figure 4.17).

A closer look at the Hamiltonian reveals, that nontrivial topology requires the existence of both Γ terms and magnetic field. Due to the lack of dispersion, which in the honeycomb scenario was added by the bonding/antibonding solutions, a system containing solely the magnetic field in the off-diagonal matrix elements can not provide a nonzero Chern number. Moreover, the lack of a magnetic field results in a real symmetric matrix, which also prevents topological phases. Thus we require Γ and h . Additionally, the nature of the interactions dictates the need for at least two of the Γ terms to break inversion symmetry, or alternatively anisotropy in the Kitaev couplings (see the later discussed minimal model).

Figure 4.12 presents representative values for topological phases in the absence of a trigonal crystal field. For the case of comparison with the honeycomb lattice we set $\Gamma = 0.1A$ unless otherwise stated. There is however no drastic change of topology (only phase borders as implied by the presented formulas) when the roles of Γ and K are switched. We find a range of scenarios containing topologically nontrivial phases. However, in contrast to the honeycomb lattice there are noticeably many areas with trivial Chern number. We can support the results by reformulating the fact of a trivial large magnetic field limit: If we do not find a point of degeneracy aside from $h = 0$, nontrivial Chern numbers are not possible. This is the main difference to the honeycomb lattice and likely the cause for the appearance of topologically trivial phases in the diagram.

Depending on the magnetic field direction the nontrivial topology is more or less (aside from small features) located in the Kitaev regime (sometimes in the $K > 0$ case and at other times $K < 0$) or, in the $[1, 1, 1]$ case, even including the $K = 0$ limit. One should note however, that based on earlier discussions of the Heisenberg coupling in this setup, the driver of this are the Γ terms, as easily evidence by the behavior of the phase borders scaling with the coupling strength.

A prudent first step in establishing these phase borders is calculating the roots of the discriminant of the characteristic polynomial, which is still somewhat feasible, at

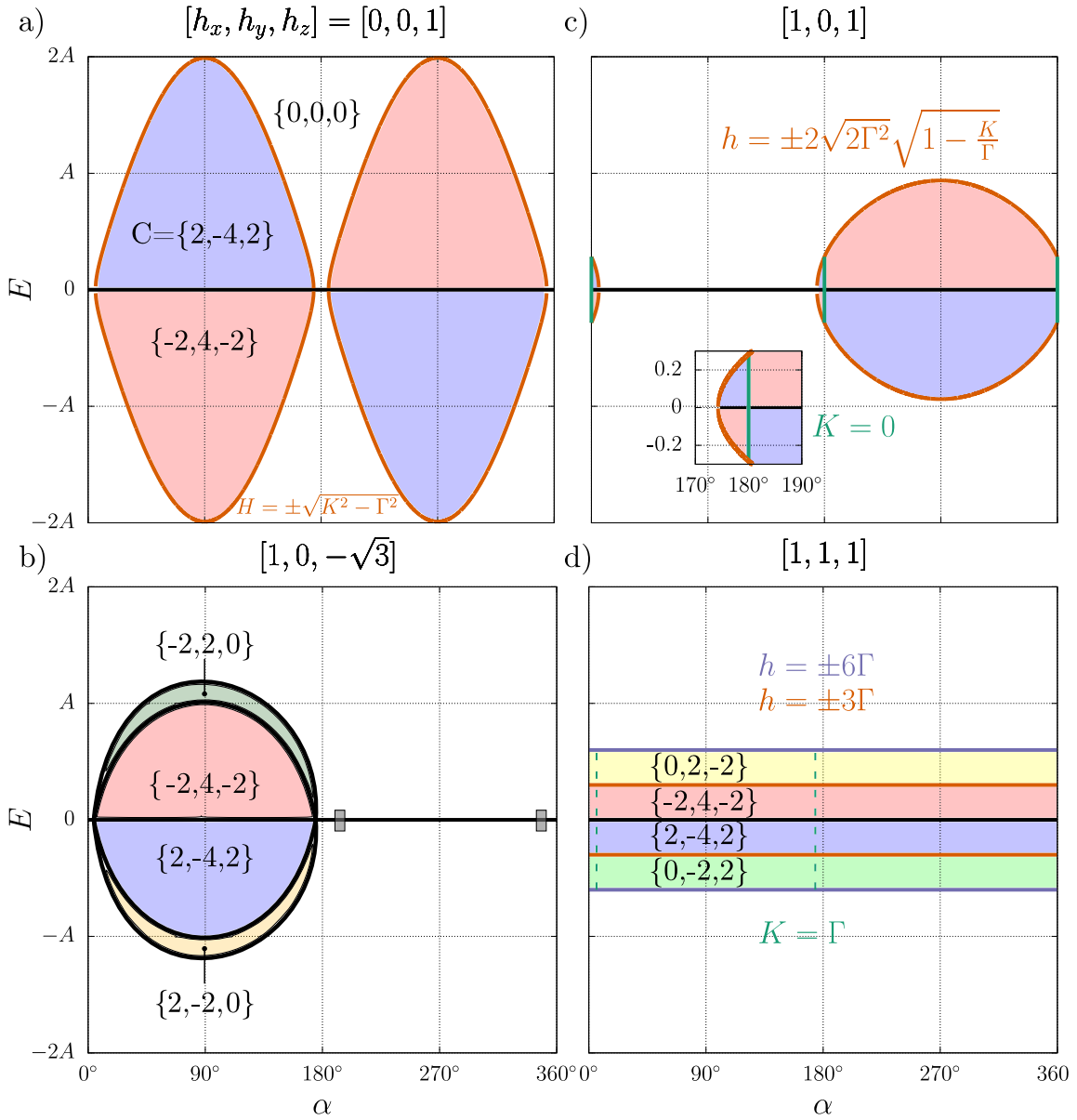


Figure 4.12. Topological phase diagrams for the triangular lattice model in absence of a trigonal crystal field: magnetic field directions are paradigmatically represented by the a) $[h_x, h_y, h_z] = [0, 0, 1]$, b) $[h_x, h_y, h_z] = [1, 0, 1]$, c) $[h_x, h_y, h_z] = [1, 0, -\sqrt{3}]$ and d) $[h_x, h_y, h_z] = [1, 1, 1]$ directions. For the trivial cases exact formulas for the phase borders are provided. The gray features in c) represent minute but existing areas of non-triviality, which is hard to evaluate due to the minuscule band gaps. All in all one may state that any area in the low-field limit can host topological band structure if the direction of the magnetic field vector is chosen appropriately.

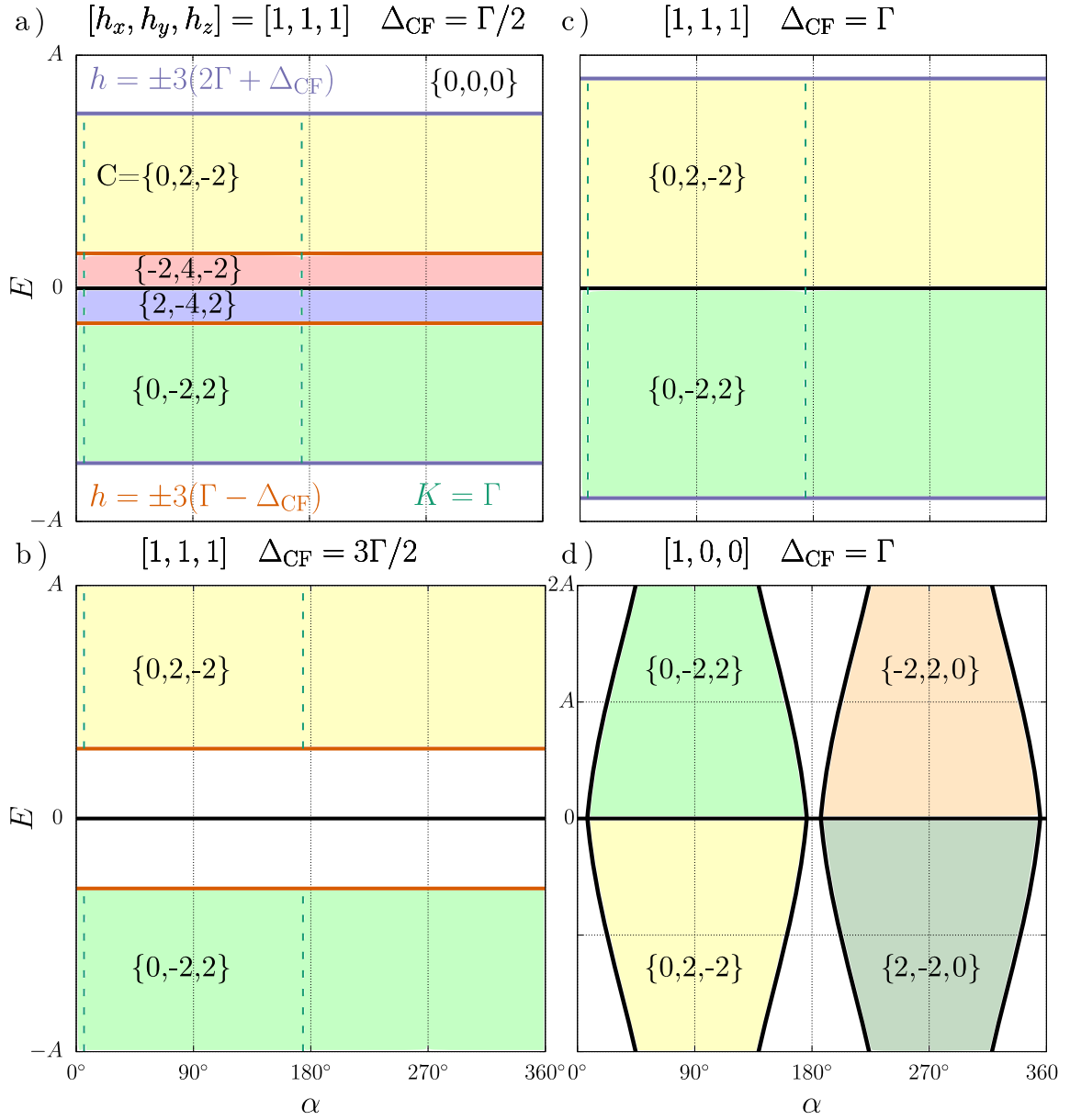


Figure 4.13. Topological phase diagrams for the triangular lattice model involving a trigonal crystal field: magnetic field directions are paradigmatically represented by the a)-c) $[h_x, h_y, h_z] = [1, 1, 1]$, where the energy scales are the most obvious, and the d) $[0, 0, 1]$ case. The trigonal crystal field supports (or in the case of $[0, 0, 1]$ creates) a phase where only two out of three bands are non-trivial. Importantly, when the crystal field is comparatively larger than the Γ interaction, the low-field limit, which is the one realistically accessible, becomes trivial. The resulting nontrivial phase moves toward higher and higher magnetic field values as Δ_{CF} increases, leading to topological band structures only being possible when magnetic field strength h and Δ_{CF} are of similar size. Additionally, in the case of the Kitaev interaction being an important quantity as in d), there the sign dictates which bands can be nontrivial, leading to four distinct phases instead of two in the absence of Δ_{CF} .

least in certain scenarios, usually with prior knowledge of the position in the Brillouin zone. These considerations can yield more general insights into the occurrence, or lack of, topological phases as seen in the aforementioned $[1, 1, 1]$ case. Moreover, it provides clean phase borders that are not subject to numerical inaccuracies. The results are provided in the figure. As the band gap closings move non-trivially in the Brillouin zone and are regularly located at some intermediate value off the beaten track of symmetry points or at least round fractions of π (we distort to a square lattice for simplicity via choice of lattice vectors analogous to the honeycomb), this is not always a practical approach, which is why no formula for the $[1, 0, -\sqrt{3}]$ case is provided.

Additionally one might be inclined to comment on the appearance of the phase diagrams in general. The $[0, 0, 1]$ case has a structure reminiscent of the Haldane model [253], although in contrast to the honeycomb lattice with next-nearest neighbors and DM interaction (and crystal field) in reference [5], we did not manage to create an obvious mapping. A reason could be that the limit $\Gamma \rightarrow 0$ is nonsensical here, at least as a topologically nontrivial model.

Another peculiarity is the $[1, 1, 1]$ case with its horizontal phase borders (aside from the $K = \Gamma$ one). Even more intriguing is the similarity of this case to the honeycomb lattice. This similarity also extends to the $K = \Gamma$ scenario, which like in the honeycomb enables the Heisenberg limit to exhibit topologically nontrivial band structure. The latter we argued to be an overall aspect of the Kitaev-Heisenberg model based on the sublattice transformation. In the triangular lattice however, the former effect is obvious. As $\gamma_{x/y/z}$ are completely real and the magnetic field enters as a completely imaginary set of numbers, the gap these interactions produce in the $[1, 1, 1]$ case is simply additive, at least when the Kitaev interactions are degenerate, i.e. at the relevant points. It is therefore expected that the Γ point in the Brillouin zone of the honeycomb lattice would host an analogous phenomenon.

We now turn to the trigonal crystal field. For the honeycomb this was only a

long side note. The crystal field only changed superficial aspects like the need to account for all six Chern numbers. It had however no impact on the topological (non-)triviality of the model. Here the result is drastically different.

Figure 4.13 contains a few exemplary phase diagrams. Other magnetic field directions fit these trends perfectly. Yet, they are less suited to describe the effects due to e.g. a superficially more complicated appearance and/or gap closing away from the symmetry points making an analytical description of the phase borders impractical.

The most important points are made by the diagrams in figure 4.13a)-c): First of all the crystal field can imbalance the Chern numbers⁷ (like Γ does here too) and therefore it prefers the topological phase fitting to this scheme. This phase gains prominence and can entirely dominate the other one, making it vanish at a critical point where the analytically determinable phase border reaches the $h = 0$ limit. At this point it appears that the crystal field is helpful for the topology, because the overall area of the phase in the parameter space has increased.

Yet, a further increase in crystal field strength changes this interpretation drastically, as a gap emerges in the low-field limit. This emerging trivial field grows with Δ_{CF} . In fact the area existing at $\Delta_{\text{CF}} = \Gamma$ is just shifted upwards in the phase diagram to an area where magnetic and crystal fields are of comparable strength.

Consequently, if a large crystal field (bigger than $J/K/\Gamma$) exists, which is a certainty in many models as can be gauged from the values we provided of Ca_2RuO_4 and even the significantly less distorted $\text{Ag}_3\text{LiRu}_2\text{O}_6$, the topology is expected to remain trivial unless the magnetic field is of comparable strength as the crystal field. A quick and dirty estimate of the magnetic field in eV units (recall that Δ_{CF} , even though it should be $\Delta_{\text{CF}}/6$ here given correct norm of direction vector $1/3$ and factor $1/2$ from projection onto the singlet-triplet model, should still have roughly two digits in meV units) would be created by looking at the Bohr magneton μ_B , which

⁷meaning that the lowest and highest band do not match anymore, here due to the crystal field splitting the triplet into a two-fold degenerate and isolated nondegenerate state

should provide an order of magnitude for the coupling (a more detailed estimate can be found in [6]). The Bohr magneton is approximately $\mu_B \approx 5.788 \cdot 10^{-2} \text{ meV/T}$. Therefore we would require a magnetic field of hundreds if not thousands of Tesla. This kind of field is incompatible with our model derivation and aside from the fact unrealistic for a laboratory setup (a low-end neutron star may only overshoot the target by an order of magnitude, thus likely presenting the most feasible option in a tongue in cheek kind of way [259]).

Leaving this comment aside, the $[0, 0, 1]$ field presents the analogous scenario with the small difference that the phases did not exist already for $\Delta_{\text{CF}} = 0$ and the trivial band is determined by the sign of K . Furthermore the new phase and trivial area do not emerge as a flat line but with a border adhering to the root function structure of the $\Delta_{\text{CF}} = 0$ model.

All in all the phase diagrams for the triangular lattice are rather tame compared to the honeycomb ones⁸. Another peculiarity is the exclusive existence of even Chern numbers. Both these aspects are very reminiscent of the result in the dipolar molecule models studied in references [249, 260–262] and at least the even Chern numbers (and high-field triviality) also emerge in the Shastry-Sutherland magnet triplon model for $\text{SrCu}_2(\text{BO}_3)_2$ [78, 124], where $C = \pm 1$ only exists in a multi-band formulation. One might suspect some underlying shared features even beyond the obvious, as the overall interactions causing the topological band structure are drastically different. For $\text{SrCu}_2(\text{BO}_3)_2$ the driver is the DM interactions and for the dipolar molecules the long-range dipole-dipole interactions enables molecule rotations to travel and change “flavor”, i.e. rotational direction, with an explicit complex phase pickup.

In particular the mantra “complicated phase diagram with likely no trivial phase for more than one atom in the unit cell and trivial phases in large areas of the

⁸Except when you add the (here) un-physical nearest neighbor DM interaction instead of the Heisenberg term. There you obtain a phase diagram akin to the $\text{SrCu}_2(\text{BO}_3)_2$ model [124] in an $h_z \neq h_x$ magnetic field in one limit and then you have two nontrivial phases like in the honeycomb intermingling. But since the high-field is still trivial these complications are limited and actually still tame compared to the honeycomb lattice.

square/triangular lattice” seems to be consistent for the dipolar molecules and our model, even beyond the honeycomb [262]. Therefore, one would suspect that the dipolar model honeycomb lattice may also have multiple nontrivial limiting cases and a model of spin-dimer triplons to likely behave similarly when looking beyond the square lattice $\text{SrCu}_2(\text{BO}_3)_2$ based scenario (cf. kagome discussion later for an explicit example).

4.3.2 Minimal Model

In order to address the presence of only even Chern numbers we need to restructure the model. One possible way to explain this “duplicity” is to reformulate the model into an artificial multilayer model [261] and show that the interactions connecting these layers are not essential for the topology by letting them go to zero without creating a gap closing. This is highly nontrivial here due to the complicated form of the interactions, which contain important on-site and hopping terms. Instead we reduce the Hamiltonian to a minimal model with the same topological phase diagram for a special scenario and find our own argument.

For the $[0, 0, 1]$ direction we find that we are able to neglect ϵ_x , ϵ_y and γ_z and still obtain the phases shown in figure 4.13 (with $\gamma_z = 0$). The Hamiltonian reduces to

$$H = \begin{pmatrix} 0 & -ih_z & \gamma_y \\ ih_z & 0 & \gamma_x \\ \gamma_y & \gamma_x & \epsilon_z \end{pmatrix}. \quad (4.19)$$

This scenario is closely related to the one argued to implement flat bands with Chern number $C = 2$ on the dice lattice [263]. In fact the Hamiltonian they analyze is more or less of the exact same form as (4.19). The difference, beyond slightly different dispersion, is the presence of a constant chemical potential instead of ϵ_z . Furthermore in their analysis they Taylor expand the touching points to make the argument we

strive for here and the magnetic field does not enter this discussion, which is good, because the mechanism of lifting the degeneracy is different. Additionally there is a spin degree of freedom with the same matrix that is not important for the point they make and we want to adopt.

As mentioned, the situation here is similar to the dice lattice. This can be made obvious if we set Γ to dominate K ($\Gamma = A$, $K = 0.1A$ if active) for the sake of an easy comparison (changes the overall look of the band structure, but not the Chern number), we can produce the band structure in figure 4.14. In the case of an absent dispersion $K = 0$ one can see that the degeneracy of all three bands takes a very simple form of a Dirac cone intercepted by a completely flat band. The magnetic field can lift this degeneracy, but the overall problem is still symmetric and the Berry curvatures cancel when the integration is performed, thus leading to a trivial Chern number.

The situation changes for $K \neq 0$. Due to the sign change of ϵ_z in different areas of the Brillouin zone we obtain two degeneracies reminiscent of the dice lattice scenario, one pair for the upper E_+ and middle band E_0 and another one for the lower band E_- and E_0 . If we follow the arguments of [263] the Chern numbers $C = \{2, -4, 2\}$ are unsurprising. The band structure degeneracy for E_+ and E_0 looks exactly the same as in the dice lattice, aside from the overall positions in the Brillouin zone, which for the dice lattice were located at the K and K' points (i.e. still at two in-equivalent points in the Brillouin zone). New in our scenario is the lower band repeating this process in the area of the Brillouin zone where ϵ_z carries the opposite sign.

Like in the dice lattice, the remaining touching points for $K \neq 0$ are quadratic dispersion relations on a flat band. The author of [263] now use this quadratic nature to argue that the Chern number should change by $\Delta C = \pm 2$ (± 1 at two points in the Brillouin zone). As we have the lower band exhibits the same touching point and the effects are additive (for the middle band, otherwise that would have $C = 0$

but E_+ and E_- would still be nontrivial), this directly explains the Chern numbers.

Nevertheless, due to the different way of lifting the degeneracy, the novel features of the dice lattice scenario with extremely flat bands and therefore motivation to look towards the possibility of fractional quantum Hall states is not warranted. The flatness is defined as the ratio of bandgap to bandwidth and the band gaps (at least the indirect ones) are basically vanishing and the bandwidth is large.

Putting this discussion aside, one might observe that the minimal model establishes the role of symmetry breaking of the Kitaev term upon a closer investigation of the Berry curvature with and without this contribution (Fig 4.14). In summary, γ_x , γ_y and h_z enable the establishment of a imaginary phase on a plaquette and the Kitaev term breaks the remaining symmetry.

An additional insight can be gained by noticing that the dice lattice phases correspond to the ones driven by the crystal field. If we allow the crystal field in the minimal model (for simplicity still $\gamma_z = 0$ entirely) we can surmise, that the touching point moves in the Brillouin zone (figure 4.14). At $\Delta = \sqrt{2}\Gamma$ (due to some interactions missing the critical points in the phase border slightly shift) the movement commences into areas of equal sign in ϵ_z therefore forcing the dice lattice scenario with only the upper and middle band being degenerate, which leads to a cancellation of Berry curvature when integrated.

4.3.3 Thermal Hall Effect

4.3.3.1 Introduction to the Thermal Hall Effect for Magnetic Excitations

We start with a short description of the thermal Hall effect in general in order to gain some context regarding the observed quantity and idea behind it. A general derivation and short side note about the difference between electrons and magnons

4.3. Triangular Lattice

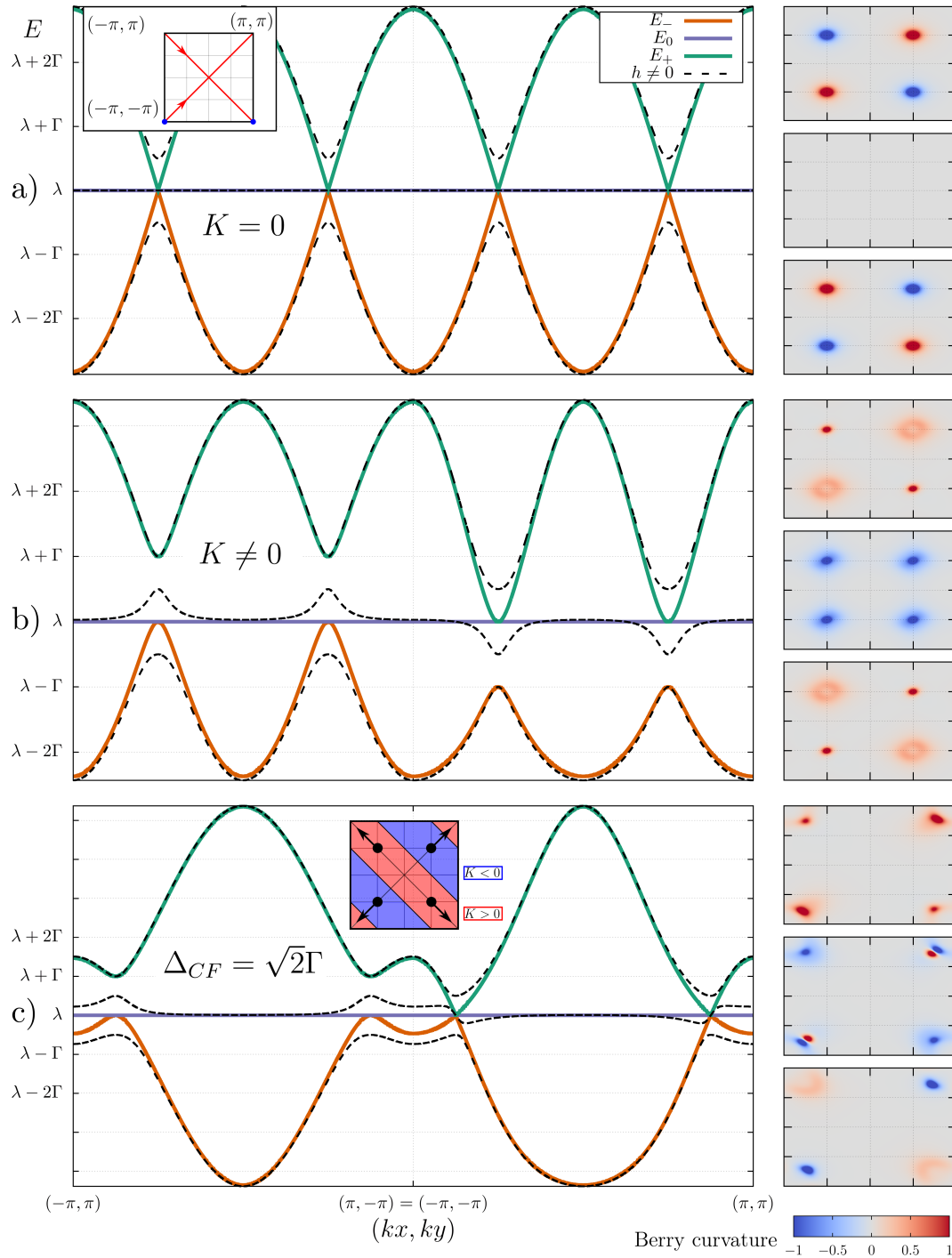


Figure 4.14. Band structures of the minimal model for the $\mathbf{h} = [0, 0, 1]$ case: a) In the absence of Kitaev interaction the band gaps can only be lifted trivially. This can be seen by observing the Berry curvature (right side, upper to lower panel belong to the energetically highest to lowest band), where the different contributions cancel each other. The Kitaev interaction in b) can enable the necessary sign change and leads to quadratic touching points of a flat band akin to the dice lattice scenario in [263]. c) The crystal field can be understood as destroying this sign change.

can be found in the review [264]. We try to use this as a basis for our own comments and point to it for explicit derivations. Moreover, a very recent review explicitly contextualizing our triplon model in regards to the overall thermal Hall effects in quantum magnets can be found in reference [265].

The original quantum Hall effect [239] and its fractional cousin [244] are build by electrons. As a result, these phenomena were established experimentally by measurements of the electrical resistance. However, the degrees of freedom in our system or bosonic/magnon excitations in general do not have a charge. Consequently, there can not be any electrical resistance or, in other words, having the Hall conductivity being a charge current is not feasible.

Nevertheless, it is prudent to start with the known quantity of comparison. The Berry curvature can be argued, either via explicit introduction to the equation of motion in a semiclassical picture or the linear response calculation of the current response via Kubo formula [240, 264], to cause a transverse charge current of the form

$$\sigma_{xy} = -\frac{e^2}{h} \sum_n \int_{\text{BZ}} d^2\mathbf{k} \rho_{\text{F}}(\epsilon_n(\mathbf{k})) \Omega_{n,z}(\mathbf{k}), \quad (4.20)$$

where e and h are the elementary charge and Planck constant, the integration goes over the Brillouin zone, $\Omega_{n,z}$ is the z-component of the Berry curvature Ω akin to equation (4.4), n denotes the band with energy ϵ_n and ρ_{F} represents the Fermi-distribution, i.e. the occupation of the band structure for a given temperature.

At zero temperature the Fermi-distribution simplifies to a Heaviside step function being either one or zero if the Fermi level is above or below the band (which in the original Hall effect are seen as flat Landau levels). Hence ρ_{F} reduces to one or zero and the integral looks exactly like the Chern number C in equation (4.4) leading to

$$\sigma_{xy} = -\frac{e^2}{h} \sum_n^{\text{occupied}} C_n. \quad (4.21)$$

Hence the current is quantized in units of $\frac{e^2}{h}$ (the novelty of reference [239]) if the Fermi level is between the bands and the system is close enough to this description (e.g. the temperature is insignificant enough compared to the band gaps).

For bosons the situation needs to be reevaluated. As the electrical current is out of the question because we do not have a charge available, the transport phenomenon considered here is the thermal one. Equivalently, a temperature gradient ∇T in a given direction, e.g. heating one side of the material, induces a transversal thermal current. One can start this discussion with the semiclassical motion of a magnon wave packet. The magnons are translated to bosons using a Holstein-Primakoff transformation and the object of study is the magnon edge current [264]

$$I = -\frac{1}{\hbar} \sum_n \int_{\text{BZ}} d^2\mathbf{k} \int_{\epsilon_n(\mathbf{k})}^{\infty} d\epsilon \rho_B(\epsilon) \Omega_{n,z}(\mathbf{k}), \quad (4.22)$$

where ρ_B is the Bose-Einstein distribution.

From this point on, the calculation gets more involved as the magnon current is not the quantity we measure. Rather the temperature gradient caused transverse thermal (Hall) conductivity is involved. Also there are complications like multiple contributions best left to literature. Derivatives of the Bose-Einstein distribution also enter and the energy integral is performed, so that the thermal Hall conductivity κ^{xy} is [264]⁹

$$\kappa^{xy} = -\frac{k_B^2 T}{\hbar} \sum_n \int_{\text{BZ}} d^2\mathbf{k} c_2[\rho_B(\epsilon_n(\mathbf{k}))] \Omega_{n,z}(\mathbf{k}), \quad (4.23)$$

where k_B is the Boltzmann constant,

$$c_2[x] = (1+x) \left[\ln\left(\frac{1+x}{x}\right) \right]^2 - [\ln(x)]^2 - 2\text{Li}_2(-x) \quad (4.24)$$

and $\text{Li}_2(-x)$ is the polylogarithm function. This quantity, although it has a compli-

⁹or detailed in the original papers [266–268], although the first one is not entirely correct. A very practical example of the calculation for a honeycomb lattice model [269] can be found in [270].

cated appearance on first glance, is not much harder to calculate than the normal Chern number (it can just be evaluated if you know the energies of the band structure and the temperature which we set externally) and is what we discuss in the figures in this section.

A few comments can be at this point. First of all the thermal Hall effect here is not quantized. This is clear when looking at the c_2 function taking the place of the Fermi-distribution when comparing equations (4.20) and (4.23). Unless of course one finds a very specific restriction for this being the case, which is why the suggested half-integer thermal Hall effect for α -RuCl₃ [53] was a big deal (before the complications mentioned in the introduction arose)¹⁰. Moreover [264] also mentions that pair creation and annihilation terms inherent in the Holstein-Primakoff transformation of spins (cf. our triplon model) and magnon-magnon interactions (e.g. the fact that we do not have bosons but hard-core bosons and/or higher order terms in the Holstein-Primakoff expansion) are a cause for loss of quantization.

Secondly, the c_2 function serves as an instrument populating the excitations, while the overall (e.g. sign) structure of the response relies on the Berry curvature. Moreover, c_2 increases for larger temperatures and obviously vanishes for $T \rightarrow 0$. “Large” concretely means that the energies of the excitations, i.e. their gap to the ground state, is of a magnitude where the thermal energy $k_B T$ can overcome the gap. A consequence is that the lowest band often governs the thermal Hall response.

Thirdly, in practice the thermal conductivity is hard to handle. A thermal Hall effect is not restricted to the topology of magnons. Heat transport can happen by other means and the contributions need to be accounted for experimentally. An illustrating example can be found in [272], where the thermal Hall effect in a magnetic skyrmion lattice accounts for phonons and skyrmions, the latter of which contributes with opposite sign.

¹⁰The thermal Hall effect for the Landau levels, i.e. in the traditional playground of quantum Hall effect physics, remains quantized, as e.g. demonstrated by the observation for fractional quantum Hall state $\nu = 5/2$ via 2.5-quantized thermal data in [271].

Fourthly, one should spell out what the magnon-magnon interaction comment implies: Spins are not normal bosons. E.g. spin-1/2 can be directly mapped to a hard-core boson. We mentioned before that this can be understood as bosons with infinitely strong on-site repulsion. More importantly, hard-core bosons do not adhere to pure boson commutation relations and thus technically the Bose-Einstein statistics. Of course this is remedied if you account for this as an interaction. Thankfully, the thermal Hall effect for magnons is well established enough to suggest that this way of handling it remains a prudent idea. However, a recent review [77] declares accounting for the magnon-magnon or triplon-triplon interactions an important need and succinctly points to the fact that inelastic neutron scattering had been successfully used to find possible signatures of topological triplons in $\text{SrCu}_2(\text{BO}_3)_2$, while the thermal Hall conductivity had not done the same. Moreover, one could ask about the character of the excitations in our model, i.e. triplons, being a potential issue. Triplon and magnon are technically different entities. However for the present discussions this would not matter for spin triplons [124], which is why the terms are often used interchangeably (see e.g. the review [76]). The fact that we do not have spin but spin-orbital triplons, although important for many things in this thesis, went overboard when we simplified the magnetization to the Zeeman term of equation (4.2).

Lastly, we should shortly address one of the possible motivations of searching for topological magnons. As evidently established by the 2007 Nobel prize in physics for the giant magnetoresistance, which is prominently responsible for skyrocketing the information density one can store on a hard drive, using spin degrees of freedom (or even beyond orbital) instead of the electron charge can possibly provide advantages. This is the subject of spintronics. In that sense the topological magnons have been suggested to be a possible platform for magnon waveguides (i.e. how a spin signal can travel) [273], interferometers [274] or dissipationless transport linked directly to the Kitaev model [275]. For the former the proposal is directly based on the material

$\text{Lu}_2\text{V}_2\text{O}_7$ [276], which has been studied in an experiment [277].

In that sense, one should point out and later discuss one possible major advantage in magnon systems. In the case of the Bose-Einstein condensation the, e.g., triplon condensates usually survive to higher temperatures, sometimes even room temperature, in contrast to gases of ultracold atoms [70]. The same advantage can exist regarding the topological magnons surviving to room temperature, which can then be attributed as an extra motivation for the practicality of the spintronics as mentioned in the paper establishing such magnon topology in YMn_6Sn_6 [278]. Hence, we require temperature to find the topological bands, but the temperature itself might not be as big of a problem as it would be in the Landau level electron picture.

4.3.3.2 The Thermal Hall Effect for Triplons

First and foremost one has to address the elephant in the room: Due to the the earlier discussed scaling of the magnetic field strength with the Bohr magneton $\mu_B \approx 5.788 \cdot 10^{-2} \text{ meV/T}$ in real materials, the expected signal of the thermal Hall conductivity in experiments is seemingly too minuscule to be measured as of today. Details can be found in reference [6], which uses the same “arbitrary units” as we do (and an unnormalized magnetic field vector, meaning the scaling is even worse than discussed there).

One does not expect this scaling problem to change by going from one lattice to another (except maybe for a stack as discussed subsequently), because the main problem is the band structure roughly existing (energy wise) around the value of the spin-orbit coupling λ . And for the paramagnetic phase, the central assumption for the topology discussion so far, this energy has to be significantly larger than J, K, Γ and Δ_{CF} .

Consequently, what we employ here is a pure model study that could only enter relevance e.g. if an alternative way of establishing Kitaev interactions provides a

similar setup (cf. earlier discussions in this chapter) or if another way of increasing the signal can be found. For the earlier discussed $\text{Lu}_2\text{V}_2\text{O}_7$ case for example, the theoretical investigation [276] points out that the three-dimensional pyrochlore lattice can be treated as a stack of two-dimensional kagome lattices, with the consequence that the “three-dimensional” thermal Hall conductivity is significantly larger than the one on the kagome.

As a pure model study, providing thermal Hall conductivities for random phases in the phased diagrams does not serve a purpose, especially because most of the calculations look rather random and the honeycomb has already been addressed [6]. We instead focus on two aspects: First of all we make comments about topics not addressed in reference [6], such as the earlier one relating to $\text{Lu}_2\text{V}_2\text{O}_7$. Secondly, we focus on some specific aspects of the triangular lattice results.

We start with an aspect making the thermal Hall conductivity an even worse tool beyond the scaling. As mentioned, a big advantage of the topology in magnetic excitations is that it might be feasible to survive to room temperature. However, our analysis is based on a low-energy effective model and even beyond that the assumption of a Mott insulator for the Kugel-Khomskii type perturbation theory. The former problem is hard to gauge, as, e.g., possible quintet involvement is model specific. The latter observation, however, can be directly connected to experimental analysis of the metal-insulator-transition in materials of interest.

For example Li_2RuO_3 (aside from having different physics) has a Mott phase surviving up to 540 K [9]. Ca_2RuO_4 however has a magnetic [279] and a Mott transition [18], where the latter is located at roughly 360 K, slowly approaching a region where non-Mott influences might be of note at room temperature of ≈ 293 K. For $\text{Ag}_3\text{LiRu}_2\text{O}_6$, i.e. a material of direct interest, originally a metallic behavior was suggested [280]. Yet, the more recent study [8] suggest a semiconducting regime slightly below room temperature and a weak Mott regime beyond, thus a very problematic setup in regard to temperature based surviveability.

Next we attempt to contribute to the previously introduced sign structure discussion of the thermal Hall conductivity in α -RuCl₃ based on statements of it being consistent with Kitaev Majorana fermion structure [54] or a general feature found in topological magnons in a KΓΓ' model [59].

For the honeycomb lattice we already mentioned that the answer is rather obvious. In the description of the thermal Hall conductivity and the subsequent statement of the Berry curvature (Chern number) of the lowest band being expected to be the deciding factor, now there is a reason available. For the high-field Kitaev model this follows directly, obviously and without constraints for the entire phase diagram in figure 4.2. Given the discussions for the Kitaev-Heisenberg model ($\Gamma = 0$) in the $[1, 1, 1]$ and $[1, 1, -2]$ case, the sign structure is most likely similar if the phase survives (so not in all regions of the phase diagram). However, changes in Chern numbers of the higher bands can be ignored and the likelihood of this is therefore very reasonable. Similarly, the Γ terms might complicate things in certain scenarios, but the new phases they create usually also just adhere to the sign of the magnetic field vector components (with the same phase survival assumption as the Kitaev-Heisenberg case). All in all, we find that the triplons on the honeycomb also usually have a/the characteristic sign structure.

For the triangular lattice things are more complicated. As established by the phase diagrams there are areas where more or less only the AFM Kitaev region can be nontrivial and some where only the FM does the same. Additionally there are the regions where only the Γ interaction alone seems to be responsible like the $[1, 1, 1]$ case, which causes an overall sign flip. Therefore the sign structure does not translate to this model if the magnetic field sweep is not chosen to actively seek out the few regions where it does. E.g. the $[0, 0, 1]$ and $[1, 0, -\sqrt{3}]$ cases (also of course $[0, 0, -1]$) fit the description for the AFM Kitaev regime.

We finally turn to concrete calculations for the triangular lattice. Why could there even be interest in them if the nontrivial topology already and more stably exists

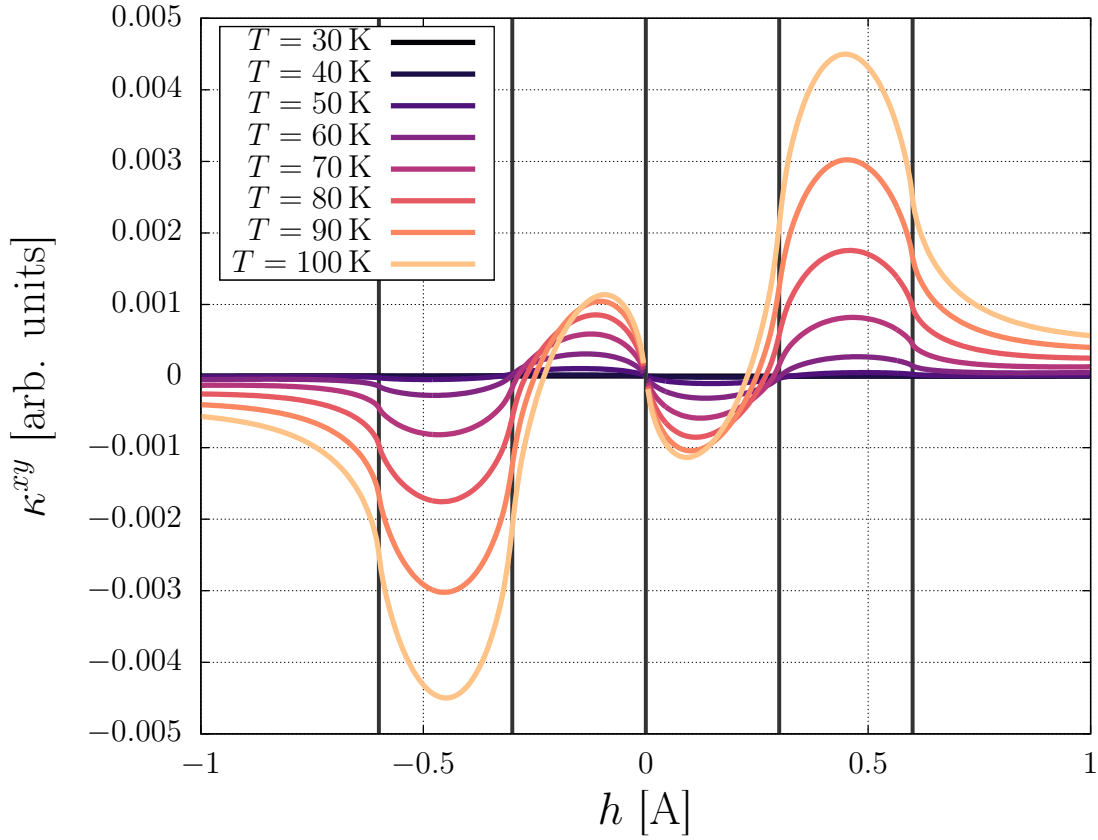


Figure 4.15. Thermal Hall conductivity for various temperatures for the $\mathbf{h} = [1, 1, 1]$ magnetic field: topological phase transitions are visualized by vertical lines. In contrast to the honeycomb lattice where there is regularly a plethora of topological phases one passes through by increasing h , the triangular lattice provides very simple and characteristic signatures of the thermal Hall conductivity κ^{xy} .

on the honeycomb lattice? First and foremost the phase diagrams of the triangular lattice are far simpler and more manageable than their honeycomb counterparts. As such one might even reliably pinpoint the regime a material is in via ab-initio calculations. This feature translates to the thermal Hall conductivity, as exemplified by the $[1, 1, 1]$ case in figure 4.15 ($\lambda = 10A$ is set hereinafter as an energy scale and the phase border cf. figure 4.12 are shown by the black vertical lines.). The structure remains simple, understandable and visually comparable to the one in the $\text{SrCu}_2(\text{BO}_3)_2$ model in [124].

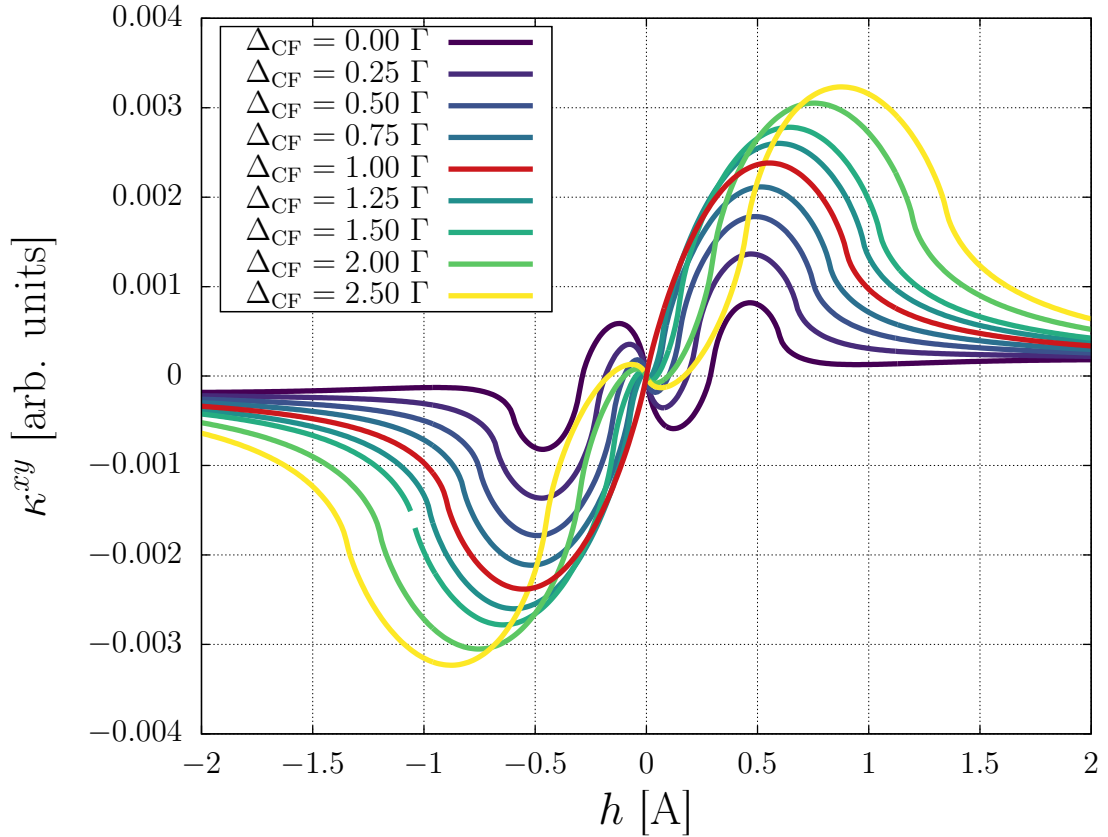


Figure 4.16. Thermal Hall conductivity for various crystal field strengths Δ_{CF} for the $\mathbf{h} = [1, 1, 1]$ magnetic field at a temperature of $T = 70$ K: the thermal Hall conductivity κ^{xy} can be driven to a sign change as a result of e.g. pressure increasing the crystal field contribution. Additionally, the overall splitting of the bands is increased and (if the sign is chosen so that the twofold degenerate crystal field state decreases in energy) the gap created by the spin-orbit coupling λ decreases, leading to a gain in signal strength.

If we can pinpoint where we are in the phase diagram, the magnetic field can be reliably chosen to switch the sign of the thermal Hall conductivity or even switch it of altogether, thus enabling a factor of control of the resulting edge modes and therefore possible use for the spintronic setups at least in principle.

Additionally one can also switch the sign or enable/destroy the topology via crystal field (i.e. pressure) as shown in figure 4.16. Switching of via pressure does not work for the honeycomb, as mentioned before. Also, reliable predictions in the

kaleidoscope of phases seems unfeasible there, while for the triangular lattice the overall structure remains predictable.

4.4 Other Geometries and Interactions

Analyzing Kitaev-Heisenberg models for different geometries is a very established idea [257], which we already started when considering the triangular lattice. Here we try to find out whether or not triplon topology exists in various lattices, in particular the ones sketched in figure 4.17.

4.4.1 Kagome Lattice

We start with the kagome lattice [figure 4.17c)]. Summarizing the result in one sentence: The kagome lattice works like the honeycomb with even more phase transitions. In essence: we tried more or less everything we discussed for (the numerical results on) the honeycomb lattice and have not found any trivial phase (aside from scenarios like $[1, -1, 0]$ and others discussed before).

Because there are nine bands and there is not necessarily a symmetry of Chern numbers of the lowest and highest bands, presenting a full phase diagram like in figure 4.9 seems unreasonable. Also, the model seems to complicated for an analysis of the limits as before. Our observations are of a purely numerical nature. Additionally, the sheer amount of phase transitions (note that we only look at $0^\circ \leq \alpha \leq 180^\circ$ here) provides a reason not to look too closely at the results and rather talk about the overarching narrative.

Instead of outright providing a full phase diagram, we sketch the result of the $[1, 1, 1]$ case with $\Gamma = 0$ and provide practical insight, so anyone attempting to do a similar calculation can see how we e.g. established the honeycomb phase diagrams (and realize why we do not want to do the same here). Figure 4.18 shows a plot

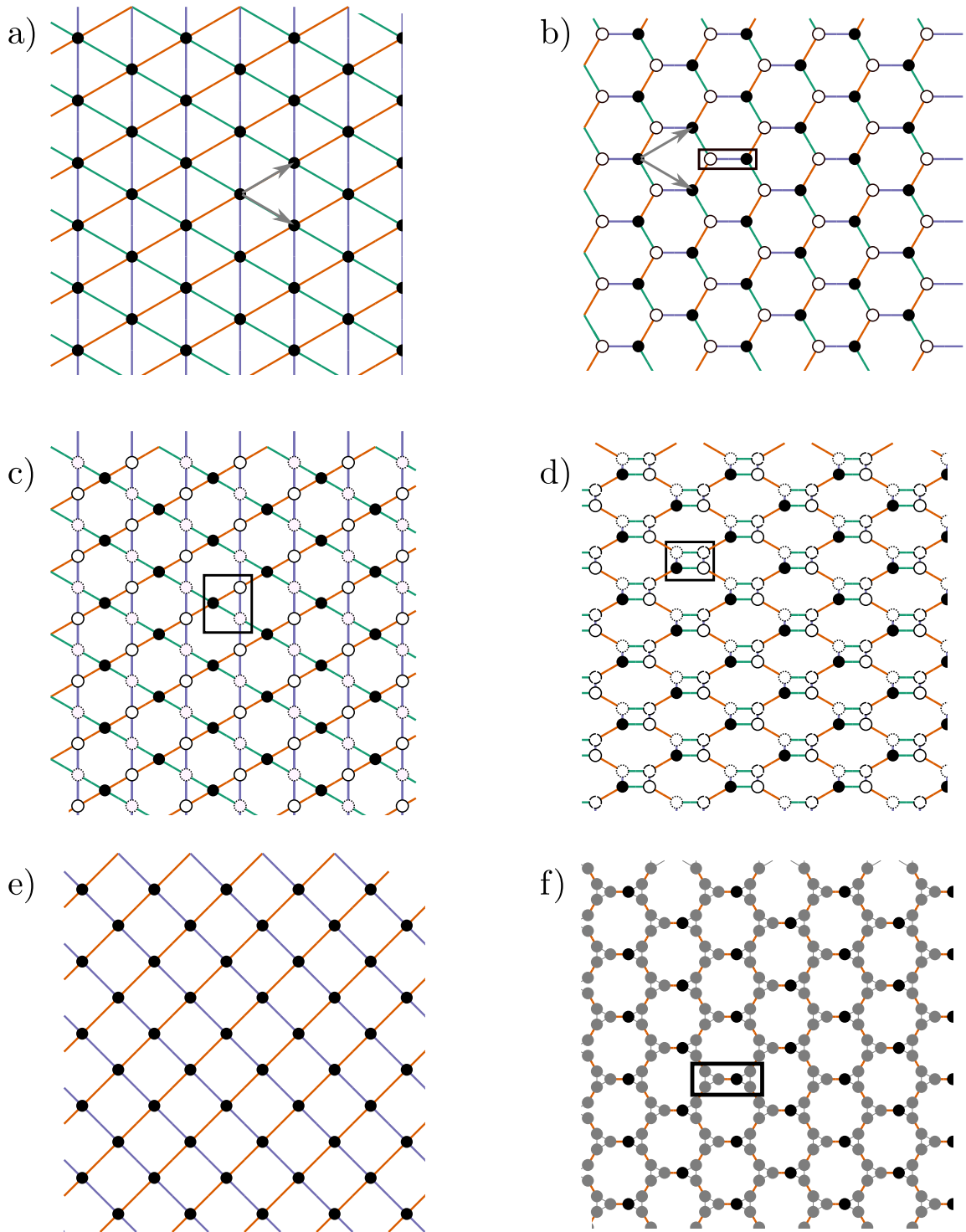


Figure 4.17. Various lattice setup studied for their triplon topology: The three bond types of the Kitaev-Heisenberg model are colored in orange, green and purple (except for f)). Lattice vectors (gray arrows, stay consistent for all lattices pictured) and basis sites (black boxes) for the unit cells are provided. The lattices are a) the triangular lattice, b) the honeycomb lattice, c) the kagome lattice, d) the square-octagon lattice, e) the square lattice and f) the star lattice (dimer bonds orange).

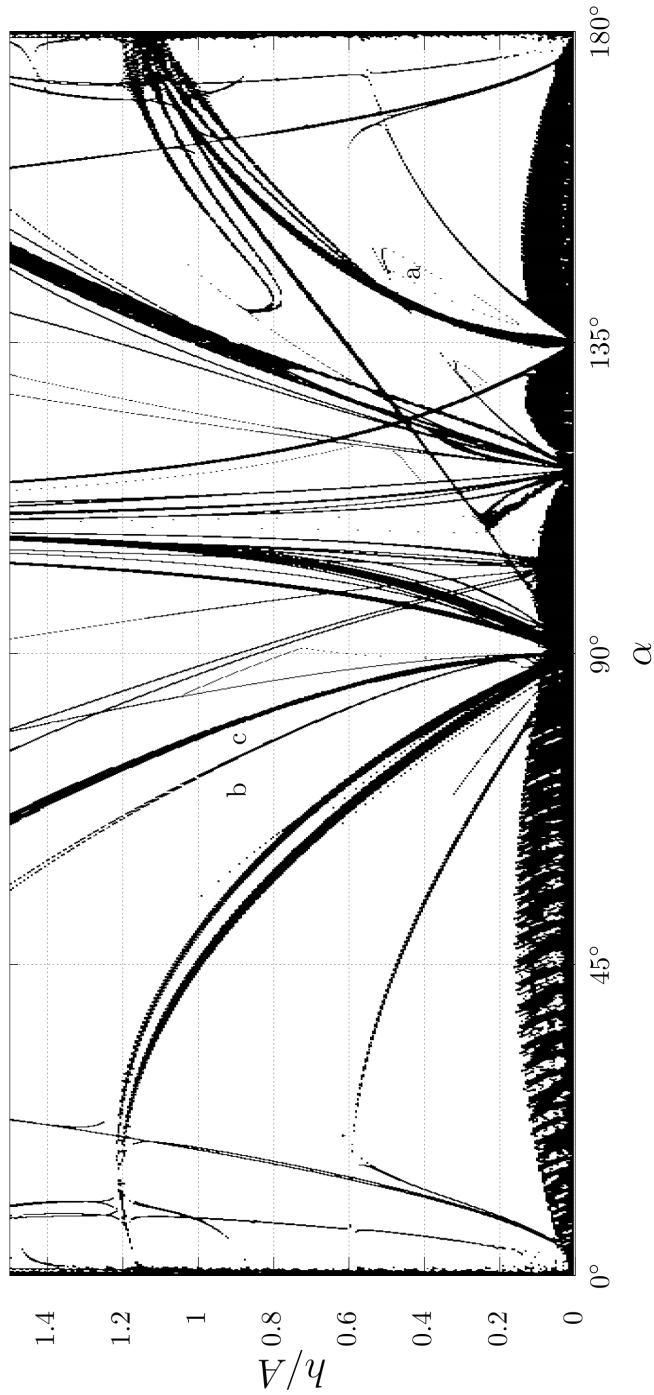


Figure 4.18. Chern number calculation for the Kitaev-Heisenberg model on a kagome lattice in a $[1, 1, 1]$ magnetic field with $\Gamma = 0$: Only the Chern number calculations obviously erroneous due to minute band gaps are highlighted in a black color, because this can imply phase transitions. Exemplary, three locations denoted by letters are connected to Chern numbers. One finds $\{1, -3, 2, -3, 6, -3, 2, -3, 1\}$ for a, $\{-1, 0, 1, -1, 0, 1, -1, 0, 1, -2, 1, -1, 0, 1\}$ for b and $\{-1, 0, 1, 1, -1, 0, 1\}$ for c.

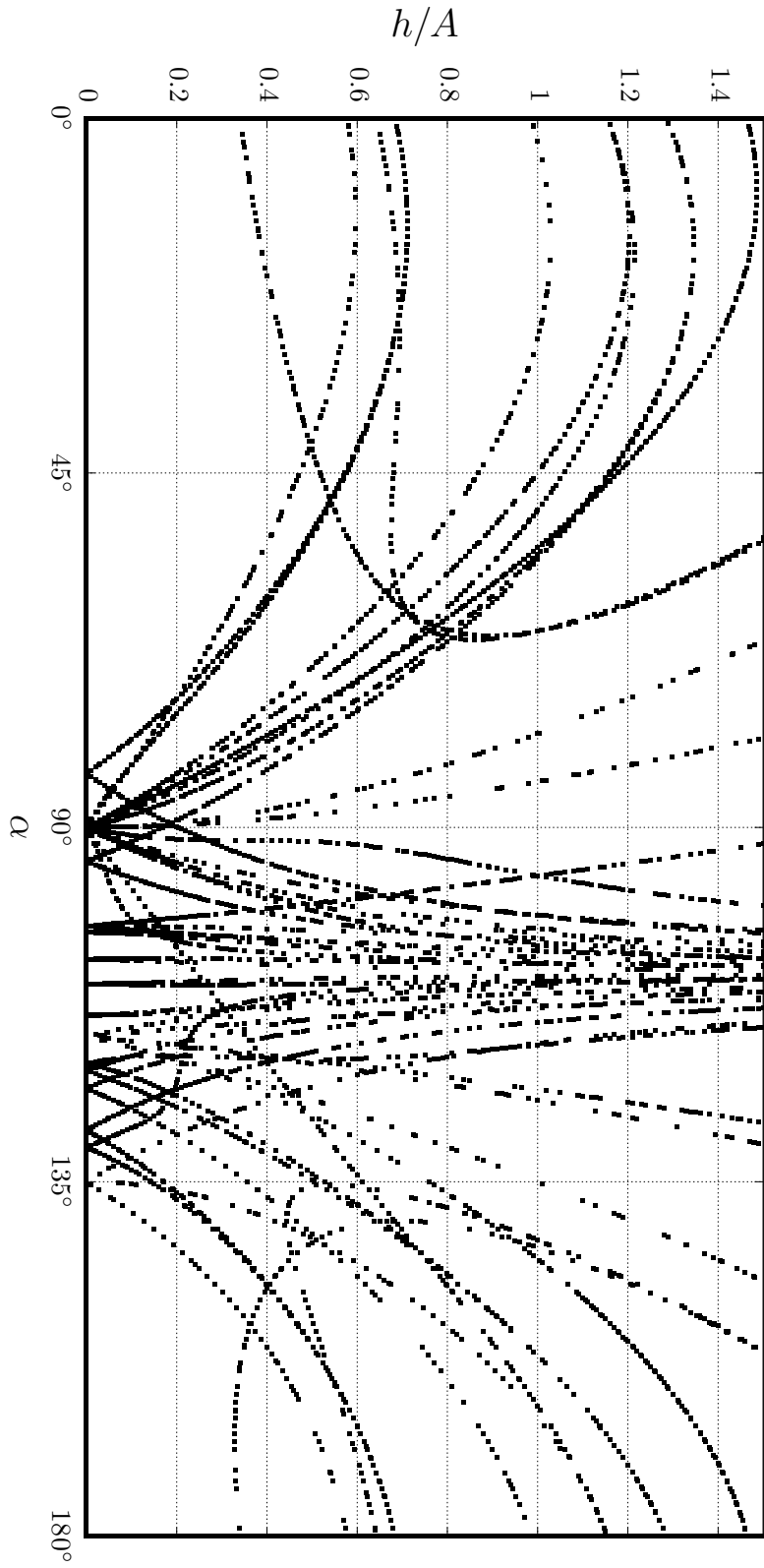


Figure 4.19. Band gap closing at the Γ , K and M symmetry points for the Kitaev-Heisenberg model on a kagome lattice in a $[1, 1, 1]$ magnetic field with $\Gamma = 0$: Even without evaluation of the off-symmetry point degeneracies (which exist based on figure 4.18), the topological phase diagram for the kagome lattice can be gauged as rather complicated.

of the Chern number calculations (for the first half of the Kitaev-Heisenberg model for simplicity) where only the results that are obviously wrong (due to (almost) degenerate bands making an integration with the chosen accuracy, read number of points in the Brillouin zone, unfeasible) colored black. Additionally, figure 4.19 shows the band gap closings (only at the Γ , K and M symmetry points in the Brillouin zone) found by explicitly calculating the zeroes of the band gaps at the specific \mathbf{k} values, which obviously has the advantage of not having to perform an integration. For the honeycomb in the absence of Γ interaction the latter provides almost all necessary information for the phase diagram (cf. figures 4.7 and 4.8).

In a practical estimation of the phase diagram one can overlay these plots. Some black spots in 4.18 are obviously just a numerical issue, while others, where a change of Chern numbers follows, can be band gap closings away from the obvious symmetry points. Other transitions happening quickly are not found in 4.18 as not hitting them exactly can mean that just the Chern number changes without numerical issues. This approach however enables one to see if any such search for these kind of gap closings away from the symmetry points has to be performed (which is not hard, but naturally more effort than searching at a single point). For the kagome lattice this is the case even in the absence of Γ interactions. Here, we do not present such results as 4.19 looks crowded enough as presented.

As a result we have all phase transitions and can try to fill in the diagram. For this one can turn to the other results established by the Chern number calculation in 4.18. Yet an absence of obviously nonsensical results like the black points in that picture does not mean that the remaining ones are reliable. Numerical difficulties of the integration (i.e. its accuracy settings) still might not provide a useable result everywhere. In complicated cases like the honeycomb with $\Gamma \neq 0$ and the kagome, one might only obtain a big majority of phases in a first overall sweep. It is on that level that we make the assertion of not having found any trivial phase yet. For a phase diagram you have to then make the effort and fill all the gaps, which is arduous

work given the sometimes minute band gaps and overall amount of phases found. It is probably therefore that the paper discussed subsequently [252] also only provides three phases explicitly.

Ergo we point out the phases a, b and c in figure 4.18 explicitly. The Chern numbers from the lowest to highest band in “a” are $\{1, -3, 2, -3, 6, -3, 2, -3, 1\}$ (which represents multiple large areas with Chern number 6). For b, which seemingly survives down to the low-field Kitaev limit, we find $\{-1, 0, 1, -1, 0, 1, -1, 0, 1\}$, which is reminiscent of the low-field limit spin- L calculation (just for three instead of two sublattices consistent with the unit cell size of the kagome lattice). The big neighboring phase c is defined by $\{-1, 0, 1, 1, -2, 1, -1, 0, 1\}$, i.e. a ± 2 transition between bands 4 and 5.

Now we consider the results of the very recent paper [252] to find a practical application of the knowledge we gained. The authors consider a spin-1/2 Kitaev-Heisenberg model on a star-lattice (cf. figure 4.17). In one of the resulting phases, the ground state is found to be described by a valence bond singlet, where the spins on the orange colored bonds in figure 4.17 host a spin-1/2 dimer singlet and triplet excitations in an effective model framework (which is why you can not directly compare phase transitions). If one treats the singlets as new lattice sites, the emerging geometry is a kagome lattice.

Following naive predictions based on our model, given that their setup should work in rough analogy, we would expect a kaleidoscope of nontrivial topological phases everywhere when a magnetic field is involved, a lot of very chaotic looking phase transitions and maybe even Chern number 6 to be the reliably biggest topological invariant involved. In [252] they find exactly that. Moreover, the $\{-1, 3, -5, 6, -6, 6, -5, 3, -1\}$ phase they point out also seems to exist in a small area in our phase diagram, but that might be by accident because the location in our diagram is near the Heisenberg limit (as suggested by the first three Chern numbers when compared to the honeycomb).

Concluding, we would like to point out an extremely recent study of a model based on a class of materials with an emerging kagome lattice (and DM interactions), which also shares the feature of kaleidoscopic topological phase diagrams [281].

All in all one may be able use our model, especially the fact that nontrivial Chern numbers exist everywhere, as a blueprint to understand singlet-triplet topology in other setups.

4.4.2 Square-Octagon Lattice

The natural question arising from the results of the kagome lattice is: Does the triplon topology continue to work out when going to bigger unit cells? One such model is the square-octagon lattice (cf. figure 4.17), which has been discussed in the context of the regular Kitaev model [207, 282, 283] due to it sharing one important feature with the honeycomb lattice: each site has exactly three bonds (constructed as one of each type).

For us this feature is also a practical one. In the pure Kitaev case, each flavor is located on a bond without the option of leaving, thus leading to the same kind of nondispersive band structure as the honeycomb model (cf. figure 4.4). As a result we obtain the same kind of starting point in the high- and low-field limits, just with extra degeneracy. For the low-field case one obtains exactly two copies of the anti-bonding spin- $L = 1$ and the bonding spin- $L = 1$, i.e. two sixfold degenerate flat bands. In the high-field limit the sublattice produces two copies of each two band model, i.e. three fourfold degenerate bands. In principle those could be evaluated, although this is nontrivial as everything exchanges nontrivially and the perturbation theory needs to be revised.

However, there is no need to do so. The answer provided by purely numerical evaluation of the entire Kitaev-Heisenberg model suggests that we can never produce band gaps in this model. Degeneracies always remains, which seems logical as we

only have three flavors to lift at minimum a degeneracy involving 4 states. The touching points are located at more often than not entire lines in the Brillouin zone, which implies that even more involved approaches like introducing anisotropy in e.g. the Kiteav interactions can not help.

Just to illustrate this point by a simple example: At the Γ point ($\mathbf{k} = \mathbf{0}$) the entire model in the basis $\{|x_1\rangle, |x_2\rangle, |x_3\rangle, |x_4\rangle, |y_1\rangle, |y_2\rangle, \dots\}$, where the letter denotes the triplon flavor and the index the sublattice reads:

$$H = \begin{pmatrix} \epsilon & -\mathbf{h}_z & \mathbf{h}_y \\ \mathbf{h}_z & \epsilon & -\mathbf{h}_x \\ -\mathbf{h}_y & \mathbf{h}_x & \epsilon \end{pmatrix}, \quad (4.25)$$

$$\epsilon = \begin{pmatrix} 0 & 3J + K & 0 & 0 \\ 3J + K & 0 & 0 & 0 \\ 0 & 0 & 0 & 3J + K \\ 0 & 0 & 3J + K & 0 \end{pmatrix}, \quad \mathbf{h}_\alpha = \begin{pmatrix} ih_\alpha & 0 & 0 & 0 \\ 0 & ih_\alpha & 0 & 0 \\ 0 & 0 & ih_\alpha & 0 \\ 0 & 0 & 0 & ih_\alpha \end{pmatrix}.$$

This matrix is simple enough that the eigenvalues can be solved exactly by an algebraic program of choice. For the $[1, 1, 1]$ case one obtains three threefold degenerate solutions. Likewise, any magnetic field with two matching components, e.g. $h_x = h_y \neq h_z$, results in three twofold degeneracies. Other cases can be analyzed similarly e.g. at the M point. There is no lack of choice when it comes to degenerate points. Including Γ interactions or crystal field does not remedy the overall problem of non-existing band gaps.

Hence we managed to find a case where the topology becomes ill-defined due to remaining degeneracies that seemingly can not be lifted, likely due to the size of the unit cell.

4.4.3 Ca_2RuO_4 -Based Lattice Model

For the Shastry-Sutherland magnet $\text{SrCu}_2(\text{BO}_3)_2$ topological triplon excitations have been implied via inelastic neutron scattering [125]. Additionally, the experimental spectra suggest a nontrivial interplay with two-triplon bound states, which the topology survives. Naturally, one is reminded of the inelastic neutron scattering experiment establishing the Higgs mode in Ca_2RuO_4 [2], a material with significantly more established research compared to e.g. $\text{Ag}_3\text{LiRu}_2\text{O}_6$.

Why has there been no sign of a topological triplon excitation in Ca_2RuO_4 ? First of all, Ca_2RuO_4 is not a paramagnet, but rather in the condensed AFM phase¹¹. Therefore one could excuse the absence of a topological band structure by it not surviving into the condensed phase, which is a valid point worth of study beyond this thesis. That however is not the main point we want to make here. One could easily suggest considering for example an iridate based counterpart where the SOC could feasibly be strong enough.

So we turn to the second argument against a topological band structure in these materials: the model itself. In [1] it was found that the h_2 (cf. equation (1.77)) are

$$H = \frac{t^2}{U} \sum_{\gamma} \sum_{\langle i,j \rangle_{\gamma}} \left[\frac{11}{3} \mathbf{v}_i \cdot \mathbf{v}_j - v_{i\gamma} v_{j\gamma} + \frac{1}{3} (\mathbf{u}_i \cdot \mathbf{u}_j - u_{i\gamma} u_{j\gamma}) \right], \quad (4.26)$$

with the author's choice of $\mathbf{T} = \mathbf{u} + i\mathbf{v}$ we¹² find (again discarding pair creation and

¹¹We drop the point of questioning whether SOC is really important or one should rather understand Ca_2RuO_4 as a more regular spin-1 model due to the tetragonal crystal field, which was mentioned in earlier discussions. That is not the issue here and some kind of triplon based model can always be created when crystal field and SOC are handled on equal footing (cf. section 3.3.1).

¹²[1] uses additional approximations such as $v_{i\gamma} v_{j\gamma} \rightarrow 1/3 \cdot \mathbf{v}_i \cdot \mathbf{v}_j$, which are avoided here because the bond dependence is essential

annihilation terms)

$$H = \frac{t^2}{U} \sum_{\gamma} \sum_{\langle i,j \rangle_{\gamma}} \left(\mathbf{T}_i^{\dagger} \mathbf{T}_j - \frac{1}{3} T_{\gamma,i}^{\dagger} T_{\gamma,j} + \text{h.c.} \right). \quad (4.27)$$

Paired with the different and more symmetric lattice and bond structure compared to the honeycomb (see 4.17), this model is actually not well suited for nontrivial triplon topology. Even with a more free parameter choice akin to the Kitaev-Heisenberg model it stays trivial because the Γ interactions are lacking. And even adding Γ interactions does not help. Neither does a less simplified Kugel-Khomskii model including Hund's coupling influences (cf. model in appendix A.4) or the idea of adding (well motivated based on the material) next-nearest neighbor terms [134].

Luckily, one does not have to be concerned about the exact structure of the model and what kind of interactions are necessary to create a topological triplon band structure (e.g. DM interactions). The third argument against nontrivial topology seems to be significantly stronger anyways: With one atom in the unit cell, Ca_2RuO_4 has the same problem regarding the crystal field as the triangular lattice.

The tetragonal crystal field, like the trigonal one, introduces a trivial gap (can be tested e.g. with the triangular lattice model and understood easily). It is of the same size and therefore intrinsically connected to the same problems as the trigonal field, namely that, if it is larger than the $J/K/\Gamma$ terms (which it significantly is in Ca_2RuO_4 as established previously), the magnetic field needs to be of the same magnitude as the crystal field to be even able to produce a topological band structure, which we deemed extremely unrealistic.

All in all, one has reasons to not expect any Ca_2RuO_4 related material to host topological triplons.

4.4.4 Triplon Topology in Other Dimensions

Calculating the topological invariant in different dimensions can be a radically distinct process in practice [240]. The same is naturally true for the topology itself. Here we do not strive to provide any real kind of analysis of the triplon model in different dimensions. Nevertheless, the previously discussed results imply which research foci might be fruitful and what to expect. We want to make these implications clear.

First we consider a look into three-dimensional problems. Trivially, a model that does not really need to be treated as a three-dimensional entity, such as earlier the earlier pointed out example of $\text{Lu}_2\text{V}_2\text{O}_7$ where a pyrochlore lattice can be treated as a stack of two-dimensional kagome lattices, will work and might even be a good idea to gain a more noticeable thermal Hall conductance.

More importantly, however, is the fact, that many of the three-dimensional compounds where the Kitaev or Kitaev-Heisenberg models are discussed are lattices with comparatively large unit cells. The fcc lattice with the bond setup of [257] has four sites per unit cell and our own efforts suggest the same problems as the square-octagon lattice: the bands stay trivially degenerate (in the fcc at the corners of the Brillouin zone because the dispersion relations vanish like in the Heisenberg case). This does not bode well for the hyperhoneycomb [284] or its various cousins [285]¹³ (for which the magnetic phases on the other hand show an intriguing 2D-3D correspondence) and examples beyond that [207].

A seemingly more intriguing topic seems to be the one-dimensional environment. Here we try to establish this via example. It should, however, be noted that no detailed study of the subsequent model has been done, mainly due to it bringing its own challenges.

For a certain 1D model, results can be obtained practically for free by reconsidering

¹³see especially the supplementary information

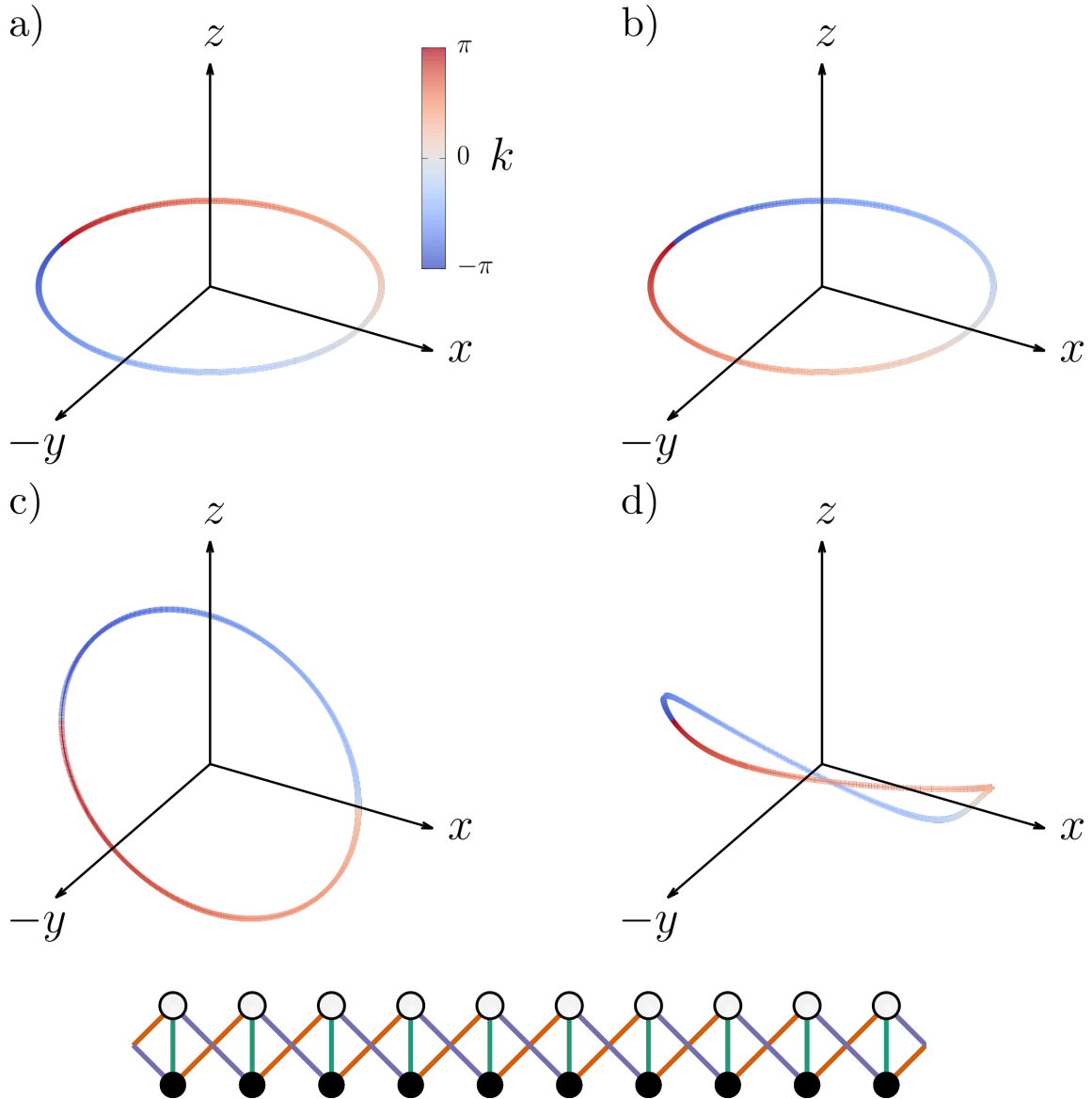


Figure 4.20. Winding number vector \hat{n} for the triplon Kitaev model based on the one-dimensional SSH-inspired lattice at the bottom, where bond colors denote the bond types: a) $[0, 0, 1]$ magnetic field, b) $[0, 1, 0]$, c) $[1, 1, 1]$ and d) $[1, 2, 3]$. In the first two cases the movement is localized entirely in the x - y -plane and the chiral symmetry is therefore intact. In c) the winding circle is orthogonal to the x - y -plane, while in d) the movement is irregular.

the high-field limit of the honeycomb lattice. Therein we reformulated the problem as a set of effective two-band models and commenced with an analysis of the winding number. Similarly, the Su-Schrieffer-Heeger (SSH) model is a two band model which often serves as a paradigmatic example for the topology in one dimension [286]. As such, we can reuse results and discussions pertaining to it, such as the one-dimensional winding number

$$W_n = \frac{1}{2\pi} \int_{\text{BZ}} dk \left(\hat{\mathbf{n}} \times \frac{\partial \hat{\mathbf{n}}}{\partial k} \right)_z, \quad (4.28)$$

where $(\)_z$ refers to the z component of the vector.

If we propose a bipartite lattice model as seen in the bottom of figure 4.20 but involving our triplon setup, the high-field limit expressions derived in section 4.2.1 can just be reused with a changed dispersion ϵ (we set $\Gamma = 0 = J$, because we only want to create a proof-of-principle and not a full study) via, e.g., $\epsilon_z = J e^{ik} + J e^{-ik} + (J + K)$ (other flavors accordingly).

Some resulting $\hat{\mathbf{n}}$ vectors for different magnetic fields are presented in figure 4.20. We find well defined nontrivial winding numbers of ± 1 for the examples in a) and b). Therefore we have established that nontrivial topology exists for our model in one dimension. In the case of a $[1, 1, 1]$ magnetic field the winding number vanishes exactly as the vector travels orthogonal to the x-y-plane, but this result should be handled with care as we try to explain with the subsequent discussion. Moreover, the case where all three components of the magnetic field are different leads to a non-integer winding number.

One should explain the latter two results. First of, the so called chiral symmetry is an important point when classifying the topology [287]. For the SSH model, reference [286] neatly derives via a simple calculation that the chiral symmetry can be expressed in terms of the sublattice symmetry, i.e. the object we tried to break in the two-dimensional case. According to this, the sublattice operator $\Sigma = P_1 - P_2$,

where P_i is a projector onto the sublattice i , can be used to find that the chiral symmetry being fulfilled can be stated as

$$\Sigma H \Sigma = -H \quad \implies \quad n_z = 0. \quad (4.29)$$

If this symmetry is upheld, i.e. if the \mathbf{n} vector stays in the x-y-plane, the winding number is a properly defined integer [286] and the topological class is AIII [287] (so a \mathbb{Z} number, which for the SSH chain is 0 or 1), while any nonzero n_z breaks this restriction and lets the winding number interpolate between those integers [161].

As such our results are easy to explain. Additionally, any component of the magnetic field vector being 0 leads to $n_z = 0$ (cf. earlier discussion), which in a twist of irony compared to the two-dimensional case is now exactly what we require. If 3 components are active n_z is not trivially vanishing and furthermore, if the flavors and thus the dispersions ϵ are not treated on a somewhat equal footing, susceptible to rather sporadic behavior.

We conclude this part by making two statements about the relevance of this topic. First of all, Malki et. al. discuss a spin-dimer singlet-triplet model in the quasi one-dimensional system BiCu_2PO_6 [288], which is also directly related to the SSH model and in their case yields peculiarities pertaining to the absence of edge-states.

Moreover, the question of how to handle the chiral symmetry breaking itself seems to be a novel topic, with the extremely recent SSH-based analysis [289], which tries to establish a description of cases such as figure 4.20d) via projection of the origin. It furthermore proposes a connection to second-order topological insulators.

All in all, the one-dimensional case seems to be a worthwhile, although nontrivial, topic of future study beyond this thesis.

4.4.5 Condensed Phase and Fractional Quantum Hall Effect

There are adjacent topics left that can be addressed given our results. However, in contrast to the previous discussion, these appear to be less promising outlooks.

So far we have restricted our analysis to the paramagnetic phase of the triplon model. Yet, the question of possible topological bands in the condensed phase remains open. First of all, the triplon interactions and higher order terms (cf. section 1.4.5.2) are a problem for the single-particle and band structure based description. Even leaving this aside, the magnetic field Van Vleck term was argued to at least be somewhat reasonable to ignore (which, for a realistic material, is a limiting and likely often unrealistic approximation anyways) due to the SOC induced gap, which is a line of thought that breaks down when triplon states overcome this gap to condense. Last but not least, while we pointed out many materials with possible $J = 0$ physics in the introduction, the triplon condensation especially when not connected with Ca_2RuO_4 does not seem to be prominently discussed on the material and experimental side of things.

Consequently, it seems to be prudent to first look into the spin-dimer singlet-triplet setups, where at least experimental support and the form of the magnetic field seem to be more convenient. If choosing to do so there seem to be two obvious angles of attack: One could use what is usually done in the condensed phase and rewrite the model by introducing a new ground state that is a mix of singlet and triplet $|\tilde{s}\rangle = \cos(\alpha)|s\rangle + \sin(\alpha)|t\rangle$, leading to at least a new form of the Hamiltonian (cf. [6]). Alternatively one could try to just attack the magnetic order as one would a normal magnet, using spin-waves and their boson expansion while outright ignoring the underlying triplon. However, this thesis and model are likely not the place to do it. We note, however, that the ferromagnetic regime of the spin Kitaev-Heisenberg

model has been argued to exhibit topologically nontrivial excitations [290]. Similarly, topologically protected edge-states have been proposed for the high magnetic-field phase (i.e. polarized paramagnet) [291].

The existence of bosons, e.g. via condensation, directly connects to the next point of interest. As the triplons are hard-core bosons they intrinsically interact via the on-site constraint. This naturally leads to the question of whether or not these interactions could feasibly enable fractional quantum Hall states. Even more so when considering that for the dipolar molecule model we used as a comparison multiple times, the possibility of realizing one such scenario, namely the Halperin state for the $\nu = 2/3$ fractional level, has been proposed [261].

Likewise, the closeness to the dice lattice [263] mentioned previously could be seen as motivating further investigation. A very recent study for example [292] exemplified the richness of the physics in such systems by finding Majorana corner states when an attractive Hubbard interaction is added.

Yet, here we try to point out why the triplon model in this thesis does not seem suited to such pursuits. In order to do this we recap what one strives for when trying to find fractional Chern insulators based on the review [293]. Based on this it would be nice to have higher Chern number $|C| > 1$ to enable more fractional Hall states. In principle high Chern numbers are a feature of our model. However, the lowest band, i.e. the one that is filled most noticeably via boson condensation, magnetic field or temperature, is almost exclusively characterized by $|C| = 1$.

Further, one requires flat bands. One can understand this requirement either by taking it as mimicking Landau levels (which are perfectly flat bands) or just as needing a regime where interactions play a major role (high density of states, limited mobility). Concretely, one also needs the interactions to be in a window of opportunity that enables the interaction to be dominant without destroying the

foundation build by the non-interacting bands, which the review puts succinctly as

$$\Delta E(\text{band gap}) \gg U(\text{interaction scale}) \gg W(\text{band width}). \quad (4.30)$$

As pointed out earlier, the flatness, i.e. the ratio of band gap to band width is usually extremely small in our model. This was not the case for the dice lattice because the mechanism of lifting the degeneracy is more favorable and there is also a spin degeneracy leading to a second flat band (one starts with six bands in that case, with each of the three energy levels being twofold degenerate).

Lastly, our model does not seem to have a reliable mechanism of predicting and setting the amount of bosons, i.e. the filling. One of the obvious difficulties is even gauging the interactions and predict the dynamics of the filling process. Another is the temperature and magnetic or crystal field filling the levels nontrivially. This is in stark contrast to the dipolar molecule model, where an excitation consists of a molecule rotation that can be separately enabled by a microwave field for each lattice site.

In summary, while the possibility of a fractional quantum Hall state exists on paper, this model does not seem suited for further research in this direction at all.

5

Conclusion and Outlook

In this thesis, we investigate effective models based on compounds with d^4 transition-metal ions like Ru^{4+} and Ir^{5+} . In chapter two, we review the previous ventures into basic versions of the triplon Kitaev-Heisenberg model. We emphasize the nature of the zigzag and stripy regimes, which distinguish themselves by possessing a unique Brillouin zone M point for the condensation of each triplon flavor.

Furthermore, we explain why the previous analysis via “classical” Monte-Carlo simulations is seemingly indistinguishable from the quantum mechanical flavor-wave theory. This line of thought naturally invites a wave function ansatz and resulting attempt at using a variational approach in order to calculate the ground state. By fixing the variational parameters with Monte-Carlo, we effectively use what we dub a semiclassical Monte-Carlo framework, which we deem to have a lot of promise not only for this thesis but applications beyond (notably Ca_2RuO_4 based application of our code in reference [134]). Especially for Kugel-Khomskii type models, a classical simulation is found to be likely inadequate, motivating our suggestion that the semiclassical Monte-Carlo scheme might be useful when applied to this kind of problem. Moreover, the sMC simulation produces a significant part of the results in this thesis.

These results mainly represent an attempt to find out what might change when including influences beyond the simplest form of the model, namely the pure \mathbf{v} vector boson based Kitaev-Heisenberg analogue. One may interpret this as an effort to,

first of all, see what parts of the simple approach the more complicated realistically present influences leave intact. Secondly, we investigate the interplay with magnetic field and pressure, which are drivers of novel effects like the triplon/magnon Bose-Einstein condensation in spin-dimers and host nontrivial effects for the Kitaev-Heisenberg physics based on related d^5 materials. As the inherent spin-orbital singlet-triplet degrees of freedom and influences beyond the simplest model change the coupling with magnetic field and pressure, we reevaluate the model with these additions in this thesis.

One addition consists of quadrupoles, modeled as \mathbf{u} boson contributions, naturally arising as a byproduct of the low-energy projection of the Kugel-Khomskii Hamiltonian. We find that their competition with the dipolar \mathbf{v} is straightforward: As both objects are disjoint in the semiclassical picture, the more energetically favorable phase wins outright, which by overall estimation of the interactions is found to be almost certainly the dipolar contributions even in a more generalized analysis of the underlying physics. As a result, we suggest that neglecting those contributions may be appropriate in many cases.

Nevertheless, we find that the multi-triplon terms, which are generally expected to be active when a significant number of triplet/triplon bosons can enter the ground state, may significantly impact the simple model. This is most evident with the emergence of the canted zigzag phase and bias, at least in our model, toward the ferromagnetic regime.

These findings partly imply some behavioral peculiarities for the triplon model in a magnetic field. More fundamental, however, is the competition between two distinct terms in the magnetic dipole moment. The flavor-changing contribution is the linear Zeeman splitting that represent the sole interaction with the magnetic field in spin-dimer systems. In these “regular” dimers, this term is found to drive Bose-Einstein condensation by reducing the singlet-triplet gap. In contrast to this, the spin-orbital system studied in this thesis has an additional excitonic term increasing

the gap. We find that the excitonic part should be expected to dominate and therefore counteract the formation of a BEC. Moreover, we suggest that previous studies suggesting something different, namely a proposal based on NiRh_2O_4 , is flawed due to inappropriate handling of the t-p-correspondence. As a result, we suggest that a magnetic field may be an unsuitable tool for driving Bose-Einstein condensation in Van Vleck-type materials like the ones studied in this thesis.

Nevertheless, the dominance of the excitonic term of the magnetic dipole moment provides an advantage for the intuitive understanding of the evolution of the magnetically ordered phase in magnetic fields. The semiclassical Hamiltonian (with neglect of the Zeeman term and higher-order triplon contributions) is found to have the same form as a classical spin model. As a result, a large part of the behavior in magnetic fields can seemingly be directly interpolated from classical models, which are still complicated and host a plethora of phases, but are well studied. There is a normalization due to effective spin length provided by the condensate density, which should be kept in mind. Additionally, the incorporation of the multi-triplon terms can significantly alter the expectations when the interactions are compatible with the magnetic field, which leads to a significant extension of the canted antiferromagnetic phase in our phase diagram. We therefore suggest that the overall interplay with the magnetic field is often intuitive, namely trivial for the paramagnet and simply spin-like for the magnetic phases, except for some specific higher-order effects, which are a direct consequence of compatible phases and need to probably be evaluated individually for each new model.

Finally, investigations of the fate of the Kitaev phase itself in the magnetic field seem inconclusive. The problem directly connects to topical interest in possible intermediate spin-liquid phases for general spin-S Kitaev models and experiment-based suggestions concerning the intermediate magnetic field phase in $\alpha\text{-RuCl}_3$. Yet, there seems to be no intermediate phase in the ED simulations of our model. In fact, we seemingly only find the transition known from the classical energy scale. We are

unsure if this is simply an artifact of the simulation solely establishing a correlated paramagnet in this regime and suggest that further analysis may be necessary. The question of the fate of the triplon Kitaev phase in this model remains open.

The last part of chapter three provides a look at the impact of a trigonal crystal field, which is directly motivated by experimental analysis of $\text{Ag}_3\text{LiRu}_2\text{O}_6$ under pressure. We find that the crystal field should, in contrast to the magnetic field, expected to drive BEC. In particular, the simple incorporation via perturbation theory suggest a close analogy between spin-dimers in magnetic fields and spin-orbital dimers under pressure. This directly contrasts with the experiment attesting the emergence of two “nonmagnetic” phases, the intermediate of which has been suggested to possibly be connected to the triplon model. A nonperturbative inclusion of the crystal field does seemingly not solve this discrepancy, although we find it to imply intriguing interplay with the Heisenberg regime that may motivate a more thorough future study. As the trend of the triplon model toward BEC seems to be the norm, however, we suggest that the intermediate phase has a different origin. In any case, a focused investigation of the competition between molecular orbital and SOC induced triplon model should be attempted. This might also possibly connect to discussion of the nature of Li_2RuO_3 and the behavior of $\alpha\text{-RuCl}_3$ under pressure.

In the final chapter, we discuss the topologically nontrivial phases arising in the edge-case of the magnetic field interacting with the triplon model solidly considered to be in the paramagnetic regime. Topological magnons/triplons are prominently addressed in regular spin-dimer systems, where Dzyaloshinskii-Moriya Interaction is regularly the key ingredient. In our spin-orbital model, the role of this interaction can seemingly be substituted by the Kitaev or Γ terms. In this document, we chart the plethora of topological phases and assess their origin as bosonic Dirac-cone physics. Additionally, we provide models in the limiting cases that seemingly provide intuitive ways of formulating expectations regarding topological nontriviality of the model.

For the case of the honeycomb model we find that, in contrast to previous sugges-

tions, almost any magnetic field direction has the potential to induce topologically nontrivial phases. This is attributed to multiple limits being nontrivial and should be expected to extend to the kagome lattice. Additionally, influences like the crystal field seem to be unable to destroy the topological nontriviality. Yet, this interpretation also suggest that a more trivial lattice with a single site atomic basis, like the triangular lattice, should be expected to be topologically trivial for realistic parameters due to crystal field distortions. In general, the thermal Hall response in the spin-orbital triplon systems seems to be minute. Consequently, this setup should be set aside as far as experiments are concerned, until an alternative scheme to induce Kitaev interactions in a singlet-triplet system with more suitable energy scales emerges. Moreover, the analysis also implies four (or more) atoms per unit cell being unable to fully gap in magnetic fields, which may discourage ventures into the topology of this model kind of model in many three-dimensional compounds. Finally, we demonstrate the viability and potential of this model for one-dimensional objects by providing a proof-of-principle with possibly intriguing implications regarding chiral/sublattice symmetry.

All in all, one may summarize the results in a rough overarching manner by stating the following: The spin-orbital triplon model has the potential to host a plethora of novel physical phenomena. Yet, a lot of these can seemingly be predicted and naively understood by carefully taking stock of some fundamental concepts. For the magnetic and crystal field evaluations, on-site analysis of the influences paired with simple formulation of the singlet-triplet wave function ansatz provides the intuitive interpretations as a mostly normal spin without BEC in the former and analogue to a spin-dimer in the other. Similarly, the topological nature of the model can be gauged by a look at the limiting cases. Consequently, a thorough look at the model in this manner might be a useful first estimate for future studies of similar concepts.

A

Appendix

A.1 Additional Magnetic Orders

In this part of the appendix we present two additional magnetic orders found for the sMC simulations of the pure h_3 - h_4 higher-order term model at $A = 2\lambda$. The existence of these magnetic orders has been noted in the discussion of the respective model in the later parts of section 3.1.2. As mentioned in the section, these figures are a results of $N = 16$ lattice size sMC simulations. For representative angles we choose $\alpha = 90^\circ$ in figure A.1 and $\alpha = 254^\circ$ in figure A.2.

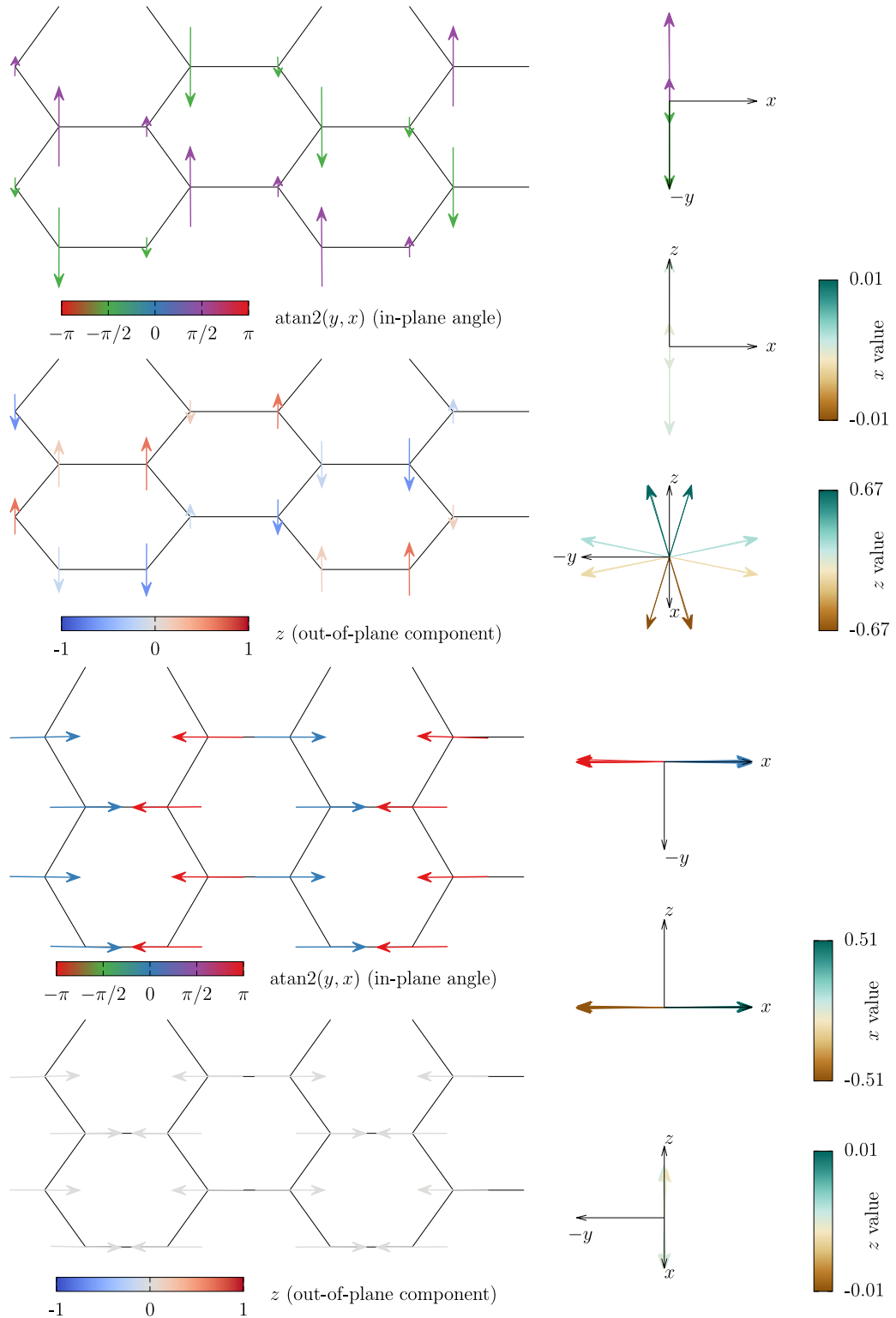


Figure A.1. SMC simulation of the triplon model with solely higher-order contributions at $A = 2\lambda$ and $\alpha = 90^\circ$: A magnetic field with partly zigzag-like features is present. The top two diagrams represent the \mathbf{v} bosons and the lower two \mathbf{u} .

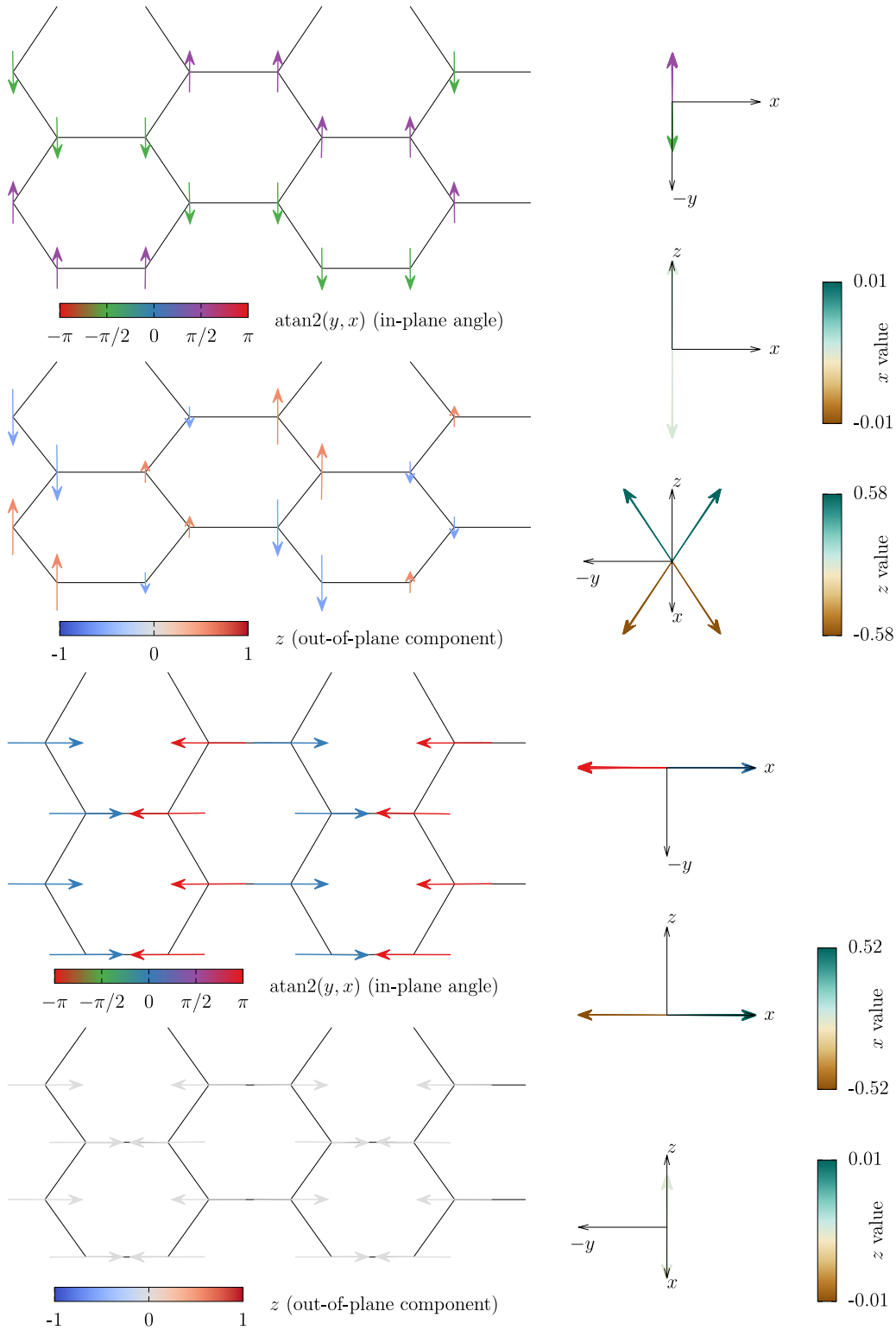


Figure A.2. SMC simulation of the triplon model with solely higher-order contributions at $A = 2\lambda$ and $\alpha = 254^\circ$: A magnetic field with partly zigzag-like features is present. The top two diagrams represent the \mathbf{v} bosons and the lower two \mathbf{u} .

A.2 More Details: Crystal Field Analysis

In this part of the appendix we present results that support the points made in the main text. Figure A.3 includes the h_2 matrix elements of the Heisenberg $\alpha = 0$ case of the full crystal field model as a function of the crystal field strength Δ . The kinks are due to the basis phase fixing at $\Delta = 0$ noted in the main text.

Figure A.4 represents ED data of the simple crystal field with more data points in the paramagnetic regime. The subsequent figure A.5 visualizes the analogous data for the full crystal field model. Furthermore, figure A.6 contains the equivalent to the full field ED analysis of the main text without the inclusion of higher-order terms.

The remaining two figures present the phase diagrams for the α sweeps in absence of higher-order terms. Figure A.7 represents the simple crystal field scheme while figure A.8 visualizes the full model. As expected, the canted zigzag phase is absent in the simple scheme and minute shifts of the condensation points can be found.

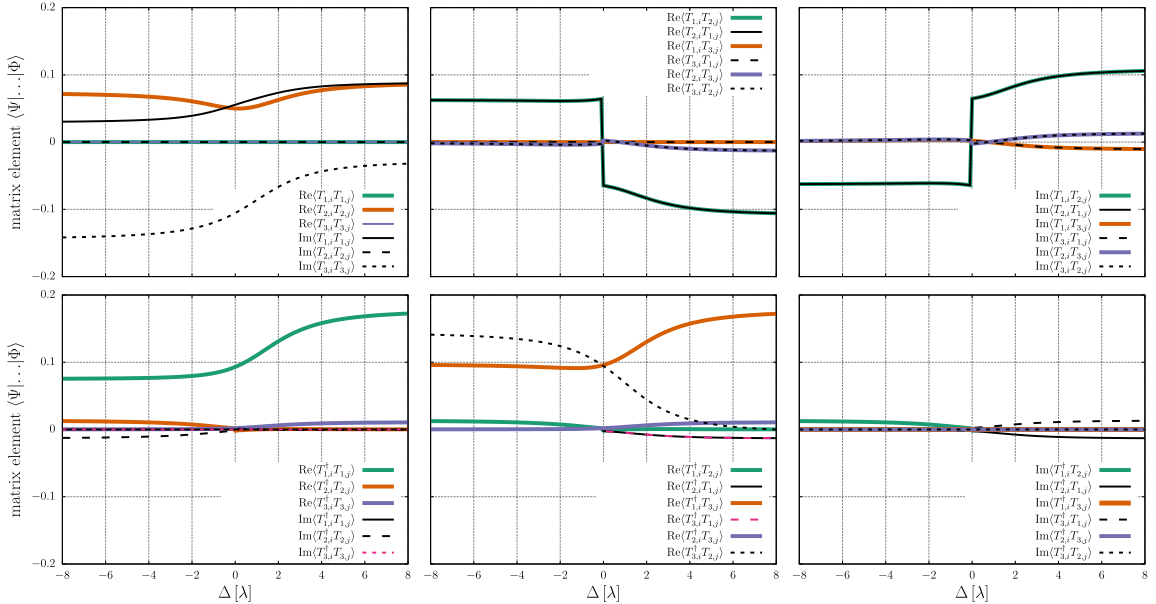


Figure A.3. Matrix elements (h_2 terms) of the triplon model in the Heisenberg $\alpha = 0$ case in the full crystal field regime: The crystal field does not drastically suppress the interactions per se.

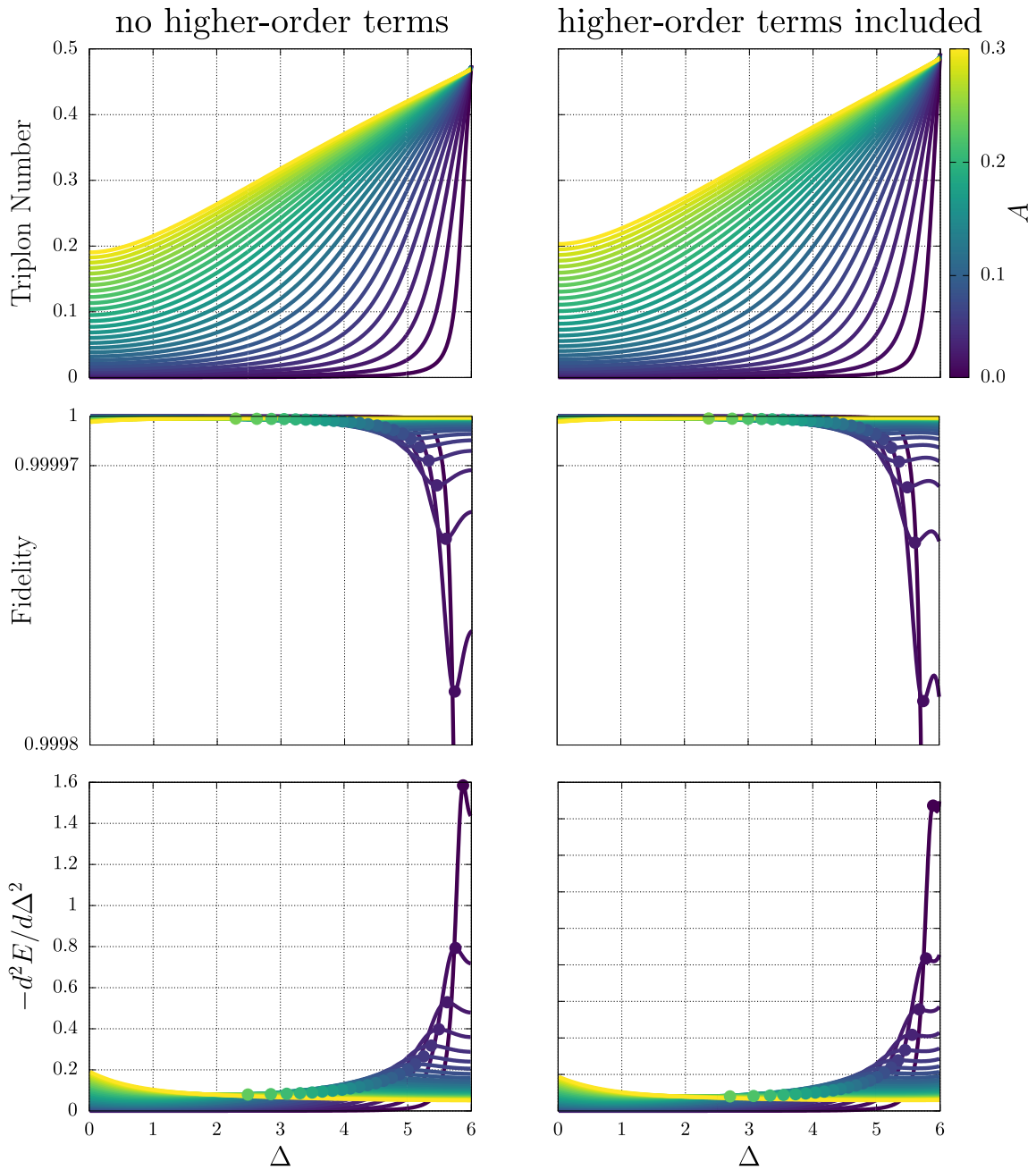


Figure A.4. Ground state properties calculated via ED for the AFM Heisenberg model in the simple crystal field scheme: Here additional values of Heisenberg interaction A are provided in order to give a more detailed view of the paramagnetic regime and the emergence of the magnetic phase. No previously unmentioned irregularities are found.

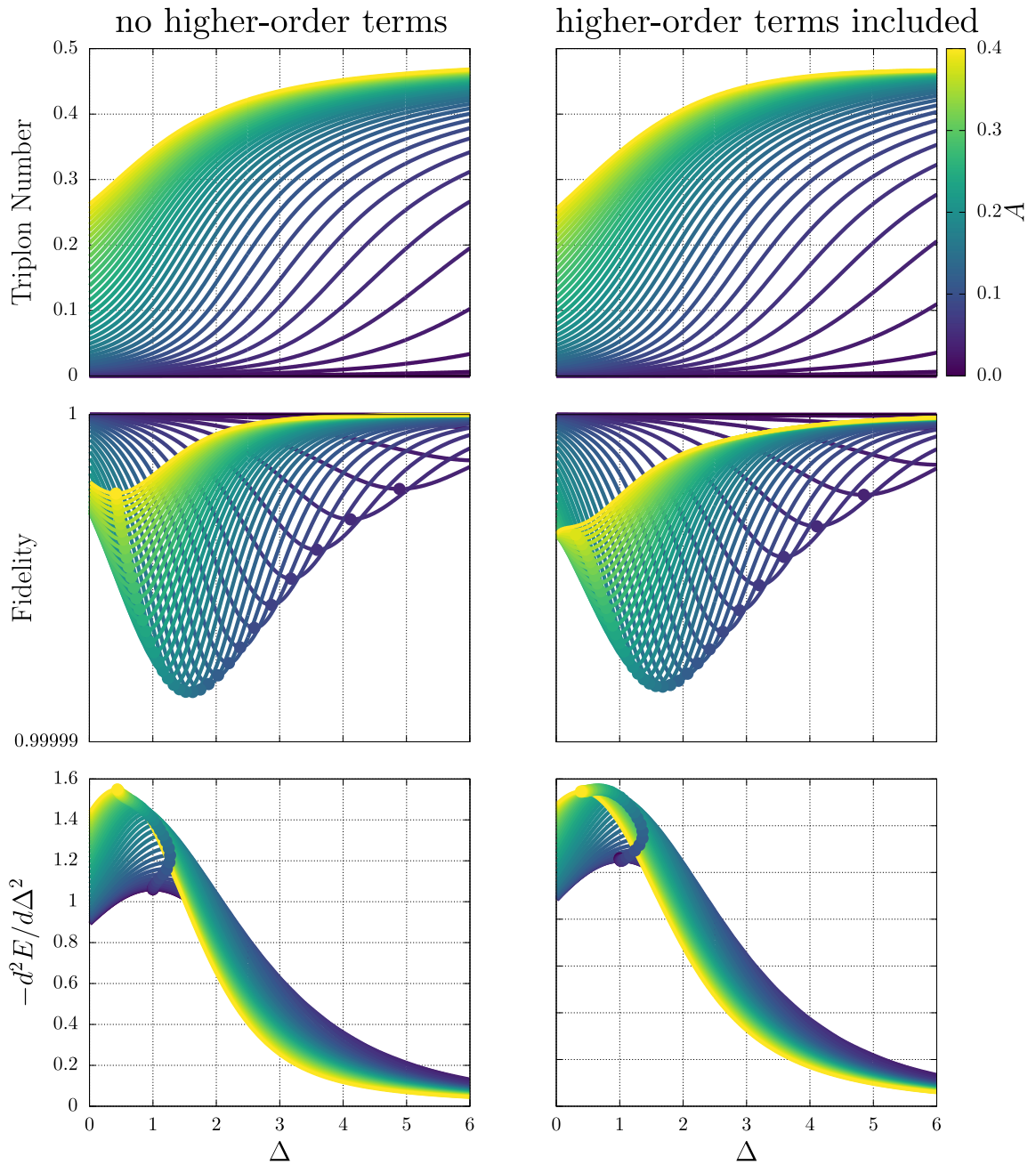


Figure A.5. Ground state properties calculated via ED for the AFM Heisenberg model in the full crystal field scheme: In direct equivalence to the previous picture, additional values of Heisenberg interaction A are provided in order to give a more detailed view of the paramagnetic regime and the emergence of the magnetic phase. No previously unmentioned irregularities are found.

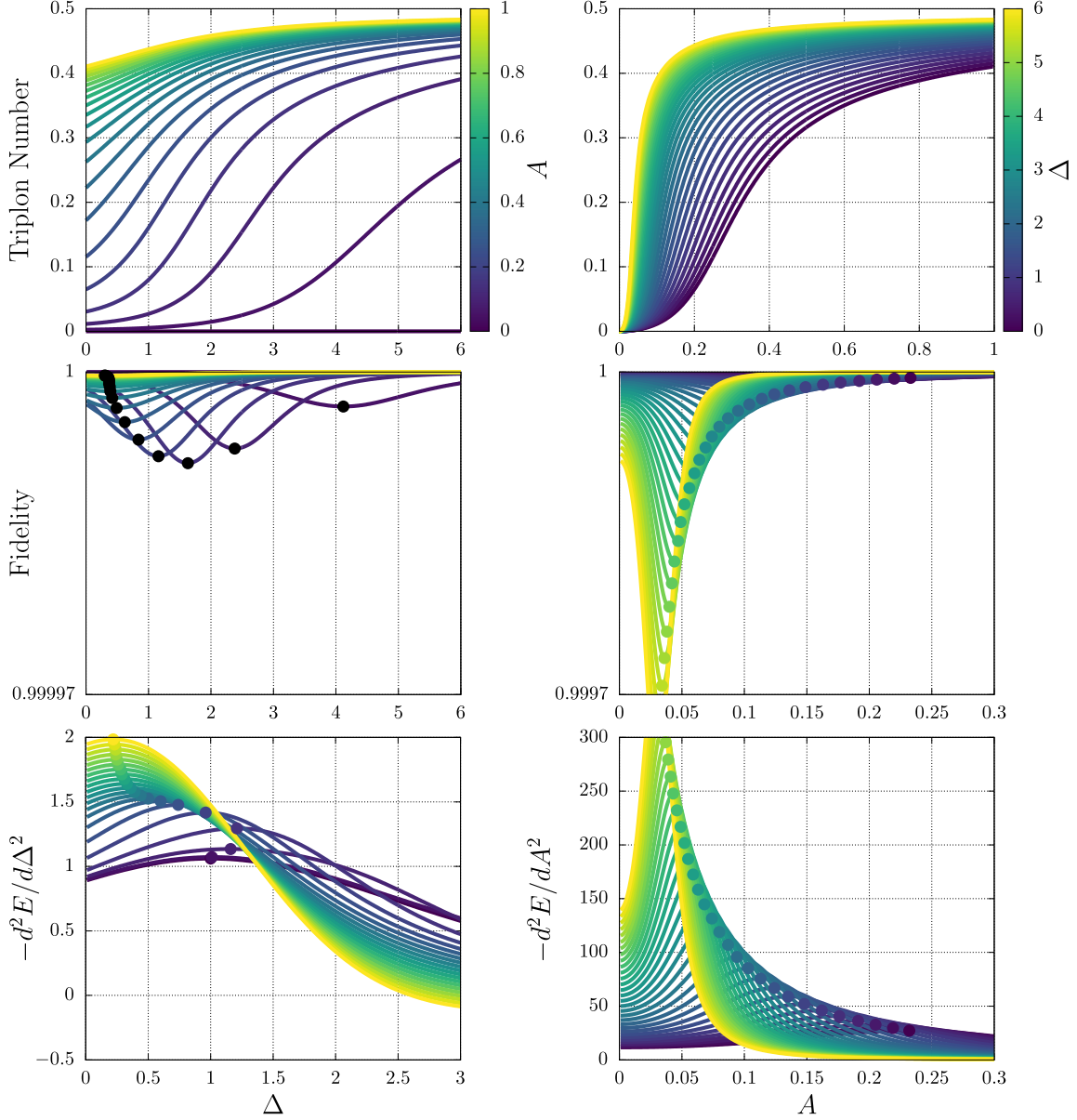


Figure A.6. Ground state properties calculated via ED for the AFM Heisenberg model in the full crystal field scheme without higher-order terms: This figure is the h_2 equivalent of the corresponding analysis in the main part of this document. Its purpose is to show that the higher-order terms do not restrict another singlet phase from emerging. There remains a single phase transition into the magnetic order.

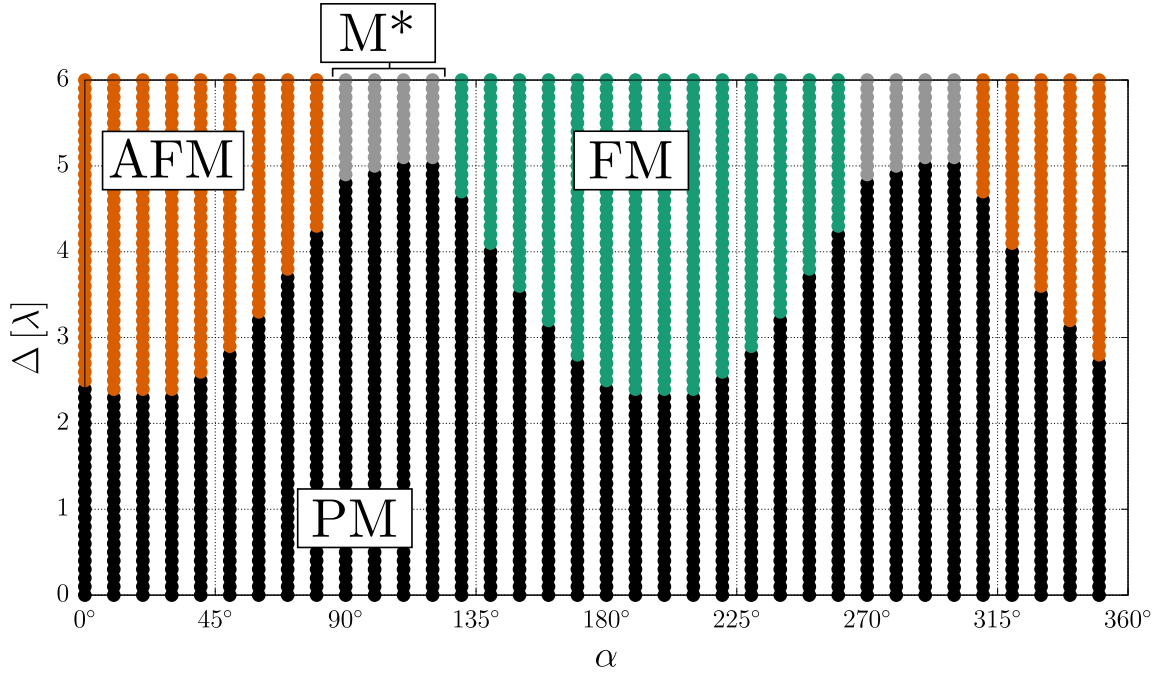


Figure A.7. Semiclassical Monte-Carlo phase diagram for the Kitaev-Heisenberg model without higher-order h_3 - h_4 terms, $A = 0.1\lambda$ and various values of interaction angle α and crystal field Δ . This result represents the simple crystal field scheme.

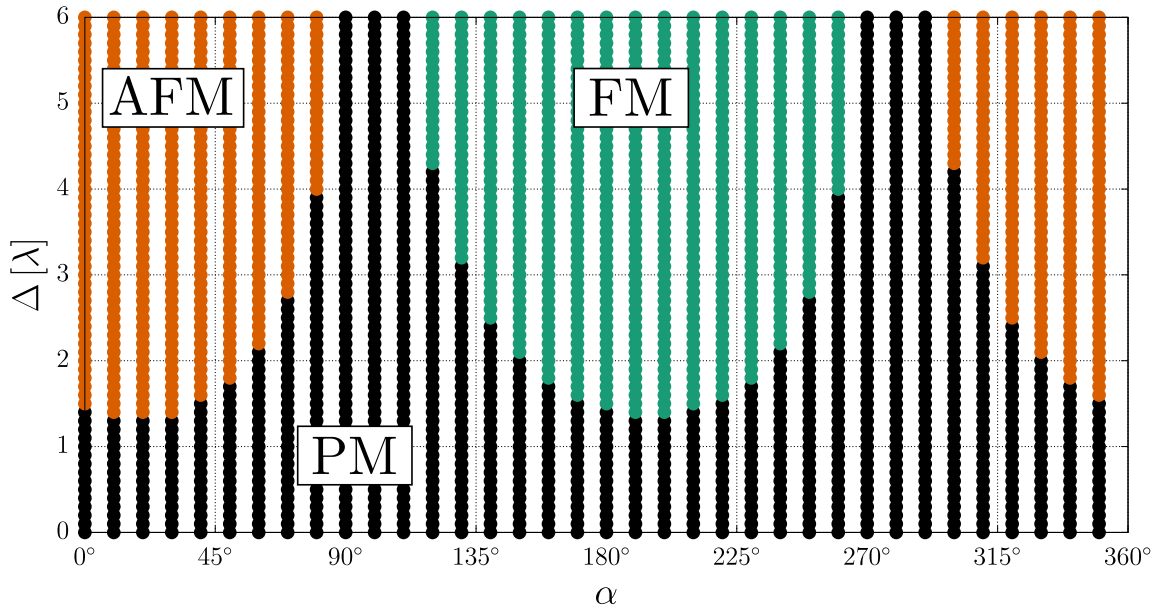


Figure A.8. Semiclassical Monte-Carlo phase diagram for the Kitaev-Heisenberg model without higher-order h_3 - h_4 terms, $A = 0.1\lambda$ and various values of interaction angle α and crystal field Δ . This result represents the full crystal field scheme.

A.3 Matrix Elements and States of the Full Crystal Field Model

As mentioned, we provide a matrix and states at arbitrarily chosen values in order to help with reproduction or refutation of our results. The matrix elements are designated by their indices, e.g., $H_{\alpha_i, \text{out} \beta_j, \text{out} \gamma_i, \text{in} \delta_j, \text{in}}^{(c)}$, where i and j are nearest neighbor lattice sites on the (c) bond (cf. equation (1.62)) and $\alpha/\beta/\gamma/\delta$ are singlet or triplet states. The labels “in” and “out” reflect the matrix elements, i.e. $H_{\alpha_i, \text{out} \beta_j, \text{out} \gamma_i, \text{in} \delta_j, \text{in}}^{(c)} = \langle \alpha_i \beta_j | H^{(c)} | \gamma_i \delta_j \rangle \alpha_i^\dagger \beta_j^\dagger \gamma_i \delta_j$. In other words, we write down a matrix akin to the one in figure 1.13, just with a slightly different notation for the indices. In regards to the (c) bond Hamiltonian one should recall that switching $x \rightarrow y \rightarrow z \rightarrow x$ to get the other bonds is fine, but a pure index switch does not translate to the $t_{1/2/3}$ triplon basis. Finally, we write the state indices like α with s for the singlet and $1/2/3$ for the $t_1/t_2/t_3$ triplet. The matrix represents the arbitrarily chosen values $\lambda = 1$, $\alpha = 7^\circ$, $\Delta = 2.13$ and $A = 0.84$ (thus setting t^2/U and t'^2/U). We only provide the top half of the matrix and the diagonal entries. The remaining offdiagonal elements can obviously be constructed by complex conjugation and transposition (Hermitian matrix).

$$\begin{array}{lll}
H_{ss,ss}^{(c)} = 4.1947 + 0.0000i & H_{ss,s1}^{(c)} = 0.0484 - 0.0484i & H_{ss,s2}^{(c)} = 0.0395 + 0.0000i \\
H_{ss,s3}^{(c)} = -0.0000 + 0.0000i & H_{ss,1s}^{(c)} = 0.0484 - 0.0484i & H_{ss,11}^{(c)} = 0.0000 + 0.6189i \\
H_{ss,12}^{(c)} = -0.7264 + 0.7264i & H_{ss,13}^{(c)} = 0.0000 - 0.0609i & H_{ss,2s}^{(c)} = 0.0395 + 0.0000i \\
H_{ss,21}^{(c)} = -0.7264 + 0.7264i & H_{ss,22}^{(c)} = 0.5673 + 0.0000i & H_{ss,23}^{(c)} = -0.0745 + 0.0745i \\
H_{ss,3s}^{(c)} = -0.0000 + 0.0000i & H_{ss,31}^{(c)} = 0.0000 - 0.0609i & H_{ss,32}^{(c)} = -0.0745 + 0.0745i \\
H_{ss,33}^{(c)} = 0.0000 - 0.5597i & H_{s1,s1}^{(c)} = 4.2655 + 0.0000i & H_{s1,s2}^{(c)} = -0.0276 - 0.0276i \\
H_{s1,s3}^{(c)} = 0.3902 + 0.0000i & H_{s1,1s}^{(c)} = 1.1416 + 0.0000i & H_{s1,11}^{(c)} = 0.0579 - 0.0579i \\
H_{s1,12}^{(c)} = -0.0164 + 0.0000i & H_{s1,13}^{(c)} = -0.2127 + 0.2127i & H_{s1,2s}^{(c)} = -0.0045 - 0.0045i \\
H_{s1,21}^{(c)} = 0.0363 + 0.0000i & H_{s1,22}^{(c)} = 0.0068 + 0.0068i & H_{s1,23}^{(c)} = 0.1333 + 0.0000i \\
H_{s1,3s}^{(c)} = 0.0770 + 0.0000i & H_{s1,31}^{(c)} = 0.3487 - 0.3487i & H_{s1,32}^{(c)} = -0.2313 + 0.0000i \\
H_{s1,33}^{(c)} = -0.0110 + 0.0110i & H_{s2,s2}^{(c)} = 4.3107 + 0.0000i & H_{s2,s3}^{(c)} = -0.4779 + 0.4779i \\
H_{s2,1s}^{(c)} = -0.0045 + 0.0045i & H_{s2,11}^{(c)} = 0.0000 + 0.0053i & H_{s2,12}^{(c)} = 0.0577 - 0.0577i \\
H_{s2,13}^{(c)} = 0.0000 - 0.2140i & H_{s2,2s}^{(c)} = 1.1489 + 0.0000i & H_{s2,21}^{(c)} = -0.0067 + 0.0067i \\
H_{s2,22}^{(c)} = 0.0581 + 0.0000i & H_{s2,23}^{(c)} = 0.2127 - 0.2127i & H_{s2,3s}^{(c)} = -0.0943 + 0.0943i
\end{array}$$

A. Appendix

$$\begin{aligned}
 H_{s2,31}^{(c)} &= 0.0000 + 0.3381i & H_{s2,32}^{(c)} &= -0.3487 + 0.3487i & H_{s2,33}^{(c)} &= 0.0000 + 0.0090i \\
 H_{s3,s3}^{(c)} &= 4.1844 + 0.0000i & H_{s3,1s}^{(c)} &= 0.0770 + 0.0000i & H_{s3,11}^{(c)} &= 0.0046 - 0.0046i \\
 H_{s3,12}^{(c)} &= -0.3059 + 0.0000i & H_{s3,13}^{(c)} &= 0.0031 - 0.0031i & H_{s3,2s}^{(c)} &= -0.0943 - 0.0943i \\
 H_{s3,21}^{(c)} &= 0.2984 + 0.0000i & H_{s3,22}^{(c)} &= -0.0046 - 0.0046i & H_{s3,23}^{(c)} &= 0.0025 + 0.0000i \\
 H_{s3,3s}^{(c)} &= 0.3770 + 0.0000i & H_{s3,31}^{(c)} &= 0.0242 - 0.0242i & H_{s3,32}^{(c)} &= 0.0198 + 0.0000i \\
 H_{s3,33}^{(c)} &= -0.0000 + 0.0000i & H_{1s,1s}^{(c)} &= 4.2655 + 0.0000i & H_{1s,11}^{(c)} &= 0.0579 - 0.0579i \\
 H_{1s,12}^{(c)} &= 0.0363 + 0.0000i & H_{1s,13}^{(c)} &= 0.3487 - 0.3487i & H_{1s,2s}^{(c)} &= -0.0276 - 0.0276i \\
 H_{1s,21}^{(c)} &= -0.0164 + 0.0000i & H_{1s,22}^{(c)} &= 0.0068 + 0.0068i & H_{1s,23}^{(c)} &= -0.2313 + 0.0000i \\
 H_{1s,3s}^{(c)} &= 0.3902 + 0.0000i & H_{1s,31}^{(c)} &= -0.2127 + 0.2127i & H_{1s,32}^{(c)} &= 0.1333 + 0.0000i \\
 H_{1s,33}^{(c)} &= -0.0110 + 0.0110i & H_{11,11}^{(c)} &= 5.1470 + 0.0000i & H_{11,12}^{(c)} &= -0.4020 - 0.4020i \\
 H_{11,13}^{(c)} &= 0.5617 + 0.0000i & H_{11,2s}^{(c)} &= 0.0000 - 0.0053i & H_{11,21}^{(c)} &= -0.4020 - 0.4020i \\
 H_{11,22}^{(c)} &= 0.0000 + 0.3040i & H_{11,23}^{(c)} &= -0.0533 - 0.0533i & H_{11,3s}^{(c)} &= 0.0046 + 0.0046i \\
 H_{11,31}^{(c)} &= 0.5617 + 0.0000i & H_{11,32}^{(c)} &= -0.0533 - 0.0533i & H_{11,33}^{(c)} &= 0.2410 + 0.0000i \\
 H_{12,12}^{(c)} &= 3.4953 + 0.0000i & H_{12,13}^{(c)} &= -0.4715 + 0.4715i & H_{12,2s}^{(c)} &= -0.0067 - 0.0067i \\
 H_{12,21}^{(c)} &= 0.2366 + 0.0000i & H_{12,22}^{(c)} &= 0.3196 + 0.3196i & H_{12,23}^{(c)} &= -0.0462 + 0.0000i \\
 H_{12,3s}^{(c)} &= 0.2984 + 0.0000i & H_{12,31}^{(c)} &= -0.0533 + 0.0533i & H_{12,32}^{(c)} &= 0.2953 + 0.0000i \\
 H_{12,33}^{(c)} &= 0.0729 - 0.0729i & H_{13,13}^{(c)} &= 4.1375 + 0.0000i & H_{13,2s}^{(c)} &= 0.0000 - 0.3381i \\
 H_{13,21}^{(c)} &= -0.0533 - 0.0533i & H_{13,22}^{(c)} &= 0.0000 - 0.0462i & H_{13,23}^{(c)} &= -0.0795 - 0.0795i \\
 H_{13,3s}^{(c)} &= 0.0242 + 0.0242i & H_{13,31}^{(c)} &= 0.0671 + 0.0000i & H_{13,32}^{(c)} &= -0.0185 - 0.0185i \\
 H_{13,33}^{(c)} &= 0.3214 + 0.0000i & H_{2s,2s}^{(c)} &= 4.3107 + 0.0000i & H_{2s,21}^{(c)} &= 0.0577 - 0.0577i \\
 H_{2s,22}^{(c)} &= 0.0581 + 0.0000i & H_{2s,23}^{(c)} &= -0.3487 + 0.3487i & H_{2s,3s}^{(c)} &= -0.4779 + 0.4779i \\
 H_{2s,31}^{(c)} &= 0.0000 - 0.2140i & H_{2s,32}^{(c)} &= 0.2127 - 0.2127i & H_{2s,33}^{(c)} &= 0.0000 + 0.0090i \\
 H_{21,21}^{(c)} &= 3.4953 + 0.0000i & H_{21,22}^{(c)} &= 0.3196 + 0.3196i & H_{21,23}^{(c)} &= 0.2953 + 0.0000i \\
 H_{21,3s}^{(c)} &= -0.3059 + 0.0000i & H_{21,31}^{(c)} &= -0.4715 + 0.4715i & H_{21,32}^{(c)} &= -0.0462 + 0.0000i \\
 H_{21,33}^{(c)} &= 0.0729 - 0.0729i & H_{22,22}^{(c)} &= 5.2816 + 0.0000i & H_{22,23}^{(c)} &= -0.5780 + 0.5780i \\
 H_{22,3s}^{(c)} &= -0.0046 + 0.0046i & H_{22,31}^{(c)} &= 0.0000 + 0.0462i & H_{22,32}^{(c)} &= -0.5780 + 0.5780i \\
 H_{22,33}^{(c)} &= 0.0000 - 0.1219i & H_{23,23}^{(c)} &= 4.2673 + 0.0000i & H_{23,3s}^{(c)} &= 0.0198 + 0.0000i \\
 H_{23,31}^{(c)} &= -0.0185 + 0.0185i & H_{23,32}^{(c)} &= 0.0974 + 0.0000i & H_{23,33}^{(c)} &= -0.3936 + 0.3936i \\
 H_{3s,3s}^{(c)} &= 4.1844 + 0.0000i & H_{3s,31}^{(c)} &= 0.0031 - 0.0031i & H_{3s,32}^{(c)} &= 0.0025 + 0.0000i \\
 H_{3s,33}^{(c)} &= -0.0000 + 0.0000i & H_{31,31}^{(c)} &= 4.1375 + 0.0000i & H_{31,32}^{(c)} &= -0.0795 - 0.0795i \\
 H_{31,33}^{(c)} &= 0.3214 + 0.0000i & H_{32,32}^{(c)} &= 4.2673 + 0.0000i & H_{32,33}^{(c)} &= -0.3936 + 0.3936i \\
 H_{33,33}^{(c)} &= 4.1844 + 0.0000i & & & &
 \end{aligned}$$

The digits of the previous matrix are not rounded and do not imply precision. A

cutoff after 4 decimal places was chosen arbitrarily, as this should suffice for the purpose of checking the overall end result in this scheme and saves considerable amount of space. Similarly, one might provide the values of the singlet and triplet states at this point. One finds (same decimal cutoff):

$$\begin{aligned}
 |s\rangle &= 0.5403i(|m_L = 0, m_S = 0\rangle - |1, -1\rangle - |-1, 1\rangle) - 0.1016(1+i)(|1, 0\rangle + |0, 1\rangle) \\
 &\quad - 0.1016(1-i)(|-1, 0\rangle + |0, -1\rangle) + 0.1438(|1, 1\rangle - |-1, -1\rangle), \\
 |t_1\rangle &= -0.1621(1+i)|0, 0\rangle - 0.1621(1-i)|-1, -1\rangle - 0.1502|0, 1\rangle + 0.3795|1, 0\rangle \\
 &\quad + 0.1062(1+i)|-1, 1\rangle - 0.2684(1+i)|1, -1\rangle + 0.5298i(|0, -1\rangle - |-1, 0\rangle), \\
 |t_2\rangle &= -0.1323i|0, 0\rangle - 0.3712(1+i)|0, 1\rangle + 0.2776(1+i)|1, 0\rangle \\
 &\quad - 0.5250i|-1, 1\rangle + 0.3926i|1, -1\rangle + 0.0936(1-i)(|0, -1\rangle + |-1, 0\rangle) \\
 &\quad + 0.2647|1, 1\rangle + 0.1323|-1, -1\rangle
 \end{aligned}$$

Obviously, the t_3 triplon remains constant.

A.4 Matrix Elements of the Triplon Model for Ca_2RuO_4

The triplon Hamiltonian of the Ca_2RuO_4 Kugel-Khomskii Hamiltonian studied in reference [20] and [134] has never been published. As they stem from a Mathematica notebook written by us and an implementation of this model in sMC and ED was also our contribution, it seems to be appropriate to write down the model here. One may note that equation (3.9) provides the definitions and the equations following it contain the h_2 matrix elements (which we therefore do not have to reiterate here). Subsequently, we provide expressions for the other nontrivial matrix elements. The indices and presentation are analogous to the previous section, with the difference that the $t_x/t_y/t_z$ triplon basis and corresponding indices are used.

$$\begin{aligned}
 h_{ss,ss}^{\text{NNN}} &= \frac{4t_{\text{NNN}}^2(-5J_{\text{H}}^2+6J_{\text{H}}U+3U^2)}{9U(-3J_{\text{H}}+U)(2J_{\text{H}}+U)} & h_{sx,sx}^{\text{NNN}} &= \frac{t_{\text{NNN}}^2(-16J_{\text{H}}^2+15J_{\text{H}}U+9U^2)}{6U(-3J_{\text{H}}+U)(2J_{\text{H}}+U)} \\
 h_{sy,sy}^{\text{NNN}} &= \frac{t_{\text{NNN}}^2(-10J_{\text{H}}^2+19J_{\text{H}}U+7U^2)}{6U(-3J_{\text{H}}+U)(2J_{\text{H}}+U)} & h_{sz,sz}^{\text{NNN}} &= \frac{t_{\text{NNN}}^2(-7J_{\text{H}}^2+7J_{\text{H}}U+4U^2)}{3U(-3J_{\text{H}}+U)(2J_{\text{H}}+U)} \\
 h_{xs,sy}^{\text{NNN}} &= \frac{t_{\text{NNN}}^2(-16J_{\text{H}}^2+15J_{\text{H}}U+9U^2)}{6U(-3J_{\text{H}}+U)(2J_{\text{H}}+U)} & h_{xx,xx}^{\text{NNN}} &= \frac{t_{\text{NNN}}^2(-13J_{\text{H}}^2+10J_{\text{H}}U+7U^2)}{4U(-3J_{\text{H}}+U)(2J_{\text{H}}+U)} \\
 h_{xy,xy}^{\text{NNN}} &= \frac{t_{\text{NNN}}^2(-8J_{\text{H}}^2+11J_{\text{H}}U+5U^2)}{4U(-3J_{\text{H}}+U)(2J_{\text{H}}+U)} & h_{xz,xz}^{\text{NNN}} &= \frac{t_{\text{NNN}}^2(-11J_{\text{H}}^2+9J_{\text{H}}U+6U^2)}{4U(-3J_{\text{H}}+U)(2J_{\text{H}}+U)} \\
 h_{ys,ys}^{\text{NNN}} &= \frac{t_{\text{NNN}}^2(-10J_{\text{H}}^2+19J_{\text{H}}U+7U^2)}{6U(-3J_{\text{H}}+U)(2J_{\text{H}}+U)} & h_{yx,yx}^{\text{NNN}} &= \frac{t_{\text{NNN}}^2(-8J_{\text{H}}^2+11J_{\text{H}}U+5U^2)}{4U(-3J_{\text{H}}+U)(2J_{\text{H}}+U)} \\
 h_{yy,yy}^{\text{NNN}} &= \frac{t_{\text{NNN}}^2(-J_{\text{H}}^2+4J_{\text{H}}U+U^2)}{U(-3J_{\text{H}}+U)(2J_{\text{H}}+U)} & h_{yz,yz}^{\text{NNN}} &= \frac{t_{\text{NNN}}^2(-8J_{\text{H}}^2+11J_{\text{H}}U+5U^2)}{4U(-3J_{\text{H}}+U)(2J_{\text{H}}+U)} \\
 h_{zs,zs}^{\text{NNN}} &= \frac{t_{\text{NNN}}^2(-7J_{\text{H}}^2+7J_{\text{H}}U+4U^2)}{3U(-3J_{\text{H}}+U)(2J_{\text{H}}+U)} & h_{zx,zx}^{\text{NNN}} &= \frac{t_{\text{NNN}}^2(-11J_{\text{H}}^2+9J_{\text{H}}U+6U^2)}{4U(-3J_{\text{H}}+U)(2J_{\text{H}}+U)} \\
 h_{zy,zy}^{\text{NNN}} &= \frac{t_{\text{NNN}}^2(-8J_{\text{H}}^2+11J_{\text{H}}U+5U^2)}{4U(-3J_{\text{H}}+U)(2J_{\text{H}}+U)} & h_{zz,zz}^{\text{NNN}} &= \frac{t_{\text{NNN}}^2(-9J_{\text{H}}^2+8J_{\text{H}}U+5U^2)}{4U(-3J_{\text{H}}+U)(2J_{\text{H}}+U)} \\
 h_{sx,yy}^{\text{NNN}} &= \frac{J_{\text{H}}t_{\text{NNN}}^2}{\sqrt{6}U(-3J_{\text{H}}+U)} & h_{xs,zz}^{\text{NNN}} &= h_{sx,yy}^{\text{NNN}} = -h_{sz,yx}^{\text{NNN}} = -h_{xy,zs}^{\text{NNN}} \\
 h_{sx,zy}^{\text{NNN}} &= \frac{t_{\text{NNN}}^2(-5J_{\text{H}}^2-3J_{\text{H}}U+U^2)}{2\sqrt{6}U(-3J_{\text{H}}+U)(2J_{\text{H}}+U)} & h_{sy,xz}^{\text{NNN}} &= h_{sx,zy}^{\text{NNN}} = h_{xs,yz}^{\text{NNN}} = h_{ys,zx}^{\text{NNN}} \\
 h_{xy,yx}^{\text{NNN}} &= \frac{t_{\text{NNN}}^2(1/U+1/(2J_{\text{H}}+U))}{8} & h_{sy,zx}^{\text{NNN}} &= -h_{sx,zy}^{\text{NNN}} = h_{sz,xy}^{\text{NNN}} = h_{xz,sy}^{\text{NNN}} = h_{yx,zs}^{\text{NNN}} \\
 & & h_{yz,zy}^{\text{NNN}} &= h_{xy,yx}^{\text{NNN}} = -h_{xx,yy}^{\text{NNN}} = -h_{yy,zz}^{\text{NNN}}
 \end{aligned}$$

$$\begin{aligned}
 h_{ss,ss}^x &= \frac{2(J_{\text{H}}^2(-6t_l^2+t_l t_s-10t_s^2)+2J_{\text{H}}(5t_l^2+6t_s^2)U+(4t_l^2+t_l t_s+6t_s^2)U^2)}{9U(-3J_{\text{H}}+U)(2J_{\text{H}}+U)} \\
 h_{sx,sx}^x &= \frac{-4J_{\text{H}}^2(t_l^2+4t_s^2)+J_{\text{H}}(16t_l^2+15t_s^2)U+(4t_l^2+9t_s^2)U^2}{6U(-3J_{\text{H}}+U)(2J_{\text{H}}+U)} \\
 h_{sy,sy}^x &= \frac{-10J_{\text{H}}^2(t_l^2+t_s^2)+J_{\text{H}}(12t_l^2+19t_s^2)U+(6t_l^2+7t_s^2)U^2}{6U(-3J_{\text{H}}+U)(2J_{\text{H}}+U)} \\
 h_{sz,sz}^x &= \frac{J_{\text{H}}^2(-5t_l^2+t_l t_s-7t_s^2)+J_{\text{H}}(6t_l^2+7t_s^2)U+(3t_l^2+t_l t_s+4t_s^2)U^2}{3U(-3J_{\text{H}}+U)(2J_{\text{H}}+U)} \\
 h_{xs,xs}^x &= \frac{-4J_{\text{H}}^2(t_l^2+4t_s^2)+J_{\text{H}}(16t_l^2+15t_s^2)U+(4t_l^2+9t_s^2)U^2}{6U(-3J_{\text{H}}+U)(2J_{\text{H}}+U)} \\
 h_{xx,xx}^x &= \frac{-13J_{\text{H}}^2 t_s^2+2J_{\text{H}}(7t_l^2+5t_s^2)U+(2t_l^2+7t_s^2)U^2}{4U(-3J_{\text{H}}+U)(2J_{\text{H}}+U)} \\
 h_{xy,xy}^x &= \frac{-4J_{\text{H}}^2(t_l^2+2t_s^2)+J_{\text{H}}(9t_l^2+11t_s^2)U+(3t_l^2+5t_s^2)U^2}{4U(-3J_{\text{H}}+U)(2J_{\text{H}}+U)} \\
 h_{xz,xz}^x &= \frac{-(J_{\text{H}}^2(4t_l^2+11t_s^2))+9J_{\text{H}}(t_l^2+t_s^2)U+3(t_l^2+2t_s^2)U^2}{4U(-3J_{\text{H}}+U)(2J_{\text{H}}+U)} \\
 h_{ys,ys}^x &= \frac{-10J_{\text{H}}^2(t_l^2+t_s^2)+J_{\text{H}}(12t_l^2+19t_s^2)U+(6t_l^2+7t_s^2)U^2}{6U(-3J_{\text{H}}+U)(2J_{\text{H}}+U)} \\
 h_{yx,yx}^x &= \frac{-4J_{\text{H}}^2(t_l^2+2t_s^2)+J_{\text{H}}(9t_l^2+11t_s^2)U+(3t_l^2+5t_s^2)U^2}{4U(-3J_{\text{H}}+U)(2J_{\text{H}}+U)} \\
 h_{yy,yy}^x &= \frac{-(J_{\text{H}}^2(9t_l^2+4t_s^2))+8J_{\text{H}}(t_l^2+2t_s^2)U+(5t_l^2+4t_s^2)U^2}{4U(-3J_{\text{H}}+U)(2J_{\text{H}}+U)} \\
 h_{yz,yz}^x &= \frac{-(J_{\text{H}}^2(7t_l^2+8t_s^2))+J_{\text{H}}(7t_l^2+11t_s^2)U+(4t_l^2+5t_s^2)U^2}{4U(-3J_{\text{H}}+U)(2J_{\text{H}}+U)} \\
 h_{zs,zs}^x &= \frac{J_{\text{H}}^2(-5t_l^2+t_l t_s-7t_s^2)+J_{\text{H}}(6t_l^2+7t_s^2)U+(3t_l^2+t_l t_s+4t_s^2)U^2}{3U(-3J_{\text{H}}+U)(2J_{\text{H}}+U)} \\
 h_{zx,zx}^x &= \frac{-(J_{\text{H}}^2(4t_l^2+11t_s^2))+9J_{\text{H}}(t_l^2+t_s^2)U+3(t_l^2+2t_s^2)U^2}{4U(-3J_{\text{H}}+U)(2J_{\text{H}}+U)} \\
 h_{zy,zy}^x &= \frac{-(J_{\text{H}}^2(7t_l^2+8t_s^2))+J_{\text{H}}(7t_l^2+11t_s^2)U+(4t_l^2+5t_s^2)U^2}{4U(-3J_{\text{H}}+U)(2J_{\text{H}}+U)} \\
 h_{zz,zz}^x &= \frac{J_{\text{H}}^2(-9t_l^2+2t_l t_s-9t_s^2)+8J_{\text{H}}(t_l^2+t_s^2)U+(5t_l^2+2t_l t_s+5t_s^2)U^2}{4U(-3J_{\text{H}}+U)(2J_{\text{H}}+U)}
 \end{aligned}$$

$$\begin{aligned}
 h_{sx,yz}^x &= \frac{J_H^2(5t_l^2-3t_l t_s+4t_s^2)+J_H(3t_l^2+t_l t_s+2t_s^2)U-t_l^2 U^2}{2\sqrt{6}U(-3J_H+U)(2J_H+U)} \\
 h_{sx,zy}^x &= \frac{J_H^2(-5t_l^2+t_l t_s-5t_s^2)-J_H(3t_l^2+4t_l t_s+3t_s^2)U+(t_l^2-t_l t_s+t_s^2)U^2}{2\sqrt{6}U(-3J_H+U)(2J_H+U)} \\
 h_{sy,xz}^x &= \frac{J_H^2(-4t_l^2+3t_l t_s-5t_s^2)-J_H(2t_l^2+t_l t_s+3t_s^2)U+t_s^2 U^2}{2\sqrt{6}U(-3J_H+U)(2J_H+U)} \\
 h_{sy,zx}^x &= \frac{J_H^2(5t_l^2-t_l t_s+5t_s^2)+J_H(3t_l^2+4t_l t_s+3t_s^2)U-(t_l^2-t_l t_s+t_s^2)U^2}{2\sqrt{6}U(-3J_H+U)(2J_H+U)} \\
 h_{sz,xy}^x &= \frac{J_H^2(4t_l^2-2t_l t_s+5t_s^2)+J_H(2t_l^2+t_l t_s+3t_s^2)U+(t_l-t_s)t_s U^2}{2\sqrt{6}U(-3J_H+U)(2J_H+U)} \\
 h_{sz,yx}^x &= \frac{J_H^2(-5t_l^2+2t_l t_s-4t_s^2)-J_H(3t_l^2+t_l t_s+2t_s^2)U+t_l(t_l-t_s)U^2}{2\sqrt{6}U(-3J_H+U)(2J_H+U)} \\
 h_{xs,yz}^x &= \frac{J_H^2(-5t_l^2+t_l t_s-5t_s^2)-J_H(3t_l^2+4t_l t_s+3t_s^2)U+(t_l^2-t_l t_s+t_s^2)U^2}{2\sqrt{6}U(-3J_H+U)(2J_H+U)} \\
 h_{xs,zy}^x &= \frac{J_H^2(5t_l^2-3t_l t_s+4t_s^2)+J_H(3t_l^2+t_l t_s+2t_s^2)U-t_l^2 U^2}{2\sqrt{6}U(-3J_H+U)(2J_H+U)} \\
 h_{xx,yy}^x &= \frac{-(J_H(t_l^2+t_l t_s+t_s^2)+(t_l^2+t_s^2)U)}{4U(2J_H+U)} \\
 h_{xx,zz}^x &= \frac{-(t_l(J_H(t_l+t_s)+t_l U))}{4U(2J_H+U)} \\
 h_{xy,yx}^x &= \frac{(J_H+U)(J_H(-3t_l^2+2t_l t_s-3t_s^2)+(t_l^2+t_l t_s+t_s^2)U)}{4U(-3J_H+U)(2J_H+U)} \\
 h_{xy,zs}^x &= \frac{J_H^2(-5t_l^2+2t_l t_s-4t_s^2)-J_H(3t_l^2+t_l t_s+2t_s^2)U+t_l(t_l-t_s)U^2}{2\sqrt{6}U(-3J_H+U)(2J_H+U)} \\
 h_{xz,ys}^x &= \frac{J_H^2(5t_l^2-t_l t_s+5t_s^2)+J_H(3t_l^2+4t_l t_s+3t_s^2)U-(t_l^2-t_l t_s+t_s^2)U^2}{2\sqrt{6}U(-3J_H+U)(2J_H+U)} \\
 h_{xz,zx}^x &= \frac{t_l(2t_s(1/U+2/(-3J_H+U))+3t_l(1/U+1/(2J_H+U)))}{24} \\
 h_{ys,zx}^x &= \frac{-(J_H^2(4t_l^2-3t_l t_s+5t_s^2)+J_H(2t_l^2+t_l t_s+3t_s^2)U-t_s^2 U^2)}{2\sqrt{6}U(-3J_H+U)(2J_H+U)} \\
 h_{yx,zs}^x &= \frac{J_H^2(4t_l^2-2t_l t_s+5t_s^2)+J_H(2t_l^2+t_l t_s+3t_s^2)U+(t_l-t_s)t_s U^2}{2\sqrt{6}U(-3J_H+U)(2J_H+U)} \\
 h_{yy,zz}^x &= \frac{-(t_s(J_H(t_l+t_s)+t_s U))}{4U(2J_H+U)} \\
 h_{yz,zy}^x &= \frac{t_s(2t_l(1/U+2/(-3J_H+U))+3t_s(1/U+1/(2J_H+U)))}{24}
 \end{aligned}$$

Bibliography

- [1] G. Khaliullin, *Excitonic Magnetism in Van Vleck-type d^4 Mott Insulators*, Phys. Rev. Lett. **111**, 197201 (2013).
- [2] A. Jain, M. Krautloher, J. Porras, G. H. Ryu, D. P. Chen, D. L. Abernathy, J. T. Park, A. Ivanov, J. Chaloupka, G. Khaliullin, B. Keimer, and B. Kim, *Higgs mode and its decay in a two-dimensional antiferromagnet*, Nature Physics **13**, 633–637 (2017).
- [3] S.-M. Souliou, J. Chaloupka, G. Khaliullin, G. Ryu, A. Jain, B. J. Kim, M. Le Tacon, and B. Keimer, *Raman Scattering from Higgs Mode Oscillations in the Two-Dimensional Antiferromagnet Ca_2RuO_4* , Phys. Rev. Lett. **119**, 067201 (2017).
- [4] A. Kitaev, *Anyons in an exactly solved model and beyond*, Annals of Physics **321**, 2–111 (2006), january Special Issue.
- [5] P. S. Anisimov, F. Aust, G. Khaliullin, and M. Daghofer, *Nontrivial Triplon Topology and Triplon Liquid in Kitaev-Heisenberg-type Excitonic Magnets*, Phys. Rev. Lett. **122**, 177201 (2019).
- [6] P. S. Anisimov, *Triplons in the excitonic Kitaev-Heisenberg model on the honeycomb lattice: condensation, interactions and topology*, Ph.D. thesis, Universität Stuttgart (2019), <http://dx.doi.org/10.18419/opus-10366>.
- [7] F. Aust, *Cluster Perturbation Theory for hard-core bosons*, Master thesis, Universität Stuttgart (2018).
- [8] T. Takayama, M. Blankenhorn, J. Bertinshaw, D. Haskel, N. A. Bogdanov, K. Kitagawa, A. N. Yaresko, A. Krajewska, S. Bette, G. McNally, A. S. Gibbs, Y. Matsumoto, D. P. Sari, I. Watanabe, G. Fabbris, W. Bi, T. I. Larkin, K. S. Rabinovich, A. V. Boris, H. Ishii, H. Yamaoka, T. Irifune, R. Bewley, C. J. Ridley, C. L. Bull, R. Dinnebier, B. Keimer, and H. Takagi, *Competing spin-orbital singlet states in the $4d^4$ honeycomb ruthenate $Ag_3LiRu_2O_6$* , Phys. Rev. Res. **4**, 043079 (2022).
- [9] Y. Miura, Y. Yasui, M. Sato, N. Igawa, and K. Kakurai, *New-Type Phase Transition of Li_2RuO_3 with Honeycomb Structure*, Journal of the Physical Society of Japan **76**, 033705 (2007).
- [10] Y. Miura, M. Sato, Y. Yamakawa, T. Habaguchi, and Y. Ōno, *Structural Transition of Li_2RuO_3 Induced by Molecular-Orbit Formation*, Journal of the Physical Society of Japan **78**, 094706 (2009).

- [11] J. C. Wang, J. Terzic, T. F. Qi, F. Ye, S. J. Yuan, S. Aswartham, S. V. Streltsov, D. I. Khomskii, R. K. Kaul, and G. Cao, *Lattice-tuned magnetism of $Ru^{4+}(4d^4)$ ions in single crystals of the layered honeycomb ruthenates Li_2RuO_3 and Na_2RuO_3* , Phys. Rev. B **90**, 161110 (2014).
- [12] H. Suzuki, H. Gretarsson, H. Ishikawa, K. Ueda, Z. Yang, H. Liu, H. Kim, D. Kukusta, A. Yaresko, M. Minola, J. A. Sears, S. Francoual, H.-C. Wille, J. Nuss, H. Takagi, B. J. Kim, G. Khaliullin, H. Yavaş, and B. Keimer, *Spin waves and spin-state transitions in a ruthenate high-temperature antiferromagnet*, Nature Materials **18**, 563–567 (2019).
- [13] T. Feldmaier, P. Strobel, M. Schmid, P. Hansmann, and M. Daghofer, *Excitonic magnetism at the intersection of spin-orbit coupling and crystal-field splitting*, Phys. Rev. Res. **2**, 033201 (2020).
- [14] I. Vergara, M. Magnaterra, P. Warzanowski, J. Attig, S. Kunkemöller, D. I. Khomskii, M. Braden, M. Hermanns, and M. Grüninger, *Spin-orbit coupling and crystal-field splitting in Ti-doped Ca_2RuO_4 studied by ellipsometry*, Phys. Rev. B **106**, 085103 (2022).
- [15] S. Kunkemöller, D. Khomskii, P. Steffens, A. Piovano, A. A. Nugroho, and M. Braden, *Highly Anisotropic Magnon Dispersion in Ca_2RuO_4 : Evidence for Strong Spin Orbit Coupling*, Phys. Rev. Lett. **115**, 247201 (2015).
- [16] G. Zhang and E. Pavarini, *Higgs mode and stability of xy -orbital ordering in Ca_2RuO_4* , Phys. Rev. B **101**, 205128 (2020).
- [17] S. Mohapatra and A. Singh, *Magnetic reorientation transition in a three orbital model for Ca_2RuO_4 —interplay of spin-orbit coupling, tetragonal distortion, and Coulomb interactions*, Journal of Physics: Condensed Matter **32**, 485805 (2020).
- [18] G. Zhang and E. Pavarini, *Mott transition, spin-orbit effects, and magnetism in Ca_2RuO_4* , Phys. Rev. B **95**, 075145 (2017).
- [19] D. Sutter, C. G. Fatuzzo, S. Moser, M. Kim, R. Fittipaldi, A. Vecchione, V. Granata, Y. Sassa, F. Cossalter, G. Gatti, M. Grioni, H. M. Rønnow, N. C. Plumb, C. E. Matt, M. Shi, M. Hoesch, T. K. Kim, T.-R. Chang, H.-T. Jeng, C. Jozwiak, A. Bostwick, E. Rotenberg, A. Georges, T. Neupert, and J. Chang, *Hallmarks of Hund's coupling in the Mott insulator Ca_2RuO_4* , Nature Communications **8**, 15176 (2017).
- [20] P. Strobel, F. Aust, and M. Daghofer, *Magnetic phases for strongly correlated t_{2g}^4 electrons on the square lattice: Impact of spin-orbit coupling and crystal field*, Phys. Rev. B **104**, 115148 (2021).
- [21] G. Cao, S. McCall, M. Shepard, J. E. Crow, and R. P. Guertin, *Magnetic and transport properties of single-crystal Ca_2RuO_4 : Relationship to superconducting Sr_2RuO_4* , Phys. Rev. B **56**, R2916–R2919 (1997).

-
- [22] Y. Maeno, H. Hashimoto, K. Yoshida, S. Nishizaki, T. Fujita, J. G. Bednorz, and F. Lichtenberg, *Superconductivity in a layered perovskite without copper*, Nature **372**, 532–534 (1994).
- [23] Y. Maeno, S. Yonezawa, and A. Ramires, *Still Mystery after All These Years — Unconventional Superconductivity of Sr_2RuO_4 —*, Journal of the Physical Society of Japan **93**, 062001 (2024).
- [24] C. Sow, S. Yonezawa, S. Kitamura, T. Oka, K. Kuroki, F. Nakamura, and Y. Maeno, *RETRACTED: Current-induced strong diamagnetism in the Mott insulator Ca_2RuO_4* , Science **358**, 1084–1087 (2017).
- [25] G. Mattoni, S. Yonezawa, and Y. Maeno, *Diamagnetic-like response from localized heating of a paramagnetic material*, Applied Physics Letters **116**, 172405 (2020).
- [26] J. Bertinshaw, N. Gurung, P. Jorba, H. Liu, M. Schmid, D. T. Mantadakis, M. Daghofer, M. Krautloher, A. Jain, G. H. Ryu, O. Fabelo, P. Hansmann, G. Khalullin, C. Pfleiderer, B. Keimer, and B. J. Kim, *Unique Crystal Structure of Ca_2RuO_4 in the Current Stabilized Semimetallic State*, Phys. Rev. Lett. **123**, 137204 (2019).
- [27] P. Warzanowski, M. Magnaterra, P. Stein, G. Schlicht, Q. Faure, C. J. Sahle, T. Lorenz, P. Becker, L. Bohatý, M. Moretti Sala, G. Monaco, P. H. M. van Loosdrecht, and M. Grüninger, *Electronic excitations in $5d^4 J = 0 Os^{4+}$ halides studied by resonant inelastic x-ray scattering and optical spectroscopy*, Phys. Rev. B **108**, 125120 (2023).
- [28] Y. Zhang, L.-F. Lin, A. Moreo, and E. Dagotto, *$J = 0$ nonmagnetic insulating state in K_2OsX_6 ($X=F, Cl, \text{ and } Br$)*, Phys. Rev. B **106**, 155148 (2022).
- [29] A. Paramekanti, D. J. Singh, B. Yuan, D. Casa, A. Said, Y.-J. Kim, and A. D. Christianson, *Spin-orbit coupled systems in the atomic limit: rhenates, osmates, iridates*, Phys. Rev. B **97**, 235119 (2018).
- [30] S. Fuchs, T. Dey, G. Aslan-Cansever, A. Maljuk, S. Wurmehl, B. Büchner, and V. Kataev, *Unraveling the Nature of Magnetism of the $5d^4$ Double Perovskite Ba_2YIrO_6* , Phys. Rev. Lett. **120**, 237204 (2018).
- [31] A. Nag, S. Bhowal, A. Chakraborty, M. M. Sala, A. Efimenko, F. Bert, P. K. Biswas, A. D. Hillier, M. Itoh, S. D. Kaushik, V. Siruguri, C. Meneghini, I. Dasgupta, and S. Ray, *Origin of magnetic moments and presence of spin-orbit singlets in Ba_2YIrO_6* , Phys. Rev. B **98**, 014431 (2018).
- [32] M. Kusch, V. M. Katukuri, N. A. Bogdanov, B. Büchner, T. Dey, D. V. Efremov, J. E. Hamann-Borrero, B. H. Kim, M. Krisch, A. Maljuk, M. M. Sala, S. Wurmehl, G. Aslan-Cansever, M. Sturza, L. Hozoi, J. van den Brink, and J. Geck, *Observation of heavy spin-orbit excitons propagating in a nonmagnetic background: The case of $(Ba, Sr)_2YIrO_6$* , Phys. Rev. B **97**, 064421 (2018).

- [33] H. Schnait, D. Bauernfeind, T. Saha-Dasgupta, and M. Aichhorn, *Small moments without long-range magnetic ordering in the zero-temperature ground state of the double perovskite iridate Ba_2YIrO_6* , Phys. Rev. B **106**, 035132 (2022).
- [34] H. Takahashi, H. Suzuki, J. Bertinshaw, S. Bette, C. Mühle, J. Nuss, R. Dinnebier, A. Yaresko, G. Khaliullin, H. Gretarsson, T. Takayama, H. Takagi, and B. Keimer, *Nonmagnetic $J = 0$ State and Spin-Orbit Excitations in K_2RuCl_6* , Phys. Rev. Lett. **127**, 227201 (2021).
- [35] Z. Porter, P. M. Sarte, T. Petersen, M. H. Upton, L. Hozoi, and S. D. Wilson, *Spin-orbit excitons and electronic configuration of the $5d^4$ insulator $Sr_3Ir_2O_7F_2$* , Phys. Rev. B **106**, 115140 (2022).
- [36] Y. Haraguchi, D. Nishio-Hamane, and H. A. Katori, *Magnetic ordering in the $J_{\text{eff}} = 0$ nickelate $NiRh_2O_4$ prepared via a solid-state metathesis*, Phys. Rev. Mater. **7**, 084413 (2023).
- [37] B. Yuan, B. H. Kim, Q. Chen, D. Dobrowolski, M. Azmanska, G. M. Luke, S. Fan, V. Bisogni, J. Pelliciari, and J. P. Clancy, *Highly Tunable Ru-dimer Molecular Orbital State in 6H-perovskite $Ba_3MRu_2O_9$* , arXiv e-prints , arXiv:2405.09418 (2024).
- [38] H. Takagi, T. Takayama, G. Jackeli, G. Khaliullin, and S. E. Nagler, *Concept and realization of Kitaev quantum spin liquids*, Nature Reviews Physics **1**, 264–280 (2019).
- [39] S. M. Winter, A. A. Tsirlin, M. Daghofer, J. van den Brink, Y. Singh, P. Gegenwart, and R. Valentí, *Models and materials for generalized Kitaev magnetism*, Journal of Physics: Condensed Matter **29**, 493002 (2017).
- [40] M. Hermanns, I. Kimchi, and J. Knolle, *Physics of the Kitaev Model: Fractionalization, Dynamic Correlations, and Material Connections*, Annual Review of Condensed Matter Physics **9**, 17–33 (2018).
- [41] L. Janssen and M. Vojta, *Heisenberg–Kitaev physics in magnetic fields*, Journal of Physics: Condensed Matter **31**, 423002 (2019).
- [42] C. Broholm, R. J. Cava, S. A. Kivelson, D. G. Nocera, M. R. Norman, and T. Senthil, *Quantum spin liquids*, Science **367**, eaay0668 (2020).
- [43] T. Lancaster, *Quantum spin liquids*, arXiv e-prints , arXiv:2310.19577 (2023).
- [44] A. Kitaev, *Fault-tolerant quantum computation by anyons*, Annals of Physics **303**, 2–30 (2003).
- [45] F. Arute, K. Arya, R. Babbush, D. Bacon, J. C. Bardin, R. Barends, R. Biswas, S. Boixo, F. G. S. L. Brandao, D. A. Buell, B. Burkett, Y. Chen, Z. Chen, B. Chiaro, R. Collins, W. Courtney, A. Dunsworth, E. Farhi, B. Foxen, A. Fowler, C. Gidney, M. Giustina, R. Graff, K. Guerin, S. Habegger, M. P. Harrigan, M. J. Hartmann, A. Ho, M. Hoffmann, T. Huang, T. S. Humble, S. V. Isakov, E. Jeffrey, Z. Jiang,

- D. Kafri, K. Kechedzhi, J. Kelly, P. V. Klimov, S. Knysh, A. Korotkov, F. Kostritsa, D. Landhuis, M. Lindmark, E. Lucero, D. Lyakh, S. Mandrà, J. R. McClean, M. McEwen, A. Megrant, X. Mi, K. Michielsen, M. Mohseni, J. Mutus, O. Naaman, M. Neeley, C. Neill, M. Y. Niu, E. Ostby, A. Petukhov, J. C. Platt, C. Quintana, E. G. Rieffel, P. Roushan, N. C. Rubin, D. Sank, K. J. Satzinger, V. Smelyanskiy, K. J. Sung, M. D. Trevithick, A. Vainsencher, B. Villalonga, T. White, Z. J. Yao, P. Yeh, A. Zalcman, H. Neven, and J. M. Martinis, *Quantum supremacy using a programmable superconducting processor*, *Nature* **574**, 505–510 (2019).
- [46] K. J. Satzinger, Y.-J. Liu, A. Smith, C. Knapp, M. Newman, C. Jones, Z. Chen, C. Quintana, X. Mi, A. Dunsworth, C. Gidney, I. Aleiner, F. Arute, K. Arya, J. Atalaya, R. Babbush, J. C. Bardin, R. Barends, J. Basso, A. Bengtsson, A. Bilmes, M. Broughton, B. B. Buckley, D. A. Buell, B. Burkett, N. Bushnell, B. Chiaro, R. Collins, W. Courtney, S. Demura, A. R. Derk, D. Eppens, C. Erickson, L. Faoro, E. Farhi, A. G. Fowler, B. Foxen, M. Giustina, A. Greene, J. A. Gross, M. P. Harrigan, S. D. Harrington, J. Hilton, S. Hong, T. Huang, W. J. Huggins, L. B. Ioffe, S. V. Isakov, E. Jeffrey, Z. Jiang, D. Kafri, K. Kechedzhi, T. Khattar, S. Kim, P. V. Klimov, A. N. Korotkov, F. Kostritsa, D. Landhuis, P. Laptev, A. Locharla, E. Lucero, O. Martin, J. R. McClean, M. McEwen, K. C. Miao, M. Mohseni, S. Montazeri, W. Mruczkiewicz, J. Mutus, O. Naaman, M. Neeley, C. Neill, M. Y. Niu, T. E. O’Brien, A. Opremcak, B. Pató, A. Petukhov, N. C. Rubin, D. Sank, V. Shvarts, D. Strain, M. Szalay, B. Villalonga, T. C. White, Z. Yao, P. Yeh, J. Yoo, A. Zalcman, H. Neven, S. Boixo, A. Megrant, Y. Chen, J. Kelly, V. Smelyanskiy, A. Kitaev, M. Knap, F. Pollmann, and P. Roushan, *Realizing topologically ordered states on a quantum processor*, *Science* **374**, 1237–1241 (2021).
- [47] G. Jackeli and G. Khaliullin, *Mott Insulators in the Strong Spin-Orbit Coupling Limit: From Heisenberg to a Quantum Compass and Kitaev Models*, *Phys. Rev. Lett.* **102**, 017205 (2009).
- [48] J. Chaloupka, G. Jackeli, and G. Khaliullin, *Kitaev-Heisenberg Model on a Honeycomb Lattice: Possible Exotic Phases in Iridium Oxides A_2IrO_3* , *Phys. Rev. Lett.* **105**, 027204 (2010).
- [49] J. Chaloupka, G. Jackeli, and G. Khaliullin, *Zigzag Magnetic Order in the Iridium Oxide Na_2IrO_3* , *Phys. Rev. Lett.* **110**, 097204 (2013).
- [50] J. G. Rau, E. K.-H. Lee, and H.-Y. Kee, *Generic Spin Model for the Honeycomb Iridates beyond the Kitaev Limit*, *Phys. Rev. Lett.* **112**, 077204 (2014).
- [51] P. A. Maksimov and A. L. Chernyshev, *Rethinking α - $RuCl_3$* , *Phys. Rev. Res.* **2**, 033011 (2020).
- [52] S.-H. Baek, S.-H. Do, K.-Y. Choi, Y. S. Kwon, A. U. B. Wolter, S. Nishimoto, J. van den Brink, and B. Büchner, *Evidence for a Field-Induced Quantum Spin Liquid in α - $RuCl_3$* , *Phys. Rev. Lett.* **119**, 037201 (2017).

- [53] Y. Kasahara, T. Ohnishi, Y. Mizukami, O. Tanaka, S. Ma, K. Sugii, N. Kurita, H. Tanaka, J. Nasu, Y. Motome, T. Shibauchi, and Y. Matsuda, *Majorana quantization and half-integer thermal quantum Hall effect in a Kitaev spin liquid*, Nature **559**, 227–231 (2018).
- [54] T. Yokoi, S. Ma, Y. Kasahara, S. Kasahara, T. Shibauchi, N. Kurita, H. Tanaka, J. Nasu, Y. Motome, C. Hickey, S. Trebst, and Y. Matsuda, *Half-integer quantized anomalous thermal Hall effect in the Kitaev material candidate α -RuCl₃*, Science **373**, 568–572 (2021).
- [55] Y. Kasahara, K. Sugii, T. Ohnishi, M. Shimozawa, M. Yamashita, N. Kurita, H. Tanaka, J. Nasu, Y. Motome, T. Shibauchi, and Y. Matsuda, *Unusual Thermal Hall Effect in a Kitaev Spin Liquid Candidate α -RuCl₃*, Phys. Rev. Lett. **120**, 217205 (2018).
- [56] M. Yamashita, J. Gouchi, Y. Uwatoko, N. Kurita, and H. Tanaka, *Sample dependence of half-integer quantized thermal Hall effect in the Kitaev spin-liquid candidate α -RuCl₃*, Phys. Rev. B **102**, 220404 (2020).
- [57] J. A. N. Bruin, R. R. Claus, Y. Matsumoto, N. Kurita, H. Tanaka, and H. Takagi, *Robustness of the thermal Hall effect close to half-quantization in α -RuCl₃*, Nature Physics **18**, 401–405 (2022).
- [58] P. Czajka, T. Gao, M. Hirschberger, P. Lampen-Kelley, A. Banerjee, J. Yan, D. G. Mandrus, S. E. Nagler, and N. P. Ong, *Oscillations of the thermal conductivity in the spin-liquid state of α -RuCl₃*, Nature Physics **17**, 915–919 (2021).
- [59] L. E. Chern, E. Z. Zhang, and Y. B. Kim, *Sign Structure of Thermal Hall Conductivity and Topological Magnons for In-Plane Field Polarized Kitaev Magnets*, Phys. Rev. Lett. **126**, 147201 (2021).
- [60] Z.-D. Fan, X.-Q. Sun, and J.-Y. Chen, *On the Thermal Transport Puzzles in α -RuCl₃*, arXiv e-prints, arXiv:2312.06601 (2023).
- [61] C. Xu, J. Feng, M. Kawamura, Y. Yamaji, Y. Nahas, S. Prokhorenko, Y. Qi, H. Xiang, and L. Bellaiche, *Possible Kitaev Quantum Spin Liquid State in 2D Materials with $S = 3/2$* , Phys. Rev. Lett. **124**, 087205 (2020).
- [62] Z. Zhou, K. Chen, Q. Luo, H.-G. Luo, and J. Zhao, *Strain-induced phase diagram of the $S = \frac{3}{2}$ Kitaev material CrSiTe₃*, Phys. Rev. B **104**, 214425 (2021).
- [63] W. M. H. Natori, H.-K. Jin, and J. Knolle, *Quantum liquids of the $S = \frac{3}{2}$ Kitaev honeycomb and related Kugel-Khomskii models*, Phys. Rev. B **108**, 075111 (2023).
- [64] P. P. Stavropoulos, D. Pereira, and H.-Y. Kee, *Microscopic Mechanism for a Higher-Spin Kitaev Model*, Phys. Rev. Lett. **123**, 037203 (2019).

- [65] X.-Y. Dong and D. N. Sheng, *Spin-1 Kitaev-Heisenberg model on a honeycomb lattice*, Phys. Rev. B **102**, 121102 (2020).
- [66] I. Khait, P. P. Stavropoulos, H.-Y. Kee, and Y. B. Kim, *Characterizing spin-one Kitaev quantum spin liquids*, Phys. Rev. Res. **3**, 013160 (2021).
- [67] C. Hickey, C. Berke, P. P. Stavropoulos, H.-Y. Kee, and S. Trebst, *Field-driven gapless spin liquid in the spin-1 Kitaev honeycomb model*, Phys. Rev. Res. **2**, 023361 (2020).
- [68] Z. Zhu, Z.-Y. Weng, and D. N. Sheng, *Magnetic field induced spin liquids in $S = 1$ Kitaev honeycomb model*, Phys. Rev. Res. **2**, 022047 (2020).
- [69] S. Sachdev and R. N. Bhatt, *Bond-operator representation of quantum spins: Mean-field theory of frustrated quantum Heisenberg antiferromagnets*, Phys. Rev. B **41**, 9323–9329 (1990).
- [70] T. Giamarchi, C. Rüegg, and O. Tchernyshyov, *Bose–Einstein condensation in magnetic insulators*, Nature Physics **4**, 198–204 (2008).
- [71] V. Zapf, M. Jaime, and C. D. Batista, *Bose-Einstein condensation in quantum magnets*, Rev. Mod. Phys. **86**, 563–614 (2014).
- [72] M. Matsumoto, B. Normand, T. M. Rice, and M. Sgrist, *Field- and pressure-induced magnetic quantum phase transitions in $TlCuCl_3$* , Phys. Rev. B **69**, 054423 (2004).
- [73] C. Rüegg, B. Normand, M. Matsumoto, A. Furrer, D. F. McMorrow, K. W. Krämer, H. U. Güdel, S. N. Gvasaliya, H. Mutka, and M. Boehm, *Quantum Magnets under Pressure: Controlling Elementary Excitations in $TlCuCl_3$* , Phys. Rev. Lett. **100**, 205701 (2008).
- [74] M. Matsumoto, B. Normand, T. M. Rice, and M. Sgrist, *Magnon Dispersion in the Field-Induced Magnetically Ordered Phase of $TlCuCl_3$* , Phys. Rev. Lett. **89**, 077203 (2002).
- [75] P. Merchant, B. Normand, K. W. Krämer, M. Boehm, D. F. McMorrow, and C. Rüegg, *Quantum and classical criticality in a dimerized quantum antiferromagnet*, Nature Physics **10**, 373–379 (2014).
- [76] P. A. McClarty, *Topological Magnons: A Review*, Annual Review of Condensed Matter Physics **13**, 171–190 (2022).
- [77] M. Malki and G. S. Uhrig, *Topological magnetic excitations*, Europhysics Letters **132**, 20003 (2020).
- [78] J. Romhányi, K. Penc, and R. Ganesh, *Hall effect of triplons in a dimerized quantum magnet*, Nature Communications **6**, 6805 (2015).

- [79] Y. Li, S. M. Winter, D. A. S. Kaib, K. Riedl, and R. Valentí, *Modified Curie-Weiss law for j_{eff} magnets*, Phys. Rev. B **103**, L220408 (2021).
- [80] S. Lower, *Chem1 Virtual Textbook: A Reference Text for General Chemistry (electronic edition)*, [https://chem.libretexts.org/Bookshelves/General_Chemistry/Chem1_\(Lower\)](https://chem.libretexts.org/Bookshelves/General_Chemistry/Chem1_(Lower)), Accessed: 2024-09-20.
- [81] E. Pavarini, E. Koch, F. Anders, and M. E. . Jarrell, *Correlated electrons: from models to materials*, Schriften des Forschungszentrums Jülich. Reihe Modeling and simulation, Vol. 2 (Forschungszentrum Jülich GmbH, ISBN 9783893367962, Jülich, 2012).
- [82] W. Nolting, *Quantum Mechanics - Methods and Applications* (Springer International, ISBN 9783319633244, 2017).
- [83] P. Atkins, T. Overton, J. Rourke, M. Weller, F. Armstrong, and M. Hagerman, *Shriver and Atkins' Inorganic Chemistry, Fifth Edition*, Vol. 5 (W. H. Freeman and Company, ISBN 9781429218207, New York, 2010).
- [84] Periodic Table of the Elements, <https://www.periodictable.one/element/44>, accessed: 2024-07-16.
- [85] D. I. Khomskii, *Transition Metal Compounds* (Cambridge University Press, ISBN 9781139096782, 2014).
- [86] S. Agrestini, F. Borgatti, P. Florio, J. Frassinetti, D. Fiore Mosca, Q. Faure, B. Detlefs, C. J. Sahle, S. Francoual, J. Choi, M. Garcia-Fernandez, K.-J. Zhou, V. F. Mitrovic, P. M. Woodward, G. Ghiringhelli, C. Franchini, F. Boscherini, S. Sanna, and M. Moretti Sala, *Origin of Magnetism in a Supposedly Nonmagnetic Osmium Oxide*, Phys. Rev. Lett. **133**, 066501 (2024).
- [87] K. Momma and F. Izumi, *VESTA3 for three-dimensional visualization of crystal, volumetric and morphology data*, Journal of Applied Crystallography **44**, 1272–1276 (2011).
- [88] C. Ballhausen, *Introduction to Ligand Field Theory* (McGraw-Hill Book Company, New York, 1962).
- [89] J. Rasch and A. C. H. Yu, *Efficient Storage Scheme for Precalculated Wigner $3j$, $6j$ and Gaunt Coefficients*, SIAM Journal on Scientific Computing **25**, 1416–1428 (2004).
- [90] M. Dresselhaus, G. Dresselhaus, and A. Jorio, *Group Theory: Application to the Physics of Condensed Matter* (Springer Berlin Heidelberg, ISBN 9783540328995, 2007).
- [91] J. Chaloupka, *Emergent transverse-field Ising model in d^4 spin-orbit Mott insulators*, Phys. Rev. B **109**, L020403 (2024).

- [92] F.-Y. Li and G. Chen, *Spin-orbital entanglement in d^8 Mott insulators: Possible excitonic magnetism in diamond lattice antiferromagnets*, Phys. Rev. B **100**, 045103 (2019).
- [93] H. Gong, K. Kim, B. H. Kim, B. Kim, J. Kim, and B. Min, *Is the ground state of $5d^4$ double-perovskite Iridate Ba_2YIrO_6 magnetic or nonmagnetic?*, Journal of Magnetism and Magnetic Materials **454**, 66–70 (2018).
- [94] A. Abragam and B. Bleaney, *Electron Paramagnetic Resonance of Transition Ions*, Oxford Classic Texts in the Physical Sciences, ISBN 9780191023002 (OUP Oxford, 2012).
- [95] H. Liu, J. Chaloupka, and G. Khaliullin, *Kitaev Spin Liquid in 3d Transition Metal Compounds*, Phys. Rev. Lett. **125**, 047201 (2020).
- [96] G. L. Stamokostas and G. A. Fiete, *Mixing of $t_{2g} - e_g$ orbitals in 4d and 5d transition metal oxides*, Phys. Rev. B **97**, 085150 (2018).
- [97] J. Owen and J. Thornley, *Covalent bonding and magnetic properties of transition metal ions*, Reports on Progress in Physics **29**, 675 (1966).
- [98] C. Jørgensen, ed., *Absorption Spectra and Chemical Bonding in Complexes* (Pergamon, ISBN 9780080096278, 1962) pp. 351–355.
- [99] H. B. Gray, *Electrons and Chemical Bonding* (W. A. Benjamin, Inc., 1965).
- [100] H. Gretarsson, H. Suzuki, H. Kim, K. Ueda, M. Krautloher, B. J. Kim, H. Yavaş, G. Khaliullin, and B. Keimer, *Observation of spin-orbit excitations and Hund’s multiplets in Ca_2RuO_4* , Phys. Rev. B **100**, 045123 (2019).
- [101] H. Suzuki, H. Liu, J. Bertinshaw, K. Ueda, H. Kim, S. Laha, D. Weber, Z. Yang, L. Wang, H. Takahashi, K. Fürsich, M. Minola, B. V. Lotsch, B. J. Kim, H. Yavaş, M. Daghofer, J. Chaloupka, G. Khaliullin, H. Gretarsson, and B. Keimer, *Proximate ferromagnetic state in the Kitaev model material α - $RuCl_3$* , Nature Communications **12**, 4512 (2021).
- [102] H. Gretarsson, H. Fujihara, F. Sato, H. Gotou, Y. Imai, K. Ohgushi, B. Keimer, and H. Suzuki, *$J=\frac{1}{2}$ pseudospins and $d-p$ hybridization in the Kitaev spin liquid candidates RuX_3 ($X=Cl, Br, I$)*, Phys. Rev. B **109**, L180413 (2024).
- [103] C. A. Occhialini, V. Bisogni, H. You, A. Barbour, I. Jarrige, J. F. Mitchell, R. Comin, and J. Pelliciari, *Local electronic structure of rutile RuO_2* , Phys. Rev. Res. **3**, 033214 (2021).
- [104] B. Zager, J. R. Chamorro, L. Ge, F. Bahrami, V. Bisogni, J. Pelliciari, J. Li, G. Fabbris, T. M. McQueen, M. Mourigal, and K. W. Plumb, *Electronic structure of the frustrated diamond lattice magnet $NiRh_2O_4$* , Phys. Rev. B **106**, 045134 (2022).

- [105] A. E. Taylor, S. Calder, R. Morrow, H. L. Feng, M. H. Upton, M. D. Lumsden, K. Yamaura, P. M. Woodward, and A. D. Christianson, *Spin-Orbit Coupling Controlled $J = 3/2$ Electronic Ground State in $5d^3$ Oxides*, Phys. Rev. Lett. **118**, 207202 (2017).
- [106] B. Yuan, J. P. Clancy, A. M. Cook, C. M. Thompson, J. Greedan, G. Cao, B. C. Jeon, T. W. Noh, M. H. Upton, D. Casa, T. Gog, A. Paramekanti, and Y.-J. Kim, *Determination of Hund's coupling in $5d$ oxides using resonant inelastic x-ray scattering*, Phys. Rev. B **95**, 235114 (2017).
- [107] M. Haverkort, *Spin and orbital degrees of freedom in transition metal oxides and oxide thin films studied by soft x-ray absorption spectroscopy*, Ph.D. thesis, Universität zu Köln (2005).
- [108] S. V. Streltsov and D. I. Khomskii, *Jahn-Teller Effect and Spin-Orbit Coupling: Friends or Foes?*, Phys. Rev. X **10**, 031043 (2020).
- [109] G. Khaliullin, *Orbital Order and Fluctuations in Mott Insulators*, Progress of Theoretical Physics Supplement **160**, 155–202 (2005).
- [110] H. Liu and G. Khaliullin, *Pseudo-Jahn-Teller Effect and Magnetoelastic Coupling in Spin-Orbit Mott Insulators*, Phys. Rev. Lett. **122**, 057203 (2019).
- [111] Y. Kubota, H. Tanaka, T. Ono, Y. Narumi, and K. Kindo, *Successive magnetic phase transitions in α - $RuCl_3$: XY-like frustrated magnet on the honeycomb lattice*, Phys. Rev. B **91**, 094422 (2015).
- [112] J. G. Rau, E. K.-H. Lee, and H.-Y. Kee, *Spin-Orbit Physics Giving Rise to Novel Phases in Correlated Systems: Iridates and Related Materials*, Annual Review of Condensed Matter Physics **7**, 195–221 (2016).
- [113] G. Cao and P. Schlottmann, *The challenge of spin-orbit-tuned ground states in iridates: a key issues review*, Reports on Progress in Physics **81**, 042502 (2018).
- [114] K. V. Shanavas, Z. S. Popović, and S. Satpathy, *Theoretical model for Rashba spin-orbit interaction in d electrons*, Phys. Rev. B **90**, 165108 (2014).
- [115] F. Hellman, A. Hoffmann, Y. Tserkovnyak, G. S. D. Beach, E. E. Fullerton, C. Leighton, A. H. MacDonald, D. C. Ralph, D. A. Arena, H. A. Dürr, P. Fischer, J. Grollier, J. P. Heremans, T. Jungwirth, A. V. Kimel, B. Koopmans, I. N. Krivorotov, S. J. May, A. K. Petford-Long, J. M. Rondinelli, N. Samarth, I. K. Schuller, A. N. Slavin, M. D. Stiles, O. Tchernyshyov, A. Thiaville, and B. L. Zink, *Interface-induced phenomena in magnetism*, Rev. Mod. Phys. **89**, 025006 (2017).
- [116] L. Landau and M. Lifshits, *Quantum Mechanics: Non-Relativistic Theory*, Course of theoretical physics (Elsevier Science, ISBN 9780750635394, 1991).

-
- [117] G. Jha and T. Heine, *DFTB Parameters for the Periodic Table: Part III, Spin-Orbit Coupling*, Journal of Chemical Theory and Computation **18**, 4472–4481 (2022).
- [118] Q. Gu, S. K. Pandey, and R. Tiwari, *A computational method to estimate spin–orbital interaction strength in solid state systems*, Computational Materials Science **221**, 112090 (2023).
- [119] T. Feldmaier, *Excitonic antiferromagnetism in two-dimensional t_{2g}^4 systems*, Ph.D. thesis, Universität Stuttgart (2020), <http://dx.doi.org/10.18419/opus-10716>.
- [120] I. Dzyaloshinsky, *A thermodynamic theory of “weak” ferromagnetism of antiferromagnetics*, Journal of Physics and Chemistry of Solids **4**, 241–255 (1958).
- [121] T. Moriya, *Anisotropic Superexchange Interaction and Weak Ferromagnetism*, Phys. Rev. **120**, 91–98 (1960).
- [122] A. Fert, M. Chshiev, A. Thiaville, and H. Yang, *From Early Theories of Dzyaloshinskii–Moriya Interactions in Metallic Systems to Today’s Novel Roads*, Journal of the Physical Society of Japan **92**, 081001 (2023).
- [123] R. E. Camley and K. L. Livesey, *Consequences of the Dzyaloshinskii–Moriya interaction*, Surface Science Reports **78**, 100605 (2023).
- [124] M. Malki and K. P. Schmidt, *Magnetic Chern bands and triplon Hall effect in an extended Shastry–Sutherland model*, Phys. Rev. B **95**, 195137 (2017).
- [125] P. A. McClarty, F. Krüger, T. Guidi, S. F. Parker, K. Refson, A. W. Parker, D. Prabhakaran, and R. Coldea, *Topological triplon modes and bound states in a Shastry–Sutherland magnet*, Nature Physics **13**, 736–741 (2017).
- [126] D. Bhowmick and P. Sengupta, *$U(1)$ -Symmetry protected Dirac nodal loops of triplons in $SrCu_2(BO_3)_2$* , arXiv e-prints, arXiv:2003.12998 (2020).
- [127] D. Bhowmick and P. Sengupta, *Weyl triplons in $SrCu_2(BO_3)_2$* , Phys. Rev. B **104**, 085121 (2021).
- [128] D. G. Joshi and A. P. Schnyder, *Topological quantum paramagnet in a quantum spin ladder*, Phys. Rev. B **96**, 220405 (2017).
- [129] D. G. Joshi and A. P. Schnyder, *\mathbb{Z}_2 topological quantum paramagnet on a honeycomb bilayer*, Phys. Rev. B **100**, 020407 (2019).
- [130] A. Haldar, G. Massarelli, and A. Paramakanti, *Higher-order topology and corner triplon excitations in two-dimensional quantum spin-dimer models*, Phys. Rev. B **104**, 184403 (2021).
- [131] W. Nolting, *Fundamentals of Many-body Physics* (Springer International, ISBN 9783319983264, 2018).

- [132] H. Strand, *Correlated Materials - Models & Methods*, Ph.D. thesis, University of Gothenburg (2013).
- [133] J. Kanamori, *Electron Correlation and Ferromagnetism of Transition Metals*, Progress of Theoretical Physics **30**, 275–289 (1963).
- [134] P. Strobel, *Effective Kugel-Khomskii type models for d^4 and d^5 materials*, Ph.D. thesis, Universität Stuttgart (2023), <http://dx.doi.org/10.18419/opus-13869>.
- [135] G. Khaliullin, P. Horsch, and A. M. Oleś, *Spin Order due to Orbital Fluctuations: Cubic Vanadates*, Phys. Rev. Lett. **86**, 3879–3882 (2001).
- [136] A. M. Oleś, G. Khaliullin, P. Horsch, and L. F. Feiner, *Fingerprints of spin-orbital physics in cubic Mott insulators: Magnetic exchange interactions and optical spectral weights*, Phys. Rev. B **72**, 214431 (2005).
- [137] J. Hubbard, *Electron correlations in narrow energy bands*, Proceedings of the Royal Society of London A: Mathematical, Physical and Engineering Sciences **276**, 238–257 (1963).
- [138] S. B. Roy, *Mott Insulators*, 2053-2563 (IOP Publishing, ISBN 9780750315968, 2019).
- [139] M. Imada, A. Fujimori, and Y. Tokura, *Metal-insulator transitions*, Rev. Mod. Phys. **70**, 1039–1263 (1998).
- [140] E. Pavarini, E. Koch, R. Scalettar, and R. Martin, eds., *The Physics of Correlated Insulators, Metals, and Superconductors*, Schriften des Forschungszentrums Jülich. Reihe Modeling and Simulation, Vol. 7 (Forschungszentrum Jülich GmbH, ISBN 9783958062245, Jülich, 2017).
- [141] K. I. Kugel' and D. I. Khomskii, *The Jahn-Teller effect and magnetism: transition metal compounds*, Soviet Physics Uspekhi **25**, 231 (1982).
- [142] P. W. Anderson, *Antiferromagnetism. Theory of Superexchange Interaction*, Phys. Rev. **79**, 350–356 (1950).
- [143] H. Liu, *Towards Kitaev spin liquid in 3d transition metal compounds*, International Journal of Modern Physics B **35**, 2130006 (2021).
- [144] H. Liu, J. Chaloupka, and G. Khaliullin, *Exchange interactions in d^5 Kitaev materials: From Na_2IrO_3 to $\alpha\text{-RuCl}_3$* , Phys. Rev. B **105**, 214411 (2022).
- [145] P. Strobel and M. Daghofer, *Comparing the influence of Floquet dynamics in various Kitaev-Heisenberg materials*, Phys. Rev. B **105**, 085144 (2022).
- [146] P. Strobel and M. Daghofer, *From linear to circular polarized light: Floquet engineering in Kitaev-Heisenberg materials with Lissajous figures*, Phys. Rev. B **108**, 035132 (2023).

-
- [147] O. Friedt, M. Braden, G. André, P. Adelman, S. Nakatsuji, and Y. Maeno, *Structural and magnetic aspects of the metal-insulator transition in $\text{Ca}_{2-x}\text{Sr}_x\text{RuO}_4$* , Phys. Rev. B **63**, 174432 (2001).
- [148] J. Kuneš, *Excitonic condensation in systems of strongly correlated electrons*, Journal of Physics: Condensed Matter **27**, 333201 (2015).
- [149] N. Kaushal, R. Soni, A. Nocera, G. Alvarez, and E. Dagotto, *BCS-BEC crossover in a $(t_2g)^4$ excitonic magnet*, Phys. Rev. B **101**, 245147 (2020).
- [150] N. Kaushal, J. Herbrych, A. Nocera, G. Alvarez, A. Moreo, F. A. Reboredo, and E. Dagotto, *Density matrix renormalization group study of a three-orbital Hubbard model with spin-orbit coupling in one dimension*, Phys. Rev. B **96**, 155111 (2017).
- [151] T. Sato, T. Shirakawa, and S. Yunoki, *Spin-orbital entangled excitonic insulator with quadrupole order*, Phys. Rev. B **99**, 075117 (2019).
- [152] B. A. Ivanov and A. K. Kolezhuk, *Effective field theory for the $S=1$ quantum nematic*, Phys. Rev. B **68**, 052401 (2003).
- [153] C. Lacroix, P. Mendels, and F. Mila, *Introduction to Frustrated Magnetism* (Springer Berlin, Heidelberg, ISBN 9783642105890, 2011).
- [154] J. Lotze, *Variational cluster approximation at finite temperatures*, Ph.D. thesis, Universität Stuttgart (2022), <http://dx.doi.org/10.18419/opus-12231>.
- [155] G. Pan and Z. Y. Meng, in *Encyclopedia of Condensed Matter Physics (Second Edition)*, edited by T. Chakraborty (Academic Press, ISBN 9780323914086, Oxford, 2024) second edition ed., pp. 879–893.
- [156] T. Sato, B. J. Ramshaw, K. A. Modic, and F. F. Assaad, *Scale-invariant magnetic anisotropy in $\alpha\text{-RuCl}_3$: A quantum Monte Carlo study*, arXiv e-prints, arXiv:2312.03080 (2023).
- [157] Y. Fan and Y. Wan, *Fluctuation-induced first-order phase transitions in the Kitaev-like d^4 honeycomb magnet*, Phys. Rev. B **107**, 075130 (2023).
- [158] J. Q. Liu, F.-Y. Li, G. Chen, and Z. Wang, *Featureless quantum paramagnet with frustrated criticality and competing spiral magnetism on spin-1 honeycomb lattice magnet*, Phys. Rev. Res. **2**, 033260 (2020).
- [159] A. Läuchli, F. Mila, and K. Penc, *Quadrupolar Phases of the $S = 1$ Bilinear-Biquadratic Heisenberg Model on the Triangular Lattice*, Phys. Rev. Lett. **97**, 087205 (2006).
- [160] T. Holstein and H. Primakoff, *Field Dependence of the Intrinsic Domain Magnetization of a Ferromagnet*, Phys. Rev. **58**, 1098–1113 (1940).

- [161] N. Lang, *One-Dimensional Topological States of Synthetic Quantum Matter*, Ph.D. thesis, Universität Stuttgart (2019), https://serv.n15.de/theses/PhD_Nicolai_Lang_2019-DIGITAL-A4-08-08-19-V11.pdf.
- [162] E. Manousakis, *The spin-1/2 Heisenberg antiferromagnet on a square lattice and its application to the cuprous oxides*, Rev. Mod. Phys. **63**, 1–62 (1991).
- [163] A. Mulder, R. Ganesh, L. Capriotti, and A. Paramakanti, *Spiral order by disorder and lattice nematic order in a frustrated Heisenberg antiferromagnet on the honeycomb lattice*, Phys. Rev. B **81**, 214419 (2010).
- [164] G. Ramachandran, *Competing Orders in Strongly Correlated Systems*, Ph.D. thesis, University of Toronto (2012), http://www.imsc.res.in/~ganesh/Ramachandran_Ganesh_201206_PhD_thesis.pdf.
- [165] L. Janssen, E. C. Andrade, and M. Vojta, *Honeycomb-Lattice Heisenberg-Kitaev Model in a Magnetic Field: Spin Canting, Metamagnetism, and Vortex Crystals*, Phys. Rev. Lett. **117**, 277202 (2016).
- [166] A. Akbari and G. Khaliullin, *Magnetic excitations in a spin-orbit-coupled d^4 Mott insulator on the square lattice*, Phys. Rev. B **90**, 035137 (2014).
- [167] E. Dagotto, *Correlated electrons in high-temperature superconductors*, Rev. Mod. Phys. **66**, 763–840 (1994).
- [168] H. Fehske, R. Schneider, and A. Weiße, *Computational Many-Particle Physics* (Springer Berlin, Heidelberg, ISBN 9783540746867, 2007).
- [169] E. Pavarini, E. Koch, J. van den Brink, and G. Sawatzky, eds., *Quantum Materials: Experiments and Theory*, Schriften des Forschungszentrums Jülich. Reihe modeling and simulation, Vol. 6 (Forschungszentrum Jülich GmbH, ISBN 9783958061590, Jülich, 2016).
- [170] J. Chaloupka and G. Khaliullin, *Highly frustrated magnetism in relativistic d^4 Mott insulators: Bosonic analog of the Kitaev honeycomb model*, Phys. Rev. B **100**, 224413 (2019).
- [171] A. Koga, H. Tomishige, and J. Nasu, *Ground-state and Thermodynamic Properties of an $S = 1$ Kitaev Model*, Journal of the Physical Society of Japan **87**, 063703 (2018).
- [172] K. Fukui, Y. Kato, J. Nasu, and Y. Motome, *Ground-state phase diagram of spin- S Kitaev-Heisenberg models*, Phys. Rev. B **106**, 174416 (2022).
- [173] O. N. Meetei, W. S. Cole, M. Randeria, and N. Trivedi, *Novel magnetic state in d^4 Mott insulators*, Phys. Rev. B **91**, 054412 (2015).
- [174] C. Svoboda, M. Randeria, and N. Trivedi, *Effective magnetic interactions in spin-orbit coupled d^4 Mott insulators*, Phys. Rev. B **95**, 014409 (2017).

- [175] M. Cuoco, F. Forte, and C. Noce, *Probing spin-orbital-lattice correlations in $4d^4$ systems*, Phys. Rev. B **73**, 094428 (2006).
- [176] D. Sénéchal, *An introduction to quantum cluster methods*, arXiv e-prints , arXiv:0806.2690 (2008).
- [177] J. Lotze and M. Daghofer, *Suppression of effective spin-orbit coupling by thermal fluctuations in spin-orbit coupled antiferromagnets*, Phys. Rev. B **104**, 045125 (2021).
- [178] M. Schmid, *From ground state properties to high energy spectroscopy : extending the application of DMFT for correlated quantum materials*, Ph.D. thesis, Universität Stuttgart (2020), <http://dx.doi.org/10.18419/opus-11046>.
- [179] J. Chaloupka and G. Khaliullin, *Spin-State Crossover Model for the Magnetism of Iron Pnictides*, Phys. Rev. Lett. **110**, 207205 (2013).
- [180] K. Hukushima and K. Nemoto, *Exchange Monte Carlo Method and Application to Spin Glass Simulations*, Journal of the Physical Society of Japan **65**, 1604–1608 (1996).
- [181] T. Hotta and E. Dagotto, *Prediction of Orbital Ordering in Single-Layered Ruthenates*, Phys. Rev. Lett. **88**, 017201 (2001).
- [182] E. M. Stoudenmire, S. Trebst, and L. Balents, *Quadrupolar correlations and spin freezing in $S = 1$ triangular lattice antiferromagnets*, Phys. Rev. B **79**, 214436 (2009).
- [183] K. Tanaka and C. Hotta, *Finite-temperature thermodynamic properties of spin-1 nematics in an applied magnetic field*, Phys. Rev. B **102**, 140401 (2020).
- [184] K. Remund, R. Pohle, Y. Akagi, J. Romhányi, and N. Shannon, *Semi-classical simulation of spin-1 magnets*, Phys. Rev. Res. **4**, 033106 (2022).
- [185] R. Pohle, N. Shannon, and Y. Motome, *Eight-color chiral spin liquid in the $S = 1$ bilinear-biquadratic model with Kitaev interactions*, Phys. Rev. Res. **6**, 033077 (2024).
- [186] M. Cuoco, F. Forte, and C. Noce, *Interplay of Coulomb interactions and c -axis octahedra distortions in single-layer ruthenates*, Phys. Rev. B **74**, 195124 (2006).
- [187] I. Rozada, M. Aramon, J. Machta, and H. G. Katzgraber, *Effects of setting temperatures in the parallel tempering Monte Carlo algorithm*, Phys. Rev. E **100**, 043311 (2019).
- [188] J. Greitemann, K. Liu, and L. Pollet, *Probing hidden spin order with interpretable machine learning*, Phys. Rev. B **99**, 060404 (2019).
- [189] K. Liu, N. Sadoune, N. Rao, J. Greitemann, and L. Pollet, *Revealing the phase diagram of Kitaev materials by machine learning: Cooperation and competition between spin liquids*, Phys. Rev. Res. **3**, 023016 (2021).

- [190] N. Rao, K. Liu, M. Machaczek, and L. Pollet, *Machine-learned phase diagrams of generalized Kitaev honeycomb magnets*, Phys. Rev. Res. **3**, 033223 (2021).
- [191] K. Tanaka and C. Hotta, *Multiple quadrupolar or nematic phases driven by the Heisenberg interactions in a spin-1 dimer system forming a bilayer*, Phys. Rev. B **101**, 094422 (2020).
- [192] A. Paramekanti, D. D. Maharaj, and B. D. Gaulin, *Octupolar order in d-orbital Mott insulators*, Phys. Rev. B **101**, 054439 (2020).
- [193] P. P. Stavropoulos, Y. Yang, I. Rousochatzakis, and N. B. Perkins, *Complex orders and chirality in the classical Kitaev- Γ model*, arXiv e-prints, arXiv:2311.00037 (2023).
- [194] C. Rüegg, N. Cavadini, A. Furrer, H.-U. Güdel, K. Krämer, H. Mutka, A. Wildes, K. Habicht, and P. Vorderwisch, *Bose-Einstein condensation of the triplet states in the magnetic insulator $TlCuCl_3$* , Nature **423**, 62–65 (2003).
- [195] N. Cavadini, G. Heigold, W. Henggeler, A. Furrer, H.-U. Güdel, K. Krämer, and H. Mutka, *Magnetic excitations in the quantum spin system $TlCuCl_3$* , Phys. Rev. B **63**, 172414 (2001).
- [196] K. W. Plumb, J. P. Clancy, L. J. Sandilands, V. V. Shankar, Y. F. Hu, K. S. Burch, H.-Y. Kee, and Y.-J. Kim, *α - $RuCl_3$: A spin-orbit assisted Mott insulator on a honeycomb lattice*, Phys. Rev. B **90**, 041112 (2014).
- [197] A. U. B. Wolter, L. T. Corredor, L. Janssen, K. Nenkov, S. Schönecker, S.-H. Do, K.-Y. Choi, R. Albrecht, J. Hunger, T. Doert, M. Vojta, and B. Büchner, *Field-induced quantum criticality in the Kitaev system α - $RuCl_3$* , Phys. Rev. B **96**, 041405 (2017).
- [198] I. A. Leahy, C. A. Pocs, P. E. Siegfried, D. Graf, S.-H. Do, K.-Y. Choi, B. Normand, and M. Lee, *Anomalous Thermal Conductivity and Magnetic Torque Response in the Honeycomb Magnet α - $RuCl_3$* , Phys. Rev. Lett. **118**, 187203 (2017).
- [199] Z. Wang, S. Reschke, D. Hübner, S.-H. Do, K.-Y. Choi, M. Gensch, U. Nagel, T. Röm, and A. Loidl, *Magnetic Excitations and Continuum of a Possibly Field-Induced Quantum Spin Liquid in α - $RuCl_3$* , Phys. Rev. Lett. **119**, 227202 (2017).
- [200] J. Zheng, K. Ran, T. Li, J. Wang, P. Wang, B. Liu, Z.-X. Liu, B. Normand, J. Wen, and W. Yu, *Gapless Spin Excitations in the Field-Induced Quantum Spin Liquid Phase of α - $RuCl_3$* , Phys. Rev. Lett. **119**, 227208 (2017).
- [201] A. Banerjee, P. Lampen-Kelley, J. Knolle, C. Balz, A. A. Aczel, B. Winn, Y. Liu, D. Pajerowski, J. Yan, C. A. Bridges, A. T. Savici, B. C. Chakoumakos, M. D. Lumsden, D. A. Tennant, R. Moessner, D. G. Mandrus, and S. E. Nagler, *Excitations in the field-induced quantum spin liquid state of α - $RuCl_3$* , npj Quantum Materials **3**, 8 (2018).

-
- [202] T. Yamada, T. Suzuki, and S.-i. Suga, *Ground-state properties of the $K - \Gamma$ model on a honeycomb lattice*, Phys. Rev. B **102**, 024415 (2020).
- [203] D. A. S. Kaib, S. M. Winter, and R. Valentí, *Kitaev honeycomb models in magnetic fields: Dynamical response and dual models*, Phys. Rev. B **100**, 144445 (2019).
- [204] K. Imamura, Y. Mizukami, O. Tanaka, R. Grasset, M. Konczykowski, N. Kurita, H. Tanaka, Y. Matsuda, M. G. Yamada, K. Hashimoto, and T. Shibauchi, *Defect-Induced Low-Energy Majorana Excitations in the Kitaev Magnet α - RuCl_3* , Phys. Rev. X **14**, 011045 (2024).
- [205] C. Hickey and S. Trebst, *Emergence of a field-driven $U(1)$ spin liquid in the Kitaev honeycomb model*, Nature Communications **10**, 530 (2019).
- [206] Z. Zhu, I. Kimchi, D. N. Sheng, and L. Fu, *Robust non-Abelian spin liquid and a possible intermediate phase in the antiferromagnetic Kitaev model with magnetic field*, Phys. Rev. B **97**, 241110 (2018).
- [207] C. Berke, S. Trebst, and C. Hickey, *Field stability of Majorana spin liquids in antiferromagnetic Kitaev models*, Phys. Rev. B **101**, 214442 (2020).
- [208] J. Nasu, Y. Kato, Y. Kamiya, and Y. Motome, *Successive Majorana topological transitions driven by a magnetic field in the Kitaev model*, Phys. Rev. B **98**, 060416 (2018).
- [209] S. Liang, M.-H. Jiang, W. Chen, J.-X. Li, and Q.-H. Wang, *Intermediate gapless phase and topological phase transition of the Kitaev model in a uniform magnetic field*, Phys. Rev. B **98**, 054433 (2018).
- [210] M. Gohlke, R. Moessner, and F. Pollmann, *Dynamical and topological properties of the Kitaev model in a $[111]$ magnetic field*, Phys. Rev. B **98**, 014418 (2018).
- [211] S.-S. Zhang, G. B. Halász, and C. D. Batista, *Theory of the Kitaev model in a $[111]$ magnetic field*, Nature Communications **13**, 399 (2022).
- [212] S. S. Jahromi, M. Hörmann, P. Adelhardt, S. Fey, H. Karamnejad, R. Orús, and K. P. Schmidt, *Kitaev honeycomb antiferromagnet in a field: quantum phase diagram for general spin*, Communications Physics **7**, 319 (2024).
- [213] Y.-H. Chen, J. Genzor, Y. B. Kim, and Y.-J. Kao, *Excitation spectrum of spin-1 Kitaev spin liquids*, Phys. Rev. B **105**, L060403 (2022).
- [214] H.-Y. Lee, N. Kawashima, and Y. B. Kim, *Tensor network wave function of $S = 1$ Kitaev spin liquids*, Phys. Rev. Res. **2**, 033318 (2020).
- [215] S. Das, D. Nafday, T. Saha-Dasgupta, and A. Paramakanti, *NiRh_2O_4 : A spin-orbit entangled diamond-lattice paramagnet*, Phys. Rev. B **100**, 140408 (2019).

- [216] A. Biffin, C. Rüegg, J. Embs, T. Guidi, D. Cheptiakov, A. Loidl, V. Tsurkan, and R. Coldea, *Magnetic Field Dependence of Excitations Near Spin-Orbital Quantum Criticality*, Phys. Rev. Lett. **118**, 067205 (2017).
- [217] D. Ish and L. Balents, *Theory of excitations and dielectric response at a spin-orbital quantum critical point*, Phys. Rev. B **92**, 094413 (2015).
- [218] A. Oosawa, M. Fujisawa, T. Osakabe, K. Kakurai, and H. Tanaka, *Neutron Diffraction Study of the Pressure-Induced Magnetic Ordering in the Spin Gap System $TlCuCl_3$* , Journal of the Physical Society of Japan **72**, 1026–1029 (2003).
- [219] T. Biesner, S. Biswas, W. Li, Y. Saito, A. Pustogow, M. Altmeyer, A. U. B. Wolter, B. Büchner, M. Roslova, T. Doert, S. M. Winter, R. Valentí, and M. Dressel, *Detuning the honeycomb of α - $RuCl_3$: Pressure-dependent optical studies reveal broken symmetry*, Phys. Rev. B **97**, 220401 (2018).
- [220] S. V. Streltsov and D. I. Khomskii, *Covalent bonds against magnetism in transition metal compounds*, Proceedings of the National Academy of Sciences **113**, 10491–10496 (2016).
- [221] G. Jackeli and D. I. Khomskii, *Classical Dimers and Dimerized Superstructure in an Orbitally Degenerate Honeycomb Antiferromagnet*, Phys. Rev. Lett. **100**, 147203 (2008).
- [222] J. Park, T.-Y. Tan, D. T. Adroja, A. Daoud-Aladine, S. Choi, D.-Y. Cho, S.-H. Lee, J. Kim, H. Sim, T. Morioka, H. Nojiri, V. V. Krishnamurthy, P. Manuel, M. R. Lees, S. V. Streltsov, D. I. Khomskii, and J.-G. Park, *Robust singlet dimers with fragile ordering in two-dimensional honeycomb lattice of Li_2RuO_3* , Scientific Reports **6**, 25238 (2016).
- [223] K. Mehawat and Y. Singh, *First-order magnetostructural transition in single crystals of the honeycomb lattice ruthenate Li_2RuO_3* , Phys. Rev. B **95**, 075105 (2017).
- [224] S. Yun, K. H. Lee, S. Y. Park, T.-Y. Tan, J. Park, S. Kang, D. I. Khomskii, Y. Jo, and J.-G. Park, *Magnetic and electrical anisotropy with correlation and orbital effects in dimerized honeycomb ruthenate Li_2RuO_3* , Phys. Rev. B **100**, 165119 (2019).
- [225] F. Bahrami, W. Lafargue-Dit-Hauret, O. I. Lebedev, R. Movshovich, H.-Y. Yang, D. Broido, X. Rocquefelte, and F. Tafti, *Thermodynamic Evidence of Proximity to a Kitaev Spin Liquid in $Ag_3LiIr_2O_6$* , Phys. Rev. Lett. **123**, 237203 (2019).
- [226] F. Bahrami, E. M. Kenney, C. Wang, A. Berlie, O. I. Lebedev, M. J. Graf, and F. Tafti, *Effect of structural disorder on the Kitaev magnet $Ag_3LiIr_2O_6$* , Phys. Rev. B **103**, 094427 (2021).
- [227] A. Chakraborty, V. Kumar, S. Bachhar, N. Büttgen, K. Yokoyama, P. K. Biswas, V. Siruguri, S. Pujari, I. Dasgupta, and A. V. Mahajan, *Unusual spin dynamics*

- in the low-temperature magnetically ordered state of $\text{Ag}_3\text{LiIr}_2\text{O}_6$* , Phys. Rev. B **104**, 115106 (2021).
- [228] K. Kitagawa, T. Takayama, Y. Matsumoto, A. Kato, R. Takano, Y. Kishimoto, S. Bette, R. Dinnebier, G. Jackeli, and H. Takagi, *A spin-orbital-entangled quantum liquid on a honeycomb lattice*, Nature **554**, 341–345 (2018).
- [229] K. Geirhos, P. Lunkenheimer, M. Blankenhorn, R. Claus, Y. Matsumoto, K. Kitagawa, T. Takayama, H. Takagi, I. Kézsmárki, and A. Loidl, *Quantum paraelectricity in the Kitaev quantum spin liquid candidates $\text{H}_3\text{LiIr}_2\text{O}_6$ and $\text{D}_3\text{LiIr}_2\text{O}_6$* , Phys. Rev. B **101**, 184410 (2020).
- [230] P. Laurell and S. Okamoto, *Dynamical and thermal magnetic properties of the Kitaev spin liquid candidate $\alpha\text{-RuCl}_3$* , npj Quantum Materials **5**, 2 (2020).
- [231] A. Singhanian, J. van den Brink, and S. Nishimoto, *Emergence of vortex state in the $S = 1$ Kitaev-Heisenberg model with single-ion anisotropy*, Phys. Rev. Res. **6**, 033146 (2024).
- [232] X. M. Zhang, R. M. Liu, Z. Jin, T. T. Liu, D. Y. Chen, Z. Fan, M. Zeng, X. B. Lu, X. S. Gao, M. H. Qin, and J.-M. Liu, *Phase transitions in the classical exchange-anisotropic Kitaev-Heisenberg model*, Phys. Rev. E **102**, 042132 (2020).
- [233] K. Nawa, K. Tanaka, N. Kurita, T. J. Sato, H. Sugiyama, H. Uekusa, S. Ohira-Kawamura, K. Nakajima, and H. Tanaka, *Triplon band splitting and topologically protected edge states in the dimerized antiferromagnet*, Nature Communications **10**, 2096 (2019).
- [234] O. Tanaka, Y. Mizukami, R. Harasawa, K. Hashimoto, K. Hwang, N. Kurita, H. Tanaka, S. Fujimoto, Y. Matsuda, E.-G. Moon, and T. Shibauchi, *Thermodynamic evidence for a field-angle-dependent Majorana gap in a Kitaev spin liquid*, Nature Physics **18**, 429–435 (2022).
- [235] B. H. Kim, *Field-angle anisotropy of proximate Kitaev systems under an in-plane magnetic field*, Phys. Rev. Res. **3**, 043032 (2021).
- [236] K. Hwang, A. Go, J. H. Seong, T. Shibauchi, and E.-G. Moon, *Identification of a Kitaev quantum spin liquid by magnetic field angle dependence*, Nature Communications **13**, 323 (2022).
- [237] X.-G. Wen, *Colloquium: Zoo of quantum-topological phases of matter*, Rev. Mod. Phys. **89**, 041004 (2017).
- [238] M. Z. Hasan and C. L. Kane, *Colloquium: Topological insulators*, Rev. Mod. Phys. **82**, 3045–3067 (2010).
- [239] K. v. Klitzing, G. Dorda, and M. Pepper, *New Method for High-Accuracy Determination of the Fine-Structure Constant Based on Quantized Hall Resistance*, Phys. Rev. Lett. **45**, 494–497 (1980).

- [240] B. A. Bernevig, *Topological Insulators and Topological Superconductors* (Princeton University Press, ISBN 9781400846733, Princeton, 2013).
- [241] M. V. Berry, *Quantal phase factors accompanying adiabatic changes*, Proceedings of the Royal Society of London. A. Mathematical and Physical Sciences **392**, 45–57 (1984).
- [242] Q. Niu and D. J. Thouless, *Quantised adiabatic charge transport in the presence of substrate disorder and many-body interaction*, Journal of Physics A: Mathematical and General **17**, 2453 (1984).
- [243] J. E. Avron and R. Seiler, *Quantization of the Hall Conductance for General, Multiparticle Schrödinger Hamiltonians*, Phys. Rev. Lett. **54**, 259–262 (1985).
- [244] D. C. Tsui, H. L. Stormer, and A. C. Gossard, *Two-Dimensional Magnetotransport in the Extreme Quantum Limit*, Phys. Rev. Lett. **48**, 1559–1562 (1982).
- [245] M. P. A. Fisher, P. B. Weichman, G. Grinstein, and D. S. Fisher, *Boson localization and the superfluid-insulator transition*, Phys. Rev. B **40**, 546–570 (1989).
- [246] P. S. Kumar, I. F. Herbut, and R. Ganesh, *Dirac Hamiltonians for bosonic spectra*, Phys. Rev. Res. **2**, 033035 (2020).
- [247] L.-M. Duan, E. Demler, and M. D. Lukin, *Controlling Spin Exchange Interactions of Ultracold Atoms in Optical Lattices*, Phys. Rev. Lett. **91**, 090402 (2003).
- [248] A. Micheli, G. K. Brennen, and P. Zoller, *A toolbox for lattice-spin models with polar molecules*, Nature Physics **2**, 341–347 (2006).
- [249] D. Peter, N. Y. Yao, N. Lang, S. D. Huber, M. D. Lukin, and H. P. Büchler, *Topological bands with a Chern number $C = 2$ by dipolar exchange interactions*, Phys. Rev. A **91**, 053617 (2015).
- [250] K. Fukui, Y. Kato, J. Nasu, and Y. Motome, *Feasibility of Kitaev quantum spin liquids in ultracold polar molecules*, Phys. Rev. B **106**, 014419 (2022).
- [251] T. Cookmeyer and S. Das Sarma, *Engineering the Kitaev Spin Liquid in a Quantum Dot System*, Phys. Rev. Lett. **132**, 186501 (2024).
- [252] P. d’Ornellas and J. Knolle, *Kitaev-Heisenberg model on the star lattice: From chiral Majorana fermions to chiral triplons*, Phys. Rev. B **109**, 094421 (2024).
- [253] F. D. M. Haldane, *Model for a Quantum Hall Effect without Landau Levels: Condensed-Matter Realization of the “Parity Anomaly”*, Phys. Rev. Lett. **61**, 2015–2018 (1988).
- [254] H. Wang, Y. Dai, G.-M. Chow, and J. Chen, *Topological hall transport: Materials, mechanisms and potential applications*, Progress in Materials Science **130**, 100971 (2022).

- [255] L. E. Chern and C. Castelnovo, *Topological phase diagrams of in-plane field polarized Kitaev magnets*, Phys. Rev. B **109**, L180407 (2024).
- [256] F. Cramer, G. E. Shephard, and P. J. Heron, *The misuse of colour in science communication*, Nature Communications **11**, 5444 (2020).
- [257] I. Kimchi and A. Vishwanath, *Kitaev-Heisenberg models for iridates on the triangular, hyperkagome, kagome, fcc, and pyrochlore lattices*, Phys. Rev. B **89**, 014414 (2014).
- [258] J. Chaloupka and G. Khaliullin, *Hidden symmetries of the extended Kitaev-Heisenberg model: Implications for the honeycomb-lattice iridates A_2IrO_3* , Phys. Rev. B **92**, 024413 (2015).
- [259] A. P. Igoshev, S. B. Popov, and R. Hollerbach, *Evolution of Neutron Star Magnetic Fields*, Universe **7**, 351 (2021).
- [260] S. V. Syzranov, M. L. Wall, V. Gurarie, and A. M. Rey, *Spin-orbital dynamics in a system of polar molecules*, Nature Communications **5**, 5391 (2014).
- [261] D. Peter, *Quantum states with topological properties via dipolar interactions*, Ph.D. thesis, Universität Stuttgart (2015), <http://dx.doi.org/10.18419/opus-5169>.
- [262] F. Aust, *Dirac Point and Topological Band Structures with Dipolar Exchange Interaction*, Bachelor thesis, Universität Stuttgart (2015).
- [263] F. Wang and Y. Ran, *Nearly flat band with Chern number $C = 2$ on the dice lattice*, Phys. Rev. B **84**, 241103 (2011).
- [264] S. Murakami and A. Okamoto, *Thermal Hall Effect of Magnons*, Journal of the Physical Society of Japan **86**, 011010 (2017).
- [265] X.-T. Zhang, Y. H. Gao, and G. Chen, *Thermal Hall effects in quantum magnets*, Physics Reports **1070**, 1–59 (2024).
- [266] H. Katsura, N. Nagaosa, and P. A. Lee, *Theory of the Thermal Hall Effect in Quantum Magnets*, Phys. Rev. Lett. **104**, 066403 (2010).
- [267] R. Matsumoto and S. Murakami, *Theoretical Prediction of a Rotating Magnon Wave Packet in Ferromagnets*, Phys. Rev. Lett. **106**, 197202 (2011).
- [268] R. Matsumoto and S. Murakami, *Berry phase and thermal transport coefficients in magnon systems*, Journal of Physics: Conference Series **302**, 012025 (2011).
- [269] S. A. Owerre, *A first theoretical realization of honeycomb topological magnon insulator*, Journal of Physics: Condensed Matter **28**, 386001 (2016).

- [270] S. A. Owerre, *Topological honeycomb magnon Hall effect: A calculation of thermal Hall conductivity of magnetic spin excitations*, Journal of Applied Physics **120**, 043903 (2016).
- [271] M. Banerjee, M. Heiblum, V. Umansky, D. E. Feldman, Y. Oreg, and A. Stern, *Observation of half-integer thermal Hall conductance*, Nature **559**, 205–210 (2018).
- [272] M. Akazawa, H.-Y. Lee, H. Takeda, Y. Fujima, Y. Tokunaga, T.-h. Arima, J. H. Han, and M. Yamashita, *Topological thermal Hall effect of magnons in magnetic skyrmion lattice*, Phys. Rev. Res. **4**, 043085 (2022).
- [273] A. Mook, J. Henk, and I. Mertig, *Magnon waveguide with nanoscale confinement constructed from topological magnon insulators*, Phys. Rev. B **91**, 174409 (2015).
- [274] R. Shindou, R. Matsumoto, S. Murakami, and J.-i. Ohe, *Topological chiral magnonic edge mode in a magnonic crystal*, Phys. Rev. B **87**, 174427 (2013).
- [275] D. Takikawa, M. G. Yamada, and S. Fujimoto, *Dissipationless spin current generation in a Kitaev chiral spin liquid*, Phys. Rev. B **105**, 115137 (2022).
- [276] A. Mook, J. Henk, and I. Mertig, *Magnon Hall effect and topology in kagome lattices: A theoretical investigation*, Phys. Rev. B **89**, 134409 (2014).
- [277] Y. Onose, T. Ideue, H. Katsura, Y. Shiomi, N. Nagaosa, and Y. Tokura, *Observation of the Magnon Hall Effect*, Science **329**, 297–299 (2010).
- [278] H. Zhang, X. Feng, T. Heitmann, A. I. Kolesnikov, M. B. Stone, Y.-M. Lu, and X. Ke, *Topological magnon bands in a room-temperature kagome magnet*, Phys. Rev. B **101**, 100405 (2020).
- [279] M. Braden, G. André, S. Nakatsuji, and Y. Maeno, *Crystal and magnetic structure of Ca_2RuO_4 : Magnetoelastic coupling and the metal-insulator transition*, Phys. Rev. B **58**, 847–861 (1998).
- [280] S. A. J. Kimber, C. D. Ling, D. J. P. Morris, A. Chemseddine, P. F. Henry, and D. N. Argyriou, *Interlayer tuning of electronic and magnetic properties in honeycomb ordered $\text{Ag}_3\text{LiRu}_2\text{O}_6$* , J. Mater. Chem. **20**, 8021–8025 (2010).
- [281] B. Ma, Z. D. Wang, and G. V. Chen, *Upper-branch thermal Hall effect in quantum paramagnets*, Phys. Rev. Res. **6**, 023044 (2024).
- [282] A. C. Y. Li, M. S. Alam, T. Iadecola, A. Jahin, J. Job, D. M. Kurkcuoğlu, R. Li, P. P. Orth, A. B. Özgüler, G. N. Perdue, and N. M. Tubman, *Benchmarking variational quantum eigensolvers for the square-octagon-lattice Kitaev model*, Phys. Rev. Res. **5**, 033071 (2023).
- [283] M. G. Yamada, *Topological \mathbb{Z}_2 invariant in Kitaev spin liquids: Classification of gapped spin liquids beyond projective symmetry group*, Phys. Rev. Res. **3**, L012001 (2021).

- [284] E. K.-H. Lee, R. Schaffer, S. Bhattacharjee, and Y. B. Kim, *Heisenberg-Kitaev model on the hyperhoneycomb lattice*, Phys. Rev. B **89**, 045117 (2014).
- [285] W. G. F. Krüger, M. Vojta, and L. Janssen, *Heisenberg-Kitaev models on hyperhoneycomb and stripy-honeycomb lattices: 3D-2D equivalence of ordered states and phase diagrams*, Phys. Rev. Res. **2**, 012021 (2020).
- [286] J. K. Asboth, L. Oroszlany, and A. Palyi, *A Short Course on Topological Insulators* (Springer International, ISBN 9783319256078, 2016).
- [287] A. P. Schnyder, S. Ryu, A. Furusaki, and A. W. W. Ludwig, *Classification of Topological Insulators and Superconductors*, AIP Conference Proceedings **1134**, 10–21 (2009).
- [288] M. Malki, L. Müller, and G. S. Uhrig, *Absence of localized edge modes in spite of a non-trivial Zak phase in BiCu₂PO₆*, Phys. Rev. Res. **1**, 033197 (2019).
- [289] Q. Wang and N. Hao, *Generalized Topology in Lattice Models without Chiral Symmetry*, arXiv e-prints , arXiv:2407.00795 (2024).
- [290] D. G. Joshi, *Topological excitations in the ferromagnetic Kitaev-Heisenberg model*, Phys. Rev. B **98**, 060405 (2018).
- [291] P. A. McClarty, X.-Y. Dong, M. Gohlke, J. G. Rau, F. Pollmann, R. Moessner, and K. Penc, *Topological magnons in Kitaev magnets at high fields*, Phys. Rev. B **98**, 060404 (2018).
- [292] N. Mohanta, R. Soni, S. Okamoto, and E. Dagotto, *Majorana corner states on the dice lattice*, Communications Physics **6**, 240 (2023).
- [293] E. J. Bergholtz and Z. Liu, *Topological Flat Band Models And Fractional Chern Insulators*, International Journal of Modern Physics B **27**, 1330017 (2013).

Acknowledgments

A work like this thesis is always not solely an effort of just one person. Many people have contributed to the success of this project - each in their own unique way. This section presents the futile attempt to account for all of this help.

First and foremost, I want to thank Prof. Dr. Maria Daghofer for supervising this thesis, many fruitful ideas and discussions, invaluable input as well as a lot of patience. Similarly, I am very grateful for Prof. Dr. Ronny Nawrodt and Prof. Dr. Sebastian Loth agreeing to their respective roles for the doctorate examination. To Maria and Sebastian, I would also like to apologize for the absurd amount of coffee consumption and likely resulting wear and tear of the shared FMQ coffee machine.

Naturally, my colleagues of the FMQ institute have been instrumental in the success of this thesis. In particular, I would like to acknowledge Pascal Strobel and Pavel Anisimov, both of which I cooperated with on parts of the project. Moreover, I would like to thank Alexander Sattler, Marco Schönleber and Benjamin Heinrich for proof-reading the thesis. Beyond that, I would like to thank Jan Lotze, Michael Schmid, Teresa Feldmaier, Jonas Heverhagen and all other workmates past and present for viable input and companionship. I look forward to the next alumni meeting.

Additionally, I am also extremely grateful for a lot of interactions with other work groups, namely the Sebastian Loth and Johannes Roth groups, which we share the FMQ label, a building floor and break room with, as well as the Philipp Hansmann group. Specifically, I would like to thank Lukas Arnhold for the shared misery during the writing process and Dominic Klein for a lot of conversations. Last but not least, I would like to express my appreciation to the people in the secretary's office, who are often the unsung heroes of keeping the entire operation running smoothly.

Acknowledgments

Concluding, I am deeply indebted to my family and friends. The former has provided an overwhelming amount of support on every step of the way. The latter, no matter if long-time friends, former fellow students, acquaintances from hobbies like handball or any combination thereof, are what keeps a person sane and happy.

**Schriftliche Erklärung gemäß §6 Absatz 3 der Promotionsordnung
von 2016 der Universität Stuttgart**

Hiermit erkläre ich, Friedemann Aust, geboren am 31.03.1993 in Stuttgart, dass die eingereichte Dissertation zum Thema **Exciton Bose-Einstein Condensation and Topology in Van Vleck-Type Mott Insulators** selbständig verfasst habe.

Ich versichere nach bestem Wissen und Gewissen alle Hilfsmittel sowie inhaltliche und wörtliche Nutzung von Bestandteilen anderen Quellen als solche angegeben und kenntlich gemacht zu haben.

Stuttgart, den 17. Oktober 2024

Friedemann Aust